

ON

OF MINERALS

APPLIED

LARGE SCALES

thesis for the purpose of
their own thesaurus for

RITY, PRESSURE

SCALING, LAWS

paper, micro, electronic, may

reproduction on paper or in

for the three years following

phic database, often needs to
help, through providing the

blication)

Date: 10/07/2002

idate's options regarding
the completed form to the
ton Campus.

Date: 10/7/02

MONASH UNIVERSITY
THESIS ACCEPTED IN SATISFACTION OF THE
REQUIREMENTS FOR THE DEGREE OF
DOCTOR OF PHILOSOPHY

ON..... 7 March 2003

for Sec. Research Graduate School Committee

Under the copyright Act 1968, this thesis must be used only under the normal conditions of scholarly fair dealing for the purposes of research, criticism or review. In particular no results or conclusions should be extracted from it, nor should it be copied or closely paraphrased in whole or in part without the written consent of the author. Proper written acknowledgement should be made for any assistance obtained from this thesis.

ERRATA

In response to comments made by the Examiners of this Thesis, a number of additions and alterations have been made to the text by the author. These are given below.

- (1) Additional paragraph to be inserted in Section 1.2 (page 6) as the 5th paragraph of this section:

"As can be seen in Figure 1.3, issues of physical size and operating temperature (or indeed pressure) are addressed separately in the empirical approach to fluidized bed scale-up. Ultimately, however, the goal is to increase the physical scale of the system from experimental reactor to full-scale production plant, maintaining the *same* pressure and temperature conditions. So whilst the effects of pressure and temperature on fluidization phenomena are very important, as far as the overall objective of process scale-up is concerned, it is the physical size of the unit which changes. Therefore, knowledge of the effect of altering size alone is of fundamental importance in successful large-scale fluidized bed design. And as will be seen, it is the effect of size that is the focus of the present work."

- (2) Additional paragraph to be inserted as the penultimate paragraph of Section 1.3 (page 8) as follows:

"The overall aim of this work is to determine whether, and to what extent, the simplified scaling laws for bubbling fluidized beds hold over a wide range of operating conditions and large change in operating scale. In order to satisfy this aim, a comprehensive range of physical experiments was carried out. Rather than limit the evaluation to one measurement technique alone, several independent experimental approaches were employed, which will be elaborated upon in subsequent chapters. In brief, the measurements and analyses performed were:

- Pressure fluctuations – Single-ended pressure probes were placed at geometrically similar locations in all scales of fluidized beds. Comparisons of average pressure, fluctuation amplitude, average cycle frequency,

probability density function and frequency spectrum were made for both correctly scaled and various mis-scaled scenarios.

- Voidage fluctuations – Electrical Capacitance Tomography measurements were made at geometrically similar locations in the two smallest fluidized beds. Comparisons of average voidage, voidage fluctuation amplitude, average cycle frequency, probability density function and frequency spectrum were made for both scaled and mis-scaled conditions; further investigations of the measurement system itself were performed using scaled artificial glass voids in packed beds at both scales.
- Solids motion – The motion of neutrally-buoyant geometrically scaled spheres was studied using video footage of the bed surface at the three largest scales. Based on the time between appearances of the spheres at the bed surface, a comparison of the distribution of circulation times was made for both scaled and mis-scaled conditions.
- Solids mixing – Using a novel application of the Electrical Capacitance Tomography technology, the solids downflow velocity was measured for tracer materials in the two smallest fluidized beds. The downflow velocity was compared for both scaled and mis-scaled conditions with correlations from the existing literature.

As can be seen from the layout summarised below, the results and discussion sections of this thesis have been organised in terms of measurement technique and presented in separate chapters. This structure, rather than the more conventional thesis format, was chosen due to the wide variety of experimental techniques employed."

- (3) To qualify the application of Equation 2.5 (page 11) the following comment to be added:

"Being derived from the simple two-phase theory, it should be noted that Equation 2.5 only holds for low gas velocities where a significant splash zone does not exist and H is the overall height of the dense bed. In general practical terms, the bed voidage is more often obtained from the pressure drop across a certain portion of the dense bed, viz:

$$\varepsilon = 1 - \frac{\Delta P}{\Delta H} \left(\frac{1}{\rho_p g} \right) \quad (2.5a)$$

where ΔP is the pressure drop measured across a certain height differential ΔH of the dense bed, ρ_p is the density of the particles and g is the acceleration due to gravity."

- (4) In Section 2.6 (page 37), the following comments should be appended to the end of the third paragraph:

"Horio (1997) pointed out that the original approach taken by Glicksman (1984) was seriously flawed by not considering the appropriate boundary conditions in his development of the scaling laws. Instead, Glicksman arbitrarily introduced the particle diameter as the reference scale. Furthermore, Horio rejected Glicksman's requirement that the particle Reynolds number (based on the superficial gas velocity) be kept less than 4 for the viscous-dominated regime, pointing out that the superficial gas velocity is not related to the criterion for particle size selection."

- (5) The first sentence of the second paragraph in Section 2.9.1 (page 50) should be replaced by the following:

"Following on from the initial study, Fitzgerald *et al.*, (1983) – also reported on in more detail in Fitzgerald *et al.*, (1984) – measured global pressure fluctuations in an atmospheric fluidized bed combustor and a one-quarter scale cold model (air-fluidized copper particles)."

- (6) In Section 2.9.2, the paragraph entitled "4. Limiting Particle Reynolds Number for the Simplified Scaling Parameters" (pages 61-62) should be replaced in its entirety with the following:

"In his original publication, Glicksman (1984) recommended that the viscous-dominated form of the simplified scaling laws be limited to low particle Reynolds number of 4 or less, and the inertial-dominated form to $Re_p > 400$. Glicksman's reasoning for this was so that either the viscous or inertial term in the Ergun equation could be neglected (in situations when drag was either predominantly inertial or predominantly viscous). The full set of scaling laws would be required in the intermediate region. Horio (1997) disputed the

limitation on particle Reynolds number for the viscous-dominated regime and pointed out that since the superficial gas velocity was not related to the criterion for particle size selection, Glicksman's proposed particle Reynolds number limitation was irrelevant. Certainly, in light of the experimental studies, this restriction on the simplified parameters was found to be conservative; Zhang and Yang (1987) proposing that for approximate similarity, the simplified scaling criteria could be applied in the intermediate region $4 < Re_p < 400$, and they verified this up to $Re_p = 78$ by experiment, (note that they inadvertently maintained the density ratio constant). In later work Glicksman *et al.* (1993a) modified Glicksman's previous requirements after determining the extent of the error when the simplified scaling parameters were used in the intermediate region. With the proviso that the solid to gas density ratio was matched in the scaled beds and the Ergun equation was valid for the drag coefficient, Glicksman suggested that the simplified scaling laws could be applied over a considerably wider range of conditions and bed sizes than the original viscous scaling law without appreciable error. They demonstrated this in accompanying verification experiments using a range of fluidization regimes, and used a model to suggest that a pressurized bubbling bed of 1 mm (or smaller) diameter particles operating at particle Reynolds numbers up to 1000 could be successfully modelled (less than 20% error in drag coefficient) with a ¼ scale model constructed using the simplified criteria. Thus, despite the differences of opinion, both the Glicksman *et al.* (1993a) relaxation of the Reynolds number requirement and the Horio (1997) argument that the limitation was invalid in the first place both lead us to the conclusion that for most practical purposes, a limiting particle Reynolds number does *not* apply.

(7) -To be read in conjunction with Sections 3.2.1 to 3.2.4 (pages 65 - 74):

For the purposes of comparison, plenum chamber volumes for the four experimental fluidized beds were as follows:

Bed Diameter (mm)	Plenum Volume (L)
146	2.3
300	29
600	110
1560	2700

- (8) In the first paragraph of Section 4.6.1 (page 121), the sentence "This is a good indicator of relative bed expansion." should be replaced by "The average pressure reflects the amount of solids between the probe position and the bed surface, which increases as the bed expands."
- (9) In Section 4.8, paragraph 6 (spanning pages 146 and 147) points out the significant differences anticipated in frequency spectra results for the mis-scaled scenarios. In support of this statement, the following Figure 4.26a should be added:

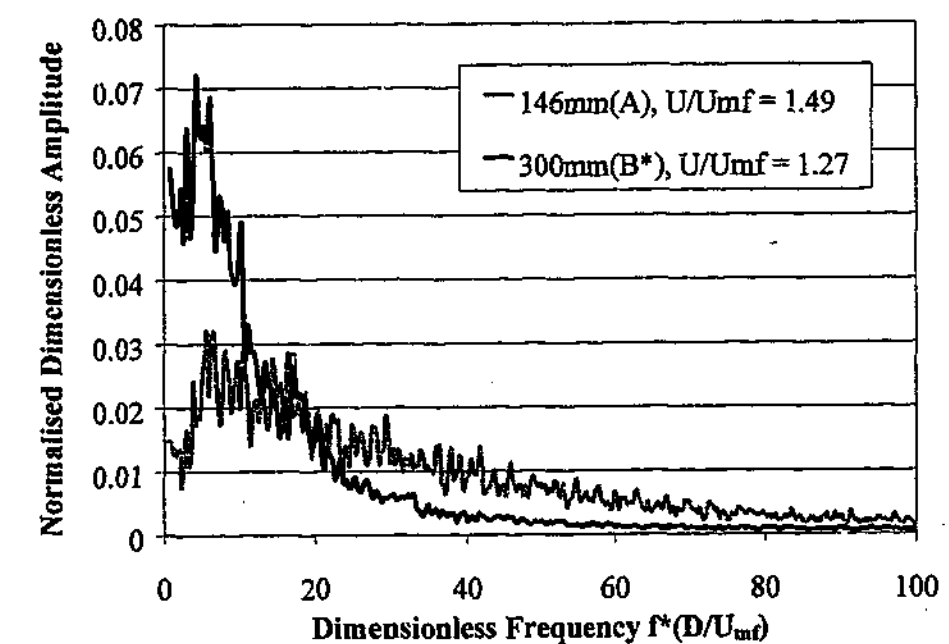


Figure 4.26a Comparison of the normalised ensemble-averaged amplitude spectra for the dimensionless pressure fluctuations from the 146 mm bed with material A and the 300 mm bed with mis-matched bed material B* at low gas velocity.

(10) In the References (pages 303 - 320), the following to be added:

Fitzgerald, T., Bushnell, D. B., Crane, S., and Shieh, Y. (1983) "Testing of cold scaled bed modelling for fluidized bed combustor" in Proceedings of the 7th International Conference on Fluidized Bed Combustion, DOE/METC, vol. 2, p766 - 780.

Horio (1997) "Hydrodynamics" In: "Circulating Fluidized Beds", Grace J.R., Avidan, A. A. and Knowlton, T. M. (Eds.) Blackie Academic and Professional, Great Britain.

(11) In order to clarify the significance of **Figure D.1** (page 353), the following explanation should be added, immediately prior to the figure:

"The reason that identical distributor pressure drop profiles are expected when the simplified scaling laws are applied is because the distributors are geometrically scaled. That is, the same number of orifices are located at the same dimensionless positions on the distributor plate assemblies, with the orifice diameters the same proportion of the overall bed diameter in each case. Thus each distributor will have the same fraction of open cross-sectional area, irrespective of size. Therefore, at the same gas flowrate, the pressure drop across the distributor plate will be the same in all cases, provided that the orifice discharge coefficients are the same (a reasonable assumption). Figure D.1 shows that in practice, the pressure drop profiles of all distributors are indeed well-matched with each other.

When beds are operated in accordance with the scaling laws, gas velocities are in fact scaled by \sqrt{m} , so for a bed double the diameter, the gas velocity is increased by a factor of $\sqrt{2}$. Because the pressure drop across an orifice is proportional to the *square* of the gas velocity, the distributor pressure drop in the larger bed will be exactly *double* that of its smaller counterpart. And due to the scaling of the length dimensions, the larger bed will also be double the bed depth (and thus have double the bed pressure drop when fluidized). Thus, the larger bed will actually have the same ratio of distributor-to-bed pressure drops as the smaller one when operated in accordance with the simplified scaling laws."

Experimental Verification of the Simplified Scaling Laws for Bubbling Fluidized Beds at Large Scales

by

Philip John Sanderson
Bachelor of Engineering (Honours)
University of Adelaide

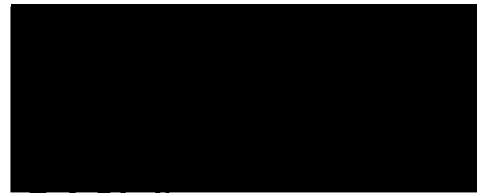
A thesis submitted in fulfillment of the
requirements for the degree of
Doctorate of Philosophy

Department of Chemical Engineering
Monash University

August, 2002

DECLARATION

To the best of my knowledge and belief this thesis contains no material that has been accepted for the award of any other degree or diploma in any University, and contains no material previously published or written by another person, except where due reference is given in the text.



P. J. Sanderson

Department of Chemical Engineering

Monash University

August, 2002

ACKNOWLEDGMENTS

There are many people to whom I am greatly indebted for their advice, assistance and support throughout the course of my candidature. First and foremost is my academic supervisor, Professor Martin Rhodes, whose guidance and support on both a professional and personal level has been absolutely outstanding and greatly appreciated. What's more, he is a Chuck Berry fan. Other researchers at Monash University Department of Chemical Engineering who have lent their valuable advice or technical assistance are Dr Ming Mao, Dr Shan Wang, and Dr Shintaro Takeuchi. I thank them for their input. The technical contributions of the excellent workshop staff, Paul Beardsley, Gerry Skipper, Ron Graham and in particular Peter Froud were an essential part of the extensive experimental program, and I thank them for a job well done. Likewise, the assistance and advice of the electronics technicians Roy Harrip and Gamini Ganegoda (Roy and H.G.) is greatly appreciated. The personal support and friendship of my fellow students deserves a special note; in particular those from the original Room 117 (Cafe Giovanni Magnifico) and Yum Cha club - Eric Hsieh, Nina Jiang, especially Mr Looi (for being a prankster), and Mr Chang (for unprecedented exposure to fine wine, food and music). More recently, Igor Sidorenko and Dr Belinda Mathers have provided friendship, advice and support. The various members of the Chemical Engineering Departmental "family" - Stelios, Judy, Paul, Yvonne, Chris and especially Irene - thank you for day-to-day assistance in ways too numerous to mention!

At CSIRO Division of Minerals my thanks go to Alfi Zakhari for his friendship and engineering assistance with the large fluidized bed cold models; thanks are also due to Terry Joyce, Ross Close, Peter Phillips and Robert White for technical support. The suggestions and advice of Dr Seng Lim and Dr Paul Peeler are also greatly appreciated.

Of course, such a project goes nowhere without financial support. The original Cooperative Research Centre for New Technologies for Power Generation from Low-Rank Coal and its successor, the Cooperative Research Centre for Clean Power from Lignite provided the project and the funding, as well as valuable opportunities for industry contact, training and conference attendance. The support of their management staff has been excellent and it has been a pleasure to be associated with them. In the CRC "family" I am especially grateful to David Brockway, Peter Jackson, Howard Mitchell, Lynn Hollamby, and Dawn Rankin for all manner of advice and assistance along the way.

Over time I have also had fruitful long-distance discussions with Dr Ravi Kumar from the National Chemical Laboratory in Pune, India and encouragement, advice and the odd bit of computer programming from my long-time friend and cohort Dr Richard van Wegen. In the broader context of extra-curricular fluidization activities, I must thank Robin Cooke of the Mutoid Waste Company for a great friendship and some highly successful collaborative fluidized bed artistry; and "Dr" Aaron Beaucaire for many great years of friendship, unusual jobs and, of course, fluidized bed TV opportunities.

Finally, I want to thank my family. Firstly my dad, Robin Sanderson, who was involved in fluidization research back when the Davidson bubble model was a new concept... For all your advice, suggestions, proof-reading, machine-shop work on bubble cap distributors and little wooden balls, and technical assistance in operating large-scale fluidized bed facilities at CSIRO - thanks heaps for your timely contributions. And to both my parents thankyou for giving me the freedom and the courage to do anything I set my mind to. Thankyou so much for all your support all this time. Finally to my partner Kirstie and daughter Emily... Emily, may you be all you can be, and have fun above all else. And Kirstie, thankyou for everything, your love and support and energy has kept me going through some tough times. You have been there for me when I needed it, you are my angel.

ABSTRACT

Due to the complexity of the hydrodynamic behaviour present in fluidized beds, issues of design and scale-up can be complicated. Although the economic benefits of an appropriate fluidized bed system can be large, developing a successful full-scale unit for a new process can be a risky business. Most of the fundamental work on fluidization and the development of engineering correlations has been carried out using laboratory equipment with a range of bed diameters up to about 0.6 metres. Commercial reactors, however, are usually of the order of several metres in diameter. As a consequence there is always a concern about the reliability of the design correlations at these scales.

One option for reducing design risk is to use scaling laws in the design of a small-scale unit. Scaling laws are common in many areas of science. The scaling laws for fluidized beds could provide a means of reducing the expense of scale-up by providing a greater degree of certainty in the behaviour of the final large-scale unit, based on experiments and data obtained from a correctly scaled small unit.

However, experimental verification of the scaling laws has produced mixed outcomes regarding the range of conditions over which the various forms of the laws would apply. Of particular concern is the number of so-called verification studies which did not include a deliberately mis-scaled control experiment and/or relied solely on one type of measurement for hydrodynamics characterisation. The lack of verification data at large scales and for non-ideal distributor geometries as well as are uncertainties regarding the importance of solid-to-gas density ratio also indicate that scaling law verification work is far from complete.

This investigation has considered hydrodynamic the so-called "simplified" similarity criteria for bubbling fluidization from an experimental standpoint, with emphasis on the abovementioned areas which have been overlooked in previous analyses.

In this work, where possible, experimental work was carried out in four bubbling beds from 146 mm in diameter to 1560 mm in diameter, representing the largest scale change over which experimental verification of the simplified scaling laws has been carried out thus far. Scaled bubble-cap distributors were used in all beds and a number of deliberate mis-match control experiments were performed. The work has employed a multiple-

measurement approach and the larger range of independent experimental results provides a broader basis from which to draw conclusions about the success or failure of the simplified similarity criteria than previous studies. Pressure fluctuations, voidage fluctuations, solids downflow velocities and the motion of large neutrally-bouyant spheres have been used at various (and in some cases all) bed scales.

Global pressure fluctuations (*ie* those originating from a single-ended in-bed probe) were found to be an adequate means of distinguishing between scaled and mis-scaled bubbling bed hydrodynamics. Electrical Capacitance Tomography, on the other hand, was found to be far less useful (even at the small scales) in fluidized bed diagnostics of the type required in this work. In its novel use as a detector for glass ballotini tracer in solids mixing experiments, the ECT system was moderately effective and this approach is worthy of further consideration. The use of the large neutrally-buoyant spherical tracers was found to be an adequate indicator of bed hydrodynamics and the motion of the tracers was found to follow the scaling laws.

For the majority of the operating conditions and the full range of bed sizes, the measurements made at the different scales indicated that hydrodynamic similarity had been achieved when the scaling laws were satisfied.

For a small scale change (from 146 mm to 300 mm bed diameters) involving particle Reynolds numbers from 1 to 12, the simplified criteria were successful in terms of the overall quantitative agreement of pressure fluctuations. Qualitative agreement was also observed in solids downflow velocities for the low velocity conditions investigated. In control experiments, deliberate particle size mis-matches resulted in a lack of similarity, but solid-to-gas density ratio appeared to be unimportant for the conditions investigated.

For the case of a large scale change (from 146 mm to 1560 mm diameter beds), agreement was found to be generally good for gas velocities in the range from 1.3 to 3.5 times the minimum fluidization velocity (particle Reynolds numbers from 1 to 13). Pressure fluctuations showed best agreement towards the radial centre and in the lower portions of the bed. At higher velocities, discrepancies in pressure fluctuation results were found in the behaviour of the largest bed when compared with the smaller three, but could not be discerned from the large spherical tracer particle results. The difference in pressure fluctuation results at high velocity appears to represent a deviation from similarity not accounted for by the simplified scaling criteria and should be considered as an area for future work.

TABLE OF CONTENTS

Table of Contents.....	i
List of Figures.....	vii
List of Tables.....	xxi

Chapter 1. Introduction

1.1 Fluidization of Solids.....	1
1.1.1 Particle Classification.....	1
1.1.2 Gas Fluidization Regimes.....	2
1.1.3 Applications of Fluidization.....	4
1.2 The Problem of Fluidized Bed Scale-up.....	5
1.3 Objective and Scope of Thesis.....	7

Chapter 2. Literature Review

2.1 Introduction.....	9
2.2 Bubbling Fluidized Bed Dynamics.....	9
2.2.1 Generally Observed Bubble Behaviour.....	9
2.2.2 Two-Phase Theory of Fluidization.....	10
2.2.3 The Davidson Bubble Model.....	12
2.2.4 Shape of Bubbles.....	13
2.2.5 Coalescence.....	15
2.2.6 Splitting.....	15
2.2.7 Rise Velocity.....	16
2.2.8 Bubble Size.....	17
2.2.9 Slugging.....	18
2.3 Solids Motion and Mixing in Bubbling Fluidized Beds.....	20
2.3.1 Variables Influencing the Rate of Solids Mixing.....	22
2.3.2 Estimating Solids Particle Velocity.....	24
2.3.3 Solids Circulation Flux.....	24
2.3.4 Bed Turnover Time.....	25
2.3.5 Solids Mixing Models.....	26
2.3.6 Motion of Neutrally-Buoyant Objects in Bubbling Fluidized Beds.....	29

2.4	The Need for Scaling Laws for Bubbling Fluidized Beds.....	30
2.5	Scaling Laws from Dimensional Similarity.....	31
2.5.1	Early Work on Dimensionless Groups.....	31
2.5.2	Development of the Scaling Law of Glicksman (1984).....	33
2.6	Model-Based Similarity Rule of Horio <i>et al.</i> , (1986a).....	37
2.6.1	Equivalence of the Scaling Rules of Glicksman and Horio.....	38
2.7	Scaling Parameters Based on Chaos Theory.....	40
2.7.1	Ordered, Stochastic and Chaotic Systems.....	40
2.7.2	The Chaotic Similarity Group.....	41
2.8	Overview of Measurement Techniques in Fluidized Beds.....	46
2.9	Experimental Verification of the Scaling Laws for Bubbling Beds.....	48
2.9.1	Review of Previous Experimental Verification Studies.....	50
2.9.2	Outcomes of Previous Studies.....	57
	1. Scaling Laws and the Geldart Classification.....	58
	2. Solid-to-Gas Density Ratio.....	59
	3. Sphericity and Particle Size Distribution.....	61
	4. Limiting Particle Reynolds Number for the Simplified Scaling Parameters.....	61
	5. Maximum Scale Change Possible.....	62
2.10	Conclusions.....	63

Chapter 3. Experimental Equipment

3.1	Introduction.....	65
3.2	Fluidized Bed Vessels and Operating Equipment.....	65
3.2.1	146 mm System.....	65
3.2.2	300 mm System.....	68
3.2.3	600 mm System.....	70
3.2.4	1560 mm System.....	72
3.3	Bed Materials.....	74
3.4	Operating Gas Velocities.....	78
3.5	Bubble Cap Distributor Design.....	78
3.5.1	Distributor Types Used in Previous Work.....	79
3.5.2	Bubble Cap Design.....	81
3.5.3	Distributor Pressure Drop Considerations.....	82
3.6	Pressure Probe Design and Instrumentation.....	87
3.6.1	Influence of Probe Internal Diameter and Length on Measurements.....	88

3.6.2	Influence of Probe External Diameter on Bed Behaviour.....	89
3.6.3	Chosen Probe Design.....	90
3.6.4	Tapping Points for Pressure Probes.....	93
3.6.5	Pressure Transducers and Data Acquisition.....	94
3.7	Electrical Capacitance Tomography.....	96
3.7.1	3.7.1 The UMIST PTL-300 System.....	97
3.7.2	Use of the ECT System.....	98
3.7.3	Hydrodynamic Similarity Investigations Using ECT.....	100
3.7.4	Solids Mixing Studies Using ECT.....	101
3.8	Setup for Monitoring Float Tracers.....	102
3.9	Conclusion.....	103

Chapter 4. Pressure Fluctuations

4.1	Introduction.....	104
4.2	Background – Pressure Fluctuations in Bubbling Fluidization.....	104
4.2.1	Sources of Pressure Fluctuations.....	105
4.2.2	Models for Pressure Oscillations in Gas-Fluidized Beds.....	106
4.2.3	Hydrodynamics Similarity Evaluations by Pressure Fluctuation Analysis.....	111
4.2.4	Experimental Criteria for Similarity Comparison.....	111
4.3	Preliminary Signal Testing.....	112
4.3.1	Background Electrical Noise.....	112
4.3.2	Bandwidth Check for Pressure Fluctuation Signals.....	114
4.4	Pressure Fluctuation Analysis Techniques.....	115
4.5	Approach for Pressure Fluctuation Experiments at Small Scales.....	118
4.5.1	Experimental Setup.....	118
4.5.2	Analysis and Comparison of the Pressure Fluctuations.....	119
4.6	Results of the Preliminary Experiments.....	120
4.6.1	Average Pressure Drop Comparison.....	121
4.6.2	Comparison of Average Absolute Deviation.....	125
4.6.3	Comparison of Average Cycle Frequency.....	126
4.7	Comparison of Single Number and Distribution Results.....	132
4.7.1	Comparison of Probability Density Functions.....	132
4.7.2	Comparison of Amplitude Spectra.....	137
4.8	Discussion of Small-Scale Pressure Fluctuation Results.....	145
4.9	Large-Scale Pressure Fluctuation Experiments.....	149
4.9.1	Initial Comparison of Bed Pressure Drops.....	150

4.9.2	Comparison of Pressure Probe Results.....	156
4.9.3	Pressure Fluctuations at Higher Gas Velocities.....	173
4.10	Discussion of Large-Scale Pressure Fluctuation Results.....	177
4.10.1	Spatial Variation in Hydrodynamics Similarity.....	177
4.10.2	Changes in Bed Behaviour with Changing Gas Velocity.....	180
4.11	Conclusions	184

Chapter 5. Voidage Fluctuations

5.1	Introduction.....	186
5.2	Background – Capacitance Measurements in Fluidized Beds.....	186
5.3	Introduction to Electrical Capacitance Tomography.....	189
5.4	Experimental Usage of ECT.....	191
5.5	Limitations of the ECT System Used in This Work.....	195
5.6	The Approach for the Similarity Experiments Using ECT.....	196
5.6.1	Calibration of the ECT Sensors.....	198
5.6.2	Baseline Drift.....	199
5.6.3	Experimental Setup.....	204
5.6.4	Analysis and Comparison of Voidage Fluctuations.....	206
5.7	Results of the Voidage Fluctuation Similarity Experiments.....	206
5.7.1	Comparison of Time-Averaged Average Solids Volume Fraction.....	214
5.7.2	Average Absolute Deviation of Cross-Sectionally Averaged Solids Volume Fraction.....	217
5.7.3	Dimensionless Average Cycle Frequency of Cross-Sectionally Averaged Solids Volume Fraction.....	219
5.7.4	Comparison of Probability Density Functions.....	222
5.7.5	Comparison of Amplitude Spectra.....	224
5.8	ECT Sensitivity Differences.....	226
5.9	Discussion.....	231
5.10	Conclusions.....	235

Chapter 6. Solids Mixing

6.1	Introduction.....	237
6.2	Previous Experimental Approaches to Solids Mixing.....	238
6.2.1	Motion of Large Neutrally-Buoyant Objects in Bubbling Beds.....	240
6.2.2	The Effect of Scale on Solids Mixing.....	241

6.2.3	Previous Solids Mixing Investigations of the Similarity Rule.....	245
6.3	Electrical Capacitance Tomography Study of Axial Solids Mixing.....	246
6.3.1	Development of Technique.....	247
6.3.2	Preliminary Study – Effect of Tracer Particle Size.....	257
6.3.3	Solids Mixing Comparisons Between 146 mm and 300 mm Scales.....	267
6.4	Float Tracer Study of Solids Motion.....	274
6.4.1	Basis for Comparison.....	274
6.4.2	Float Tracer Logging Procedure.....	275
6.4.3	Float Tracer Manufacture.....	277
6.4.4	Preliminary Experiment – Effect of Tracer Density.....	278
6.4.5	Comparison of Float Tracer Results at 300 mm, 600 mm and 1560 mm Scales.....	281
6.5	Conclusions from Solids Mixing Experiments.....	290

Chapter 7. Conclusions and Recommendations

7.1	Overview.....	292
7.2	Work Summary.....	293
7.3	Conclusions.....	294
7.3.1	Measurement Techniques.....	294
7.3.2	Verification of the Simplified Similarity Criteria for Bubbling Fluidization....	296
7.4	Recommendations and Future Work.....	297

Nomenclature.....	299
--------------------------	------------

References.....	303
------------------------	------------

Appendix A. Literature Data.....	321
---	------------

Appendix B. Flow Measurements.....	324
---	------------

B.1	Introduction – Sources of Error.....	324
B.2	Flowmeter Calibration Charts and Error Estimates.....	325
B.2.1	146 mm System.....	325
B.2.2	300 mm System.....	328
B.3	Orifice Plate Flow Measurements.....	331
B.3.1	Orifice Plate Sample Calculation.....	331

B.3.2	Estimated Errors in Flow From Orifice Plate Measurements.....	333
B.4	Assumed Transport Properties for Other Calculations.....	335
Appendix C. Particle Characteristics.....		337
C.1	Particle Size Analysis Results.....	337
C.2	Minimum Fluidization Velocity Results.....	345
Appendix D. Distributor Characteristics.....		353
Appendix E. Pressure Transducer Calibration Data.....		355
Appendix F. Pressure Fluctuation Results.....		361
Appendix G. Solids Mixing Results.....		389

LIST OF FIGURES

- Figure 1.1 Schematic representation of gas fluidization regimes
- Figure 1.2 General flow regime diagram for gas-solids contacting (after Grace, 1986)
- Figure 1.3 Graphical representation of the typical approach to process scale-up
- Figure 2.1 Schematic representation of the idealised bubble showing bubble and wake volume
- Figure 2.2 2-dimensional representation of the bubble coalescence model of Darton *et al.*, (1977)
- Figure 2.3 Modes of slugging observed in fluidized beds
- Figure 2.4 Wake and drift fractions of an idealised bubble (after Baeyens and Geldart, 1986)
- Figure 2.5 Solids circulation patterns in various aspect ratio bubbling fluidized beds (after Kunii and Levenspiel, 1991)
- Figure 2.6 The counter-current backmixing model of solids motion in bubbling beds (after Kunii and Levenspiel, 1991)
- Figure 3.1 Flow diagram for the 146 mm fluidized bed
- Figure 3.2 Flow diagram for the 300 mm fluidized bed
- Figure 3.3 Flow diagram for the 600 mm fluidized bed
- Figure 3.4 Flow diagram for the 1560 mm fluidized bed
- Figure 3.5 Cross-sectional view of bubble cap design used in all beds
- Figure 3.6 Bubble cap layout on distributor plate for each bed
- Figure 3.7 Details of pressure probes used in 146 mm, 300 mm and 600 mm beds for in-bed measurements

- Figure 3.8 Modification to pressure probe to allow measurements to be taken flush with the vessel wall
- Figure 3.9 Pressure probe arrangement for use in the 1560 mm bed
- Figure 3.10 Cross-section of the sealed support collar design used on the 1560 mm bed for mounting pressure probes
- Figure 3.11 Axial location of pressure probes in all beds
- Figure 3.12 General layout of the Electrical Capacitance Tomography system
- Figure 3.13 Electrode layout for Electrical Capacitance Tomography measurements at the 146 mm and 300 mm scales
- Figure 3.14 Experimental arrangement for dynamic voidage measurements using Electrical Capacitance Tomography
- Figure 3.15 Bed arrangement for solids mixing experiments carried out using Electrical Capacitance Tomography
- Figure 3.16 General arrangement for solids motion experiments using neutrally-buoyant tracers conducted in the 300 mm, 600 mm and 1560 mm beds
- Figure 4.1 Preliminary amplitude spectra results for pressure signals from the four scales of fluidized beds
- Figure 4.2 Dimensionless average pressure comparison for the 146 mm and 300 mm beds at 2:1 aspect ratio with materials A and B
- Figure 4.3 Dimensionless average pressure comparison for the 146 mm and 300 mm beds at 2:1 aspect ratio with materials A, A*, B and B*
- Figure 4.4 Dimensionless average pressure comparison for the 146 mm and 300 mm beds at 2:1 aspect ratio with materials A*, G and B*
- Figure 4.5 Comparison of the average absolute deviation of dimensionless pressure for the 146 mm and 300 mm beds at 2:1 aspect ratio with materials A, A*, G, B and B*
- Figure 4.6 Comparison of the pressure fluctuation average cycle frequency for the 146 mm and 300 mm beds with materials A and B

- Figure 4.7 Comparison of the pressure fluctuation re-scaled average cycle frequencies for the 146 mm and 300 mm beds with materials A and B
- Figure 4.8 Comparison of the pressure fluctuation average cycle frequency for the 146 mm and 300 mm beds with materials A, A*, B and B*
- Figure 4.9 Comparison of the pressure fluctuation re-scaled average cycle frequency for the 146 mm and 300 mm beds with materials A, A*, B and B*
- Figure 4.10 Comparison of the pressure fluctuation re-scaled average cycle frequency for the 146 mm and 300 mm beds with materials A*, G and B*
- Figure 4.11 Comparison of the pressure fluctuation dimensionless average cycle frequencies for the 146 mm and 300 mm beds with materials A, A*, G, B and B*
- Figure 4.12 Example of how the average and average absolute deviation relate to the overall probability density function for pressure fluctuation results
- Figure 4.13 Comparison of the normalised probability distribution for dimensionless pressure fluctuations from the 146 mm bed with material A and the correctly-scaled 300 mm bed with material B at low gas velocity
- Figure 4.14 Comparison of the normalised probability distribution for dimensionless pressure fluctuations from the 146 mm bed with material A and the correctly-scaled 300 mm bed with material B at intermediate gas velocity
- Figure 4.15 Comparison of the normalised probability distribution for dimensionless pressure fluctuations from the 146 mm bed with material A and the correctly-scaled 300 mm bed with material B at high gas velocity
- Figure 4.16 Comparison of the normalised probability distribution for dimensionless pressure fluctuations from the 146 mm bed with material A*; the 146 mm bed with material G (density mis-match); and the correctly-scaled 300 mm bed with material B* at low gas velocity

- Figure 4.17 Comparison of the normalised probability distribution for dimensionless pressure fluctuations from the 146 mm bed with material A*; the 146 mm bed with material G (density mis-match); and the correctly-scaled 300 mm bed with material B* at intermediate gas velocity
- Figure 4.18 Comparison of the normalised probability distribution for dimensionless pressure fluctuations from the 146 mm bed with material A*; the 146 mm bed with material G (density mis-match); and the correctly-scaled 300 mm bed with material B* at high gas velocity
- Figure 4.19 Comparison of one-sided spectral estimate (employing the Hanning window) from a sample pressure fluctuation time-series using different ensemble-averaging approaches
- Figure 4.20 Comparison of the peak frequency and the average cycle frequency from an example time-series taken from the 146 mm bed with material A, at $U/U_{mf} = 8.37$
- Figure 4.21 Comparison of the normalised ensemble-averaged amplitude spectra for the dimensionless pressure fluctuations from the 146 mm bed with material A and the correctly-scaled 300 mm bed with material B at low gas velocity
- Figure 4.22 Comparison of the normalised ensemble-averaged amplitude spectra for the dimensionless pressure fluctuations from the 146 mm bed with material A and the correctly-scaled 300 mm bed with material B at medium gas velocity
- Figure 4.23 Comparison of the normalised ensemble-averaged amplitude spectra for the dimensionless pressure fluctuations from the 146 mm bed with material A and the correctly-scaled 300 mm bed with material B at high gas velocity
- Figure 4.24 Comparison of the normalised ensemble-averaged amplitude spectra for the dimensionless pressure fluctuations from the 146 mm bed with material A* and material G (mis-matched density) and the correctly-scaled 300 mm bed with material B* at low gas velocity
- Figure 4.25 Comparison of the normalised ensemble-averaged amplitude spectra for the dimensionless pressure fluctuations from the 146 mm bed with

material A* and material G (mis-matched density) and the correctly-scaled 300 mm bed with material B* at intermediate gas velocity

- Figure 4.26 Comparison of the normalised ensemble-averaged amplitude spectra for the dimensionless pressure fluctuations from the 146 mm bed with material A* and material G (mis-matched density) and the correctly-scaled 300 mm bed with material B* at high gas velocity
- Figure 4.27 Comparison of the dimensionless average pressure measured from pressure probes located at $h/H_s=0.46$ and $r/R=0$ in all four scaled fluidized beds for a range of dimensionless gas velocities
- Figure 4.28 Dimensionless average pressure drop comparison for the four correctly scaled beds after adjusting results to account for errors in bed height and bulk density
- Figure 4.29 Average pressure measurements from the windbox of the 1560 mm bed when fluidized at low gas velocity and distributor pressure drop measurements (empty vessel) for a similar velocity range are used to estimate the pressure drop due to the presence of the bed alone
- Figure 4.30 Comparison of the subsequent dimensionless average pressure measured from pressure probes located at $h/H_s=0.46$ and $r/R=0$ in all four scaled fluidized beds for a range of dimensionless gas velocities -bed inventories scaled by mass
- Figure 4.31 Comparison of the dimensionless average pressure measured from pressure probes located at $h/H_s=0.46$ and $r/R=0.5$ in all five fluidized beds for a range of dimensionless gas velocities. All beds, with the exception of the 600mm bed with material D, have been scaled using the simplified scaling criteria
- Figure 4.32 Comparison of the dimensionless average absolute deviation of pressure measured from pressure probes located at $h/H_s=0.77$ and $r/R=0$ in all five fluidized beds for a range of dimensionless gas velocities. All beds, with the exception of the 600mm bed with material D, have been scaled using the simplified scaling criteria
- Figure 4.33 Comparison of the dimensionless average absolute deviation of pressure measured from pressure probes located at $h/H_s=0.77$ and $r/R=1$ in all

five fluidized beds for a range of dimensionless gas velocities. All beds, with the exception of the 600mm bed with material D, have been scaled using the simplified scaling criteria

- Figure 4.34 Comparison of the dimensionless average cycle frequency of pressure measured from pressure probes located at $h/H_s=0.46$ and $r/R=0$ in all five fluidized beds for a range of dimensionless gas velocities. All beds, with the exception of the 600mm bed with material D, have been scaled using the simplified scaling criteria
- Figure 4.35 Agreement map showing qualitatively how well the pressure fluctuations from the various probe locations and superficial gas velocities from 1.25 to $3.5 \cdot U_{mf}$ match for the scaled fluidized beds
- Figure 4.36 Comparison of the normalised probability distributions for the four correctly scaled beds (146 mm, material A; 300 mm, material B; 600 mm, material C; and 1560 mm, material D) at low gas velocity for the probe located at $r/R = 0$ and $h/H = 0.2$
- Figure 4.37 Comparison of the normalised probability distributions for the correctly scaled beds (300 mm, material B; and 1560 mm, material D) with the mis-matched bed (600 mm, material D) at low gas velocity for the probe located at $r/R = 0$ and $h/H = 0.2$
- Figure 4.38 Comparison of the normalised probability distributions for the correctly scaled beds (146 mm, material A; 300 mm, material B; 600 mm, material C, and 1560 mm, material D) at low gas velocity for the probe located at $r/R = 0$ and $h/H = 0.77$
- Figure 4.39 Comparison of the normalised probability distributions for the correctly scaled beds (300 mm, material B and 1560 mm, material D) with the mis-scaled bed (600 mm, material D) at low gas velocity for the probe located at $r/R = 0$ and $h/H = 0.77$
- Figure 4.40 Comparison of the normalised probability distributions for the correctly scaled beds (146 mm, material A; 300 mm, material B and 1560 mm, material D) at high gas velocity for the probe located at $r/R = 0$ and $h/H = 0.77$

- Figure 4.41 Comparison of the dimensionless amplitude spectra from the correctly-scaled 146 mm and 300 mm beds at low gas velocity, with probe located at $r/R = 0$ and $h/H = 0.2$
- Figure 4.42 Comparison of the dimensionless amplitude spectra from the correctly-scaled 146 mm and 600 mm beds at low gas velocity, with probe located at $r/R = 0$ and $h/H = 0.2$
- Figure 4.43 Comparison of the dimensionless amplitude spectra from the correctly-scaled 146 mm and 1560 mm beds at low gas velocity, with probe located at $r/R = 0$ and $h/H = 0.2$
- Figure 4.44 Comparison of the dimensionless amplitude spectra from the correctly-scaled 146 mm and the mis-scaled 600 mm bed at low gas velocity, with probe located at $r/R = 0$ and $h/H = 0.2$
- Figure 4.45 Comparison of the dimensionless amplitude spectra from the correctly-scaled 146 mm and 300 mm beds at low gas velocity, with probe located at $r/R = 0$ and $h/H = 0.77$
- Figure 4.46 Comparison of the dimensionless amplitude spectra from the correctly-scaled 146 mm and 600 mm beds at low gas velocity, with probe located at $r/R = 0$ and $h/H = 0.77$
- Figure 4.47 Comparison of the dimensionless amplitude spectra from the correctly-scaled 146 mm and 1560 mm beds at low gas velocity, with probe located at $r/R = 0$ and $h/H = 0.77$
- Figure 4.48 Comparison of the dimensionless amplitude spectra from the correctly-scaled 146 mm and the mis-scaled 600 mm bed at low gas velocity, with probe located at $r/R = 0$ and $h/H = 0.77$
- Figure 4.49 Comparison of the dimensionless amplitude spectra from the correctly-scaled 146 mm and 300 mm beds at high gas velocity, with probe located at $r/R = 0$ and $h/H = 0.77$
- Figure 4.50 Comparison of the dimensionless amplitude spectra from the correctly-scaled 146 mm and 1560 mm beds at high gas velocity, with probe located at $r/R = 0$ and $h/H = 0.77$

- Figure 4.51 Comparison of the dimensionless average pressure measured for the correctly-scaled 146 mm (material A), 300 mm (material B), 600 mm (material C) and mis-scaled 600 mm (material D) beds for higher superficial gas velocities. Pressure probe is positioned at $r/R = 0.5$ and $h/H = 0.2$
- Figure 4.52 Comparison of the dimensionless average absolute deviation of pressure measured for the correctly-scaled 146 mm (material A), 300 mm (material B), 600 mm (material C) and mis-scaled 600 mm (material D) beds for higher superficial gas velocities. Pressure probe is positioned at $r/R = 0$ and $h/H = 0.46$
- Figure 4.53 Comparison of the dimensionless average cycle frequency of pressure fluctuations measured for the correctly-scaled 146 mm (material A), 300 mm (material B), 600 mm (material C) and mis-scaled 600 mm (material D) beds for higher superficial gas velocities. Pressure probe is positioned at $r/R = 1$ and $h/H = 0.46$
- Figure 4.54 Data of Figure 4.53 re-plotted with results for the 600 mm bed adjusted by non-dimensionalising the frequency with the "ideal" scaled minimum fluidization velocity of $U_{mf} = 0.082$ m/s instead of the actual $U_{mf} = 0.07$ m/s of the bed material
- Figure 4.55 Dimensionless bubble size predictions from the Darton *et al.* (1977) correlation for the four scaled and one mis-scaled beds over the range of gas velocities considered experimentally. Bubble sizes are predicted for the axial location of the upper pressure probe, ie $h/H = 0.77$
- Figure 5.1 Example of an ECT image of a bubbling fluidized bed
- Figure 5.2 The procedure used to generate the voidage fluctuation time series from capacitance measurements
- Figure 5.3 ECT baseline drift for a gently fluidized bed silica sand after improper calibration (fluidization time during calibration procedure too short)
- Figure 5.4 Stable ECT baseline for gently fluidized silica sand after calibration (fluidization time of 15 minutes during calibration procedure)

- Figure 5.5 ECT baseline for garnet sand after improper calibration (fluidization time during calibration procedure too short)
- Figure 5.6 ECT baseline for glass beads after calibration (with short fluidization time during calibration procedure)
- Figure 5.7 ECT baseline for a gently fluidized bed of silica sand after correct calibration in the 300 mm bed
- Figure 5.8 Long-term calibration drift for a packed bed of silica sand in the 146 mm bed after correct calibration
- Figure 5.9 Series of reconstructed images (using standard linear back-projection algorithm) from the 146 mm bed with material A operated at $U/U_{mf} = 1.49$
- Figure 5.10 Series of reconstructed images (using standard linear back-projection algorithm) from the 300 mm bed with material B operated at $U/U_{mf} = 1.58$
- Figure 5.11 Series of reconstructed images (using standard linear back-projection algorithm) from the 146 mm bed with material A operated at $U/U_{mf} = 8.37$
- Figure 5.12 Series of reconstructed images (using standard linear back-projection algorithm) from the 300 mm bed with material B operated at $U/U_{mf} = 8.47$
- Figure 5.13 Series of reconstructed images (using standard linear back-projection algorithm) from the 300 mm bed with material A* operated at $U/U_{mf} = 1.41$
- Figure 5.14 Series of reconstructed images (using standard linear back-projection algorithm) from the 300 mm bed with material B* operated at $U/U_{mf} = 1.51$
- Figure 5.15 Series of reconstructed images (using standard linear back-projection algorithm) from the 300 mm bed with material A* operated at $U/U_{mf} = 3.84$

- Figure 5.16 Series of reconstructed images (using standard linear back-projection algorithm) from the 300 mm bed with material B* operated at $U/U_{mf} = 3.93$
- Figure 5.17 Series of reconstructed images (using standard linear back-projection algorithm) from the 300 mm bed with material G operated at $U/U_{mf} = 1.46$
- Figure 5.18 Series of reconstructed images (using standard linear back-projection algorithm) from the 300 mm bed with material G operated at $U/U_{mf} = 3.98$
- Figure 5.19 Typical average solids volume fraction time-series generated from reconstructed ECT image data
- Figure 5.20 ECT overall average solids volume fraction for the correctly-scaled 146 mm (material A) and 300 mm (material B) beds for a range of dimensionless superficial gas velocities
- Figure 5.21 ECT overall average solids volume fraction for the correctly-scaled 146 mm (material A*) and 300 mm (material B*) beds for a range of dimensionless superficial gas velocities
- Figure 5.22 ECT overall average solids volume fraction. Comparison between the original correctly scaled beds (materials A and B in the 146mm and 300 mm beds) with the second set of correctly scaled materials in the same scale beds (materials A* and B* in the 146 mm and 300 mm beds)
- Figure 5.23 ECT overall average solids volume fraction for the correctly-scaled 146 mm (material A*) and 300 mm (material B*) beds compared with the correctly-scaled but higher density material G in the 146 mm bed
- Figure 5.24 Comparison of the average absolute deviation of overall solids volume fraction fluctuations for the 146 mm (materials A, A* and G) and 300 mm beds (materials B and B*)
- Figure 5.25 Comparison of the dimensionless average cycle frequency of the ECT average solids volume fraction fluctuations for the correctly-scaled 146

mm (material A) and 300 mm (material B) beds for a range of dimensionless superficial gas velocities

Figure 5.26 Comparison of the dimensionless average cycle frequency of the ECT average solids volume fraction fluctuations for the correctly-scaled 146 mm (material A* and higher-density material G) and 300 mm (material B*) beds for a range of dimensionless superficial gas velocities

Figure 5.27 Comparison of the re-scaled average cycle frequency of the ECT average solids volume fraction fluctuations for all beds. (Bed materials A, A* and G in the 146 mm bed and material B* in the 300 mm bed for a range of dimensionless superficial gas velocities)

Figure 5.28 Comparison of the normalised probability density function for the correctly-scaled 146 mm bed and 300 mm bed with materials A and B respectively, operated at the intermediate gas velocity of $U/U_{mf} \approx 5$

Figure 5.29 Comparison of the normalised probability density function for the correctly-scaled 146 mm bed with material A*, and the 300 mm bed with material B*, with additional data for the correctly-scaled 146 mm bed with higher-density material G. The beds were operated at the intermediate gas velocity of $U/U_{mf} \approx 2.5$

Figure 5.30 Comparison of the normalised dimensionless amplitude spectra for the correctly-scaled 146 mm bed with material A and the correctly-scaled 300 mm bed with material B, operated at the intermediate gas velocity of $U/U_{mf} \approx 5$

Figure 5.31 Comparison of the normalised dimensionless amplitude spectra for the correctly-scaled 146 mm bed with material A and the correctly-scaled 300 mm bed with material B, plus the correctly-scaled 146 mm bed with higher-density material G, operated at the intermediate gas velocity of $U/U_{mf} \approx 2.5$

Figure 5.32 Arrangement for testing ECT sensitivity to phantom voids placed at various radial locations in the 300 mm bed

Figure 6.1 Typical transient tracer response for the addition of ballotini tracer (at $t = 100$ s) to a 146 mm diameter bubbling bed of sand, measured with the ECT system

- Figure 6.2 Tracer response profiles for five consecutive runs with a 5 second moving average applied to the data
- Figure 6.3 Tracer response profiles for five consecutive runs after the initial concentration off-set has been removed
- Figure 6.4 Average transient tracer concentration response profile for the original five runs
- Figure 6.5 Transient trace response profile for tracer with $U_{mf}(\text{tracer}) > U > U_{mf}(\text{bed})$
- Figure 6.6 Transient trace response profile for tracer with $U > U_{mf}(\text{tracer}) > U_{mf}(\text{bed})$
- Figure 6.7 Transient trace response profile for tracer with $U > U_{mf}(\text{tracer}) \approx U_{mf}(\text{bed})$
- Figure 6.8 Transient trace response profile for tracer with $U \gg U_{mf}(\text{tracer}) \approx U_{mf}(\text{bed})$
- Figure 6.9 Transient trace response profile for tracer with $U \gg U_{mf}(\text{bed}) > U_{mf}(\text{tracer})$
- Figure 6.10 Average tracer response profile for the 146 mm bed, (Pair 1), with $U/U_{mfBM} = 1.44$ and $U_{mfT}/U_{mfBM} = 1.23$. The system was scaled using the simplified criteria to match the 300 mm bed, results of which are shown in Figure 6.11
- Figure 6.11 Average tracer response profile for the 300 mm bed, (Pair 1), with $U/U_{mfBM} = 1.45$ and $U_{mfT}/U_{mfBM} = 1.36$. The system was scaled using the simplified criteria to match the 146 mm bed with results presented in Figure 6.10
- Figure 6.12 Average tracer response profile for the 146 mm bed, (Pair 2), with $U/U_{mfBM} = 1.43$ and $U_{mfT}/U_{mfBM} = 1.04$. The system was scaled using the simplified criteria to match the 300 mm bed, results of which are shown in Figure 6.13
- Figure 6.13 Average tracer response profile for the 300 mm bed, (Pair 2), with $U/U_{mfBM} = 1.43$ and $U_{mfT}/U_{mfBM} = 1.13$. The system was scaled using

the simplified criteria to match the 146 mm bed with results presented in Figure 6.12

- Figure 6.14 Average tracer response profile for the 146 mm bed, (Pair 3), with $U/U_{mfBM} = 1.44$ and $U_{mfT}/U_{mfBM} = 1.00$. The system was scaled using the simplified criteria to match the 300 mm bed, results of which are shown in Figure 6.15
- Figure 6.15 Average tracer response profile for the 300 mm bed, (Pair 3), with $U/U_{mfBM} = 1.44$ and $U_{mfT}/U_{mfBM} = 0.68$. The system was scaled using the simplified criteria to match the 146 mm bed with results presented in Figure 6.14, however, there was a significant discrepancy in tracer particle size
- Figure 6.16 Illustration of the technique used to record float tracer location
- Figure 6.17 Conceptual example of the method for approximating the time spent below the bed surface from the tracer appearance log file
- Figure 6.18 Schematic of float tracer particles used in similarity experiments
- Figure 6.19 Distribution of circulation times for float tracers of the same size but different density in the 1560 mm bed fluidized at $U/U_{mf} = 2.7$
- Figure 6.20 Comparison of the dimensionless circulation time distribution for geometrically scaled float tracers in scaled fluidized beds at $U/U_{mf} \approx 2.75$
- Figure 6.21 Tracer circulation time distributions for the lowest gas velocity studied ($U/U_{mf} \approx 1.27$)
- Figure 6.22 Comparison of the dimensionless circulation time distribution for geometrically scaled float tracers in scaled fluidized beds at $U/U_{mf} \approx 3.85$
- Figure 6.23. Peak circulation times for float tracers in the correctly scaled fluidized beds at all gas velocities considered
- Figure 6.24 The effect of using a larger float tracer ($D/D_t = 20.5$) on the dimensionless circulation time distribution results, compared with the

original size used in the similarity experiments ($D/D_t = 41.1$) for the 300 mm bed fluidized at $U/U_{mf} = 2.72$

- Figure 6.25 The effect of using a larger float tracer ($D/D_t = 20.5$) on the dimensionless circulation time distribution results
- Figure 6.26 The effect of using a coarser bed material for a given bed diameter, float tracer size and dimensionless superficial gas velocity
- Figure 6.27 The reduced effect of mis-scaled bed material at higher gas velocity ($U/U_{mf} = 3.83$) on the dimensionless circulation time distribution results for the float tracers

LIST OF TABLES

Table 2.1	Examples of measurement techniques used in bubbling fluidized beds
Table 2.2	Summary of bubbling bed scaling law experimental verification work
Table 2.3	Summary of scaling law verification results with regards to Geldart classification
Table 3.1	Bed material particle characteristics for hydrodynamic similarity tests
Table 3.2	Scaling factor errors for materials used in the low aspect-ratio similarity experiments
Table 3.3	Scaling factor errors for materials used in the higher aspect-ratio similarity experiments
Table 3.4	Range of operating conditions for similarity experiments in terms of gas velocity and particle Reynolds number
Table 3.5	Bubble cap dimensions for all beds
Table 3.6	Layout measurements for bubble caps in all beds
Table 3.7	Settled bed depths and distributor orifice diameters for all beds
Table 3.8	Pressure probe tapping point locations (height above distributor)
Table 3.9	Pressure transducer operating ranges
Table 3.10	Standard run-times and sampling rates used for pressure fluctuation measurements
Table 3.11	Electrical Capacitance Tomography Electrode dimensions for the 146 mm and 300 mm scales
Table 3.12	Bed operating conditions for similarity experiments involving Electrical Capacitance Tomography

Table 4.1	Comparison of average absolute deviation of transducer signal to electrical noise for low-value pressure signals
Table 4.2	Comparison of experimental dominant frequency results (in Hz) with predictions of various models
Table 4.3	Results of bulk density measurements for bed materials used in similarity experiments
Table 4.4	Bed masses required for correct scaling based on the estimated mass of material in the 1560 mm bed
Table 4.5	Comparison of minimum slugging criteria with experimental conditions
Table 5.1	Comparison of the dimensionless ECT electrode sizes in the 146 mm and 300mm fluidized bed vessels.
Table 5.2	Sizes of spherical thin-walled hollow glass phantom voids used in comparative ECT sensitivity tests
Table 5.3	Comparison of the ECT-measured solids volume fraction with the known solids volume fraction for thin-walled hollow glass spheres placed in packed beds of silica sand at both the 146 mm and 300 mm scale. Volume fraction is expressed as a percentage of the packed bed volume fraction.
Table 6.1	Tracer and bed material combinations for investigating the effect of tracer to bed material particle size mis-match
Table 6.2	Results for solids downflow velocities of tracer particles of different sizes for the same bed material and superficial gas velocity
Table 6.3	Operating conditions and tracer/bed material combinations for the solids mixing similarity experiments
Table 6.4	Comparison of the experimentally measured solids downflow velocities and those calculated from the correlations of Kunii and Levenspiel (1969) and Baeyens and Geldart (1986)
Table 6.5	Comparison of the similarity criteria scaling ratio \sqrt{m} calculated from bed geometry, measured bed material minimum fluidization velocity,

measured solids downflow velocity and predicted solids downflow velocities

Table 6.6 Qualitative observations of density variation on float tracer behaviour in the 1560 mm bed (material D)

Table 6.7 Float tracer specifications for hydrodynamic similarity experiments

Table 6.8 Operating conditions for the float tracer circulation time similarity experiments

1. INTRODUCTION

The purpose of this short introductory chapter is to provide a summary of the background information relevant to this research and to establish a context for the original work reported in the remainder of the document. This chapter includes a brief introduction to the concepts of fluidization, means of categorizing fluidized particles and fluidization regimes, example applications of fluidization and some of the issues associated with the scale-up of fluidized bed processes. The chapter concludes with a summary of the research objectives and scope of the present work.

1.1 Fluidization of Solids

Fluidization occurs when solid particles are transformed into a fluid-like state by being suspended in a gas or liquid. In this state the bed of particles behaves somewhat like a fluid because it tends to establish a level and flows in response to a pressure gradient. Gas flows through the bed in the form of bubbles, and the bed can take on the appearance of a boiling liquid. Characteristics of fluidization are good mixing and fluid-solid contact. For this reason, fluidized beds lend themselves to applications requiring isothermal operation and good mass transfer.

1.1.1 Particle Classification

Particle systems are frequently classified in terms of their fluidization behaviour by the Geldart classification diagram (Geldart, 1973). When classified in this way, particles fall into four groups: A (small low density particles); B (sand-like particles); C (cohesive, very small particles difficult to fluidize); and D (large particles which can form spouts). In fluidized beds the particles can range in size from a few microns to several millimetres in diameter, and particles with a wide range of densities can be fluidized.

1.1.2 Gas Fluidization Regimes

In fluidization, various types of behaviour are encountered depending on the type of system and operating conditions. These fluidization regimes can be broadly summarised for gas-solids fluidization as follows (Kunii and Levenspiel, 1991):

- At low gas velocity the bed behaves as a packed bed with gas flowing through the interstices between particles. The particles themselves are stationary. The pressure drop through the bed is described by the Carman-Kozeny equation (Carman, 1956) in the laminar flow regime and the Ergun equation (Ergun, 1952) in general.
- As the gas velocity increases, a point is reached where the upward drag force on the particles due to the gas flow balances the downward force on the particles due to gravity. The particles are lifted by the fluid, the separation between the particles increases and the bed becomes fluidized. The gas velocity at which this occurs is termed the minimum fluidization velocity and is usually referred to as U_{mf} . The pressure drop through the bed reaches a constant value, independent of further increases in gas velocity.
- For particles of Geldart Group A, increasing the gas flowrate beyond minimum fluidization leads to homogeneous expansion of the bed (that is, bubbles do not form).
- As the gas velocity increases further, a point is reached that is referred to as the minimum bubbling velocity, (often termed U_{mb}), corresponding to the onset of instabilities with bubbling and channelling of gas through the bed and more vigorous movement of solids. This is known as a *bubbling fluidized bed*. (For Group A materials, $U_{mb} > U_{mf}$; for Group B materials, $U_{mb} = U_{mf}$.) The characteristics of the bubbles (size, frequency and velocity) depend on the operating conditions.
- Bubbles tend to coalesce and grow as they rise through the bed, and if the bed is sufficiently deep with a small enough diameter, bubbles can grow to a point where they spread across the vessel. This is known as a *slugging fluidized bed*.
- At gas velocities higher than the terminal velocity of the particles, entrainment occurs and the upper surface of the bed effectively disappears. These type of systems are known as *fast* or *circulating fluidized beds*, and recycling of solids is required for bed operation.
- At very high gas velocities, the pneumatic transport regime is attained.

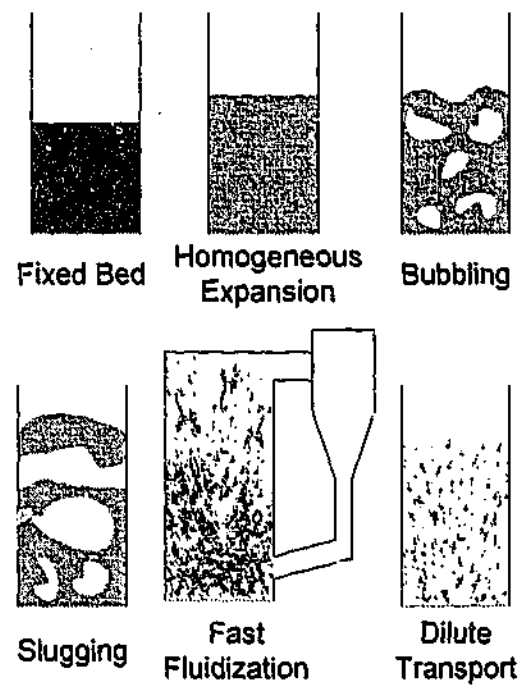


Figure 1.1: Gasfluidization regimes

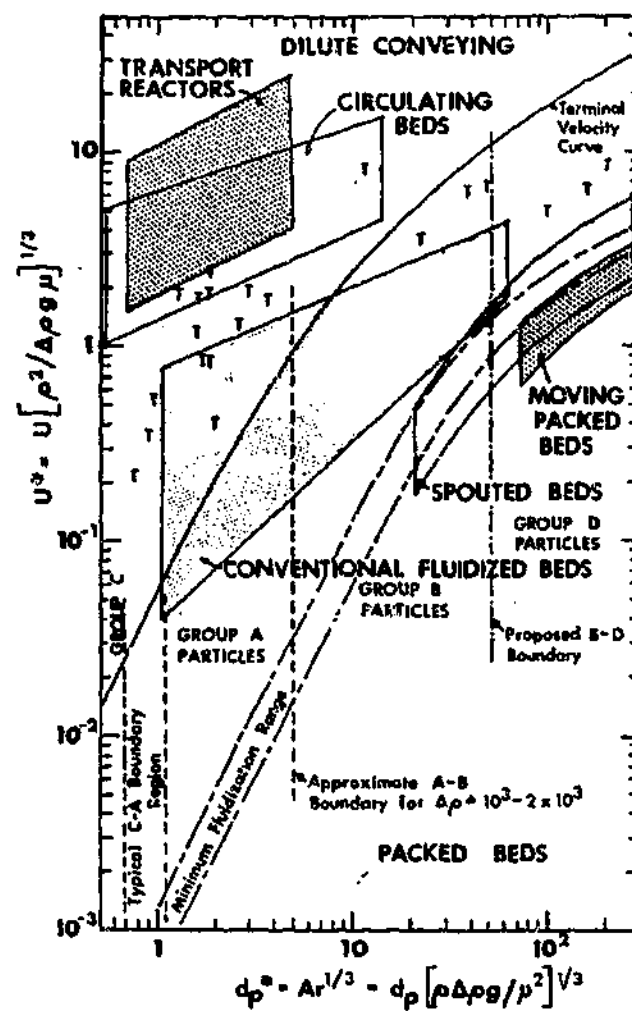


Figure 1.2 General flow regime diagram for the whole range of gas-solids contacting.
(from Grace, 1986)

A number of investigators have constructed charts to map these fluidization regimes and thus assist the bed design process. The one shown above (Figure 1.2) was developed by Grace (1986) and provides a fast way of determining which fluidization regime is likely to be encountered under specific conditions.

1.1.3 Applications of Fluidization

Fluidized beds have found applications in a wide variety of industries since the early part of the 20th century. Such applications include fluid catalytic cracking (FCC) reactors; combustion or gasification of coal, biomass or solid waste; ore roasting; cultivation of micro-organisms (biofluidization); production of polythene; drying of solids; plastic powder coating; and heat treatment of metal components.

The advantages of fluidized beds stem from their fluid-like behaviour and good mixing characteristics, and include the following points (Kunii and Levenspiel, 1991). Fluidized solids are easy to handle, and relatively high rates of heat and mass transfer are possible in the bed, where near isothermal conditions exist. Because the rate of heat transfer between a fluidized bed and an immersed object is high, fluidized bed heat exchangers require relatively small surface areas, and circulating solids between two fluidized beds allows large quantities of heat to be added or removed. Fluidized beds are also quite suitable for large-scale operations, and compared with a fixed bed of the same bed height and gas velocity, the pressure drop of the fluidized bed is much lower.

However, fluidized beds are not suitable for all applications. There are limitations on the types of fluid/solid systems which can be fluidized effectively, and bubbles can cause gas bypassing, lowering the conversion in a reactor. The movement of the solids causes a non-uniform solids residence time, which may be undesirable. The movement of the bed material can also erode the walls of pipes and vessels, and cause attrition of the solids. In wet or high temperature situations, agglomeration and sintering of the bed material can seriously affect bed performance. And due to the complexity of the hydrodynamic behaviour present in fluidized beds, issues of design and scale-up can be complicated.

1.2 The Problem of Fluidized Bed Scale-up

The scale-up and design of fluidized bed reactors is an uncertain undertaking because of the complexity of fluidized beds and limitations in the extent to which their behaviour can be predicted. Although the economic benefits of an appropriate fluidized bed system can be large, developing a successful full-scale unit for a new process can be a risky business.

Most of the fundamental work on fluidization and the development of engineering correlations has been carried out using laboratory-scale and pilot-scale equipment with a range of bed diameters up to about 1 metre in some cases, but less than 0.6 metres in most. Commercial reactors, however, are usually of the order of several metres in diameter, and as a consequence there is always a concern about the reliability of the design correlations at these scales.

In order to "fill the gap" and link data obtained from a small-scale model with a commercial reactor, the behaviour of the model must represent the commercial reactor as accurately as possible. Whilst chemical kinetics are usually considered separately and are assumed to be independent of the reactor scale, there are several approaches to scaling up the physical behaviour (hydrodynamics) of the fluidized bed system.

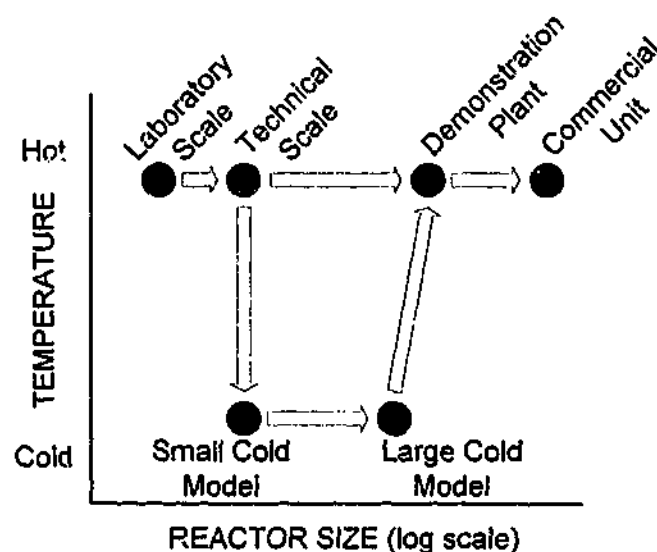


Figure 1.3 The typical approach to scale-up. Note that the vertical axis could also represent pressure.

One approach is to rely heavily on empirical data, constructing various small and intermediate scale beds to try and iron out any difficulties before committing resources to the design of the full-scale plant. Although this is a cautious and costly approach, it is still the most common route taken for scaling up a fluidized bed process. Figure 1.3 shows an example of the typical scale-up approach diagrammatically.

A second approach is the theoretical approach, involving computer models that simulate fluidized bed behaviour from a fundamental mathematical description of the physics. This type of consideration is becoming more popular as the availability of high power computers increases, although simplifications and assumptions are still necessary to make simulation possible. The two main bases for simulations are Computational Fluid Dynamics (CFD) incorporating the so-called "two-fluid model" (TFM) and the Discrete (or Distinct) Element Method (DEM). The CFD approach describes the fluidized bed as two continuous, interpenetrating phases – the particle phase and the fluid phase. Mass and momentum balances are derived for each phase and solved numerically by simulating the whole fluidized bed using a finite grid. The so-called DEM approach is usually a combination of DEM and CFD techniques in which all particles are traced individually by solving Newton's equations of motion, while the fluid phase is treated as a continuum. Whilst CFD and DEM simulations show promise, and reasonable agreement between simulations and experiments has been achieved by a number of workers (eg Tsuji *et al.*, 1993; Witt *et al.*, 1997), we are not yet at the stage where a large fluidized bed could be designed directly from these models alone.

The third approach is to use some form of scaling law in the design of a small-scale unit such that it will replicate the physical behaviour of the full-scale unit in proportion to its size. Scaling laws are nothing new in many areas of science. Bunde *et al.* (2002) provide a broad transdisciplinary analysis of scaling laws in non-linear systems. In economics, scaling laws have been widely applied (Brock, 1999). The so-called "universal scaling laws in biology" are well known (West *et al.*, 1997), and the scaling law approach has also been applied to many engineering situations, -one example being the scaling of turbulent combustion phenomena (Arpaci and Agarwal, 1999). In engineering situations, dimensional analysis is often used to put scaling laws into a convenient practical form. The approach is to keep a set of characteristic dimensionless numbers the same at both scales.

In a fluidized bed these numbers could be, for example, appropriate forms of the Froude number, the bed aspect ratio, the particle-to-gas density ratio or the particle Reynolds number. The specific dimensionless numbers are chosen by dimensional analysis of the characteristic variables of the fluidized beds or the non-dimensionalized governing equations. In bubbling fluidization, the major scaling law contributions were originally made by Glicksman, (1984) and Horio *et al.*, (1986a). In theory, if the scaling rules are followed, then a small unit should closely mimic the behaviour of the large one.

The scaling laws for fluidized beds could provide a means of reducing the expense of scale-up by providing a greater degree of certainty in the behaviour of the final large-scale unit, based on experiments and data obtained from a correctly scaled small unit. However, experimental verification of the scaling laws has produced mixed outcomes regarding the range of conditions over which the various forms of the laws would apply. Of particular concern are uncertainties regarding the importance of solid-to-gas density ratio. The experimental work has also been restricted to relatively small increases in system size. Whether the same scaling laws will work over a large increase in bed size with complicating factors such as non-ideal distributor geometries is still unknown.

1.3 Objective and Scope of Thesis

The main objectives of this project are as follows:

- To provide a comprehensive review of the literature covering scaling laws and scaling law verification work in the area of bubbling fluidization.
- To investigate the effects of scale on bubbling fluidized beds across a wider range of system sizes than has been possible previously.
- To test the so-called *simplified scaling laws* at this range of scales.
- To test deliberately mis-matched scenarios as a form of control experiment.
- To evaluate the effect of solid to gas density ratio at low particle Reynolds numbers.
- To investigate the reliability of different measurement techniques for evaluating hydrodynamic similarity. (Specifically these measurement techniques will employ pressure probes, Electrical Capacitance Tomography, solids mixing and float-tracer experiments.)
- To confirm that beds with a bubble-cap distributor design will scale successfully.

Since this work focuses on experimental verification of scaling laws, the project is experimentally intensive as a consequence. The study involves comparative experiments using fluidized bed cold models with a wide range of diameters (0.15, 0.3, 0.6 and 1.56 metres), and as stated above, a variety of measurements are employed. (It should be noted, however, that not all the measurements could be applied at all scales for practical reasons.)

The layout of the thesis can be summarised as follows. In Chapter 2, a literature review is conducted that covers the relevant fluidization phenomena and conventional theories as well as the approach to fluidized bed measurements. A thorough review of scaling laws and previous verification work is presented with a useful summary provided in Appendix A. Chapter 3 outlines the experimental equipment and bed materials in detail and also covers important design aspects such as tuyere and pressure probe design. Chapter 4 covers the experimental verification work employing the use of pressure measurements. Chapter 5 reports on the verification work involving voidage fluctuations from Electrical Capacitance Tomography measurements and identifies a number of technical issues regarding the use of the instrumentation, and Chapter 6 presents a solids mixing study (also employing ECT) as well as a similarity study involving float-tracers. Finally, Chapter 7 presents the conclusions of the present study and provides recommendations for areas of future work that arise from this investigation.

2. LITERATURE REVIEW

2.1 Introduction

This project, concerning scaling laws in fluidized beds, is restricted in scope to the investigation of the behaviour of bubbling gas-fluidized beds of Group B materials. In this chapter, all relevant background information upon which the present work is based will be summarised.

Firstly, the generally observed behaviour of bubbles and solids in bubbling fluidized beds will be considered, as will the transition from bubbling to slugging behaviour and the motion of solids within the dense phase. The review of these phenomena is primarily based on the comprehensive summaries contained in Geldart, (1992) and Baeyens and Geldart, (1986) and Kunii and Levenspiel, (1991). The development of the scaling laws for the bubbling fluidized bed will then be reviewed. Measurement techniques for bubbling bed experimentation are then given a general introduction, and finally all major previous work concerning the experimental verification of the scaling laws for bubbling fluidization is reviewed.

2.2 Bubbling Fluidized Bed Dynamics

A dense bubbling gas-fluidized bed contains regions of low solids density, known as *bubbles* or *voids*, as well as regions of higher density called the *emulsion* or *dense phase*. The main characteristics associated with bubbles in fluidized beds are the bubble size, bubble rise velocity, and bubble interactions (splitting and coalescence).

2.2.1 Generally Observed Bubble Behaviour

The bubbles in a fluidized bed appear very similar in many ways to gas bubbles in a liquid of low viscosity (Kunii and Levenspiel, 1991):

- The shape of the bubbles is often similar, close to spherical when small, flattened and distorted when larger, and spherical cap-shaped when large.

- In both systems, large bubbles rise more quickly than smaller ones, and the expressions for bubble rise velocity in the two systems depend on the same factors.
- Bubble coalescence (small train of bubbles joins together to form a larger one) occurs in both systems; the resulting change in rise velocity also has the same direction.
- Wall effects act in the same direction on the bubble's rise velocity.

Further observations of bubbling fluidized beds indicate that roughly all gas in excess of that required for minimum fluidization flows through the bed in the form of bubbles, with the dense phase remaining close to minimum fluidization conditions and relatively quiescent at low gas flows. As the gas velocity increases, the increasing bubble activity causes the churning and flow of the solids which gives rise to the excellent mixing characteristics of the bubbling fluidized bed.

2.2.2 Two-Phase Theory of Fluidization

This model was first proposed by Toomey and Johnstone (1952) and is able to explain many of the properties of fluidized beds. In the two-phase theory it is assumed that the fluidized bed consists of a dense phase of particles surrounding bubbles of gas which are essentially free of particles. In the dense phase the flow rate of gas is equal to that required to just fluidize the bed and the voidage is constant and equal to the voidage at minimum fluidization (ϵ_{mf}).

If the total gas flowrate is given by:

$$Q = \frac{U}{A} \quad (2.1)$$

Then the flowrate can be divided between the dense-phase:

$$Q_{mf} = U_{mf} A \quad (2.2)$$

and the bubbles:

$$Q - Q_{mf} = Q_B = (U - U_{mf})A \quad (2.3)$$

Q_B is known as the "visible" bubble flowrate and is invariably less than $(U - U_{mf})A$. Thus the two-phase theory was modified in order to account for this, leading to:

$$\frac{Q_B}{A} = U - U_D(1 + n\bar{\varepsilon}_B) \quad (2.4)$$

where $\bar{\varepsilon}_B$ is the fraction of the bed occupied by the bubbles (or the bubble hold-up);

$$\bar{\varepsilon}_B = \frac{H - H_{mf}}{H} = \frac{Q_B}{A} \cdot \frac{1}{U_A} \quad (2.5)$$

and U_D is the dense-phase gas velocity ($\geq U_{mf}$). In the above equation, U_A is the average velocity of bubbles in the bed. Reported values of n varied; Grace and Clift (1974) showed that n may be as high as 27. Thus to simplify the above, Equation 2.3 can be rewritten as:

$$\frac{Q_B}{A} = Y(U - U_{mf}) \quad (2.6)$$

and Y is approximately 0.67 for sands (Werther, 1978 & 1983). Y also increases towards the bed surface. Additionally, various workers' experimental results for Y have been correlated against Archimedes number and presented in Baeyens & Geldart (1986).

The two-phase theory is an attempt to explain the distribution of gas in the bed and this is of interest because it affects the degree of chemical conversion. Equation 2.4 provides a reasonable estimate where $\bar{\varepsilon}_B$ is obtained from bed expansion data, n is taken as 2, and $U_D = U_{mf}$ for Group B and D powders (or is obtained from collapse-tests for Group A materials).

It is important to note that U_D represents the *superficial* velocity of the gas in the dense phase; and the *relative* velocity between gas and particles in the dense phase will be higher due to the reduced cross-sectional area (equal to $\varepsilon_D A$). Thus

$$U_D = \varepsilon_D U_{Drel} \quad (2.7)$$

But the effect of solids circulation may mean that locally the dense phase as a whole could be moving up or down, and therefore the *absolute* velocity of the gas in the dense phase (relative to the wall) could be many times greater than U_D and be positive or negative (upwards or downwards).

2.2.3 The Davidson Bubble Model

With the basic behaviour of bubbling beds accounted for by the two phase theory, it is now necessary to account for the formation of the bubbles themselves. Davidson's well-known model (Davidson and Harrison, 1963) accounts for the movement of both gas and solids and the pressure distribution about rising bubbles. The model is developed on the following postulates:

- 1) A gas bubble is solids-free and circular in shape, thus being spherical in a three-dimensional bed and cylindrical in a two-dimensional (thin-walled) bed.
- 2) As a bubble rises, particles move aside as would an incompressible, inviscid fluid of bulk density $\rho_p(1-\varepsilon_m)$.
- 3) The gas in the emulsion phase flows as an incompressible viscous fluid.

The following boundary conditions are also used:

- Far from the bubble an undisturbed pressure gradient exists
- The pressure in the bubble is constant

The above postulates and boundary conditions are sufficient to give the flow-pattern for solids and for gas, as well as the pressure distribution in the vicinity of the rising bubble. The theory also leads to two quite different gas flow patterns depending on the relative velocity of the bubble and the emulsion gas.

If the emulsion gas is rising faster than the bubble, the emulsion gas uses the bubble as a convenient short-cut on its way through the bed. It enters at the bottom of the bubble and leaves at the top and an annular ring of gas circulates within the bubble, moving upwards with it. This is known as a *cloudless* or *slow bubble*.

If, on the other hand, the bubble rises faster than the gas in the emulsion phase, a different flow pattern results. This is called the *clouded* or *fast bubble*. As with the slow bubble, emulsion gas still enters at the bottom of the bubble and leaves at the top. But because the bubble is rising faster than the emulsion gas, the gas leaving the top of the bubble is swept around and returns to the base of the bubble. The region around the bubble in which this circulating gas flows is called the cloud. The rest of the gas in the bed does not mix with the recirculating gas but moves aside as the fast bubble with its cloud passes by.

Davidson's theory is successful in that it predicts the formation of bubbles. The theory agrees reasonably well with observations of both clouded and cloudless bubbles from experiments. There are some discrepancies though. First of all, real bubbles are often not spherical, but have a flat or indented base, and the model does not fit the data for the back end of the bubble. In addition, the cloud around a clouded bubble is thinner than predicted, and real bubbles may contain a small amount of solids. Davidson's model is, however, by far the simplest to use.

The remaining parts of Section 2.2 deal with the observed characteristics of bubbles and slugs. Unless otherwise referenced, the information has been taken from the comprehensive summary of the observations of bubbles and slugs provided in Geldart (1992).

2.2.4 Shape of Bubbles

Experimental observations of bubbles in fluidized beds indicate that the bubbles have a spherical cap, similar to air bubbles in a liquid. Rowe *et al* (1971) carried out a comprehensive study of the shape of bubbles in a number of powders using X-ray pictures. The wake of the bubble is often referred to in terms of the wake fraction, which can be defined in two ways:

$$f_w = \frac{V_w}{V_b + V_w} \quad (2.8)$$

or

$$\beta_w = \frac{V_w}{V_b} \quad (2.9)$$

where V_w is the volume of the wake and V_b is the volume of the bubble. Note that by these definitions;

$$\beta_w = \frac{f_w}{1-f_w} \quad (2.10)$$

The wake region most probably forms because the pressure in the lower part of the bubble is less than the surrounding emulsion phase. Thus gas is drawn into the bubble at that point causing instability, partial collapse of the bubble and turbulent mixing. The turbulence causes solids to be drawn up behind the bubble, forming the wake region. Thus a rising bubble tends to draw up a wake of solids behind it, and the wake is observed to shed and leak solids as it rises. So there is a continuous, (although not necessarily large), exchange of solids between the wake and the emulsion.

The fraction occupied by the wake is generally taken as $\beta_w = 0.33$ (Geldart, 1992) – as compared with 0.9 for air bubbles in water. In 2D beds the bubbles appear to have similar shape but drag at the walls of the vessel lengthens the bubble, making the wake fraction appear smaller.

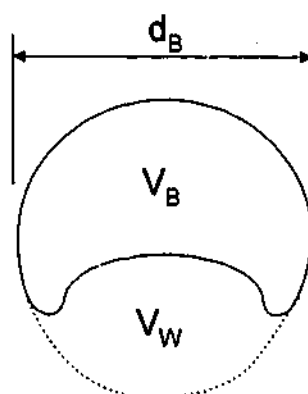


Figure 2.1 – Idealised bubble showing bubble and wake volume

2.2.5 Coalescence

Of course, in the real world only a very small fraction of bubbles resemble the ideal shapes presented in the models. This is because the bubbles are continually growing, splitting, coalescing, forming and disappearing. Observations show that if two bubbles are close enough together, they will *coalesce*, that is, the trailing one accelerates and is drawn into the leader. The trailing bubble becomes elongated as it accelerates into the leading bubble. If the bubbles are not vertically aligned, the trailing one will tend to move into line behind the leading one and then be drawn into it. When a large fast rising bubble overtakes smaller slow bubbles, it may sweep them up, always by absorbing them through its base. There have been many investigations carried out into bubble coalescence (eg Argyriou *et al.*, 1971, Clift & Grace, 1971) and there are a number of models for bubble coalescence, (eg Darton *et al.*, 1977), which can be used to successfully predict the increase in bubble size with bed height. The diagram below shows the bubble paths during coalescence for the Darton model.

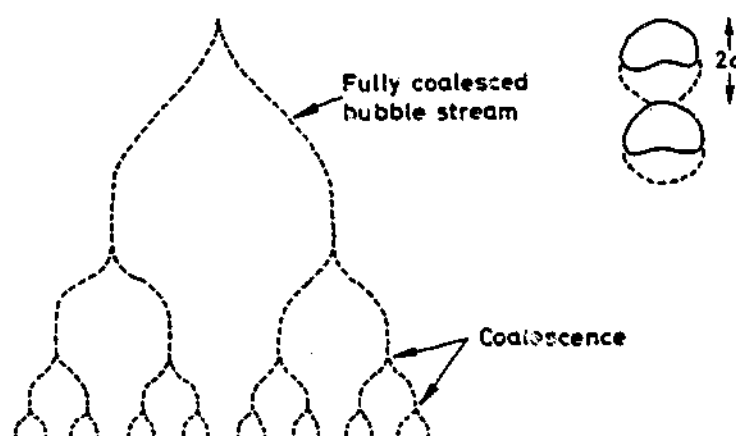


Figure 2.2 2-Dimensional view of the bubble coalescence model of Darton *et al.* (1977). ("a" refers to the radius of a spherical bubble of equivalent volume to the actual bubble)

2.2.6 Splitting

Sometimes the roof of a bubble is seen to develop a downward cusp, which then frequently grows rapidly to cause the bubble to split vertically. In most cases where a bubble splits, the larger portion reabsorbs the smaller portion almost immediately. When the two bubbles formed are almost the same size, the larger one first grows at the

expense of the smaller one, before recalescence occurs. In some cases the larger bubble pulls away from the smaller one, leaving two bubbles. Recalescence occurs more frequently in beds of large particles than beds of fine ones.

2.2.7 Rise Velocity

The rise velocity of a single bubble in a fluidized bed has been shown to follow the same type of relationship as that for a gas bubble rising through a liquid. See, for example, Davidson *et al.* (1959), Harrison and Leung (1961) and Rowe (1971). Although the experimental data are somewhat scattered, leading to some doubts about the value of the coefficient, the expression

$$U_B = 0.7\sqrt{gd_{eq}} \quad (2.11)$$

is still widely accepted. Here U_B is the bubble rise velocity, g is the acceleration due to gravity, and d_{eq} is the diameter of a sphere of equivalent volume to the bubble. Many modifications to this basic expression have been proposed. For example; to account for vessel constraints rise velocity can be estimated from a choice of two equations (Kunii and Levenspiel, 1991);

$$U_B = 0.711\sqrt{gd_{eq}} \quad \text{for } \frac{d_{eq}}{D} < 0.125 \quad (2.12)$$

$$U_B = \left[0.711(gd_{eq})^{\frac{1}{2}} \right] 1.2 \exp\left(-1.49 \frac{d_{eq}}{D}\right) \quad \text{for } 0.125 < \frac{d_{eq}}{D} < 0.6 \quad (2.13)$$

where D is the diameter of the container. (Note that for $d_b/D > 0.6$ the bed should be considered to be *slugging*, not bubbling.) Werther (1983) also proposed different values of the coefficient in Equation 2.11 depending on the type of powder and the bed diameter. However, the motion of bubbles is complicated by the fact that they tend to accelerate whilst coalescing, and are also influenced by the direction of motion of the surrounding solids. This all leads to a great deal of scatter in the experimental values of

bubble rise velocity, making it hard to know whether greater effort in fine-tuning the correlations is worthwhile.

2.2.8 Bubble Size

Bubble size in fluidized beds increases with excess gas velocity and with increasing height above the distributor. Suggested reasons for this are:

1. Decreasing hydrostatic pressure on the bubbles as they rise through the bed. This is significant only in very deep beds.
2. Bubbles continue to grow by depleting the emulsion phase of gas locally. This appears to occur with beds of large (Group D) particles.
3. Two small bubbles may coalesce to form a bigger one. This seems to be the most important mechanism for bubble growth.

A consequence of coalescence and splitting is that a maximum bubble size may exist in the bed. Because bubble splitting is more frequent in beds of fine (Group A) particles and less frequent in beds of coarser particles (Group B), the maximum bubble size in a large bed of coarse particles is large; but is small in beds of fine particles.

A number of correlations for bubble size exist, (eg Mori and Wen, 1975; Darton *et al.* 1977; Rowe, 1976), most of which focus on Group B materials. The Darton *et al.* correlation for bubble diameter is:

$$d_{eq} = 0.54(U - U_{mf})^{0.4} (h + 4\sqrt{A_0})^{0.8} / g^{0.2} \quad (2.14)$$

where h is the distance of the bubble from the distributor, g is the acceleration due to gravity and A_0 is the "catchment area" for the bubble stream at the distributor plate (which characterises different distributors and is usually the area of plate per orifice).

Note that this equation is only applicable for $d_{eq} \leq \frac{1}{3}D$. Most bubble size correlations

have been based on data obtained from small beds, however Werther (1978) developed an equation based on experiments in larger beds (0.45 m and 1 m diameter) for Group B solids (note: cgs units):

$$d_{eq} = 0.00853 \left[1 + 27.2(U - U_{mf}) \right]^{\frac{1}{3}} (1 + 6.84h)^{1.21} \quad (2.15)$$

The prediction of bubble sizes in beds of Group A or Group D solids has also been investigated and separate correlations proposed to account for differences in observed behaviour. These are not relevant to the current work, however.

2.2.9 Slugging

When bubbles grow to a size greater than approximately one-third of the bed diameter, slugging can occur. In slugging fluidization, 3 types of slugs can be formed. Axi-symmetric (axial) slugs, wall slugs and flat (solids or square-nosed) slugs, which are all depicted in Figure 2.2 below. Axi-symmetric slugging tends to occur in smooth-walled beds of fine powders at moderate gas velocity where the particles will rain down at the bed wall to match the rise rate of the slugs. Wall slugs occur at higher velocities in beds with angular solids and/or a rough vessel wall. Flat slugs occur in beds of Group D solids where the bed separates into slices of emulsion separated by gas. Particles rain down continuously from one slice of emulsion to the next as the slices rise up the bed. The topmost slice eventually disappears as it is not replenished with solids.

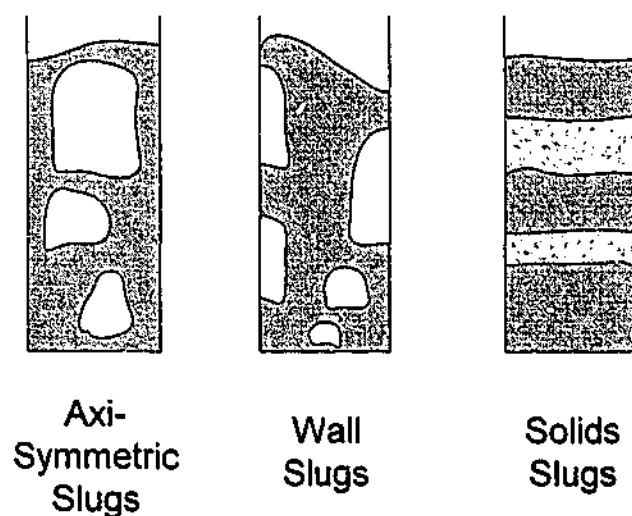


Figure 2.3 Modes of slugging observed in fluidized beds

The point of operation at which slugging commences in an otherwise bubbling fluidized bed is a function of the bed depth and the superficial gas velocity. Various predictions

for the onset of slugging have been proposed. Yagi and Muchi (1952) stated that slugging is unlikely at any velocity if the bed height to bed diameter ratio is less than:

$$\frac{H_{mf}}{D} = \frac{1.9}{(\rho_p d_p)^{0.3}} \quad (2.16)$$

(The equation is in S.I. units.) For beds deeper than 1m, Stewart and Davidson (1967) suggested that the minimum gas velocity at which slugging commences is:

$$U_{ms} = U_{mf} + 0.07\sqrt{gD} \quad (2.17)$$

For bed depths between 0.3m and 1m, the gas velocity is generally higher than that predicted by Equation 2.17 and the equation of Baeyens and Geldart (1974) can be used:

$$U_{ms} = U_{mf} + 0.16(H_L - H_{mf})^2 + 0.07\sqrt{gD} \quad (2.18)$$

where H_L is the critical bed height beyond which slugging can occur and is given by:

$$H_L = 1.34D^{0.175} \quad (2.19)$$

Darton *et al.*, (1977) also presented a correlation for minimum slugging, with the bed aspect ratio condition given by:

$$\frac{H}{D} > 3.5 \left(1 - \frac{1}{\sqrt{N_0}} \right) \quad (2.20)$$

and the superficial gas velocity for minimum slugging given by the Stewart and Davidson criterion (Equation 2.17).

Slugs tend to travel more slowly than bubbles, and because of this the chemical conversion in a slugging bed may be higher (for the same $U - U_{mf}$) than in a freely bubbling bed. Slugs give rise to regular pressure fluctuations in the bed which can be significant enough in large diameter fluidized beds to cause structural damage. In this

case, internals can be used to help break up the slugs. Unlike a freely bubbling bed, in a slugging bed, the pressure drop across the bed increases steadily beyond $\frac{Mg}{A}$ as the superficial gas velocity increases, due to acceleration of the solids.

2.3 Solids Motion and Mixing in Bubbling Fluidized Beds

Experimental investigations in bubbling fluidized beds have shown that the emulsion is not stagnant, but develops distinct flow patterns as a consequence of the influence of bubbles. Typically, solids tend to rise up in the locations where bubbles predominate; in the areas which are essentially bubble-free, solids flow downwards. Thus circulation patterns develop within the bubbling bed. In the idealised case, solids are carried upwards in the *wake* of the bubble (solids occupying the bottom of the completed sphere), and the *drift* (the region behind the completed sphere).

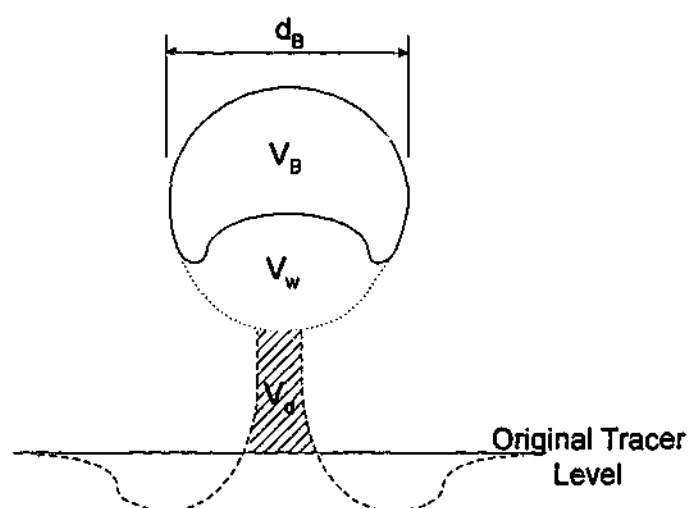


Figure 2.4 Wake and drift in an idealised bubble, redrawn from Baeyens & Geldart (1986).

The flow patterns in the emulsion of bubbling beds can vary significantly with different distributor designs and bed height-to-diameter ratios. Kunii and Levenspiel (1991) give a summary of the observed patterns for different beds of Group B particles:

- At low fluidizing velocity in beds of aspect ratio (height to diameter) close to, but less than unity, the emulsion solids circulate as a vortex ring with upflow near the wall and downflow at the bed axis (Fig 2.4a).

- At higher flowrates the pattern may reverse because of the predominance of large rising bubbles at the bed centre (Fig 2.4b).
- As the bed aspect ratio approaches unity, the emulsion solids tend to move down the wall near the bed surface (Fig 2.4c).
- In beds with an aspect ratio greater than unity, a second vortex ring forms above the original vortex ring, and the upflow is in the centre of the bed (Fig 2.4d).
- At higher gas flows, the solids circulation in the upper vortex ring becomes more vigorous and dominates the overall emulsion movement.
- In very shallow beds with aspect ratio less than one half, beds with a uniform distributor may exhibit vortex rings of aspect ratio approximately 1, (Fig 2.4e), but with high pressure drop tuyeres in the distributor, the location of the tuyeres may determine the circulation pattern of the emulsion (Fig 2.4f).

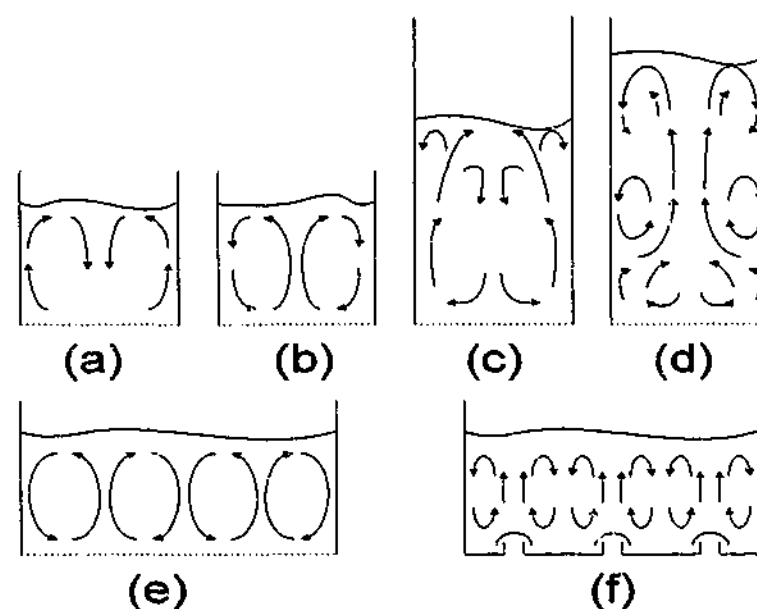


Figure 2.5 Solids circulation patterns in fluidized beds of different aspect ratios (redrawn from Kunii & Levenspiel, 1991)

Vertical mixing in fluidized beds is much faster than lateral mixing. Lateral mixing seems to result primarily from particles either being carried to the bed surface where they are dispersed sideways by bursting bubbles or carried down to the distributor where they are carried sideways by bubble-free flows of emulsion phase.

Solids motion is of interest to the fluidized bed designer because it influences gas-solid contacting, gas backmixing, heat transfer, the position of stagnant zones within the bed, and the choice of solids feed and withdrawal locations. Various approaches have been

used to try and model solids motion and mixing in fluidized beds, and some of these will now be discussed.

2.3.1 Variables Influencing the Rate of Solids Mixing

A comprehensive introduction to a basic model approach to solids circulation is given in Baeyens & Geldart (1986), who developed a number of parameters for evaluating solids mixing in bubbling fluidized beds. The major points of their approach will now be summarised.

Given the general observations of solids mixing in fluidized beds, the rate of mixing of solids in a fluidized bed is expected to be a function of:

- the volumetric flowrate of bubbles through the bed (Q_B),
- the quantity of material dragged upwards by each bubble (β_s),
- the rise velocity of the solids (U_s), and
- the fraction of the bed consisting of bubbles (ϵ_B).

The volumetric flowrate of the bubbles Q_B can be determined from Equation 2.6 presented earlier:

$$\frac{Q_B}{A} = Y(U - U_{mf}) \quad (2.6)$$

(where the parameter Y is used to account for the fact that the visible flow of bubbles is less than that predicted directly by the two-phase theory).

From the idealised case of a rising bubble (see Figure 2.3), the fraction of solids dragged upwards (β_s), is the sum of the solids dragged upwards in the bubble wake (β_b) and the fraction of solids in the drift (β_d):

$$\beta_s = \beta_w + \beta_d \quad (2.21)$$

with

$$\beta_w = \frac{V_w}{V_b} \quad (2.22)$$

and

$$\beta_d = \frac{V_d}{V_b} \quad (2.23)$$

Rowe and Partridge (1962) showed that β_w decreased with increasing particle size. Baeyens and Geldart (1973) found that β_d also decreased with increasing particle size. For Group B materials, β_d is usually larger than β_w , with β_w averaging approximately 0.35 (Baeyens and Geldart, 1986).

The rise velocity of the solids (U_s) has been found to be dependent on the bubble rise velocity. Baeyens and Geldart (1973) found that the particles travelling in the wake of the bubble rise at the same velocity as the average bubble rise velocity (U_A), and the particles carried up on the drift travel at some fraction of the bubble rise velocity, typically around 38% of U_A . Values of U_A could be calculated directly from the single bubble rise velocity correlations presented in Section 2.2.7, or estimated from the following equation (Davidson & Harrison, 1963) which relates the average bubble rise velocity U_A to the rise velocity of a single isolated bubble U_B .

$$U_A = (U - U_{mf}) + U_B \quad (2.24)$$

The fraction of the bed consisting of bubbles can be obtained simply from a consideration of the bed expansion, viz:

$$\varepsilon_B = \frac{H - H_{mf}}{H} \quad (2.25)$$

or it could be predicted approximately by re-arranging Equation 2.6 (and substituting U_A according to Equation 2.24):

$$\varepsilon_B = \frac{Q_B / A}{U_A} = \frac{Y(U - U_{mf})}{U_A} = \frac{Y(U - U_{mf})}{U - U_{mf} + U_B} \quad (2.26)$$

2.3.2 Estimating Solids Particle Velocity

If the assumption is made that the particles travel upwards in the wake and drift of bubbles and downwards elsewhere, a mass balance in any horizontal plane across the bed can be written (Baeyens and Geldart, 1986):

$$\begin{array}{|c|} \hline \text{Bed fraction} \\ \text{containing} \\ \text{downward} \\ \text{moving} \\ \text{solids} \\ \hline \end{array} \times \begin{array}{|c|} \hline \text{Average} \\ \text{downwards} \\ \text{particle} \\ \text{velocity} \\ \hline \end{array} = \begin{array}{|c|} \hline \text{Bed} \\ \text{fraction} \\ \text{containing} \\ \text{upwards} \\ \text{moving} \\ \text{solids} \\ \hline \end{array} \times \begin{array}{|c|} \hline \text{Average} \\ \text{upwards} \\ \text{solids} \\ \text{velocity} \\ \hline \end{array} \quad (2.27)$$

The mass balance can now be written in terms of the parameters discussed above:

$$1 - \varepsilon_B - (\beta_w + \beta_d)\varepsilon_B v_p = U_A \beta_w \varepsilon_B + 0.38 U_A \beta_d \varepsilon_B \quad (2.28)$$

Substituting for U_A (using Equation 2.26) and rearranging for v_p :

$$v_p = \left(\frac{\beta_w + 0.38\beta_d}{1 - \varepsilon_B - \varepsilon_B(\beta_w + \beta_d)} Y \right) (U - U_{mf}) \quad (2.29)$$

The first bracketed term depends strongly on particle properties and decreases with increasing particle size and it has been found experimentally (Baeyens & Geldart 1973) for a number of materials that v_p varies linearly with $(U - U_{mf})$. It should be pointed out that v_p is an average particle velocity and the local value of particle velocity could be several times greater or smaller than the value of v_p estimated in this way.

2.3.3 Solids Circulation Flux

The mass balance established in Equation 2.27 can be re-written to express solids circulation flux by considering the upwards moving solids:

$$\begin{array}{|c|} \hline \text{Solids} \\ \text{circulation} \\ \text{rate} \\ \hline \end{array} = \begin{array}{|c|} \hline \text{Dense} \\ \text{phase} \\ \text{bulk} \\ \text{density} \\ \hline \end{array} \times \begin{array}{|c|} \hline \text{Bed fraction} \\ \text{containing} \\ \text{upwards} \\ \text{moving} \\ \text{solids} \\ \hline \end{array} \times \begin{array}{|c|} \hline \text{Average} \\ \text{upwards} \\ \text{solids} \\ \text{velocity} \\ \hline \end{array} \times \begin{array}{|c|} \hline \text{Bed cross-} \\ \text{sectional} \\ \text{area} \\ \hline \end{array} \quad (2.30)$$

which leads to an expression for solids flux (J):

$$J = \rho_p (1 - \varepsilon_{mf}) (U_A \beta_w \varepsilon_B + 0.38 U_A \beta_d \varepsilon_B) \quad (2.31)$$

and substituting for ε_b :

$$J = \rho_p (1 - \varepsilon_{mf}) (U - U_{mf}) Y (\beta_w + 0.38 \beta_d) \quad (2.32)$$

This expression has been found to be reasonably consistent with experiments for Group B materials. Equation 2.32 can be compared with the expression for solids flux given by Kunii and Levenspiel (1969):

$$J = \alpha \rho_p (1 - \varepsilon_{mf}) (U - U_{mf}) \quad (2.33)$$

where the term $Y(\beta_w + 0.38 \beta_d)$ is lumped into a single value α .

2.3.4 Bed Turnover Time

The time taken for the bed material to circulate once is simply calculated as the total bed mass divided by the mass flow of the bed material:

$$t_T = \frac{M}{JA} \quad (2.34)$$

and substituting for M and J gives the bed turnover time (t_T):

$$t_T = \frac{H_{mf}}{(\beta_w + 0.38 \beta_d) Y (U - U_{mf})} \quad (2.35)$$

2.3.5 Solids Mixing Models

In addition to the parameters of Baeyens and Geldart (1986) introduced above, a number of mathematical models for solids mixing have been developed. The various approaches have been reviewed by Potter (1971), van Deemter (1985) and Kunii and Levenspiel (1991), of which the two major modelling approaches employed are diffusion models and counter-current backmixing models. Both approaches require empirical coefficients as inputs.

Diffusion (or Dispersion) Models for Solids Mixing

The advantage of applying a diffusion model to solids mixing in bubbling fluidization is that the calculations in the model are relatively straightforward. The diffusion model for solids mixing in axial and radial directions can be expressed in cylindrical coordinates as:

$$\frac{\partial c_{si}}{\partial t} = D_{sa} \frac{\partial^2 c_{si}}{\partial z^2} + D_{sr} \frac{1}{r} \frac{\partial}{\partial r} \left(r \frac{\partial c_{si}}{\partial r} \right) \quad (2.36)$$

where c_i is the concentration of species i and D_{sa} and D_{sr} are the diffusion coefficients in the axial and radial directions respectively.

Although the diffusion modelling approach is attractive, unfortunately, solids mixing in bubbling beds does not really appear to be a diffusion process. Some of the assumptions necessary to apply a diffusion model are that the system is homogeneous, the interaction distance is small compared to the system size, and the particle motion is random. None of these is strictly true in a bubbling fluidized bed. Bubbles represent local inhomogeneities, and voidage may vary with bed height. The particles are displaced a distance of the order of a bubble diameter with each interaction (eg Rowe *et al.*, 1965) which may or may not represent a small interaction distance depending on the size of the bed and the operating conditions. Finally, the particle motion is not random, but the result of a specific pattern of displacement associated with the passage of each bubble (Rowe *et al.*, 1965).

Verloop *et al.* (1968/69) found that the diffusion coefficients measured in various previous studies differed by up to several orders of magnitude. A number of other workers, including Valenzuela and Glicksman (1984) and Avidan and Yerushalmi (1985) have also pointed out the shortcomings of using diffusion models for solids mixing in the bubbling regime.

Counter-Current Backmixing Model

This approach to modelling solids mixing was taken by van Deemter (1967) with the model later developed further by Gwyn *et al.* (1970) and others.

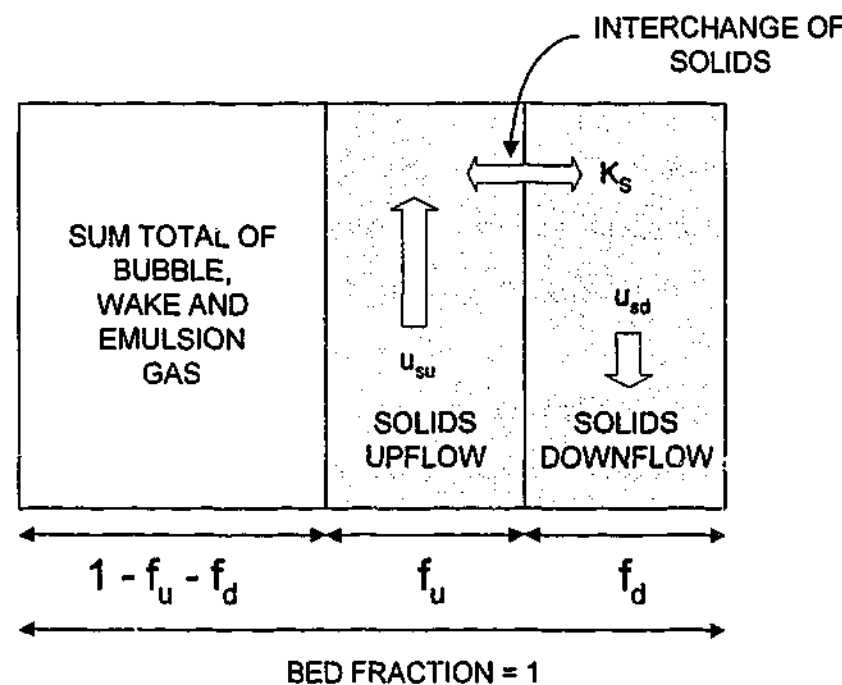


Figure 2.6 The counter-current backmixing model (redrawn from Kunii and Levenspiel 1991)

The model separates the axial flow in the bed into three layers; two counter-current flowing streams of solids and a single stream of gas flow. The model is illustrated pictorially in Figure 2.5.

In the model, the solids upflow and downflow velocities are given by u_{su} and u_{sd} respectively, with the volume fractions of solids travelling in each direction given by f_u and f_d . The two streams of solids are assumed to move in plug flow. The upward solids stream is the result of solids displaced vertically in the wakes of bubbles and by bubble

induced drift. A downflow of solids must be present in order to balance this upflow, so that there is no net mass flux at any horizontal layer:

$$f_u u_{su} = f_d u_{sd} \quad (2.37)$$

Solids (of component i) are exchanged in the horizontal direction according to a solids exchange coefficient K_{si} . Mass conservation of component i requires that:

$$f_d \frac{\partial c_{sdi}}{\partial t} + f_d u_{sd} \frac{\partial c_{sdi}}{\partial z} + K_{si} (c_{sdi} - c_{sui}) = 0 \quad (2.38)$$

and

$$f_u \frac{\partial c_{sui}}{\partial t} + f_u u_{su} \frac{\partial c_{sui}}{\partial z} + K_{si} (c_{sui} - c_{sdi}) = 0 \quad (2.39)$$

where c_{sui} and c_{sdi} refer to the concentrations of component i in the upflow and downflow regions respectively. Thus the input parameters to the model are f_u, f_d, u_{su}, u_{sd} and K_{si} , with an additional constraint given by the relationship in equation 2.37.

The basic model has been enhanced by various workers over the years. Sitnai (1981) included an additional downflowing solids layer to account for faster solids downflow at the walls of the bed. Shen *et al.* (1995) incorporated lateral mixing effects by discretizing the bed across its width and adding a lateral diffusion model for the solids exchange between the downflowing layers in adjacent elements, and found favourable comparisons between their model results and the experimental work of May (1959) and Valenzuela and Glicksman (1984).

The countercurrent backmixing model seems to represent the mixing in bubbling beds somewhat better than other models, despite the fact that other mixing mechanisms such as splashing at the bed surface and turbulent mixing at the distributor are not accounted for. The main limitation of the model appears to be the difficulty in determining an appropriate solids exchange coefficient K_s .

In this work, a number of experiments have been performed in order to compare the characteristics of solids mixing behaviour at different scales. Relevant experimental work involving the solids mixing models introduced above will be covered in Chapter 6,

where solids mixing experiments used for similarity comparison in the current work will be reported on.

2.3.6 Motion of Neutrally-Buoyant Objects in Bubbling Fluidized Beds

When particles in fluidized beds differ sufficiently in size and or density, segregation effects start occurring. Materials are described as either flotsam or jetsam, depending on their tendency to remain in the top or bottom of the bed respectively. Segregation has been found to depend on the relative sizes and densities of the particles, and also on the fluidizing velocity.

When the size difference between the particles is at least an order of magnitude, a pseudo-hydrostatic effect starts to occur. This is usually reported for cases of only a few large particles or objects present, so the overall bed behaviour is not significantly affected by their presence. In this case, the difference between the density of the large particles and the density of the bulk emulsion then determines the segregation tendency of the large particles and the following general observations have been made (*eg Rios et al., 1986*):

- Low density objects float on the bed surface;
- Objects with a density near that of the bulk emulsion at minimum fluidization conditions circulate throughout the whole bed;
- High density objects settle to the bottom of the bed and stay there.

Flat objects may not follow the above guidelines (*Nienow and Cheesman, 1980*) and even low-density flat objects tend to settle to the distributor, particularly at low gas velocities. For large objects with a density that promotes circulation throughout the bed, the object is carried upwards to the bed surface in an irregular fashion under the influence of rising bubbles, and moves downwards under the influence of the dense phase (*Nienow et al., 1978*).

Lim and Agarwal (1994) made detailed observations of the motion of large and lighter objects under the influence of bubbles using a two-dimensional bubbling bed of ballotini with plastic spheres and coal particles. They found that the large particle most often descended near the wall region of the bed with a velocity comparable to the calculated solids dense-phase velocity. They also found extensive interaction between

the large particle and the bubbles in the middle section of the bed, with the particle subjected to large upwards and downwards velocities in that region. The average upward component of the particle was found to be about $0.3U_B$, with the particle travelling a significant distance upwards in the bubble wake, but overall, the average upwards velocity was only $0.07U_B$. (due to the particle being shed-off intermittently along the way). Their data agreed well with the previous work of Nienow *et al.* (1978) and Rios *et al.* (1986) who made observations in three-dimensional beds.

Because they are affected by bubble and solids behaviour, the motion of these large, neutrally buoyant objects can be used in hydrodynamic studies. Apart from the work of Lim and Agarwal (1994) mentioned above, Merry and Davidson (1973) used a large "radio-pill" as a tracer in an experimental investigation of gulf-streaming; Bellgardt and Werther (1986) used subliming dry-ice pellets to study solids mixing and Linjewile and Hull *et al.*, (1993) used various larger and lighter spheres equipped with thermocouples to investigate heat transfer coefficients between bed and sphere.

In this work, a solids motion investigation using large, neutrally buoyant spheres was undertaken as an alternative means of comparing bed behaviours at different scales. This will be covered in Chapter 6.

2.4 The Need for Scaling Laws for Bubbling Fluidized Beds

As previously mentioned, the behaviour of large fluidized beds can differ significantly from smaller ones and several physical models of different sizes are usually required as part of the development of the full-scale fluidized bed unit. For reasons of chemical kinetics (or sometimes just convenience), the same bed material has often been employed in the different sized units as part of the scale-up process. However, it is now well recognised that the bed diameter has a marked effect on the bed hydrodynamics and simply using the same particles in a smaller container can lead to problems. Werther (1974) found that for a fine quartz sand the bed diameter had to be at least 500 mm before wall effects could be considered negligible in the bubbling regime; and Glicksman and McAndrews (1985) showed that for coarse particles (combustor bed material) the bed width had to be at least 5 times the mean bubble diameter for the bubble behaviour to be independent of wall effects. Therefore, if smaller scale models are to be used effectively, a different approach (scaling laws) must be employed.

Although in principle, the behaviour of a system of particles suspended in a fluid is completely determined by the Navier-Stokes equations and Newton's equations of motion, the problem becomes far too complicated to permit direct solution when considering more than a few particles. Early attempts to describe momentum conservation equations for bubbling fluidized beds were made (eg Anderson and Jackson, 1967), but could only be applied with limited success because of the simplifications necessary to make calculations possible.

Whilst complete and reliable numerical simulation of bed behaviour eludes us, simplification to the scale-up methodology could still be achieved with the application of a suitable scaling law by reducing the number of intermediate steps in development from laboratory to commercial scale. This fact was appreciated decades ago, but for many years, it was believed that the bubbling behaviour of a fluidized bed was too random to develop any form of scaling law for it.

2.5 Scaling Laws from Dimensional Similarity

Although the approach of dimensional similarity had been applied to fluidized beds before, it wasn't until the 1980's that dimensionless groups were applied specifically to the problem of bubbling fluidized bed scale-up. The rationale was that if fluidization phenomena are geometrically similar like other fluid dynamic problems, scale-up methodology could be greatly simplified by dimensional analysis. Thus the use of appropriate groups of dimensionless numbers would enable a large-scale fluidized bed to be modelled accurately by laboratory experiments. The following section outlines the development of the various proposed sets of dimensionless groups and their application to scaling fluidized beds.

2.5.1 Early Work on Dimensionless Groups

The first hint of a scaling law came in 1962, when Romero and Johanson considered dimensionless groups in an investigation of what factors influenced bubbling fluidized bed behaviour. They recognised that a comparison of several dimensionless terms in

different beds gave a better indication of the likely bed behaviour than considering one term in isolation.

Starting with a theory which treats the fluidizing medium and dense bed as physically separate phases, they considered two cases: In the first case the bed was more or less homogeneous with relatively small differences between the densities and viscosities of the dense bed and the support fluid; corresponding to liquid-solid fluidization. In the second case the dense phase was treated as an emulsion and the bed viscosity was considerably higher than that of the support fluid; this was used to describe gas-solid fluidization.

By considering a sinusoidal disturbance through the bed and the equations for stability at the bed surface, Romero and Johanson were able to derive dimensionless groups from the stability equations, for the cases of liquid-solid and gas-solid fluidization:

liquid-solid fluidization:

$$\frac{\rho_s - \rho_f}{\rho_f}, \frac{U_{mf}^2}{gd_p}, \frac{d_p U_{mf} \rho_f}{\mu}, \frac{d_p}{L}$$

(2.35)

gas-solid fluidization:

$$\frac{U_{mf}^2}{gd_p}, \frac{d_p U_{mf} \rho_s}{\mu}, \frac{d_p}{L}$$

(2.36)

In the set proposed for liquid-solid fluidization, the first group is the density ratio, the second is a form of Froude number, the third is particle Reynolds number and the fourth group is the length ratio. In gas-solid fluidization, the density ratio is absent, and the Reynolds number is defined somewhat differently, involving solid density and bed viscosity. It is interesting to note that Romero and Johanson did not think the density ratio was an important parameter in gas-solid fluidization; subsequent workers (eg Fitzgerald *et al.* 1984, Glicksman, 1984) chose to include this term for similarity in gas-solid fluidization, and it was later shown to be important under certain conditions (Leu & Lan 1992; Farrel *et al.*, 1998).

A similar set of criteria were proposed by Broadhurst and Becker (1973), developed using the approach of the Buckingham-Pi method. They chose to use the superficial gas velocity in place of the minimum fluidization velocity as a way of ensuring that "no

prior knowledge of the fluidized system is required other than the properties of the solid and fluid, and the dimensions of the bed". The groups proposed are as follows:

$$\frac{\rho_f}{\rho_s}, \frac{Lg}{U^2}, \frac{d_p U \rho_f}{\mu}, \frac{L}{d_p} \quad (2.37)$$

Note that in this set of groups the length parameter in the Froude group is a characteristic bed length such as bed diameter; not the particle diameter as used by Romero and Johanson. Also, the Reynolds number term here is the more conventional particle Reynolds number (based on fluid density and viscosity).

Fitzgerald *et al.* (1984) used the same set of four dimensionless groups as Broadhurst and Becker to test the scaling relationships on large industrial fluidized bed combustors.

Glicksman (1984) also proposed a set of dimensionless groups identical to those of Fitzgerald; however the approach used in obtaining them was somewhat different, making it possible to consider separately the cases of inertial-dominated or viscous-dominated flow. Because of this, Glicksman's approach offered some new insight and is summarised below:

2.5.2 Development of the Scaling Law of Glicksman (1984)

Glicksman derived his scaling laws by non-dimensionalising the equations of motion for the particulate and gas phases. These governing equations for motion and mass conservation were originally derived by Anderson and Jackson (1967, 1969). Conservation of mass for the fluid and the particles leads to the following equations:

$$\text{Fluid:} \quad \text{div}(\varepsilon \bar{u}) = 0 \quad (2.38)$$

$$\text{Particles:} \quad \text{div}[(1 - \varepsilon) \bar{v}] = 0 \quad (2.39)$$

where ε is the void fraction and \bar{u} and \bar{v} are the velocities of the gas and particles as vectors. Similarly, the equations of motion for the fluid and particles are given by:

$$\text{Fluid:} \quad \rho_f \varepsilon \left[\frac{\partial \bar{u}}{\partial t} + \bar{u} \cdot \text{grad}(\bar{u}) \right] + \bar{i} \rho_f g \varepsilon + \text{grad}(p) + \beta(\bar{u} - \bar{v}) = 0 \quad (2.40)$$

$$\text{Particle:} \quad \rho_s (1 - \varepsilon) \left[\frac{\partial \bar{v}}{\partial t} + \bar{v} \cdot \text{grad}(\bar{v}) \right] + \bar{i} \rho_s g (1 - \varepsilon) - \beta(\bar{u} - \bar{v}) = 0 \quad (2.41)$$

where \bar{i} is the unit vector in the vertical direction, and p is pressure. The term $\beta(\bar{u} - \bar{v})$ represents the drag force between the fluid and the particles. β is not constant but can be determined from a general expression for fluid drag such as the Ergun equation (Ergun, 1952). In the above expressions for conservation of momentum, forces resulting from inter-particle collisions and electrostatics effects are neglected. Possible boundary conditions are:

$$\text{At the distributor:} \quad \bar{u} = \frac{\bar{i}U}{1 - \theta} ; \quad \bar{v} = 0 \quad (2.42)$$

(θ is the fractional area of the distributor available for flow)

$$\text{At the walls:} \quad \bar{u} = 0 ; \quad \bar{v} = 0 \quad (2.43)$$

$$\text{Above the bed surface:} \quad \bar{u} = \bar{i}U ; \quad \bar{v} = 0 \quad (2.44)$$

After non-dimensionalising Equations 2.38 to 2.44, the resulting scaling parameters are:

$$\frac{\beta d_p}{\rho_s U}, \frac{gD}{U^2}, \frac{d_p}{D}, \frac{\rho_f}{\rho_s}, \frac{P_0}{\rho_s U^2} \quad (2.45)$$

where P_0 is the pressure in the freeboard. Usually the last term is neglected because the absolute pressure does not vary sufficiently within the bed to change fluid properties. In addition to these groups, particle sphericity (Φ_s) and particle size distribution (commonly abbreviated to psd) must also be maintained. When these dimensionless groups are compared with those of Fitzgerald *et al.* (1984) in (2.37), it can be seen that the only difference is that the Glicksman groups contain a more general drag expression

in place of the particle Reynolds number. The drag coefficient β in this expression can be determined (for example) from the Ergun equation:

$$\beta|\bar{u} - \bar{v}| = \frac{\Delta P}{L} = 150 \frac{\varepsilon(1-\varepsilon)^2}{\varepsilon^3} * \frac{\mu|\bar{u} - \bar{v}|}{(\phi_s d_p)^2} + 1.75 \frac{\varepsilon^2(1-\varepsilon)}{\varepsilon^3} * \frac{\rho_f |\bar{u} - \bar{v}|^2}{\phi_s d_p} \quad (2.46)$$

and for perfectly spherical particles ($\phi_s = 1$):

$$\frac{\beta d_p}{\rho_s U} = 150 \frac{\varepsilon(1-\varepsilon)^2}{\varepsilon^3} \left[\frac{\mu}{\rho_f U d_p} \right] \frac{\rho_f}{\rho_s} + 1.75 \frac{\varepsilon^2(1-\varepsilon)}{\varepsilon^3} \frac{|\bar{u}' - \bar{v}'|}{U} \frac{\rho_f}{\rho_s} \quad (2.47)$$

where \bar{u}' and \bar{v}' are the dimensionless fluid and particle velocity vectors. The term in square brackets in Equation 2.47 is the inverse of particle Reynolds number, hence the first group of Equation 2.45 can be re-written in terms of particle Reynolds number as well as the solid-gas density ratio. In other words, the Glicksman groups (except for the last term) are identical to the Fitzgerald groups.

The first term on the right hand side of Equation 2.47 represents the viscous contribution to the drag, and the second term represents the contribution of fluid inertia. Glicksman proposed simplifications to the dimensionless groups of Equation 2.45 under conditions where either the viscous or inertial effects dominated.

Viscous limit

In situations where the viscous contribution to the drag is more than ten times the inertial contribution, the second term of the R.H.S. of (2.47) becomes insignificant when compared to the first, and can be neglected. This occurs in situations where the particle Reynolds number is 4 or lower. Taking the resulting equation and multiplying both sides by the density ratio (ρ_s/ρ_f) gives:

$$\frac{\beta d_p}{\rho_s U} \frac{\rho_s}{\rho_f} = 150 \frac{\varepsilon(1-\varepsilon)^2}{\varepsilon^3} \left[\frac{\mu}{\rho_f U d_p} \right] \quad (2.48)$$

This shows that the first and fourth groups in (2.45) do not have to be individually satisfied, but can be combined together into one group, the particle Reynolds number. This means that for viscous dominated flow (neglecting the pressure group), the Glicksman groups simplify to:

$$\frac{\rho_f U d_p}{\mu}, \frac{gD}{U^2}, \frac{d_p}{D}, \text{geometry}, \Phi, \text{particle size distribution} \quad (2.49)$$

Inertial limit

In situations where the inertial contribution to the drag is more than ten times the viscous contribution, the first term of the right hand side of Equation 2.47 becomes insignificant when compared to the second, and can be neglected. This occurs for particle Reynolds numbers of 400 or higher. Thus the dimensionless term on the left hand side of Equation 2.47 is a function of the gas-solid density ratio, and the number of dimensionless groups required for similarity are again reduced to 3:

$$\frac{gD}{U^2}, \frac{d_p}{D}, \frac{\rho_f}{\rho_s}, \text{geometry}, \Phi, \text{particle size distribution} \quad (2.50)$$

Later, Glicksman *et al* (1993) revised the simplified scaling laws for bubbling fluidized beds by recognizing that the applicable range of the laws could be extended if the additional requirement of constant solid to gas density ratio was met, with the same set of simplified parameters applying at both the viscous and inertial limits. The modified form of the simplified laws was presented thus:

$$\frac{gD}{U^2}, \frac{\rho_f}{\rho_s}, \frac{U}{U_{mf}}, \text{geometry}, \Phi, \text{particle size distribution} \quad (2.50a)$$

2.6 Model-Based Similarity Rule of Horio *et al.* (1986a)

An entirely different approach to scaling of bubbling fluidized beds was taken by Horio *et al.* in 1986. One of the limitations of formulations involving conservation of momentum equations (such as Glicksman, 1984) is that they cannot explicitly include bubbles. So rather than approach the problem by applying conservation of momentum equations to the gas and particulate phases, Horio *et al.* based their equations on a model of a bubbling fluidized bed developed in earlier work.

The basic assumptions of Horio's model are:

- 1) The two phase theory originally proposed by Toomey and Johnstone (1952) applies.
- 2) The velocities of bubbles in a freely bubbling bed are calculated using the bubble interaction model of Clift and Grace (1971).
- 3) The flow of particles around a bubble is the same as the case of an isolated bubble (Davidson, 1961).
- 4) Bubble splitting is estimated from the data of Toei *et al.* (1974) where the splitting frequency is found to be proportional to $U_{mf}^{-0.5}$.

Horio *et al.* argue that the particle diameter is not the representative length for the macroscopic flow field in the bed and should therefore not be used to non-dimensionalize the variables. Since the particle phase is treated as a continuous phase, the bed diameter is chosen as the characteristic length.

The scaling parameters that emerge from Horio's scheme are:

$$\frac{U - U_{mf}}{\sqrt{gD}}, \frac{U_{mf}}{\sqrt{gD}} \quad (2.51)$$

which can be rearranged to:

$$\frac{U^2}{gD} \text{ and } \frac{U}{U_{mf}} \quad (2.52)$$

Horio *et al.* expressed their scaling law in the form of equations:

$$U - U_{mf} = \sqrt{m}(U - U_{mf})^0 \quad (2.53)$$

Corresponding to the condition for geometrically similar bubble coalescence, and

$$U_{mf} = \sqrt{m} U_{mf}^0 \quad (2.54)$$

Corresponding to the condition for geometrically similar flow-field around a bubble and for similar bubble splitting.

Note that the superscript ⁰ refers to conditions in the original scale bed.

2.6.1 Equivalence of the Scaling Rules of Glicksman and Horio

When we compare Equation 2.52 with Equation 2.45 it is clear that Horio's scaling law requires less dimensionless parameters be kept constant. Glicksman (1988) showed that Horio's two scaling groups are actually equivalent to the subset of his own dimensionless groups (Glicksman 1984) for the viscous limit (low particle Reynolds numbers).

This was also shown by Roy (1989) using an different approach -as follows. Consider Equation 2.48 for the viscous regime:

$$\frac{\beta d_p}{\rho_s U} \frac{\rho_s}{\rho_f} = 150 \frac{\varepsilon(1-\varepsilon)^2}{\varepsilon^3} \left[\frac{\mu}{\rho_f U d_p} \right] \quad (2.48)$$

multiplying both sides by $\frac{D}{d_p}$ and then multiplying the R.H.S. by $\frac{g}{g}$ leads to

$$\frac{\beta d_p}{\rho_s U} \frac{\rho_s}{\rho_f} \frac{D}{d_p} = 150 \frac{\varepsilon(1-\varepsilon)^2}{\varepsilon^3} \frac{gD}{U} \frac{\mu}{\rho_f g d_p^2} \quad (2.48a)$$

multiplying both sides by a factor of $\frac{\rho_f}{\rho_s - \rho_f}$ gives:

$$\frac{\beta d_p}{\rho_s U} \frac{\rho_s}{\rho_s - \rho_f} \frac{D}{d_p} = 150 \frac{\varepsilon(1-\varepsilon)^2}{\varepsilon^3} \frac{gD}{U} \frac{\mu}{(\rho_s - \rho_f) g d_p^2} \quad (2.48b)$$

Now consider the expression for minimum fluidization velocity from Davidson and Harrison (1963):

$$U_{mf} = 0.00114 * \frac{gd_p^2(\rho_s - \rho_f)}{\mu} \quad (2.55)$$

Inverting and rearranging:

$$\frac{\mu}{(\rho_s - \rho_f)gd_p^2} = \frac{0.00114}{U_{mf}} \quad (2.55a)$$

Substituting this into Equation 2.48b and multiplying the R.H.S by $\frac{U}{U}$:

$$\frac{\beta d_p}{\rho_s U} \frac{\rho_s}{\rho_s - \rho_f} \frac{D}{d_p} = 150 \frac{\epsilon(1-\epsilon)^2}{\epsilon^3} \frac{gD}{U} \frac{0.00114}{U_{mf}} * \left(\frac{U}{U} \right)$$

$$\frac{\beta d_p}{\rho_s U} \frac{\rho_s}{\rho_s - \rho_f} \frac{D}{d_p} = 0.0171 \frac{\epsilon(1-\epsilon)^2}{\epsilon^3} \left(\frac{gD}{U^2} \right) \left(\frac{U}{U_{mf}} \right) \quad (2.56)$$

The resulting expression (Equation 2.56) for the viscous regime has now been written in terms of Horio's groups (Equation 2.52). It is encouraging that despite the reasoning between these approaches being quite different, they arrive at the same requirements for similarity under the stated conditions.

Note: The current work considers only *bubbling* bed hydrodynamics, and as such, scaling laws for *circulating* fluidized beds are outside the scope of this work. However, for reference it is worth mentioning that more recently, Horio extended his scheme to include circulating fluidized beds (Horio; 1989) as did Glicksman (1990, 1993a).

2.7 Scaling Parameters Based on Chaos Theory

In the early 1990's a number of workers provided experimental evidence to suggest that a gas-solids fluidized bed reactor is actually a chaotic system which could be characterised with a low-dimensional strange attractor (Daw *et al.*, 1990, Daw and Halow 1991; Schouten *et al.*, 1992). This suggested that the hydrodynamics of fluidization could be defined within the context of non-linear dynamic theory.

The consequence of the chaotic features of fluidization was that chaotic time-series analysis could be used to facilitate dimensionless scaling of fluidized beds (Schouten and van den Bleek, 1992) in several ways:

- 1) Chaotic time-series analysis could be applied to pressure fluctuation measurements to quantitatively assess and compare the *extent* of the chaos present within the fluidized bed systems under given operating conditions.
- 2) An indication of the number of significant degrees of freedom present within the systems could be obtained and related to the number of dimensionless groups required for hydrodynamic similarity.
- 3) The chaotic dynamics of fluidization could be incorporated into the scaling laws by extending them with an extra similarity group accounting for the time-dependency of the non-linear fluidization dynamics.

2.7.1 Ordered, Stochastic and Chaotic Systems

There are two kinds of system normally encountered in engineering situations. They are *deterministic ordered systems*, and *non-ordered stochastic systems*. Furthermore, there are two sub-classes of deterministic ordered systems; *conservative* systems in which the energy balance is restricted to the conservation of kinetic and potential energy (such as the ideal frictionless pendulum), and *dissipative ordered* systems where part of the energy can transform into other forms (*eg* sensible heat and friction) and dissipate.

Dissipative ordered systems are the ones most common to engineers. For this type of deterministic ordered system it is possible (and usual) to predict its evolution in time over an interval $[t_1, t_2]$. This is done by solving the combined energy, mass and momentum balances, given the initial conditions of the system (at $t = t_1$). In fact, it is

possible to predict the state of the system over any time interval up to infinity, based on a knowledge of the system's initial conditions.

The non-ordered stochastic system on the other hand, differs markedly from the ordered systems, especially with respect to its predictability. A *stochastic* system is completely unpredictable over the interval $[t_1, t_2]$. This means that given the initial conditions of the system at t_1 , it is *impossible* to predict the system's evolution over time even to the next fraction of a second. It is only possible to calculate an *expectation value*, which is a mean value of all possible states weighted by their probability density distribution.

The *predictability* of a given system can be defined in terms of Kolmogorov entropy (Grassberger, 1986) as follows: The information I (in bits) needed to predict the time evolution of a system over the interval $[t_1, t_2]$ given the information at t_1 (I_{t_1}) is given by:

$$I_{[t_1, t_2]} = I_{t_1} + K(t_2 - t_1) \quad \text{for } (t_2 - t_1) \rightarrow \infty \quad (2.57)$$

where K is the Kolmogorov entropy (expressed in bits per unit time). For a dissipative ordered system the Kolmogorov entropy equals zero. Thus from Equation 2.57 it follows that this type of system is completely predictable over any time interval, given the state of the system at the start of the interval. For a stochastic system the Kolmogorov entropy equals infinity. In other words, an infinite amount of information is needed to predict the system over any time interval.

For a *chaotic* system, the Kolmogorov entropy lies somewhere between zero and infinity. This means that a chaotic system is only to some extent predictable over a restricted time interval. This is the case for fluidized beds.

2.7.2 The Chaotic Similarity Group

Schouten and van den Bleek (1992) applied chaos theory to calculate the number of degrees of freedom (correlation dimension) at different operating conditions in a one-dimensional fluidized bed model and later compared these results with correlation dimensions obtained from chaos analysis of pressure fluctuations in a real fluidized bed

(Schouten *et al.* 1992). They concluded that a change in the correlation dimension corresponded to a change in fluidization regime.

Van den Bleek and Schouten (1993) subsequently suggested that the Kolmogorov entropy was an important parameter to consider when comparing the behaviour of scaled fluidized beds. The suggestion was that in addition to the energy, mass and momentum balances normally considered in engineering problems, an *information balance* should be included for chaotic systems. Their reasoning was that in both dissipative ordered systems and stochastic (infinitely chaotic) systems the Kolmogorov entropy is set (either zero or infinity respectively), and hence from Equation 2.57 *conservation of information* was obeyed implicitly. But in chaotic systems the Kolmogorov entropy has a non-zero finite value which can vary depending on system conditions. Applying the conservation of information rule in this situation results in a constant chaotic similarity group, $K\tau_0$ in which K is the Kolmogorov entropy and τ_0 is a characteristic time of the system involved. For a fluidized bed, van den Bleek and Schouten (1993a) proposed that

$$\tau_0 = \frac{d_p}{U} \quad (2.58)$$

where d_p is the particle diameter and U the superficial gas velocity. Thus the appropriate chaotic similarity group for a fluidized bed would be:

$$\frac{Kd_p}{U} \quad (2.59)$$

Note that for consistency with the simplified parameters, appropriate choices of a length dimension and velocity would produce a chaotic similarity group of:

$$\frac{KD}{U_{mf}} \quad (2.59a)$$

Their suggestion was that this law be applied in conjunction with previously proposed similarity laws (Glicksman, 1984), but they admitted that "In practice... it is impossible to fulfil all the similarity rules." So a reduced set of similarity rules, selected on the

basis of their importance to the specific system, should be employed instead, and "...although one cannot obey all similarity rules, one should try to obey this (chaotic) one at least."

There is a difficulty in predicting the value of K in a given system, for if one wishes to maintain $\frac{Kd_p}{U}$ constant in different systems, one must know the value of the Kolmogorov entropy in order to evaluate the chaotic similarity group.

Van den Bleek and Schouten (1993) found that the Kolmogorov entropy was both quantitatively and qualitatively related to fluidized bed hydrodynamics. In experimental investigations (van der Stappen *et al.*, 1995) the values for Kolmogorov entropy were generated from chaos analysis of "global" bed pressure fluctuations. As has been widely reported (eg Roy & Davidson, 1989; van der Schaaf *et al.*, 1998) global pressure fluctuation measurements mostly register the effect of bubble eruption at the bed surface, reflecting the behaviour of the whole bed, rather than a localised region near the probe itself.

Following on from the reasoning that the Kolmogorov entropy values generated in this way were dependent on the influence of bubbles at the bed surface, van der Stappen *et al.* proposed a semi-theoretical relationship between Kolmogorov entropy and bed properties.

They proposed that the Kolmogorov entropy K (the rate of information loss) would be proportional to the flow of erupting bubbles (N_b), and that each bubble eruption would cause a certain amount of information loss. The amount of information lost per bubble eruption depended on how severely the bed was affected by the eruption; a large bubble erupting would have a greater effect than a small one. They termed the effect of the bubble eruption on the bed behaviour the bubble "impact" (I_b). Hence:

$$K \propto N_b * I_b \quad (2.60)$$

The flow of erupting bubbles (the number of bubbles erupting per unit time per unit area) can be expressed in the form of the correlation of Darton *et al.*, (1977) under the assumption that all excess gas is transported in the form of bubbles:

$$N_b = \frac{(U - U_{mf})}{V_B} \quad (2.61)$$

Where V_B is the bubble volume. As a first approximation, the bubble impact I was assumed to be proportional to relative bubble size (D_B/D). So Equation 2.61 becomes:

$$K \propto N_b * I_b = N_b \frac{\pi}{4} D^2 \left(\frac{D_B}{D} \right) = \frac{1.5(U - U_{mf})D}{D_B^2} \quad (2.62)$$

By applying their experimental data to this expression, van der Stappen *et al.*, arrived at the following expression for bubble size:

$$D_B = 0.44(U - U_{mf})^{0.3} H_s^{0.8} g^{-0.2} \quad (2.63)$$

which is of similar form to the bubble diameter correlation of Darton *et al.* and agrees generally with this and other bubble diameter correlations to within about 20%. This agreement therefore shows some validity for the expression (2.62).

For the same experimental data they fitted an expression for Kolmogorov entropy in terms of the system parameters; superficial gas velocity, minimum fluidization velocity, bed diameter and settled bed height:

$$K = 10.7 \left(\frac{U - U_{mf}}{U_{mf}} \right)^{0.4} \frac{D^{1.2}}{H_s^{1.6}} \quad (2.64)$$

where H_s is the height of the settled bed. (K will be in bits/second when the other parameters are expressed in S.I. form.) If generally applicable, this expression would solve the difficulty in evaluating K and thus the chaotic similarity group (Kd_p/U) could be calculated based on system parameters. Experimental verification of this expression for a limited range of operating conditions has followed (Schouten, *et al.*, 1996), although the value of K derived from experiment is somewhat dependent on the location of the measurement probe, indicating that K is not constant throughout the bed under given operating conditions.

Finally, van der Stappen (1996) and Schouten *et al.*, (1996) made the observation that when the simplified scaling parameters were employed experimentally, it appeared that the value of K remained constant when using \sqrt{m} to normalise the time-scale. In other words, the chaotic similarity group in fact appears to be matched *automatically* at the different scales when following simplified scaling. At face value this makes sense considering that their measurements of K are derived from pressure fluctuations originating as bubble phenomena, and these bubble phenomena are precisely what formed the basis for deriving the original Horio *et al.*, (1986a) scaling law.

Following this idea, it can be seen that in the van der Stappen *et al.*, (1995) development for a K correlation and corresponding bubble size correlation (Equation 2.63), the bubble size D_B very nearly follows perfect geometric scaling. That is, for perfect scaling (employing the length ratio scaling factor m of Horio *et al.*, 1986a) we would expect:

$$D_{B2} = m D_{B1} \quad (2.65)$$

and applying the Horio similarity criteria into Equation 2.63 we arrive at:

$$D_{B2} = m^{0.95} D_{B1} \quad (2.66)$$

which is quite close. Additionally, from Equation 2.64 by applying the simplified parameters for a scale change we can arrive at:

$$K_2 = m^{-0.4} K_1 \quad (2.67)$$

which, as is pointed out by Schouten *et al.* (1996) is close to the required scaling factor of $m^{-0.5}$ required for complete consistency with the simplified parameters.

To conclude, if the measurements of K are made from pressure fluctuations originating as bubbles (and indeed the value of K can be correlated with bubble phenomena), then this author tentatively suggests that the chaotic similarity group may not be an independent parameter in bubbling bed scaling but in fact simply a different representation of the existing similarity criteria.

2.8 Overview of Measurement Techniques in Fluidized Beds

The measurement techniques that have been used in fluidized beds are many and varied. The current work employs three measurement techniques, (pressure probes, electrical capacitance tomography and tracer particles) which will be dealt with in detail later. The purpose of this introduction is to illustrate the wide range of techniques that have been applied to fluidized beds. Recent review articles on this topic are Grace and Baeyens (1986), Yates and Simons (1994), Louge (1997) and Werther (1999).

The first and possibly the most valuable piece of measurement equipment for the experimental study of fluidized beds is the eyeball. For this reason, many laboratory fluidized bed systems are constructed of transparent materials so that the bed can be visually observed. Visual observation however is limited to the bed surface and wall regions; it is not possible to see what is going on in the middle of a bubbling bed. Thin slice or "two-dimensional" fluidized beds have been extensively used to observe bubble behaviours, these have the drawback that the wall effects on the bed behaviour are considerable.

Visual observation is only a qualitative tool unless images can be recorded and analysed. Thus the use of photography, cine film, analog and (more recently) digital video cameras has allowed visual observation of fluidized beds to be quantified.

The methods of measuring bed behaviours fall into two categories; *intrusive* and *non-intrusive*. Intrusive techniques involve some sort of probe inserted into the bed to make measurements, and have the disadvantage that they will affect the bed behaviour in the vicinity of the probe and quite possibly influence the very thing they are trying to measure. A study was carried out by Rowe and Masson (1981) to evaluate the effect of various probe designs on bed behaviour using x-ray cine photography. They concluded that all probes disturb the bubbles to a greater or lesser extent depending on their design. Non-intrusive measurement techniques on the other hand measure internal bed behaviours from outside, without disrupting the flow which is a distinct advantage. Unfortunately non-intrusive techniques are in general much more expensive than intrusive ones. Table 2.1 shows the various intrusive and non-intrusive techniques that have been widely used in bubbling fluidized beds.

Intrusive Measurement Techniques	Application	Non-Intrusive Measurement Techniques	Application
Optical probe	Local bed voidage	Eyeball	Fluidization regime, qualitative bed behaviour
Boroscope	Local visual observations	Photography, Cine and Video	Bubble and particle motion at walls or bed surface
Pressure probe	Local or global bed pressure	Wall pressure tappings	Bed pressure near wall
Gas sampling probe	Tracer gas sampling	Inductance loops	Ferromagnetic tracer detection
Capacitance probe	Local bed voidage	X-ray photography and tomography	Bubble imaging, bed voidage
Solids-sampling probe	Tracer particle sampling	γ -ray tomography	Bubble imaging, bed voidage
Particle impact probe	Particle momentum	Positron emission particle tracking (PEPT)	Single particle tracking
Solids pressure probe	Solids pressure	Electrical capacitance tomography (ECT)	Bubble imaging, bed voidage

Table 2.1 Some bubbling bed measurement techniques

Tracers and sampling systems have often been employed to examine the mixing of solids and gases within fluidized beds. Coloured gases such as NO_2 (eg Wace & Burnett 1961) have been used and the mixing observed visually, or chemically different gases have been introduced into the bed and sampled at a different bed location. For solids mixing studies, the idea is to manufacture a particle which has the desired fluidization characteristics, but which can be identified from the bulk bed material in some other way. Tracers which have been used include coloured particles (eg Basesme & Levy 1992), radioactive particles (eg Weinell *et al*, 1997), salt particles (eg Rhodes *et al*, 1991), ferromagnetic particles (eg Avidan & Yerushalmi, 1985), heated particles (eg White & Zakhari, 1998) and phosphorescent particles (eg Wei *et al*, 1998); specific means of detection have been developed in each case.

All measurement techniques have advantages and limitations, it is very important that any technique employed is appropriate for its intended application and that the limitations of the technique are well understood by the user. In the relevant chapters to follow, the techniques used in the current scaling law investigation will be described in

detail along with their limitations. First, however, the experimental work carried out in previous scaling law investigations will be reviewed.

2.9 Experimental Verification of the Scaling Laws for Bubbling Beds

Numerous measurement techniques have been used to verify the proposed scaling laws in fluidized beds. When two fluidized beds are hydrodynamically similar, their dependent hydrodynamic phenomena, when expressed in dimensionless form, will be identical. The objective of experimental verification is to measure and compare dependent hydrodynamic phenomena in fluidized beds constructed according to the scaling laws. Examples of dependent hydrodynamic phenomena (such as the bubble diameter, frequency and rise velocity, as well as solids particle velocity and bed turnover time) have been introduced in Sections 2.3 and 2.4. These can either be measured directly (where possible) by visual observation (*eg* Horio *et al*, 1986a), or inferred from time-resolved pressure fluctuation or voidage measurements (*eg* Almstedt & Zakkay, 1990). This section summarises the experiments performed and their results.

Glicksman (1999a) provides an excellent overview of the approach to fluidized bed scale-up generally, as well as a detailed summary of scaling law experimental verification work. On the following page, Table 2.2 outlines the systems investigated by other workers and for further information a complete summary of the experimental conditions for all previous scaling law work in bubbling fluidization is given in Appendix A.

Although the present work deals only with experimental verification of the simplified scaling laws for bubbling fluidized beds, the full and simplified scaling laws are closely associated, hence investigations of the full set of scaling laws have also been included in this review.

Reference	Scaling Laws	System and Measurements
Fitzgerald & Crane (1980)	Full	Rectangular beds of cork/air & sand/freon with "bead" distributors; average frequency of pressure signal (from wall taps); movies of various beds
Fitzgerald <i>et al</i> (1984)	Full	Limestone/hotair (combustor) & copper/air (model) +2D beds; autocorrelation function of pressure signal (wall taps); movies in 2D beds
Nicastro & Glicksman (1984)	Full	Coal combustor & iron grit/air (model); pressure signal (from double probe); probability density and power spectra
Horio <i>et al</i> (1986a)	Simplified	3 cold models with various glass beads; bubble parameters calculated from video of bed surface
Horio <i>et al</i> (1986b)	Simplified	4 cold models with sand; magnetic sand and large float tracers were used to look at solids mixing. Tapered bed and different orifice pitch also investigated.
Newby & Keairns (1986)	Full	Rectangular beds of glass/air and steel/pressurised air or CO ₂ ; movies and single pressure wall tappings
Zhang & Yang (1987)	Simplified	2D beds of sand/air; photograph, average pressure and entrainment rate (collected solids in test-tube above bed)
Roy & Davidson (1989)	Full and Simplified	Low vs high temperature, and low vs high pressure bed pairs with various solids; single and double pressure probes used for pressure fluctuation frequency and amplitude comparison
Almstedt & Zakkay (1990)	Full	Hot pressurised vs cold pressurised beds of sand-like bed materials; capacitance probes used to infer bubble characteristics
Leu & Lan (1992)	Full and Simplified	2D beds hot and cold with various fluids (Air/He/Freon) and particles (alumina/sand/cork/silica) Compared pressure fluctuations from probes
Di Felice <i>et al</i> (1992a)	Full	5 ambient or pressurised cold models with various solids; bed height plus variance and spectra of pressure fluctuations (from wall tapping) sampled at 20Hz for at least 10 seconds.
Di Felice <i>et al</i> (1992b)	Full	6 ambient or pressurised cold models with various solids to compare pairs of A, B and D materials; amplitude and frequency data from pressure fluctuations (wall tapping).
Rapagna <i>et al</i> (1992)	Full	10 ambient or pressurised cold models (5 matched pairs) of group A materials, compared by amplitude and frequency of pressure fluctuations (wall tapping).
Van der Stappen (1996)	Simplified	Air/sand ambient beds compared by amplitude, frequency and KML of pressure fluctuations from wall tappings. Very large number of data points collected at high sampling frequency
Farrell <i>et al</i> (1998)	Simplified	Same-sized bed used with 2 materials with mis-matched particle densities but same U_{mf} .
Stein <i>et al</i> (1998)	Simplified	Small ambient cold models (air with various particles); PEPT used to quantify movement of single particle within bed by an average circulation frequency
Brue and Brown (2001)	Full	Small beds, ambient air/sand and pressurised air/steel shot; differential pressure "probes" used for frequency spectra comparison (20 to 40 Hz sampling).

Table 2.2 – Summary of bubbling bed scaling law experimental verification work.

2.9.1 Review of Previous Experimental Verification Studies

Fitzgerald and Crane (1980) evaluated the full set of hydrodynamic scaling parameters in bubbling fluidized beds. Pressure fluctuations between bed and freeboard (so-called "global" fluctuations) and movie films of two correctly scaled rectangular cross-section beds were compared. One bed was cork particles fluidized with air, the other was sand fluidized with Refrigerant-12 vapour. The distributors were made of approximately scaled glass and lead beads respectively. The movies, which were filmed at different frame-rates in anticipation of the different time-scales of the two beds, were reported to show similarities in bubble growth and solids flow patterns in the fluidized beds. The ratio of the minimum fluidization velocities in each bed was within 20% of the theoretical value, with the authors suggesting that the difference was due to interlocking of the cork particles (particle sphericity was not matched between the beds). The fast Fourier transform of the pressure fluctuations was used to determine their average frequency, and the ratio of the average frequencies in the two beds agreed reasonably well with the predicted velocity-time scale factor. As well as some additional movies involving beds of tungsten-carbide/water and expanded-polystyrene/air, a comparison was made of slug behaviour, with movies showing that the slugs appeared to have the same scaled lengths and velocities. Unfortunately, no mis-scaled system was reported in the work to check the methods of comparison.

Following on from the initial study, Fitzgerald *et al.*, (1984) measured global pressure fluctuations in an atmospheric fluidized bed combustor and a one-quarter scale cold model (air-fluidized copper particles). They extended the modelling concept to include two-dimensional cold models (also following the scaling laws) of helium-fluidized sand and air-fluidized copper. The full set of hydrodynamic scaling parameters was matched between the beds. In the case of the two-dimensional beds, a comparison of the autocorrelation function of the pressure fluctuations showed that it was qualitatively similar, but not within the 95% confidence interval that they had expected. In the case of the combustor and scaled cold-model, the amplitude of the autocorrelation function of the combustor was considerably lower, and the experimentally determined time-scaling factor differed from the theoretical value by 24%. In both comparisons, the authors suggested electrostatic effects might be a cause of the discrepancy, which is certainly a possibility. However, they do not mention particle size distribution or particle sphericity, and failure to match these could also account for the differences.

Also, the combustor had a bubble-cap distributor, while their cold model had a perforated plate distributor. Although the ratio of distributor to bed pressure drops were similar, the different distributor geometries as well as the presence of internals may have had some effect. Once again, no deliberate mis-match of the beds was performed for comparison.

Nicastro and Glicksman (1984) experimentally verified the full set of hydrodynamic scaling laws for bubbling fluidized beds between a bubbling fluidized bed combustor and a scaled cold model. They compared the time-resolved pressure fluctuations from differential (so-called "local") pressure measurements. The power spectra and probability distributions of the fluctuations agreed well for the correctly scaled systems. When the hot bed material was used directly in the scaled cold bed (a deliberate mis-match), the agreement was poor. Attention was paid to particle sphericity and particle size distribution and the effects of these variables on the local bed voidage, and its consequences for local bed pressure drop were stressed. Although the full set of similarity rules were adhered to, there was a reasonably large discrepancy in the solid to gas density ratio (about 23%). However, experimental verification was only carried out at low particle Reynolds number (approximately 5), hence only the viscous dominated regime was investigated (where it is suggested that the density ratio can be neglected).

Horio *et al.*, (1986a) used three geometrically similar bubbling beds of different sized glass beads fluidized with ambient air to verify their proposed scaling laws. Because the solid to gas density ratio was not varied, they were essentially using an equivalent of the "simplified" set of scaling parameters as defined by Glicksman *et al.* (1993). Video analysis of the bubble bursts at the bed surface were used to determine the cross-sectional average bubble diameter, bubble diameter distribution and radial distribution of the superficial bubble velocity. Similarity was generally achieved in these results when the simplified scaling law was followed, however there were some anomalous results in the comparisons of superficial bubble velocity.

Horio *et al.*, (1986b) verified the bubbling bed scaling laws introduced in Horio *et al.*, (1986a) for solids mixing and the motion of large particles. Air-fluidized beds of silica sand were used with both straight and tapered bed geometries. A bed sectioning technique was employed to determine the transient radial dispersion coefficient from a column of tracer particles placed at the bed centre, and the distribution of float tracers. The conclusion was that the simplified scaling laws were obeyed for mixing and

segregation in both straight and tapered geometries. The particle Reynolds numbers in the investigation were quite low (approximately 1) hence the experiments fall within the viscous-dominated regime. In these experiments, the minimum fluidization velocities ratio and the geometric ratio m , were not perfectly matched according to the scaling criteria (in one case the error is around 40%) although this appears to have had little effect on the results. Apart from this discrepancy, there was no deliberate system mismatch investigated, so there is no information about how this would influence the solids mixing behaviour.

Newby and Keairns (1986) compared two different cold models scaled using the full set of scaling laws. The larger bed consisted of glass powder fluidized by ambient air, the smaller bed was a half-scale version of the first, consisting of steel powder fluidized with air under pressure. The non-dimensional bubble frequencies taken from high-speed movies of the beds agreed well. They also found reasonably good agreement between the non-dimensional amplitude of the pressure fluctuations in the beds. No mis-matched systems were considered.

Zhang and Yang (1987) compared a pair of scaled two-dimensional cold models where the simplified scaling laws (including constant solid-to-gas density ratio) were employed. The beds consisted of air-fluidized sand at ambient pressure. Photographs showed that the beds appeared qualitatively similar and they also found the dimensionless bed heights and freeboard entrainment rates were similar. They suggested that their version of the simplified scaling laws (equivalent to Horio *et al* 1986a) was appropriate for particle Reynolds numbers in the range $4 \leq Re_p \leq 400$ if one assumed that only the *total* drag force acting on the particle had to be similar, rather than the specific contributions of viscous and inertial drag. Their experiments, which were conducted at relatively high particle Reynolds numbers (from 24 to 78) would seem to confirm this, but unfortunately, no mis-matched system was investigated to verify the sensitivity of their measurements.

Roy and Davidson (1989), tested the validity of the full set and the viscous limited scaling laws for a number of bubbling bed systems including some at elevated temperatures and pressures. Experiments were performed in two scaled pairs of fluidized beds; one pair examined the effect of temperature, the other pair examined pressure effects. Measurements of global and local pressure fluctuations were made, with emphasis given to the different phenomena contributing to each type of

measurement. The non-dimensional dominant frequency and amplitude of the pressure fluctuations were used as the basis for the comparison. From their results they concluded that 2 groups (forming the simplified scaling laws) were sufficient for bed similarity for particle Reynolds numbers less than 30, but for particle Reynolds numbers higher than this, the additional requirements of similar solid-to-gas density ratio (ρ_s/ρ_f) and particle to bed diameter ratio (d_p/D) had to be satisfied. Although the various dimensionless parameters have been relaxed in different runs, presumably to evaluate the importance of each, it does not appear to have been carried out in a systematic way. It would also seem that the particle density and gas to solid density ratio data have been incorrectly reported for some runs, and the use of logarithmic axes on the plots leave the distinction between scaled and mis-scaled results open to different interpretations.

Almstedt and Zakkay, (1990) used the full set of scaling laws in the comparison of a hot pressurised fluidized bed combustor (PFBC) and a pressurised cold scale-model. They used a capacitance probe to measure the mean values of bubble frequency, bubble pierced length, bubble rise velocity and bubble volume fraction. Scaling comparisons were made by non-dimensionalising the bubble parameters. The cold bed was tested with three different bed materials: Olivine sand and two different size distributions of the original bed material from the hot bed. The sand differed from the hot bed material in terms of sphericity and density. The hot bed material with the incorrect particle size distribution was used to show the sensitivity of the scaling to the particle-to-bed-diameter ratio. The non-dimensional form of the capacitance measurements agreed within 25% for the properly scaled bed material and the olivine sand, with the agreement best in the upper portion of the bed. The olivine sand showed only slightly worse agreement than the hot bed material, so the small mismatch in particle sphericity and density did not have a significant effect on the results. In the cold bed, the improperly scaled hot bed material showed a maximum deviation of 38% from the hydrodynamics of the PFBC. They concluded that a correctly scaled cold model can be used to successfully model the hydrodynamics of a large scale PFBC.

Leu and Lan (1992) investigated both the full and simplified scaling laws in a comprehensive set of experiments using three two dimensional models, with pressure fluctuations measured between in-bed probe and freeboard used for the comparison. They found that the full set of scaling laws could be successfully applied to different materials in the same bed (air-fluidized alumina at 270°C modelled by helium fluidized silica at ambient conditions) with a mismatch (air-fluidized alumina at ambient

conditions) showing poor similarity with the previous two in pressure fluctuation amplitude. Like Fitzgerald *et al.*, (1984) they also considered the autocorrelation function of the pressure fluctuations but concluded that for large time lags the autocorrelation function is likely to vary even for correctly scaled systems, hence the requirement of Fitzgerald that the results agree within the 95% confidence interval was unreasonable. They then considered the effect of scale change using the full set of scaling laws by comparing a large air-fluidized cork bed with a smaller matched freon-12-fluidized sand bed and mis-matched air-fluidized sand bed. Results for probability density function were inconclusive, but the autocorrelation function showed good agreement between the correctly matched beds and almost no agreement at all with the mis-matched bed. Finally they explored the simplified scaling laws by comparing two same-sized matched ambient beds (air-fluidized silica with a same-sized bed of air-fluidized alumina) and two same-sized matched hot and cold beds (air-fluidized silica at 270°C and air-fluidized silica at ambient conditions). They found that in the first case although the pressure fluctuation amplitudes agreed well, there were discrepancies in the fluctuation frequencies, and in the second case, although the fluctuation frequencies were similar, the fluctuation amplitudes were different. Note that although the simplified scaling criteria were matched in both these cases, the solid to gas density ratio was mis-matched in both cases, as was the Froude number in case 2. And there is a further technical criticism; the probe lengths are not provided but there is a chance that the small diameter of the probes used (approximately 1.6 mm) may have affected frequency responses due to over-damping of certain signal frequencies (van Ommen, *et al.*, 1999).

Di Felice *et al.*, (1992a) investigated the full set of scaling laws for bubbling and slugging fluidized beds. They pressurised different diameter fluidized bed columns to match the scaling parameters. Pressure fluctuation data, video measurements of bed expansion and minimum fluidization velocity were used to compare the similarity of five different bed configurations. Three beds matched the scaling laws closely, the fourth had a mis-matched particle sphericity and the fifth was out of scale. There was good agreement in the non-dimensional bed expansion measurements and the voidage at minimum fluidization velocity for all but the bed with the mis-scaled sphericity. (The lower particle sphericity in this case increased the minimum fluidization velocity for the system which effectively shifted the bed expansion curve.) In the bubbling regime, the pressure fluctuations for the three properly scaled beds showed good agreement while the mis-scaled beds showed poor agreement with the other three. In the slugging

regime, however, they found that the pressure fluctuation characteristics for all five beds were in poor agreement with each other, although the bed expansion characteristics were similar to those in the bubbling regime. They suggested that this was because particles within the solids plug experience conditions more like a packed bed and as a result the similarity rules which were developed for *fluidized* particles did not apply.

Subsequently, Di Felice *et al.* (1992b) evaluated the full set of scaling laws for bubbling and slugging beds of Geldart A, B and D particles using pressure fluctuations as a basis for comparison. For bubbling beds, the dominant frequency and the RMS of the pressure fluctuations agreed well for all particle types. For slugging beds, only Geldart type B and D particles were considered. Results showed reasonable agreement in the RMS of the pressure fluctuations, but poor agreement in the dominant frequency. They concluded that whilst the full set of scaling parameters were valid for bubbling beds, they were not appropriate for slugging beds where particle interactions in the solids plug were thought to be important.

Rapagna *et al* (1992) showed the full set of scaling laws could work for Geldart A powders in both the homogeneous and bubbling regimes, as suggested by Foscolo *et al.* (1990). The experiments were performed in 5 pairs of matched cold models of various Group A powders fluidized by air at different pressures. The RMS of the pressure fluctuations, the minimum fluidization and minimum bubbling velocities, and corresponding voidages were used for comparison and all showed good agreement. They cautioned against simplifying the scaling laws by neglecting the density ratio for Group A powders because of the strong influence gas density has on the minimum bubbling voidage for small particles with low terminal velocities. However, they suggested that the length ratio could be omitted if the bubbles were small in comparison with the bed diameter. It does not appear that any of the tests corresponded to a deliberate system mis-match.

Van der Stappen (1996) considered the application of chaos theory to the problem of fluidized bed scale-up and performed some similarity tests in a pair of air-fluidized beds of silica sand which were operated under conditions of the simplified scaling criteria with constant solid to gas density ratio. Global pressure fluctuation measurements were made at different scaled heights in each bed and their analysis showed good agreement in bed expansion, average absolute deviation of pressure fluctuations, probability density function, frequency spectra and Kolmogorov entropy but some discrepancies.

were noted near the distributor, most significant in Komogorov entropy. The author noted that the distributors were not specifically scaled and that the choice and design of distributor and windbox may have had significant effects on the resultant bed pressure fluctuations. Further experiments were performed using air-fluidized polystyrene particles in the larger bed which satisfied the simplified similarity criteria but resulted in different solid to gas density ratio, particle size distribution and particle shape. They found that the agreement in Kolmogorov entropy was poor (best at low gas velocity) near the bed surface and non-existent near the distributor. Unfortunately no other comparison was made of these results. A mis-scaled silica sand bed material was also used in the smaller bed; this also shows a discrepancy in Kolmogorov entropy (particularly bad at the distributor) but these experiments were also performed with a different distributor, so the results are open to different interpretations.

In order to address the question about the importance of the solid to gas density ratio, Farrel *et al.* (1998) carried out experiments in bubbling, slugging and circulating fluidized beds where the full set of scaling parameters were maintained, except the solid-to-gas density ratio, which was deliberately mis-matched. It appears that the bed materials compared were not from the same Geldart group (B and D materials were compared). Measurements of bed pressure profiles and global pressure fluctuations were carried out. Results for bubbling beds were presented in terms of bed expansion (inferred from pressure profiles), and the probability density function and power spectrum of the pressure fluctuations. The comparison showed that the beds did *not* exhibit hydrodynamic similarity. The authors concluded that the density ratio was an important parameter that could *not* be neglected in simplification of the scaling laws, however they did not mention the issue of crossing boundaries within the Geldart classification.

Stein, *et al.* (1998) used the technique of positron emission particle tracking (PEPT) to follow the motion of a single bed particle in several different sized bubbling beds fluidized by ambient air. The bed materials used were resin beads, foamed glass and glass ballotini, and ranged in size from 0.65 to 4 mm in diameter. The beds were scaled using the simplified scaling parameters. A comparison of solids cycle frequency showed reasonably similar results, however, results for the smallest scaled column were completely different from the two larger columns, which the authors attributed to slugging behaviour in the small column. In this work, no deliberately mis-scaled system was reported on.

Brue and Brown (2001) carried out a study using the full set of scaling laws on a small ambient cold prototype bed (102 mm diameter) and a half-scale pressurised model (50.8 mm diameter). In the prototype bed they tested three different size of glass beads fluidized by ambient air and in the model they used three appropriately scaled fractions of steel shot fluidized by air at 295 kPa. Their range of test gas velocities was reasonably low (from $U/U_{mf} = 1.1$ to 2.2) and they tested three bed heights (from $H/D \approx 1$ to 2). Their test measurement for hydrodynamic similarity was differential pressure fluctuations recorded at 20 to 40 Hz from various bed locations, and these were analysed using power spectral density functions. Transfer functions were fitted to their spectral results and the fitted parameters for the models then used as a means of comparison between beds. The authors defined numerical ranges for agreement between the parameters corresponding to excellent, fair and poor matches. Considering that they matched the full set of scaling laws in all the cases they tested, they found a surprisingly poor number of excellent matches overall. In particular, they found that poor agreement occurred when the differential probe was located close to the bed surface (such that it was periodically uncovered) and also when the bed aspect ratio was high, as the small model had a tendency to slug - a similar observation to that of Stein *et al.*, (1998) who also used a very small column for experiments. Like many before them, Brue and Brown (2001) also did not report on any deliberately mis-matched runs.

2.9.2 Outcomes of Previous Studies

Various conclusions can be drawn from the assorted previous studies, but they must be made with caution, because many of the studies carried out have significant drawbacks. Most notable is the number of investigations (half of those reviewed) in which the experimenters failed to carry out (or report on) a control experiment in which there was a *deliberate mis-match* of some (or all) of the scaling law parameters. The use of a control experiment cannot be over-stressed. When comparing hydrodynamic phenomena in bubbling fluidized beds, there will always be some degree of similarity in the behaviour of the beds because they are operating in the same fluidization regime (*ie* bubbling). If no deliberate mis-match study is undertaken, it is not possible to be sure that "similarities" detected with the given measurement technique are a direct result of scaling law success (true hydrodynamic similarity), or just the result of general behaviour which is inherently similar in bubbling fluidization anyway.

1. Scaling Laws and the Geldart Classification

It should be noted that in the development of the scaling laws, both simplified and full, the particle type (Geldart classification) is not specified explicitly. Thus the small-scale model which the scaling laws predict to be suitable must also be checked to ensure that the required particles are not so small that they are of the Geldart C group (and hence unable to be conventionally fluidized). Furthermore, the question arises as to whether the scaling laws will be successful not only *within* the Geldart classifications A, B and D, but also *between* them.

With regards to achieving hydrodynamic similarity *within* a Geldart classification, it is quite clear from the previous studies that both the full and simplified scaling laws are generally successful for the sand-like Group B materials. The full set of scaling laws are likewise successful for Group D materials, however there has been no comparison between a pair of Group D materials scaled using the simplified criteria. And despite the absence of any explicit term to describe the influence of interparticle forces in the development of the scaling laws, it would appear (as proposed by Foscolo *et al* 1990) that the full set of scaling laws are likewise suitable for scaling between bed materials of Group A (Di Felice *et al* 1992b, Rapagna *et al* 1992) although no control experiments were performed. No study has been carried out using Group A materials with the simplified laws.

As for the success of the scaling laws *between* Geldart groups, it would seem that the full set of scaling laws can be used to scale materials of Group D with Group B; this is possibly also true for the simplified laws, however this conclusion depends on the results from Zhang and Yang (1987), Stein *et al* (1998), neither of whom performed control experiments; and a single result from Roy and Davidson (1989) who only partly satisfied the simplified law. The only scaling comparison between a Group A and Group B material was carried out by Roy and Davidson (1989) under conditions which could be argued correspond to either the full or simplified set of scaling laws depending on the allowable error in matching the particle Reynolds number. Table 2.3 summarises the conclusions with regards to Geldart classification.

Scaling Law	A to A	A to B	B to B	B to D	D to D
Full	Yes	Possibly	Yes	Yes	Yes
Simplified	Unknown	Possibly	Yes	Possibly	Unknown

Table 2.3 Success of the scaling laws with regards to Geldart classification

2. Solid-to-Gas Density Ratio

The issue of matching the solid-to-gas density ratio was highlighted by Broadhurst and Becker (1973) in their early dimensional analysis study of bubbling fluidization. In their comparison of four different-sized columns, they found that the solid-to-gas density ratio was important for phenomena such as the minimum bubbling velocity. The question of matching the solid-to-gas density ratio with the simplified scaling parameters was pointed out by Glicksman *et al* (1993b), experimentally reported on by Farrel *et al* (1998) and also highlighted by Glicksman (1999b). In the full set of scaling laws, one of the requirements is that the solid to gas density ratio be kept the same in the different sized beds. With the simplified parameters of Horio *et al* (1986a), the solid to gas density ratio is not explicitly mentioned, although in the accompanying verification work, the ratio is kept constant inadvertently by the use of the same type of bed material and fluidizing gas. In the equivalent simplified criteria of Glicksman (1984), the density ratio term is also absent. In Glicksman's development, the density ratio term disappears from the scaling law requirements when viscous-dominated drag is assumed to occur (low particle Reynolds numbers) and the inertial term containing the density ratio is dropped from the Ergun equation (see Section 2.5.2).

However, Glicksman *et al* (1993b) made the following observation. Since the minimum fluidization velocity is a function of the particle to gas density ratio, if the density ratio is altered in the small-scale model (scaled by the simplified parameters), the required particle diameter must then be changed in order that the minimum fluidization velocity is still scaled correctly between the two units. Changing the particle diameter will thus alter the particle Reynolds number which may significantly increase the error in the drag coefficient in the scale model. Glicksman therefore recommended that for scaling beds with intermediate or large Reynolds numbers the solid to gas density ratio should be included in the set of scaling parameters. It should be pointed out, however, that this requirement does not really constitute a limitation to the simplified scaling laws because

the same type of bed material and fluidizing gas can be used; whereas with the full set of scaling laws, when the density ratio is maintained constant, the absolute values of the solid and gas density required to satisfy all the parameters may necessitate the use of unusual solids and fluids.

A number of the previously mentioned studies have explored the use of the simplified scaling laws with mis-matched solid to gas density ratios. Roy and Davidson (1989) conducted three runs with a density ratio mis-match, in which it could be argued that the simplified criteria were met, although they only satisfied Condition 1 (Equation 2.53) of Horio's criteria. The runs in which the particle Reynolds numbers were relatively low ($Re_p=33$, $Re_p=12$) showed similarity whereas the run conducted at the higher particle Reynolds number ($Re_p=105$) did not. Leu and Lan (1992) also investigated a density mis-match with the use of the simplified scaling criteria. Contrary to Roy and Davidson, they found that similarity was not achieved, even though their experiments were conducted at low particle Reynolds numbers ($6 < Re_p < 14$ and $2 < Re_p < 8$) and they satisfied both requirements of the similarity rule in their first comparison and Condition 2 alone in the second. Van der Stappen (1996) also explored a density mis-match for the range $10 < Re_p < 35$ and found similarity was not achieved for gas velocities exceeding $2.5 \cdot U_{mf}$ (corresponding to $Re_p=13$), although the particle size distribution and sphericity were also mis-matched and the choice of distributor may also have influenced the results. Farrel *et al* (1998) carefully matched all parameters except the density ratio in their study of the simplified scaling law and found that similarity was not achieved at all for $10 < Re_p < 25$. Note that they carried out their comparison on materials from different Geldart groups (B and D), thus spanning a boundary for which insufficient verification work for the simplified scaling laws has been carried out (as shown earlier in this section) and this casts some doubt on their conclusions. Finally, Stein *et al* (1998) carried out one run in their study of the simplified criteria in which the density ratio was mis-matched (for $17 < Re_p < 42$) and they did claim to find similar behaviour, although they presented limited data and their results may be open to different interpretations.

Given the somewhat contradictory evidence from the previous studies and the recommendations from Glicksman *et al* (1993), it can only be concluded from review that when using the simplified scaling laws a conservative approach should be adopted. That is, the solid to gas density ratio should be maintained constant between different units for particle Reynolds numbers above 4 until further work has clarified the matter. Note that various workers have also presented results for conditions in which the *full* set

of scaling laws were used with a mis-matched density ratio (to a greater or lesser extent). Again, the results are somewhat contradictory. Since similar solid to gas density ratio is a *requirement* of the full set of scaling laws, this parameter should certainly be matched, although errors of up to $\pm 20\%$, may be allowable, as the results from Nicastro and Glicksman (1984) and Almstedt and Zakkay (1990) would tend to indicate.

3. Sphericity and Particle Size Distribution

Because of their influence on bed expansion properties, sphericity and particle size distribution are required to be similar in the case of both the simplified and full set of scaling criteria. Unfortunately, these parameters are not often reported in verification studies. Almstedt and Zakkay (1990) found only a minor influence of sphericity on their scaling results between two different angular materials (crushed limestone and olivine sand). On the other hand, Di Felice *et al* (1992a) and van der Stappen (1996) both scaled angular materials with spherical materials and in both cases found poor agreement (although in the latter case this could equally be attributed to the density mismatch). Particle size distribution has also not been examined in detail, although workers often mention that attempts have been made to keep the distributions narrow (and of similar mode or shape). Based on the limited evidence available, it should be considered adequate for both particle size distribution and sphericity to be maintained *qualitatively* similar when applying the scaling laws (*ie* both the particle and the distribution to have a qualitatively similar shape).

4. Limiting Particle Reynolds Number for the Simplified Scaling Parameters

In his original publication, Glicksman (1984) recommended that the viscous-dominated form of the simplified scaling laws be limited to low particle Reynolds number of 4 or less, and the inertial-dominated form to $Re_p > 400$. This is so that either the viscous or inertial term in the Ergun equation can be neglected (in situations when drag is either predominantly inertial or predominantly viscous). The full set of scaling laws would be required in the intermediate region. In light of the experimental studies, however, this restriction on the simplified parameters was found to be conservative; Zhang and Yang (1987) proposing that for approximate similarity, the simplified scaling criteria could be

applied in the intermediate region $4 < Re_p < 400$, and they verified this up to $Re_p = 78$ by experiment, (note that they inadvertently maintained the density ratio constant). This was further developed by Glicksman *et al.* (1993) who sought to determine the extent of the error when the simplified scaling parameters were used in the intermediate region. With the proviso that the solid to gas density ratio is matched in the scaled beds and the Ergun equation is valid for the drag coefficient, Glicksman suggested that the simplified scaling laws could be applied over a wider range of conditions and bed sizes than the original viscous scaling law without appreciable error. They demonstrated this in accompanying verification experiments using a range of fluidization regimes, and used a model to suggest that a pressurized bubbling bed of 1 mm (or smaller) diameter particles operating at particle Reynolds numbers up to 1000 could be successfully modelled (less than 20% error in drag coefficient) with a $\frac{1}{4}$ scale model constructed using the simplified criteria.

5. Maximum Scale Change Possible

Although both the simplified scaling criteria (with constant density ratio) and the full set of scaling laws should be applicable over a wide range of bed sizes, few scaling law experiments have been performed in beds of significant size. Fitzgerald *et al* (1984) tested the full set of scaling laws in their comparison of a 460 mm square cold model with an atmospheric fluidized bed combustor of 1830mm square; this represents the largest bed in which scaling law verification work has been undertaken. Unfortunately, they did not achieve hydrodynamic similarity between the two units to the extent that they considered it statistically significant. Nicastro and Glicksman (1984) tested the full set of scaling laws (successfully) in a 610 mm square combustor and a 150 mm cold model. Almstedt and Zakkay (1990) used a 780 mm circular combustor and a 394 mm cold model in their (successful) test of the full set of scaling laws. The largest bubbling bed used in simplified scaling law verification was the 600 mm diameter cold model used in the solids mixing studies of Horio *et al* (1986b).

In light of the evidence that wall effects can play a significant role in bed hydrodynamics at small scales (*eg* Werther, 1974; Glicksman and McAndrews, 1985) and the lack of large-scale data on scaling law verification, (particularly notable with the simplified scaling laws), the applicability of the scaling laws to large scale changes cannot be automatically assumed. The use of such scaling criteria for large scale

changes must therefore be considered with caution until verification work is extended to cover larger bed sizes.

2.10 Conclusions

In this review chapter the generally observed phenomena of bubbling fluidization have been summarised. Simple treatments of bubble characteristics, criteria for slugging and models for solids motion have been presented in order to provide a suitable background for work in subsequent chapters. The principal aspects of scaling law development for bubbling fluidization have then been reviewed, and it can be seen that despite their different developments and forms, the various scaling laws show some encouraging equivalence in certain instances. Measurement techniques for fluidized beds are then given a brief introduction, followed by a thorough review of the experimental verification work carried out previously for both full and simplified criteria.

Several issues arise from an examination of the previous verification work. It can be seen that many of the previous workers did not carry out -or at least report on- any deliberate experimental mis-match in scaling law parameters. This constitutes a significant oversight, as such a control experiment is necessary to demonstrate the validity of the test procedure being employed to verify similarity. Consequently, the results of many of the previous studies must be treated with a certain amount of caution.

Although both the full and simplified criteria have been tested extensively for Geldart B particles, verification work for the simplified criteria has seldom been carried out for Geldart A or D solids (and success for these powder types cannot be automatically assumed).

From the limited studies of the effect of solid-to-gas density ratio on scaled bed behaviour, further investigation is required and presently it can only be concluded that a conservative approach be adopted and the solid-to-gas density ratio matched for flow conditions exceeding a particle Reynolds number of 4. It has been pointed out that in some ways this requirement presents more of a restriction to the use of the full set of similarity criteria, because in the case of the simplified criteria the same solids and gases may be conveniently used whilst applying the full set of parameters may result in a requirement for unusual solids and fluids. A conservative approach should also be

adopted for the choice of particle shape and particle size distribution – with these being maintained at least qualitatively similar through a scale change. There does not appear to be a restrictive limit to the application of the simplified scaling laws in terms of an upper limit particle Reynolds number – provided that the solid-to-gas density ratio is matched.

Finally, there is evidence to suggest that wall effects can play a significant part in determining overall bed behaviour and there have been very few studies carried out at large scales where wall effects diminish significantly. There is experimental evidence to suggest that small columns (less than 100 mm in diameter) should be avoided in any similarity work as slugging (not accounted for by the similarity criteria) may occur. Due to the lack of large-scale studies there is certainly a need for verification work to be carried out across a more extensive range of bed sizes.

3. EXPERIMENTAL EQUIPMENT

3.1 Introduction

This chapter provides equipment specifications and all the necessary background information about the equipment and the approaches used to perform the experimental verification of the simplified scaling laws at large scales. The fluidized bed equipment is first described, then a summary of the bed materials and operating conditions is given. Some specific design aspects of the equipment are then presented; namely the approach to distributor design, the selection criteria and design of pressure probes, the pressure data acquisition system, the electrical capacitance tomography system and lastly, the equipment for monitoring float tracers.

3.2 Fluidized Bed Vessels and Operating Equipment

Four different diameter bubbling fluidized bed cold models were employed in the experimental work. They were all of circular cross-section, with bed diameters (internal diameter of the vessel) of 146 mm, 300 mm, 600 mm and 1560 mm. Throughout the remainder of this text, the different sized beds will be referred to by their diameters. All of the beds were fluidized with ambient air (that is, the beds were operated at or extremely close to atmospheric pressure with the fluidizing air at room temperature, or slightly above room temperature depending on the heating effects of the supply systems). The two smaller scale systems were located in the Chemical Engineering Department of Monash University at the Clayton Campus; the two larger units were installed at the CSIRO Division of Minerals Clayton site, adjacent to the Clayton Campus of Monash University. Each system will now be described in detail.

3.2.1 146 mm System

The smallest-scale cold model, (as is often the case when comparing engineering equipment of different sizes), was also by far the simplest. The bed vessel consisted of a 150 mm internal diameter acrylic tube which (for the majority of the experiments) was

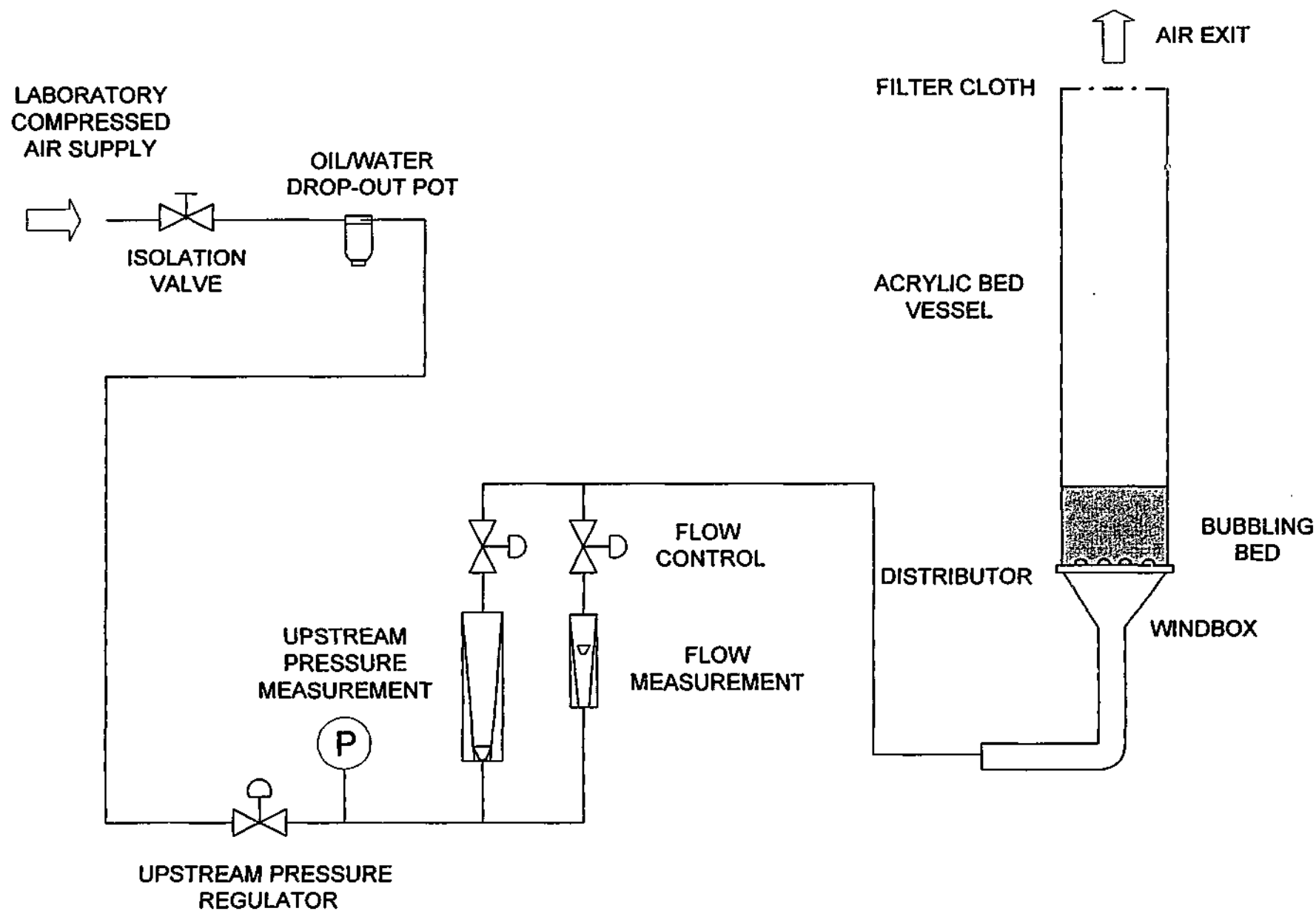
completely lined with grounded aluminium flashing to prevent electrostatic buildup. The aluminium lining reduced the vessel internal diameter to 146 mm. A second acrylic tube without metal lining and with an original internal diameter of 146 mm was used for experiments involving Electrical Capacitance Tomography (ECT). In both cases the tube was 1000 mm long (except for the case of the solids mixing experiments, - see Section 3.7.4).

The top of the tube was covered with a low pressure drop filter cloth where required (higher gas velocity operation and/or dust coming from the bed). The pressure between the bed freeboard region and atmosphere with the filter in place was measured on several occasions and found to be in all cases negligible (less than 10 Pa). After runs where it was observed or suspected that dusts had been generated, the filter material was cleaned with a vacuum cleaner.

The tubes had flanged bases so that they could be bolted to the windbox with the chosen distributor plate "sandwiched" in between. Neoprene gaskets and silicone sealant were used to seal the flanged joints. The windbox was made from PVC and conical in shape. Solids were poured into the vessel from the top opening; the vessel was usually emptied of contents by unbolting it from the support frame and pouring bed materials into a handy bucket. A modified distributor arrangement with a central drain port was employed to remove solids during ECT solids mixing experiments; see Section 3.7.4.

The supply air for this rig was taken from the laboratory compressed air supply (at 15°C) with gas flow measurements made using two variable area flowmeters whose specifications and calibration data are given in Appendix B. Gas exit temperature was occasionally tested in the freeboard region and always found to match the supply temperature of 15°C. The air flowrate was controlled manually using bronze screwed needle valves. Figure 3.1 shows the layout of the 146 mm bubbling bed equipment.

Figure 3.1 The 146 mm cold model system



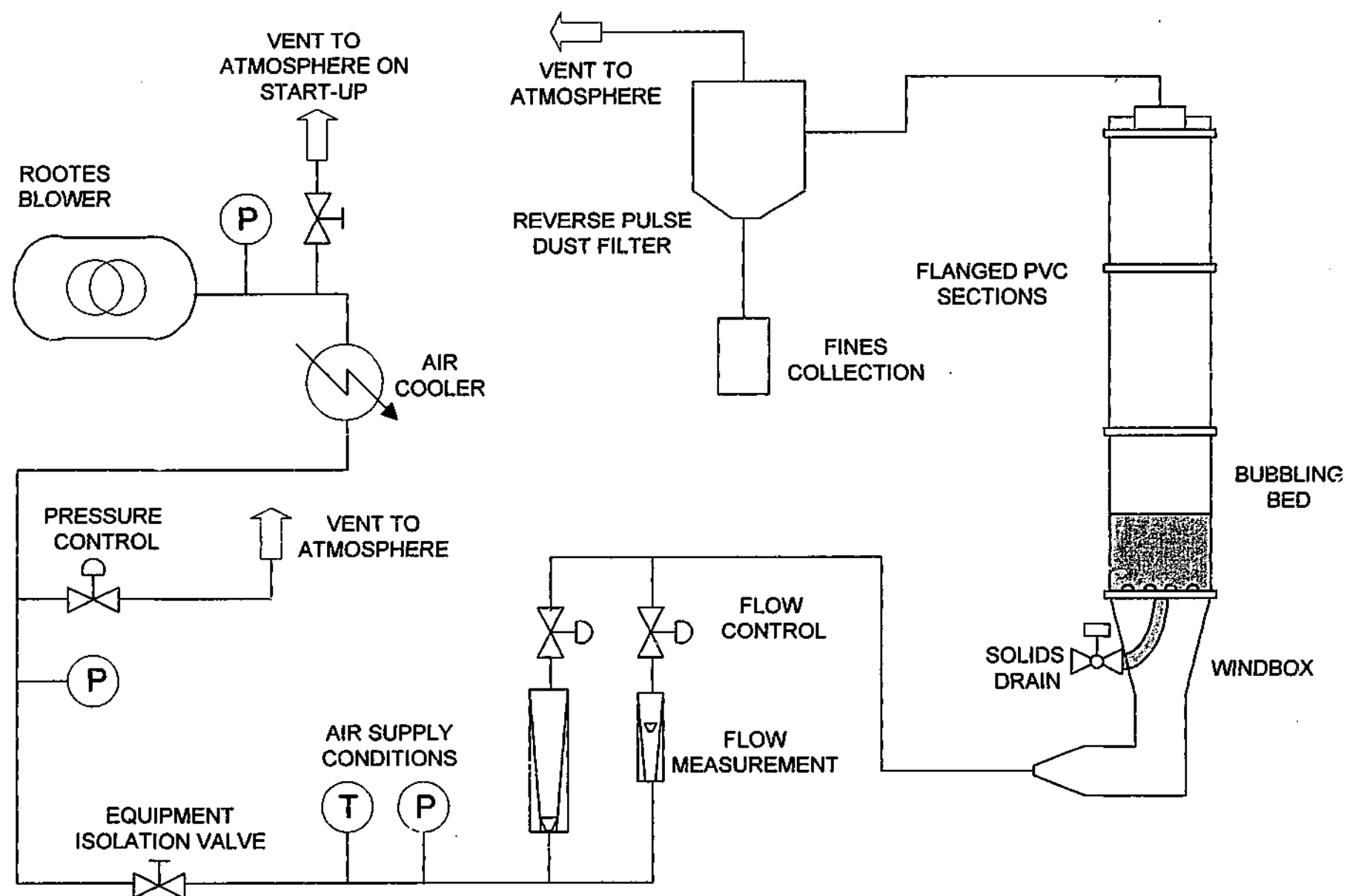
3.2.2 300 mm System

The 300 mm cold model was constructed of transparent PVC flanged sections with internal diameters of 300 mm. Under normal operation (all except solids mixing experiments) the vessel stood 2200 mm high (above the distributor) and the gas exit was connected via a 100 mm reinforced hose to a reverse pulse dust collector for exit gas cleanup. No allowance was made for solids return to the bed as the quantities of material elutriated from the bed were minimal. Pressure measurements in the freeboard of this unit again showed the difference between freeboard pressure and atmosphere to be negligible, and also that there were no pressure pulses associated with dust collector operation.

Once again, the flanged bed sections were bolted to the windbox with the chosen distributor plate sandwiched in between. Neoprene gaskets and silicone sealant were used to seal the flanged joints. The PVC windbox was conical in shape, although with a different aspect ratio from the windbox of the 146 mm bed. Solids were generally poured into the vessel through the top opening (normally connected to the 100 mm hose) and removed from the vessel using a 50 mm drain port located at the centre of the distributor.

The air was supplied to this cold model from a Rootes blower located outside the laboratory. The air from the blower was passed through an after-cooler heat exchanger cooled by refrigerated brine to reduce its temperature prior to entering the building. Air temperatures were measured at the air inlet to the cold model by Type K thermocouple and ranged from 15 to 35°C with the refrigeration system operating correctly. Occasional testing of the air temperature in the freeboard indicated a range of 15 to 25°C. Supply pressure was controlled by the manual operation of a bypass valve which vented air from the supply line to atmosphere. The air flowrate to the fluidized bed was measured by means of variable area flowmeters (specifications and calibration data in Appendix B) and controlled manually using diaphragm valves. Figure 3.2 shows the layout of the 300 mm bubbling bed equipment.

Figure 3.2 The 300 mm cold model system



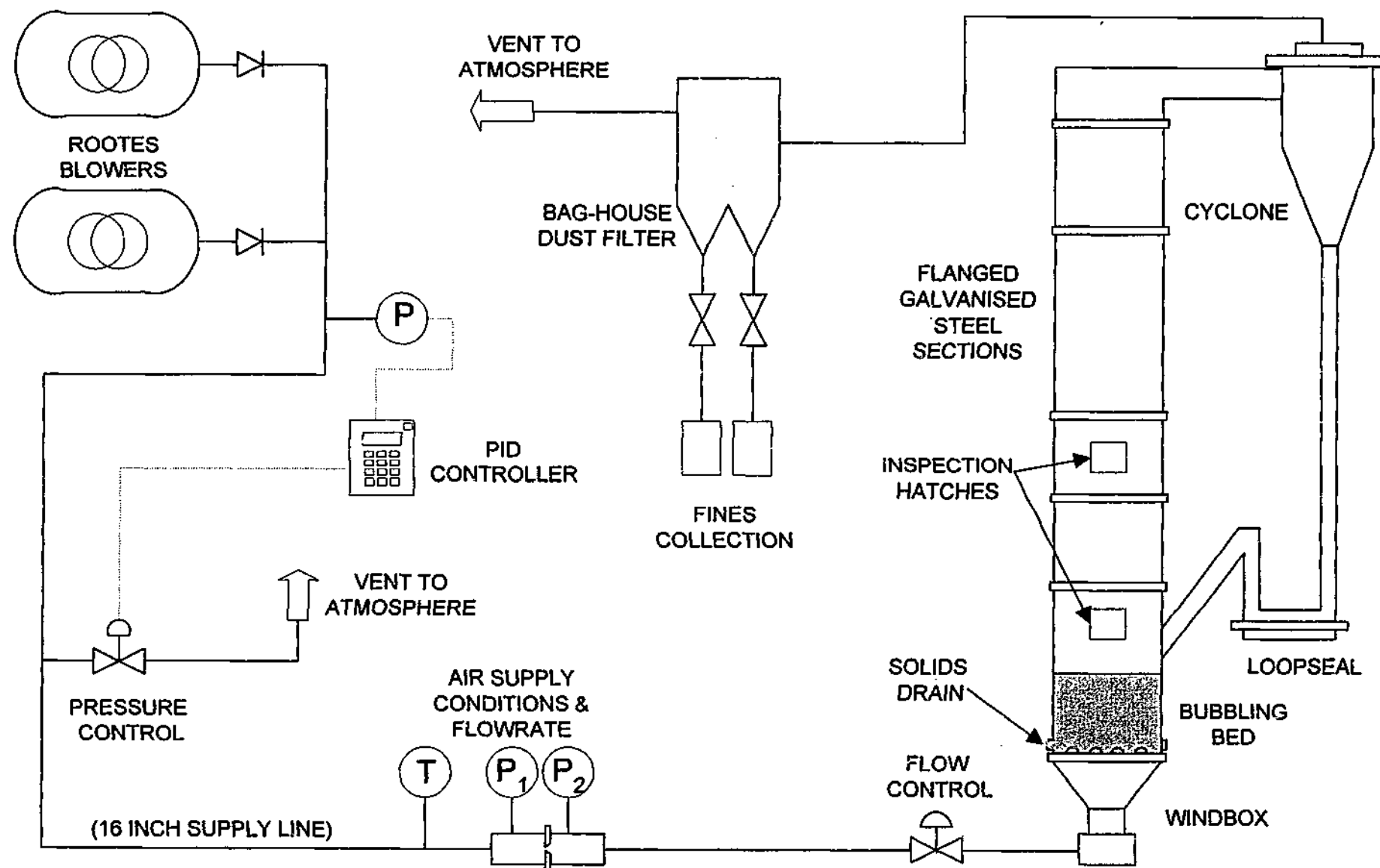
3.2.3 600 mm System

The 600 mm cold model was of galvanized steel construction. The riser section, of 600 mm internal diameter was 9.8 m high and consisted of a number of flanged sections bolted together. The flanged bed sections were bolted to a conical windbox with the distributor plate sandwiched in between. Neoprene gaskets and silicone sealant were used to seal the flanged joints. Because the equipment was originally designed for use in both bubbling and circulating modes, the riser exit gas passed through a cyclone allowing solids to be separated and returned to the bottom of the riser via a loopseal if required. In all operations described here, the bed was only operated in bubbling mode and the loopseal was turned off. Note that the lowest point of the solids return entry to the riser was located at a height of 620 mm above the distributor plate, and did not interfere with the geometry of the bubbling bed at the bed depths used in this study. Air from the cyclone gas exit was passed to a large bag-house dust filter system for cleanup.

At this scale, the consequences of larger size equipment become apparent. Distributor alteration and removal operations required the use of a small forklift. Air supply for this bed was from two Rootes blowers feeding a common 16 inch (406 mm) supply line. At higher gas velocities, (particularly in the 1560mm bed), the combined total power drawn by the blowers could exceed 250 kW. The air supply pressure was controlled by venting air from the supply line to atmosphere using a butterfly control valve, which was adjusted by altering the value of the line pressure set-point on the associated PID controller. Air flow measurements were carried out by measuring the pressure 406 mm upstream and 203 mm downstream of a 2 inch (50.8 mm) orifice plate in the 16 inch supply line. The pressure drop was measured using a calibrated EIRELEC MP320 digital manometer.

Flow conditions were set by manually adjusting the butterfly valve on the inlet to the windbox, and/or by adjusting the pressure in the supply line. Supply air temperature was measured by Type K thermocouple 420 mm upstream of the orifice plate and in the bed windbox so that air temperature (and hence density) change could be compensated for in the flow measurement calculation. The air temperature at the windbox always remained between 15 and 20°C, although the air temperature at the orifice plate could get as high as 45°C. Air temperatures in the freeboard region were occasionally tested, and always found to be within the range 15 to 18°C.

Figure 3.3 The 600 mm cold model system



Solids were loaded into the bed through a 230 mm square inspection hatch located 620 mm above the distributor in the riser wall, and were removed through a pair of 65 mm discharge ports located in the vessel wall 50 mm above the distributor plate. Figure 3.3 shows the layout of the 600 mm bubbling bed equipment.

3.2.4 1560 mm System

The 1560 mm cold model was also of galvanized steel construction and was supported in a 5-storey high free-standing structure. Like the 600 mm system it was designed to operate in both bubbling and circulating modes and was equipped with twin cyclones, solids return legs and loopseals. (For operation in bubbling mode the loopseals were turned off.) The riser section, of 1560 mm internal diameter was 10.6 m high and consisted of a number of large flanged sections bolted together. The bottom flanged section was bolted to the conical windbox with the distributor plate sandwiched in between. Silicone sealant was used to seal the flanged joints. In the case of this system, the angled twin solids return points to the riser were located at a height of 500 mm above the distributor plate, and therefore did alter cross-sectional shape of the bed to some extent for the bed depth considered in this study. Air from the cyclone gas exit was passed to the large bag-house dust filter system for cleanup.

Air supply for this bed was from the two Rootes blowers feeding the common 16 inch supply line and joining into a 36 inch (914 mm) supply line from a diesel engine driven centrifugal fan. The fan was only for use in low pressure-drop applications and was isolated from the system for the bubbling bed experiments. Like the 600 mm system, air supply pressure was controlled by venting air from the supply line to atmosphere using the butterfly control valve, adjusted by altering the value of the line pressure set-point on the PID controller. Air flow measurements were carried out by measuring the pressure 406 mm upstream and 203 mm downstream of a 4 inch (101.6 mm) orifice plate in the 16 inch supply line. The orifice pressure drop was measured using a calibrated EIRELEC MP320 digital manometer.

Flow conditions were set by manually adjusting the 36 inch butterfly valve on the inlet to the windbox, and/or by adjusting the pressure in the supply line. Supply air temperature was measured by Type K thermocouple 420 mm upstream of the orifice

Figure 3.4 The 1560 mm cold model system

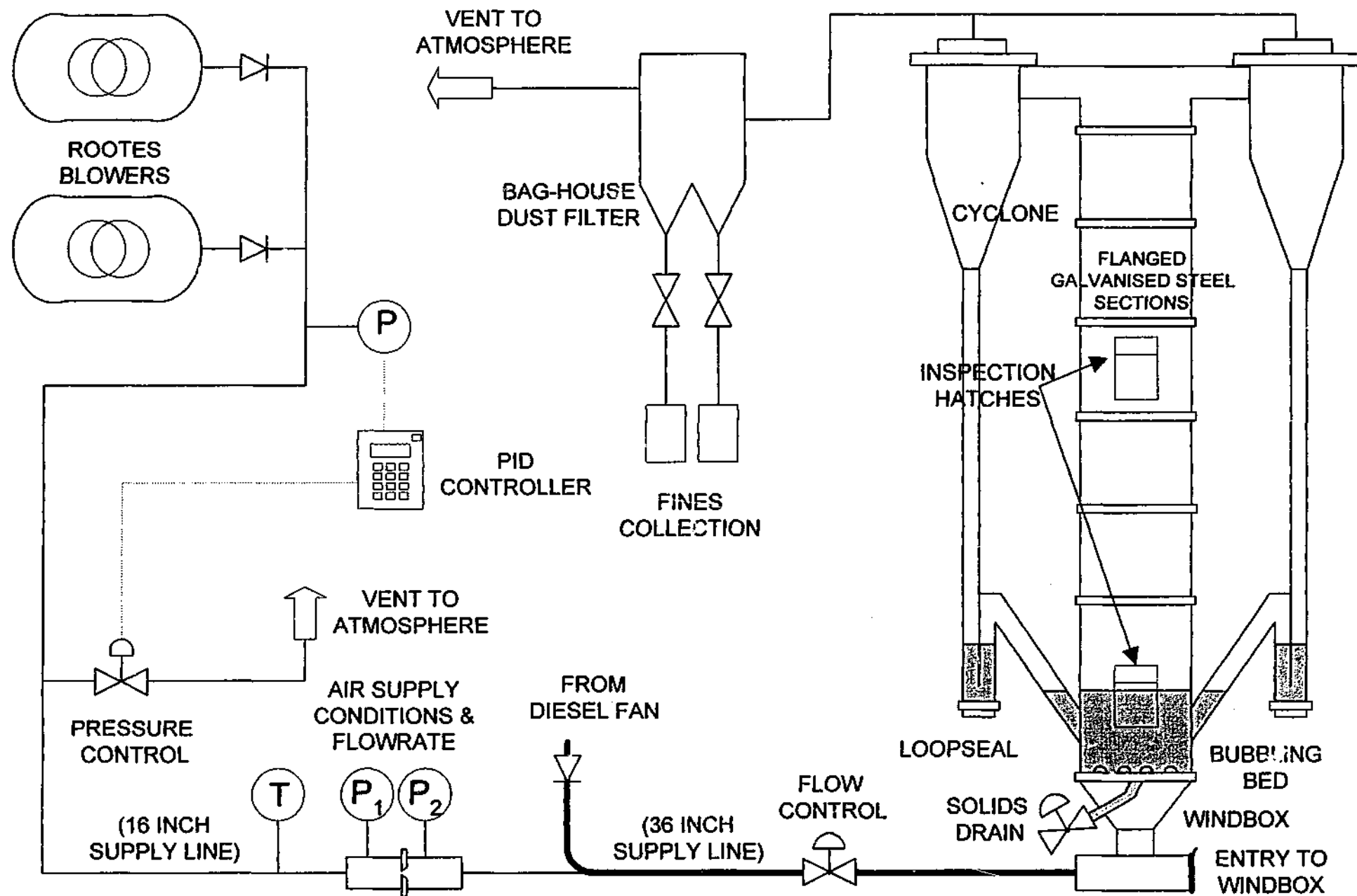


plate and in the bed windbox so that the air temperature change could be compensated for in the flow measurement calculation. The air temperature at the windbox varied from 15 to 45°C, air temperatures at the orifice plate typically ranged from 30 to 90°C. The freeboard air temperature was occasionally measured, and reliably fell within the range 15 to 35°C. Freeboard pressure was found to be very close to atmospheric (within 20 Pa) even at high gas velocities.

At this large scale, major distributor alteration and removal operations were never attempted. The design of the tuyeres (see Section 3.5.2) allowed for pressure drop adjustment to be carried out with the distributor *in situ*. This was effected by removing the blank from the end of the 36 inch supply line, entering the line and erecting a ladder inside the windbox so that the underside of the distributor could be reached and tuyere orifice sizes changed over. The skirt-to-plate distance of the bubble caps could be altered from inside the bed vessel when solids were not present.

Solids were pneumatically loaded into the bed through an angled 220 mm feed port located 2800 mm above the distributor in the riser wall, and were removed through a central 100 mm drain port in the distributor. A large 500 x 800 mm hatch in the riser wall could be opened in sections at bed level for vessel entry; a similar hatch was available for access to the freeboard region (5.0 m above the distributor). Figure 3.4 shows the layout of the 1560 mm bubbling bed equipment.

3.3 Bed Materials

The bed materials chosen for use in the similarity experiments were silica sand and garnet sand, all angular-shaped materials of Geldart group B. The majority of experiments were conducted with different silica sands, the garnet sand was only used in one series of experiments designed to investigate a mis-scaled solid to gas density ratio. Bed materials are specified in Table 3.1. The bed material D used in the largest bed was used as the basis for scaling bed materials A, B, and C which were used in the smaller, correctly-scaled scenarios. Bed materials A* and B* were used in the 146 mm and 300 mm beds in order to investigate the effect of mis-matched particle size and bed material G was used in the 146 mm bed to investigate the mis-scaled density ratio.

Bed Material	Sand Type	Bed Used	d_{sv} (μm)	ρ_s (kg/m^3)	U_{mf} (m/s)
A	Silica	146 mm	225	2650	0.039
B	Silica	300 mm	280	2650	0.058
C	Silica	600 mm	330	2650	0.070
D	Silica	1560 mm	425	2650	0.127
A*	Silica	146 mm	337	2650	0.085
B*	Silica	300 mm	398	2650	0.125
G	Garnet	146 mm	300	4100	0.082

Table 3.1 Characteristics of the bed materials used in the similarity experiments

The similarity experiments were divided into two sets, based on the aspect ratios of the beds involved. Across the full range of bed sizes, beds with a shallow aspect ratio of 0.67:1 (H:D) were used. At the 146 and 300 mm scales, additional similarity experiments were conducted with aspect ratios of 2:1 (H:D).

Unlike the full set of scaling laws, the simplified parameters do not specify particle diameter directly. As can be seen from the first requirement of the simplified scaling laws as presented by Horio *et al* (1986a) the minimum fluidization velocity is the scaled property, the particle diameter is only selected indirectly in order to satisfy this requirement:

$$U_{mf2} = \sqrt{m} * U_{mf1} \quad (3.1)$$

where m is the ratio of bed diameters. So, in the case of the shallow aspect ratio experiments, the minimum fluidization velocity of the bed material D was measured, and the correctly-scaled bed materials were then sieved from commercially available silica sand until the required (correctly scaled) minimum fluidization velocities were obtained according to the scaling law requirement (Equation 3.1). Details of the minimum fluidization experiments and particle size distributions for all materials are contained in Appendix C.

The matching of bed material properties to bed properties was not perfect, as can be seen from the relative errors in the scaling factor m , calculated as follows:

Consider the scaling factor m as dictated by the characteristic length ratios of the scaled beds, which will be referred to as m_{geo} :

$$m_{geo} = \frac{D_2}{D_1} \quad (3.2)$$

Given the first requirement of the scaling law (Equation 3.1), the ratio can also be written in terms of the particles' minimum fluidization velocities:

$$m_{part} = \left(\frac{U_{mf2}}{U_{mf1}} \right)^2 \quad (3.3)$$

And relative error between the particle-based and geometry-based scaling factors is given by:

$$\%m = \left(\frac{m_{part}}{m_{geo}} - 1 \right) * 100 \quad (3.4)$$

Which can be written in terms of Equations 3.2 and 3.3 as:

$$\%m = \left[\left(\frac{U_{mf2}}{U_{mf1}} \right)^2 * \left(\frac{D_1}{D_2} \right) - 1 \right] * 100 \quad (3.5)$$

Errors in the scaling factor for the bed materials used in the shallow aspect ratio experiments (with the minimum fluidization velocity of the material (D) in the 1560 mm bed taken as the reference) are shown in Table 3.2.

Materials A and B scale reasonably well with D, however there is some error in C, and the case where material D has been used in the 600 mm bed (deliberate particle size mis-match) gives a large error.

Material	D (mm)	U_{mf} (m/s)	m_{geo}	m_{part}	%m (%)
A	146	0.039	0.094	0.094	0.8
B	300	0.058	0.192	0.209	7.8
C	600	0.07	0.385	0.304	-26.6
D	1560	0.127	1	1	Basis
D	600	0.127	0.385	1	160

Table 3.2 Scaling factor errors for materials used in the shallow aspect ratio similarity experiments

In the deeper aspect ratio experiments, two different sets of correctly scaled materials were used. Bed materials A and B were correctly scaled with each other. Bed materials A* and B* were also correctly scaled with each other. Comparing A with B* or A* with B, however, can be used to demonstrate a particle size mis-match. Material G was designed to match the A* and B* systems, however the density ratio in this case is completely mis-scaled. Below, in Table 3.3, errors in scaling ratio are presented with bed material A in the 146 mm bed taken as the basis. (Note that although materials A*, B* and G have large errors on this basis, the errors are of similar size, because these systems are in fact similar to each other.)

Material	D (mm)	U_{mf} (m/s)	m_{geo}	m_{part}	%m (%)
A	146	0.039	1	1	Basis
B	300	0.058	2.055	2.21	7.6
A*	146	0.085	1	4.75	375
B*	300	0.125	2.055	10.3	400
G	146	0.082	1	4.42	342

Table 3.3 Scaling factor errors for materials used in the deeper aspect ratio similarity experiments

3.4 Operating Gas Velocities

The range of superficial gas velocities used in the similarity experiments were as shown in Table 3.4. Within the ranges shown, it was endeavored to make measurements at the same dimensionless velocity in each bed, although this was not always possible.

0.67:1 (H/D) Aspect Ratio Experiments				
Material	Bed	U range (m/s)	U/U_{mf} range	Re_p range
A	146 mm	0.042-0.146	1.06-3.75	0.7-2.3
B	300 mm	0.062-0.217	1.06-3.75	1.2-4.1
A (HV)	146 mm	0.048-0.362	1.23-9.28	0.8-5.7
B (HV)	300 mm	0.071-0.539	1.22-9.29	1.4-10.3
C	600 mm	0.082-0.660	1.17-9.43	1.8-14.8
D	1560 mm	0.173-0.515	1.36-4.06	5.3-15.7
D	600 mm	0.141-0.646	1.11-5.09	4.6-21.2
2:1 (H/D) Aspect Ratio Experiments				
Material	Bed	U range (m/s)	U/U_{mf} range	Re_p range
A	146 mm	0.058-0.327	1.49-8.37	0.9-6.4
B	300 mm	0.092-0.614	1.58-10.59	1.8-11.7
A*	146 mm	0.101-0.327	1.18-3.84	2.4-9.5
B*	300 mm	0.159-0.614	1.51-4.91	4.1-15.9
G	146 mm	0.101-0.402	1.23-4.90	2.1-8.3

Table 3.4 Ranges of superficial and dimensionless superficial gas velocities and particle Reynolds number (based on fluid density at exit conditions and surface volume mean diameter) for the hydrodynamic similarity experiments. "HV" refers to separate runs conducted at higher gas velocity.

3.5 Bubble Cap Distributor Design

In this section the design of the distributors used in the hydrodynamic similarity experiments is presented. Firstly, the previous work is reviewed in order to demonstrate a relative lack of variety in distributor designs used, and the possible influence of distributor design on hydrodynamic similarity. Specific details of the bubble cap

geometry, pressure drop requirements, and orifice sizes for this work are summarized, and a check for minimum gas velocity to ensure complete tuyere operation based on an empirical correlation is carried out.

3.5.1 *Distributor Types Used in Previous Work*

In the previous experimental verification work, distributor design has not been considered in great detail, although it is generally accepted that the distributors must be geometrically similar, with distributor pressure drops scaled relative to the bed pressure drop (eg Nicastro and Glicksman, 1984; Horio *et al*, 1986a). The majority of workers have chosen to use geometrically scaled perforated plate distributors, or high pressure drop porous plates, with exceptions noted below.

Fitzgerald *et al* (1980) used glass and lead beads as distributors in their initial comparative study. The bead diameter was not scaled especially closely in the different units, however hydrodynamic similarity was achieved. In their subsequent work (Fitzgerald *et al*, 1984) the two-dimensional cold models had geometrically similar distributors with correctly scaled pressure drops, but the three-dimensional cold model had a perforated plate distributor, different from the bubble-cap design used in the combustor, (although the pressure drops were scaled appropriately). In the latter instance, they found the agreement between cold model and combustor to be relatively poor, and one of the possible causes they suggested was incorrect distributor plate scaling.

Nicastro and Glicksman (1984) used correctly scaled nozzle type distributors in their comparison of combustor and cold model, with good results.

Roy and Davidson (1989) used perforated plates (occasionally with filter paper or cotton added as a porous layer to prevent fine particles escaping) in their similarity experiments. The plates were intended to be geometrically scaled, although the pair of beds used in the low and high temperature comparison had distributor geometries that were slightly (20%) out-of-scale (Roy, 1989). This does not appear to have had a significant effect on the similarity results they report.

An interesting practical issue relating to the distributor design of cold models was identified by Almstedt and Zakkay (1990), who used geometrically scaled perforated plate distributors in their comparison between combustor and cold model. In the combustor, the distributor was air and water cooled to 150°C whilst the bed itself operated at 870°C. This resulted in the gas transport properties being different in the distributor than in the bed; effectively the cooling of the distributor reduced the pressure drop across it for a given orifice diameter and air flow-rate (when compared with air at combustor temperature). So whilst the cold model had a *geometrically* scaled distributor, the scaled pressure drop across it was effectively higher than its combustor counterpart. There were some discrepancies in the bubble parameters reported between the two systems, with the distributor differences suggested as one of the possible causes. They attempted to address this issue by carrying out some experiments with a larger orifice size in the distributor of the cold model which lowered the pressure drop (but also introduced a mis-scaled orifice gas velocity), however, this did not appear to influence the results.

Van der Stappen (1996) employed porous (sintered bronze) distributors for the similarity comparisons and these were not scaled in any way between the columns. Significant differences were found in Kolmogorov entropy at distributor level, which were postulated to have been caused by mis-scaling of the initial bubble formation in the zone near the distributor. Further evidence of differing Kolmogorov entropy (significant at distributor level) was presented for three 0.1 m diameter bubbling beds, identical in all respects except distributor, windbox and upstream equipment, however more detailed analysis of the results was not presented.

In an internal technical report, Brown and Schroeder (1997) also suggested that mismatched distributor characteristics were the source of discrepancies in pressure fluctuation measurements and associated deviations from hydrodynamic similitude between a bubbling bed combustor and a cold model. They used the frequency spectrum of pressure fluctuations to demonstrate the dramatic effect of removing a fine mesh screen from the (improperly scaled) perforated plate distributor in the cold model. No comment was made about the effect of the screen on the distributor to bed pressure drop ratio and the possibility of mal-distribution, however.

Apart from the work of Nicastro and Glicksman (1984), hydrodynamic similarity experiments have not been performed using scaled down "industrial" style distributors,

and there is some evidence to indicate that incorrect distributor scaling can lead to problems achieving hydrodynamic similarity even if the pressure drops are matched. Consequently, in this work a less usual type of distributor design (for laboratory studies) has been employed, and care has been taken to ensure that the distributor geometry and pressure drops are scaled between the different sized units.

3.5.2 Bubble Cap Design

The bubble cap (or tuyere) distributors used in this work are based on a simple design where a short vertical standpipe is fixed into a flat distributor plate, and the top end of the standpipe is covered with an overhanging cap to prevent solids falling from the bed into the windbox. The gas therefore enters the bed laterally through the space between each cap skirt and the distributor plate. Under idealised circumstances the gas flows evenly outwards from all sides of each cap. The dimensions of the bubble caps have been scaled in proportion with the diameters of the cold models. The design of the bubble cap is shown in Figure 3.5, with dimensions given in Table 3.1.

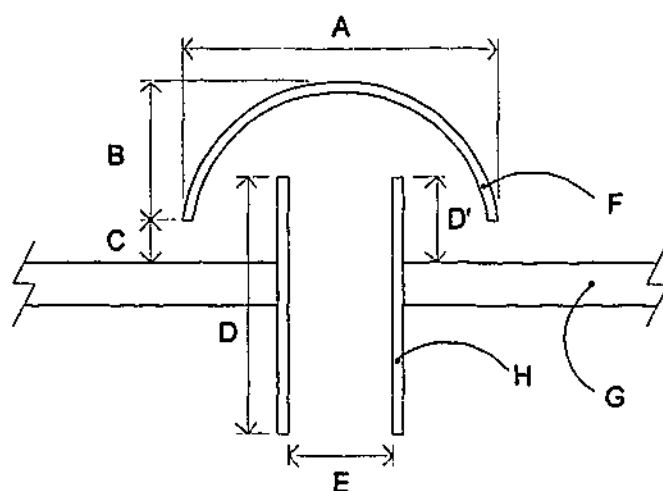


Figure 3.5 Cross-sectional view of the design of bubble caps used in the scaled cold models

The bubble caps (18 in total) were arranged in a geometrically similar triangular pattern on the distributor plates as shown in Figure 3.6.

Bed:	A	B	C	D	D'	E	F	G	H
146 mm	16.0	10.0	2.4	14.0	4.7	8.2	1.0	6.0	1.0
300 mm	30.0	16.5	4.8	23.5	9.4	20.1	1.5	8.0	1.0
600 mm	57.0	33.0	9.6	43.8	18.8	40.2	0.5	9.5	2.0
1560 mm	150	89	25	105	49	100	9.2	16	7.1

Table 3.5 Dimensions of the bubble caps used in each cold model (all dimensions given in mm)

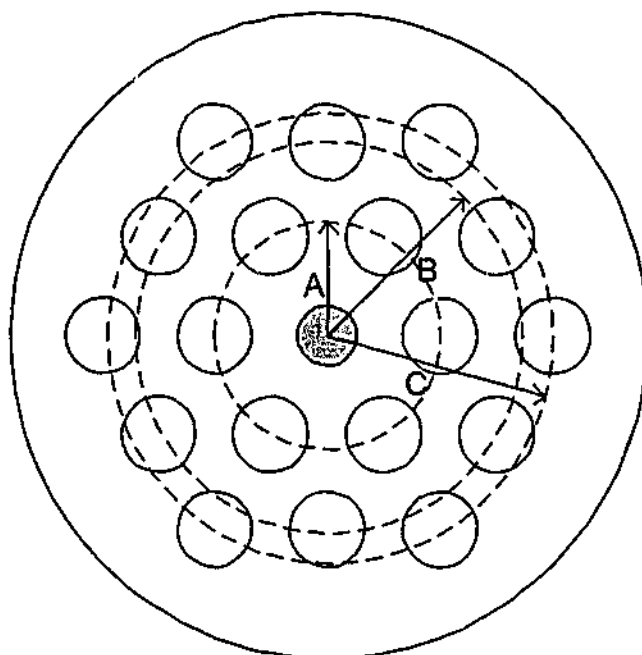


Figure 3.6 Layout of the bubble caps used in each scaled cold model. The central position is reserved for a drain port.

Bed Diameter:	A	B	C
146 mm	30.0	52.0	60.0
300 mm	59.5	104	120
600 mm	119	208	240
1560 mm	310	540	625

Table 3.6 Geometric layout of bubble caps on each distributor plate (all dimensions in mm)

3.5.3 Distributor Pressure Drop Considerations

Note that the overall pressure drop of such an arrangement (as drawn in Figure 3.5) is quite low. For the similarity experiments, the pressure drop through the distributors was increased by placing a constriction (orifice) into the base of each stand-pipe. This

approach allowed the distributor pressure drop to be adjusted independently of the rest of the bubble cap geometry.

The choice of distributor pressure drop was (as usual) a trade-off between the desire for good gas distribution to ensure uniform fluidization and the limits of blower capacity. Because the distributor pressure drops were to be scaled across four different units, ultimately the limitation was imposed by the system with the "weakest" blower for its size. This was the 1560 mm bed system, with maximum blower capacity of 1 m³/s at 70 kPa. The relatively low blower capacity of this system meant that compromises had to be made in terms of both distributor pressure drop and total bed depth.

After some initial "back of the envelope" calculations, the aspect ratio of the 1560 mm bed was chosen to be 0.67:1, which gave a bed depth of 1040 mm (and consequently sets the settled bed depths of all the smaller scaled units). The bed pressure drop could be estimated approximately by Equation 3.6:

$$\Delta P_{bed} = H(1 - \varepsilon)(\rho_p - \rho_f)g \quad (3.6)$$

-With ε , ρ_p and ρ_f initially estimated to be 0.45, 2650 kg/m³ and 1.15 kg/m³ respectively (silica sand fluidized by air), this gives a bed pressure drop of $\Delta P_{bed}=14.9$ kPa. For the distributor, the design pressure drop was determined from the popular maxim (Knowlton, 1997):

$$\Delta P_{dist} = 0.3 * \Delta P_{bed} \quad (3.7)$$

giving a distributor pressure drop requirement of $\Delta P_{dist}=4.5$ kPa, which was deemed to be the pressure drop required across the distributor *at minim fluidization conditions*. The required orifice diameter for flow restriction in each bubble cap could then be estimated using a modified form of the procedure given by Knowlton (1997), and assuming a discharge coefficient of $C_d=0.8$ for each orifice, (which is likely to be conservative):

(1) The ideal gas law was used to estimate the density of the air passing through each orifice, assuming the gas conditions in the orifice are the same as those in the windbox (Kunii and Levenspiel, 1991):

$$\rho_h = \frac{P_w}{RT_w} \quad (3.8)$$

where P_w and T_w are the absolute pressure and temperature in the windbox respectively. R is the universal gas constant, taken as 287.0 Nm/kgK. Conditions in the windbox were assumed to be as follows:

$$P_w = \Delta P_{dist} + \Delta P_{bed} + P_{atm} \quad (3.9)$$

ie $P_w = 4500 + 14900 + 101325 = 120725$ Pa (absolute),

and $T_w = 303K$.

That is, the windbox pressure is estimated to be the sum of pressure differentials from freeboard to windbox (based on the proposed bed depth and distributor pressure drop), and the windbox temperature is assumed to be 30°C, (representing anticipated average operating conditions). So:

$$\rho_h = \frac{P_w}{RT_w} = \frac{120725}{303 * 287} = 1.39 \text{ kg/m}^3. \quad (3.10)$$

(2) The gas velocity through the orifice, U_h is calculated viz:

$$U_h = C_d \sqrt{\frac{2\Delta P_{dist}}{\rho_h}} = 0.8 * \sqrt{\frac{2 * 4500}{1.39}} = 64.4 \text{ m/s}. \quad (3.11)$$

(3) The orifice diameter is then calculated from:

$$d_h = \sqrt{\frac{\rho_f UA}{\rho_h U_h N \pi / 4}} \quad (3.12)$$

where ρ_f is the gas density in the bed (assumed to be the same as the freeboard), A is the bed cross-sectional area, U is the superficial gas velocity –which for the design

conditions stated is the U_{mf} of the bed material, and N is the number of orifices in the distributor (ie 18). Substituting the values leads to:

$$d_h = \sqrt{\frac{1.15 * 0.127 * 1.91}{1.39 * 64.4 * 18 * (\pi/4)}} = 0.0148 \text{ m} \quad (3.13)$$

That is, the required orifice size for each bubble cap is 14.8 mm.

Once this initial orifice size had been determined for the 1560 mm bed, the geometric scaling ratio could be used to determine a first-estimate of the required orifice diameters for the other beds (*estimate* only, because it has to be assumed that ρ_h and C_d are invariant with scale change).

Because the orifice diameter was estimated based on a number of assumptions which may not be entirely accurate (in particular, the conservatively assumed discharge coefficient) the actual distributor pressure drop resulting from the given orifice size was measured (without bed present) to confirm that the desired bed pressure drop at minimum fluidization velocity had been achieved. This procedure was adopted to confirm distributor pressure drop for all distributors at all scales. Generally, the initial orifice size was slightly too small (intentional, by using a conservative C_d value) and after measuring the distributor pressure drop with the initial orifice size and comparing it with the desired value, a new hole size could be calculated from:

$$\frac{\Delta P_{new}}{\Delta P_{old}} = \left[\frac{d_{h(old)}}{d_{h(new)}} \right]^4 \quad (3.14)$$

which can be derived from Equation 3.11 assuming constant ρ_h , C_d and volumetric flowrate. The final orifice sizes and bed depths are listed in Table 3.7. The pressure drop characteristics of the bubble cap distributors at all four scales are presented in Appendix D.

Bed Diameter	Settled Bed Depth (mm)	Orifice Diameter (mm)
146 mm	96 (295)	1.5
300 mm	200 (590)	3.6
600 mm	400	6.4
1560 mm	1040	16.0

Table 3.7 Bed depths and orifice diameters for scaled bubble cap distributors. Bed depths for the deeper aspect ratio experiments are given in brackets.

Finally, a consideration was made regarding a problem specific to bubbling fluidized beds operating with bubble-cap distributors; -the issue of intermittent tuyere operation reported by Whitehead and Dent (1967). This situation occurs for superficial gas velocities below a certain minimum velocity, U_M , and results in the gas flow through individual bubble caps temporarily (and randomly) dropping to a low flowrate, with associated stagnation of the bed material in the vicinity of the non-operating cap. The possibility that this situation might occur was of concern, because a bubbling bed with randomly changing patterns of bubble-cap operation and associated zones of defluidization is likely to deviate from hydrodynamic similarity (due to the fact that the scaling laws are not expected to account for this random defluidization behaviour).

Whitehead and Dent (1967) presented a correlation to determine the value of U_M as follows:

$$\frac{U_M}{U_{mf}} = 0.7 + \left[0.49 + \frac{3.23 \cdot 10^{-7} (N^{0.22} K_D^2 \rho_s H_s)}{U_{mf}^2} \right]^{1/2} \quad (3.15)$$

where K_D is the grate flow factor, given by

$$K_D = \frac{K_T N}{A} \quad (3.16)$$

K_T is the tuyere flow factor:

$$K_T = \frac{60 Q_T}{\sqrt{\Delta P_{dist}}} \quad (3.17)$$

and Q_T is the volumetric flow of gas through a tuyere:

$$Q_T = \frac{UA}{N} \quad (3.18)$$

Note that the correlation is in Imperial units: (U , U_M and U_{mf} in ft/s, H_s in ft, ρ_s in lb/ft³, A in ft², Q_T in ft³/s and ΔP_D in inches of water). A general note also that this equation as reproduced in Whitehead (1970) is incorrectly printed.

This expression was used to determine U_M in the 1560 mm fluidized bed, with a settled bed height of 1040 mm and distributor pressure drop characteristic as shown in Appendix D. The resulting value of $U_M/U_{mf} = 1.45$, indicated that for the majority of gas velocities considered (see Table 3.4), intermittent tuyere operation was not expected to cause trouble. The correlation was also applied to the smaller beds, and indicated that U_M/U_{mf} was slightly higher in the smaller units. It is not known however, whether this correlation which was developed from large-scale experiments (of similar size to the 1560 mm equipment) would be reliable at smaller scales.

Whitehead and Dent (1967) also reported a hysteresis effect with regards to tuyere operation; if the gas velocity was increased to a high level and then reduced, the value of U_M at which the tuyeres became non-operational was *lower* than if the gas velocity was simply increased from zero until all tuyeres were operating. Note that Equation 3.15 is applicable to the former situation. Consequently, when operating any of the fluidized beds, the procedure was to always "overshoot" the desired gas velocity and then reduce the flow back to the target value.

3.6 Pressure Probe Design and Instrumentation

In this section, the design of the pressure probes used in the similarity experiments is presented. (A detailed review of pressure fluctuations in bubbling fluidized beds will be given in Section 4.2). Many previous studies of fluidized beds have employed the use of pressure probes, and a variety of designs have been developed. Ideally, a pressure probe should be sensitive to the pressure fluctuations present within the bubbling bed, convey the pressure signal without distortion or attenuation to the pressure transducer,

and influence the bed behaviour as little as possible. The pressure probe design chosen for the current work was designed using these general guidelines, with the further proviso that the same probe be appropriate for use *at all bed scales*.

3.6.1 Influence of Probe Internal Diameter and Length on Measurements

It has been shown that the design of the pressure probe and the resulting probe response characteristics can have a significant influence on the measurements obtained from it (eg Clark and Atkinson, 1988). Even the early study of Shuster and Kisliak (1952) includes a cautionary note about the choice of tube length and diameter.

A comprehensive review of the application of pressure probes to fluidized bed studies was presented by van Ommen *et al* (1999), who thoroughly investigated the response characteristics of the probe and transducer system, and considered the effect of probe length and probe internal diameter on the measured signal from a bubbling fluidized bed and a "noisy" turbulent gas stream. They compared a number of previous probe-transducer models and rules of thumb for probe design, concluding that in general, optimum probe internal diameters lie in the range 2 to 5 mm. For statistical and chaos analysis of pressure signals, probe lengths up to 2.5 m are acceptable because the typical range of frequencies under investigation are low (*ie* only up to 20 Hz or so). For spectral analysis, however, the probe length is dependent on the frequencies of interest; higher frequencies require shorter probe lengths. Therefore they conclude that although probe lengths up to 2.5 m may be acceptable, in general it is desirable to keep the probe length as short as possible.

For beds with identical aspect ratio, it is known that the characteristic frequencies present in the pressure fluctuations will be a function of scale, with smaller (shallower) systems exhibiting higher frequencies and larger (deeper) systems exhibiting lower frequencies (eg Lirag and Littman, 1971, Fan *et al*, 1981). Thus in the hydrodynamic similarity comparisons, the measured frequencies are expected to be highest in the smallest bed and lowest in the largest bed. For the purposes of probe design, the idea is to ensure that the frequency range of interest is correctly transmitted to the pressure sensor, and given the probe design suggestions of van Ommen *et al* (1999), the limiting factor is the highest frequencies of interest that the probe must transmit accurately. These will occur in the smallest bed and the *dominant* frequency of the spectrum

generated can be estimated from (for example) the equation of Verloop and Heertjes (1974):

$$f = \frac{1}{2\pi} \sqrt{\frac{g}{L} \left(\frac{2-\varepsilon}{\varepsilon} \right)} \quad (3.19)$$

For the 146 mm bed with voidage (ε) assumed to be 0.45 and bed depth (L) assumed to be 0.0973 m (conservative, since this is the *settled* bed depth from Table 3.7) the dominant frequency of the pressure fluctuations will be $f \approx 3$ Hz. Even if the signal has a relatively broad bandwidth, it is unlikely that significant power will exist at frequencies beyond the 20 Hz guideline suggested by van Ommen *et al.* Thus, the choice of probe length is not likely to be especially critical, provided it is kept less than 2.5 m.

3.6.2 Influence of Probe External Diameter on Bed Behaviour

The influence of probe *external* diameter on the local bed behaviour in the probe's vicinity has been demonstrated by various workers, *eg* Geldart and Kelsey (1972); Rowe and Masson, (1981). It can be concluded that all probes disturb the bed to a greater or lesser extent (depending on the design). Horizontal probes were found by Rowe and Masson (1981) to decelerate bubbles and promote bubble splitting, and the smaller the bubble, the greater the effect of the probe (for a given probe size). Vertical probes were found to have a lesser effect.

Roy and Davidson (1989) showed that differential pressure measured from a double probe (*ie* a probe with two separate tubes set close together in the bed) mainly registers the effects of local bubble passage; whereas a differential pressure measurement from a single probe with respect to atmospheric (or freeboard) pressure mainly registers the effect of bubbles bursting at the bed surface. Van der Schaaf *et al* (1998) attributed pressure fluctuations in a fluidized bed to two main sources. Like Roy and Davidson, they found that a bubble passing a probe causes a local pressure fluctuation which will be registered by a double probe. They also found that bubble generation at the bottom of the bed, bubble coalescence in the bed and bubble eruption at the bed surface all contribute to the generation of pressure waves that pass through the bed at high speed.

Single pressure probes are sensitive to both the fast pressure waves and the passage of local bubbles; however the effect of the pressure waves normally predominates (except when the probe is located near to the bed surface) When local differential pressure measurements are made with a double probe, the effects of the fast pressure waves are largely filtered out, with mainly local bubble behaviour being registered. It is therefore likely that measurements from a double probe will be more adversely affected by the probe's own influence on the bed than measurements from a single probe.

3.6.3 Chosen Probe Design

Consequently the approach to the pressure probe design for hydrodynamic similarity comparisons in this work was to use horizontally mounted single-ended pressure probes. Although the horizontally mounted probe causes more disruption to bubble passage than the vertical-stemmed probe, horizontal mounting was chosen because the probes could be located more easily and would be less prone to flexing due to the dynamic forces of the bed on the probe. The probe was made single-ended because that way the effects of the fast pressure waves resulting from the hydrodynamic phenomena occurring throughout the bed would be registered, representing the "global" hydrodynamics in the bed more effectively. Also, because the local effects registered by the single probe are likely to be small, the disruptive effect of the probe on the local bed conditions is less likely to influence the measured fluctuations.

To completely rule out the possibility of differences in probe design affecting signals from one bed and not another, the same data acquisition system was used throughout the study and all the pressure probes used (in every bed) had identical internal dimensions (as recommended by Fuller and Daw, 1993). The probe internal dimensions were selected in line with the rules of thumb proposed by van Ommen *et al* (1999).

The probe tubes were stainless steel with internal diameters of 2.5 mm and the probe lengths (from tip to pressure transducer connection) were all 500 mm. The probe tips were fitted with a fine stainless-steel gauze to prevent solids ingress. This was held in place with a sleeve of heat-shrink tubing. The probe tubes were fixed into a 10 mm OD stainless steel support tube which was inserted through a thermocouple connector assembly. Threaded tapping points at various locations in the bed wall allowed the probes to be inserted into the bed (via the thermocouple assembly) to almost any desired

radial position. The external configuration of the probes differed somewhat to account for the scale of the bed in which the probes were used or the radial position required (a special probe had to be made for taking pressure measurements flush with the wall).

Figure 3.7 shows the detail of the probes generally used in the 146 mm, 300 mm and 600 mm beds. Figure 3.8 shows the probe used for taking measurements at the bed wall in the same beds.

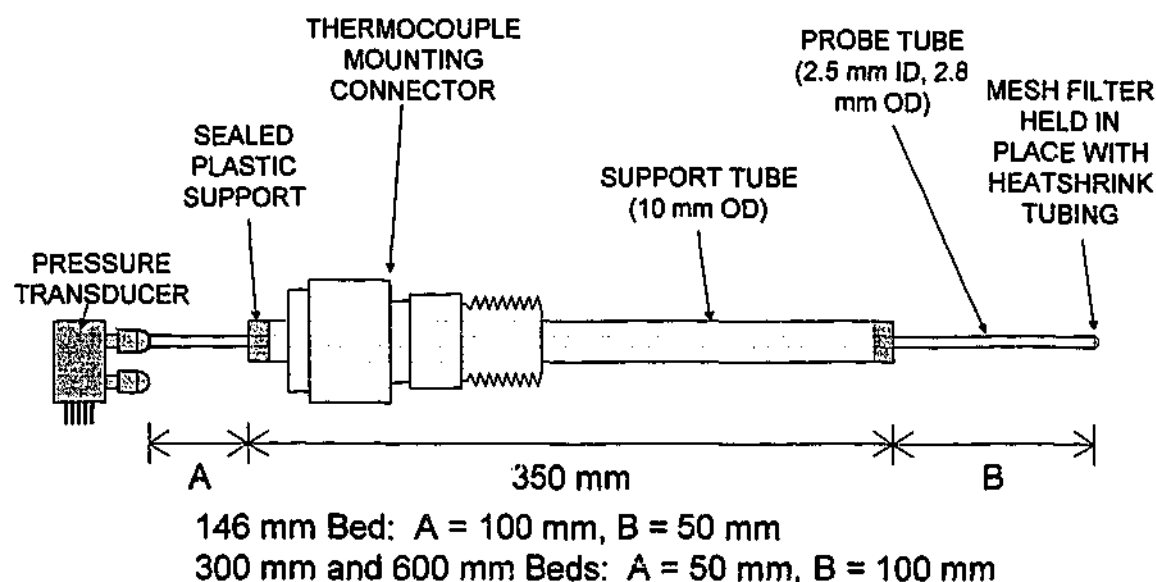


Figure 3.7 Details of the pressure probe used in hydrodynamic similarity experiments for the 146 mm, 300 mm and 600 mm beds. Although the probe length is the same, the dimensions A and B were altered between the 146 mm beds and the other beds to allow for ease of mounting.

The situation for the 1560 mm bed was a little different, because the chosen probe length of 500 mm was less than the radius of the bed. A 38 mm OD stainless-steel mounting tube was used to house and support the original 500 mm probe and pressure transducer as shown in Figure 3.9. An open tube feeding in through the end of the assembly allowed the reference side of the transducer access to atmospheric pressure.

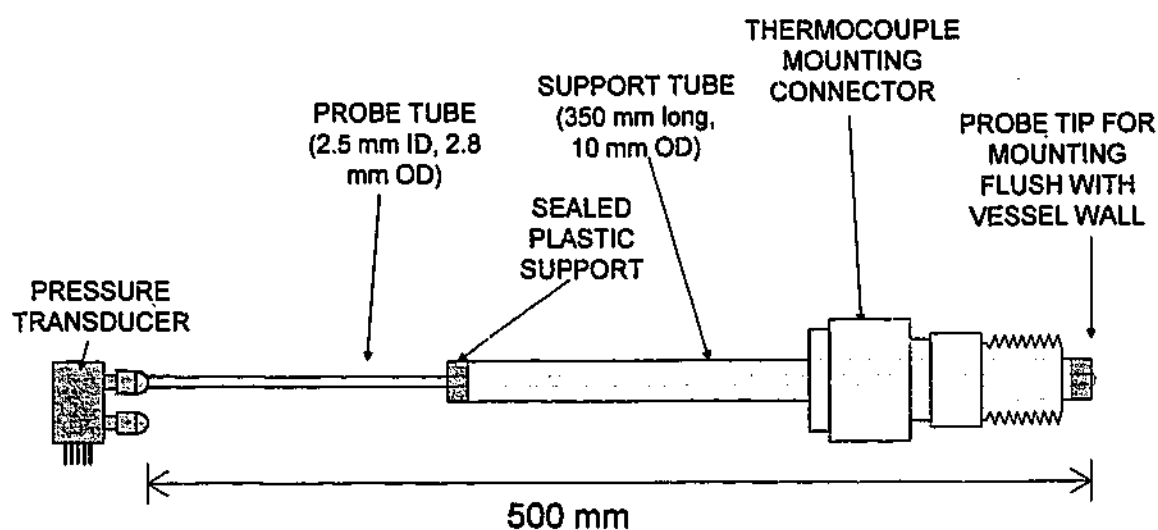


Figure 3.8 Modification to the probe for use flush with the bed wall in the 146 mm, 300 mm and 600 mm beds. Note that the thermocouple connector could be slid along the probe support tube the required amount so that the end of the probe remained exactly flush with the inside surface of the vessel wall.

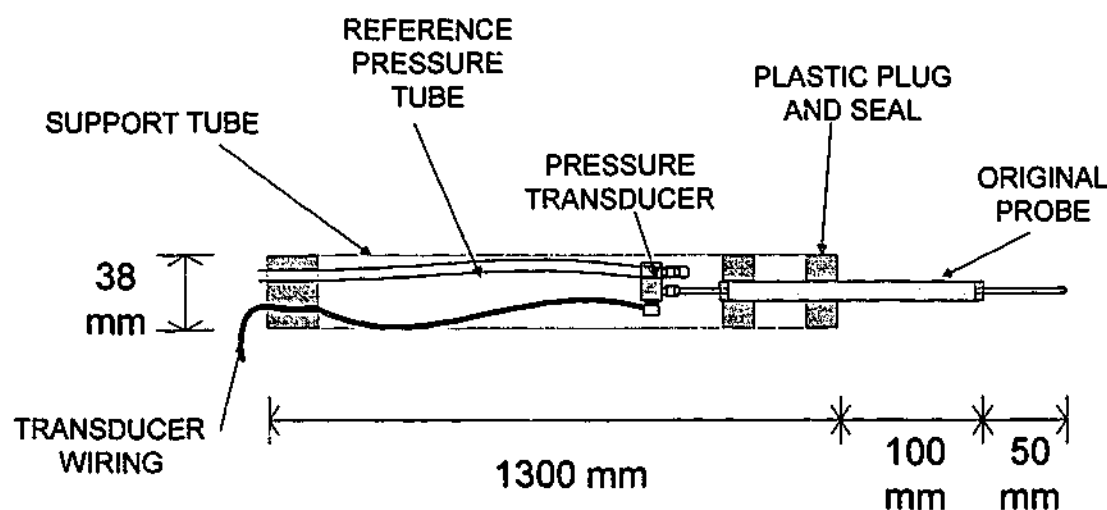


Figure 3.9 "Scaled-up" probe assembly used for experiments in the 1560 mm bed. The same probe design that was used in the smaller beds was supported in a 38 mm OD tube for insertion into the large cold model. A nylon tube fed air to the reference side of the pressure transducer.

Transducer wires were also fed out through the end of the assembly. The "scaled-up" probe was inserted through threaded sockets in the 1560 mm bed wall and fixed in place with a sealed support collar (fabricated along similar lines to the small thermocouple connectors used at the other scales). A deliberate 0.5 to 1 mm clearance fit between the probe support tube and the inside of the support collar allowed a small quantity of solids back as far as the o-ring. This arrangement worked exceptionally well, as particle

ingress "locked" the probe into the collar, yet when the probe was required to move, twisting it within the collar pulverised the particles and allowed easy movement for repositioning. For wall measurements, the wall-probes used at smaller scales were fixed in the mounting tube flush with its end; the tube was then inserted through the side of the vessel so that it was flush with the inside wall.

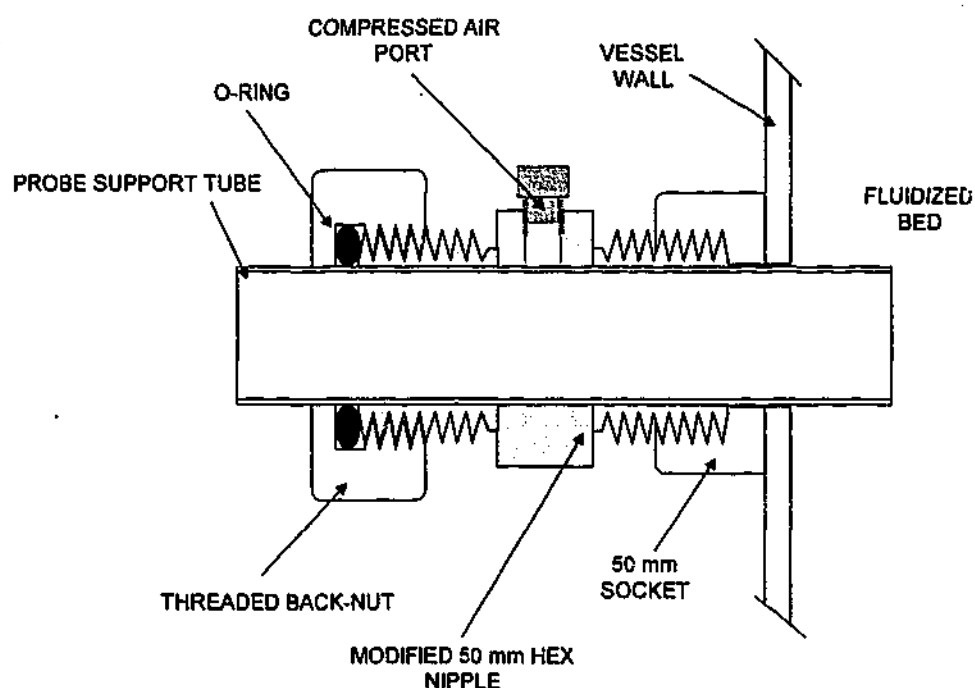


Figure 3.10 Sectioned view of the sealed support collar design for large probes in the 1560 mm bed. The fitting was sealed with an O-ring; as it turned out, the tapping point for compressed air was never required for clearing solids from the inside of the fitting.

3.6.4 Tapping Points for Pressure Probes

Tapping points for probes were placed at various heights along the walls of the bed vessels. (Each system was also equipped with a tapping point in the windbox for air temperature or pressure monitoring.) The tapping points were arranged so that the dimensionless height of the probes (h/H , where h is the height of the probe from the distributor) would be the same in all beds. Tapping points for all beds are shown in Figure 3.11; different tapping points were used in the lower aspect ratio bed experiments than in the higher aspect ratio bed experiments. Tapping point distances are given in Table 3.7. In most instances, three probes were used simultaneously in adjacent axial positions, with three radial positions investigated during different runs: at

the vessel wall, at the radial centre, and the halfway point between the wall and the radial centre.

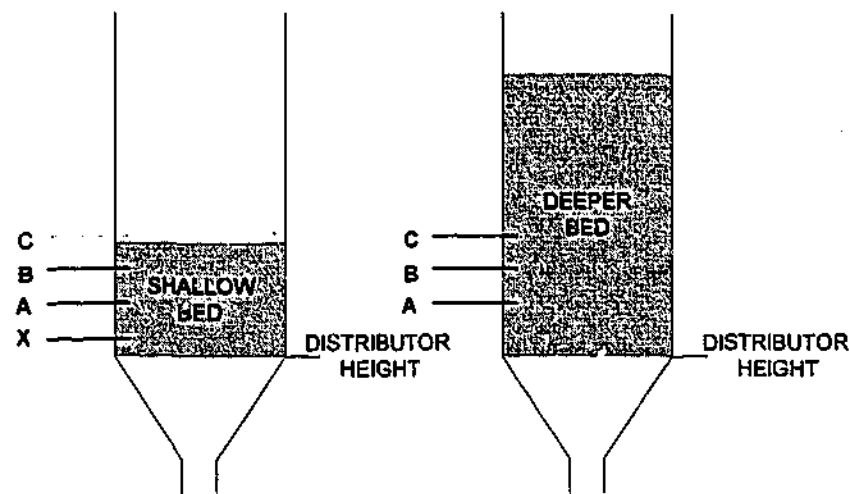


Figure 3.11 Location of tapping points for use with pressure probes. Solid lines indicate where probes were used in the case of each bed aspect ratio. A tapping point was also provided in the windbox of each unit for distributor characterisation.

Bed:	X	A	B	C
146 mm	19.5	48	75	103
300 mm	40	96	154	212
600 mm	80	192	308	424
1560 mm	210	500	800	1100

Table 3.8 Distance from top surface of distributor plate to the centre of each tapping point. The tapping point heights correspond to the same dimensionless probe height (h/H) at each scale.

3.6.5 Pressure Transducers and Data Acquisition

A range of fast-response pressure transducers was used with the pressure probes. To improve accuracy, transducers with the most appropriate pressure measurement range were used for given experimental conditions. (The probes were designed to facilitate quick transducer changeover). The transducers were manufactured by Data Instruments; they were accurate to $\pm 1\%$ of full scale output, and had a response time of less than 1 millisecond. The following specifications apply:

Transducer	Range (kPa)	Output* (mV)
XCX 0.3DNQ	0 to ± 2.07	0 to ± 10
XCX 01DNQ	0 to ± 6.90	0 to ± 9
XCX 05DNQ	0 to ± 34.5	0 to ± 30

* at 25°C and 12v DC excitation

Table 3.9 Pressure transducer operating ranges.

The pressure transducers were calibrated (with the appropriate excitation voltage) against a Druck DPI 601 calibrated digital pressure reference before use and at various times during the experimental program. Calibration data for all transducers used is presented in Appendix E. It was found that the slope of the calibration lines remained unchanged throughout the experimental program, however, there were changes in the transducer measurement offset on a day-to-day basis. Therefore a "baseline" measurement was carried out at the start of each similarity experiment. That is, the output signals from all transducers were recorded at zero differential pressure. The voltage offset for each transducer was thus known and could be removed from the subsequent measurements. The baseline measurements also served as confirmation that the level of background electrical noise was acceptable before each experiment commenced.

The outputs from the pressure transducers were logged on a data acquisition personal computer via a PCL-818HG data acquisition card using Advantech Genie v2.12 software. Up to 16 inputs could be logged simultaneously, although generally only 3 were used at any one time. The data acquisition card had 12 bit A/D conversion and a maximum sampling rate of 100 kHz. The Genie software could sample at frequencies up to 20kHz.

Signal amplification and low pass filtering were *not* generally used between pressure transducer and data acquisition computer, as preliminary tests indicated that the level of noise in the raw signal was low, and the low-pass filter electronics available actually tended to *increase* the noise. (The issues of noise and filtering will be elaborated on in Chapter 4.) Signal cables were always kept as short as possible (usually ~ 1 m) and care was taken not to place signal cables near other (eg power) cables. It was found that spurious signals were developed in the system when the computer was run with its

original switch-mode power supply. Replacement of the power supply with an older-style transformer/filter supply solved this problem.

The actual sampling rate used in the similarity experiments was usually in the range 80 Hz to 250 Hz, with lower sampling frequencies and longer run-times being used in the largest bed; higher sampling frequencies and shorter run-times used in the smallest bed. The rationale for this was that given the expectation of higher signal frequencies at smaller scales, the signal would be better represented in those cases by increasing the sample rate. By limiting the run-time at the smaller scales, a similar number of data points could be acquired at each scale. The sampling frequency was chosen (somewhat arbitrarily) to be approximately 80 times the expected dominant frequency for each bed as calculated from Equation 3.19. (Note that this can also be thought of as scaling the sampling frequency by $\frac{1}{\sqrt{m}}$ where m is the geometric scaling ratio, as Equation 3.19 gives $f \propto \sqrt{\frac{1}{L}}$ and the beds are geometrically similar.) For the majority of runs, slightly over 16,384 (2^{14}) data points were recorded from each pressure probe. The standard data logging conditions are summarised in Table 3.10.

Bed	Run Time (s)	Sampling Rate (Hz)	Number of Points
146 mm	65	257.9	16763
300 mm	90	186.6	16794
600 mm	130	130.6	16978
1560 mm	200	83.3	16660

Table 3.10 Standard run-times and sampling rates used for pressure fluctuation measurements

3.7 Electrical Capacitance Tomography

The purpose of the Electrical Capacitance Tomography experiments was two-fold:

- (1) To measure and compare the overall voidage fluctuation data in the scaled beds and determine if these were similar when the beds were operated under the conditions specified by the scaling criteria.

- (2) To carry out some basic solids mixing experiments in the scaled beds by exploiting the measurement system's ability at distinguishing between materials with different dielectric constant.

The ECT system consisted of a set of electrodes surrounding the region of interest in the fluidized bed, a data acquisition unit containing the sensor electronics, and a computer to log the data and reconstruct the capacitance measurements into the cross-sectional image of the vessel contents. The general setup is shown in Figure 3.12.

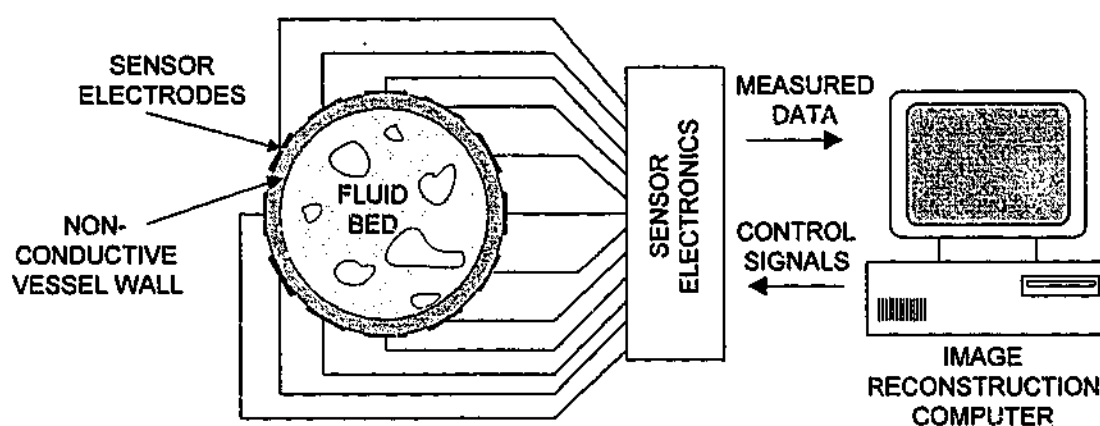


Figure 3.12 General layout of an ECT system

3.7.1 The UMIST PTL-300 System

The system used in the current work was the Process Tomography PTL300 single-plane unit developed at UMIST (University of Manchester Institute of Technology). The sensors consist of 12 electrodes equi-spaced around the outside of the fluidized beds. The PTL-300 system uses the *single excitation method*; excitation voltage is applied to only one electrode at a given time and the charges on the other electrodes are then measured. In *dual excitation* ECT systems such as the one developed at METC (Morgantown Energy Technology Centre) a pair of opposite electrodes are energized simultaneously.

In the UMIST system, during an individual measurement, fast CMOS switching electronics hold one electrode at a positive voltage for short periods, while the other electrodes are grounded. The rapid discharges of the excited electrode through each grounded electrode are recorded in parallel to provide a measurement of their mutual

capacitances. Then a different electrode is made the excitation electrode and measurements are again made from the remaining sensor electrodes. Because the switching is rapid, the imaging can be repeated at a rate of up to 100 Hz.

The PTL-300 system allows for either earthed-shield or driven-shield electrodes to be used both above and below the measurement electrodes. The purpose of the driven shield electrodes is to maintain a parallel electric field pattern across the sensor in the region of the measuring electrodes by preventing the field lines from spreading axially at the ends of the measurement electrodes. The appropriate driven shield electrode pair (above and below each measurement electrode) is held at the same voltage as the measurement electrodes during measurements. Generally speaking, electrode systems with driven shield electrodes are expected to be more accurate than those without (eg Kühn *et al.*, 1996).

The Linear Back-Projection (LBP) reconstruction algorithm has been the most common one used for ECT image reconstruction. However, there is much evidence to suggest that the reconstruction algorithm is the limiting factor in image accuracy (see Huang, *et al.*, 1992; Bair and Oakley, 1993). Therefore the UMIST ECT system allows the user to select the standard LBP algorithm, or use an optional iterative LBP algorithm (Yang *et al.*, 1997) which takes considerably more processing time but reproduces images more faithfully.

3.7.2 Use of the ECT System

The ECT system was applied to specific areas of the hydrodynamic similarity investigation where it was most likely to yield successful, reliable information about the behaviour of the fluidized beds. In this work there was little emphasis given to the reconstructed images or their interpretation. The main focus here was on the dynamic information yielded by the voidage fluctuations themselves.

Sensor electrodes were developed for the 146mm bed and an existing set of electrodes was used in the 300mm bed. (An attempt to extend the technology to the 600 mm scale at CSIRO Division of Minerals failed due to the fact that the sensitivity of the technique became too poor at that scale.)

Although it was desirable to keep the electrode heights geometrically scaled in the two beds, this was not possible due to the design requirements of the electrode area (Byars, 1998). It was, however, possible to keep the axial centre of the electrode assemblies at the same dimensionless bed height. (The heights of the electrode axial centres were 150 mm and 300 mm in the 146 mm and 300 mm beds respectively.) Also, for reasons of electrode area, the beds were required to have aspect ratios of approximately 2:1 (H/D) or more. Figure 3.13 shows the unrolled layout of the ECT sensors which were wrapped around the exterior of the bed vessels. The corresponding dimensions are given in Table 3.11.

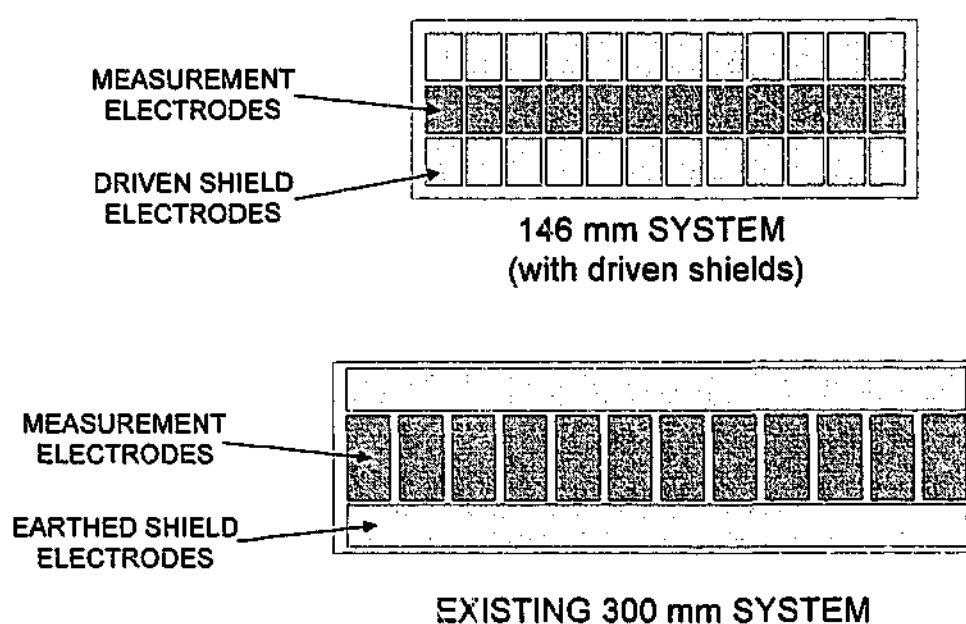


Figure 3.13 ECT electrode layouts represented graphically (not to scale). The diagrams show the sensors as they appear when "unrolled" from around the exterior of the fluidized bed vessels.

Bed Diameter	Electrode Height (mm)	Electrode Width (mm)	Construction
300 mm	152	76	Electrodes externally mounted around the PVC vessel. Earthed shield electrodes.
146 mm	50 (shields also 50 mm)	37 (shields also 37 mm)	Electrodes externally mounted around the acrylic vessel. Driven shield electrodes (above and below)

Table 3.11 Details of measurement electrodes for the two fluidized beds

3.7.3 Hydrodynamic Similarity Investigations Using ECT

For hydrodynamic similarity comparisons, the imaging system was used to record data at its maximum rate; 16,000 frames at 80 frames per second (with the given computing hardware) and was principally used to record the dynamic overall average voidage data from various fluidized bed configurations and conditions listed in Table 3.12. The information was outputted as a time-series of the average solids concentration present at the cross-sectional layer of the fluidized bed corresponding to the axial centre of the electrodes. Figure 3.14 shows the experimental arrangement for the dynamic voidage measurements.

Material	Bed	U range (m/s)	U/U_{mf} range	Re_p range
A	146 mm	0.058-0.402	1.49-10.32	0.9-6.4
A*	146 mm	0.101-0.402	1.18-4.73	2.4-9.5
G	146 mm	0.101-0.402	1.23-4.91	2.1-8.3
B	300 mm	0.092-0.614	1.58-10.59	1.8-11.7
B*	300 mm	0.224-0.614	1.8-4.91	5.8-15.9

Table 3.12 Bed configurations used for dynamic bed voidage comparisons

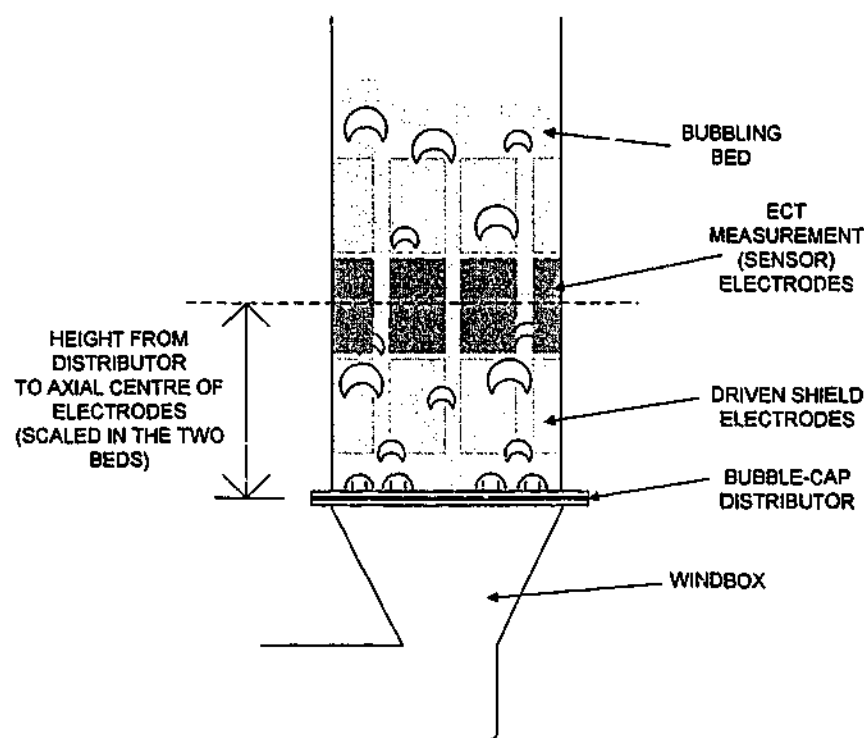


Figure 3.14 Experimental arrangement used for the dynamic voidage experiments

3.7.4 Solids Mixing Studies Using ECT

The second application of the ECT system in this work was to the study of solids mixing within the smaller-scale fluidized beds. Given that the ECT system uses the differences in dielectric constant (or permittivity) of the solids and the fluidizing gas to distinguish the emulsion from the bubbles in imaging of gas fluidization, the question arose as to whether the ECT would be able to distinguish between two different solids if they had different permittivities.

Initial trials with glass beads as a tracer in beds of silica sand, and using a modified calibration procedure showed promise, so this approach was incorporated into the similarity study. This, however required the addition of a solids drain port to the 146 mm bed so that the bed could be emptied in situ.

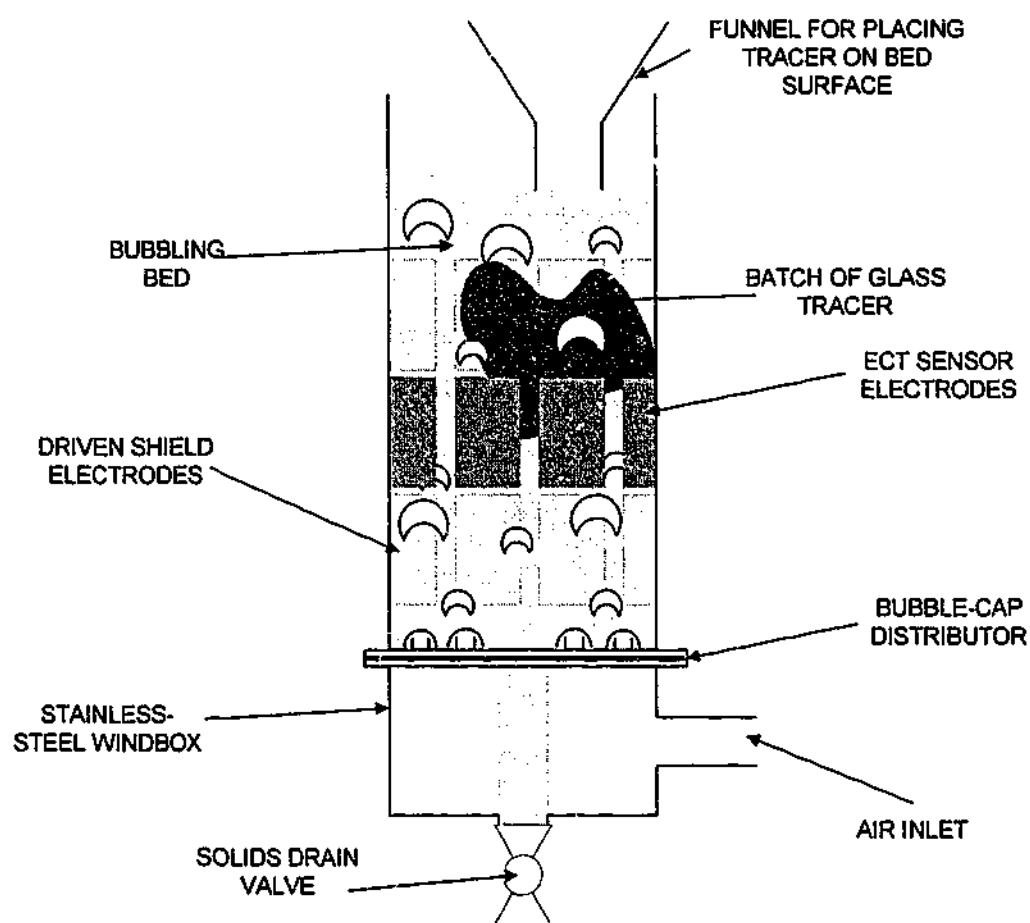


Figure 3.15 Bed arrangement used for the solids mixing experiments carried out with the ECT system.

Additionally the vessel walls were reduced to a height of 400 mm to aid in tracer solids placement. The modified 146 mm bed arrangement is shown in Figure 3.15, which also

illustrates the concept of the experiment. Specific details of the calibration procedure, bed materials, tracers and operating conditions are given in Chapter 6.

3.8 Setup for Monitoring Float Tracers

Solids motion was characterised in the three larger scaled beds using neutrally-buoyant spherical float tracers. (Details of the tracers themselves are given in Chapter 6). Three tracers with identical diameter and density (but different colour) were placed into a given bed for each experiment. The appearance and disappearance of the float tracers at the bed surface was recorded using a Sony TRV-89E Hi-8 video camera, mounted above the bed surface. The camera was contained in a sealed housing (of the type normally used for underwater filming) to prevent solids ingress into the mechanism.

Each float tracer was painted with a different colour fluorescent paint (red, green and blue), and the bed surface was illuminated with "soft" ultraviolet light from blacklight fluorescent tubes, so that each time a tracer appeared at the bed surface it could be easily and clearly distinguished in the video images.

Because the range of wavelengths of light captured by the video camera is somewhat wider than the "visible" spectrum (extending both into the near UV and the near IR for most modern cameras), the camera was fitted with an ultraviolet filter (Kodak Wratten gelatin filter 2A) to ensure the background image of the bed itself remained dark whilst the coloured tracers showed up clearly.

The height of the camera from the bed surface and the height of the fluorescent lamp assemblies were adjusted in each bed to ensure that the bed surface was fully contained in the camera's field of view and the lamp assembly was as close as possible to the bed surface whilst remaining out of the field of view. The arrangement is shown in Figure 3.16.

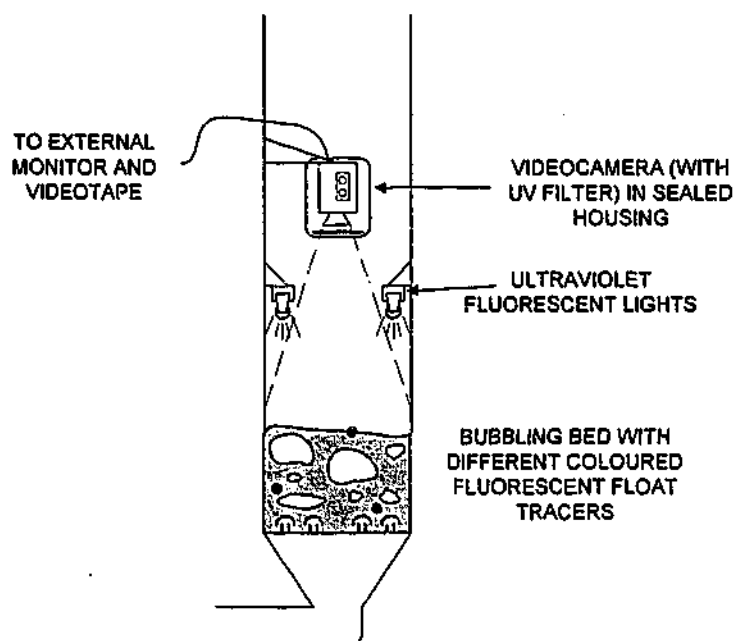


Figure 3.16 General arrangement for solids motion experiments carried out at the 300 mm, 600 mm and 1560 mm scales. The camera was set up so that the field of view was wide enough to cover the entire bed surface when fluidized; the height of the lamps was then adjusted so that they were just clear of frame. Three geometrically scaled spherical float tracers covered with different colours of fluorescent paint were used at any one time.

Note that no pressure probes were present in the beds during these experiments. The run-times for the solids mixing experiments were 90, 60 and 45 minutes in the 1560, 600 and 300 mm beds respectively. The reason that three tracers were used in each experiment was to increase (triple) the number of statistics generated for a given length of experiment. After the experiments were recorded, videotapes were viewed and the quantity of interest, namely the time between appearances of a given coloured tracer was logged. The details of this logging procedure are given in Chapter 6.

3.9 Conclusion

In this chapter, all pertinent information regarding the experimental equipment used in this study has been presented. Operating conditions have also been specified and the various equipment items used for measurements have been described. In the next three chapters, the experimental verification study for the simplified scaling criteria will be presented in detail. Chapters have been organised according to measurement technique.

4. PRESSURE FLUCTUATIONS

4.1 Introduction

In order to assess the simplified scaling laws, experimental comparisons have been made to establish the existence and extent of hydrodynamic similarity between the four cold model fluidized beds. This chapter presents the background to, results of, and discussion concerning those hydrodynamic similarity comparisons carried out using pressure fluctuations. (Parts of this work were presented in Sanderson *et al.* 2001 and Sanderson and Rhodes 2001).

4.2 Background – Pressure Fluctuations in Bubbling Fluidization

Pressure measurements and pressure fluctuation analyses have been popular experimental tools for investigations of fluidized bed behaviour for a considerable length of time. This is due to the relative simplicity with which the measurements can be made, and the wealth of information which can be derived from the measurements. Measurement of the overall bed pressure drop as a function of the gas velocity is used to determine the minimum fluidization velocity of the bed material. Time averaged values of the pressure difference between different locations are routinely used on industrial units to give an indication of bed height.

It has long been known that by studying pressure fluctuations within the bed, detailed information about the bed hydrodynamics can be obtained. The earliest studies of pressure fluctuations were carried out in the 1950's. Shuster and Kisliak, (1952) relied upon the visual interpretation of chart records for the analysis of bed behaviour, and developed a statistical index for measuring fluidization quality based on earlier work of Morse and Ballou (1951) who used a capacitance probe for similar investigations. Since these early studies, many statistical, spectral and more recently, chaotic analyses have been applied to pressure fluctuations as a means of attempting to fingerprint the behaviour of fluidized beds. The analyses of these time varying pressure signals have become more complex and involved over the years, and the actual mechanisms by which the pressure fluctuations are produced within the bed have also been the subject of much discussion.

4.2.1 Sources of Pressure Fluctuations

The pressure fluctuations occurring within a bubbling fluid bed are generally acknowledged to be both directly and indirectly due to the flow of bubbles, but the exact details of the cause and effect have been difficult to identify, and a great deal of work has been published on the subject. In the early stages of pressure fluctuation analysis it was felt that bubbles were the *only* cause of these fluctuations and the single remaining question was whether the fluctuations were due to the presence of local bubbles close to the measuring probe or bubbles erupting at the bed surface. Tamarin (1964), Hiby (1967), and Lirag and Littman (1971) concluded that the passage of bubbles through the upper surface of the bed and corresponding fluctuations in bed height were the major cause of the fluctuations. Lirag and Littman (1971) observed that the dominant frequency in the fluctuating signal did not alter with a change in the probe location, an observation also supported by the work of Fan *et al* (1981). Both workers did observe that the dominant frequency in the pressure fluctuations was related to bed height, and varied approximately by $\frac{1}{\sqrt{H}}$. It should be noted that Roy and Davidson (1989) showed that measurements from single pressure probes were predominantly influenced by bed surface effects, and double pressure probes mainly register the passage of local bubbles. Since both Lirag and Littman (1971) and Fan *et al* (1981) used a single probe, it is not surprising that they found that bed surface effects predominated.

But there was also evidence suggesting that bubble activity was not the only source of pressure fluctuations; Hiby (1967) also showed that particles could undergo coherent oscillations when the bed was very shallow, and work by Davidson (1968), Wong and Baird (1971) and Baird and Klein (1973) indicated that the plenum chamber could behave like a Helmholtz resonator with the bed acting like a piston above it, although the effect was only significant in beds with low pressure drop distributors. Fan *et al* (1984) extended this idea and related the instantaneous bed height to the residence time of a bubble in the bed.

Foscolo and Gibilaro (1984) showed that pressure disturbances within a bed propagate in the form of either dynamic or continuity waves and used the relative velocities of each wave type as the basis for a criterion for bed stability. Roy *et al.* (1990) derived an expression for the velocity of sound in fluidized beds and verified this experimentally by cross-correlating pressure fluctuation measurements. More recently Bi *et al.* (1995), Musmarra *et al.* (1995), and van der Schaaf *et al.* (1998), have also explored the issue of

pressure wave propagation in fluidized beds. Van der Schaaf *et al* (1998) disputed the existence of particle collision waves as proposed by Musmarra *et al.* (1995), and also rejected the damping mechanism suggested by both Bi *et al.*, (1995) and Musmarra *et al.* (1995) for the attenuation of compression waves in fluidized beds. They attributed pressure fluctuations in a fluidized bed to slow upward-moving pressure waves caused by rising gas bubbles; and fast compression waves which move upwards and downwards. The fast upwards moving compression waves were found to be caused by gas bubble formation and coalescence, with the downwards moving compression waves resulting from bubble eruptions at the bed surface, bubble coalescence and changes in bed voidage. They also pointed out the types of pressure waves which would predominate for a given pressure probe configuration (single or double probe) – See Section 3.6.2.

4.2.2 Models for Pressure Oscillations in Gas-Fluidized Beds

A number of workers have proposed models for the pressure fluctuation oscillations in fluidized beds. Tamarin (1964) described a fluidized bed as consisting of a fluid phase and “self-excited” particles. Through a combination of theoretical reasoning and experimental data an empirical correlation for the frequency of oscillation in two-phase beds was proposed:

$$f = 0.585 \left(\frac{U}{U_{mf}} - 1 \right)^{0.275} \frac{\sqrt{gD}}{d_{eq}} \quad (4.1)$$

This empirical model is limited in usefulness because the bubble diameter (d_e) has to be known in order to estimate the frequency of oscillation. Hiby (1967) and Verloop and Heertjes (1974) both proposed mechanisms for bed oscillation which are similar to each other in many respects, although the derivations differ slightly. Hiby proposed a system of oscillating layers being “pulled into tune” *ie* layers of bubble production which coincide with the natural oscillations of the bed. The changes in bed voidage as the bed lifts and falls back to its original position result in the fluctuations in static pressure drop across the bed. Verloop and Heertjes, on the other hand, considered shallow incipiently fluidized beds and suggested that the entire incipiently fluidized bed oscillates in phase. The resulting equations from the different workers proposed for predicting the natural frequency of bed oscillation are as follows:

$$\text{Hiby (1967)} \quad f = \sqrt{\frac{g(1-\varepsilon)}{(0.75\pi^2)H\varepsilon}} \quad (4.2)$$

$$\text{Verloop and Heertjes (1974)} \quad f = \frac{1}{2\pi} \sqrt{\frac{g(2-\varepsilon)}{H\varepsilon}} \quad (4.3)$$

Fan *et al.* (1984) developed a piston-like model for bubbling beds by an extension of previous work by Davidson (1968), Wong and Baird (1971) and Baird and Klein (1973). The major assumption in this approach was that the bed oscillates as a coherent whole. The natural frequency of the bed can be calculated, accounting for the mass of particles in the bed and the compressibility of the gas in the windbox. Unfortunately, the complex algebra required for the piston model does not allow easy solution, except for the trivial case where the distributor pressure drop is zero:

$$f = \frac{1}{2\pi} \sqrt{\frac{P_c A}{V_c \rho_{mf} H_{mf}}} \quad (4.4)$$

(P_c and V_c are the the windbox pressure, and volume respectively.)

A different approach was taken by Baskakov *et al.* (1986) who proposed a direct analogy between fluidized bed hydrodynamics and a hydraulic pendulum (eg U tube manometer). The changes in bed voidage (and hence pressure) are due to the change in the height of the bed surface caused by the rising of a single large bubble and the associated entrainment of solids to the bed surface. Solids then return downwards along the sides of the bed to restore equilibrium. Their resulting equation for the natural frequency of bed oscillation is similar to the previous workers except that it includes no dependence on bed voidage:

$$\text{Baskakov et al. (1986)} \quad f = \frac{1}{\pi} \sqrt{\frac{g}{H}} \quad (4.6)$$

Brown and Brue (1996) made comparisons between experimental pressure fluctuation measurements and the equations of Hiby (1967), Verloop and Heertjes (1974) and Baskakov *et al.* (1986). They found that in their system (local pressure measurements in a bubbling fluidized bed of various glass beads), the equation of Hiby most closely

predicted the observed frequency phenomena. They also proposed a modification to the Hiby equation, after observing a decrease in the measured fluctuation frequency under certain bubbling bed conditions. They attributed this decrease to the increasing influence of bubble coalescence on bed surface fluctuations in deeper bubbling beds, and re-derived the Hiby (1967) equation basing the derivation on minimum fluidization velocity, rather than superficial gas velocity. The modified form of the Hiby equation as proposed by Brown and Brue (1996) was:

$$f = \frac{2}{3\pi} \sqrt{\frac{g}{H} \left(\frac{(3-2\varepsilon)}{\varepsilon} \right)} \quad \text{for } Re_p < 20 \quad (4.7)$$

and

$$f = \frac{2}{3\pi} \sqrt{\frac{3g}{H} \left(\frac{(1-\varepsilon)}{\varepsilon} \right)} \quad \text{for } Re_p > 20 \quad (4.6)$$

All of the bubbling bed models mentioned show the same dependence of bed fluctuation frequency on bed depth, *ie* $f \propto \frac{1}{\sqrt{H}}$. The dependence of fluctuation frequency on other

operating variables such as superficial gas velocity and particle size, shape and density varies with the models, but certainly for the self-excited oscillation models of Hiby (1967) and Verloop and Heertjes (1974), particle properties and gas velocity are only important in the extent to which they effect the bed voidage. In the U-tube model of Baskakov *et al* (1986) the *only* variable is the bed height H . Other workers, such as Sadasivan *et al.*, (1980) developed empirical correlations based on experimental data which also show the same dependence of bed fluctuation frequency on bed depth. This dependency of fluctuation frequency on bed height is consistent with the development of the simplified scaling laws if the bed heights are scaled in proportion with the bed diameters. This can be shown quite simply:

Recalling the equations from the Horio *et al.* (1986a) scaling law scheme,

$$U_2 - U_{mf2} = \sqrt{m}(U_1 - U_{mf1}) \quad (4.7)$$

and

$$U_{mf2} = \sqrt{m}U_{mf1} \quad (4.8)$$

where the subscripts 1 and 2 refer to the smaller and larger scaled systems and the scaling factor m refers to the increase in bed geometry:

$$m = \frac{D_2}{D_1} \quad (4.9)$$

So scale-up using this scaling law therefore involves increasing the characteristic length dimensions of the system by m , and the characteristic velocity (length per unit time), by \sqrt{m} , ie:

$$L_2 = mL_1 \quad (4.10)$$

and

$$\left(\frac{L}{T}\right)_2 = \sqrt{m} \left(\frac{L}{T}\right)_1 \quad (4.11)$$

Characteristic frequency (f) can be defined as

$$f = \frac{\left(\frac{L}{T}\right)}{L} \quad (4.12)$$

and therefore using Equations 4.10 and 4.11, according to the scaling law the frequency should scale by:

$$f_2 = \frac{\left(\frac{L}{T}\right)_2}{L_2} = \frac{\sqrt{m} \left(\frac{L}{T}\right)_1}{mL_1} = \frac{1}{\sqrt{m}} f_1 \quad (4.13)$$

Now the expressions for bed frequency in the proposed models all have the dependency

$$f \propto \frac{1}{\sqrt{H}} \quad (4.14)$$

If the aspect ratios are maintained the same in the two different sized units then by Equation 4.9:

$$H_2 = mH_1 \quad (4.14)$$

and

$$\frac{f_2}{f_1} = \sqrt{\frac{H_1}{H_2}} = \frac{1}{\sqrt{m}} \quad (4.15)$$

which is in agreement with Equation 4.13, thus showing that the previously proposed expressions for bed frequency are in agreement with the simplified scaling law.

In addition to investigations of the bed frequency, Lirag and Littman (1971) and other workers have found from their experiments that the amplitude of the pressure fluctuations registered by a single pressure tapping was also a strong function of bed height. Fan *et al.* (1981) also found that the pressure fluctuation amplitude registered by a single pressure tapping was influenced by the height of the tapping point in the bed to some extent. Fluctuation amplitude showed a tendency to increase and then decrease again with increasing tapping height from the distributor. From multiple axial measurements at different gas velocities they found that the height at which the fluctuation amplitude started to decrease again descended towards the distributor as the gas velocity was increased. From their results they concluded that the bed density has an important effect on the amplitude of the pressure fluctuations.

Expressions for predicting the amplitude of pressure fluctuations have also been derived. For example, Baskakov *et al.* (1986) presented an equation for the amplitude of the pressure fluctuations registered at the bottom of the bed (A_b), based on dimensional analysis and empirical constants from experimental results:

$$\frac{A_b}{\Delta P_{bed}} = 1.5 \left[\frac{\rho_b (U - U_{mf})^2}{\Delta P_{bed}} \right]^{0.42} \quad (4.16)$$

Roy and Davidson (1989) also presented an empirical expression for the amplitude of pressure fluctuations registered by a single probe:

$$\frac{P}{\rho_s (U - U_{mf})^2} = 0.08(1 - \varepsilon) \left[\frac{U - U_{mf}}{(gD)^{0.5}} \right]^{-1.6} \left[\frac{H}{D} \right]^{0.8} \quad (4.17)$$

The above expressions are consistent with the simplified scaling law in the case of the same bed expansion characteristics (ie same ρ_s , ρ_b and ε) at both scales. That is, for pressure fluctuations of amplitude A_b ;

$$A_{b2} = mA_{b1} \quad (4.18)$$

where m is the scaling factor from Horio's simplified scaling laws.

4.2.3 *Hydrodynamic Similarity Evaluations by Pressure Fluctuation Analysis*

The results of previous work indicate the complexity of the pressure fluctuation signal and the combination of sources which are likely to contribute to the signal. It is clear from the previous work that the pressure signals from single probes can be used to provide information about the overall bed hydrodynamics. It is also clear that many of the previous models proposed to explain these fluctuations agree with the simplified scaling law approach in terms of both pressure fluctuation frequency and amplitude. Therefore, it is reasonable to expect that the measured characteristics of a pressure fluctuation signal should scale according to the simplified scaling laws. Consequently, an analysis of the pressure fluctuations from a single-ended pressure probe in a bubbling fluidized bed in terms of amplitude and frequency (and statistical functions of these quantities) is likely to provide a sound basis for a quantitative hydrodynamic comparison of the simplified scaling laws.

4.2.4 *Experimental Criteria for Similarity Comparison*

If pressure fluctuation measurements are to be used for a hydrodynamic similarity comparison, it must first be shown that:

- Any contributions of noise to the recorded signal from other sources (eg electrical interference) is small enough as to not significantly influence the measurements or their analysis.
- The resultant discretely-sampled signal represents the pressure fluctuations accurately, without aliasing.
- The amplitude and frequency characteristics of the fluctuations for a given set of operating conditions are invariant and reproducible.

- The measurements and their analysis provide information which is sufficiently sensitive to correctly discriminate between known cases of hydrodynamic similarity and non-similarity.

In order to check that the above requirements had been satisfied, initial signal testing and pressure fluctuation experiments were conducted. A number of test cases were conducted to check the signal acquisition setup. Further physical experiments involving only a small scale change and deliberately matched and mis-matched scaling law parameters were then used to confirm the reliability of the measurements. These test cases were also used to identify the most practical form of analysis to carry out on the resulting fluctuation measurements.

4.3 Preliminary Signal Testing

Initial tests were conducted to evaluate the level of background electrical noise in the signals from pressure transducers at all scales. Worst-case signal-to-noise ratio situations could then be tested – these correspond to situations where the pressure transducer signal was at its lowest power (as the level of background electrical noise was relatively constant).

Test cases for the bandwidth of the signals resulting from pressure fluctuations at all scales are also presented in this section, as a check of the adequacy of the proposed signal sampling frequencies outlined in Section 3.6.5. This is in order to demonstrate that the sampling frequency (and hence the Nyquist frequency) is high enough to avoid aliasing.

4.3.1 Background Electrical Noise

Due to the low signal strengths involved, the background electrical noise level was monitored at the start of every experimental run in order to check that it was acceptable low. In fact, it was generally found that the background electrical noise in the system was extremely low. Typical results for background electrical noise recorded by the data acquisition system for the four fluidized bed scales have been expressed in terms of the average absolute deviation of the signal and are presented below in Table 4.1, along with values of the average absolute deviation of the lowest amplitude recorded pressure

signal involved in the experimental work. (The lowest amplitude recorded signals generally resulted from low gas velocities and probe locations close to the bed surface, although selecting transducers with appropriate ranges reduced the instances of extremely low signal strengths.) Note that for the purposes of the comparison, the data are presented in millivolts (mV). The average absolute deviation of the signal is a measure of the signal amplitude and is defined as:

$$AAD = \frac{1}{n} \sum |x - \bar{x}| \quad (4.19)$$

Bed Diameter	AAD of typical background noise	AAD of lowest strength signal
146 mm	0.002	0.03
300 mm	0.002	0.06
600 mm	0.004	0.05
1560 mm	0.005	0.05

Table 4.1 Comparison of the average absolute deviation (AAD) of background noise and the lowest recorded pressure fluctuation data. The values are presented in millivolts.

From the above data it can be seen that in these worst-case scenarios there is still an order of magnitude difference between the amplitude of the signal and that of the background noise, despite the low signal strength. Note that often signal amplifiers are used to boost the transducer output between transducer and data logging computer. Initially this was attempted in the present work using a solid-state amplifier and low-pass filter arrangement. This approach, however, led to a significant *increase* in the level of noise (compared to signal) and proved to be an unworkable arrangement. As mentioned in Section 3.6.5 it was found that by maintaining short connections with appropriately placed cables between transducer and data logging computer the noise was kept to a minimum without the need for amplification.

4.3.2 Bandwidth Check for Pressure Fluctuation Signals

For discrete sampling of a time series it is understandably important to select a sampling frequency which is high enough to accurately reflect all the characteristics of the original signal. The guideline is the Nyquist critical frequency (f_c), which is defined as half of the sampling frequency. If the signal being sampled is bandwidth limited to frequencies less than the Nyquist frequency, then the signal is completely determined by its samples. Or, to put it another way; in order to ensure the signal in question is accurately represented, one needs to select a sampling frequency at least double the highest frequency component of interest present in the signal.

It has been found that the typical global pressure fluctuation signal from a bubbling fluidized bed appears to be bandwidth limited to low frequencies (typically <20Hz) and contains a range of frequencies which do not alter significantly with changing gas velocity in the bubbling regime (eg van Ommen *et al.*, 1999, Dhodapkar and Klinzing, 1993). These observations imply that the sampling frequency can be kept reasonably low, and need not be changed for different operating gas velocities. The sampling frequencies used at the different scales in this work were outlined in Table 3.10. As a check that the sampling frequencies were adequately high (*ie* aliasing was not occurring), spectral analysis was carried out on some preliminary data for each scale to check that for the sampling frequency employed, the Fourier transform of the data was approaching zero as the frequency approached the Nyquist critical frequency (Press *et al.*, 1992).

Figure 4.1 shows the results of an initial comparison of the amplitude spectra from the four scaled fluidized beds under typical operating conditions. In this particular instance, the superficial gas velocity in all units is approximately twice the minimum fluidization velocity and the sampling rates have been set as shown in Table 3.10. For each bed, the amplitude spectrum has been produced by carrying out a fast Fourier transform (using the Hamming window function) on four sets of 4096 points from the pressure fluctuation time series. The resulting four spectra have then been averaged to produce a single spectrum for each bed. In this particular case a 10-point moving average has then been applied to each spectrum to make it easier to distinguish each spectrum on the chart.

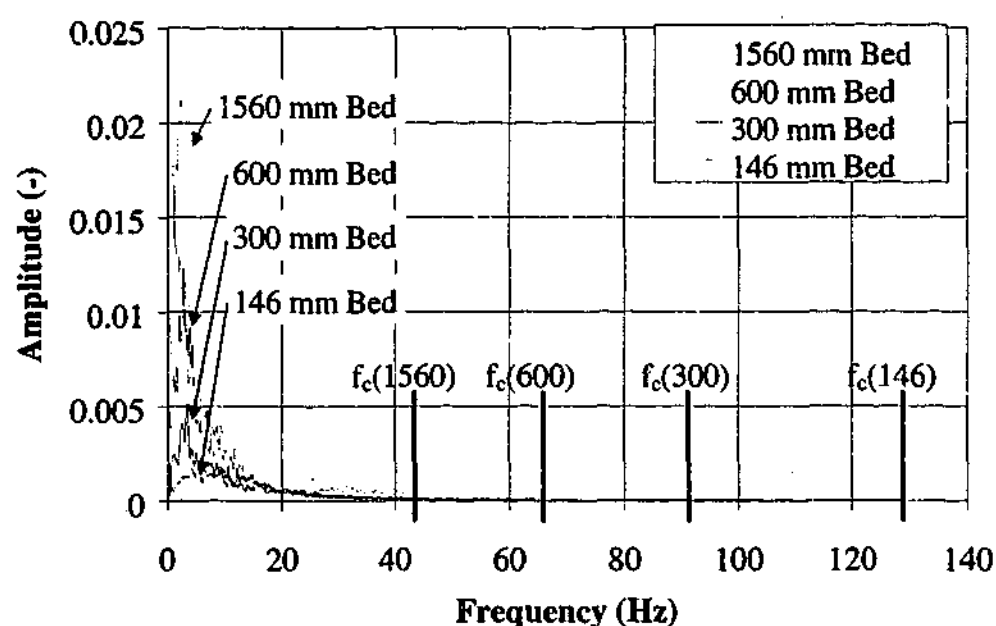


Figure 4.1 A preliminary comparison of the amplitude spectra from the four scaled bubbling fluidized beds, operating at $U/U_{mf} = 2.0$. Each spectrum is the averaged result of the fast Fourier transforms of 4 sets of 4096 points from the recorded time series, using the Hamming window function. A 10-point moving average has been applied to each spectrum to improve clarity. Vertical lines indicate the Nyquist critical frequency (f_c) for each bed with the bed diameter given in parentheses.

As can be seen from the Figure 4.1, all four spectra show the greatest signal strength at the lower frequency end of the range, *ie* less than 20 Hz. In all cases the spectra are tending towards zero signal amplitude as the frequency approaches the Nyquist critical frequency, indicating that the sampling frequency is high enough that the recorded time series accurately represents the original signal, and aliasing will be avoided with these sampling frequencies.

4.4 Pressure Fluctuation Analysis Techniques

Having demonstrated that the chosen method for pressure fluctuation signal acquisition is adequate in terms of both background electrical noise and sampling rate, the approach taken for the experimental evaluation of the pressure fluctuations will now be discussed.

Recall that when two fluidized beds are said to be hydrodynamically similar, their dependent hydrodynamic phenomena, when expressed in dimensionless form, are

expected to be identical. Experimental verification of similarity criteria is an attempt to compare these dependent hydrodynamic phenomena at different scales. In the case of the pressure fluctuations registered from a single pressure probe, the recorded signal is the result of complex interactions from within the bed and it is not possible to derive the specifics of the bed behaviour (such as bubble characteristics) from such a signal for direct comparison between one bed and another. So typically, the approach taken is to carry out some form of analysis on the recorded signals, and compare the characteristics of one signal with another (eg Fitzgerald and Crane, 1980; Leu and Lan, 1992; Brue and Brown, 2001). Thus it is commonly assumed that if the recorded signals exhibit similar characteristics, then the sources of the signals are hydrodynamically similar. The same approach will be adopted for the purposes of the current work.

In previous similarity studies involving pressure fluctuations, the characteristics of the signals investigated have included:

- Spectral or "frequency" analysis (Fitzgerald and Crane, 1980; Nicastro and Glicksman, 1984; Roy and Davidson, 1989; Leu and Lan, 1992; Di Felice *et al.*, 1992; Van der Stappen, 1996; Farrel *et al.*, 1998; Brue and Brown, 2001)
- Probability density (Nicastro and Glicksman, 1984; Leu and Lan, 1992; Farrel *et al.*, 1998)
- Fluctuation amplitude (Roy and Davidson, 1989; Leu and Lan, 1992; Di Felice *et al.*, 1992; Rapagna *et al.*, 1992; Van der Stappen, 1996)
- Autocorrelation functions (Fitzgerald *et al.*, 1984)
- Kolmogorov entropy (Van der Stappen, 1996)

Although there are a number of approaches that may be taken, generally speaking, the various workers listed above have selected analyses for the pressure fluctuations in order to compare them on two counts: Firstly, that the *size or magnitude* of the fluctuations have scaled correctly, and secondly, that the *time-scale or frequency* of the fluctuations have scaled correctly. Fluctuation magnitude is determined by some measure of the amplitude of the signal, such as the probability density distribution, root-mean-square, variance, standard deviation or average absolute deviation. Frequency or time-scale comparisons have involved autocorrelation functions, spectral analysis, and calculations of dominant frequency or average cycle frequency. Additional measurements of chaotic invariants such as the Kolmogorov entropy provide an indication of the predictability of the signal.

Since there appear to be a number of ways of looking at the magnitude and frequency of a pressure signal when investigating similitude, the question arises as to which approach gives the "best" representation of the signal. Clearly, the most comprehensive indication of the fluctuation characteristics comes from the distribution-style analysis, such as probability density function or PDF (in the case of magnitude) and power spectral density function or PSD (in the case of frequency). This is because for each time series a characteristic curve is generated showing the range of amplitudes (for the PDF) and the range of frequencies (for the PSD) encountered, and the scaled curves can be overlayed for a visual comparison. However, where many comparisons are to be made, for example in situations where a large number of scales and operating conditions are involved, this representation becomes unwieldy due to the number of distributions that must be compared. Consequently, the distributions are often replaced by a single number which in some way represents the distribution. In the case of the PDF, a measure of amplitude such as the standard deviation, average absolute deviation, variance *etc.* can be used; and in the case of the PSD, the dominant frequency or an average cycle frequency can be used. In this way, data can be compared more easily for a range of operating conditions, but information about the shape of the distributions is lost.

In the present work, due to the number of scales, operating conditions and comparisons involved, the latter approach (single number) has been used for the majority of cases. A limited number of probability density distributions and amplitude spectra have been compared in order to provide some detailed information about the magnitude and frequencies of the pressure fluctuations, but the majority of the comparisons have been carried out using the average absolute deviation (*AAD*) as a representation of fluctuation magnitude, and the average cycle frequency (\bar{f}) as a representation of the fluctuation frequency, in a similar fashion to Van der Stappen (1996). In the initial experimental appraisal of pressure fluctuations conducted between the two smallest scales of fluidized bed, a comparison between the distribution and single-number approaches is made, in order to demonstrate the consistency of the results derived from each method. The initial comparisons will provide evidence to show that the single number approach is reliable, and that in this application it does not mask any important characteristics which the distributions approach highlighted. In the next section the initial experimental study of pressure fluctuations is described in detail.

4.5 Approach for Pressure Fluctuation Experiments at Small Scales

There were a number of objectives for the preliminary experiments. They provided a complete test of the pressure probes and data acquisition system. The experiments generated sample data at scales and operating conditions similar to those previously reported in the literature so the outcomes for particular scaled and mis-scaled scenarios could be anticipated. Hence, the results could then be used to determine how well the measurements responded to known scaled and mis-scaled scenarios, and therefore used as a basis for drawing conclusions about similarity at the larger scales in subsequent work.

4.5.1 Experimental Setup

The experimental apparatus employed in the preliminary investigations has been outlined in Chapter 3, and was shown in Figures 3.1 and 3.2. The fluidized beds compared were the 146 mm and 300 mm diameter units, with settled height to diameter ratios of approximately 2:1. A single pressure probe was used in each bed, with its tip placed at the radial centreline and inserted at a height of 103 mm and 212 mm above the distributor (in the 146 mm and 300 mm diameter beds respectively). This corresponds to port C in Figure 3.11.

In these initial trials, the effects of operating gas velocity and bed material selection were investigated under the conditions specified in Sections 3.3 and 3.4. Scaled and mis-scaled bed materials were used as follows:

Experiment 1

In the 146 mm bed, Material A was used and compared with its correctly scaled counterpart, Material B, in the 300 mm bed. This experiment was designed to represent a correctly scaled system.

Experiment 2

In a secondary set of experiments, Material A* was used in the 146 mm bed, designed to scale correctly with its counterpart, Material B* in the 300 mm system. This experiment was also designed to represent a correctly scaled system, but involved larger particle sizes and hence higher particle Reynolds numbers than Experiment 1.

Note that by comparing results of Experiment 1 with Experiment 2 at appropriate operating velocities (*ie* the same U/U_{mf}), the consequences of a mis-scaled particle size can be determined.

Experiment 3

An additional experiment was conducted in the 146 mm bed with Material G, consistent with Materials A* and B* involved in Experiment 2 in terms of the simplified scaling law, but having a mis-matched particle density. The experiment was designed to explore the effect of a mis-scaled particle density.

For each bed, bed material and operating velocity, the experiment was repeated three times, with pressure fluctuations recorded from the probe for each experiment. The repetition enabled any random variation in results due to slight differences in conditions (*eg* initial bed height and gas flowrate) to be quantified to some extent.

4.5.2 Analysis and Comparison of the Pressure Fluctuations

The resulting pressure fluctuation time series from the various experiments were analysed and compared in a number of ways. First of all, the measurements were non-dimensionalised so that they could be directly compared with one another. In the case of the measured pressure, in these initial experiments non-dimensionalisation was carried out by dividing the measured pressure by the estimated weight per unit area of the bed contents, *viz*:

$$P^* = \frac{P}{\rho_b g H_s} \quad (4.20)$$

where ρ_b , the bulk density of the bed materials was taken to be 1550 kg/m³ for the silica sands (Commercial Minerals, 1998) and 2300 kg/m³ for the garnet material (GMA, 1999); H_s is the measured settled bed height for the relevant bed, and g is the acceleration due to gravity.

This choice of approach for non-dimensionalising pressure was made for several reasons. Firstly, giving the dimensionless pressure in this form makes it easy to relate the pressure measurements to the position of the probe in the bed, because (in theory)

the average dimensionless pressure should be unity for a probe at the distributor and zero for a probe at the bed surface. Since the average pressure is predominantly affected by probe position, it makes sense to do so. Secondly, although some workers (eg Nicastro and Glicksman, 1984) have chosen to non-dimensionalize pressure using a velocity-squared term in place of gH_s in the denominator of Equation 4.20 – and it is dimensionally consistent to do so, the velocity squared term can have an overriding influence on the resulting function when plotted against the dimensionless velocity expressed (as it is in this work) as multiples of U_{mf} . Additionally, because the term is squared, small errors in the value of the velocity can significantly alter the results. It is also mentally more difficult to relate the dimensionless pressure to a physical effect in this case.

Thus in this work, the approach of Equation 4.20 is preferred. However, as will be shown later, the chosen non-dimensionalisation procedure for pressure was not without its own shortcomings and in later experiments, the pressure measurements were non-dimensionalised in a slightly different way to reduce errors. This modified approach will be described in due course.

Frequency measurements were non-dimensionalised by:

$$f^* = f \left(\frac{D}{U_{mf}} \right) \quad (4.21)$$

which uses an approach similar to that of Nicastro and Glicksman, (1984), except that in the case of the simplified scaling criteria the relevant length dimension is the bed diameter, not the particle diameter, and the relevant length-per-unit-time parameter is the minimum fluidization velocity, not the superficial gas velocity.

4.6 Results of the Preliminary Experiments

The single number parameters of the pressure fluctuation time series which were investigated were the average pressure (indicating bed expansion); average absolute deviation (a measure of the fluctuation magnitude); and the average cycle frequency (a measure of the fluctuation frequency). The average absolute deviation was calculated using Equation 4.19, and the average cycle frequency (number of times the fluctuating

signal crosses its own average) was numerically evaluated using the RRChaos (ver. 2.25) software of the Reactor Research Group (Delft University of Technology). Additionally, data from selected operating conditions were used to produce probability density functions and amplitude spectra, with which to compare the single number average absolute deviation and average cycle frequency results. The method of producing these distributions will be described alongside the relevant results.

4.6.1 Average Pressure Drop Comparison

The simplest comparison to be made between the scaled fluidized beds is that of the average pressure measured by the probe. This is a good indicator of relative bed expansion. Correctly scaled average pressure drops and bed expansion have been observed by previous investigators of bubbling bed scaling laws (eg Zhang and Yang, 1987) and are to be expected for the correctly scaled small systems considered here. Figure 4.2 shows the dimensionless average pressure measured for the correctly scaled beds used in Experiment 1 for the full range of gas velocities considered.

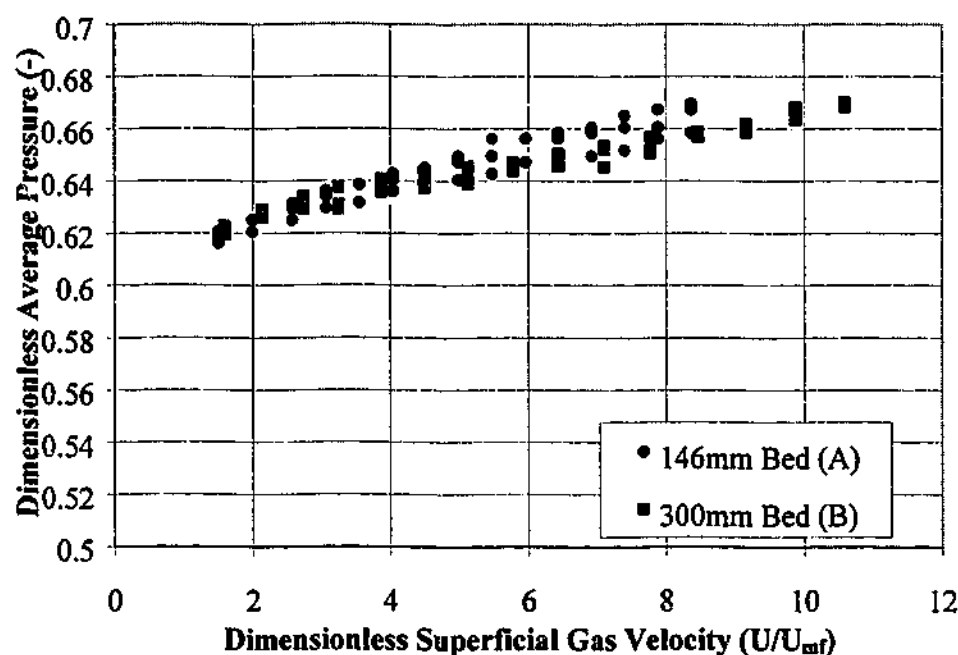


Figure 4.2 Comparison of the dimensionless average pressure measured in the 146 mm and 300 mm correctly scaled beds for a range of dimensionless superficial gas velocities.

Clearly, there is good agreement between the two beds when the average pressure is compared on this basis. There is a limited amount of scatter in the data indicating some

variation in results between the three runs performed in each bed, likely to be due to small variations in settled bed height and superficial gas velocity between runs. Note that for this experiment the settled bed heights were approximately 295 mm and 590 mm in the two scaled beds, and the probe heights were 103 and 212 mm. Ignoring bed expansion, this puts the probes at a dimensionless height of

$$\frac{H_s - h}{H_s} = \frac{0.295 - 0.103}{0.295} = 0.65 \text{ and } \frac{0.590 - 0.212}{0.590} = 0.64 \quad (4.22)$$

below the bed surface in the two beds. Since the pressure drop through a bubbling fluidized bed is often approximated by:

$$\Delta P_{bed} = \rho_b g H \quad (4.23)$$

(eg Kunii and Levenspiel, 1991), it is to be expected that the "depth" of the probes expressed in Equation 4.22 should correspond approximately to the average pressure when non-dimensionalised by Equation 4.20, which it does.

Note that whilst it was originally intended that the beds be operated at exactly the same dimensionless superficial gas velocity for each condition in the experiments, a systematic error occurred in the flow measurements during these initial small-scale experiments for the 300 mm bed. This error was caused by a damaged calibration instrument, and as a result the superficial gas velocities *indicated at the time of the experiment* were significantly less than the true gas velocity. The flow data were subsequently corrected for this error (*ie* gas velocities presented in this work are unaffected by this initial error), but consequently the dimensionless superficial gas velocities are not exactly the same at each data point for the two beds, as can be seen in Figure 4.2. The trends, however, are still clear.

Having established the agreement in bed expansion between the two correctly scaled beds it is now worthwhile comparing the results with those of Experiment 2, the second set of correctly scaled beds involving larger particle sizes.

A similar range of superficial gas velocities were involved, however the larger particle sizes (and hence greater minimum fluidization velocities) mean that the dimensionless

gas velocity is lower in this second set of experiments. Figure 4.3 shows the results for the larger particle sizes compared with the original data presented in Figure 4.2.

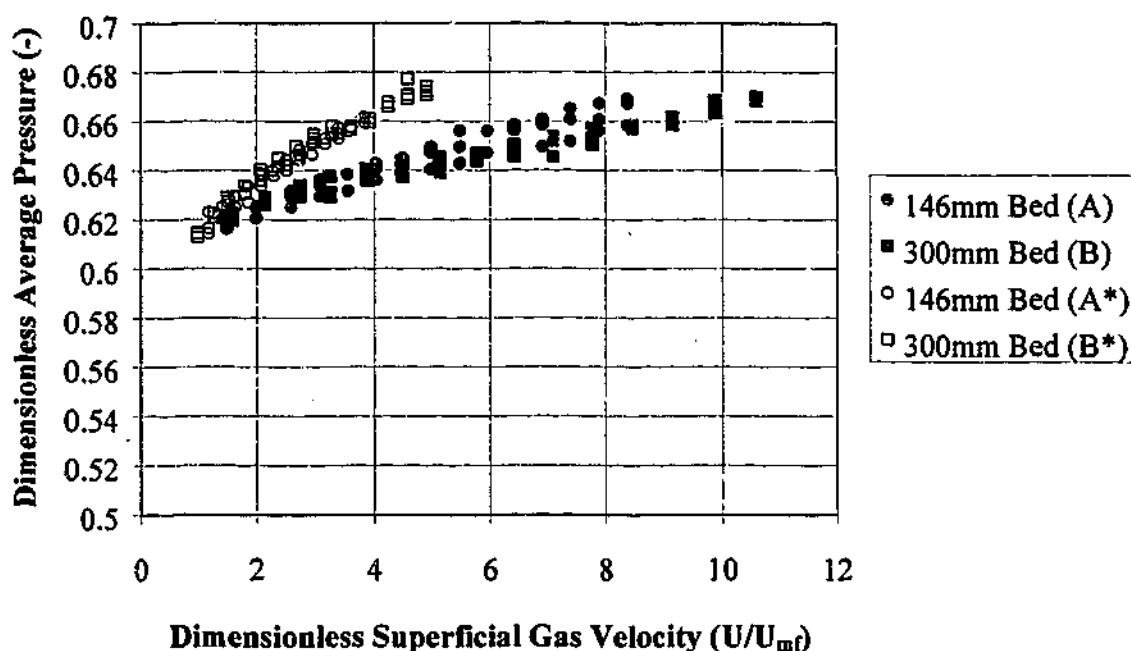


Figure 4.3 Plot of dimensionless average pressure drop against dimensionless superficial gas velocity. Comparison between the original correctly scaled beds (materials A and B in the 146 mm and 300 mm beds), with the second set of correctly scaled materials in the same scale beds (materials A* and B* in the 146 mm and 300 mm beds).

Two points can be noted from Figure 4.3. Point one is that the second pair of scaled beds (with materials A* and B* indicated by the open markers) also show good agreement with each other in dimensionless average pressure (implying similarity in dimensionless bed expansion). Point two is that the trend for this pair of bed materials is distinctly different from that of the original bed material pair. This is to be expected, since the second set of bed materials are not operating under conditions of similarity when compared to the first set. So, Figure 4.3 demonstrates the consequence of mis-scaling the bed material size (and hence U_{mf}).

Of course, one must consider the difference in these trends in the correct context. In the case of the second set of materials (A* and B*), the minimum fluidization velocities are approximately double those for the first set of materials (A and B). If we compare the two materials used in the 146 mm bed for example, the same absolute superficial gas velocity in that bed will yield only *half* the *dimensionless* superficial gas velocity for the larger material A* when compared with material A. So when plotted in dimensionless

form, the trends between A and A* appears to be significantly different. In actual fact, at the same *absolute* superficial gas velocity, the bed expansion trends would be about the same for both these materials. So it is a consequence of the way the data are plotted in Figure 4.3 that the expansion behaviour of the materials appears to be so different. In dimensionless terms the behaviour of the materials is different, but in terms of absolute superficial gas velocity, the expansion behaviour of all four materials would be very similar (not unexpected since they are all different grades of the same type of sand).

Having considered the effect of different sized bed materials on the dimensionless average pressure, the final consideration is that of the effect of changing the particle density, whilst maintaining the similarity criteria in all other respects. This was carried out in Experiment 3, where garnet sand, (designated as material G) was used in the 146 mm bed. In terms of minimum fluidization velocity, material G was very similar to material A*, and hence follows the simplified scaling criteria of Horio *et al.* (1986a) with respect to both A* and B* materials. Figure 4.4 compares the results for the denser bed material G with A* and B*.

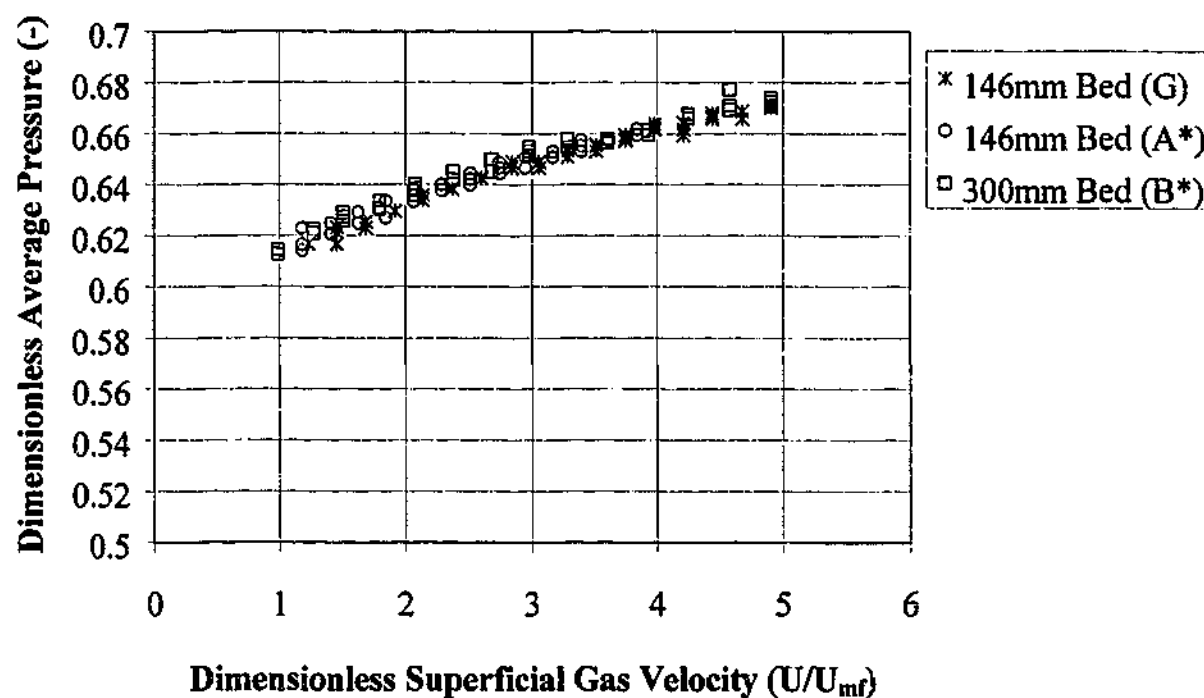


Figure 4.4 Comparison of the dimensionless average pressure over a range of dimensionless gas velocities between correctly scaled bed materials A*, B* (silica sands) and G (garnet sand). Although meeting the requirements of the Horio scaling criteria, material G has a significantly higher density.

Figure 4.4 indicates that despite its greater density, the dimensionless pressure for the garnet sand shows a similar trend to that of the two silica sand materials. Note that the increased density is accounted for in the non-dimensionalisation procedure (Equation 4.21) and the minimum fluidization velocity of material G is very close to that of material A*. As far as bed expansion goes, the result is not unexpected, since the bed expansion for group B materials is not dramatically affected by particle density. This observation is borne out by the majority of bubble size correlations (*eg* Darton *et al.*, 1977; Werther, 1978; Mori and Wen, 1975 *etc.*) which express bubble size as some function of minimum fluidization velocity, and do not specifically include a particle density term.

4.6.2 Comparison of Average Absolute Deviation

Whilst the average pressure gives an indication of the average height of bed material present above the probe, the measured amplitude of the pressure fluctuations is a little harder to directly relate to bed behaviour. As mentioned in Section 3.6.2, the sources of pressure fluctuations detected by a single probe within a bubbling bed are various, with simultaneous contributions from pressure waves originating from bubble generation, coalescence and eruption fluctuations (Van der Schaaf *et al.*, 1998). The amplitude of the fluctuations is a strong function of gas velocity and has therefore been used by many investigators undertaking hydrodynamic similarity comparisons (see Section 4.4).

As previously stated, the average absolute deviation (see Equation 4.19) has been used as a measure of the pressure fluctuation amplitude in this work. This can be easily thought of as measuring the distance between the instantaneous value of the signal and its arithmetic average for every point in the time series, and then averaging all the measured distances for the entire time series.

The average absolute deviation was calculated from the recorded pressure fluctuations for the full range of gas velocities employed in the similarity experiments. Figure 4.5 shows the result for all the bed materials (Experiments 1, 2 and 3).

The results presented in Figure 4.5 show excellent agreement between the correctly scaled beds A and B, and also between the correctly scaled beds A* and B*. There is a distinct difference in the trends for these different bed pairs, however, demonstrating the difference in dimensionless fluctuation magnitude when mis-scaled beds are compared.

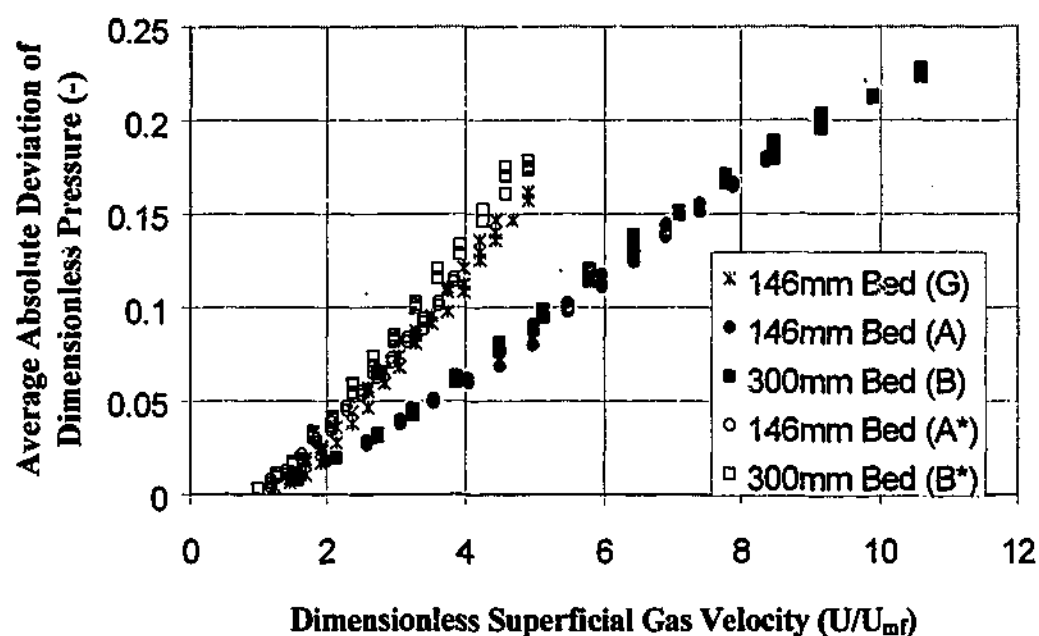


Figure 4.5 Results for the average absolute deviation of dimensionless pressure for correct and mis-scaled beds. Materials A and B in the 146 mm and 300 mm beds respectively are correctly scaled. Materials A* and B* in the 146 mm and 300 mm beds respectively are also correctly scaled, but different from the A B pair. Material G is correctly scaled with materials A* and B* in terms of the Horio criteria, but has a mis-matched particle density.

The trend for material G in the 146 mm bed (mis-scaled particle density) closely matched the results for materials A* and B*, indicating that at least for this range of gas velocities, the dimensionless amplitude of the pressure fluctuations is insensitive to the density mis-match.

4.6.3 Comparison of Average Cycle Frequency

The dimensionless average cycle frequency of the measured pressure fluctuations was calculated for the systems used in Experiments 1, 2 and 3 as a basic indicator of the frequency of the fluctuations. So that the effects of the non-dimensionalisation procedure may be better appreciated, the dimensional average cycle frequency will first be introduced, before proceeding with the comparison on a dimensionless basis. Calculated as the number of times the time-series crosses its own average per unit time,

Figure 4.6 shows the results for the dimensional cycle frequency (units in Hz) for the 146 mm and 300 mm beds with materials A and B.

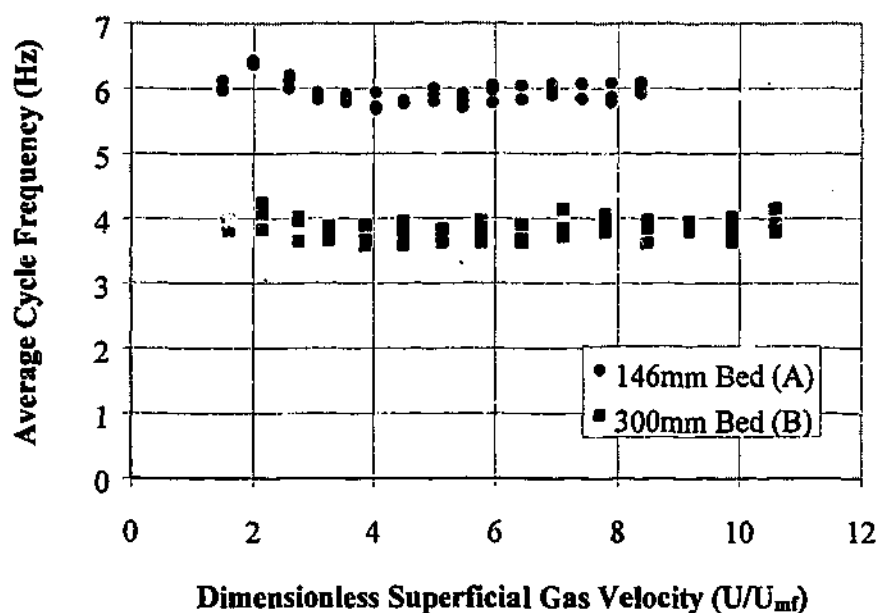


Figure 4.6 Dimensional average cycle frequency comparison between the 146 mm and 300 mm diameter beds with correctly scaled materials A and B respectively for a range of dimensionless gas velocities.

As can be seen from the above figure, in absolute terms the frequency is only slightly affected by gas velocity, the trends for the two units are similar in shape and the average cycle frequency of the smaller scale unit is higher than that for the larger unit. This is to be expected since the depth of the smaller bed is lower, and there is a generally observed height-dependency of fluctuation frequency in bubbling beds, with shallower beds exhibiting higher frequency fluctuations than deeper beds (eg Lirag and Littman, 1971; Fan *et al.*, 1981; Dhodapkar and Klinzing, 1993). As shown in Section 4.2.2, this height dependency has often been modelled by expressions consistent with the simplified scaling law. So, do the results of Figure 4.6 agree with the results expected for correctly scaled beds? To answer this, it is necessary to appreciate how the scaling law affects the time-scale and frequency behaviour of the beds in question. In the simplified scaling criteria, recall that the length scale has increased by a factor of m , but the length-per-unit-time scale has only increased by \sqrt{m} . Consequently the time-scale has changed by \sqrt{m} times and so, accordingly, frequency changes by $\frac{1}{\sqrt{m}}$. We would therefore expect that the measured frequency be lower in the larger bed, by a factor of $\frac{1}{\sqrt{m}}$. In the case of

the above beds, the value of \sqrt{m} for the scale change has been calculated as 1.49 (U_{mf} basis) from the data of Table 3.2.

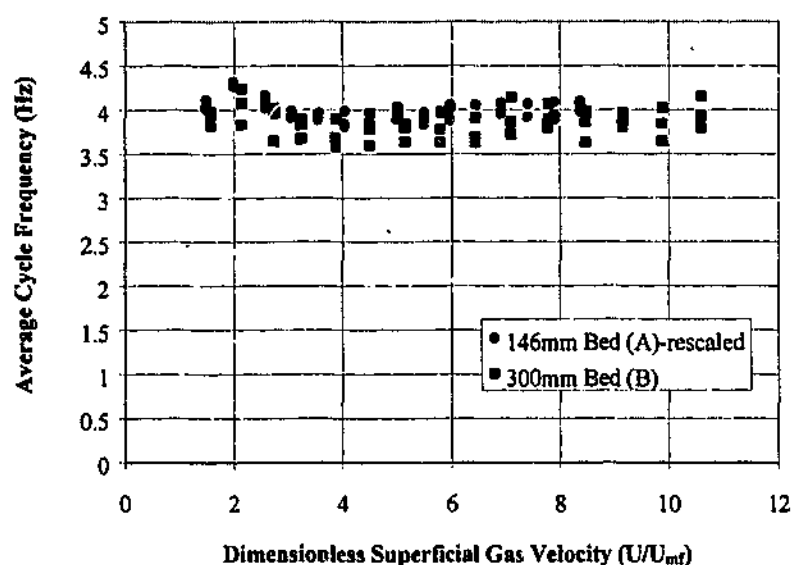


Figure 4.7 Comparison of average cycle frequency between the correctly-scaled 146 mm bed with material A and the 300 mm bed with material B for a range of dimensionless gas velocities. Results for the smaller bed have been re-scaled by the scaling factor $\frac{1}{\sqrt{m}}$ where $\sqrt{m} = \frac{U_{mf}(300\text{mmBed})}{U_{mf}(146\text{mmBed})}$.

Thus it is expected that the average cycle frequency be approximately 1.49 times higher in the smaller bed. Figure 4.7 shows the data of Figure 4.6 re-plotted with the data for the smaller bed scaled down by a factor of 1.49. Figure 4.7 clearly shows close agreement of the scaled bed frequencies. Now the comparison will be extended to include the second set of bed materials, the correctly scaled A* and B* combination. The results are shown in Figure 4.8 and 4.9 without and with the use of the scaling factor respectively.

In Figure 4.8 it can be noted that in absolute terms, the average cycle frequencies for the larger materials A* and B* in the two beds are slightly lower than for their smaller counterparts, A and B. This agrees with the experimental observations of previous workers (eg Sadasivan *et al.*, 1980; Leu and Lan, 1992) that larger particles tend to have lower bubble eruption frequencies. The low frequency outliers noted for the 146 mm (A*) and 300 mm (B*) data correspond to visual observations of incomplete fluidization at low gas velocities very close to U_{mf} . The difference (offset in the y-direction) in measured frequency between material A* in the 146 mm bed and material B* in the 300

mm bed is about the same as that for materials A and B. As can be seen from Figure 4.9, when the appropriate scaling factor of $\frac{1}{\sqrt{m}}$ is applied to the 146 mm bed A* data (where \sqrt{m} is calculated as 1.47 – on a U_{mf} basis from data in Table 3.2) correspondence with the results for the 300 mm bed B* combination is apparent.

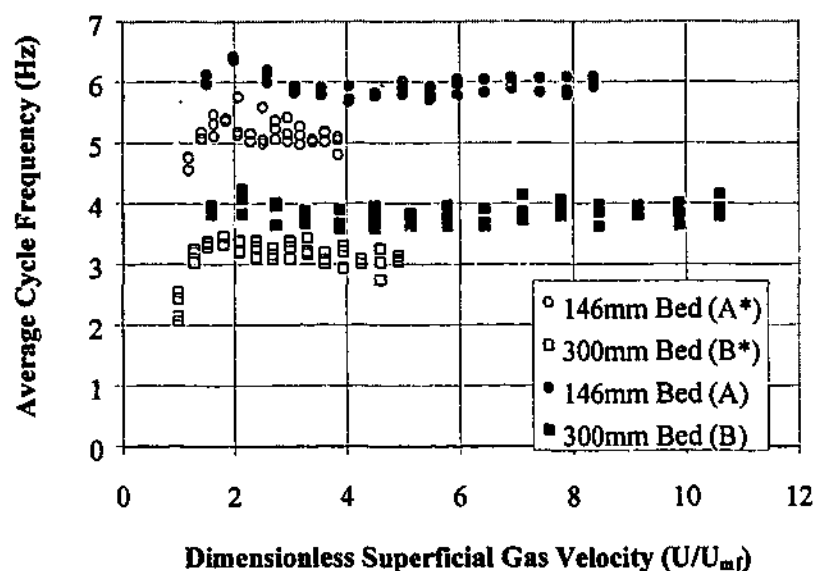


Figure 4.8 Comparison of the average cycle frequency for the 146 mm bed with materials A and A*, and the 300 mm bed with materials B and B* for a range of gas velocities. No scaling factor has been applied to the frequency data.

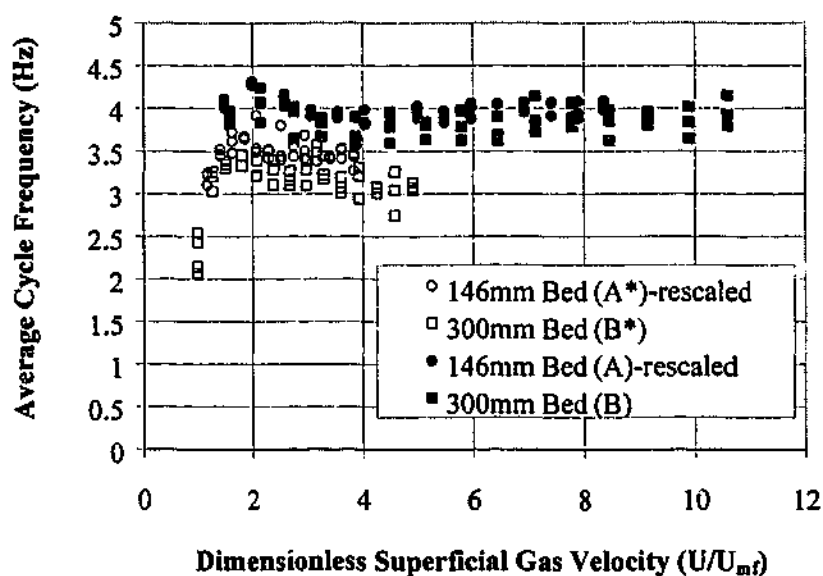


Figure 4.9 Comparison of the average cycle frequency for the 146 mm bed with materials A and A*, and the 300 mm bed with materials B and B* for a range of gas velocities. A scaling factor of $\frac{1}{\sqrt{m}}$ where $\sqrt{m} = \frac{U_{mf}(300\text{mmBed})}{U_{mf}(146\text{mmBed})}$ has been applied to the frequency data for both sets of 146 mm beds results.

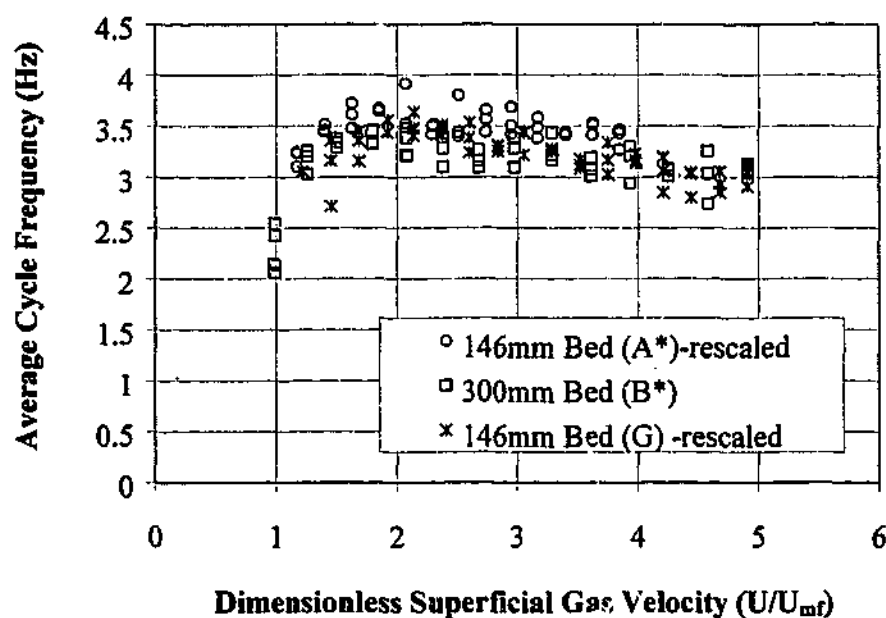


Figure 4.10 Comparison of the results for correctly scaled materials A* and B* in the 146 mm and 300 mm beds respectively, with that of the correctly scaled, but higher density material G in the 146 mm bed. A scaling factor of $\frac{1}{\sqrt{m}}$ where

$$\sqrt{m} = \frac{U_{mf}(300\text{mmBed})}{U_{mf}(146\text{mmBed})}$$

(materials A* and G) results.

Figure 4.10 shows the results for the correctly scaled materials A* and B* in the 14 mm and 300 mm beds with the data for the higher density material G in the 146 mm bed. The results for materials A* and G have been re-scaled (U_{mf} -based scaling factors of 1.49 and 1.52 respectively), and it is immediately clear that the trend for average cycle frequency of material G in the 146 mm bed is very close to that of both the other data sets, implying that the density of the particles has had no discernible effect in this instance. Although the average cycle frequency for the garnet material is perhaps slightly lower than that of silica sand A*, given the scatter in the data it is unreasonable to say that the agreement of this material with material B* is significantly different to the agreement between materials A* and B*.

In Figures 4.6 to 4.10, the average cycle frequency has been compared as a dimensional value (in Hz) in order to highlight several points which are not immediately apparent when the data are plotted in true dimensionless form. The points to be noted about the preceding comparisons for the conditions investigated are as follows:

- The average cycle frequency appears to scale by a factor of $\frac{1}{\sqrt{m}}$ between the two different sized beds, where \sqrt{m} is calculated from $\sqrt{m} = \frac{U_{mf}(300mmBed)}{U_{mf}(146mmBed)}$ for the bed materials in question, and this is consistent with the simplified scaling law.
- Significantly increasing (approximately doubling) the minimum fluidization velocity of the bed materials results in a slight reduction in the measured average cycle frequency for materials at the same bed scale, consistent with the observations of previous workers.
- For the conditions studied, the use of a bed material with a higher particle density but the same U_{mf} in the same scale of bed does not affect the measured average cycle frequency to a significant extent.

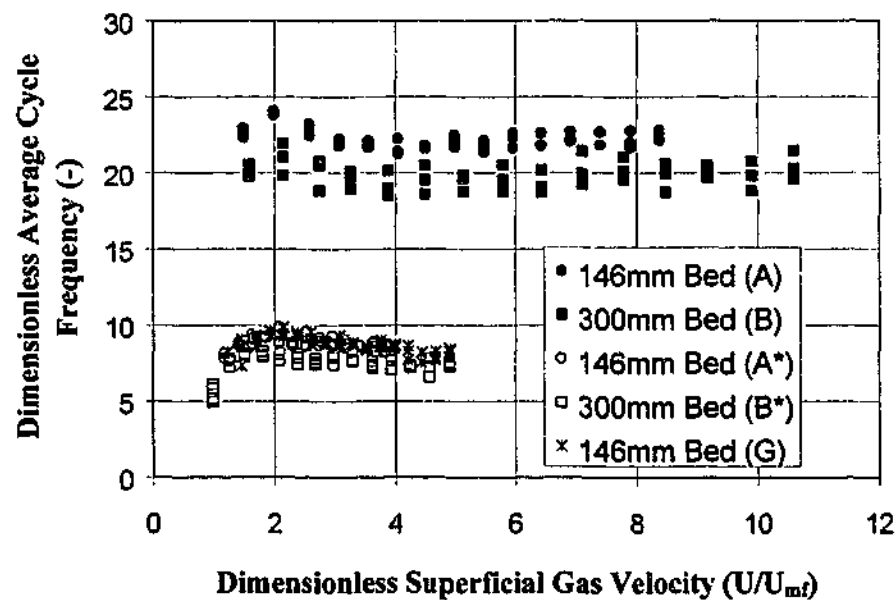


Figure 4.11 Comparison of the dimensionless average cycle frequency for the pressure fluctuation data for all preliminary experiments. Frequency is non-dimensionalised by

multiplying by the factor $\frac{D}{U_{mf}}$.

In Figure 4.11 the results for all five experimental scenarios are plotted in fully dimensionless form, with the dimensionless average cycle frequency calculated using Equation 4.21.

When plotted in dimensionless form, two points can be immediately recognised. First of all, the agreement between material A in the 146 mm bed and material B in the 300 mm bed appears to be not as good as in the previous representation (eg Figure 4.7). Secondly, there now appears to be a dramatic difference in the frequency value for the mis-scaled data sets. Both are consequences of the non-dimensionalisation calculation.

The poorer agreement between the A and B data results from the fact that the ratio of the U_{mf} values of the bed materials is not exactly as required by the scaling law for the given ratio of the bed diameters (see Section 3.3 for a description of this error). Bed diameter was not involved in the re-scaling calculations presented in the earlier charts, thus avoiding this error. The dramatic difference in frequency between the two groups of data is a consequence of the large difference in the D/U_{mf} ratio for these data. So whilst the non-dimensional frequency plot in Figure 4.11 clearly identifies which scenarios agree or disagree with reference to the scaling law, details about the relative values of the measured frequencies are not immediately obvious.

4.7 Comparison of Single Number and Distribution Results

Having compared preliminary results for the pressure fluctuations on the basis of average pressure drop, average absolute deviation of pressure, and average cycle frequency, some additional comparisons will be presented for selected data-sets using the probability density function and amplitude spectrum. The relationship of the single number results to the distribution results will be explained, and the results for the two types of approach will be shown to be consistent.

4.7.1 Comparison of Probability Density Functions

The probability density function is a way of displaying how broadly the magnitudes of the pressure fluctuations are distributed about the average, and the shape of the resulting distribution. Thus it provides a much more complete picture of the pressure fluctuation behaviour than the average or average absolute deviation alone.

It is presented as a normalised histogram with the area under the curve set to be unity for each set of data. The bin widths for the histograms, (representing a dimensionless pressure measurement) are set to be the same for the data being compared. Typically, the data were divided into 50 bins in order to generate a distribution with a meaningful shape (*ie* too few bins and the shape of the distribution is lost as it becomes too tall and narrow; too many bins and the distribution spreads widely across the x-axis and once again the shape of the distribution is lost). Figure 4.12 shows the relationship between a probability density distribution, the average and the average absolute deviation (AAD) for a sample data set. It should be appreciated that although the average and AAD provide some information about the distribution, it is possible that differently-shaped distributions could still produce similar average and AAD values.

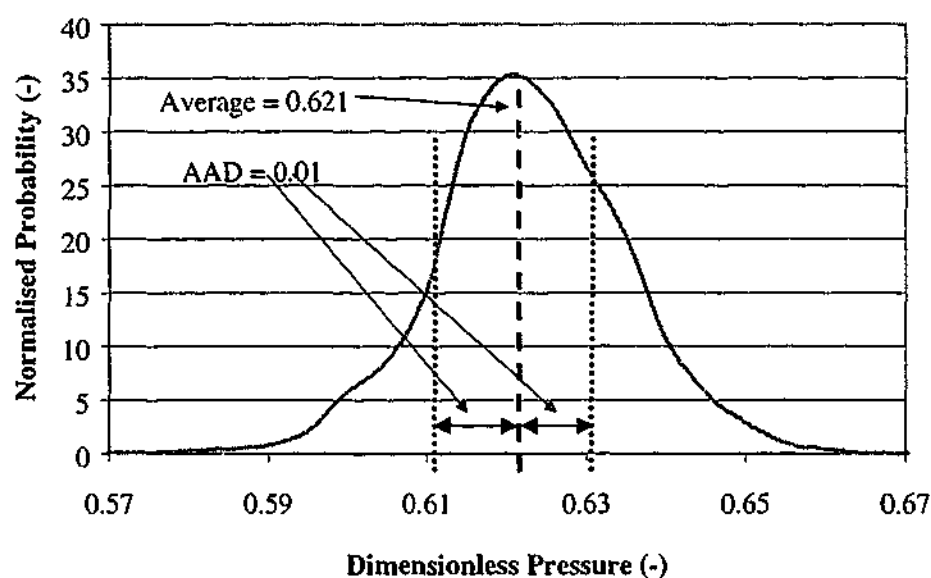


Figure 4.12 Comparison of the average and the average absolute deviation (AAD) with the probability density distribution for a sample data set.

Now, for similar pressure fluctuation statistics, one would expect the probability density functions for each data set to have the same size, shape and dimensionless pressure. For the preliminary experimental data, comparisons of the average and AAD have already shown good agreement in the cases of correct scaling across the full range of gas velocities considered, and significant differences were identified for the mis-scaled beds. In order to double-check the results for the correctly-scaled systems, probability density distribution comparisons will be made at a low, intermediate and high gas velocity for the systems where good agreement in the single values was noted.

Figures 4.13, 4.14 and 4.15 show the normalised probability density distributions for the 146 mm bed with material A and the 300 mm bed with material B for a low, medium and high gas velocity. Note that due to the previously mentioned difficulties with gas flow measurement, *exact* coincidence of dimensionless gas velocities between the two units was not achieved. However, given the similarity in the trends for average and AAD seen earlier, it is not expected that the small difference in gas velocity should have a strong influence on the distribution comparison, although some effect may be noticed at lower gas velocities.

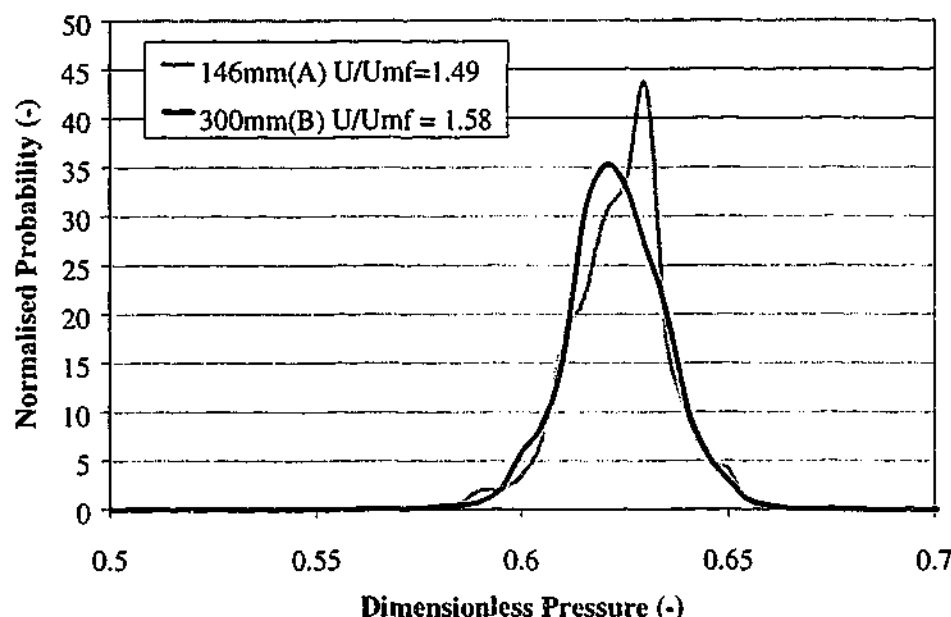


Figure 4.13 Comparison of the normalised probability distribution for dimensionless pressure fluctuations from the 146 mm bed with material A and the correctly-scaled 300 mm bed with material B at low gas velocity.

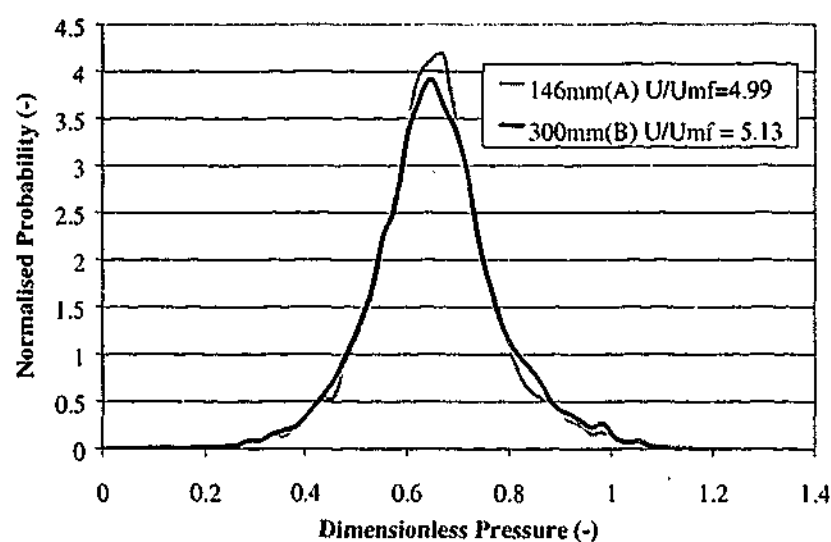


Figure 4.14 Comparison of the normalised probability distribution for dimensionless pressure fluctuations from the 146 mm bed with material A and the correctly-scaled 300 mm bed with material B at intermediate gas velocity.

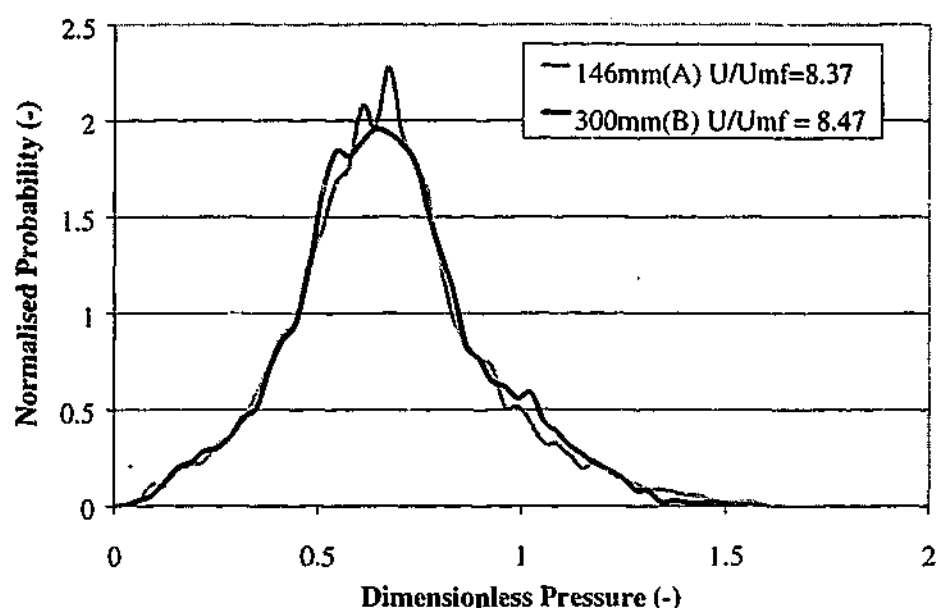


Figure 4.15 Comparison of the normalised probability distribution for dimensionless pressure fluctuations from the 146 mm bed with material A and the correctly-scaled 300 mm bed with material B at high gas velocity.

The three preceding figures show that statistically, the dimensionless pressure fluctuations from the two units are indeed very similar. Although there is a slight difference between the distributions in Figure 4.13, this is likely to be due to the difference in dimensionless gas velocity between the beds. (The significance of a given small difference in gas velocity is larger when the gas velocities are very low). As one might expect from visual observation of a bubbling bed, the distributions are narrow at low gas velocity, but become broader at higher gas velocities, indicating that the range of fluctuation magnitudes increases as gas velocity goes up. The agreement in these distributions supports the previous results for average and AAD of the pressure fluctuations and strongly indicates similar behaviour between the two beds.

Figures 4.16, 4.17 and 4.18 are presented below. They show the normalised probability density distributions for the 146 mm bed with material A* and again with material G; and the 300 mm bed with material B* for a low, medium and high gas velocity. Again, *exact* coincidence of dimensionless gas velocities between the two units was not achieved, which may have some effect at the lower gas velocities.

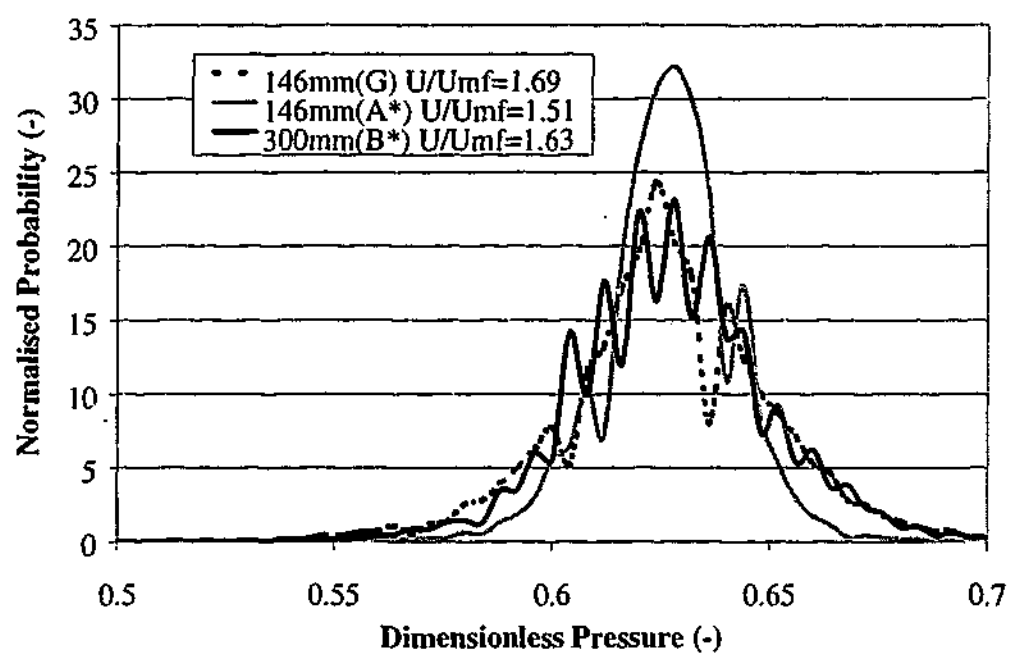


Figure 4.16 Comparison of the normalised probability distribution for dimensionless pressure fluctuations from the 146 mm bed with material A*; the 146 mm bed with material G (density mis-match); and the correctly-scaled 300 mm bed with material B* at low gas velocity.

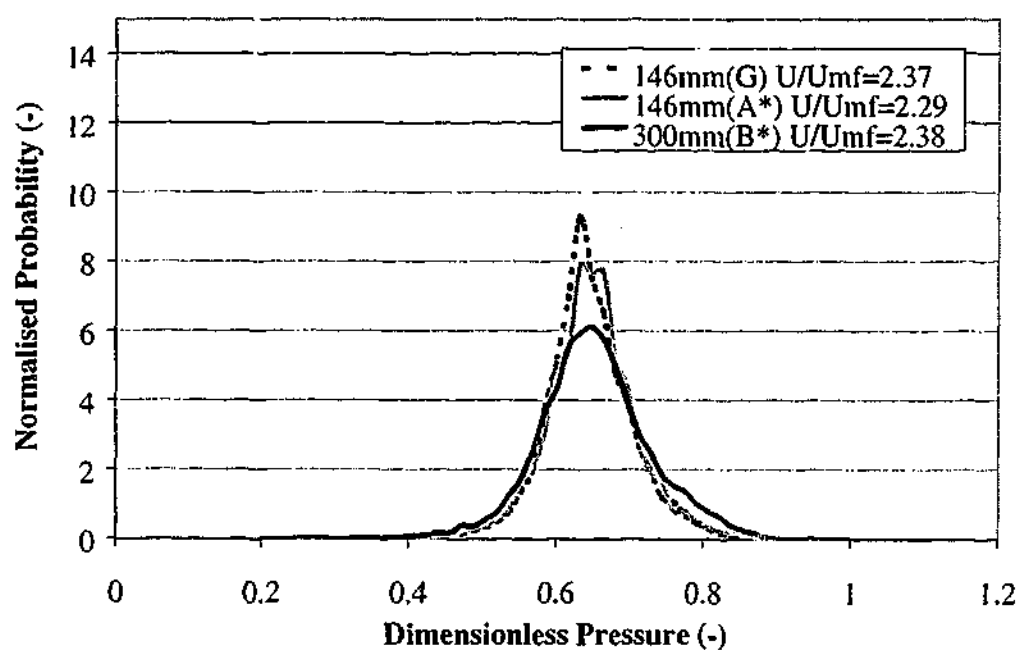


Figure 4.17 Comparison of the normalised probability distribution for dimensionless pressure fluctuations from the 146 mm bed with material A*; the 146 mm bed with material G (density mis-match); and the correctly-scaled 300 mm bed with material B* at intermediate gas velocity.

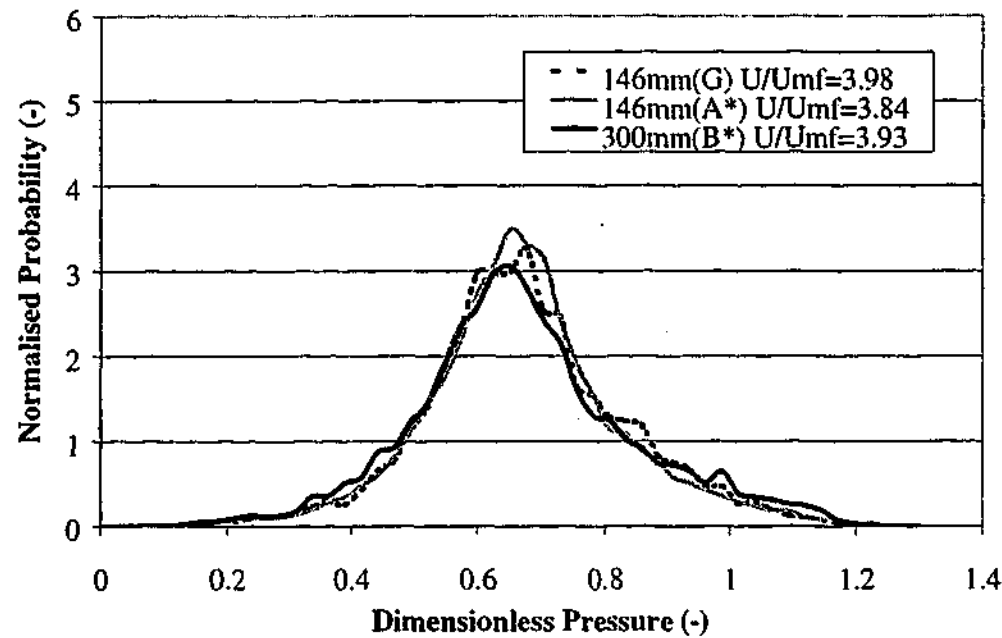


Figure 4.18 Comparison of the normalised probability distribution for dimensionless pressure fluctuations from the 146 mm bed with material A*; the 146 mm bed with material G (density mis-match); and the correctly-scaled 300 mm bed with material B* at high gas velocity.

Once again, agreement of the distributions is good, although they are perhaps not quite as well-matched as the previously compared A and B beds. In Figure 4.16, the distribution for the bed with the A* material is somewhat taller and narrower than its counterparts, and although this difference is reflected by the value of the average absolute deviation for the data, it is not really apparent in Figure 4.5, due to the scale of that chart. The most likely reason for this difference is the error in gas velocity (which is somewhat lower for this bed than the other two). It should also be noted that at low gas velocity there is the possibility of incomplete tuyere operation leading random bed stagnation in these 2:1 aspect ratio beds. This phenomenon has been discussed in Section 3.5.3. At higher gas velocity (Figures 4.17 and 4.18), the agreement in probability density distribution between the three beds is good, and there does not appear to be any significant difference in result for the higher density material.

4.7.2 Comparison of Amplitude Spectra

The second type of distribution comparison is that of the amplitude spectrum, produced by carrying out a fast Fourier transform on selected pressure fluctuation time-series, once again, for low, medium and high gas velocity in the various beds. The Fourier

transform is a widely used analysis tool that has been applied to pressure and voidage fluctuations in fluidized beds by many workers (eg Kang, *et al.*, 1967; Lirag and Littman, 1971; Taylor *et al.*, 1973; Fan *et al.*, 1981; Roy and Davidson, 1989; Dhodapkar and Klinzing, 1993; Svensson *et al.*, 1996). The Fourier transform and its inverse establish a one-to-one relation between the time domain, function $f(t)$ and the frequency domain, spectrum $F(\omega)$. The Fourier transform is defined by:

$$F(\omega) = \int_{-\infty}^{\infty} f(t)e^{-i\omega t} dt \quad (4.24)$$

The inverse Fourier transform is

$$f(t) = \frac{1}{2\pi} \int_{-\infty}^{\infty} F(\omega)e^{i\omega t} d\omega \quad (4.25)$$

The Fourier transform can be viewed as the decomposition of a function $f(t)$ into a sum of frequency components, the coefficients of which are given by the inner product of $f(t)$ and $e^{i\omega t}$. This transform uses sine and cosine as its bases to map a time domain function into the frequency domain. So the spectrum $F(\omega)$ shows the overall strength with which any frequency ω is contained in the function $f(t)$. The Fourier transform does not show how the frequencies vary with time in $f(t)$.

The Short-time (or "Windowed") Fourier Transform is currently the most common method for studying time-varying signals. The idea is to create a "window" which slides over the signal in time, and then compute the Fourier transform for every portion within each window. The general definition of the Windowed Fourier Transform (WFT) is as follows:

$$F(t, \omega) = \int_{-\infty}^{\infty} f(\tau)g(\tau - t)e^{-i\omega\tau} d\tau \quad (4.26)$$

Commercial software is used in the procedure of obtaining the frequency spectrum from an experimental time-series. Often called the Fast Fourier Transform (FFT), the calculation is performed using one of a number of available numerical algorithms. It is important to note that the FFT of a set of sampled data is not the true Fourier transform of the process from which the data was obtained. The choice of the sample size, the

numerical algorithm and the window function can affect the appearances of and the signal concentration in the transform.

In the present work, Microcal Origin 5.0 was the software used to perform one-sided windowed Fourier transforms on selected data. The Hanning window function was used in these analyses in order to eliminate discontinuities at the beginning and end of the time-series, and an ensemble averaging procedure was used in order to reduce the random error in the spectrum estimate. Normalisation was carried out on the resultant spectra so that the area under each curve was unity. Note: the ensemble-averaging procedure is as follows. A given time series is broken up into a number of smaller, equally-sized segments. Each segment is then Fourier transformed and all the transforms corresponding to all the segments taken from the time-series, are then averaged to provide a single spectrum. For a time-series of finite length, increasing the number of segments involved reduces the random error in the resulting spectrum, but as the number of segments increases, their length decreases and consequently the resolution of the estimate decreases. So a choice of segment length is made in order to compromise between reducing the random error and the resolution. Note that a common practice is overlapping of the segments by half their length, as this can be used as a means of increasing the number of segments a given time-series can yield.

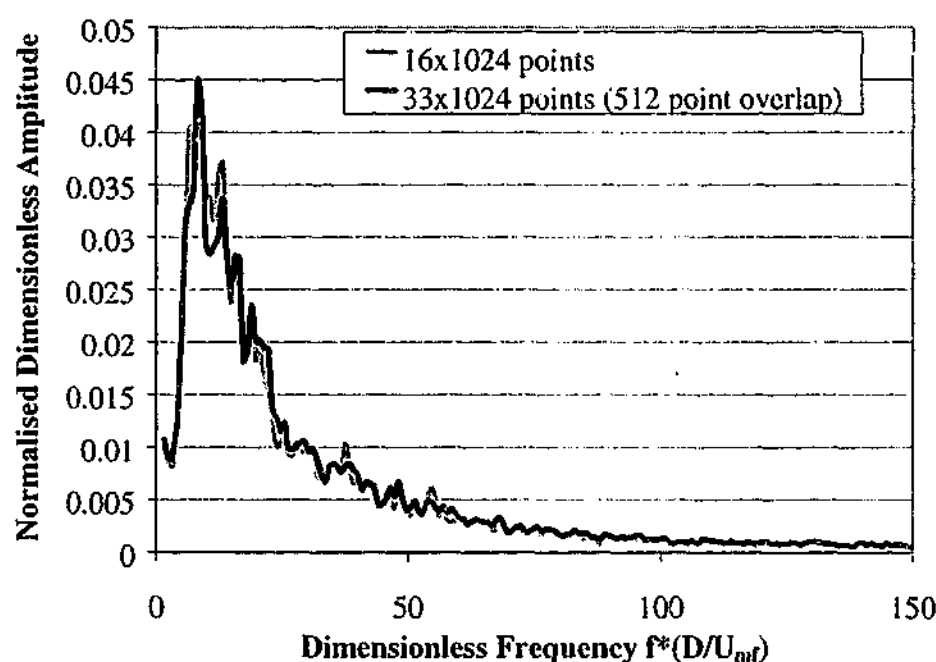


Figure 4.19 Comparison of one-sided spectral estimate (employing the Hanning window) from a sample pressure fluctuation time-series using different ensemble-averaging approaches. In the first approach, 16 consecutive sets of 1024 points were used; in the second approach, 33 sets of 1024 points (overlapping by 512 points) were used.

It should be noted that the choice for segment length in ensemble-averaging procedures for FFT analyses vary greatly in fluidization studies. For example, in recent works involving spectral comparisons Farrell (1996) used a total of 128 overlapping segments of 256 points length; whereas Brue and Brown (2001) used 15 overlapping segments of 8192 points. In this study, some initial work was performed in order to determine a suitable segment length for the ensemble averaging procedure, and it was found that dividing the time-series into 16 segments 1024 points long was a reasonable compromise between random error, resolution and computation procedure time. The potential improvement of overlapping the segments was explored, however as shown by Figure 4.19, the difference in results for a typical run was marginal.

In the preceding section, comparisons were made of the average cycle frequency in both dimensional and dimensionless form for the various fluidized beds. When comparing the results to those derived from spectral estimates, it is worth noting the difference between the average cycle frequency and the peak frequency. The peak (or dominant) frequency is simply the frequency at which the signal exhibits its peak power and can be quite clearly identified on the previous figure (dimensionless frequency of approximately 10). Peak frequencies have been used previously in similarity comparisons (see Roy and Davidson, 1989, Di Felice *et al.*, 1992, Leu and Lan 1992).

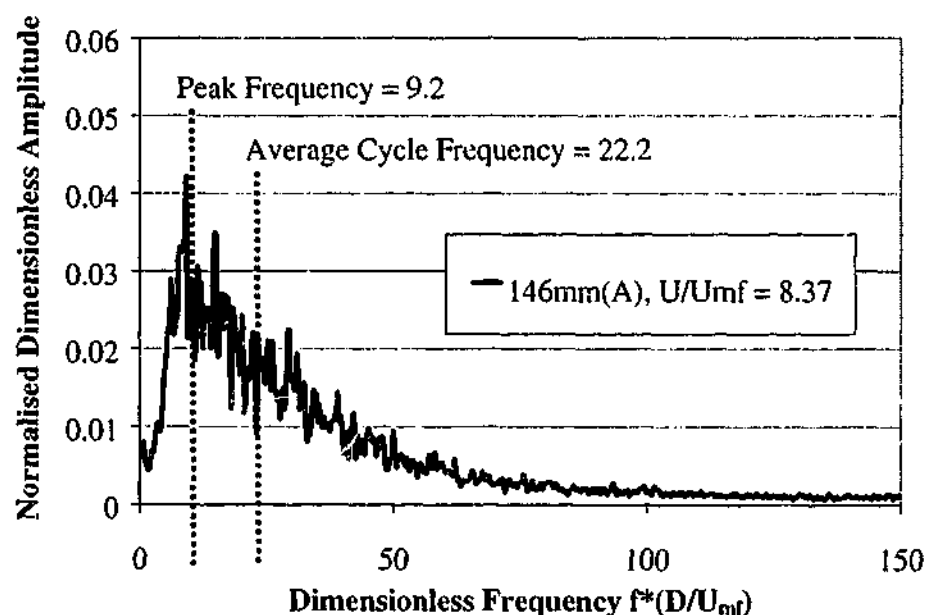


Figure 4.20 Comparison of the peak frequency and the average cycle frequency from an example time-series taken from the 146 mm bed with material A, at $U/U_{mf} = 8.37$. Note that the frequencies are presented in non-dimensional form.

The average cycle frequency on the other hand, is generally higher than the peak frequency as it corresponds to the average number of times the signal crosses its own mean per unit time (regardless of amplitude). Van der Stappen (1996), employed the average cycle frequency in similarity comparisons. In the asymmetrically-shaped spectra typical of fluidized beds, one would not expect the values for peak frequency and average cycle frequency to coincide. Figure 4.20 shows the relative (dimensionless) frequency values for a sample pressure-fluctuation time-series.

In the following figures, comparisons of selected spectra are presented for the 146 mm bed with material A, and corresponding 300 mm bed with material B at low, intermediate and high gas velocities. (Note that mis-matched data are not presented, because it is already clear from the single-value results that they exhibit a significant difference in results.)

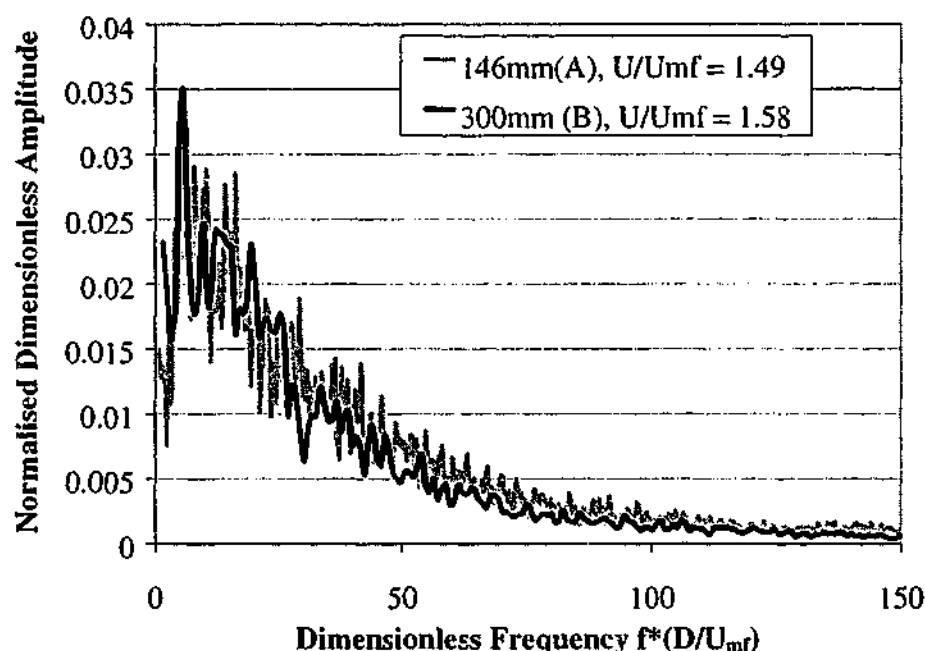


Figure 4.21 Comparison of the normalised ensemble-averaged amplitude spectra for the dimensionless pressure fluctuations from the 146 mm bed with material A and the correctly-scaled 300 mm bed with material B at low gas velocity.

The agreement in the shape and size of the amplitude spectra presented in Figures 4.21 to 4.23 is indicative of closely-matching behaviour in the scaled beds. The spectra for the larger bed with material B show a slight tendency to more activity at the peak frequency with less "tail", but as mentioned earlier with regards to Figure 4.11, this is most likely due to the contribution of the error in the non-dimensionalisation calculation, (because the U_{mf} ratios and diameter ratios do not correspond perfectly to the scaling law

requirements). Similar to the results for average cycle frequency, the spectra show little dependence on gas velocity.

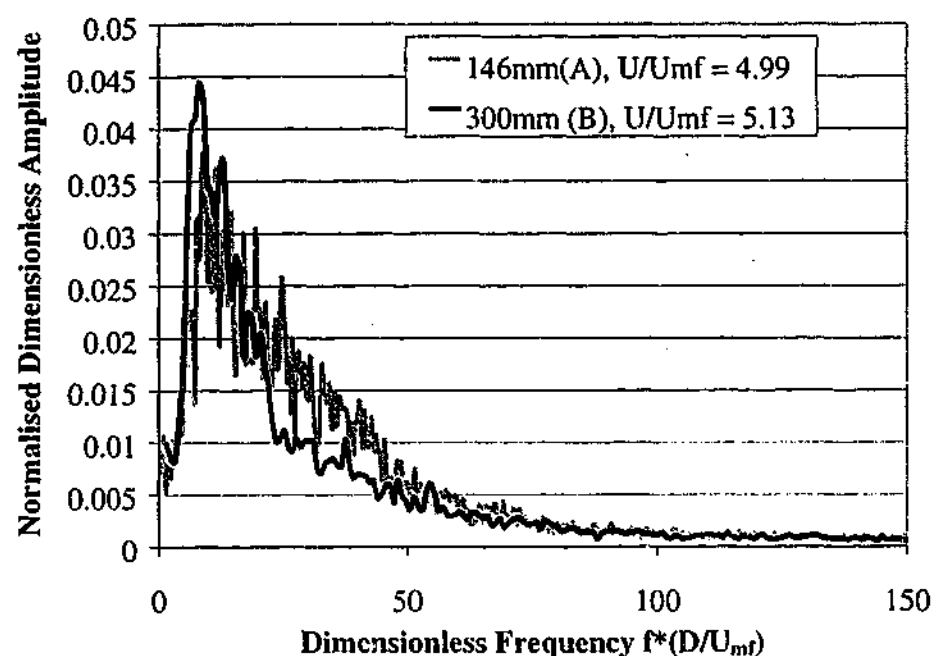


Figure 4.22 Comparison of the normalised ensemble-averaged amplitude spectra for the dimensionless pressure fluctuations from the 146 mm bed with material A and the correctly-scaled 300 mm bed with material B at medium gas velocity.

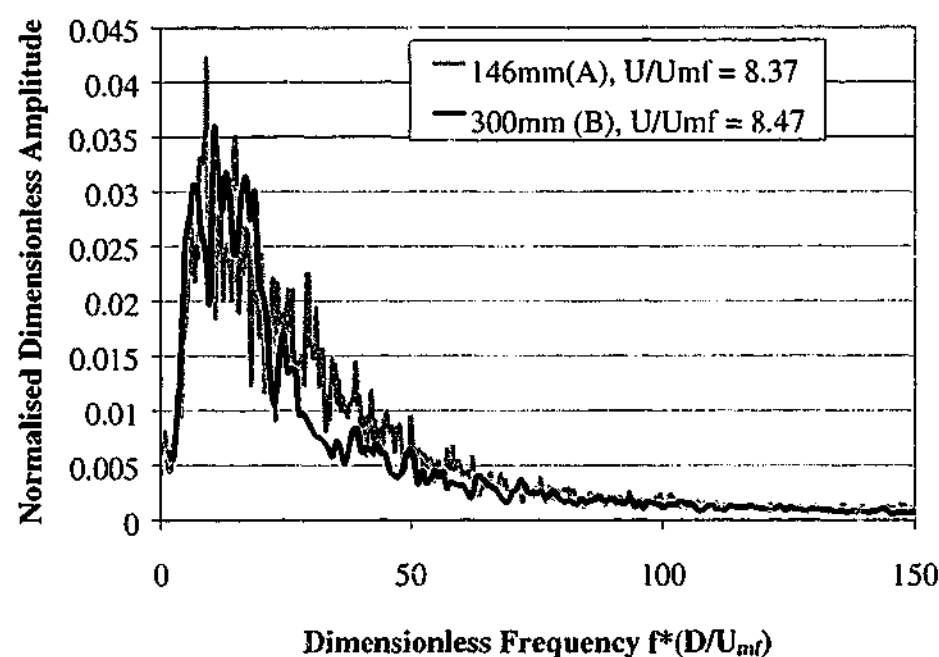


Figure 4.23 Comparison of the normalised ensemble-averaged amplitude spectra for the dimensionless pressure fluctuations from the 146 mm bed with material A and the correctly-scaled 300 mm bed with material B at high gas velocity.

Figures 4.24 to 4.26 show the results for the materials A* and G in the 146 mm bed and material B* in the 300 mm bed.

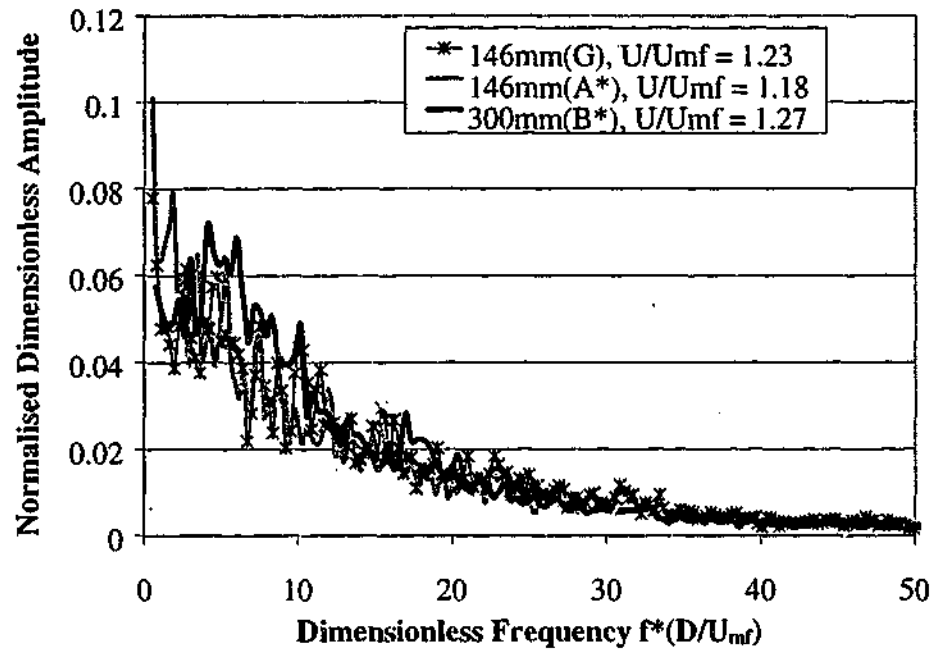


Figure 4.24 Comparison of the normalised ensemble-averaged amplitude spectra for the dimensionless pressure fluctuations from the 146 mm bed with material A* and material G (mis-matched density) and the correctly-scaled 300 mm bed with material B* at low gas velocity.

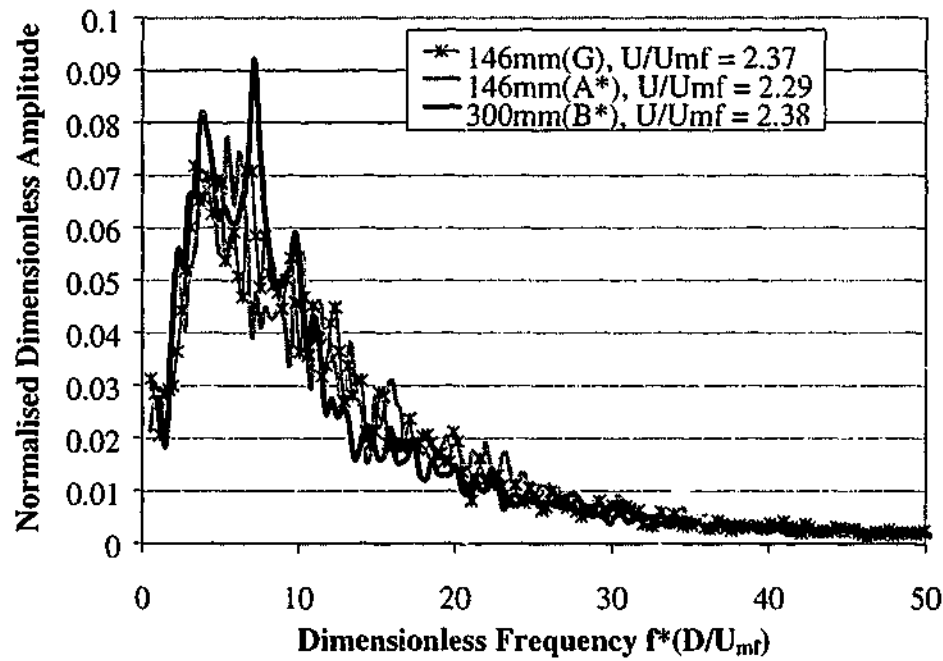


Figure 4.25 Comparison of the normalised ensemble-averaged amplitude spectra for the dimensionless pressure fluctuations from the 146 mm bed with material A* and material G (mis-matched density) and the correctly-scaled 300 mm bed with material B* at intermediate gas velocity.

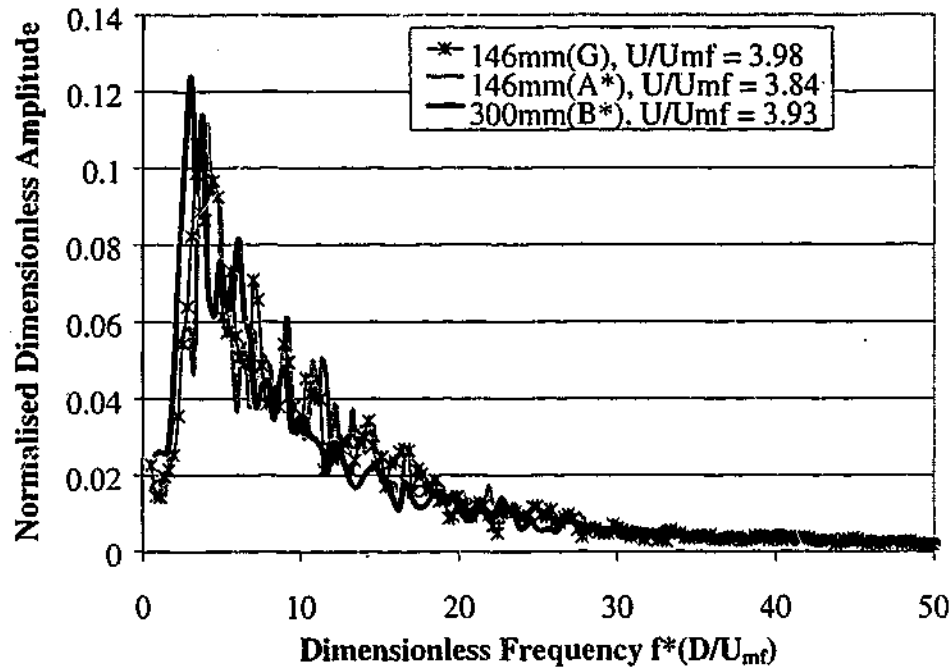


Figure 4.26 Comparison of the normalised ensemble-averaged amplitude spectra for the dimensionless pressure fluctuations from the 146 mm bed with material A* and material G (mis-matched density) and the correctly-scaled 300 mm bed with material B* at high gas velocity.

Once again, the dimensionless amplitude spectra appear to be very similar, indicating that the three beds are producing dimensionless pressure signals with correctly scaled spectral content. As indicated previously by the average cycle frequency results, there does not appear to be any distinct difference in the results for the garnet sand when compared with the other two beds, indicating that as far as this measurement is concerned, the density difference is not contributing to mis-scaled behaviour.

The dominant frequencies derived from the amplitude spectra presented above can be loosely compared with the frequency-of-oscillation predictions of some of the models presented in Section 4.2.2. Recall that the *dimensional* dominant frequencies (f) are related to the *dimensionless* frequencies (f^*) presented in the preceding spectra by:

$$f^* = f \left(\frac{D}{U_{mf}} \right) \quad (4.27 - \text{and presented earlier as 4.21})$$

In the following rough comparison, experimental data has been lumped together, regardless of superficial gas velocity. The reasons for ignoring the gas velocity are:

- the experimental observations showed almost no effect of gas velocity on measured frequencies;
- the models and correlations considered (Hiby, 1967; Verloop and Heertjes, 1974; Sadasivan *et al.*, 1980; Baskakov *et al.*, 1986) show no direct dependence of frequency on gas velocity; and
- ignoring gas velocity simplifies the comparison.

Following the example of Verloop and Heertjes (1974), the bed voidage (where required) in the comparison will be assumed to lie between 0.4 and 0.5 – a reasonable assumption for the sands considered here. Table 4.2 shows the results:

Reference	146mm (A)	146mm (A*)	300mm (B)	300mm (B*)	146mm (G)
Experimental	1.5-2.5	1.1-3.1	1.1-2.0	1.3-3.0	1.5-3.9
Hiby	2.1-2.6	2.1-2.6	1.5-1.8	1.5-1.8	2.1-2.6
Verloop/Heertjes	1.6-1.8	1.6-1.8	1.1-1.3	1.1-1.3	1.6-1.8
Sadasivan <i>et al.</i>	3.3	2.9	2.2	1.9	2.8
Baskakov <i>et al.</i>	1.8	1.8	1.3	1.3	1.8

Table 4.2 Comparison of experimental dominant frequency results (in Hz) with predictions of various models.

For the dominant frequencies obtained in Figures 4.21 to 4.26, the results are reasonably close to those predicted by the various equations. It seems likely that with a more detailed comparison (*ie* better estimate of bed voidage and more numerous experimental data from which to obtain an average dominant frequency), closer agreement would be observed. However, the point of this comparison is not to make a detailed analysis concerning the predictions of these models, but merely to indicate that the dominant frequencies observed are within the range expected from literature correlations.

4.8 Discussion of Small-Scale Pressure Fluctuation Results

By considering the results of the comparison of the pressure fluctuations in the small-scale beds, a number of points of interest can be highlighted.

First of all, there is an overall consensus in the results with regards to the scaling laws. That is, for systems which follow the Horio similarity criteria, good agreement in all the pressure fluctuation characteristics is observed. For the systems involving materials A and B, this is hardly surprising, since it involves a relatively small change in bed size (146 mm to 300 mm); the beds are operated at relatively low particle Reynolds numbers (1 to 12); all the parameters of the simplified scaling laws (including density ratio) have been met to a reasonable degree of accuracy (*ie* within 10%). Thus the A and B systems correspond to a scale-change well within the bounds of what has already been considered by other workers, and present a good standard with which to compare other results.

Given that this pair of beds is expected to produce well-matched results, the only surprise is the slight off-set noted (within some scatter) in the average cycle frequencies, and this is attributed to small inconsistencies between minimum fluidization velocity and bed dimensions, and some experimental variation in the settled bed heights in the different units.

Now considering the A* and B* systems, for this correctly matched pair of beds, once again the agreement in results is good. These systems also follow the simplified scaling criteria reasonably closely (within 10%); involve the same change in bed dimensions; correspond to particle Reynolds numbers in the range 2 to 16; and have correctly matched particle density ratios. The same comments concerning the average cycle frequency apply to these systems also.

The agreement in single number comparisons for the correctly scaled bed pairs is further supported by the similarity in shape and size of the probability density functions and amplitude spectra for selected time-series at low, intermediate and high gas velocities.

By contrast, the *dis*-agreement in trends for the deliberately mis-scaled particle sizes is pronounced. When trends for materials A* and B* are compared with the original A and B materials, there are (as expected), significant differences in bed expansion, fluctuation amplitude, and cycle frequencies. The comparison shows how the mis-scaling is reflected in the experimental measurements and demonstrates, not only the mis-match associated with not following the scaling laws, but also that the measurements used are able to correctly distinguish between scaled and mis-scaled systems. (Given the differences noted in the single number comparisons for the mis-

matched scenarios, it is not necessary to compare these results using the distributions, as it is already clear that significant discrepancies will be observed.)

Note that in all of the single value comparisons there is some scatter in experimental results from one run to the next. The scatter from repeating experiments several times helps to evaluate the extent of random error, and demonstrates that the random error in the results is not so significant as to prevent the scaled and mis-scaled systems from being correctly distinguished. Although there were differences in dimensionless gas velocity from one bed scale to the other (due to a systematic flow measurement error mentioned earlier) trends for the single number comparisons made across the full range of gas velocities were not affected, and within the data, gas velocities considered were close enough that probability density and amplitude spectra distributions from the different beds could be reasonably compared.

For the range of particle Reynolds numbers considered in the correctly-matched beds, the results of the present work are consistent with the findings of other workers (Zhang and Yang, 1987; Roy and Davidson, 1989; van der Stappen, 1996; Stein *et al.*, 1998) concerning the success of the simplified scaling laws; and support the suggestions of Glicksman *et al.* (1993), that providing the solid-to-gas density ratio is matched between the units, the simplified scaling laws will be successful over a wide range of particle Reynolds numbers.

However, comparisons concerning the bed material G in this work have led to results which appear to be somewhat at odds with previous literature work. Having identified the extent of agreement in the various measurement parameters when beds are correctly scaled (and the extent of dis-agreement for a particle size mis-match), material with a deliberately mis-matched particle density was introduced for comparison with the A* and B* materials. In contrast to some of the previous findings reported (Leu and Lan, 1992; Farrell *et al.*, 1998) there was no distinct difference in the appearance of *any* of the trends for the mis-matched particle density run. It seems that in these experiments, the more dense material G agrees with the behaviour of the material B* at least as well as the correctly matched material A* does.

In the relevant experimental comparison of Leu and Lan, (1992) where the criteria of the simplified scaling laws were followed in the same bed with the exception of only the density ratio, particle Reynolds numbers in the range 4 to 10 and 6 to 14 were used. In other words, their experiments were conducted beyond the viscous-dominated region

($Re_p \leq 4$) in which it is not necessary to match the solid-to-gas density ratio (Glicksman *et al.*, 1993). However, in this work (comparing material A* and material G in the 146 mm bed), the particle Reynolds numbers were somewhat lower, - from 2 to 8 for material G and also from 2 to 8 for material A, putting these experiments closer to the theoretical region where density ratio can be ignored. One possibility, therefore, is that the range of particle Reynolds numbers involved in the experiments here was low enough for the density difference not to contribute significantly to mis-scaled behaviour. Additional evidence to support this idea can be found in the original verification work of Nicastro and Glicksman (1984) in which the full set of scaling laws was matched, however there was a 23% mis-match in density ratio. At their operating conditions ($Re_p \approx 5$) their results showed that similarity was still achieved.

Secondly, in their comparison, Leu and Lan noticed a discrepancy in the dominant frequency between the two beds of about 0.4 Hz for all gas velocities considered, although it should be noted that they found that the amplitude of the pressure fluctuations scaled correctly. In this work, the amplitudes scale correctly, and the scatter in the relevant frequency data for the multiple runs spans a range of 0.4Hz or more, but this is not different from the previous comparisons of *correctly* scaled beds not involving a density mis-match. Unfortunately, Leu and Lan provide no comparison of the simplified scaling laws in correctly-scaled beds (*ie* with density ratio correctly matched) as a reference, so one cannot be sure that the 0.4 Hz discrepancy they attributed to density ratio mis-match may not have been present anyway.

In the work of Farrell *et al.*, (1998), once again the particle Reynolds numbers involved (from 6 to 14 and 10 to 25) were higher than in the present study making it more likely that a discrepancy would arise from a density ratio mis-match. Their comparison of power spectral and probability density functions showed clear differences in the pressure fluctuations for the different materials, and it is possible that their use of a differential pressure probe to measure local fluctuations rather than global ones may have increased the sensitivity of the comparison, (as opposed to the single pressure probe measurements carried out in this work). Unfortunately, despite matching all the other particle properties extremely carefully, it seems that the materials compared in the Farrell *et al.*, (1998) study may well have been from different Geldart groups (B and D), and the success of the simplified scaling laws across this boundary is still uncertain (see Section 2.9.2).

In conclusion, the results of the small-scale pressure fluctuation study have demonstrated that the simplified scaling laws are successful in scaling up a bubbling fluidized bed from 146 mm to 300 mm for a variety of Geldart group B powders. The experimental results are predominantly consistent with previous work published in the literature, and the measurements used in this work have provided clear evidence for distinguishing correctly-scaled or mis-scaled situations. For the range of conditions studied, mis-matching the particle-to-gas density ratio does not result in a deviation from scaled behaviour. The results at the small scales present a benchmark from which to evaluate further similarity comparisons for larger changes in bed dimensions.

4.9 Large-Scale Pressure Fluctuation Experiments

The large-scale comparison of pressure fluctuations was carried out in all four fluidized beds, of diameters 146 mm, 300 mm, 600 mm and 1560 mm. Due to blower limitations in the 1560 mm bed, all four beds were operated with settled aspect ratios of 2:3 (H_s/D). Silica sands, with properties outlined previously in Section 3.3 (further details in Appendix C) were fluidized under the conditions shown in Table 3.4. In all, there were five fluidized bed setups explored: All four bed sizes were first scaled according to the simplified scaling laws and an additional mis-scaled run was then carried out where material from the 1560 mm bed was fluidized in the 600 mm bed (particle size mismatch).

Pressure probes were installed at three axial locations in each bed corresponding to the same dimensionless height (see Table 3.8). Using a combination of positioning techniques outlined in Section 3.6.3, the probe tips could be located at any radial location from the radial centre of the beds to the vessel walls. For the similarity experiments three radial positions were chosen: At the bed wall ($r/R = 1$), halfway between the vessel wall and the bed centre ($r/R = 0.5$), and at the bed centre ($r/R = 0$). This meant that pressure fluctuations were recorded from a total of nine probe locations in each bed over the course of the experiments. In a similar fashion to the small-scale work, experiments were repeated three times to give some indication of the reproducibility of the results, (except in the case of the mis-scaled run in the 600 mm bed, carried out only once for each probe location).

The analysis of the pressure fluctuations followed similar lines to that established in the small-scale work; namely comparisons were made of the average pressure drop, the

average absolute deviation and the average cycle frequency of fluctuations registered from the individual probes within each of the beds. Similar procedures were again used for the non-dimensionalisation of the results. However, as will be shown, initial poor agreement in the average pressure drops motivated a change in approach for non-dimensionalising the pressure and an alternative method for scaling the bed material quantities.

4.9.1 Initial Comparison of Bed Pressure Drops

Initially, bed pressure drop measurements were compared with the probes all positioned at $r/R = 0$ for the correctly-scaled beds. For comparison, the measured pressures were non-dimensionalised using the same procedure as in Section 4.5.2 (Equation 4.20). A discrepancy was noted in the results – namely, that the dimensionless average bed pressure drops appeared to be off-set from one bed size to the next. The off-set was repeatable (*ie* could not be accounted for by random error) and indicted that for some reason, the average quantity of bed material present above the probes was not scaled correctly from one bed to the next.

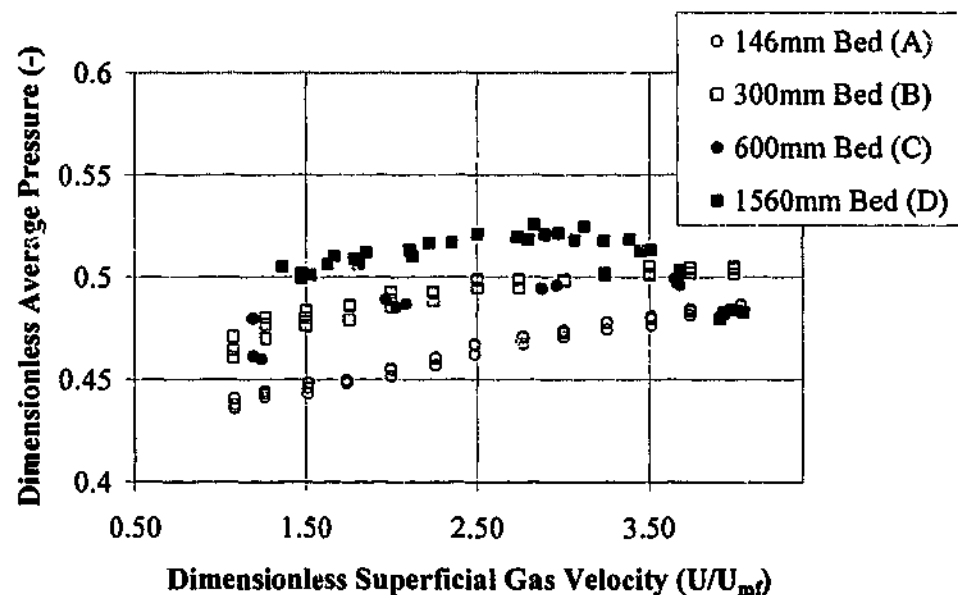


Figure 4.27 Comparison of the dimensionless average pressure measured from pressure probes located at $h/H_f=0.46$ and $r/R=0$ in all four scaled fluidized beds for a range of dimensionless gas velocities.

There is also a difference in the trend at higher gas velocities for the 1560 mm bed – *this will be discussed later (see Section 4.10.2)*. Typical results are shown in Figure 4.27, for

the probe positioned at the radial centreline and $h/H_s = 0.46$ (a similar observation was made for the other axial locations). In this figure the scale in the y-direction has been reduced somewhat in order to show the effect more clearly.

Given that the dimensionless probe positions in the axial direction were accurate, and the observation that the off-set was present from the lowest gas velocities onwards, the cause was narrowed down to errors in bed material mass initially present above the respective probes. Errors in the mass of material could be caused by:

- Inaccurate settled bed height measurements
- Differences in bulk density

In fact, the errors resulted from a combination of the two and were to some extent a consequence of the way in which the bed inventories were scaled.

Geometric similarity requires that the linear dimensions of all the fluidized beds be scaled in the same proportion. So it seems logical to scale the settled bed heights in the same ratio as bed diameters, thus maintaining aspect ratio, and consequently, bed volume. Certainly this approach seemed to work well in the initial small-scale comparisons. However, in the large-scale work the lower bed aspect ratios increase the relative error in bed height measurement, making the settled bed height measurement all the more critical, particularly at the small scale. Following along this line of reasoning, a close inspection of the 146 mm bed soon revealed that alterations to the flange and gasket arrangement above the distributor in preparation for these experiments was leading to an over-estimation of bed height by some 4 mm. This systematic error went some way towards explaining why the average pressure measured in this bed was a little lower than its larger-scale counterparts. In the 1560 mm bed, the settled bed height was found to be some 10 mm higher than it should have been (1050 mm instead of 1040 mm). No other systematic errors in height measurements could be found.

Having checked the settled bed height measurements (and identified one source of error), the next thing to consider was bed density, as it seemed that the assumption that all the bed materials involved had exactly the same bulk density may not have been correct. Bulk densities for the silica sands were initially assumed to correspond to the literature value of 1550 kg/m^3 (Commerical Minerals, 1998). In order to check this, some samples of the bed materials were gently fluidized and settled in the 146 mm bed (configured for U_{mf} measurements) and the settled bed heights carefully measured. The total bed inventories were then weighed. Results (estimated error $\approx 7 \text{ kg/m}^3$) are shown

in Table 4.3, indicating that the bulk densities of the larger materials were somewhat higher than that of the smaller ones.

Material	Measured Bulk Density (kg/m ³)
A	1530
B	1535
C	1536
D	1566

Table 4.3 Results of bulk density measurements for bed materials used in similarity experiments

Note that the larger material used in the 1560 mm bed is the only one which was used directly as it came from the supplier, (*ie* without sieving), and additional fines present in this material may be one reason for a higher bulk density. Certainly, as can be seen in the particle size distribution presented in Appendix C, there is a somewhat broader size distribution for this grade of sand. Changes in particle size distribution affect the bulk density of granular materials because small particles can fill the gaps between the larger particles, increasing the mass of a sample without increasing its overall volume.

So, having established two sources of systematic experimental error likely to have influenced these results, the dimensionless pressure drops were re-calculated using Equation 4.20, accounting for errors in bed heights and using the experimentally determined bulk densities. Results, shown in Figure 4.28 are an improvement on the initial comparison, although there is still some off-set between the smallest bed and the largest bed.

In order to reduce the chance of these discrepancies in further experiments, a new method was adopted for setting the bed inventory and non-dimensionalising the pressure results. This involved scaling the mass of material in the smaller beds directly with a careful estimate of the bed mass in the largest bed. In other words, rather than expressing the bed pressure drop as

$$\Delta P_{bed} = \rho_b g H \quad (4.23)$$

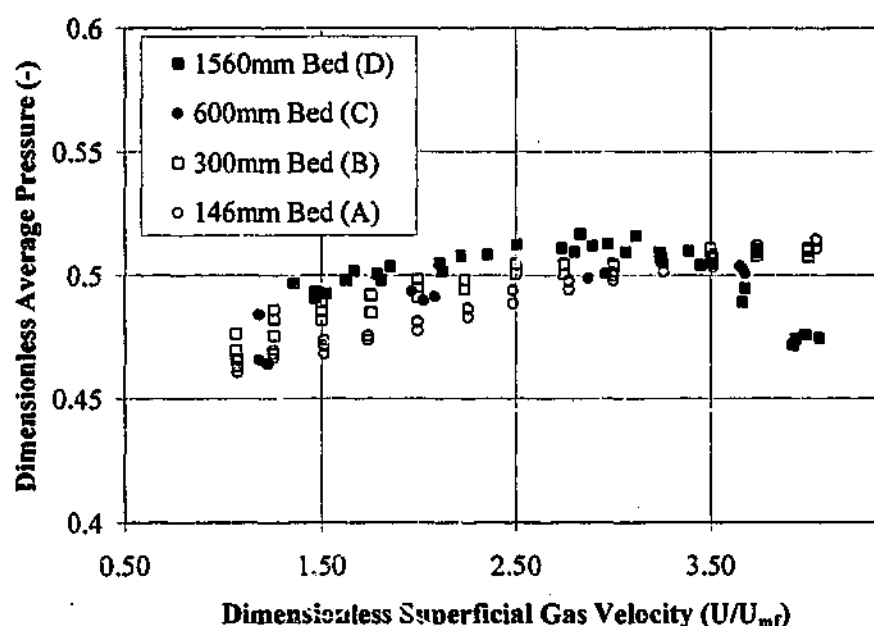


Figure 4.28 Dimensionless average pressure drop comparison for the four correctly scaled beds after adjusting results to account for errors in bed height and bulk density.

and relying on estimates of ρ_b and measurements of H_s for each of the beds in question, the mass of bed material was scaled directly with the bed cross sectional area from the equivalent expression:

$$\Delta P_{bed} = \frac{Mg}{A} \quad (4.28)$$

Thus in the repeated experiments, the mass of material in the largest bed was first determined from bed pressure drop measurements using Equation 4.28 (unfortunately there was no opportunity to measure this mass directly) and the mass of material required in the three smaller beds was scaled down from this.

Procedure for estimating and scaling bed masses

Specifically, the windbox tapping point in the 1560 mm bed was employed to determine the total average pressure drop across the distributor and bed at several gas velocities from $U/U_{mf} = 1.5$ to 2.0 and the known pressure drop characteristics of the distributor (see Appendix D) were then subtracted from the windbox pressure measurement, yielding the pressure drop due to the bed (note that the difference between freeboard pressure and atmosphere was found to be negligible – see Section 3.2.4). Figure 4.29 shows the

windbox pressure measurements, pressure drop curve for the distributor and the resulting calculated bed pressure drop for that range of gas velocities.

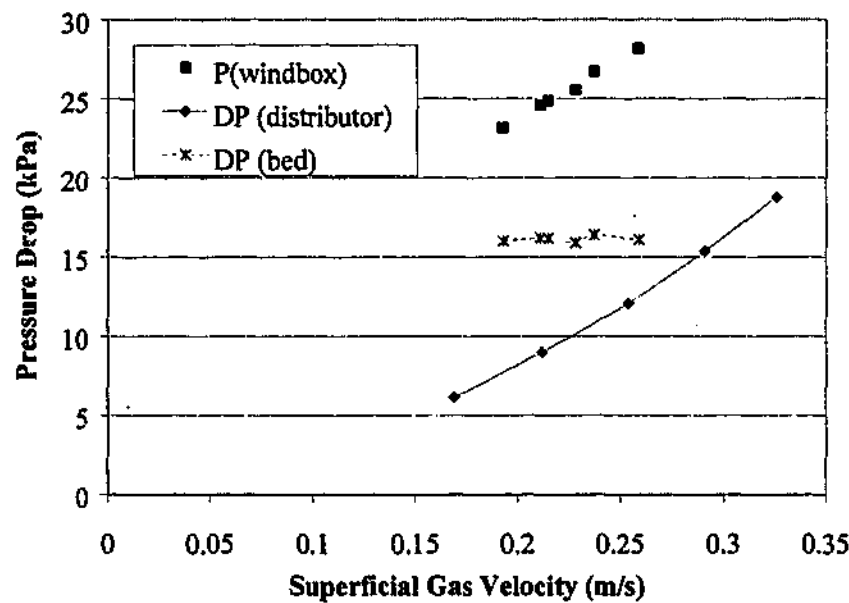


Figure 4.29 Average pressure measurements from the windbox of the 1560 mm bed when fluidized at low gas velocity and distributor pressure drop measurements (empty vessel) for a similar velocity range are used to estimate the pressure drop due to the presence of the bed alone.

The calculated bed pressure drop of 16.0 (± 0.2) kPa was then used in Equation 4.28 to determine the mass of material in the bed, viz:

$$M = \frac{\Delta P_{bed} A}{g} = \frac{16.0 \times 10^3 \times \pi \left(\frac{1.56}{2} \right)^2}{9.81} = 3117 \text{ kg} \quad (4.29)$$

which is reasonable since it was known from loading the bed material that slightly more than 3 tonnes of sand had been used to fill the bed. From this estimate of bed mass in the large bed, the masses required in the smaller beds could be calculated by applying the geometric scaling factor, m (based on the ratio of bed diameters). In this instance, the large bed geometry is used as the basis:

$$M_{bed2} = M_{bed1} \left(\frac{D_2}{D_1} \right)^3 \quad (4.30)$$

for example,

$$M_{600} = M_{1560} \left(\frac{D_{600}}{D_{1560}} \right)^3 = 3117 \left(\frac{600}{1560} \right)^3 = 177.3 \text{ kg} \quad (4.31)$$

Thus the desired masses of sand to be used in the beds was found to be as follows:

Bed	Mass Required (kg)
146 mm	2.555
300 mm	22.17
600 mm	177.3
1560 mm	3117

Table 4.4 Bed masses required for correct scaling based on the estimated mass of material in the 1560 mm bed.

Bed pressures were non-dimensionalised by the use of Equation 4.28 and the scaled masses presented above, eliminating the need for bed heights or density values to be used in the calculation *ie*:

$$P^* = \frac{PA}{Mg} \quad (4.32)$$

where P^* is the dimensionless pressure, P is the dimensional pressure, A is the bed cross-sectional area, M is the mass of the bed in question, and g is the acceleration due to gravity.

Once the bed material quantities had been scaled in this way, subsequent dimensionless bed pressure drop measurements in all four beds showed far better agreement. This can be seen in Figure 4.30, where the original 1560 mm bed data are compared with pressure drop measurements from the other three beds scaled by bed mass directly. There is still some error, as can be expected, given the fact that the bed mass in the 1560 mm bed was never directly measured, and random errors are still present. However, the agreement here is much improved over that of Figure 4.27 and somewhat better than Figure 4.28, since bulk density and bed height values are no longer required for non-dimensionalisation. It was noted that the settled bed heights for the 146 mm, 300 mm and

600 mm beds were all slightly higher than they had been when scaled geometrically in the original experiment; this corresponds to the fact that the bulk densities of these materials all turned out to be slightly lower than the density of the 1560 mm bed material. (Typical settled bed heights for the revised procedure are included towards the bottom of Table 4.5).

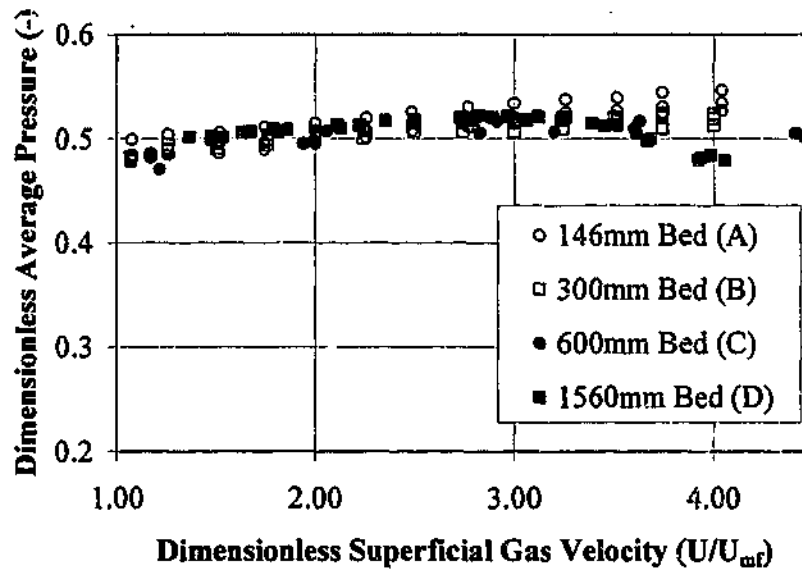


Figure 4.30 Comparison of the dimensionless average pressure measured from pressure probes located at $h/H_s=0.46$ and $r/R=0$ in all four scaled fluidized beds for a range of dimensionless gas velocities. These data are taken from subsequent experiments where the amount of bed material in the 146mm, 300 mm and 600 mm beds was scaled by mass with the estimated amount of material present in the 1560 mm bed.

4.9.2 Comparison of Pressure Probe Results

The full complement of pressure drop measurements from the nine probe locations investigated are presented in graphical form in Appendix F. Very similar trends can be seen for all of the results. For the purposes of discussion, typical results for all five cases (four scaled and one mis-scaled) are presented below in Figure 4.31. The probe is located at $h/H = 0.46$ and $r/R = 0.5$ in this instance.

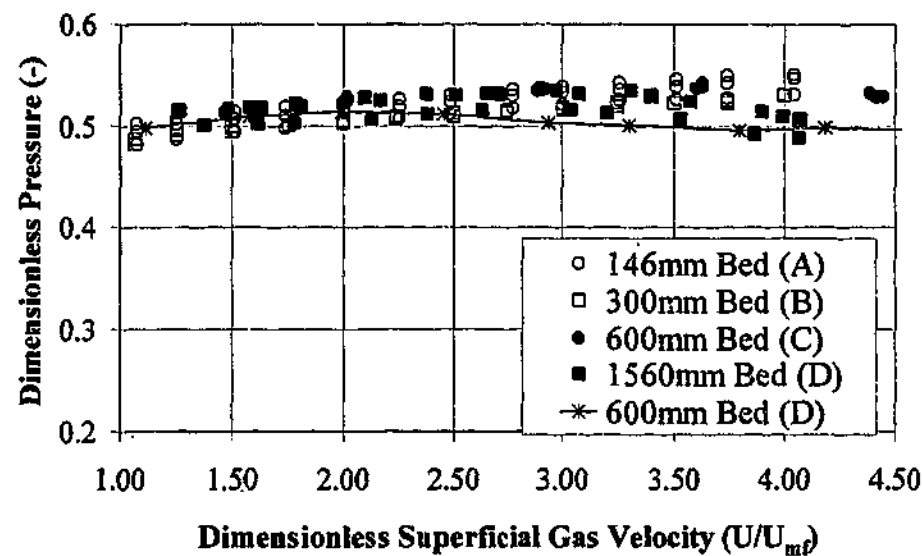


Figure 4.31 Comparison of the dimensionless average pressure measured from pressure probes located at $h/H_s=0.46$ and $r/R=0.5$ in all five fluidized beds for a range of dimensionless gas velocities. All beds, with the exception of the 600mm bed with material D, have been scaled using the simplified scaling criteria.

The agreement in the pressure drop trend is apparent for the correctly scaled 146 mm, 300 mm and 600 mm beds. A discrepancy is noted in the results for the 600 mm mis-scaled bed, with the pressure dropping away slightly when compared with the correctly scaled beds from a velocities of about $3*U_{mf}$ onwards. The material in this mis-scaled scenario is larger than it should be; consequently the size of bubbles is likely to be larger at the same dimensionless superficial gas velocity. Given the shallow nature of these beds, it is quite possible that the passage of these larger bubbles causes momentary exposure of the probes to freeboard pressure from time to time, resulting in an overall reduction in the measured average pressure. Furthermore, the simultaneous presence of multiple large bubbles may momentarily generate a region of low solids content extending from distributor to bed surface. As can be seen from the results for other probe locations, the drop in average pressure is detected by all probes, but is most strongly noted for the probes near the bed surface.

The agreement of the 1560 mm bed with the smaller correctly-scaled units is good for the majority of the gas velocities, but poorer as the velocity increases beyond about $3.5*U_{mf}$. For this unit, the average pressure begins to decrease in a fashion not unlike that of the 600 mm mis-scaled bed; but commencing at a higher dimensionless superficial gas velocity. Once again, the decrease in pressure is associated with a

reduction in the average quantity of bed material between probe tip and freeboard, and may well be a consequence of large bubble size in the low aspect ratio beds. However, it should be pointed out that the trend is not observed at all in the smaller scale beds, (apart from the mis-scaled one), and hence this behaviour at high velocity in the 1560 mm bed constitutes a deviation from scaled behaviour. The decrease in pressure can be noted at all probe locations, but is most dramatic near the bed surface and at the radial centerline.

A comparison of the average absolute deviation results for the probe positioned near the bed surface and at the bed centre is presented in Figure 4.32. These results are reasonably typical of those measured generally at all probe locations (the full set of results are presented in Appendix F). The trend for the mis-scaled bed is (as expected from the results of the small-scale work) dramatically different, clearly indicating the increase in fluctuation amplitudes associated with the larger-than-scaled bubbles present in this bed. Agreement between the other four beds is good, except for the 1560 mm bed results at the highest gas velocities, where the average absolute deviation of the pressure signals increases rather dramatically compared to its correctly-scaled counterparts. Note that the velocity at which this occurs corresponds to the velocity at which the average pressure (mentioned previously) in this bed starts to decrease.

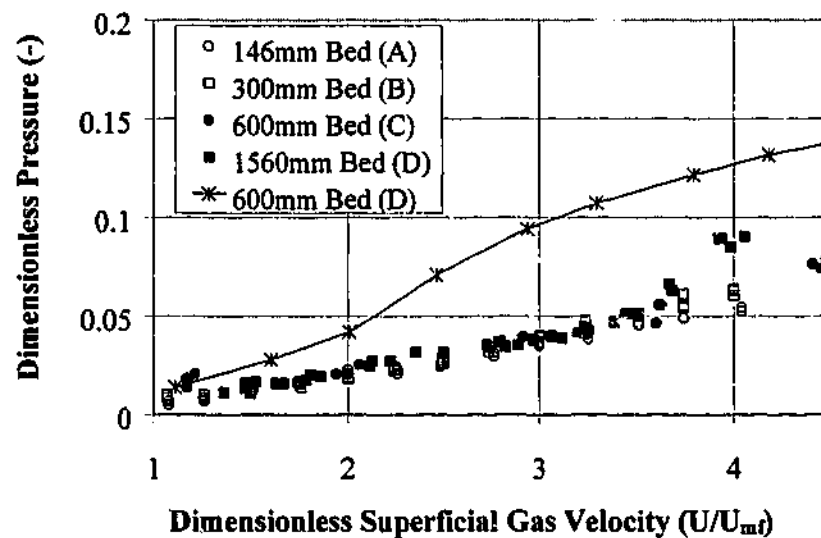


Figure 4.32 Comparison of the dimensionless average absolute deviation of pressure measured from pressure probes located at $h/H_s=0.77$ and $r/R=0$ in all five fluidized beds for a range of dimensionless gas velocities. All beds, with the exception of the 600mm bed with material D, have been scaled using the simplified scaling criteria.

The particular probe location from which the results of Figure 4.32 are derived shows the most dramatic discrepancy in the average absolute deviation (at high gas velocity) of any of the probe positions considered. For the probes located near the bottom of the bed and at the bed wall, the change varies from slight to unnoticeable. This tends to indicate that the phenomenon causing this deviation from scaled behaviour in the large bed is occurring predominantly near the bed surface and away from the walls.

Although in general the agreement in the lower velocity results for the average absolute deviation from correctly-scaled beds is good, it is better towards the radial centre of the bed than at the walls. Figure 4.33 shows the "worst case" in terms of agreement of the average absolute deviation results, which was for the probe located at the bed wall ($r/R = 1$) and near the bed surface ($h/H = 0.77$). In this case the agreement between correctly-scaled beds is only slightly better than that with the mis-scaled bed. This may be due to wall effects influencing the measured fluctuations in an unscaled way; however in repeated runs performed later (see Appendix F), the agreement at the walls was considerably better and the reason for this difference is unclear.

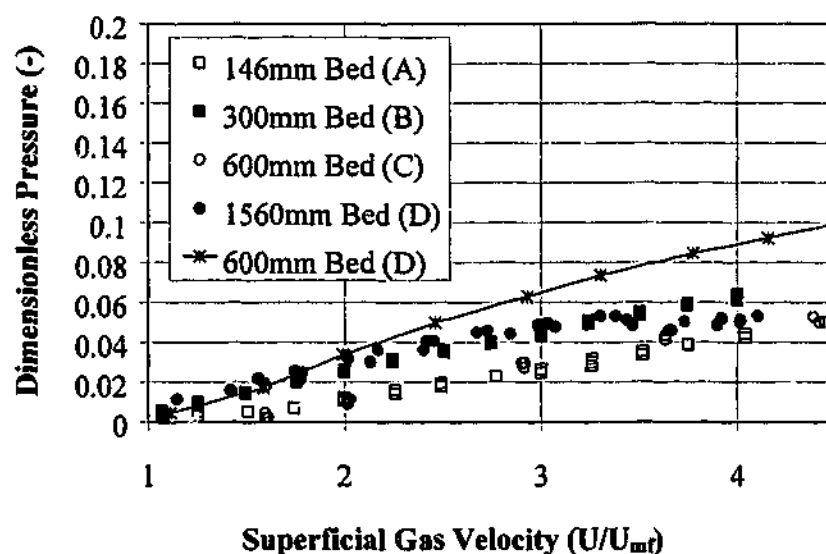


Figure 4.33 Comparison of the dimensionless average absolute deviation of pressure measured from pressure probes located at $h/H_s = 0.77$ and $r/R = 1$ in all five fluidized beds for a range of dimensionless gas velocities. All beds, with the exception of the 600mm bed with material D, have been scaled using the simplified scaling criteria.

One possibility is that some slight variation in the positioning of the probes from one set of runs to the next has influenced the measurement, but no evidence for this kind of location-dependent sensitivity could be found in the literature.

A typical comparison of average cycle frequency results for the five beds is shown in Figure 4.34. (The full set of results is presented in Appendix F). The agreement is reasonable between correctly-scaled beds, and there is a clear distinction between the correct and mis-scaled scenarios. Generally speaking, frequency results were a little more scattered for the larger beds (1560 mm and 600 mm) than for the smaller beds, and the scatter was most noticeable at low gas velocities for probe positions towards the bed surface. There was no discernible change in the average cycle frequency trend for the largest bed at gas velocities where the previously mentioned differences in average and average absolute deviation were noticed. The dimensionless average cycle frequency in the correctly-scaled 600 mm bed appears somewhat higher than its smaller counterparts; this is a consequence of the slightly larger error in the minimum fluidization velocity for this bed material. (A correct match requires $U_{mf} \approx 0.08$ m/s and this bed material has $U_{mf} = 0.07$, hence when non-dimensionalising the measured frequency, a slightly higher dimensionless value is obtained).

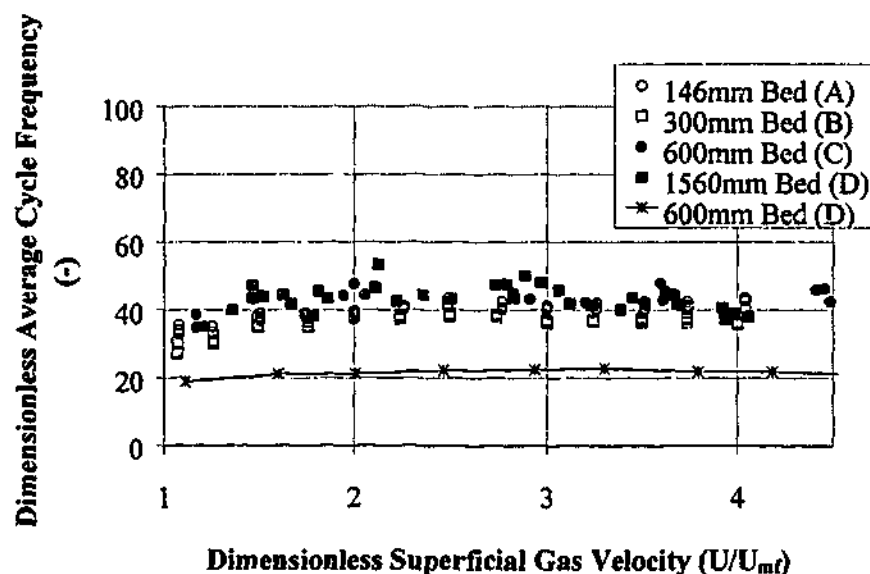


Figure 4.34 Comparison of the dimensionless average cycle frequency of pressure measured from pressure probes located at $h/H_s = 0.46$ and $r/R = 0$ in all five fluidized beds for a range of dimensionless gas velocities. All beds, with the exception of the 600mm bed with material D, have been scaled using the simplified scaling criteria.

To summarise the results with regards to the success of the scaling criteria, an "agreement map" has been generated, which indicates qualitatively how well the pressure fluctuations agree (in terms of average, average absolute deviation and average cycle frequency) for the four scaled beds. The map is only based on a qualitative comparison of the results and is designed to show how the agreement varies with probe location. (Excellent agreement = trends are indistinguishable; Good agreement = trends are similar with some scatter; Poor agreement = trends are only marginally better than for the mis-scaled scenario). The diagram is drawn assuming axi-symmetric behaviour, thus extending the results across the full bed width. Results are mapped for the scaled beds at velocities up to $3.5 \cdot U_{mf}$, to exclude the change in behaviour observed in the 1560 mm bed at high velocity, which will be addressed separately.

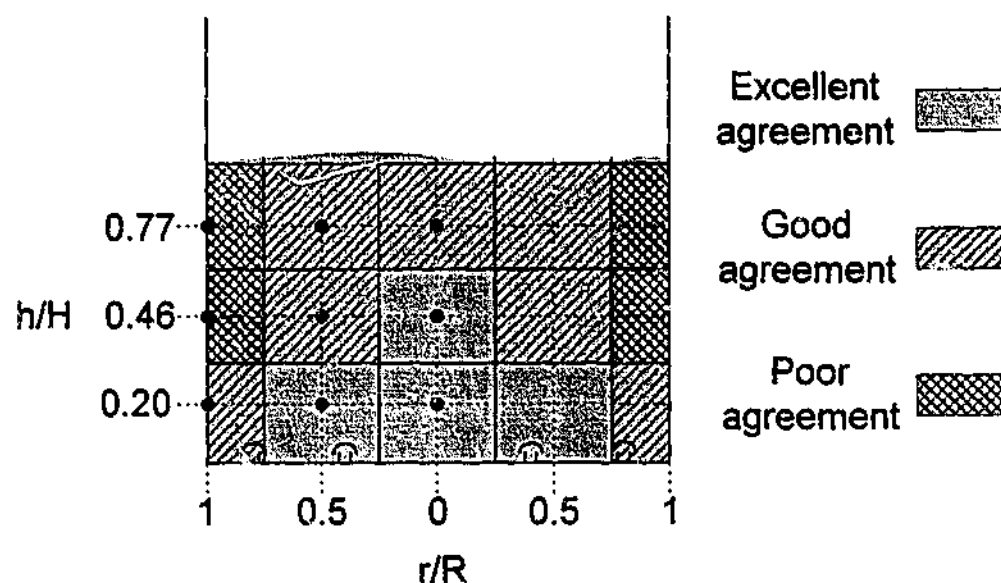


Figure 4.35 Agreement map showing qualitatively how well the pressure fluctuations from the various probe locations and superficial gas velocities from 1.25 to $3.5 \cdot U_{mf}$ match for the scaled fluidized beds. Black dots indicate the location of the probe tips in the actual measurement runs; the results have been extended across the bed width assuming the behaviour to be axi-symmetric. (Excellent agreement = trends are indistinguishable; Good agreement = trends are similar with some scatter; Poor agreement = trends are only marginally better than for the mis-scaled scenario).

As can be seen from the figure above, in general terms results near the distributor and the bed centre compare well, with the agreement becoming worse towards the bed surface and wall. Overall, the agreement between the correctly scaled beds is good.

Having gained an overall impression of the pressure fluctuation results, a number of more specific comparisons will now be made using probability density functions and amplitude spectra in a similar fashion to the earlier small-scale work. Specifically, distributions will be used to compare examples of good and poor agreement identified from the single number comparisons presented above.

First of all, the results for low velocity that typically agreed well in terms of average and average absolute deviation can be examined more closely with a comparison of probability distributions. Due to the difficulties in controlling air flowrate to the larger fluidized beds, the dimensionless superficial gas velocities do not match exactly between all four beds, however for the purposes of the probability density comparisons, points with reasonably closely-matching gas velocities can be compared. Figure 4.36 shows the results for the comparison of probability density distributions for the four correctly scaled beds at U/U_{mf} around 2.00, for the probe located at $r/R = 0$ and $h/H = 0.20$.

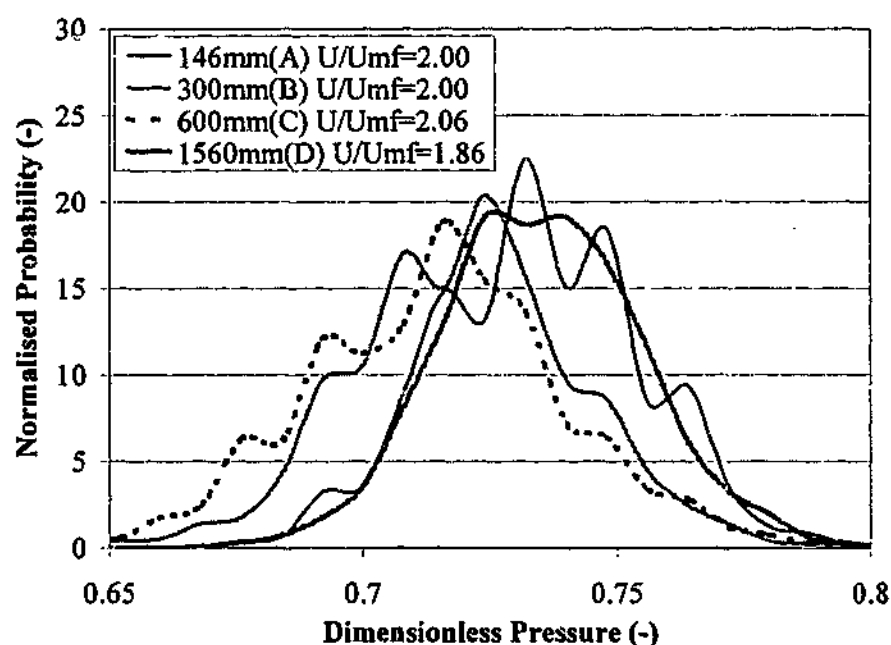


Figure 4.36 Comparison of the normalised probability distributions for the four correctly scaled beds (146 mm, material A; 300 mm, material B; 600 mm, material C; and 1560 mm, material D) at low gas velocity for the probe located at $r/R = 0$ and $h/H = 0.2$.

At first glance, these distributions do not appear particularly well matched, but this is mainly as a result of an off-set in the average pressure (likely due to small bed mass errors). If one ignores the off-set, the shape and size of the distributions are actually reasonably similar. This corresponds well with the single-value results for this probe

location, which show an off-set in the average pressure but similar average absolute deviation.

In Figure 4.37, the results for the 300 mm and 1560 mm bed presented above in Figure 4.36 are compared with the mis-matched 600 mm bed results, in order to demonstrate the significant difference between the distributions for a correctly matched and a mis-matched bed pair. Although the distributions are centered approximately around the same average value, the distribution for the mis-matched bed is much wider, indicating a much wider range of dimensionless pressure fluctuation amplitudes is present.

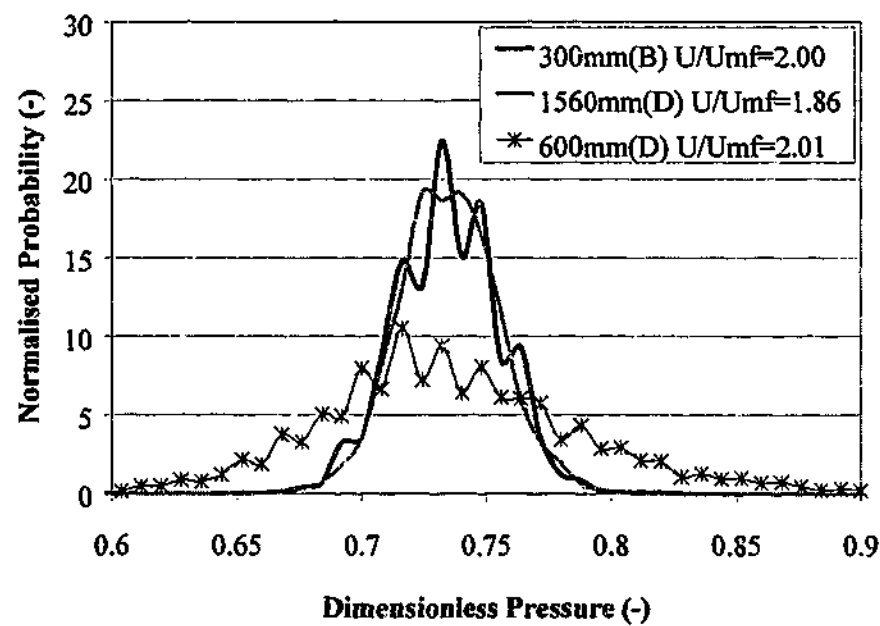


Figure 4.37 Comparison of the normalised probability distributions for the correctly scaled beds (300 mm, material B; and 1560 mm, material D) with the mis-matched bed (600 mm, material D) at low gas velocity for the probe located at $r/R = 0$ and $h/H = 0.2$.

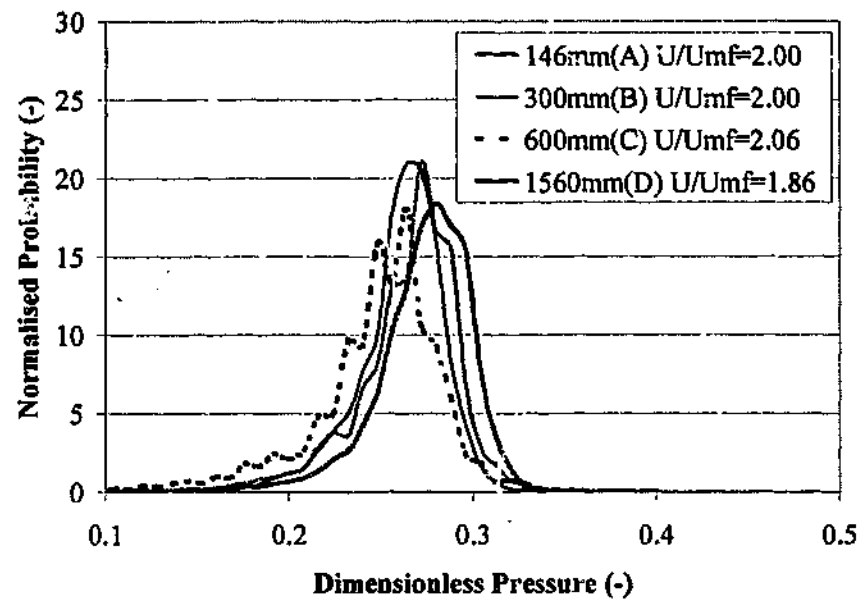


Figure 4.38 Comparison of the normalised probability distributions for the correctly scaled beds (146 mm, material A; 300 mm, material B; 600 mm, material C, and 1560 mm, material D) at low gas velocity for the probe located at $r/R = 0$ and $h/H = 0.77$.

Figure 4.38 shows the normalised probability distributions for the correctly scaled beds with pressure fluctuations measured at the radial centre, but close to the bed surface.

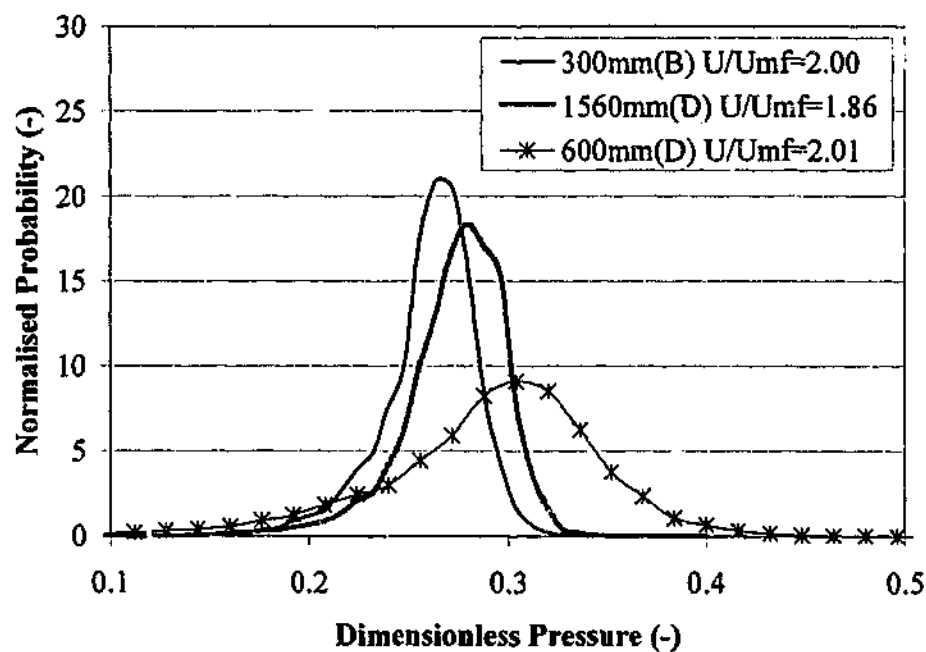


Figure 4.39 Comparison of the normalised probability distributions for the correctly scaled beds (300 mm, material B and 1560 mm, material D) with the mis-scaled bed (600 mm, material D) at low gas velocity for the probe located at $r/R = 0$ and $h/H = 0.77$.

Once again, the shape and size of the distributions are reasonably similar, although there is some off-set in the mean value. By contrast, the results for the mis-scaled 600 mm bed look vastly different to the correctly scaled 300 mm and 1560 mm beds. This is shown in Figure 4.39.

The above comparisons are examples of good agreement between the scaled beds. It is now of interest to examine the probability density function results for operating conditions where the agreement has already been identified as poor. Of particular interest is the region of high-velocity operation ($U/U_{mf} = 4$) where the largest bed shows an increase in average absolute deviation and a decrease in average pressure drop. For the exact velocity in question, results for the 600 mm correctly-scaled bed are unavailable, however as can be seen from the trends in single values presented earlier, (and as will also be shown for results at higher gas velocities presented in Section 4.9.3) this bed maintains a reasonable agreement with the smaller beds at velocities above and below $U/U_{mf} = 4$, so it is reasonable to expect that good agreement would be observed at this velocity also. Figure 4.40 shows the comparison of the probability density function for the correctly-scaled beds (excluding the 600 mm bed) at the high gas velocity.

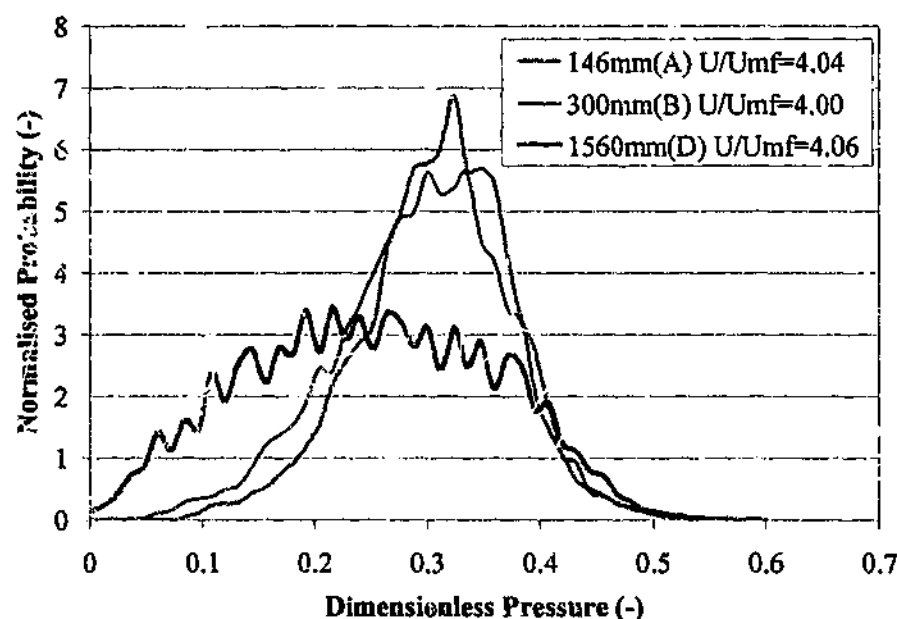


Figure 4.40 Comparison of the normalised probability distributions for the correctly scaled beds (146 mm, material A; 300 mm, material B and 1560 mm, material D) at high gas velocity for the probe located at $r/R = 0$ and $h/H = 0.77$.

The probability density function results clearly show the unusual spread of the pressure fluctuation amplitudes and the reduction in the average bed pressure drop for the 1560

mm bed when compared with its smaller-scale counterparts. It now becomes quite apparent that at this gas velocity the large bed is clearly not operating in the same way as the smaller beds.

In addition to the detail provided by the use of the probability density functions, the amplitude spectra of the beds can be used to provide more detailed information about the dominant frequencies or time-scales present within the measured pressure fluctuation signals. From the comparisons of the average cycle frequencies, it has been noted that the cycle frequencies are somewhat scattered, particularly for the larger beds at low gas velocity and towards the bed surface.

In Figure 4.41 results are presented for the amplitude spectra from the probe located at $r/R = 0$ and $h/H = 0.2$ for the correctly-scaled smaller beds. Note that the comparisons have been broken up into pairs of beds to aid the evaluation process, as it is difficult to make a reasonable comparison of a large set of spectra which all show approximately the same peak frequency and roll-off in signal content as the frequency increases – the chart becomes too congested. The 146 mm bed is taken as the reference.

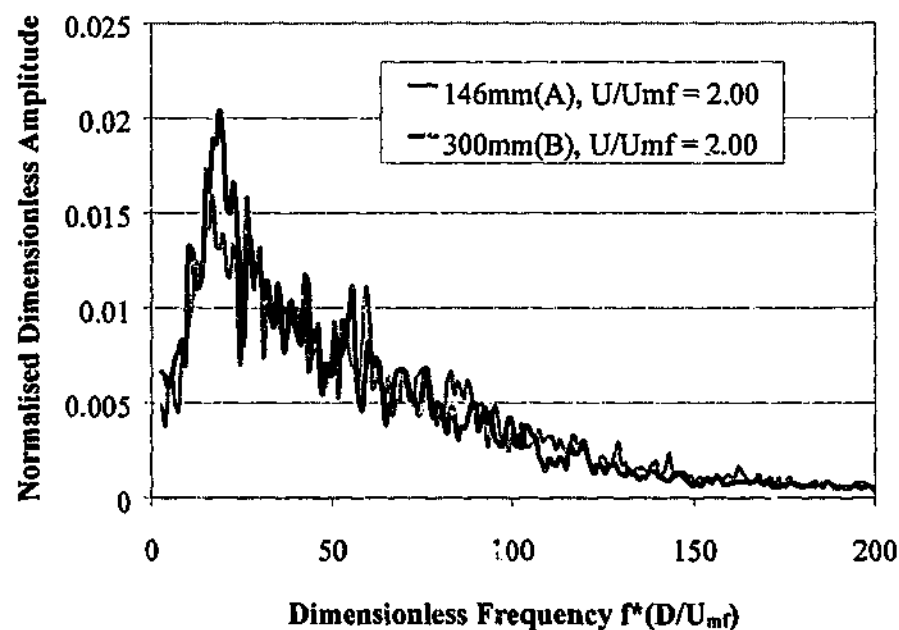


Figure 4.41 Comparison of the dimensionless amplitude spectra from the correctly-scaled 146 mm and 300 mm beds at low gas velocity, with probe located at $r/R = 0$ and $h/H = 0.2$.

In the above figure the agreement between the small beds appears to be reasonable in terms of spectral content of the pressure signals. The same can be said for the results of the correctly scaled 146 mm and 600 mm beds, presented in Figure 4.42.

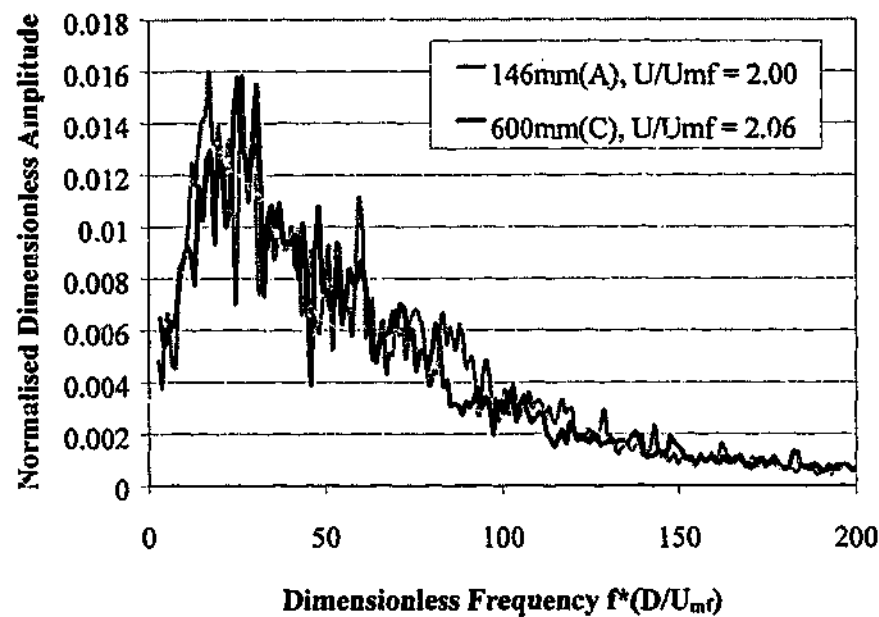


Figure 4.42 Comparison of the dimensionless amplitude spectra from the correctly-scaled 146 mm and 600 mm beds at low gas velocity, with probe located $r/R = 0$ and $h/H = 0.2$.

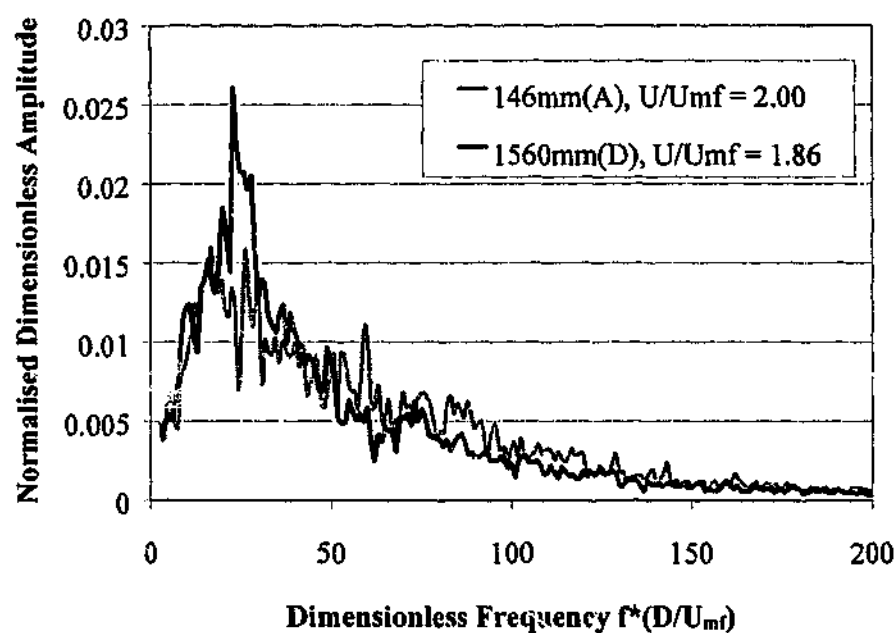


Figure 4.43 Comparison of the dimensionless amplitude spectra from the correctly-scaled 146 mm and 1560 mm beds at low gas velocity, with probe located at $r/R = 0$ and $h/H = 0.2$.

Figure 4.43, however shows some differences between the spectrum of the 1560 mm bed and the 146 mm bed; the corresponding average cycle frequencies for these particular data sets are also somewhat different, with the average cycle frequency for the larger bed being somewhat higher. The extent of the difference here is typical of the scatter in the frequency data generally seen for the larger bed. For comparison, the results for the deliberately mis-scaled 600 mm bed are shown with data from the 146 mm bed in Figure 4.44.

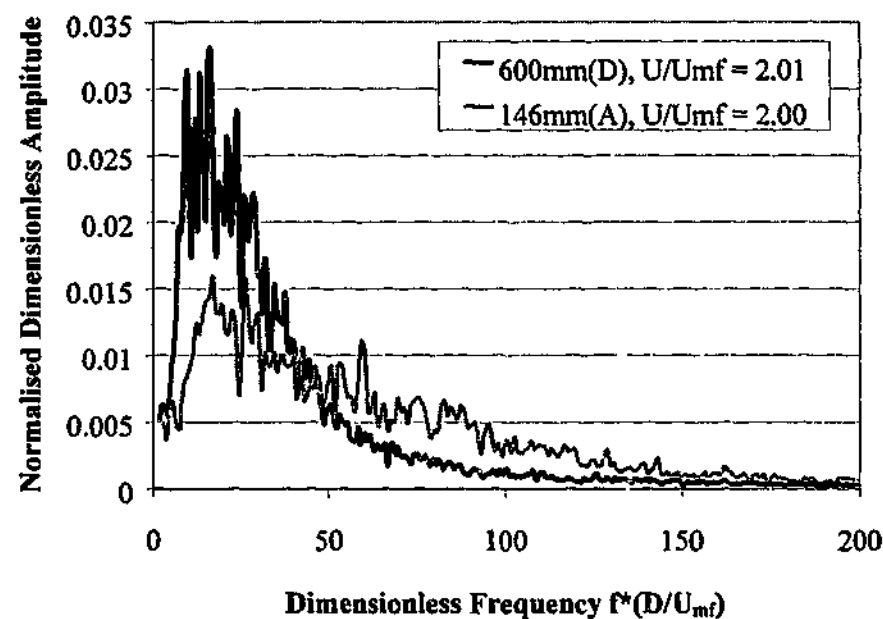


Figure 4.44 Comparison of the dimensionless amplitude spectra from the correctly-scaled 146 mm and the mis-scaled 600 mm bed at low gas velocity, with probe located at $r/R = 0$ and $h/H = 0.2$.

When the preceding figures are put in the context of the mis-scale comparison of Figure 4.44 it is clear that whilst the amplitude spectrum for the 1560 mm bed shows a somewhat limited agreement with its smaller counterparts, this agreement is far better than that for the mis-scaled 600 mm bed.

Figures 4.45 to 4.48 show comparisons of amplitude spectra from the beds (again, taken in pairs with the 146 mm bed as the reference) for the probe located at $r/R = 0$ and $h/H = 0.77$, ie near to the bed surface.

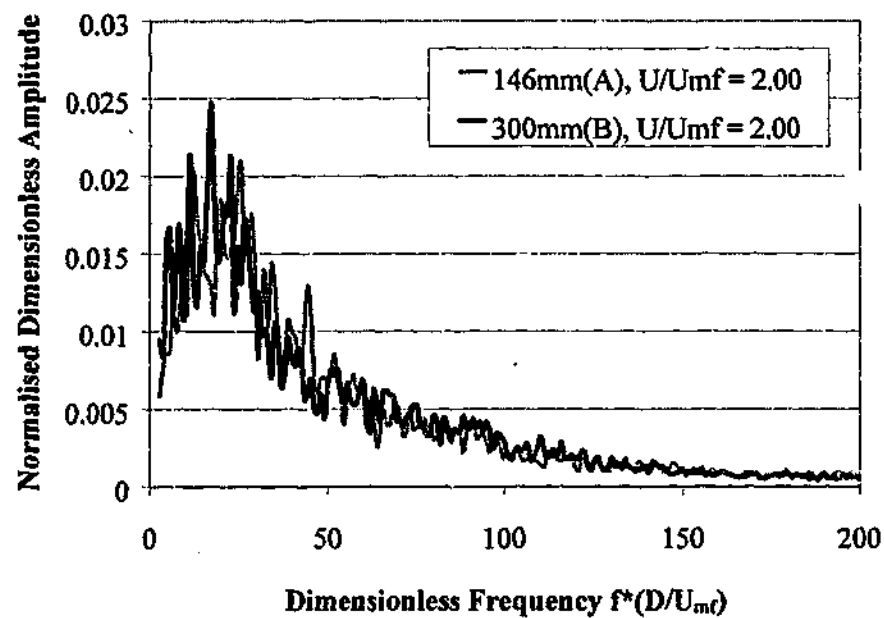


Figure 4.45 Comparison of the dimensionless amplitude spectra from the correctly-scaled 146 mm and 300 mm beds at low gas velocity, with probe located at $r/R = 0$ and $h/H = 0.77$.

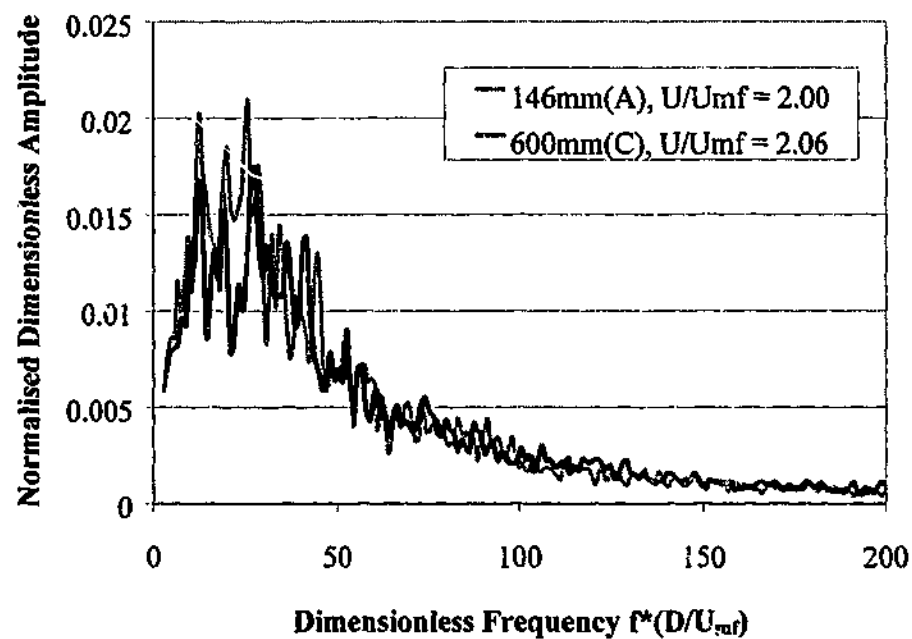


Figure 4.46 Comparison of the dimensionless amplitude spectra from the correctly-scaled 146 mm and 600 mm beds at low gas velocity, with probe located at $r/R = 0$ and $h/H = 0.77$.

At this probe position also, the agreement between the small beds appears to be reasonable in terms of spectral content of the pressure signals.

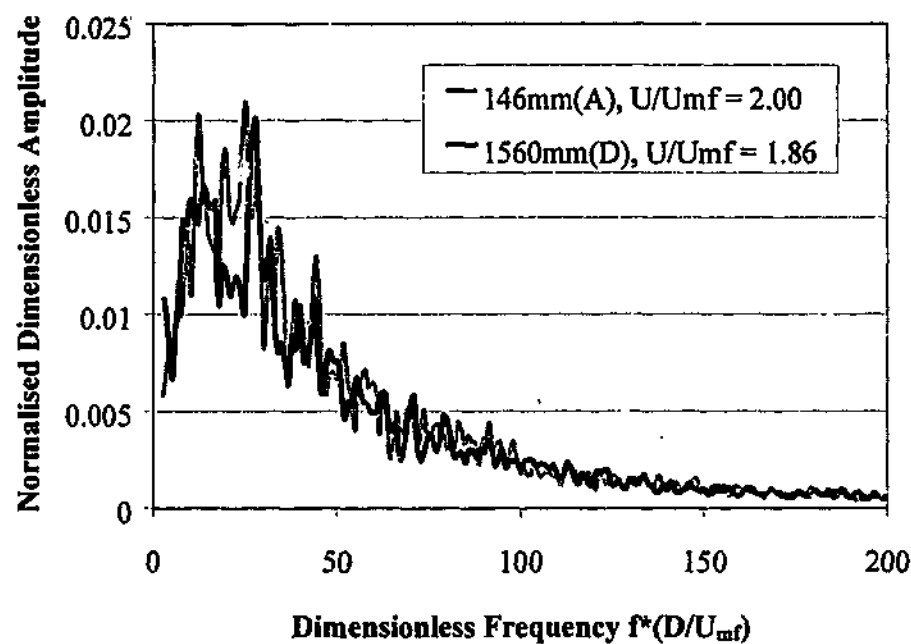


Figure 4.47 Comparison of the dimensionless amplitude spectra from the correctly-scaled 146 mm and 1560 mm beds at low gas velocity, with probe located at $r/R = 0$ and $h/H = 0.77$.

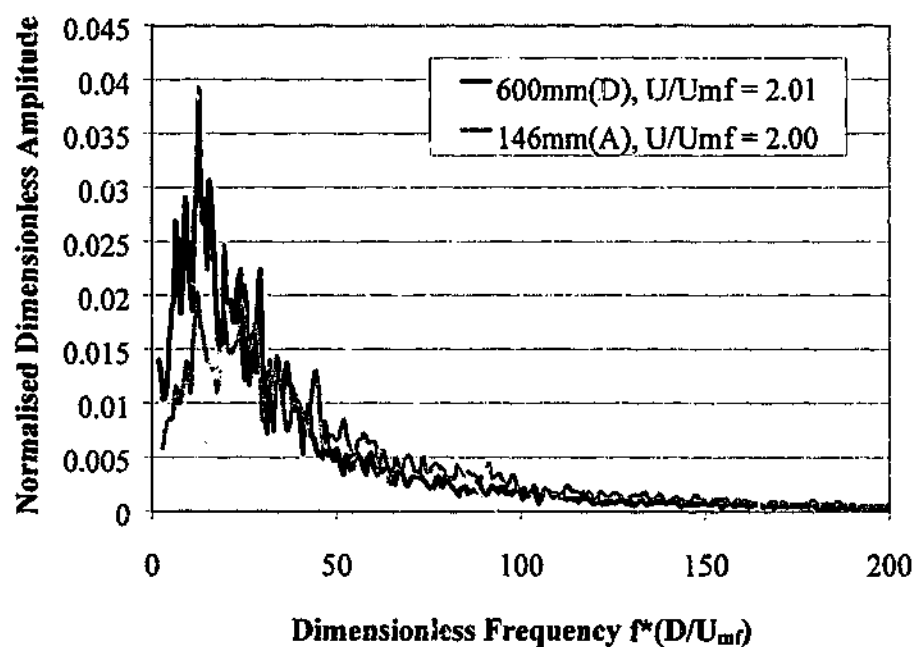


Figure 4.48 Comparison of the dimensionless amplitude spectra from the correctly-scaled 146 mm and the mis-scaled 600 mm bed at low gas velocity, with probe located at $r/R = 0$ and $h/H = 0.77$.

The results for the correctly scaled 146 mm and 600 mm beds are presented in Figure 4.46, and there is a reasonable agreement, although there is a "dip" in the spectrum for

the 600 mm bed at a dimensionless frequency of about 20. Figure 4.47, shows the results for the correctly scaled 146 mm and 1560 mm beds, and there is also a noticeable "dip" in the spectrum for the 1560 mm bed at a dimensionless frequency of about 28.

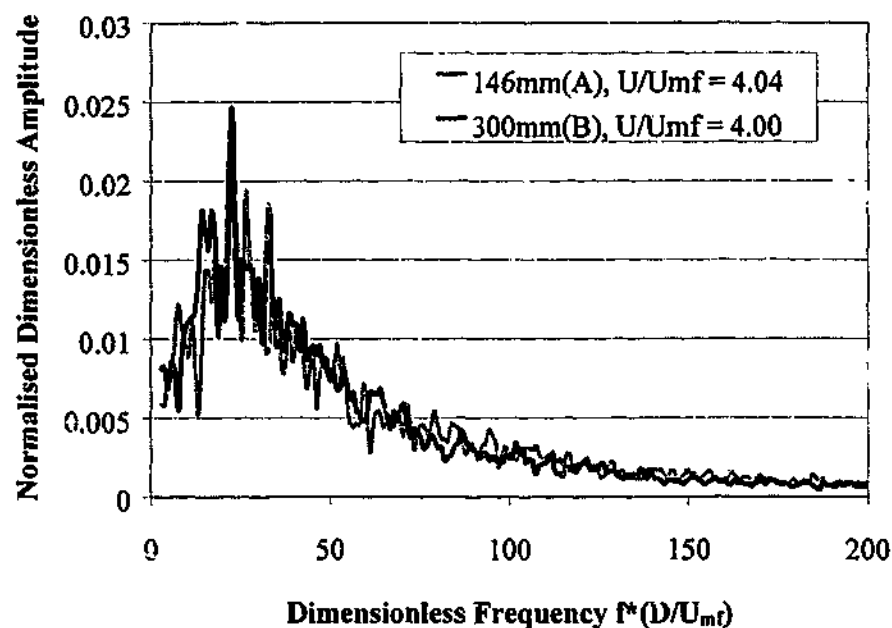


Figure 4.49 Comparison of the dimensionless amplitude spectra from the correctly-scaled 146 mm and 300 mm beds at high gas velocity, with probe located at $r/R = 0$ and $h/H = 0.77$.

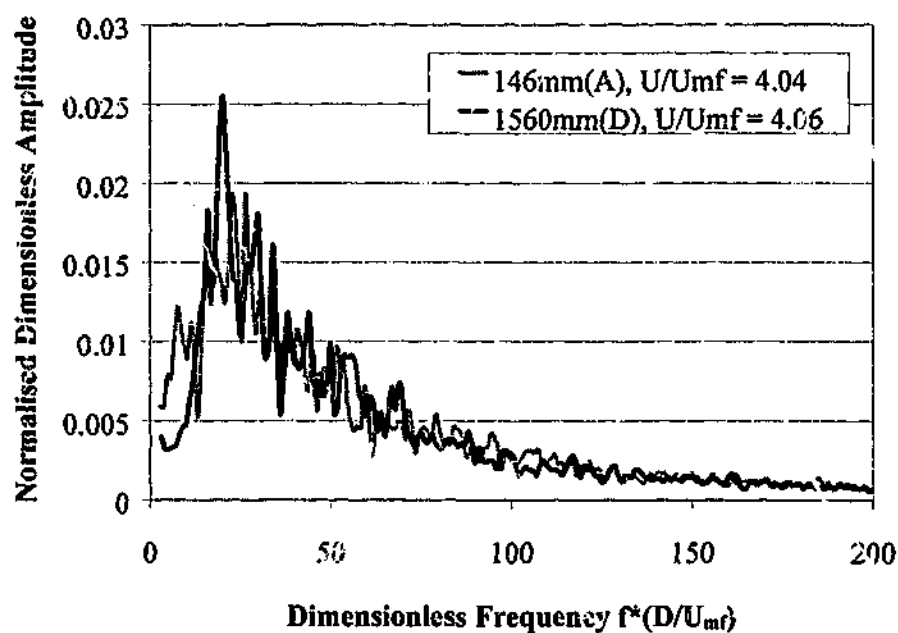


Figure 4.50 Comparison of the dimensionless amplitude spectra from the correctly-scaled 146 mm and 1560 mm beds at high gas velocity, with probe located at $r/R = 0$ and $h/H = 0.77$.

Once again, the difference between the spectra from the 146 mm and the mis-scaled 600 mm bed are significantly greater than differences observed from the scaled beds.

Figures 4.49 and 4.50 show the amplitude spectra for the 146 mm, 300 mm and 1560 mm correctly-scaled beds at the higher gas velocity (approximately $4*U_{mf}$). In both of Figures 4.49 and 4.50, the agreement between the spectra is good; of particular note is the agreement in the result between the 1560 mm bed and the 146 mm bed. This is despite a noticeable difference in the probability density function (Figure 4.40) for the large bed at this gas velocity.

The preceding comparisons of both probability density functions and amplitude spectra support the observations made regarding the single value comparisons. The general observations can be summarised as follows:

- Errors in scaling the bed inventory (mass) are clearly reflected in comparisons of the average pressure drop;
- At dimensionless gas velocities up to approximately $3.5U_{mf}$, all four beds show reasonably good agreement in pressure fluctuation amplitude, average and probability density distribution, - best towards the bottom and at the radial centre;
- At gas velocities above this, the 1560 mm bed shows an increase in fluctuation amplitude, a decrease in average pressure drop, and a dramatically different probability density function - the discrepancy being most strongly recorded by probes in the upper portion of the bed at the radial centre;
- Pressure fluctuation frequencies are generally in reasonable agreement, with some scatter in the results for the larger beds at lower gas velocities (and some double-peaks in the corresponding spectra) especially from probes positioned near the bed surface.
- In contrast to the amplitudes, the frequencies of fluctuations from the 1560 mm bed show no significant change at gas velocities beyond $3.5*U_{mf}$.

From the above observations, it is likely that wall effects and surface effects are causing some of the differences noted in the various beds at lower gas velocities. However, the most interesting feature of the four-bed comparison is the more dramatic deviation in behaviour of the 1560 mm bed at high gas velocity. The reason for this change in behaviour is not immediately clear, and it indicates an additional phenomenon not

accounted for by the scaling procedure as it does not occur in the smaller beds under similar dimensionless conditions.

It was observed that the large fluidized bed unit did exhibit considerable vibration at high gas flows; not surprising given the quantity of solids (> 3000 kg) in motion within the vessel. There is some possibility (unverified) that the vibration of the structure was of suitable magnitude and frequency to interact with the bed and influence the bed behaviour. However, the smaller-scale models also vibrated and there is no data with which to make a comparison of the vibration modes at different scales. Additionally, FFT comparisons do not show any unusual frequency peaks in the spectra from the large model. The issue of structural vibrations and their influence on bed behaviour is, however, a possible area for future work.

Unfortunately, the blower capacity was insufficient to explore the behaviour in the larger bed at higher gas velocities than $U/U_{mf} = 4.0$. It was, however, feasible to operate the smaller three beds at higher gas velocities. So another series of experiments were conducted to see whether the same sort of change in pressure fluctuations could be brought about in the smaller scale models by operating them at higher gas velocities.

4.9.3 Pressure Fluctuations at Higher Gas Velocities

In order to explore the effects of higher gas velocities further, these additional experimental runs were carried out with pressure fluctuations measured for all probe positions in the 146 mm, 300 mm and 600 mm beds. The same bed materials were used (A, B and C respectively) and the beds were operated with the same settled aspect ratio (0.67:1) as before. Gas velocities up to $9 \cdot U_{mf}$ were employed (see Table 3.4 for more details). The full set of results for all probe positions are provided in Appendix F and typical results are shown below. The mis-scaled bed (600 mm with material D) has been included for comparative purposes.

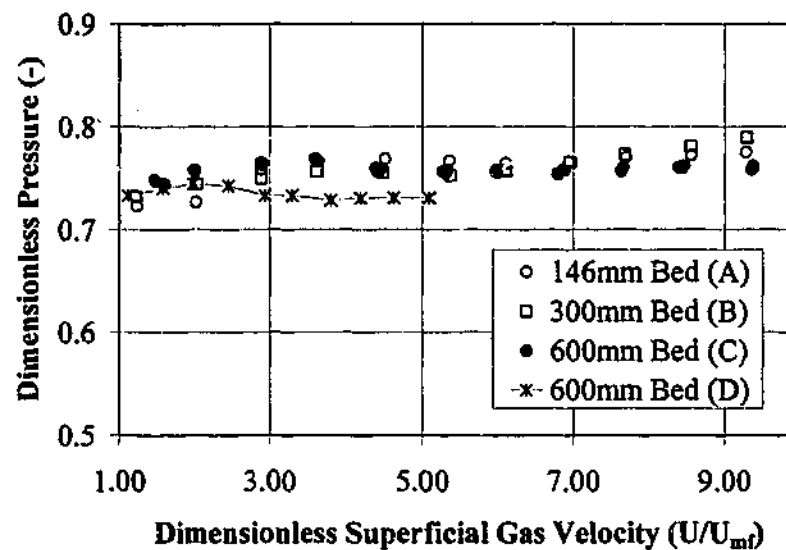


Figure 4.51 Comparison of the dimensionless average pressure measured for the correctly-scaled 146 mm (material A), 300 mm (material B), 600 mm (material C) and mis-scaled 600 mm (material D) beds for higher superficial gas velocities. Pressure probe is positioned at $r/R = 0.5$ and $h/H = 0.2$.

As can be readily seen from the results presented in Figures 4.51 to 4.53, at no point does a trend resembling that seen in the 1560 mm bed develop. If anything, there is a slight increase in both the amplitude and the average of the pressure fluctuations for the smaller beds (146 mm and 300 mm) at high gas velocities ($U/U_{mf} > 6.0$). The difference, however, is not great and certainly not of the same abrupt nature as that observed in the 1560 mm bed.

The off-set in dimensionless average cycle frequency in the 600 mm bed (Figure 4.53) is attributed to the lower-than-scaled value of the minimum fluidization velocity for this material, which affects the non-dimensionalisation calculation mentioned previously in this chapter (see for example, Section 4.6.3).

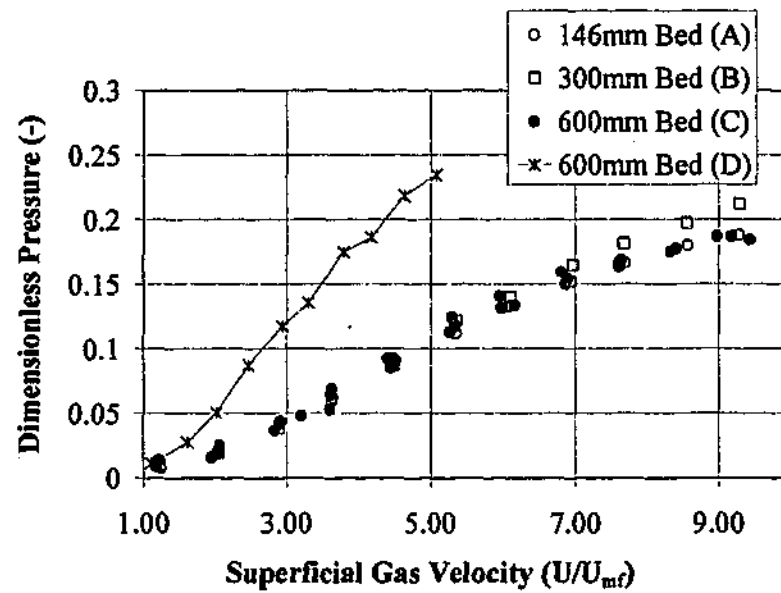


Figure 4.52 Comparison of the dimensionless average absolute deviation of pressure measured for the correctly-scaled 146 mm (material A), 300 mm (material B), 600 mm (material C) and mis-scaled 600 mm (material D) beds for higher superficial gas velocities. Pressure probe is positioned at $r/R = 0$ and $h/H = 0.46$.

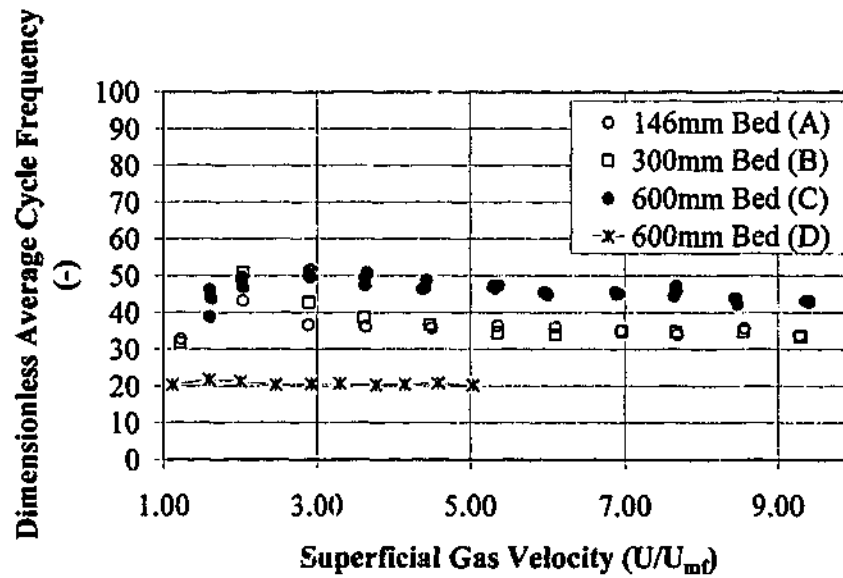


Figure 4.53 Comparison of the dimensionless average cycle frequency of pressure fluctuations measured for the correctly-scaled 146 mm (material A), 300 mm (material B), 600 mm (material C) and mis-scaled 600 mm (material D) beds for higher superficial gas velocities. Pressure probe is positioned at $r/R = 1$ and $h/H = 0.46$.

To demonstrate the significance of the effect, Figure 4.53 has been re-plotted with the 600 mm frequency data adjusted. When compared with the experimental U_{mf} and diameter of the 300 mm bed, the *ideal* U_{mf} for the 600 mm bed would be 0.082 m/s according to the scaling rules. Since the frequency is only weakly affected by the particle size and gas velocity (a point discussed earlier in this chapter), we can assume the experimentally measured dimensional frequencies for the ideal bed material case would not be vastly different. On the other hand, the *dimensionless* frequency calculated from:

$$f^* = f \left(\frac{D}{U_{mf}} \right) \quad (4.33)$$

is significantly lowered by the use of the ideal U_{mf} value in the calculation. Figure 4.54 shows results of using the *ideal* minimum fluidization velocity with the original data.

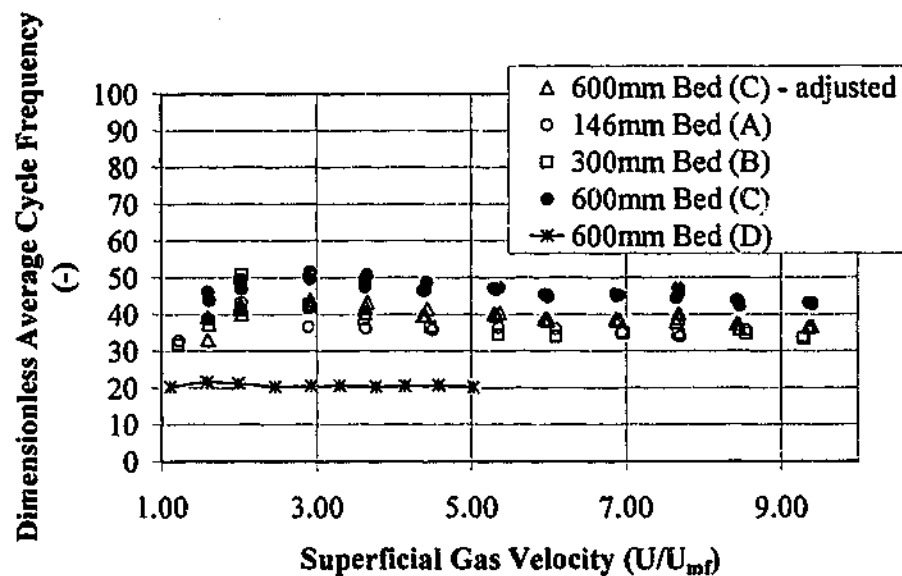


Figure 4.54 Data of Figure 4.53 re-plotted with results for the 600 mm bed adjusted by non-dimensionalising the frequency with the "ideal" scaled minimum fluidization velocity of $U_{mf} = 0.082$ m/s instead of the actual $U_{mf} = 0.07$ m/s of the bed material. Although not valid for similarity comparisons, the chart clearly demonstrates that the observed off-set in dimensionless frequency is a consequence of calculation, rather than an actual mis-scaled behaviour.

It is clear from the results of the comparison of the smaller beds at higher gas velocity that the trend seen at high gas velocity in the large (1560 mm) bed is unique to that bed alone, and cannot be replicated in the smaller units at any gas velocities considered.

4.10 Discussion of Large-Scale Pressure Fluctuation Results

Apart from some specific exceptions, the pressure fluctuation for the four scales of fluidized bed are generally similar. This is an encouraging state of affairs, as it indicates that for the most part the hydrodynamics of the beds have been scaled successfully with their dimensions. The clear distinction seen in the results between the mis-scaled bed and the scaled beds also indicates the reliability of the comparison. Some points arising from the consideration of the large-scale pressure fluctuation results will now be discussed.

4.10.1 *Spatial Variations in Hydrodynamic Similarity*

As the qualitative agreement map of Figure 4.35 shows, the best agreement across the full range of bed diameters was obtained (for gas velocities below $3.5 \cdot U_{mf}$), for pressure probes located away from the walls and the bed surface. Agreement is generally good near the distributor which tends to indicate that the initial formation of bubbles is occurring in a hydrodynamically similar way. One possible explanation for the differences in pressure fluctuation characteristics (amplitude and frequency) noted towards the walls and bed surface is presented below.

The walls and bed surface represent physical boundaries that have a local influence the "freely-bubbling" nature of the fluidized bed. The wall, for example, offers an unyielding constraint on lateral particle movement, and it has certainly been demonstrated that the presence of a vessel wall influences bubble flow patterns as well. -Typically a zone of preferential bubble flow is found near the vessel wall low down in the bed (eg Werther, 1974; Kunii and Levenspiel, 1991) and the bubbles gradually move towards the vessel centre as they rise, due to the "one-sided" coalescence behaviour that the wall imposes. (Bubbles at the wall must move inwards in order to coalesce – if they move outwards there is nothing for them to coalesce with!)

At the bed surface, bubbles burst (since the bubble internal gas pressure is greater than the surrounding freeboard pressure) and particles, predominantly from the bubble wake, are ejected upwards out of the bed (Kunii and Levenspiel, 1991). The bursting of the bubbles is a significant contributor to pressure waves recorded by the pressure probes (van der Schaaf *et al.*, 1998) and it seems reasonable to correlate the energy of the bubble burst directly with bubble size – this is supported by experimental evidence (eg Horio *et al.*, 1980 and Horio *et al.*, 1983).

If the pressure fluctuations recorded locally at the wall in the upper portion of the bed are showing differences between the scaled units, it is likely that the bubble bursts at the bed surface in regions close to the wall are not scaled perfectly. This may be due to mis-scaled distributions of bubble sizes or a mis-scaled bubble pattern at the local bed surface, -or both. A possible reason for these kind of differences in bubble characteristics at the bed surface is that the coalescence of bubbles originating near to the wall is unequally affected by the presence of the walls at different scales. Since differences in fluctuation behaviour are also noted at the wall lower down in the bed, this is a real possibility; and because the beds are relatively shallow, the coalescing bubbles will not have moved very far inwards from the wall by the time they reach the surface and burst – thus affecting surface measurements close to the wall as seen in experiments.

An additional observation relating to the large 1560 mm bed alone is that the frequencies of the pressure fluctuations are more scattered in this bed at low gas velocity when measured near the bed surface. Scatter in the frequency results for different runs conducted with similar operating conditions is an indication of some non-stationarity in the fluctuation signal; *ie* the spectrum is not perfectly invariant and reproducible at the low gas velocities. At high gas velocities however, it appears that the frequency data become more “well behaved” – there is less scatter indicating that a more regular pattern of bed behaviour has been established from one run to the next. (Note however that this is also the operating region where the *amplitudes* in this bed begin to increase rather dramatically – discussed in the subsequent section.) Although for the bubble cap arrangement used in the present work there is a possibility of random defluidization at low velocity (Whitehead *et al.*, 1967) – which has been discussed previously (see Section 3.5.3); given the agreement and repeatability of fluctuation frequencies and amplitudes in the lower part of the bed as well as the evidence from the correlation, it does not appear that this has occurred. Thus the frequency scatter noted in the upper portion of the large bed at low gas velocity cannot be explained by randomness in tuyere

operation. It is tentatively suggested that the cause of the scattering is also due to differences in the coalescence behaviour of bubbles in the larger bed.

Note that only a limited number of the previous verification studies have measured and compared pressure fluctuations results from different probe locations. Of those studies which reported on results for different probe locations, most found some form of dependence on probe location. Contrary to the present work, Vander Stappen (1996) found the agreement from single pressure probes in beds scaled by the simplified scaling laws to be particularly poor at the distributor and better further up the bed. The difference in this case was attributed to the effect of the distributors, which were not explicitly scaled, and may have caused mis-scaled behaviour in the initial bubble formation region of the bed. Amstedt and Zakkay (1990) used capacitance probes, but the results in terms of bubble behaviour are relevant here. They used the full set of scaling laws and also found poor agreement near the distributor. However once again, differences were attributed to a known difference between distributors in the two beds (namely that a significant temperature gradient across the distributor in the hot model was abruptly changing the gas transport properties – an effect which could not be replicated in an ambient model). Nicastro and Glicksman (1984) evaluated the full set of scaling laws and used differential pressure probes. They found generally good agreement, however agreement of the results was slightly poorer towards the lateral centre of the bed than at the walls. The difference, however was only slight. Finally, Brue and Brown (2001) used differential pressure measurements from wall tappings in beds scaled using the full set of scaling criteria and found quite clearly that the closer the measurements were to the bed surface, the poorer the agreement in results. They attributed the differences to bursting bubbles or sloshing of the emulsion phase - phenomena not explicitly accounted for by the scaling criteria.

So, whilst in the “ideal world” of complete hydrodynamic similarity the effect of the wall and bed surface on bed behaviour would be scaled exactly with bed dimension, the experimental results of previous studies show that it may not be the case, and that improper distributor matching may also cause trouble. In the present study there is an identifiable degradation in the observed similarity close to the wall and bed surface. A specific investigation to resolve the cause of the difference is beyond the scope of the current work; suffice it to say that these localised deviations from similarity have been identified.

4.10.2 Changes in Bed Behaviour with Changing Gas Velocity

Several observations can be made about the results with regard to increasing gas velocity. As mentioned above, for gas velocities exceeding around $3.5*U_{mf}$, the scattering in the frequency data in the 1560 mm bed is reduced, the average pressure begins to drop and the amplitude of the pressure fluctuations begins to rise dramatically. For the smaller three beds, no significant changes of this nature are noted, even when the gas velocity is increased up to $9*U_{mf}$.

Clearly this deviation in behaviour of the 1560 mm bed is velocity related, but the question remains as to what underlying phenomenon is causing the change. If the observed change in behaviour in the 1560 mm bed was due to changes in the nature of drag forces, (and thus particle-Reynolds number related), it is likely that the same kind of trend would be seen for the smaller beds at higher gas velocity. However, the discrepancy commences at a particle Reynolds number of approximately 13, which is relatively low. Zhang and Yang (1987), Roy and Davidson (1989), Van der Stappen (1996) and Stein *et al.*, (1998) have all presented results indicating success with the simplified scaling criteria with one or more scaled beds operating at particle Reynolds numbers above 13. In the higher velocity experiments of this study, the particle Reynolds number of the 600 mm bed approaches 15 at $U/U_{mf} = 9.4$, (the maximum velocity at which experiments could be performed) and a similar change in behaviour is not observed. (Although some differences in the average and the amplitude of the pressure fluctuations start to be seen in the smaller three units at these high velocities, they do not show the same characteristic trend as the 1560 mm bed at all).

In terms of experimental observations, it would appear that the large-scale shallow bed arrangement operating at relatively high gas velocity ($U/U_{mf} = 4$) with such a small number of tuyeres (18) is entering into "uncharted territory". The type of behaviour seen in the 1560 mm bed (*viz* increased amplitude, decreased average pressure and a narrower range of fluctuation frequencies at the radial bed centre) is perhaps more typical of the single bubble or exploding bubble regime identified by Svensson *et al.* (1996). However, the operating conditions for the large bed in this study are nowhere near the conditions reported in that work. In this work, the gas velocities are much lower and the distributor pressure drop at the highest gas velocities where the change in behaviour occurs is considerable (approaching 30 kPa) – far greater than the total bed pressure drop at this velocity. Despite the small number of gas entry points, one would expect this high distributor pressure drop should ensure an even gas distribution

regardless of what the bed does, putting the bubble regime for the large (and indeed all the) scaled beds firmly in the region of "multiple text-book bubbles" (Svensson *et al.*, 1996). Yet this is not what experimental observations suggest. The high distributor pressure drop (compared to bed pressure drop) also makes it unlikely that the difference in behaviour is the result of an interaction with the air-feed system (Johnsson *et al.*, 2002).

A quick review of bubble size correlations (such as those presented in Section 2.2.8) indicates that bubble sizes in these beds are likely to follow the scaling law reasonably closely, with the exception of the Werther (1978) correlation. The predictions of the Darton *et al.*, (1977) correlation for the beds used in the current work are summarized in Figure 4.55. The dimensionless bubble size has been defined based on the spherical-equivalent bubble diameter D_{eq} and the settled bed height H_s . (The reason for choosing H_s is simply that since the bed aspect ratio is less than 1, bubbles will approach H_s before they approach D so the settled bed height represents the limiting dimension).

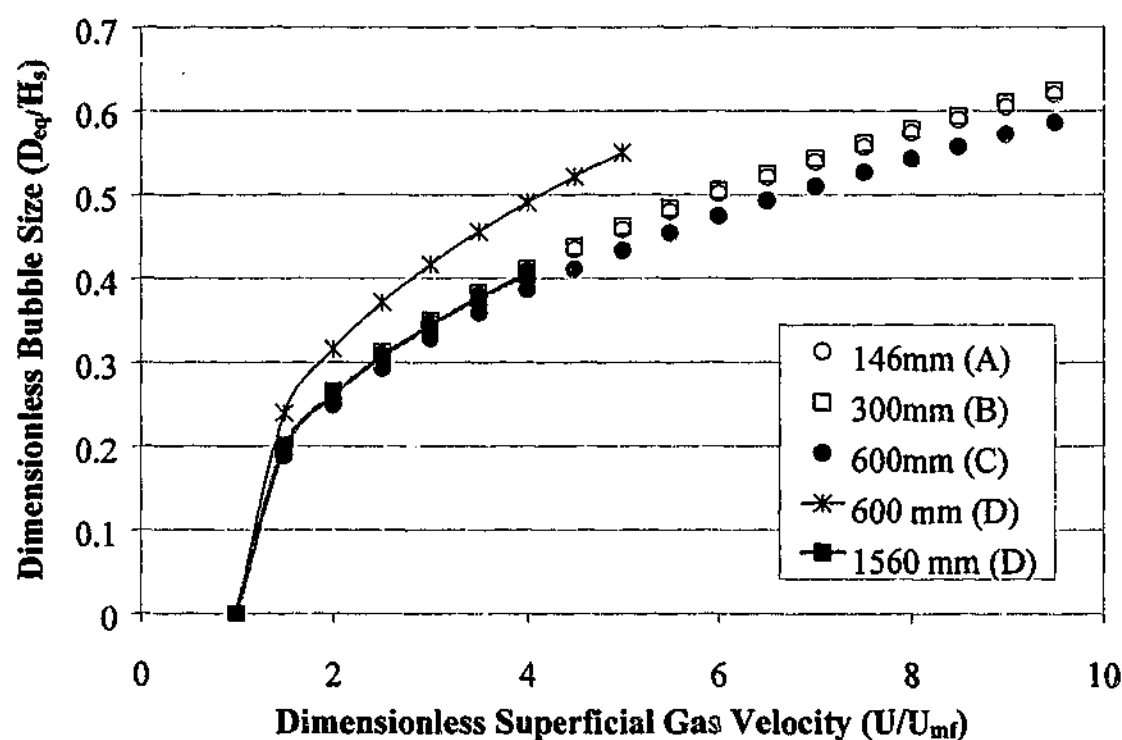


Figure 4.55 Dimensionless bubble size predictions from the Darton *et al.* (1977) correlation for the four scaled and one mis-scaled beds over the range of gas velocities considered experimentally. Bubble sizes are predicted for the axial location of the upper pressure probe, ie $h/H = 0.77$.

Bubble size is calculated for the axial position $h/H = 0.77$ corresponding to the location of the upper pressure probe. As can be seen the agreement in bubble size for the 146 mm, 300 mm and 1560 mm beds is expected to be good; slightly poorer for the 600 mm correctly scaled bed (due to the error in U_{mf} for that bed material), and very poor for the 600 mm bed with the mis-scaled bed material. This is to be expected, since the Darton *et al.*, (1977) correlation -amongst others- was identified by Horio *et al.*, (1986a) as one which satisfied their similarity rule. At gas velocities of $U/U_{mf} = 4$, the correlation predicts bubbles with equivalent diameters approximately 0.4 of the settled bed height (note that these sizes are well within the applicable range of the correlation, *ie* $d_{eq}/D < 0.33$). As expected, it does not predict any difference in dimensionless bubble size for the 1560 mm bed at this gas velocity.

The Werther (1978) correlation does not agree with the simplified scaling laws and predicts smaller bubble sizes than Darton *et al.* (1977). Although the Werther correlation predicts increasing absolute bubble size for the 146 mm, 300 mm and 600 mm correctly-scaled beds, the predicted dimensionless bubble size (*ie* D_{eq}/H_s) decreases with increasing bed size for these three beds. Notably, with this correlation the 1560 mm bed shows a dimensionless bubble size very close to that of the 300 mm bed for the full range of dimensionless gas velocities in this work. However, note that the correlation was developed for bed sizes up to 1 m, thus it may in fact not be applicable to the 1560 mm bed. In any case, the correlation shows nothing unusual at $U/U_{mf} > 3.5$ for the 1560 mm bed.

The possibility of a regime transition in the 1560 mm from bubbling to slugging can also be considered. However, the low aspect ratio of the beds makes it very unlikely that slugs can exist at *any* gas velocity. The various minimum slugging criteria introduced in Section 2.2.9 require a minimum bed height and gas velocity for slugs to be established. Table 4.5 summarizes these minimum requirements for the scaled beds employed here.

As can be clearly seen, none of the beds are deep enough for slugging to occur, although the operating gas velocities are high enough to promote slugging if the beds were deeper. Additionally, a characteristic of slugging beds is the steady increase of the bed pressure drop above $\frac{Mg}{A}$ with increasing gas velocity. As mentioned earlier, what is seen in the case of the largest bed is in fact the opposite effect.

Reference	146mm (A)	300mm (B)	600mm (C)	600mm (D)	1560mm (D)
Yagi & Muchi (1952)	$H_{mf} = 339$	$H_{mf} = 643$	$H_{mf} = 1209$	$H_{mf} = 1103$	$H_{mf} = 2868$
Baeyens & Geldart (1974)	$H_{mf} = 957$ $U_{ms} = 0.240$	$H_{mf} = 1085$ $U_{ms} = 0.301$	$H_{mf} = 1225$ $U_{ms} = 0.344$	$H_{mf} = 1225$ $U_{ms} = 0.401$	$H_{mf} = 1448$ $U_{ms} = 0.421$
Darton <i>et al.</i> , (1977)	$H_{mf} = 391$	$H_{mf} = 803$	$H_{mf} = 1605$	$H_{mf} = 1605$	$H_{mf} = 4173$
Stewart & Davidson (1967)	$U_{ms} = 0.123$	$U_{ms} = 0.178$	$U_{ms} = 0.240$	$U_{ms} = 0.297$	$U_{ms} = 0.401$
Actual Conditions	$U_{max} = 0.36$ $H_s = 103$	$U_{max} = 0.54$ $H_s = 207$	$U_{max} = 0.66$ $H_s = 413$	$U_{max} = 0.65$ $H_s = 400$	$U_{max} = 0.52$ $H_s = 1040$

Table 4.5 Requirements of various minimum slugging criteria for slugging in the scaled (and mis-scaled) fluidized beds. Gas velocities are in m/s, heights are given in mm.

The question also arises as to whether the influence of the return leg geometry in the large (1560 mm) unit had some influence on the bed behaviour. Recall (from Section 3.2.4) that this was the only bed in which the existing angled solids return points entered at a height lower than the bed surface (approximately 500 mm above the distributor). Figure 3.4 showed the arrangement. Observations relating to the angled returns are as follows: In the filling process for this bed, the small additional volume (0.04 m^3) due to the increased cross-sectional area associated with the angled returns was accounted for. (In other words, the settled bed height of 1040 mm was achieved with some solids in the lower parts of the angled return legs.) The twin loopseals contained solids from previous experiments and these were not fluidized, thus forming a relatively high pressure drop restriction against any air-flow up into the return loop. It was noted that only a small portion of very fine bed material carried over into the (non-operating) loopseals from the cyclones throughout the entire course of experiments. Furthermore, bed height remained relatively constant, confirming that little or no bed material was splashing over into the loopseals via the angled returns. The nearest angled return point was located some 0.450 m away from the pressure probe tapping points (distance measured around the circumference of the bed). Given the physical situation, it is difficult to see how the solids in the angled returns could have been fluidized, due to the high pressure restriction of the packed bed in the loop-seals. However, it is perhaps conceivable that the vigorous movement of the bed at higher gas velocities caused a plug of bed solids to be pushed up some distance into each of the angled return legs, consequently decreasing the average bed height in the riser section. (Note: Since bed

solids did not accumulate in the loopseal, any solids pushed into the angled return leg obviously were not pushed all the way to the top of it.) Thus, the maximum total volume of solids which could have "disappeared" from the bed, as calculated from the return-leg geometry (each angled return leg has length 1500 mm and diameter 250 mm) could be as large as 0.15 m^3 (approximately), corresponding to a possible bed height reduction of 80 mm. Now, the decrease in average bed pressure drop observed at high gas velocity in the 1.56 m bed was up to around 10% of the total measured pressure drop – corresponding to a change in bed height of similar order to 80 mm. So it can be said that the explanation involving angled return leg geometry is to some extent plausible.

However, the upshot of the preceding comments is that there is no single obvious explanation for the discrepancy in the 1560 mm bed behaviour that occurs at gas velocities beyond $U/U_{mf} = 3.5$. The lowering of average pressure measured by the probes towards the radial centre tends to indicate the probes are encountering an increased voidage between their location and the bed surface. The increase in amplitude implies increasingly violent fluctuations in bed height also. The change in behaviour is due to a phenomenon not accounted for in the simplified scaling laws; it is not predicted by bubble size correlations; it is not due to a transition to slugging; and the combination of high pressure drop distributor and relatively low gas velocities used suggest that the single bubble or exploding bubble regime has not been reached. Despite the lack of *prediction* for this behaviour, results from the pressure fluctuation measurements clearly indicate that a change does indeed occur in this large bed, and as the underlying cause of this change is unclear, it serves as grounds for future work.

4.11 Conclusions

The simplified scaling laws for bubbling fluidized beds have been extensively evaluated using pressure fluctuations measured from a number of bubbling fluidized beds. Initial small-scale experiments focussed on verifying the success of the scaling laws for scales and conditions similar to those used by previous workers in order to evaluate the measurement techniques used in the present work. Combinations involving mismatched particle sizes and densities were also investigated. The large-scale work was more specifically a test of the scaling laws across a very wide range of bed sizes. The major findings of the study are as follows:

- Global pressure fluctuations provide an adequate means of distinguishing between scaled and mis-scaled bubbling bed hydrodynamics.
- For the case of a small scale change involving beds of materials with the *same* solid-to-gas density ratio, hydrodynamic similarity was achieved for the full range of gas velocities considered.
- For the case of a small scale change involving beds of materials with *different* solid-to-gas density ratio, hydrodynamic similarity was also achieved for the full range of gas velocities considered. This demonstrates that for particle Reynolds numbers only slightly above the viscous limit (in this case for Re_p up to 8), the constant density ratio requirement can be safely ignored.
- The frequency of pressure fluctuations is only weakly affected by particle size, density and gas velocity, however it is more strongly affected by bed height.
- Small errors in the minimum fluidization velocity influence the resultant dimensionless frequency value through the calculation process, rather than by a direct effect on the bed behaviour.
- For shallow beds, small differences in settled bed height and particle bulk density can have a significant effect on the resultant dimensionless average pressure drop. Scaling bed inventories by bed mass directly reduces the potential for errors.
- For a large scale change in shallow beds with gas velocities up to $3.5 \cdot U_{mf}$, the agreement in bed behaviour is best towards the radial centre and in the lower portions of the bed. Agreement is poorer towards the bed surface and vessel wall.
- At gas velocities above $3.5 \cdot U_{mf}$, the largest bed (1560 mm diameter) shows a distinct deviation in average pressure drop and fluctuation amplitude which cannot be accounted for by the scaling criteria, bubble size predictions, slugging criteria, bubble regime change or a limiting particle Reynolds number. The same behaviour is not observed in smaller beds even at much higher gas velocities.
- Whilst the issue cannot be directly related to any observed hydrodynamic effects in this study, vibrations observed in the large-scale unit were impressive enough that this author would like to suggest that the influence of structural vibrations on bed behaviour may be a worthy area of future work.

Apart from the exception above, the simplified scaling laws were found to be successful for the majority of conditions studied. Areas for consideration in future work are the effects of the boundaries represented by the vessel wall and bed surface on the local bed hydrodynamics, and the unusual behaviour of very large shallow multi-tuyere fluidized beds at high gas velocity.

5. VOIDAGE FLUCTUATIONS

In this chapter, the results of the small-scale pressure fluctuation comparisons presented in Chapter 4 are augmented by voidage fluctuations measurements made using ECT under the same experimental conditions. As will be seen, the results of these voidage measurements further support the previous pressure fluctuation results, however significant limitations to the ECT measurement technique are also identified.

5.1 Introduction

In Chapter 4, pressure fluctuations were used in making comparisons of hydrodynamic behaviour between the four cold model fluidized beds. Whilst the comparison of pressure fluctuations is a robust and well-established means of comparing bed behaviour, the exact nature of the link between the measured pressure signal and the actual physical goings-on in the bed has been the subject of considerable debate (to recap, see Section 4.2.1).

Like pressure measurements, capacitance measurements have been made in fluidized beds for many years. Unlike pressure measurements however, the link between bed capacitance fluctuations and the hydrodynamics of the bed (*ie* the local bed voidage) is direct and more clearly understood. This relationship between dielectric constant and a solids volume fraction is well-established (*eg* Maxwell, 1873) and has been explored in some detail for multiphase systems (*eg* Tinga *et al.*, 1973; Louge and Opie, 1990). In addition to the common usage of capacitance probes to measure voidage in fluid beds, a more recently developed measurement systems employing the same principle is the Electrical Capacitance Tomography (ECT) system, which can be readily applied to fluidization studies.

5.2 Background - Capacitance Measurements in Fluidized Beds

Maxwell (1873) originally developed the theoretical model linking the dielectric permittivity of a two-phase mixture (of one material dispersed within another) to the volume fraction of the mixture. Other models exist. Maxwell's model applied to an

(otherwise) uniform electric field distorted by a mixture of small (relative to their separation distance), uniformly-distributed spheres of one material dispersed in a continuous phase of a second material. The model predicted that the effective dielectric permittivity of the mixture ϵ_m would be:

$$\epsilon_m = \frac{2\epsilon_1 + \epsilon_2 - 2c_v(\epsilon_1 - \epsilon_2)}{2\epsilon_1 + \epsilon_2 + c_v(\epsilon_1 - \epsilon_2)} \quad (5.1)$$

where ϵ_1 and ϵ_2 are the dielectric permittivities of the individual phases and c_v is the volume fraction of material 2 in material 1. The idea of applying a relation like the above to a measured mixture capacitance and calculating the composition of a non-conductive mixture has been in practice for many years in various gas-solid, gas-liquid and liquid-solid systems (Dyakowski *et al.*, 2000).

It is not surprising then that historically, the most commonly employed alternative dynamic measurement to pressure fluctuations in fluidized beds has been the measurement of local bed voidages using a capacitance probe. The capacitance probe approach has been in practice for as long as (if not longer than) pressure probes (*eg* Morse and Ballou, 1951). But it is the detailed work by Werther and Molerus (1973a, 1973b) that in many ways set the "standard" for capacitance probe design.

In general terms, the approach when using a capacitance probe is as follows: The capacitance is measured between two conductors separated by a portion of the fluidized bed. (Various configurations of the conductors are possible and ideally they should disturb the bed as little as possible.) The measured capacitance is proportional to the dielectric constant of the material between the conductors, and this in-turn is related to the dielectric constants of the individual materials present (the solid and the gas), and their relative quantities. If the dielectric constants of the materials are known *a priori* and the probe is suitably calibrated, then the measured capacitance can be directly related to the fractions of materials present. This is simple enough in theory, however there are some practical considerations which make the use of capacitance probes somewhat difficult:

$$C = \epsilon_r \epsilon_0 \frac{A_e}{d} \quad (5.2)$$

The above equation is commonly used to calculate the value of capacitance C between a pair of planar conductors of common area A_e , separated by a dielectric material of relative permittivity ϵ_r (ϵ_0 is the permittivity of a vacuum) and having a thickness d . (Edge effects are neglected.) Although this equation is simplified, it highlights the problem. Capacitances can only get so small before their measurement becomes difficult. And as can be seen in Equation 5.2, the further apart the conductors are (increasing d), the smaller the capacitance; and the smaller the conductor area (decreasing A_e), also the smaller the capacitance. But in order to reduce the undesirable disturbances due to the presence of a probe in a fluidized bed measurement scenario, either the probe is made very small (hence A_e is small) or the measurement is made across the whole bed using conductor plates on the vessel wall (d is large) – also the approach taken with ECT. In both situations, the resulting capacitance begins approaching the limit of what can be reliably measured, and indeed the self-capacitance of the connecting cables and nearby objects as well as any stray electric fields all begin to have a significant and deleterious effect on the measurement of such a small quantity.

The most successful approach to overcoming the problems of stray and cable capacitances in a capacitance probe is the use of a “guard” electrode, (Acree Riley and Louge, 1989). The sensor electrode is supplied with a current of constant amplitude from an oscillator via the centre conductor of a coaxial cable. The guard electrode is kept at the same voltage as the sensor via a separate circuit (supplied through the outer conductor of the coaxial cable) and absorbs the majority of the distortions to the electric field caused by external effects (so-called “stray” capacitance effects). The capacitance of the cable no longer influences the measurement because the outer conductor is now at the same potential as the inner sensor line. As will be discussed shortly, the “guard” principle has also found use in ECT systems.

Although capacitance probes can be made small, they still present an obstruction to flow. One way around this is to put the electrodes of the capacitor “probe” on opposite walls of the vessel and thus measure capacitance across the entire diameter of the vessel. However, in order to keep the capacitances measurably large across this increased distance, the size of the electrodes must be increased (Equation 5.2), so the measurement is effectively less local.

Ormiston *et al.*, (1965) were early workers who used such an approach to measure slug velocities in beds up to 140 mm in diameter. They used two pairs of electrodes at different axial heights on the outside of an acrylic tube and an automated electronic

process interpreted the capacitance measurements for counting slugs. They addressed problems with stray capacitance by placing copper shields around the outside of the capacitor plates and current leakage issues were dealt with by installing earthed screens in contact with the tube. They also adjusted the sensitivity of the two electrode pairs so that each pair would give the same reading when the tube was full of sand and when it was empty. As will be appreciated shortly, the origins of capacitance tomography can be clearly seen in early work of this type.

5.3 Introduction to Electrical Capacitance Tomography

Electrical Capacitance Tomography, (ECT) is a technique for real-time imaging of industrial flows developed in the last ten years. It is one of several tomographic techniques that have been developed in recent years for use in industrial situations. It has the advantages of being low-cost and relatively simple to set up and operate. The ECT system measures capacitance between a number of sensor electrode pairs located around the circumference of a vessel and then combines the measured values using a reconstruction algorithm in order to generate a two-dimensional density profile of the vessel contents.

The advantage of ECT in fluidized bed studies is that it is a non-intrusive measurement technique that can give measurements of volume fraction over the entire cross-section of a vessel. Being non-intrusive, the flow in the bed is not disturbed (as it is when the pressure probes are used). The main disadvantages are that it is limited to systems containing non-conductive media, and it can only be used on relatively small vessels.

The ECT system consists of a set of electrodes surrounding the region of interest in the fluidized bed, a data acquisition unit containing the sensor electronics, and a computer to log the data and reconstruct the capacitance measurements into the cross-sectional image of the vessel contents. Technical information concerning the setup of the ECT system used in the present study (the UMIST PTL-300 system) was presented in Section 3.7. Recall that the system used in this work incorporates a single plane of 12 electrodes, and uses the *single excitation method* (ie only one electrode held positive whilst measurements are made on the remaining eleven. (cf the METC ECT system which uses *dual excitation*). Currently, there are around 20 UMIST ECT systems in use around the world.

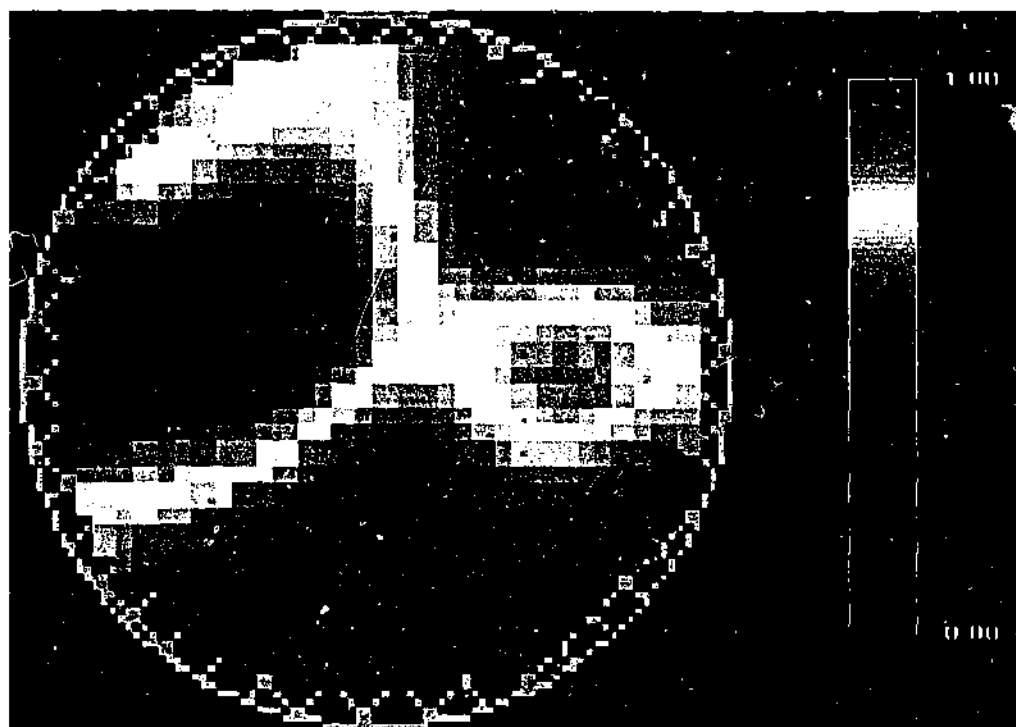


Figure 5.1 Example of an ECT image of a bubbling fluidized bed. Pixels are coloured according to a solids volume fraction defined such that a value of 1.00 corresponds to a packed bed and 0.00 corresponds to gas only.

Bair and Oakley (1993) investigated the differences between single and dual electrode excitation methods using simulations. It was expected that the method of dual excitation would produce better results because dual excitation generates a higher electric field strength in the centre of the vessel and so potentially provides more information about the centre area of the vessel. However, despite the sensitivity distributions for the measurements being quite different, reconstructed images appeared very similar, suggesting that the back-projection reconstruction algorithm used was the overall limiting factor in the system, not the selection of the excitation method.

ECT is a so-called "soft-field" measuring technique. The object space (or "measurement volume") is interrogated by electric field lines which can be envisaged as curved lines running between the measurement electrodes. If the ECT sensor is completely filled with a dielectric material (with uniform dielectric properties), then the pattern formed by the electric field lines inside the sensor will be the same, regardless of the permittivity of the material. However, if the space inside the sensor is only partially filled with the dielectric material, or if the material is dielectrically non-uniform, the pattern of electric field lines will be altered by the material inside the sensor. Consequently, any image obtained from measurements of the inter-electrode capacitances will be distorted. This

is analogous to the distortion of an optical image by an imperfect lens. It is particularly bad in physical situations where the dielectric constant is dramatically different from one phase to the other, however for the gas-solids systems of the type considered in this work, the variation in dielectric constant between the materials is not great, so the soft-field problem is less severe (Ostrowski *et al.*, 1999).

Further image distortion occurs when the sensor electrodes are located on the outside of the vessel wall because the wall material itself introduces an additional undesirable series coupling capacitance into the measurement of the inter-electrode capacitances. As the purpose of ECT is to obtain an image based on variations in the permittivity of the material inside the sensor, allowances must be made for image distortion in the image reconstruction algorithm used to generate the image.

The Linear Back-Projection (LBP) reconstruction algorithm has been the most common one used for ECT image reconstruction. This is because it is simple, and well established in the medical imaging field (from hard-field nucleonic tomography techniques such as X-ray tomography). However as mentioned, evidence suggests that the reconstruction algorithm is the limiting factor in ECT image accuracy (see Huang, *et al.*, 1992; Bair and Oakley, 1993). Much work has gone into improving the image reconstruction techniques (eg Isaksen and Nordtvedt, 1993a&b; Chen *et al.*, 1993, Lionheart, 2001; Loser *et al.*, 2001; Liu *et al.*, 2001). A summary of reconstruction algorithm developments is provided in Isaksen (1996) and more recently in Dyakowski *et al.*, (2000). Furthermore, an iterative LBP algorithm (Yang *et al.*, 1997) has been included in the PTL-300 package, but this takes more processing time to employ. However, this approach reproduces images more faithfully. (See Dyakowski *et al.*, 2000 and Liu *et al.*, 2001 for a comparison of some reconstructed images generated with both the standard and the iterative LBP.)

5.4 Experimental Usage of ECT

ECT systems from both UMIST and METC have been used in imaging a number of two-phase systems. Scenarios investigated include fluidized beds, pneumatic conveying systems and two-phase liquid systems. Halow *et al.*, (1990) tested an early version of the METC-developed 4-plane imaging system on a 152 mm fluidized bed. Four rings of 16 electrodes were placed on the inner vessel wall and used to image bubble and slug behaviour with several bed materials (nylon spheres, irregular plastic particles and a

coarse cut of FCC). The results of the measurements were generally consistent with the expected behaviour (*viz* bubble/slug size and rise velocity). They also found that the generation of an average cross-sectional voidage time series was successful for quantifying bubble properties in cases of low bubble density. Halow and Nicoletti (1992) used a modified version of the ECT equipment (4 rings of 32 electrodes each) in a 152 mm fluidized bed to investigate bubble coalescence and slug formation in various plastic materials. They highlighted some of the limitations of the images produced (limited image resolution, blurring, ghosting and a false voidage increase between two voids). A general observation of the interface between bubble and emulsion phase exhibiting a fuzzy appearance was also made, thus when calculating bubble sizes they chose to use a voidage contour of 0.7 to 0.75 to define the "edge" of the bubble. Observations of a velocity-dependent increase in emulsion-phase voidage as well as channels of increased or decreased emulsion-phase voidage were also made. The authors use these observations to highlight some of the shortcomings of the two-phase fluidized bed model. However, there is some doubt whether the fuzzy bubble appearance or voidage phenomena they report are real results or an artifact of the measurement technique.

Huang *et al.*, (1992) reported on the preliminary use of the UMIST ECT single-plane system with 8 electrodes applied to a 75 mm inclined pipe containing either an oil/water mixture or plastic particles. Limited experimental results were presented and they commented on the need for correcting image distortions created as a consequence of ECT being a soft-field technique. Huang *et al.*, (1993) further considered image distortion and the limits of image reconstruction by using various test objects ("phantoms") in the 8 electrode 75 mm pipe and also in a 12 electrode 150 mm pipe. The phantoms consisted of plastic rods in air, plastic cylinders surrounded by oil and partially filling the (horizontal) pipe with oil. They found that the rods (in air) as small as 2% of the tube diameter could be detected at the centre of the vessel, but the situation was far poorer for the hollow tubes surrounded by oil, with any tube less than 12% of the vessel diameter failing to produce an image at the vessel centre *at all* and the maximum reconstructable bubble size therefore being approximately 20% of the vessel diameter. Xie *et al.*, (1994) further reported on this work involving phantom objects, presenting similar conclusions, and highlighting the so-called "dielectric screening effect"; the implications of which are that small low permittivity objects surrounded by a higher permittivity medium are "masked" from view in the reconstructed images.

Isaksen *et al.*, (1994) presented results for an electrical capacitance tomography system applied to a model of a water/oil/gas separator. The single-plane 8-electrode ECT system was proposed as a means of on-line monitoring of the interface heights in a separation vessel in a process plant. Although not a fluidized bed application of ECT, the work is noteworthy because the acrylic separator vessel (horizontal cylinder) was quite large. The single-plane of electrodes occupied a ring 1 metre in diameter, and despite the relatively large distance between electrodes, the agreement between the actual interface levels and the detected interface levels was good (within 10 mm). The authors did, however comment on problems with static charge accumulation in the plastic vessel but suggested that this problem would be eliminated inside a real separator made from steel.

Wang *et al.*, (1995) employed the UMIST single-plane 8-electrode system to produce images of a 150 mm diameter fluidized bed of glass beads. The sensors were in this case mounted very close to the distributor of the bed and the steel windbox was used as one of the shield electrodes. They reported on bubble and slug lengths as well as "transition" behaviour at higher gas velocities. The approach used to calculate bubble and slug lengths has a significant drawback, however: A limitation to the single-plane approach is that a bubble rise velocity cannot be directly measured; it must therefore be assumed (because it is not explicitly stated in the article) that the authors employed a literature correlation to estimate the bubble rise velocity based on the bubble diameter they derived from reconstructed images of bubbles. Given the doubts cast upon the reliability of the reconstructed images in the previously-mentioned "phantom" study reported in Huang *et al.* (1993) and Xie *et al.* (1994), the results must be treated with some caution, and certainly the reliability of the reconstruction techniques employed deserved some greater mention.

Mathers and Rhodes (1996) used the UMIST single-plane 12-electrode system (precursor to the system used in the present work) on a 300 mm diameter riser operating in bubbling and slugging modes. Literature correlations were employed to estimate the expected size and rise velocity of the bubbles and slugs under the experimental conditions. These were then compared with the time-of-flight of the bubbles and slugs past the sensor electrodes as recorded by the ECT system. The ECT-observed bubble diameters and times-of-flight were also used with correlations to estimate the bubble and slug lengths at various gas velocities and compare with theory. The agreements were generally good, but better in slugging than in the bubbling mode, presumably because

the ECT system was more successful in reconstructing images for the situations where larger voids were present.

Kühn *et al.*, (1996) used a 12-electrode single-plane ECT system to measure chaotic invariants (Kolmogorov entropy and correlation dimension) in a 284 mm diameter fluidized bed. They made comment on the success of the single-plane UMIST-style sensor at small scale (100 mm diameter), but difficulties arose when trying to employ this sensor at the larger scale. They showed (qualitatively) via simulation that the normal configuration of the UMIST sensor (measurement electrodes banded axially by single earthed shield electrodes) distorted the potential distribution in the axial direction, but the METC-style system with driven shield electrodes (or indeed additional measurement planes) above and below the measurement electrode plane did not. (Note: For elucidation, the details of both these electrode configurations can be seen in Figure 3.13) Thus the workers opted instead for something closer to the METC multi-plane approach in the 284 mm scale work by modifying the original UMIST system for use with driven shield electrodes above and below the measurement electrodes. They compared the results from the ECT measurements with earlier characterization work involving pressure fluctuations (van der Stappen *et al.*, 1995), and found that the Kolmogorov entropy, average absolute deviation, average cycle frequency and peak to peak distance for the voidage fluctuations showed a distinct radial dependency (in all cases highest at the bed centre). They pointed out the need for improved image reconstruction algorithms in order to make a more detailed quantitative assessment of the voidage data.

Mathers *et al.* (1998) provided further information about the expected resolution of the standard LBP reconstruction algorithm using hollow phantom objects in packed beds of silica sand. The UMIST system with 12 electrodes was used on a 300 mm diameter vertical plastic section. Thin-walled hollow glass spheres and cardboard cylinders of various diameters and were located at a number of axial and radial positions within the bed, which was fluidized initially to aid in the object placement. Their results showed a very distinct dependency on the axial location of the phantom within the measurement volume, with the reconstructed images most closely matching the real void size and position when the void was located at the axial centre of the electrodes. These observations support the observations and simulation work of Kühn *et al.*, (1996) with regards to the axial non-uniformity in the electric field within the measurement volume when earthed shield electrodes are used. Furthermore, Mathers *et al.*, (1998) found a radial dependence similar to that observed by Huang *et al.* (1993) and Xie *et al.* (1994),

with void images progressively worsening as the voids were placed closer and closer to the radial centre of the bed (dielectric screening). For the bed size in question, they found that by using a similar approach to Halow and Nicoletti (1992) and choosing contour lines to represent the "edge" of the void, some reasonable results could be obtained for the larger voids. This contour choice however, was subjective and no formal rationale was given. Their results also indicated that a spherical void needs to be large - greater than $1/3^{\text{rd}}$ of the vessel diameter - before the reconstructed images approach the actual void size (even with the aforementioned contour line choice).

Ostrowski *et al.*, (1999) used the 12-electrode UMIST-based system for measurements of dense-powder conveying in a 52 mm plastic pipe section. Driven-shield electrodes were employed in this work. They applied a number of analyses to the ECT data, including power spectral densities, and autocorrelation functions of the types of slug flow that were observed in the system. In their conclusions they proposed that the ECT system was a suitable means of on-line monitoring of pneumatic conveying systems due to its ability to distinguish particular types of dense flow. Certainly, this work provides one of the better examples of a successful application of ECT to gas-solids flow. The large changes in capacitance associated with a slug passing through the measurement volume as well as the small diameter of the tube to which the technique is applied make it a more robust approach than in some of the previously cited applications.

Since its initial development, ECT has been applied to a wide variety of research and industrial problems, and a full review of these applications is beyond the scope of the present work. As an indication of the variety of use, however, consider the following recent applications of ECT; the visualization of dust-air explosions (Plaskowski *et al.*, 2001), measuring the mass flow of plastic pellets in tanker loading (Deloughry *et al.*, 2001), investigating the collapse of oil foams (Pacho and Davies, 2001) and a proposal to study direct injection and combustion phenomena of gasoline sprays (Sanders *et al.*, 2001).

5.5 Limitations of the ECT System Used in This Work

Before the similarity experiments involving ECT are introduced, it is worth pointing out some of the limitations of the ECT system, which have been highlighted in previous works. An understanding of these limitations is important in order to both use the ECT

equipment most effectively and interpret the results correctly. The noteworthy limitations can be summarised as follows:

- ECT can only be applied to non-conductive materials.
- Static electricity, often generated in fluidized beds, can produce noise which interferes with measurements (Plaskowski *et al.*, 1995).
- Changes in temperature, humidity and spatial position of objects nearby to the apparatus can significantly affect measurements (Yang and Stott, 1993).
- High definition measurements are not possible because the sensor size cannot be decreased without limit due to the finite resolution of the sensor electronics (Isaksen and Nordtvedt, 1993a)
- When two voids are present in the imaging field a false increase in the voidage between the two voids may be observed (Halow and Nicoletti, 1992).
- An effect known as dielectric screening can cause a region of low permittivity to be masked by a surrounding region of high permittivity. This has particular consequences for attempting to image bubbles (low permittivity) in a fluidized bed of higher permittivity sand. (Plaskowski *et al.*, 1995)
- The LBP image reconstruction algorithm can cause smoothing of sharp transitions in permittivity, resulting in indistinct boundaries between bubble and dense phases being observed when they may not in fact be present (Isaksen and Nordtvedt, 1993b)
- Measurement accuracy decreases towards the vessel centre and may limit the diameter of the vessel in which the technique can be used (Dickin *et al.*, 1992)
- In ECT systems without driven shield electrodes, measurement accuracy decreases significantly towards the top and bottom of the sensor (Mathers *et al.* 1998)
- Bubbles smaller than 30% of the vessel diameter may not be faithfully reproduced in ECT images at larger vessel scales (*ie* vessel diameter of 300 mm), and bubbles significantly smaller than this may not be imaged at all (Mathers *et al.* 1998).

As will be seen, several of these points have important consequences for the experiments reported below.

5.6 The Approach for the Similarity Experiments Using ECT

Given the information above, the ECT system was applied to specific areas of the hydrodynamic similarity investigation where it was most likely to yield successful,

reliable information about the behaviour of the fluidized beds. In the light of the work of Huang *et al.*, (1993), Xie *et al.*, (1994) and Mathers *et al.*, (1998), the reconstructed images themselves were only interpreted qualitatively.

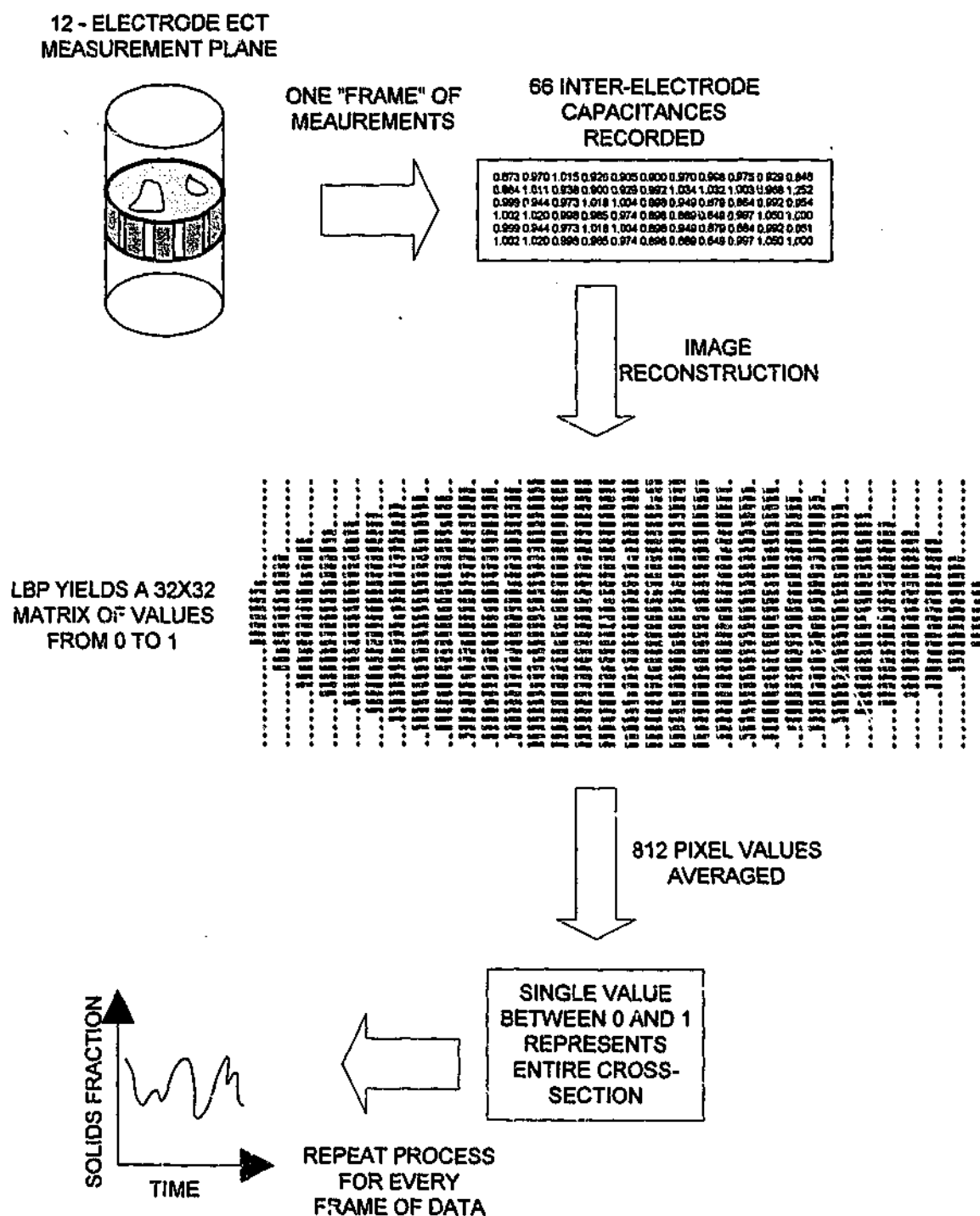


Figure 5.2 The procedure used to generate the voidage fluctuation time series from capacitance measurements. For each set of 66 capacitance measurements taken from the 12 electrodes, the linear back-projection reconstruction algorithm is used to generate the 32x32 square matrix of normalized capacitance values (between 0 for air only to 1 for packed bed of solids). For the 812 values corresponding to the circular cross-section of the vessel, an average is generated, representing the average solids fraction present within the measurement plane.

For quantitative comparisons the focus was on the *dynamic* information yielded by the voidage fluctuations themselves. The voidage fluctuations were generated by taking the average of the measured value for all pixels in the cross-section of the bed for each frame logged, to generate a single number for each reconstructed frame. The process for producing the voidage fluctuation time series is outlined in Figure 5.2.

By using this technique, the actual *size* of the reconstructed voids is not required. In other words, as long as the amount of void detected represents the physical situation in the measurement volume, it does not matter how the reconstruction algorithm distributes it in the image. Thus it is not important, for example, that the reconstructed image have sharp edges at the boundary between void and emulsion phase. As a guideline for the accuracy of the technique, Huang *et al.*, (1993) and Xie *et al.*, (1994) estimate the maximum error in estimating the component fraction from a reconstructed image (using the LBP algorithm) to be around 17%.

It must be stressed that due to the way in which the ECT system is calibrated (Section 5.6.1), the measurements do not correspond to the true voidage or solids volume as normally defined. This is because in the calibration procedure the two extremes of

- no solids at all, and
- packed bed

are used to specify the maximum range for the ECT measurements. All measurements subsequently made are normalized with respect to this range, and a packed bed thus has a measurement value of 1 and an empty vessel has a value of zero. (A bubbling fluidized bed may have measurements fluctuating around 0.8 or so.) Note also that a percentage scale (from 0% to 100%) is often used to indicate this solids fraction range. So the ECT measurement output indicates the fraction of solids present compared to the solids present in a packed bed state. In the case of the similarity work it is not necessary to perform a conversion of the results back to a true solids volume fraction or a voidage because the results are to be used comparatively and the ECT measurement output is already in a convenient dimensionless form.

5.6.1 Calibration of the ECT Sensors

Before conducting any voidage fluctuation measurements using the ECT system, careful calibration of the ECT instrument is required. The normally adopted procedure for performing an ECT calibration was as follows:

- Commence the calibration procedure with an empty vessel. This sets the lower limit of the ECT measurement scale (so that a vessel filled only with air and thus having a voidage of 1, will register on the ECT measurement scale as a value of 0%).
- Fill the bed to the desired height (which must be at least as deep as the height occupied by the measurement and shield electrodes) with the intended bed material and fluidize gently for at least 15 minutes (see Section 5.6.2 for the reasoning behind this requirement).
- Very slowly and gently reduce the airflow until the bed defluidizes and the particles settle into an evenly packed state.
- The packed bed condition thus achieved is used to set the upper limit of the ECT measurement range (thus the voidage of the packed bed corresponds on the ECT measurement scale to 100%).
- After calibration, experiments are commenced as soon as possible to minimize the effects of any gradual calibration drift.
- The ECT electrodes and connecting wires to the Data Acquisition Module are not touched or moved, nor is anything else in the laboratory within a radius of 1 metre from these items moved once calibration has been completed. This was found to reduce stray capacitance effects and calibration drift considerably.
- Calibration is carried out prior to every experimental run.

5.6.2 Baseline Drift

During the course of this work some interesting effects were noted with regard to ECT calibration drift, particularly in relation to the length of time taken to achieve a stable baseline in the ECT measurement output. It was observed that if the fluidized bed was calibrated following the above procedure but only allowing a few minutes of fluidization time prior to bed settling, a significant drift in the baseline was observed in the period following calibration. The effect varied with bed material, and was particularly severe when the bed material was silica sand.

The effect can be clearly seen in Figure 5.3. The bed has been calibrated for a grade of silica sand (of size range 125 to 355 μm), and is now fluidized at 1.44 times the minimum fluidization velocity while ECT data is logged at 10 frames per second for a period of 26 minutes. A 1-minute moving average has been applied to the ECT measured output results to smooth out the effect of short-term fluctuations associated

with bubbles so that the drift effect can be more easily distinguished. (The first 30 seconds of the plot show the original data without averaging.)

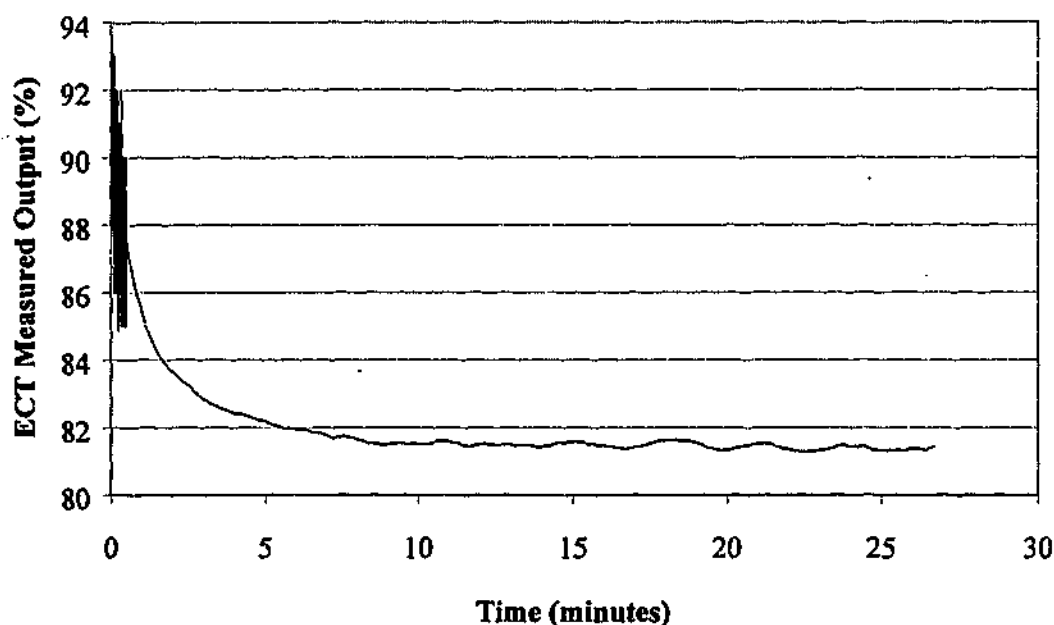


Figure 5.3 ECT baseline drift for a gently fluidized bed silica sand after improper calibration (fluidization time during calibration procedure too short). The measurement output (ordinate) corresponds to the ECT solids volume fraction scale (where empty vessel = 0% and packed bed of solids = 100%) averaged across the cross-section of the vessel. A 1-minute moving average has been applied to all but the first 30 seconds of the data.

The data of Figure 5.3 were obtained in the 146 mm bed, but the effect was observed at both scales (146 mm and 300 mm beds). Note that the baseline becomes relatively stable after 10 to 15 minutes of fluidization. If the fluidization step in the initial calibration procedure is at least this long, the baseline is stable as soon as the calibration is completed. Figure 5.4 shows this.

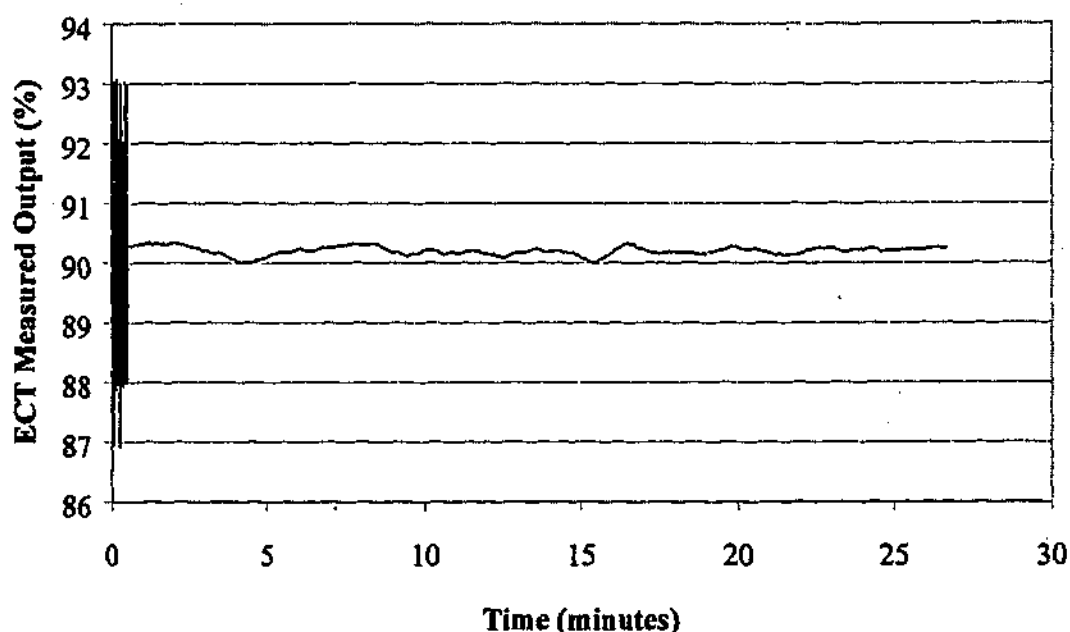


Figure 5.4 Stable ECT baseline for gently fluidized silica sand after calibration (fluidization time of 15 minutes during calibration procedure). The measurement output (ordinate) corresponds to the ECT solids volume fraction scale (where empty vessel = 0% and packed bed of solids = 100%) averaged across the cross-section of the vessel. A 1-minute moving average has been applied to all but the first 30 seconds of the data.

Interestingly, the observed baseline drift is dependent on the bed material used; with a short fluidization step in calibration, drift occurred to a lesser extent when garnet sand was used (Figure 5.5) and was not observed at all when glass beads were used as the bed material (Figures 5.6). Note that in the mixing experiments of Chapter 6, calibration was carried out using glass beads and the bed was then replaced by a bed of silica sand for the mixing experiment. In this situation, it was found that it was still necessary to fluidize the silica sand for a period of 15 minutes to achieve a stable baseline. It was noted that the baseline was generally more stable in the 146 mm bed than in the 300 mm bed, likely due to the presence of the driven shield electrodes in the former arrangement, as well as better control of the air supply at the smaller scale. For comparison, Figure 5.7 shows the baseline drift for the 300 mm diameter bed of silica sand. Once calibration was established (and with minimal ongoing external disturbances) the long-term drift of a packed bed (data logged overnight) was relatively minor, as shown in Figure 5.8 (146 mm bed).

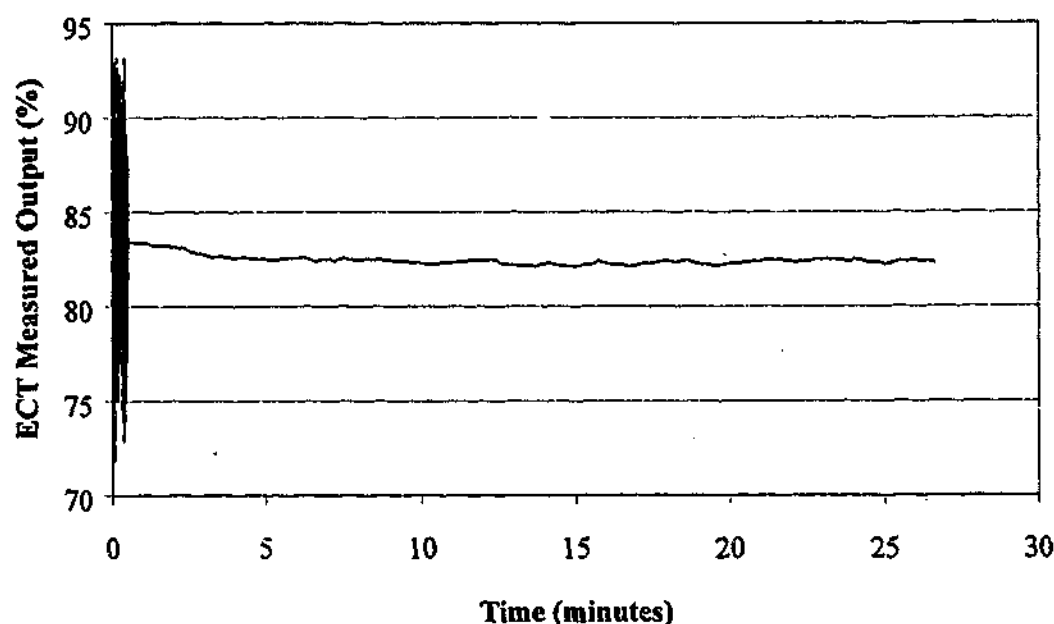


Figure 5.5 ECT baseline for garnet sand after improper calibration (fluidization time during calibration procedure too short). The measurement output (ordinate) corresponds to the ECT solids volume fraction scale (where empty vessel = 0% and packed bed of solids = 100%) averaged across the cross-section of the vessel. A 1-minute moving average has been applied to all but the first 30 seconds of the data.

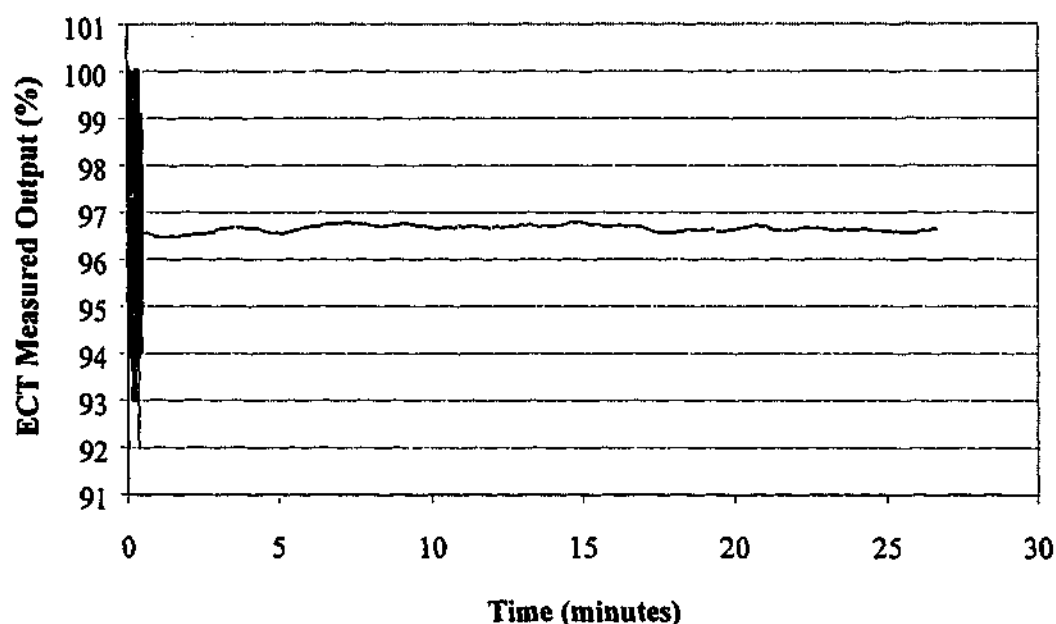


Figure 5.6 ECT baseline for glass beads after calibration (with short fluidization time during calibration procedure). The measurement output (ordinate) corresponds to the ECT solids volume fraction scale (where empty vessel = 0% and packed bed of solids = 100%) averaged across the cross-section of the vessel. A 1-minute moving average has been applied to all but the first 30 seconds of the data.

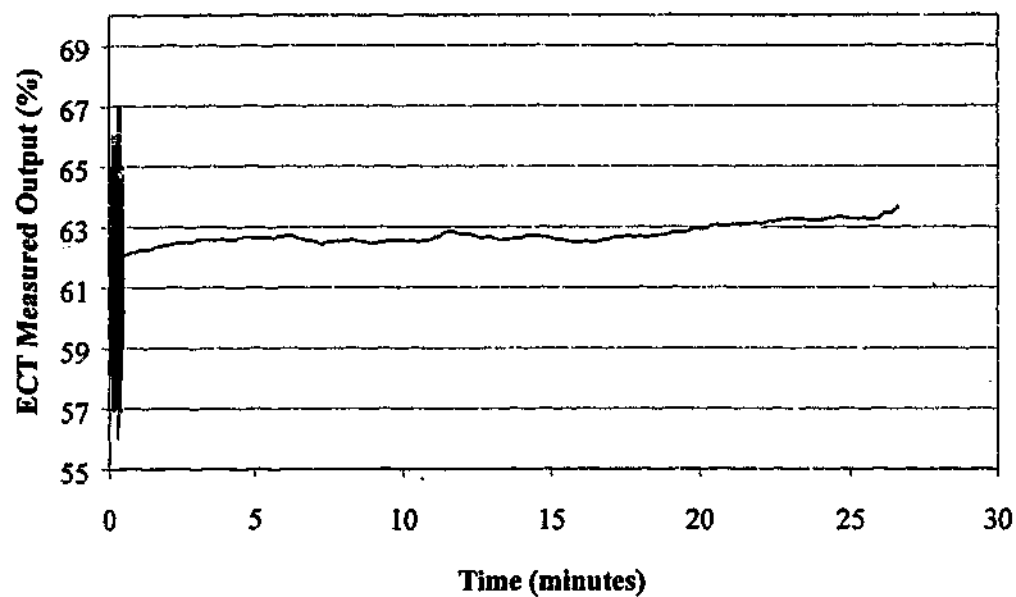


Figure 5.7 ECT baseline for a gently fluidized bed of silica sand after correct calibration in the 300 mm bed. The measurement output (ordinate) corresponds to the ECT solids volume fraction scale (where empty vessel = 0% and packed bed of solids = 100%) averaged across the cross-section of the vessel. A 1-minute moving average has been applied to all but the first 30 seconds of the data.

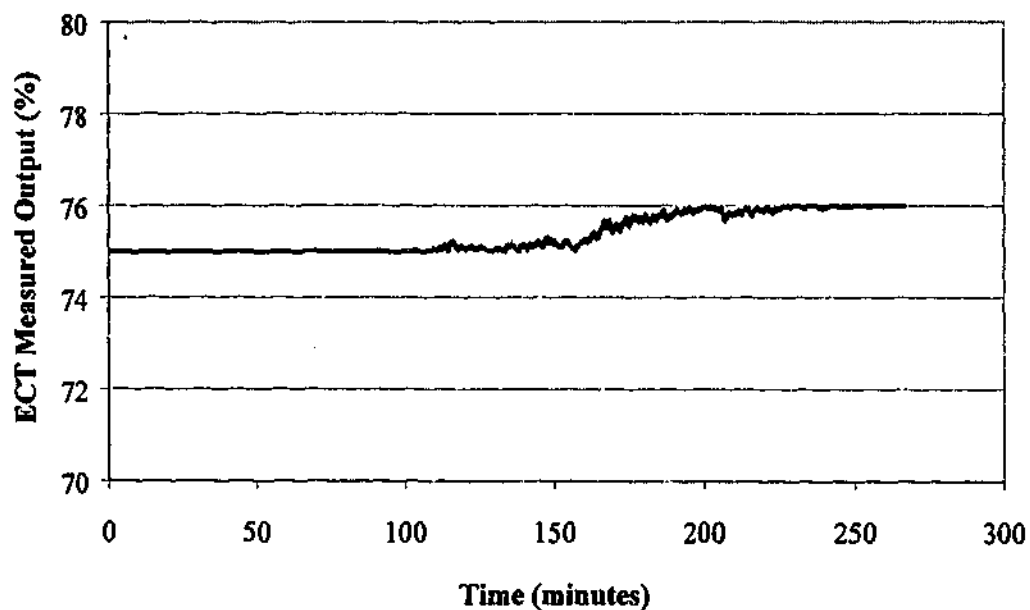


Figure 5.8 Long-term calibration drift for a packed bed of silica sand in the 146 mm bed after correct calibration.

This somewhat *ad-hoc* investigation of the baseline characteristics of the ECT system with different bed materials was carried out in order to roughly establish the degree of influence that calibration drift was likely to have on the measurements during a typical experimental run. It is clear that the type of particles involved in the fluidization are important, although the cause of the drift observed with the silica sand is not clear. One possible explanation is that in filling the fluidized bed vessel, the act of pouring the sand generates a static charge on the sand that subsequently causes an off-set in the ECT measurements. The static charge then gradually dissipates once the bed is fluidized (conduction via moisture in the supply air) until an electrostatic equilibrium is established between the bed vessel and the bed contents. Once this equilibrium is established, the baseline is stable from then onwards whether the material is fluidized or not. Provided that the experiments are carried out after allowing a suitable length of fluidization time for this equilibration to occur, subsequent calibration drift is at a slow enough rate to not significantly affect results in most instances.

5.6.3 Experimental Setup

The fluidized bed equipment employed in the hydrodynamic similarity investigations has been outlined in Chapter 3, and was shown in Figure 3.1 and 3.2. The fluidized beds compared were the 146 mm and 300 mm diameter units, with settled height to diameter ratios of approximately 2:1. The ECT electrodes (shown "unrolled" in Figure 3.13) were located so that the axial centre of the measurement electrodes was located at a correctly scaled height from the distributor in each of the beds, (namely 150 mm and 300 mm in the 146 mm and 300 mm diameter beds respectively). Note that the electrode system used at the 300 mm scale was retained from the previous work of Mathers *et al.*, (1998) and as such had only earthed shield electrodes. The smaller-scale bed was fitted with driven shield electrodes. Details of the electrode dimensions were given previously in Table 3.11.

In the voidage fluctuation experiments, the effects of operating gas velocity and bed material selection were investigated under the conditions specified in Section 3.7.5. These correspond closely to the conditions investigated in the small-scale pressure fluctuation experiments (see Section 4.5) and are re-stated below:

Experiment 1

In the 146 mm bed, Material A was used and compared with its correctly scaled counterpart, Material B, in the 300 mm bed. This experiment was designed to represent a correctly scaled system.

Experiment 2

In a secondary set of experiments, Material A* was used in the 146 mm bed, designed to scale correctly with its counterpart, Material B* in the 300 mm system. This experiment was also designed to represent a correctly scaled system, but involved larger particle sizes and hence higher particle Reynolds numbers than Experiment 1.

Note that by comparing results of Experiment 1 with Experiment 2 at appropriate operating velocities (*ie* the same U/U_{mf}), the consequences of a mis-scaled particle size can be determined.

Experiment 3

An additional experiment was conducted in the 146 mm bed with Material G, consistent with Materials A* and B* involved in Experiment 2 in terms of the simplified scaling law, but having a mis-matched particle density. The experiment was designed to explore the effect of a mis-scaled particle density.

In a similar fashion to the corresponding pressure fluctuation experiments, the experiment was repeated a minimum of three times for each bed, bed material and operating velocity. The repetition enabled any random variation in results due to slight differences in conditions (*eg* bed height, gas flowrate, packed bed density during ECT calibration, calibration drift) to be quantified to some extent.

Because the reference conditions for which the ECT system was calibrated correspond to the extremes of a packed bed and an empty vessel, it is important to remember that the value of solids volume fraction generated by ECT measurements are referenced to the packed bed condition achieved *during calibration*. This means that if the nature of the packed bed varies from one experiment to another (*ie* different degree of settling achieved during each calibration), the solids volume fraction data will appear to be different even though the same operating conditions (gas velocity, particles *etc*) are employed. For this reason, great care was taken during the calibration procedure to

defluidize and settle the bed very slowly so that the packed bed condition for calibration was as consistent as possible.

5.6.4 Analysis and Comparison of the Voidage Fluctuations

The voidage fluctuation time series resulting from the various experiments generated using the procedure described in the initial part of Section 5.6 were analysed and compared in a number of ways. The comparisons made between the voidage fluctuations were of the same form as those carried out for the pressure fluctuations in the preceding chapter, namely the single value parameters of average, average absolute deviation and average cycle frequency. Unlike the pressure measurements of the preceding chapter, however, the solids volume fraction generated by the ECT system is already in non-dimensional form, and thus no additional manipulation is required for comparisons of the average and average absolute deviation. Average cycle frequency measurements required non-dimensionalisation however, and as in other sections of this work, the following approach was employed:

$$f' = f \left(\frac{D}{U_{mf}} \right) \quad (5.3)$$

Like the pressure fluctuation analyses, the single value parameters were calculated for all gas velocities under consideration, and for selected data further comparisons were made using fast Fourier transforms and probability density functions.

5.7 Results of the Voidage Fluctuation Similarity Experiments

An initial qualitative comparison of results for the two correctly-scaled beds with materials A and B (Experiment 1) can be made by visual inspection of the reconstructed images. For this comparison, 25 successive frames of reconstructed data are presented in Figures 5.9 to 5.12. Reconstruction has been carried out using the standard linear back-projection algorithm. The images cover a similar dimensionless gas velocity operating condition for each bed at a low gas velocity ($U/U_{mf} \approx 1.5$), and again at a high gas velocity ($U/U_{mf} \approx 8.5$). Note that the sampling rate for the capacitance data is such

that frames are generated at a rate of 80 frames per second. Thus each of the figures presented below represents approximately one-third of a second of fluidization.

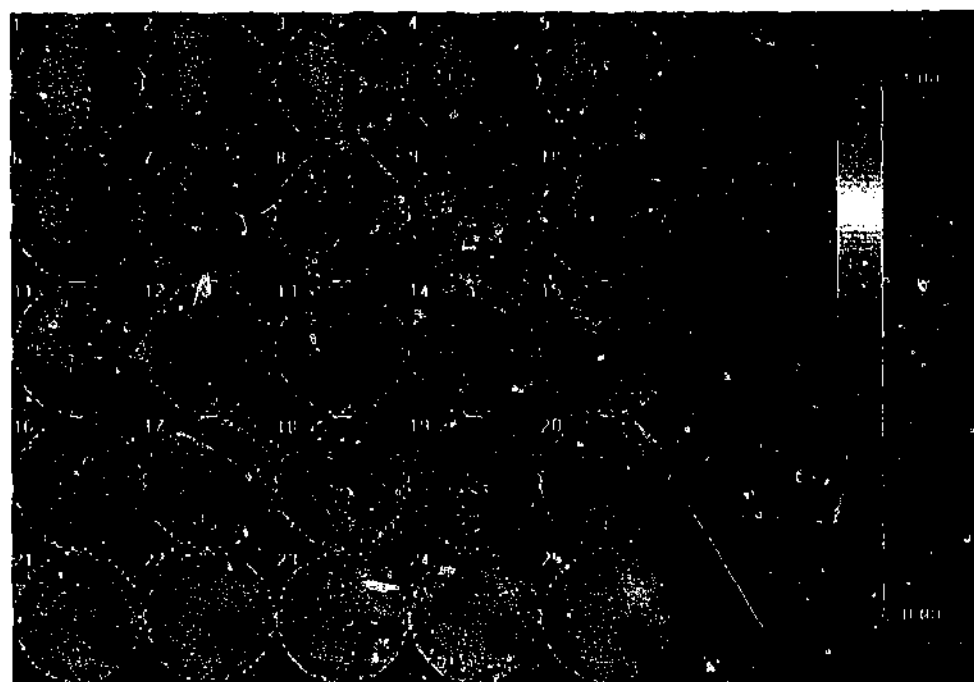


Figure 5.9 Series of reconstructed images (using standard linear back-projection algorithm) from the 146 mm bed with material A operated at $U/U_{mf} = 1.49$. (Note the scale of the colour chart at the right where empty vessel = 0.00 and packed bed of solids = 1.00). Frames recorded at 80 Hz.

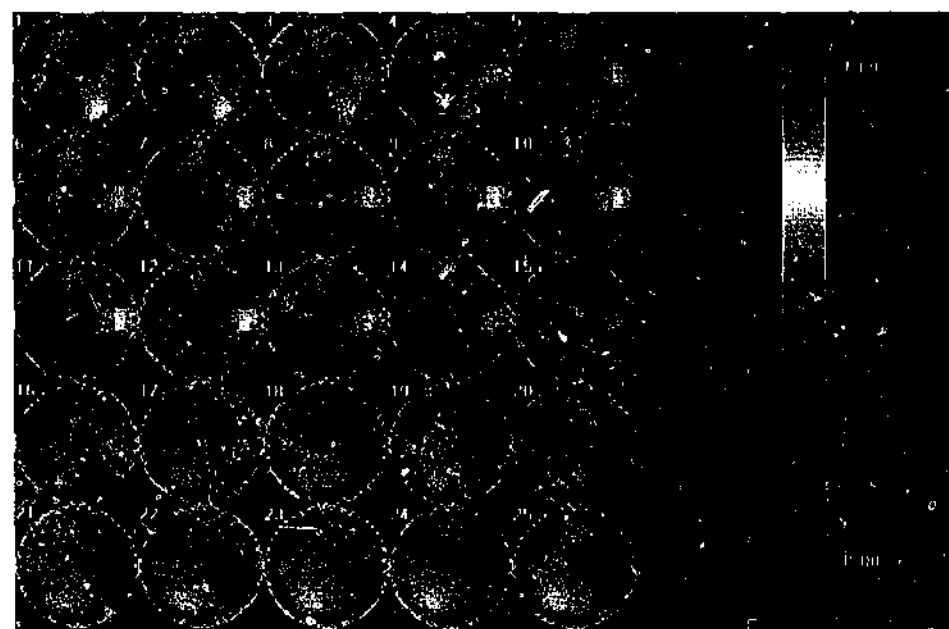


Figure 5.10 Series of reconstructed images (using standard linear back-projection algorithm) from the 300 mm bed with material B operated at $U/U_{mf} = 1.58$ (Note the scale of the colour chart at the right where empty vessel = 0.00 and packed bed of solids = 1.00). Frames recorded at 80 Hz.

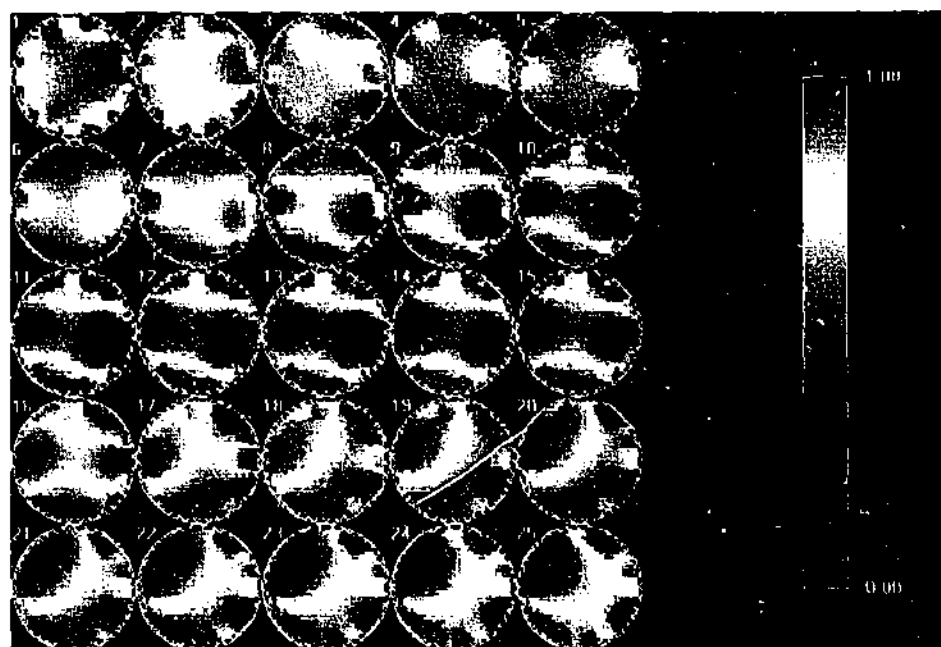


Figure 5.11 Series of reconstructed images (using standard linear back-projection algorithm) from the 146 mm bed with material A operated at $U/U_{mf} = 8.37$. (Note the scale of the colour chart at the right where empty vessel = 0.00 and packed bed of solids = 1.00). Frames recorded at 80 Hz.

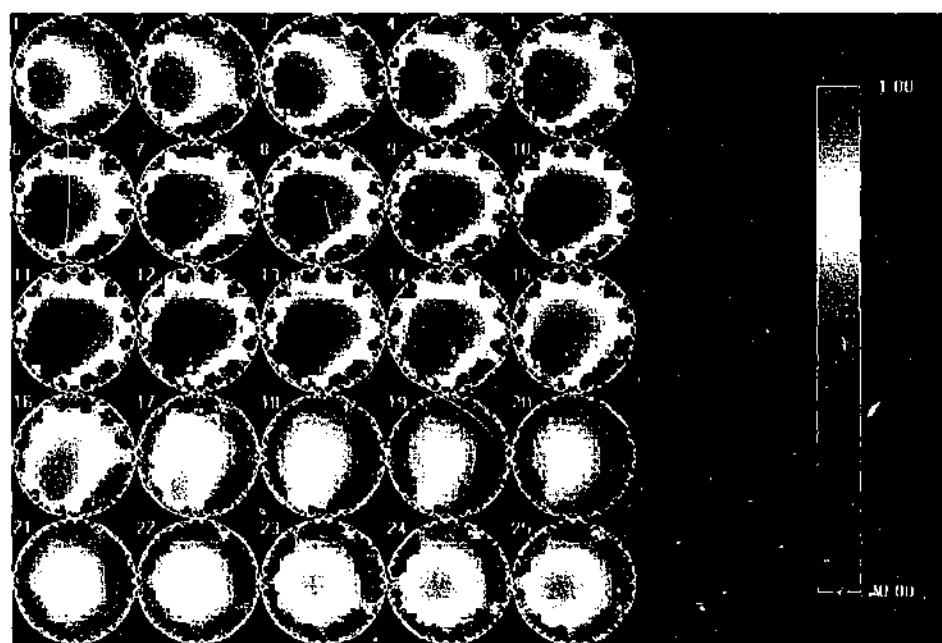


Figure 5.12 Series of reconstructed images (using standard linear back-projection algorithm) from the 300 mm bed with material B operated at $U/U_{mf} = 8.47$. (Note the scale of the colour chart at the right where empty vessel = 0.00 and packed bed of solids = 1.00). Frames recorded at 80 Hz.

Although an attempt has been made to provide representative image frames in the above figures, it must be pointed out that only 25 frames have been selected from a possible 16,000 (per gas velocity, per run), so drawing any sweeping conclusions from the comparison of such a small sample is unwise. However, some general observations concerning the reconstructed images have been made as follows:

- At low gas velocity, physical observations of the beds show that they are bubbling, however bubbles are not seen in the reconstructed images (although vague regions of decreased solids concentration are noted – see Figures 5.9 and 5.10).
- At high gas velocity, images often tend to show large singular voids which could be interpreted to mean that the beds are slugging. The presence of the ECT electrodes limited the view somewhat in these actual experiments, but in the complementary pressure fluctuation experiments (of Chapter 4) carried out for the same operating conditions, slugs were not seen. Additionally, note that the minimum bed height requirements for slugging in these beds (as calculated using the correlations of Yagi and Muchi, 1952; Bayens and Geldart 1974, and Darton *et al.*, 1977) all require an aspect ratio significantly in excess of the 2:1 aspect ratios used. It is therefore more likely that the LBP algorithm is generating false voidage increases between what are actually large discrete bubbles in the beds. Note also that generally the 146 mm system appears to resolve individual bubbles more successfully than the 300 mm system. Figures 5.11 and 5.12 are quite typical of this.
- Often, what this author terms a “clockface” pattern of solids volume fraction discontinuities is observed around the circumference of the image (clearly visible in Figure 5.12). This is likely to be an artefact of the image reconstruction, corresponding to the location of the 12 measurement electrodes around the vessel walls. (If these discontinuities were real, then during pressure fluctuation experiments at similar gas velocities, gas jets up the walls and penetrating at least half the bed height would have to be observed. This was not the case.)
- Voids tend to be imaged at the walls far more often than in the bed centre. (This observation is perhaps better supported by considering the distribution of voids reconstructed in all the images presented in Figures 5.9 to 5.18 of this section.) This may be due to preferential bubble flow near the walls of the vessels, but could also be due to the reduction in ECT measurement sensitivity towards the radial centres of the vessels.

Similar "sample" reconstructed images are now presented for the second set of scaled bed materials (A* and B*) in the two beds (corresponding to Experiment 2). The images cover a similar dimensionless gas velocity operating condition for each bed at a low gas velocity ($U/U_{mf} \approx 1.5$), and again at a high gas velocity ($U/U_{mf} \approx 3.9$). At low gas velocity, images tend to show voids more distinctly than in the former bed material pair (A and B). At high velocity, however, there is no noticeable difference in the images when compared to the former bed material pair and all of the same observations apply.

Figures 5.17 and 5.18 show sample reconstructed images for the 146 mm bed with the higher density garnet sand (material G). There are no significant differences in the reconstructed images from this bed scenario.

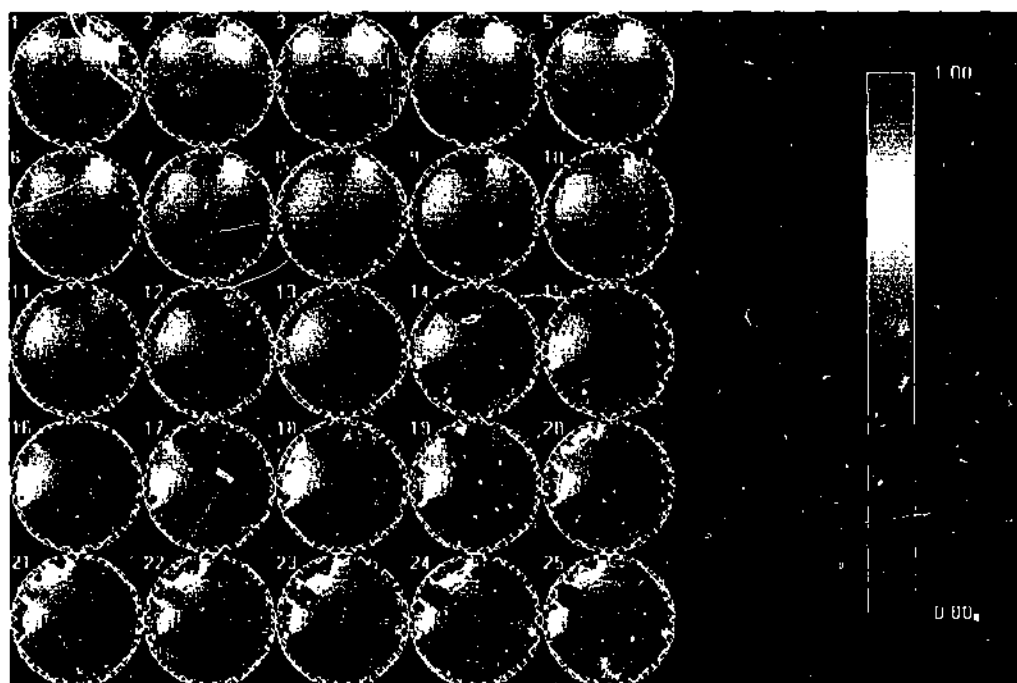


Figure 5.13 Series of reconstructed images (using standard linear back-projection algorithm) from the 300 mm bed with material A* operated at $U/U_{mf} = 1.41$. (Note the scale of the colour chart at the right where empty vessel = 0.00 and packed bed of solids = 1.00). Frames recorded at 80 Hz.

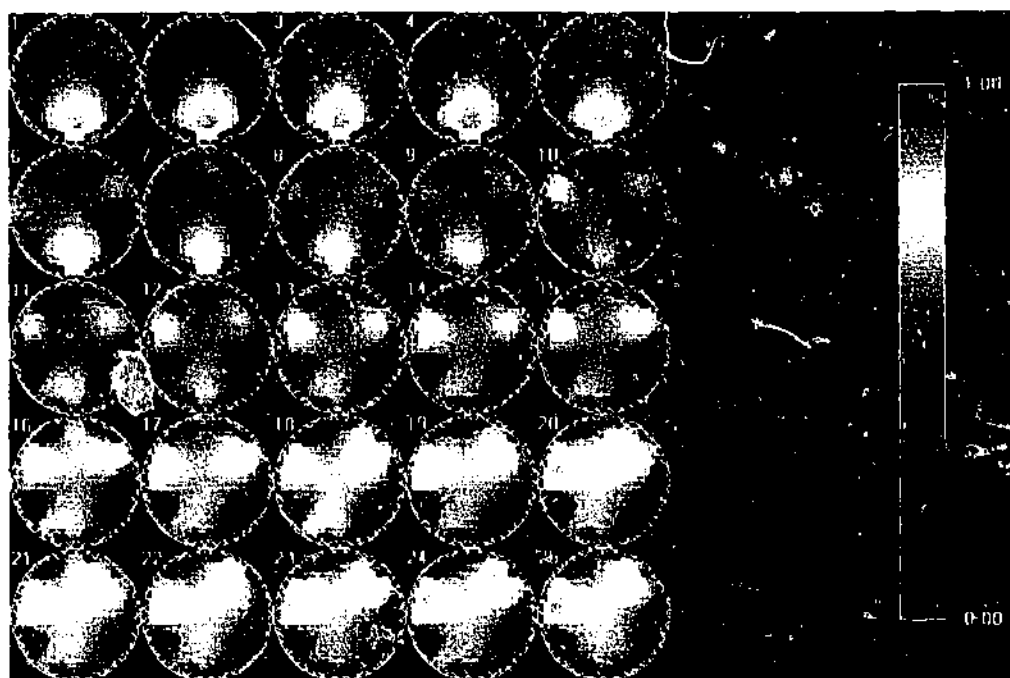


Figure 5.14 Series of reconstructed images (using standard linear back-projection algorithm) from the 300 mm bed with material B* operated at $U/U_{mf} = 1.51$. (Note the scale of the colour chart at the right where empty vessel = 0.00 and packed bed of solids = 1.00). Frames recorded at 80 Hz.

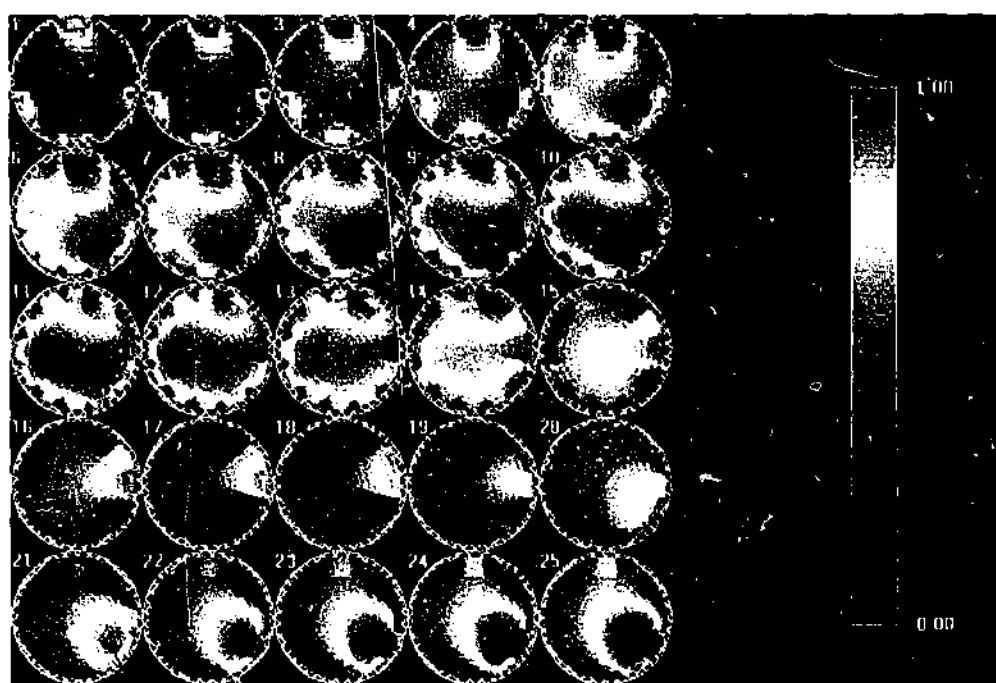


Figure 5.15 Series of reconstructed images (using standard linear back-projection algorithm) from the 300 mm bed with material A* operated at $U/U_{mf} = 3.84$. (Note the scale of the colour chart at the right where empty vessel = 0.00 and packed bed of solids = 1.00). Frames recorded at 80 Hz.

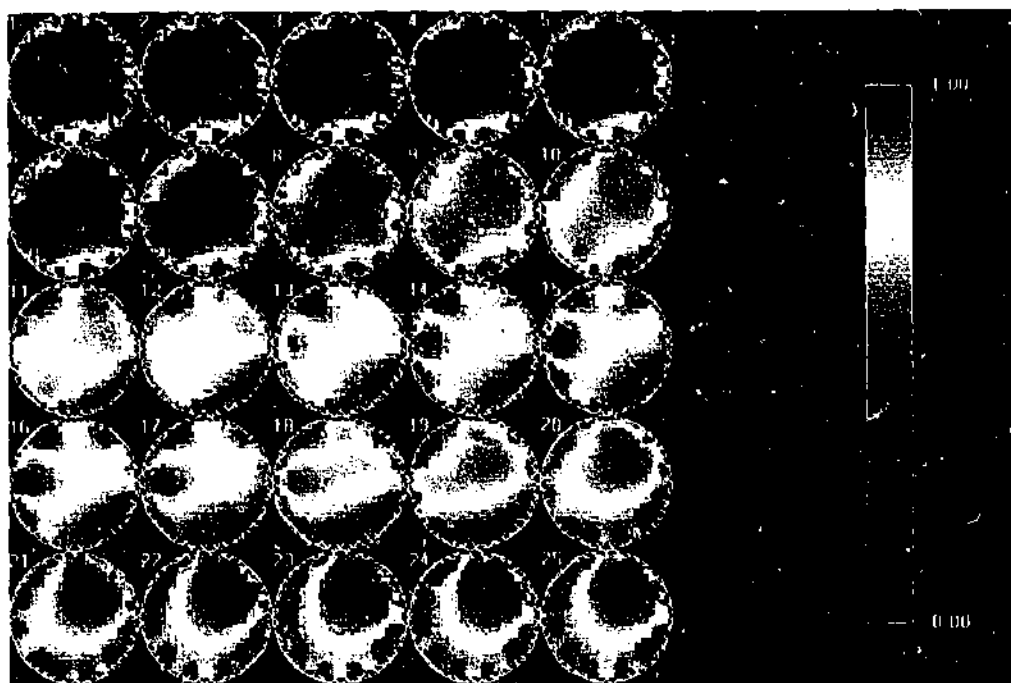


Figure 5.16 Series of reconstructed images (using standard linear back-projection algorithm) from the 300 mm bed with material B* operated at $U/U_{mf} = 3.93$. (Note the scale of the colour chart at the right where empty vessel = 0.00 and packed bed of solids = 1.00). Frames recorded at 80 Hz.

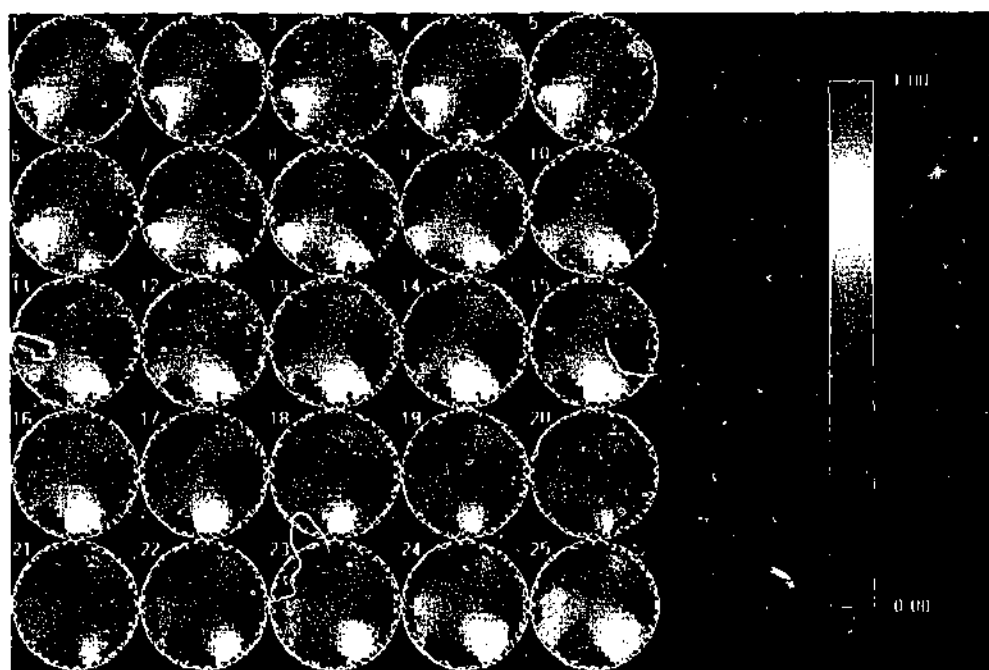


Figure 5.17 Series of reconstructed images (using standard linear back-projection algorithm) from the 300 mm bed with material G operated at $U/U_{mf} = 1.46$. (Note the scale of the colour chart at the right where empty vessel = 0.00 and packed bed of solids = 1.00). Frames recorded at 80 Hz.

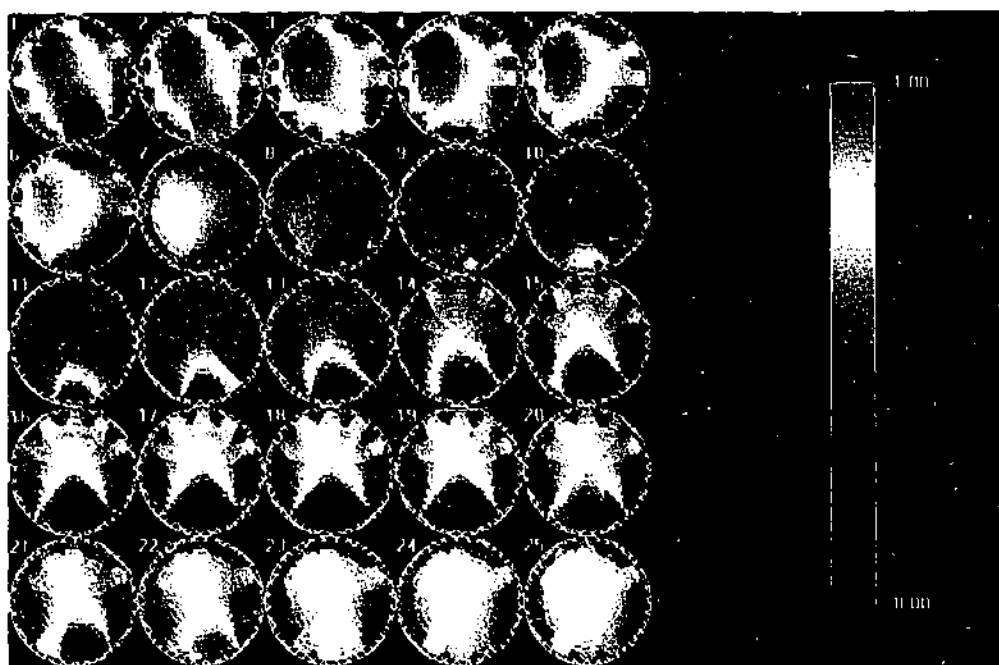


Figure 5.18 Series of reconstructed images (using standard linear back-projection algorithm) from the 300 mm bed with material G operated at $U/U_{mf} = 3.98$. (Note the scale of the colour chart at the right where empty vessel = 0.00 and packed bed of solids = 1.00). Frames recorded at 80 Hz.

Whilst it would be entirely possible to analyse reconstructed images such as those presented above from all the beds and generate bubble size data, this approach has not been taken due to the doubts cast on the accuracy of the reconstructed void sizes by Mathers *et al.*, 1998, and no sound basis from which to select a solids volume fraction "contour" that defines the actual boundary of the void.

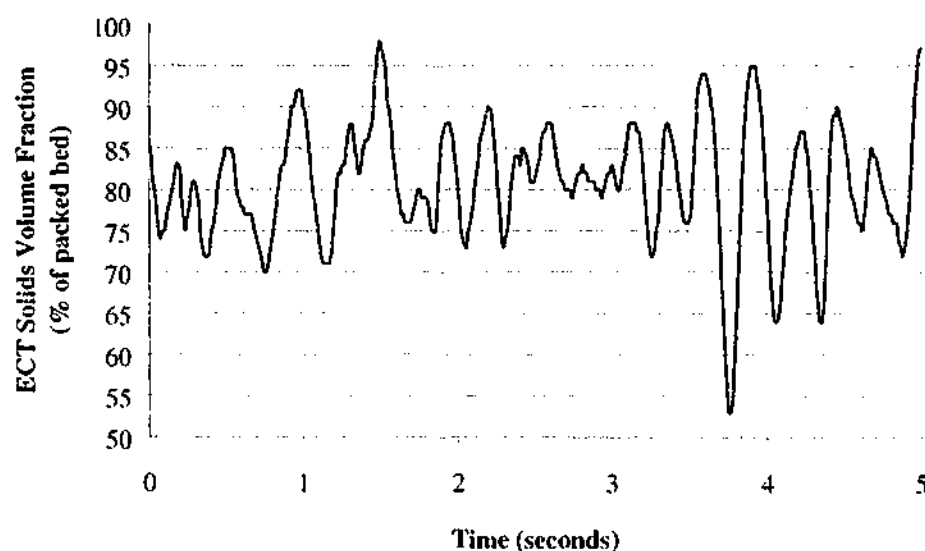


Figure 5.19 Typical average solids volume fraction time-series generated from reconstructed ECT image data.

Instead, as stated previously, the voidage fluctuation time series generated from the image data have been used for subsequent statistical comparisons for the various fluidized bed scenarios. Figure 5.19 shows a section of a typical average volume fraction time series generated in this way. The various comparisons of the volume fraction time series data are presented in the following sections.

5.7.1 Comparison of Time-Averaged Average Solids Volume Fraction

This comparison is of the time-averaged average solids volume fraction (also referred to as the "overall" average solids volume fraction) taken across the cross-section of the various fluidized beds (at measurement electrode height). It is simply the mean of the 16000 average solids volume fraction data points recorded at each gas velocity. Figure 5.20 shows the result for the 146 mm and 300 mm beds with materials A and B respectively.

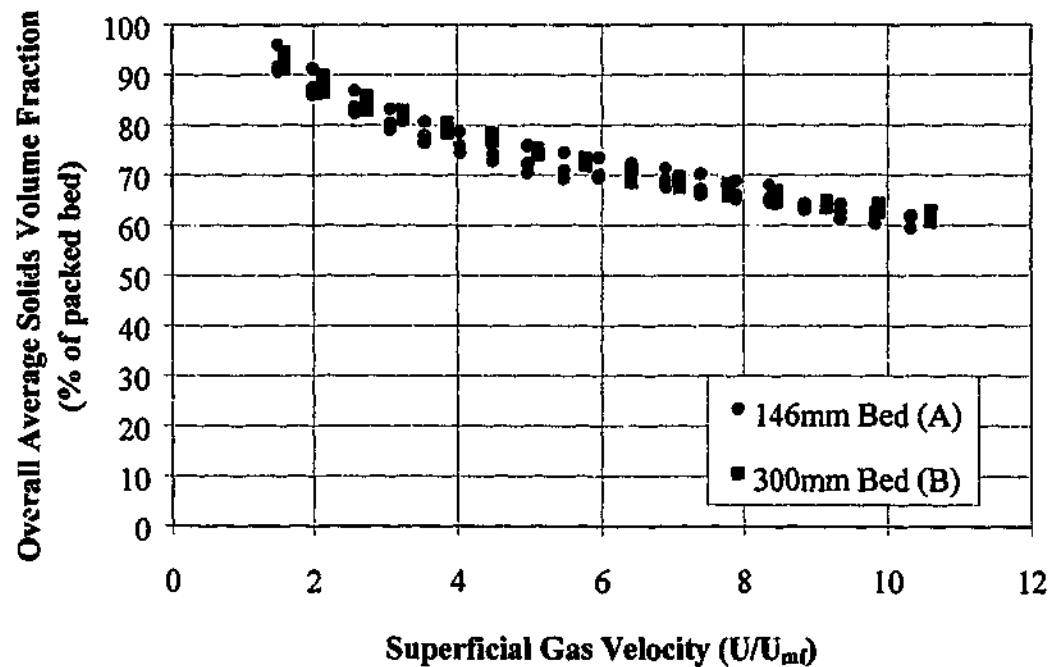


Figure 5.20 ECT overall average solids volume fraction (as a percentage of the solids volume fraction for a packed bed) for the correctly-scaled 146 mm (material A) and 300 mm (material B) beds for a range of dimensionless superficial gas velocities.

As can be easily seen from the figure, when the gas velocity increases the average solids present at measurement electrode heights in the two beds decreases as the bed expands to allow for the increasing volumes of upflowing gas. The apparent agreement in

dimensionless solids volume fraction for the two scaled beds is clear. The limited scatter in the data is likely to be due to small variations in gas velocity for the different runs, as well as differences in ECT calibration (as mentioned in Section 5.6.3). The results here appear to indicate similar bed expansion characteristics and support the corresponding pressure fluctuation results presented in Chapter 4 (see Figure 4.2).

Now the second set of scaled beds (materials A* and B* in the same bed vessels) will be considered. Recall that although a similar range of dimensional superficial gas velocities were involved in the experiments; due to the larger particle size of materials A* and B*, (and hence increased minimum fluidization velocity), the dimensionless superficial gas velocities achieved for these bed materials are *lower* than those for the previous sands. Figure 5.21 shows the comparison.

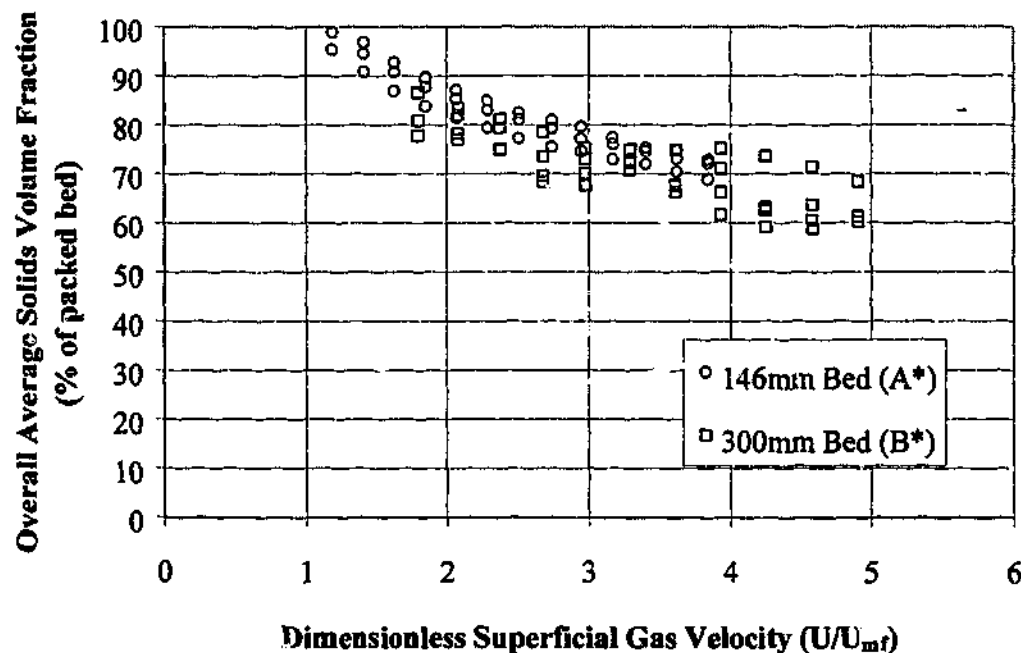


Figure 5.21 ECT overall average solids volume fraction (as a percentage of the solids volume fraction for a packed bed) for the correctly-scaled 146 mm (material A*) and 300 mm (material B*) beds for a range of dimensionless superficial gas velocities.

The agreement in trends for these bed materials is not quite so good as that of the previously compared beds. This appears to be primarily due to greater scatter in the data for the material B* at the 300 mm scale. (It was noted that during experiments with this particular material, extreme weather conditions prevailed and the baseline drift on the ECT system was particularly bad, possibly due to changing humidity in the supply air.)

The data for the second set of scaled bed materials are compared with the bed expansion results of the first pair of scaled beds (materials A and B) in Figure 5.22.

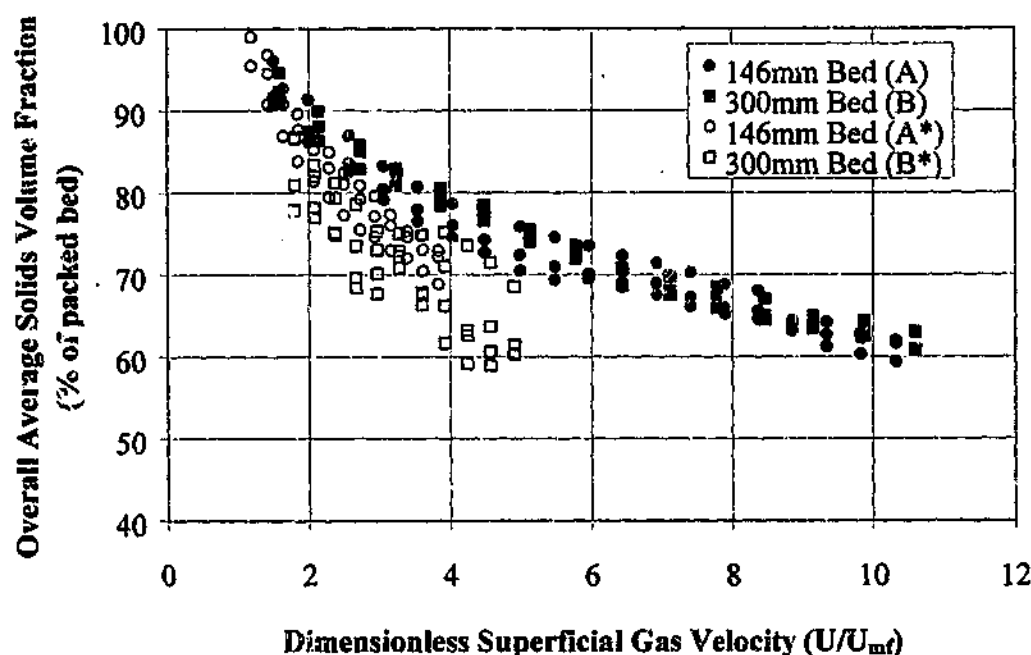


Figure 5.22 ECT overall average solids volume fraction (as a percentage of the solids volume fraction for a packed bed). Comparison between the original correctly scaled beds (materials A and B in the 146mm and 300 mm beds) with the second set of correctly scaled materials in the same scale beds (materials A* and B* in the 146 mm and 300 mm beds).

Whilst there may be a distinction between the dimensionless expansion characteristics of the materials (and indeed this is shown clearly in the corresponding pressure fluctuation data of Figure 4.3), the scatter in the ECT-based data makes it hard to judge whether the agreement between correctly scaled materials is significantly better than the agreement between mis-scaled materials (eg compare the trend for correctly-scaled A* with B* vs incorrectly-scaled A* with B). Consequently, on initial evaluation, these ECT-based average solids volume fraction results do not appear to be as good an indicator of hydrodynamics as the average pressure measurements used in the previous chapter.

The final comparison to be made using the time-averaged average solids volume fraction is a consideration of the effect of changing the particle density. The garnet sand (material G), which has the similar minimum fluidization velocity to material A*, is used as it represents a situation in which all aspects of the Horio *et al.*, (1986a) scaling criteria are matched, but the particle-to-gas density ratio is different. Figure 5.23

compares the results for the denser bed material with the previously presented results for materials A* and B*.

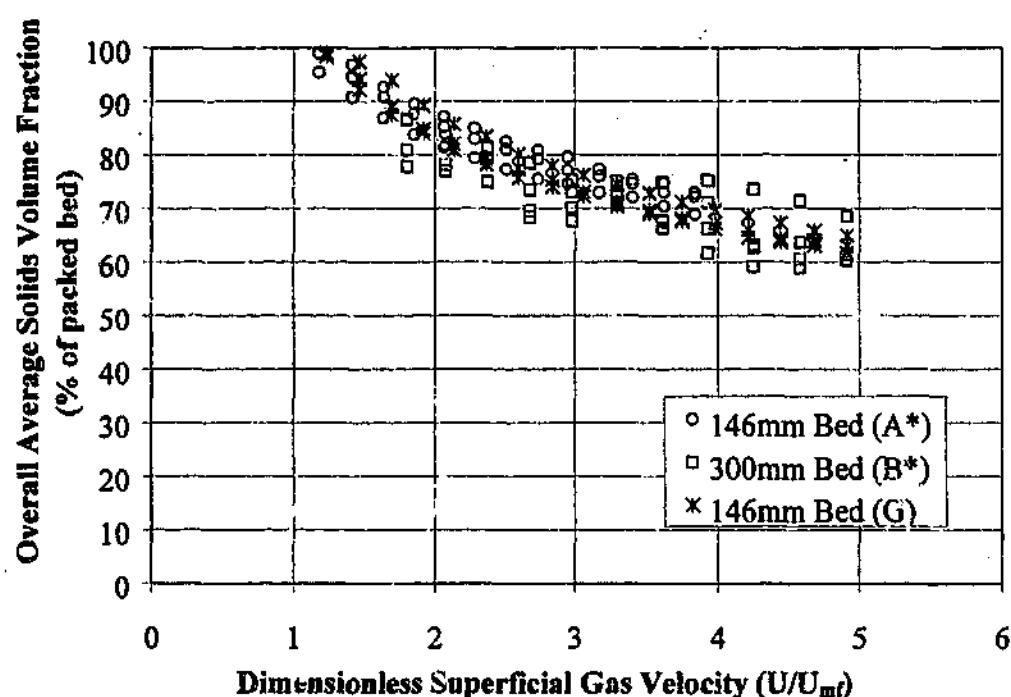


Figure 5.23 ECT overall average solids volume fraction (as a percentage of the solids volume fraction for a packed bed) for the correctly-scaled 146 mm (material A*) and 300 mm (material B*) beds compared with the correctly-scaled but higher density material G in the 146 mm bed.

The dimensionless solids volume fraction results for the higher density garnet sand agree quite well with the results for material A* as well as the more scattered material B* results. The expansion trend for the garnet sand measured in this way supports the previously presented average pressure data (Figure 4.4), indicating that there is no discernible difference in the dimensionless bed expansion behaviour for this material under these experimental conditions, despite the significant particle density difference (4100 kg/m^3 for garnet as opposed to 2650 kg/m^3 for silica sand).

5.7.2 Average Absolute Deviation of Cross-sectionally Averaged Solids Volume Fraction

Whereas the overall average solids volume fraction indicates bed expansion at the bed level where the ECT measurement plane is located, the average absolute deviation of the solids volume fraction fluctuations provides an indication of the amplitude of the

volume fraction fluctuations as seen in the ECT images. Unlike the pressure fluctuation measurements of Chapter 4 however, the ECT data is a measurement of a *slice* of the fluidized bed at the electrode level and the amplitudes should correspond to the size of the bubbles passing through this level. (The pressure probe results on the other hand, were of a more global nature, with amplitudes most strongly affected by changes in bed height.) If the bubbles are scaled correctly at the measurement levels in the two sizes of fluidized beds, (*ie* the distribution of dimensionless bubble sizes is the same at the same dimensionless height), then the average absolute deviations of the dimensionless solids volume fraction measured at these levels should also be the same. As can be seen in Figure 5.24, however, this was most certainly *not* the case.

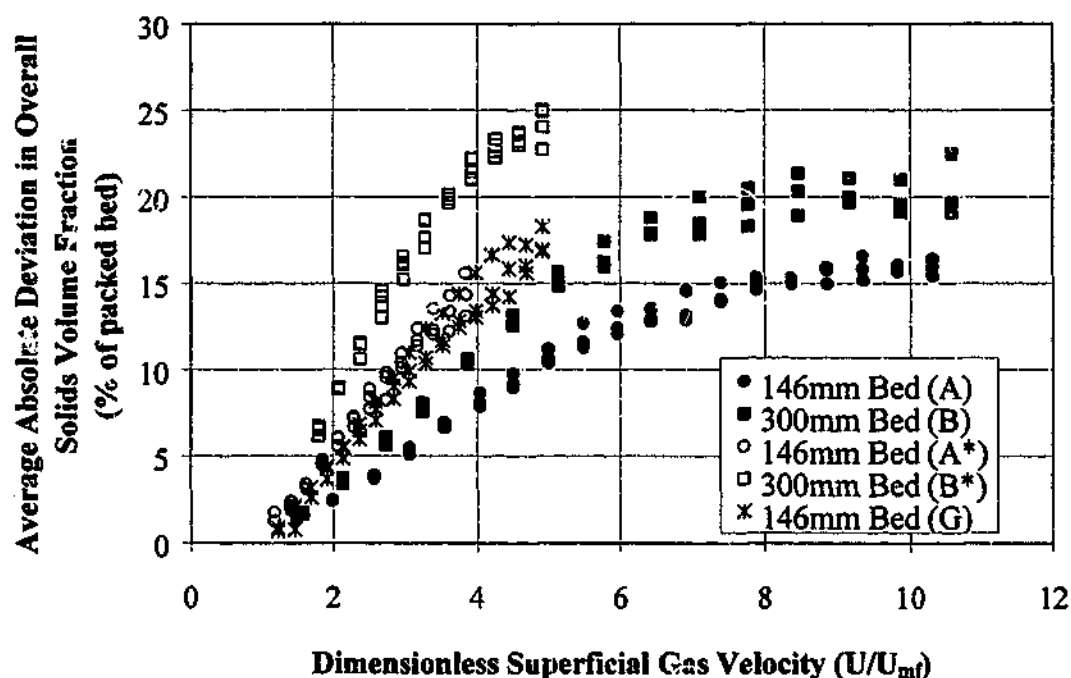


Figure 5.24 Comparison of the average absolute deviation of overall solids volume fraction fluctuations for the 146 mm (materials A, A* and G) and 300 mm beds (materials B and B*).

This result is interesting, and unexpected. Despite the agreement in the average solids volume fraction for the correctly-scaled beds, the amplitude of the fluctuations does not coincide at all, with significantly higher amplitudes registered in the large-scale bed. In fact, the *only* agreement in results is found between material A* and material G, which both have very similar minimum fluidization velocities and are both in the same bed.

There are two possibilities: Firstly, the bubble sizes in the beds at the electrode height could actually be very far from correctly-scaled (*ie* hydrodynamic similarity not

achieved), and in dimensionless terms, much larger in the 300 mm bed than in the 146 mm bed. Secondly, there could be a problem with the measurements in either one or both of the beds, leading to a discrepancy in registered amplitude. These possibilities will be discussed in greater detail in Section 5.8.

5.7.3 Dimensionless Average Cycle Frequency of Cross-sectionally Averaged Solids Volume Fraction

The dimensionless average cycle frequency has been calculated for the solids volume fraction time-series in order provide an indication of the time-scales of the solids volume fluctuations occurring in the different beds. Non-dimensionalisation of the measured average cycle frequency (average number of times the fluctuating signal crosses its own mean) was carried out via Equation 5.3. Once again, the fluctuations registered by the ECT system are *not* global; this fluctuation frequency should correspond to the local bubble passage frequency at the bed height where the electrodes are placed. Figure 5.25 shows the results for the average cycle frequency calculated for the solids volume fraction fluctuations in the correctly scaled 146 mm and 300 mm beds with materials A and B respectively.

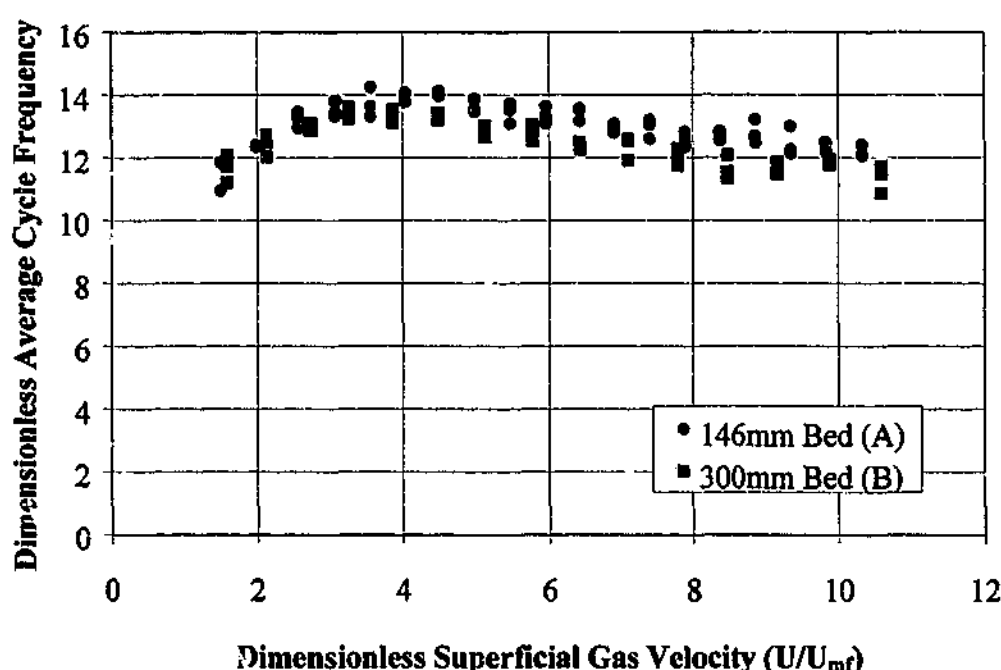


Figure 5.25. Comparison of the dimensionless average cycle frequency of the ECT average solids volume fraction fluctuations for the correctly-scaled 146 mm (material A) and 300 mm (material B) beds for a range of dimensionless superficial gas velocities.

As can be seen, the agreement in dimensionless cycle frequencies seems to be quite good. The dimensionless frequency is possibly slightly higher in the 146 mm bed than its 300 mm scaled counterpart. This is likely to be for the same reason that the dimensionless average cycle frequencies derived from pressure fluctuation measurements showed a similar off-set; (namely, the ratio of U_m/D is not perfectly matched according to the Horio scaling criteria).

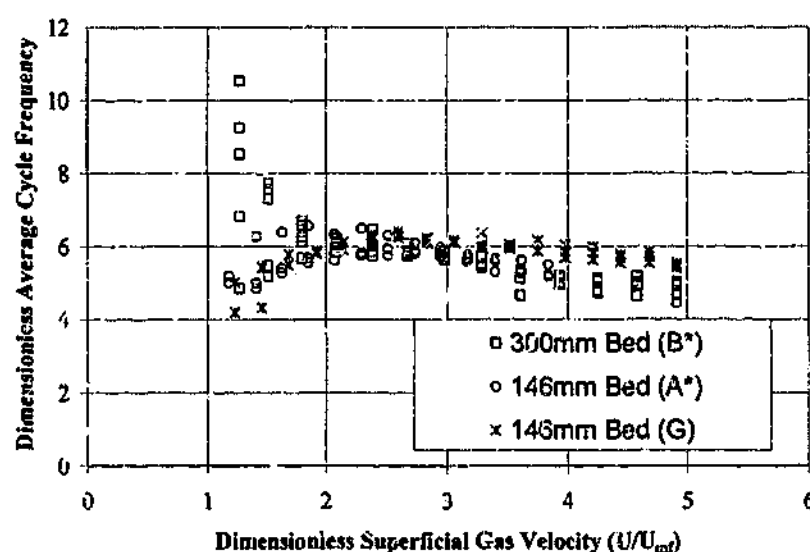


Figure 5.26 Comparison of the dimensionless average cycle frequency of the ECT average solids volume fraction fluctuations for the correctly-scaled 146 mm (material A* and higher-density material G) and 300 mm (material B*) beds for a range of dimensionless superficial gas velocities.

Figure 5.26 shows the comparison of the dimensionless average cycle frequency for the second set of correctly-scaled bed materials (A* and B*) in the 146 mm and 300 mm beds. Additionally, the dimensionless cycle frequency results for the garnet sand (material G) with the higher particle density are also shown. Overall the agreement between the A* and B* beds is reasonable, although there is much scatter in the data for B* at low gas velocity (the lowest gas velocity was only just above minimum fluidization and it is likely that there was incomplete fluidization; also one batch of B* material appeared to suffer a high attrition rate for unknown reasons – it was subsequently replaced with fresh material). Note that the absolute values of dimensionless frequency are much lower in these beds than for the previously considered pair of scaled beds (with materials A and B). Thus, in a similar fashion to the pressure fluctuation results (see Figure 4.13), the values of dimensionless frequency

once again clearly identify which scenarios agree or disagree with the scaling law. The agreement for material G in the 146 mm bed with materials A* and B* is not quite so good; once again this is likely to be a consequence of the non-dimensionalisation procedure and errors in the U_{mf}/D ratio when compared with the scaling law requirements.

In order to demonstrate the influence of the non-dimensionalisation, all the average cycle frequency data are now re-plotted in dimensional form, but with the three scenarios in the 146 mm bed (materials A, A* and G) re-scaled by the appropriate use of the scaling law scaling factor m based on minimum fluidization velocities. By using this procedure, the data can still be compared and all reference to bed diameter is removed from the calculation.

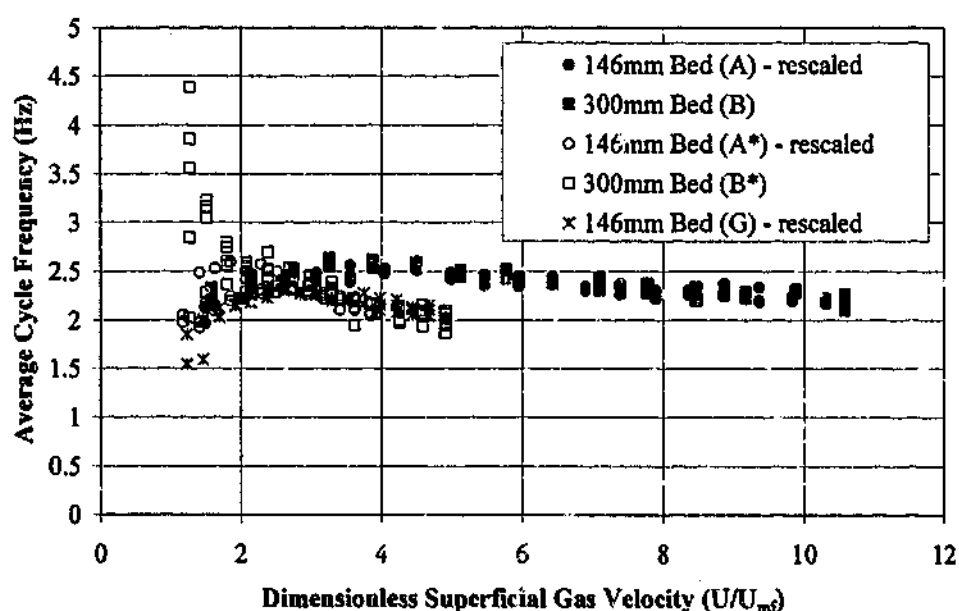


Figure 5.27 Comparison of the average cycle frequency of the ECT average solids volume fraction fluctuations for all beds. The cycle frequencies for the three 146 mm bed scenarios (bed materials A, A* and G) have been re-scaled by applying a scaling factor of $\frac{1}{\sqrt{m}}$ where $\sqrt{m} = \frac{U_{mf}(300\text{mmBed})}{U_{mf}(146\text{mmBed})}$ and 300 mm (material B*) beds for a range of dimensionless superficial gas velocities.

There is still some scatter present at the low gas velocities, but the correctly-scaled scenarios all show better agreement. Additionally, now that the cycle frequencies for the large-scale bed scenarios (materials B and B*) are used as a basis, one can appreciate than when compared in dimensional form, there is little influence of particle size on

average cycle frequency. Once again, these observations are similar to observations made regarding the pressure fluctuation cycle frequency results of Chapter 4.

5.7.4 Comparison of Probability Density Functions

The probability density function displays how the magnitudes of the voidage fluctuations are distributed about the average. It is presented as a normalised histogram with the area under the curve set to be unity for each set of data. The bin widths for the histograms, (representing a dimensionless pressure measurement) are set to be the same for the data being compared. In the case of the ECT volume fraction measurements, the data were divided into 100 bins, representing the full scale of the ECT solids volume fraction measurement.

Figure 5.28 shows the probability density function results for the 146 mm bed with material A and the 300 mm bed with material B, operated at an intermediate gas velocity of $U/U_{mf} \approx 5$. Given the appearance of the figure it should be reiterated that the beds are expected to be operating in a hydrodynamically similar fashion under these conditions.

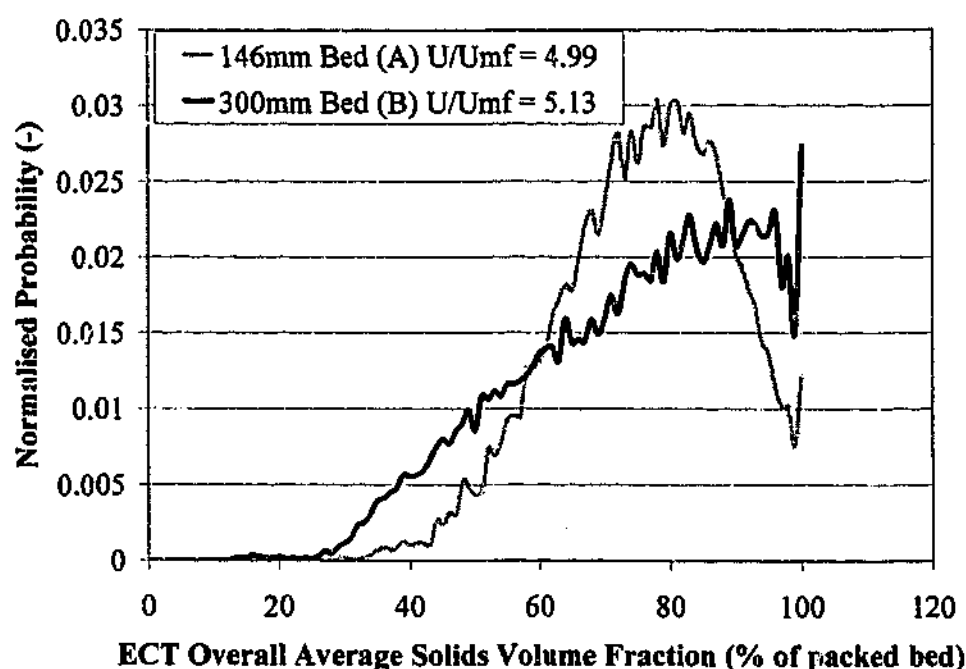


Figure 5.28 Comparison of the normalised probability density function for the correctly-scaled 146 mm bed and 300 mm bed with materials A and B respectively, operated at the intermediate gas velocity of $U/U_{mf} \approx 5$.

There is no agreement between the probability distributions here whatsoever. Several specific points can be made. First of all, the distributions appear to “leak” beyond the limiting value of 100 (packed bed condition), with the ECT imaging procedure apparently assigning all results greater than 100 into the 100 bin. In addition, the peaks of the distributions do not coincide. Finally, the lower value tails of the distributions, which are not truncated by any limit value, do not follow a similar shaped curve. Thus, the probability density function comparison supports the results of the average absolute deviation comparison (Figure 5.24) and implies that either there is no hydrodynamic similarity between these two beds, or the ECT system is responding differently at different scales.

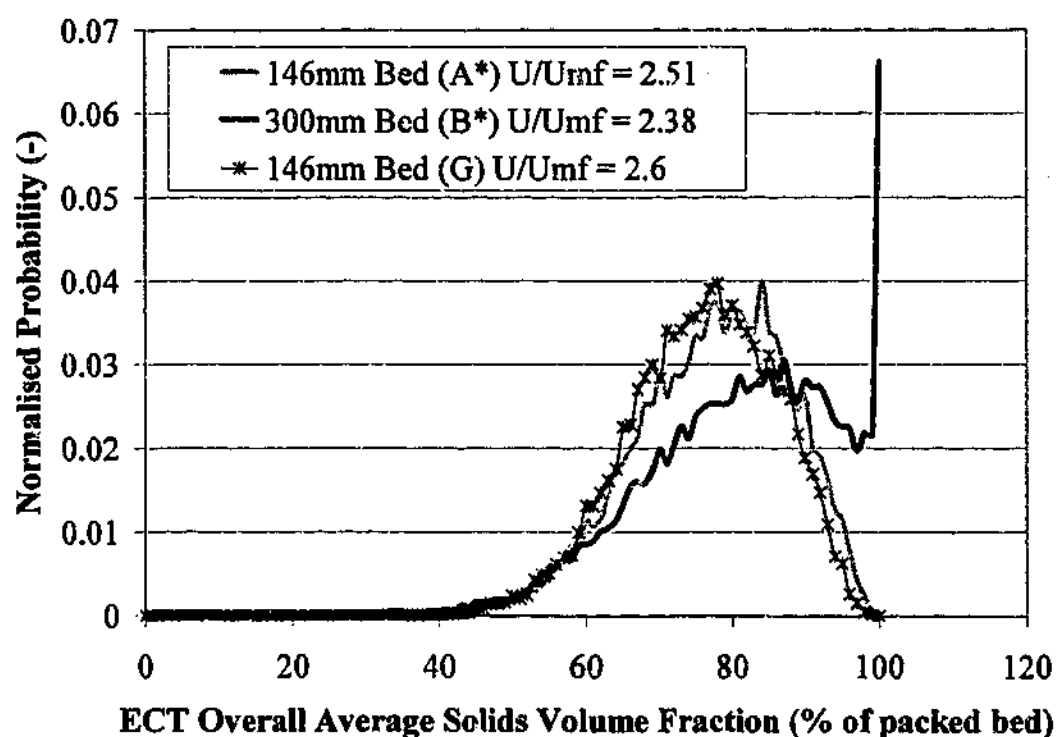


Figure 5.29 Comparison of the normalised probability density function for the correctly-scaled 146 mm bed with material A*, and the 300 mm bed with material B*, with additional data for the correctly-scaled 146 mm bed with higher-density material G. The beds were operated at the intermediate gas velocity of $U/U_{mf} \approx 2.5$.

Similarly, there is poor agreement in the results for the 146 mm bed with materials A* and G compared with the results for the 300 mm bed with material B* at the intermediate gas velocity of $U/U_{mf} \approx 2.5$ (Figure 5.29). In this case there are some distinctions, however. The results for the smaller scale bed with materials A* and G do not “leak” beyond the packed-bed limit value of 100, and, in fact, the distributions for these two bed materials agree quite well with each other. Note however, that the

distributions are not quite symmetrical, exhibiting a longer tail at the low solids volume fraction end. The comparison with the larger-scale result is a different matter. As in Figure 5.28, there is a significant amount of the distribution which has been lumped into the 100 column, (clearly if the distribution were symmetrical it would continue out until about 130). The peak is also higher than the corresponding peaks in the distributions for the materials in the smaller scale bed. Once again, the result suggest that either there is no hydrodynamic similarity between these two beds, or the ECT system is responding differently when applied at different scales.

5.7.5 Comparison of Amplitude Spectra

Here the frequency spectra for the ECT results were produced in much the same fashion as the frequency spectra for the pressure fluctuation results of Chapter 4. Microcal Origin 5.0 was used to apply a one-sided windowed Fourier transform to the data. The only difference was that in this case there was a repetition of the first few seconds worth of data from a given time series again at the end of the time series. This is because the transform requires a set of data points equal to a power of 2 and the ECT data had a maximum length of only 16,000 points, due to software limitations. Consequently, the first 384 points of the series were added on to the end of the 16,000 points, to create a "patched" time series of 16,384 points, (*ie* 2^{14}). This was considered preferable to the more mathematically correct alternative of reducing the data set to the next power of two (8192 points) – which would mean effectively throwing away half of the data. The Hanning window function was used in these analyses in order to eliminate discontinuities at the beginning and end of the time-series, and an ensemble averaging procedure (16 lots of 1024 points) was again used in order to reduce the random error in the spectrum estimate. Normalisation was carried out on the resultant spectra so that the area under each curve was unity, and the frequencies were non-dimensionalised by applying Equation 5.3.

Figure 5.30 shows the results for the correctly-scaled 146 mm bed with material A compared with the correctly-scaled 300 mm bed with material B, operated at the intermediate gas velocity of $U/U_{mf} \approx 5$. The spectra are relatively similar, showing approximately similar dominant dimensionless frequencies in the range of 10 to 15 for both beds, and a similar roll-off in signal strength as the frequency goes up.

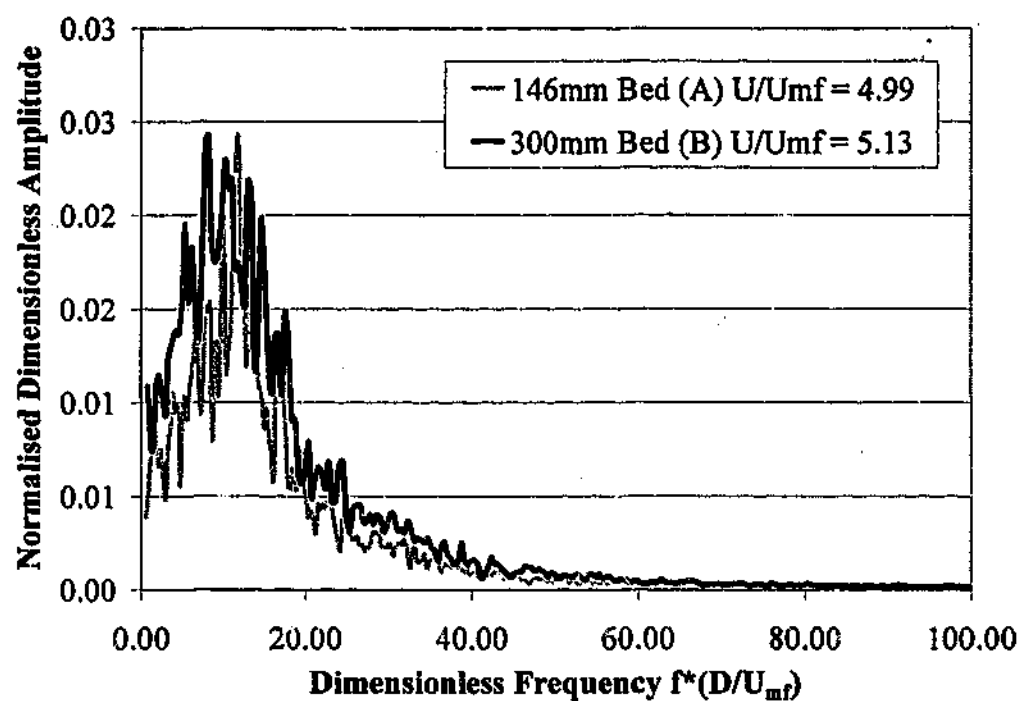


Figure 5.30 Comparison of the normalised dimensionless amplitude spectra for the correctly-scaled 146 mm bed with material A and the correctly-scaled 300 mm bed with material B, operated at the intermediate gas velocity of $U/U_{mf} \approx 5$.

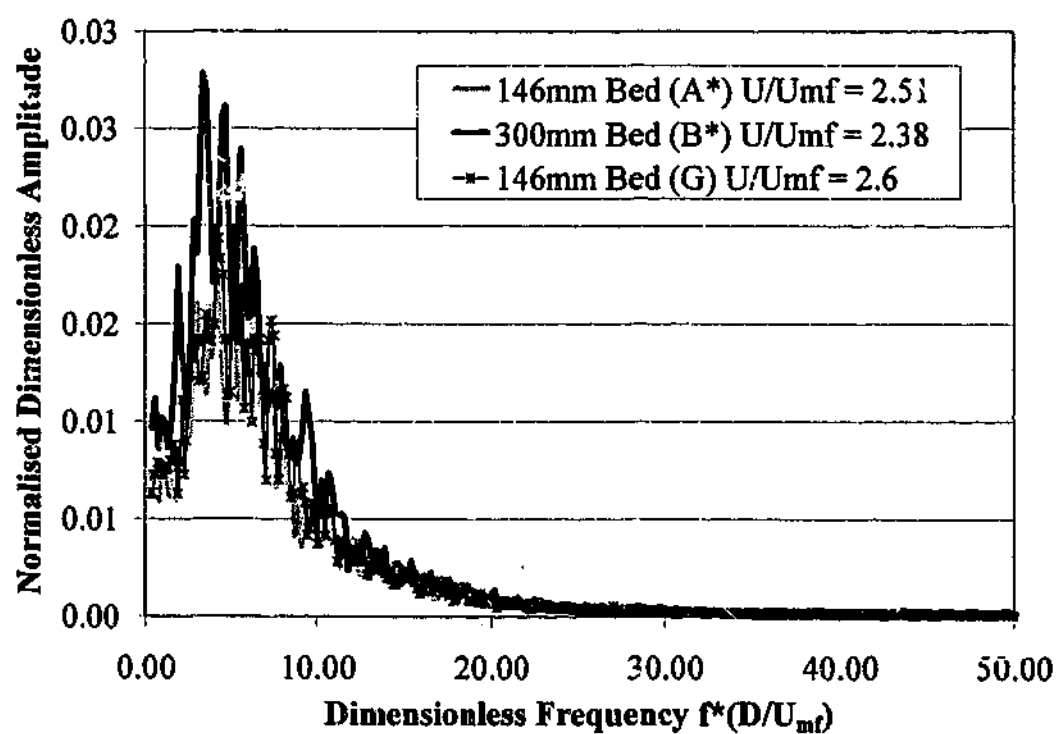


Figure 5.31 Comparison of the normalised dimensionless amplitude spectra for the correctly-scaled 146 mm bed with material A and the correctly-scaled 300 mm bed with material B, plus the correctly-scaled 146 mm bed with higher-density material G, operated at the intermediate gas velocity of $U/U_{mf} \approx 2.5$.

Figure 5.31 shows the result obtained for the comparison between the materials A* and B* in the 146 mm and 300 mm beds respectively, and for the additional comparison with the material G in the 146 mm bed at the intermediate gas velocity of $U/U_{mf} \approx 2.5$. The agreement in the spectra for the 146 mm beds of materials A* and G is very good. There is slightly less correspondence between the smaller beds and the larger counterpart with material B* (comparable with the level of agreement in Figure 5.30 for A and B materials). The larger bed shows more signal strength contained at lower dimensionless frequencies. Signal strength roll-offs are again quite similar in all cases.

5.8 ECT Sensitivity Differences

As the various comparisons of the ECT overall average solids volume fraction have been presented in the preceding section, it should be becoming increasingly clear that there are significant differences in the results. Although the average solids volume fraction and dimensionless average cycle frequency show similar trends across the range of dimensionless gas velocities considered, the average absolute deviation and probability density function show significant differences. The amplitude spectra also show differences for the comparison of the larger-particle bed materials (A* and B*).

As has been stated, differences in the result could be attributed to two possible causes. First of all, if the beds are not operating in a hydrodynamically similar fashion under the stated conditions, then it would be reasonable to expect differences in the comparisons of the dimensionless results. However, if the beds are *not* hydrodynamically similar under the stated conditions, then this constitutes a conflict with the previously presented pressure fluctuation results obtained under the same operating conditions; a failure of the scaling laws; and a contradiction to previous verification work in the literature for similar bed scales, conditions and media (eg Horio *et al.* 1986a; Zhang and Yang, 1987; van der Stappen, 1996; Stein *et al.*, 1998). Whilst possible, this is not likely.

The second option is that the measurements taken by the ECT system are significantly affected by the scale of the bed under scrutiny and the corresponding electrode configurations used. Although the same ECT system is used at both scales, the electrodes used on the vessels are different (as they have to be since the vessels are different sizes). From the review of ECT measurements and limitations presented in Sections 5.4 and 5.5, several differences which may affect measurements can be identified:

1. The electrode lengths and areas are not proportional to the bed diameters and cross-sectional areas respectively.
2. Driven shields are used in the 146 mm bed but earthed shields are used on the 300 mm bed.
3. The vessel walls are made of different materials.

Details of these differences are as follows. Due to space restrictions from the proximity of the bottom flange, the axial electrode length (L_e) on the 146 mm bed had to be truncated, resulting in a proportionally *shorter* electrode with proportionally *smaller* surface area (A_e). As a result, the ratios of L_e/D and A_e/A_{x-s} are different. (D and A_{x-s} are the bed diameter and bed cross-sectional areas respectively.) This may result in a *decreased* sensitivity to voids in the 146 mm bed when compared to the 300 mm bed (refer to comments accompanying Equation 5.2).

	146 mm Bed	300 mm Bed
L_e/D	0.34	0.51
A_e/A_{x-s}	0.11	0.16

Table 5.1 Comparison of the dimensionless ECT electrode sizes in the 146 mm and 300 mm fluidized bed vessels.

The lack of driven-shield electrodes on the pre-existing 300 mm vessel may result in *decreased* sensitivity to voids located towards the top and bottom of the electrodes, when compared with the 146 mm vessel with the driven shields (Kühn *et al.*, 1996; Mathers *et al.*, 1998).

The different material of the two vessels may also play a role, since the dielectric constants will be different (*viz* 2.84 for PMMA and 4.55 for PVC at 1 kHz – Weast, 1975). Thus despite similar wall thicknesses, the series capacitance due to the wall will be higher in the 300 mm PVC vessel, which may result in a *decrease* in void sensitivity at that scale, due to the increased dielectric screening (Huang *et al.*, 1992).

Now, although the above points constitute possible causes of a measurement discrepancy between the two scales, they are not completely convincing on their own without further experimental evidence, particularly since some of the construction

differences listed above would have counteracting effects. And, there is still the possibility, however small, that the beds really are not behaving in a scaled manner and the ECT measurements are in fact, accurate.

It was therefore decided that some additional measurements should be made comparing the sensitivity of the ECT system at each scale to voids of a known size, in a similar fashion to Mathers *et al.*, 1998. The experimental set-up was as shown in Figure 5.32, and bed materials A and B were used in the 146 mm and 300 mm beds respectively.

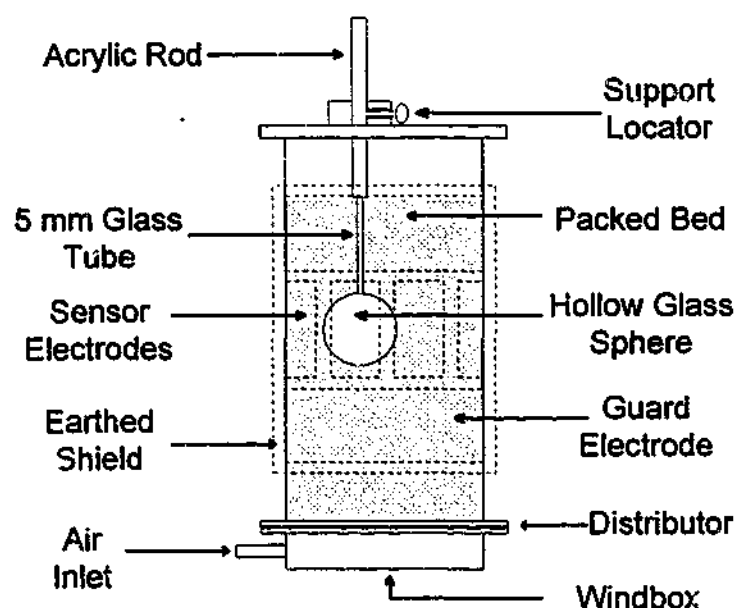


Figure 5.32 Arrangement for testing ECT sensitivity to phantom voids placed at various radial locations in the 300 mm bed. (The 146 mm bed would be similar, but with driven shields). The packed bed consisted of silica sand; material A was used in the 146 mm bed, material B in the 300 mm bed.

146 mm Bed		300 mm Bed	
Void Diameter D_v	D_v/D	Void Diameter D_v	D_v/D
64	0.44	130	0.43
40	0.27	85	0.28
20	0.14	40	0.13

Table 5.2 Sizes of spherical thin-walled hollow glass phantom voids used in comparative ECT sensitivity tests

Three sizes of thin-walled spherical glass voids were selected for use in each bed, such that they were of approximately the same dimensionless size in each bed. Table 5.2 shows the details of the phantom voids used.

The test procedure was much the same as that of Mathers *et al.*, (1998). After calibration with the bed material, the bed was gently fluidized in order to place the voids, and then allow the bed to settle back to a packed state around the void. The ECT system then logged the packed bed for 1 minute at a frame rate of 10 Hz.

146 mm Bed, Material A			
Void Diameter	Void Position	Measured Volume Fraction	Actual Volume Fraction
64 mm	Centre	84	84.7
	Wall	83	84.7
40 mm	Centre	96	96
	Wall	94.1	96
20 mm	Centre	100	99.5
	Wall	100	99.5

300 mm Bed, Material B			
Void Diameter	Void Position	Measured Volume Fraction	Actual Volume Fraction
130 mm	Centre	81.7	89.3
	Wall	80.9	89.3
85 mm	Centre	99	97
	Wall	99.1	97
40 mm	Centre	100	99.7
	Wall	100	99.7

Table 5.3 Comparison of the ECT-measured solids volume fraction with the known solids volume fraction for thin-walled hollow glass spheres placed in packed beds of silica sand at both the 146 mm and 300 mm scale. Volume fraction is expressed as a percentage of the packed bed volume fraction.

The resulting data were analysed somewhat differently, however. Rather than consider reconstructed images and the size of the voids present, the overall average solids volume

fraction was used to work out the fraction of space inside the electrode measurement volume occupied by packed bed, and the fraction occupied by the void. This was then compared with the known solids volume fraction based on the known size of the measurement volume and the void volume. The tests were conducted with the voids placed at the axial centre of the measurement volume, and either touching the vessel wall or spanning the radial centreline. Results for the phantom void tests are shown in Table 5.3.

There are several points of interest to note from these results. First of all, the results for the 146 mm bed are reasonably close. That is, the ECT image results in an estimate of the solids volume fraction quite close to the actual solids volume fraction, and the difference due to radial position of the void is not very large, with the image result almost as good at the wall as it is in the bed centre. Interestingly, the solids volume estimated via ECT measurement for the larger voids is a little *lower* than the actual case – more so at the wall. This means that the reconstructed image information is actually over-estimating the size of the larger voids to some extent.

The 300 mm diameter system is a different story, however, and these results immediately shed some light on the measurement differences seen between these two different-sized units. For the larger void (130 mm in diameter), the solids volume fraction is *under*-estimated by almost 10 percent. In other words, the ECT system is seeing a bigger void than is actually present. Yet as the void size decreases, the situation reverses. The 85 mm diameter sphere image *over*-estimates the solids volume fraction, thus *under*-estimating the size of the void. And the 40 mm sphere is not detected at all. Like the 146 mm system, there is only a small difference between measurements of the void at the radial centre when compared with the void at the wall.

So, as can be seen above, the comparison of the phantom voids in packed beds indicates certain differences in the measurement accuracy of the ECT system as a consequence of the design of the measurement electrodes. Despite the smaller ratio of electrode size to bed size in the 146 mm system, the measurements of solids volume fraction at this smaller scale are considerably more accurate than those for geometrically similar voids at the 300 mm scale. In both systems, the radial position of the void appears to have only a minor effect. The application of driven shields, as well as the reduced inter-electrode distances associated with a smaller vessel diameter are therefore significant factors in increasing the accuracy of the ECT measurement system.

5.9 Discussion

Results for the experimental program involving the use of the ECT system can be broadly split into two categories: Results pertaining to the use and usefulness of the ECT system; and results pertaining to the experimental verification of the simplified scaling laws. In this particular study, far more information has been gathered concerning the first point than the second.

The ECT system has the advantages of being non-intrusive and fast, of being able to display reconstructed images in real-time, as well as being relatively inexpensive (when compared to other non-invasive imaging techniques). However, in the actual applications of ECT explored here, significant practical drawbacks have been encountered in the use of the equipment. The difficulties involved in measuring extremely small capacitances in a physical system prone to electrostatic charging cannot be ignored. The initial baseline drift identified for fluidized beds of silica sand, (and to a lesser extent, garnet sand) can be overcome with appropriate operating procedures, however it serves as a reminder of just how easily the measurements can be perturbed by an undesirable electric field.

The finite limitations on the size of capacitance that can be physically measured place restrictions on the size of the measurement electrodes and the diameter of the vessel to which the ECT system can be applied. Recall that an attempt to employ the technique at the 600 mm bed scale in this work was abandoned, and results presented in the previous section highlight the decrease in sensitivity that may be associated with increasing the vessel diameter from 146 mm to 300 mm.

The reconstruction of images from the measured capacitance data is far from straightforward due to the distortion of the field (the soft-field problem) by the changes in the distribution of dielectrics within the measurement volume. The major consequence of these reconstruction difficulties is the limited accuracy of the resulting image. In the present work, beds operating at low gas velocity which were clearly fluidized and bubbling when the bed surface was examined by eye appeared to be quiescent in reconstructed images (*ie* no bubbles were imaged). At the other end of the scale, high gas velocities produced images in which large singular voids spanned the entire cross-section of the vessel (a result which could be interpreted as slugging); yet checks performed using existing slugging correlations indicated that slugging was unlikely, in addition to which, visual observations of the bed surface provided no

evidence of slugging whatsoever. Voids were more often imaged near the vessel walls than in the bed centre, and an imaging artifact somewhat like a clockface (and apparently corresponding to the electrode positions) was observed in some images.

Yet, despite these limitations, the reconstructed images do have one saving grace, (albeit limited only to one of the vessels used in the present work). Although the spatial distribution of solids and voids within the image may be somewhat unrepresentative, the actual amount of solids and gas present in the images appears to be relatively accurate, at least in the smaller-scale unit. Even at some of the low gas velocities where bubbles were small and not imaged, a proportional reduction was still observed in the overall average solids volume fraction data; corresponding fairly well with the volume of voids present. Huang *et al.*, (1993) and Xie *et al.*, (1994) estimated the maximum error in the component fractions calculated from a reconstructed LBP image to be around 17%. In the smaller (146 mm) vessel with the driven shields, the maximum error observed for the solids volume surrounding spherical voids was only 2%. Only minor over and under-estimations of void size were observed at this scale. However in the larger 300 mm system (with earthed shields), the maximum error in solids volume fraction was 10%, and notably, there were cases of significant *under*-estimation of solids volume fraction for this system (*ie over*-estimation of void volume). Less severe over-estimations of solids volume fraction were also observed for the smaller voids.

If the bed were fluidized, this significant over-estimation of solids volume fraction in the larger vessel could, in part be due to false increases in voidage between multiple voids generated during reconstruction (Halow and Nicoletti, 1992). This explanation is adequate for fluidized beds where several voids may exist within the measurement volume at the one time. But the case of the static tests involving phantom voids cannot be explained in this way, since only one void was present during the test, and no definitive explanation can be given. Since the error is far worse in the larger vessel, it may be related either to the larger electrode areas or inter-electrode distances involved at that scale, or possibly to the lack of driven shield electrodes. But although the cause of the error is unclear, the consequences are fairly obvious.

The unfortunate combination of over-estimating the size of large voids as well as under-estimating the size of small ones is likely to result in the distribution of measured voidage fluctuations being far more widely spread in the ECT results than actually occurs in the bubbling fluidized beds. Small voids appear to have smaller volume and large ones appear to be even bigger. Thus the amplitude (indicated by the average

absolute deviation) of the measured voidage fluctuations is larger than it should be, and the probability density function spreads out unrealistically far along the x -axis. Since the phantom void tests indicate the errors to be far greater in the 300 mm bed than in the 146 mm bed, it is likely that the significant discrepancies noted in the results for average absolute deviation and probability density function are a direct result of the large overestimate of void sizes in the 300 mm vessel. It is also likely that of the two scales, the results for the 146 mm system are the more representative. The errors may well be more severe in the fluidized systems than those measured in the static tests due to the presence of multiple voids, resulting in multiple errors (which are summed in the calculation of the overall average solids volume fraction) as well as the possible false increase in voidage measured between bubbles (Halow and Nicoletti, 1992) mentioned earlier. Additionally, if the volume of very small voids is being under-estimated - or worse - they go completely undetected, there will be a tendency for the probability density function to spread upwards. Completely undetected voids will result in an unrepresentatively high number of samples falling into the packed bed volume fraction value of 100%. This is precisely what is observed in the probability density functions of Figures 5.28 and 5.29, for the 300 mm bed results. (Note that although the result for material A in Figure 5.28 is slightly affected in this way, the results for materials A* and G in the 146 mm bed shown in Figure 5.29 are *not* affected. This is likely to be due to the operating conditions for the latter cases; the larger particles of these beds will produce correspondingly larger bubble sizes and indeed all the bubbles present may be large enough that none go undetected. Thus there is no unusual spike at the 100% (packed bed) value for those materials.)

The comparison of the probability density functions for the different-sized beds also highlights potential errors in the overall average solids volume fraction (Figures 5.20 and 5.21). Although the results *appear* to agree very well in these two figures, it is actually a consequence of the off-set in the data associated with the over-and under-estimation of solids volume fractions counteracting each other. Although less obvious, frequency results are also likely to have been affected by significant errors in voidage estimation in the 300 mm bed, with over and under-estimations of void sizes causing corresponding increases and decreases in voidage fluctuation amplitudes at different frequencies within the spectra. The increased amplitude of the lower frequencies present in signals from the 300 mm bed are likely to be a consequence of this. However, the influence does not appear to be as dramatic as that on the probability density function results, and there is still some encouraging agreement between correctly-scaled beds (as

well as disagreement between mis-scaled beds) when compared in terms of average cycle frequencies.

Finally, there is a small amount of useful data which can be interpreted in terms of scaling law verification results. Due to the aforementioned errors associated with the 300 mm scale ECT measurements, it is not realistic to draw any conclusions regarding hydrodynamic similarity from the preceding comparisons of 300 mm and 146 mm results. The only results satisfactory for comparison with regards to hydrodynamic similarity are those of materials A* and G in the 146 mm bed. These materials match relatively well according to the Horio *et al.*, (1986a) scaling criteria, although the particle-to-gas density ratio is mis-matched. However, in the previous chapter, comparison of pressure fluctuations indicated that the density mis-match associated with these materials and operating conditions may not be enough to cause notable differences in fluidization behaviour. The ECT results from this chapter also support this finding.

For the 146 mm bed with materials A* and G fluidized under similar conditions, it can be seen that the agreement in average (Figure 5.23), average absolute deviation (Figure 5.24), average cycle frequency (Figure 5.27), probability density function (Figure 5.29) and amplitude spectrum (Figure 5.31) are all quite good. Recall that the discrepancy noted in the dimensionless frequency comparisons of Figure 5.26 was explained in the accompanying text (as well as in the previous chapter) and results from the non-dimensionalisation calculation and the small difference in minimum fluidization velocity for these two materials.

Note that a comparison of these results with those from material A in the same bed at the same dimensionless superficial gas velocities (corresponding to a mis-scaled scenario) is not particularly useful in this case. This is because differences in the results for the mis-scaled scenario cannot be explicitly assigned to hydrodynamic similarity issues; the (expected) smaller bubble sizes for material A also exacerbate problems with size under-estimation and non-detection of voids (hence producing results that do not represent the "true" hydrodynamics for this material). However, as far as the comparison of materials A* and G goes, the results do show agreement and support the findings of Chapter 4: that under the operating conditions considered, the density mis-match between these materials does *not* cause a deviation from hydrodynamic similarity when the scaling laws of Horio *et al.*, (1986a) are followed.

5.10 Conclusions

The use of Electrical Capacitance Tomography for imaging bubbling fluidized beds is not without pitfalls and limitations. Many of the limitations of ECT usage have been highlighted by previous workers, and those specifically identified in the course of this work are as follows:

Due to the extremely small capacitances involved in measurements, the ECT system is quite susceptible to changes in electric fields. Consequently, it is important that the calibration procedure includes a suitable length of fluidization time for any electrostatic charges generated in the filling process to be dissipated. This time was found to be of the order of 15 to 20 minutes for silica sand (worst-case scenario).

Although not separately identified, it is likely that the use of both driven shield electrodes and small vessel diameters is important in getting the maximum measurement accuracy from an ECT system. In the present work, the errors in volume fraction estimates for the smaller vessel were significantly smaller than those for the larger vessel.

At both scales employed, images generated using the linear back-projection reconstruction algorithm did not accurately represent the behaviour of the fluidized bed. This was true of the size of the imaged voids as well as their radial distribution.

Significant over-estimation of large void sizes as well as some under-estimation of small void sizes occurred for the 300 mm electrode system. Similar, but much smaller errors were noted for the 146 mm system. These errors made quantitative comparison of voidage fluctuation results for the purposes of scaling law verification impossible for the most part.

In comparison of the voidage fluctuation results for the different scales and bed materials there was some (coincidental) agreement in trends for correctly-scaled overall average solids volume fraction data as well as some more encouraging agreement for correctly-scaled average cycle frequency results (encouraging because this parameter was less affected by the voidage measurement errors at the 300 mm scale).

However, in terms of hydrodynamic similarity criteria, the only results that are really satisfactory for comparison are those of materials A* and G in the 146 mm bed, (and this

is because the comparison has been carried out in the same sized vessel and thus is not affected by the previously described ECT scale-related issues). Results for these experiments consistently indicate that despite the density mis-match associated with these bed materials, hydrodynamic similarity is still achieved when the scaling laws of Horio *et al.*, (1986a) are followed. This is in accord with the conclusions of Chapter 4 regarding pressure fluctuation comparisons for the same bed size, materials and operating conditions.

6. SOLIDS MIXING

6.1 Introduction

In bubbling fluidization, the motion of the solids influences gas-solid contacting, gas backmixing, heat transfer, the position of stagnant zones within the bed, and can be important in the choice of optimum solids feed and withdrawal locations. A general overview of solids mixing in bubbling fluidized beds was given in Chapter 2 (Section 2.3). Basically, the mixing of solids is induced by the motion of the rising bubbles. Solids are carried up by bubbles in the bubble wake and drift and simultaneously displaced downwards elsewhere (Kunii and Levenspiel, 1969). Exchange of the wake fragments with the surroundings also occurs periodically (Rowe *et al.* 1965). Lateral mixing occurs in the bubble wake (Kunii and Levenspiel, 1969), at the bed surface due to the splashing of solids and near the distributor by bubble-free lateral solids movement (Baeyens and Geldart, 1986).

Solids mixing is critical in many different fluidized bed applications, and hence the way in which the motion of bed materials changes at different scales is of fundamental importance. Very few systematic comparisons of solids mixing have been carried out at different scales, although the results of different workers using different sized equipment have been compared in previous studies (*eg* Avidan and Yerushalmi, 1985, Kunii and Levenspiel, 1991).

In the current work, two different methods of investigating solids mixing have been applied to compare the behaviour of beds scaled using the simplified scaling laws. The first approach was a novel technique involving the use of the Electrical Capacitance Tomography system to detect tracer particles, and the second was the use of scaled large float tracers to provide information about the circulation behaviour of the bed solids. Parts of this work are to be published in Sanderson and Rhodes, (2002).

Various previous approaches to characterising and modelling bubbling fluidization solids mixing were introduced in Chapter 2. In the introductory sections of this chapter, some previous experimental techniques are introduced, including studies of the motion of large neutrally-buoyant objects in bubbling beds. The effect of scale on solids mixing

is then discussed with reference to some of the previously proposed mixing correlations. Mixing studies involving scaling law comparisons are reviewed.

The systematic development of the solids downflow velocity experiments involving Electrical Capacitance Tomography is reported, with results on the effect of tracer fluidization properties also discussed. Solids downflow velocity results for scaled systems are then compared with each other and with literature correlations.

The neutrally buoyant large float tracer experiments are then introduced. The postulate that float tracer motion should scale with the use of the similarity criteria is developed, and it is experimentally shown that within a limited range (wide enough to cover anticipated experimental errors), the density of the float tracer has negligible effect on the tracer circulation time distribution. Similarity test results are then presented, including the effects of mis-scaled bed particles and mis-scaled tracer size.

Finally, general conclusions for both experimental approaches are presented. Note that some parts of the work covered in this chapter were presented in Sanderson and Rhodes (2001a) and Sanderson and Rhodes (2002).

6.2. Previous Experimental Approaches to Solids Mixing

Experiments investigating solids mixing in fluidized beds are many and varied, and all involve some means of tracking the motion of particles in the bed. For investigating the behaviour of the bulk bed material, particles which have the desired fluidization characteristics but which can be identified from the bulk bed material in some other way are normally used. Tracers particles which have been used include coloured particles (eg Rowe *et al.*, 1965), phosphorescent particles (eg Wirth *et al.*, 1991), radioactive particles (eg Mostoufi and Chaouki, 2001), salt particles (eg Mathers, 1998), heated particles (eg Valenzuela and Glicksman, 1984) and ferromagnetic particles (eg Habermann, *et al.*, 1998). Various methods of detection have been employed to suit the tracers involved.

Tracers can be placed in layers or columns prior to fluidization, and their dispersion into the bulk bed material examined (eg Woollard and Potter, 1968; Horio, *et al.*, 1986b). Small quantities can be added to a bed (while fluidized) at the bed surface or distributor level (Whitehead *et al.*, 1976), or injected at a known position (Farrel, 1996). Tracer can

be introduced into continuous fluidized bed systems via a step change in inlet concentration, with the subsequent outlet concentration analysed over a period of time (Tailby and Cocquerel, 1961; Haberman *et al.*, 1998). Phosphorescent bed materials can be locally "activated" by UV light pulse and movement of the activated material visually observed (Wirth *et al.*, 1991).

In a few cases, larger particles with densities approaching that of the bed emulsion have been used because they also tend to circulate throughout the bed under the influence of bubbles and solids downflow (*eg* Bellgardt and Werther, 1986; Lim and Agarwal, 1994).

The complexity of the procedures for solids mixing experiments varies from one extreme to the other. Investigating the displacement of different coloured bed materials (*eg* Rowe *et al.* 1965, Whitehead *et al.* 1976) can involve tedious bed sectioning techniques to determine amount of tracer at various axial and radial positions within the bed. (The bed is defluidized after a certain time so that the sectioning can be carried out.) On the other hand, tracking the location of a single radioactive particle over an extended period of time (*eg* Garncarek *et al.*, 1997) is a far less arduous approach, but involves much more sophisticated equipment.

Results of solids mixing have been reported in many ways. Tracer concentration/time profiles, solids circulation rates, average particle velocity and particle velocity profiles have all been employed. The calculation of a directional diffusivity (also termed dispersion or diffusion coefficient) has been used by a number of workers (*eg* May, 1959; Thiel and Potter, 1978; Avidan and Yerushalmi, 1985), and is often extracted from experimental data and used for comparison with the literature, (even in some cases where a diffusion model is not directly applicable).

One of the greatest difficulties in performing solids mixing experiments and gaining useful insights from the results, is that solids mixing processes are very variable. The motion of a transient pulse of tracer solids into a bubbling bed can vary considerably from one run to the next due to the specific location, size and velocity of bubbles relative to the tracer injection point at the instant of injection (Fitzgerald *et al.*, 1977; Valenzuela and Glicksman, 1984; Farrel, 1996). Batch mixing experiments involving the mixing of carefully constructed layers of tracer can be particularly troublesome because of the unpredictable way in which the initial bubbles rise when the gas is first introduced into the bed. Transient mixing effects during the defluidization step for experiments

requiring a subsequent bed sectioning analysis may also affect the results for systems with a particularly rapid solids mixing rate.

Several models have been developed to attempt to describe the solids mixing behaviours observed in experiments; these have been reviewed by a number of authors. Early approaches to solids mixing models are covered by Potter (1971); van Deemter (1985) and Kunii and Levenspiel (1991) provide more recent reviews of the two general modelling approaches which have been most commonly employed. These are the diffusion-type models and the countercurrent backmixing models, both of which were introduced in Chapter 2. Both of these models have their limitations, with the diffusion model finding use in describing the behaviour of deep beds of fine particles, and the countercurrent backmixing model gaining greater acceptance as more appropriate for dense-phase (bubbling) fluidization in shallow beds. Baeyens and Geldart (1986), Kunii and Levenspiel (1969, 1991) and others have also developed and presented a number of parameters relating to solids mixing, with correlations for estimating them in a given bubbling bed system.

6.2.1 Motion of Large Neutrally-Buoyant Objects in Bubbling Beds

It has been observed that objects with a density near that of the bulk emulsion at minimum fluidization conditions circulate throughout the whole of a bubbling bed (eg Nguyen and Grace, 1978). Flat objects, however, have a greater tendency to settle to the distributor, particularly at low gas velocities (Nienow *et al.* 1978).

For large objects with a density that promotes their circulation throughout the bed, the object is carried upwards to the bed surface in an irregular fashion under the influence of rising bubbles, and moves downwards under the influence of the dense phase (Nienow *et al.*, 1978). Because they are affected by bubble and solids behaviour, the motion of these large, neutrally buoyant objects can be used in hydrodynamic studies. Merry and Davidson (1973) used a large "radio-pill" as a tracer in an experimental investigation of gulf-streaming; Bellgardt and Werther (1986) used subliming dry-ice pellets to study solids mixing. Linjewile and Hull *et al.*, (1993) used various larger and lighter spheres equipped with thermocouples to investigate heat transfer coefficients between bed and sphere. Lim and Agarwal (1994) studied the motion of large neutrally buoyant objects in a two-dimensional bed, relating the upwards and downwards velocities to the average

bubble rise velocity. They found good agreement with the results of the three-dimensional work of Rios *et al.* (1986), and Nienow *et al.*, (1978).

6.2.2 The Effect of Scale on Solids Mixing

Avidan and Yerushalmi (1985) presented charts showing the trend for dispersion coefficient as a function of bed diameter and of superficial gas velocity, which was reproduced with further data added by Kunii and Levenspiel (1991). From a comparison of these results it would appear that the axial dispersion coefficient varies with the bed diameter as $D^{0.5}$ (Avidan and Yerushalmi, 1985) or $D^{0.65}$ (Kunii and Levenspiel, 1991), and linearly with superficial gas velocity in small beds (Kunii and Levenspiel, 1991). These conclusions were drawn from results involving deep beds of fine (Geldart group A) powders, where typically only small-scale mixing is taking place with relatively little gulf-streaming, and the diffusion model is expected to be reasonably appropriate (Kunii and Levenspiel, 1991). In situations involving shallower gently bubbling beds where there is gulf streaming and the countercurrent backmixing model finds use, little work has been reported on the effect of scale.

The question of whether solids mixing should scale according to the simplified scaling criteria can be addressed with the following postulate: If solids mixing phenomena are *primarily* the result of bubble behaviour in the bed, and if all the bubble characteristics (including wake and drift fractions) have been scaled correctly as a result of applying the scaling criteria, then solids mixing should also scale.

Note that the above assumes that solids mixing from bed surface splashing and turbulent mixing at the distributor either also follows the scaling law, or if it doesn't, then these effects constitute a negligible contribution to the overall solids mixing behaviour. Horio *et al.*, (1986a) showed that the simplified scaling law is consistent with a number of jet diameter and height correlations of other workers, so there is some evidence that the bed behaviour near the distributor also scales. Since bubble parameters and bed expansion follow the scaling law, it may also be reasonable to extend the similarity to bed surface behaviour since this is a direct result of bubble activity. Some experimental evidence of this was provided by Zhang and Yang (1987), who report similar entrainment rates for beds scaled according to the simplified similarity criteria. However, note too that poor agreement in pressure fluctuations recorded near the surface of scaled beds has also been

reported in the literature (eg Brue and Brown, 2001) and was found to some extent in this work (see Chapter 4, Figure 4.35).

Often, axial solids velocities are correlated to bubble rise velocity, U_B . Now, U_B is expected to follow the scaling laws under most bubbling bed situations, since the majority of correlations for equivalent bubble diameter d_{eq} (eg Darton *et al.*, 1977) agree with the scaling laws (Horio *et al.* 1986a), predicting an equivalent bubble diameter which scales in proportion with bed size. Since U_B is normally related to d_{eq} by:

$$U_B = K \sqrt{g d_{eq}} \quad (6.1)$$

where K is usually taken as 0.71, the rise velocity U_B scales by \sqrt{m} , which is consistent with the expected scale change for a length-per-unit-time quantity.

For the correlation for solids downflow velocity of Kunii and Levenspiel (1969):

$$U_{sd} = \frac{\beta_w \varepsilon_B U_B}{1 - \varepsilon_B - \beta_w \varepsilon_B} \quad (6.2)$$

if the dimensionless ratios β_w (wake fraction) and ε_B (visible bubble fraction) are invariant with a scale change made in accordance with the scaling laws, then the solids downflow velocity will scale in proportion with U_B and hence follows the scaling law.

Similarly, in the case of downwards solids particle velocity as given by Baeyens and Geldart (1986):

$$U_{sd} = \left(\frac{\beta_w + 0.38\beta_d}{1 - \varepsilon_B - \varepsilon_B(\beta_w + \beta_d)} Y \right) (U - U_{mf}) \quad (6.3)$$

if the various dimensionless fractions (*ie* bubble fraction, wake fraction and drift fraction and the value Y used to account for the visible bubble fraction being less than predicted by the simple two-phase theory) are all invariant (or close to) with scaling-law scale change, then the first bracketed term of equation 6.3 becomes constant. Thus solids particle velocity should again scale in direct proportion with excess gas velocity, and hence, \sqrt{m} .

Note that for the above equation, variations in β_w and β_d with particle size (Baeyens and Geldart, 1986) will have only a marginal effect; it is the value of Y (proportion of excess gas travelling in the form of bubbles) that has the most significant effect. Although Y is found to be a function of particle diameter, (plotted as a function of Archimedes number by Baeyens and Geldart, 1986) for the range of particle diameters considered in this study, it is virtually constant, and the value given by Werther (1978 & 1983) of $Y = 0.67$ is appropriate.

Although no experimental comparison of an axial dispersion coefficient has been made under the conditions of the simplified scaling law, results for the systems summarized by Avidan and Yerushalmi (1985) and Kunii and Levenspiel (1991) indicate that the axial dispersion coefficient increases approximately with the square root of bed diameter and linearly with increasing superficial gas velocity. A crude application of the scaling rules to these trends indicates that for an m -times change in bed diameter and a \sqrt{m} -times change in superficial gas velocity, the axial dispersion coefficient will increase by m , (or at most $m^{1.15}$ if the trend of Kunii and Levenspiel, 1991 for axial dispersion coefficient with bed diameter is employed). This does not agree with the expected increase of $m^{1.5}$ which the scaling law predicts from dimensional analysis.

It has been noted by Horio *et al.* (1986a) that for fine powder catalyst beds of high fluidity, the simplified scaling law may not hold. This may possibly go some way towards explaining the above discrepancy, since the data referred to by Avidan and Yerushalmi (1985) and Kunii and Levenspiel (1991) are taken from such systems.

Horio *et al.*, (1986a) showed that the lateral dispersion model of Kunii and Levenspiel (1969) was consistent with the simplified scaling law, and Horio *et al.*, (1986b) showed that two proposed lateral dispersion models for solids mixing (Hirama *et al.*, 1975; Shi and Fan, 1985) both obeyed the simplified scaling rules. This would indicate that in systems where these models are applicable, lateral mixing is indeed scaleable.

Lim and Agarwal (1994) investigated the motion of neutrally buoyant objects in a two-dimensional bed and found that the rise velocity of the object could be related to the bubble rise velocity U_B . They found that the overall average rise velocity of the object was about $0.07U_B$, while the average upward component of rise velocity of the object (when upwardly mobile) was $0.3U_B$, a similar result to that of the three-dimensional

study of Rios *et al.* (1986). They found the average downward velocity of the object near the wall to be similar to the calculated dense-phase solids velocity.

If the observed relationship of Lim and Agarwal (1994) between the rise velocity of the body compared with that of bubbles holds generally for bubbling beds (as it may do considering the agreement with Rios *et al.*, 1986 and Nienow *et al.*, 1978), then the rise velocity of the object should scale according to the scaling laws, because the rise velocity of a bubble, U_B does (shown previously). Similarly, if the downward movement of the object is similar to that of the dense-phase velocity, then this too should scale with the scaling laws as the dense-phase velocity can be related to bubble parameters, eg Equation 6.2 (Kunii and Levenspiel, 1969) or Equation 6.3 (Baeyens and Geldart, 1986) introduced previously. Hence the solids downflow velocity (and thus the object velocity) will also be in accord with the scaling laws if the bubble properties scale.

The motion of neutrally buoyant objects was also considered by Horio *et al.*, (1986b) who derived an expression describing the motion of a floating body in the emulsion phase of a bubbling bed. By considering the force of gravity, the buoyant force on the floating body and the drag force on the body due to its relative motion in the emulsion phase, they arrived at the following equation of motion for the floating body:

$$\frac{dv^*}{dt^*} = 1 - \left(\frac{\rho_{b(mf)}}{\rho_B} \right) - \frac{3}{4} \left(|v_r^*| v_r^* \frac{\rho_{b(mf)} C_D}{d_B^* \rho_B} \right) \quad (6.4)$$

where $\rho_{b(mf)}$ is the bed density at minimum fluidization, ρ_B is the density of the body, C_D is the drag coefficient, and the dimensionless body diameter is given by:

$$d_B^* = \frac{d_B}{D} \quad (6.5)$$

the dimensionless relative velocity of the body to the emulsion is given by

$$v_r^* = \frac{u_r}{\sqrt{gD}} \quad (6.6)$$

and the dimensionless velocity of the body is given by

$$v^* = \frac{v}{\sqrt{gD}} \quad (6.7)$$

Horio *et al.* (1986b) argue that if floating bodies of the same density have their dimensions scaled with the bed dimensions, and the drag coefficient is constant (based on the assumption that there is negligible change in friction between the body and the emulsion for different scales), then the motions of the floating bodies should be identical in the scaled beds. The results of their associated experimental investigation would tend to support this.

6.2.3 Previous Solids Mixing Investigations of the Similarity Rule

Three studies of solids mixing have been carried out for beds scaled according to the simplified scaling laws. (None have been done involving the full set.) Further to the review information in Chapter 2, additional details of these previous investigations are provided below.

Horio *et al.*, (1986b) investigated lateral solids mixing and the motion of large particles in air-fluidized beds of silica sand with both straight and tapered bed geometries in beds from 50 mm to 600 mm in diameter. They used ferrite coated sands (which could be later separated from the bulk material magnetically) as a tracer material and solid polypropylene cylinders ($\rho_p = 900 \text{ kg/m}^3$), scaled proportionally for each bed as the float tracers. A bed sectioning technique was employed to determine the transient radial dispersion coefficient from a column of tracer particles placed at the bed centre, and the radial and axial distribution of the float tracers. The axial dispersion coefficients agreed well, as did the radial and axial float tracer concentrations at the same (scaled) elapsed time in each bed. The conclusion was that the simplified scaling laws were obeyed for mixing and segregation in both straight and tapered beds. There was no deliberate system mis-match investigated, however there were some unavoidable discrepancies in the minimum fluidization velocities of the bed materials employed in some of the beds. This provides (at least) some information that bed particle size may not be too critical for lateral solids mixing behaviour.

Stein, *et al.* (1998) used positron emission particle tracking (PEPT) to follow the motion of a single tagged bed particle in several air-fluidized sized bubbling beds scaled using a

combination of the simplified scaling parameters for some tests and the viscous-limit scaling parameters for others. The bed materials used were resin beads, foamed glass and glass ballotini, and ranged in size from 0.65 to 4mm in diameter. They did a basic comparison of solids circulation frequency which produced reasonably similar results, except in the smallest column (which was slugging). Their "favourable" comparison for systems with a mis-matched density ratio is at odds with the work of Farrel et al. (1998) for the range of particle Reynolds numbers considered. They compared the solids circulation frequency to the inverse of bed turnover time as estimated using the correlations of Baeyens and Geldart (1986) and Kunii and Levenspiel (1969), and found reasonable agreement. They did not report on a deliberately mis-scaled system, although the system pair operated with mis-matched density ratio that still achieved a reasonable agreement (at Re_p up to approximately 41) is cause for question.

Habermann *et al.* (1998) investigated the residence time distribution of bed particles in a small (70 mm) fluidized bed used to study an iron ore reduction process. The bed was operated at hot and cold conditions, with the simplified scaling parameters matched in the two situations and an additional cold run done with a mismatched superficial gas velocity. The bulk bed material was hematite (Fe_2O_3) with magnetite (Fe_3O_4) used as a tracer, because it has very similar particle characteristics and could be later separated from the hematite with a permanent magnet. The bed was operated in continuous mode with tracer added to the feed as a step function at a certain time. The concentration of tracer in the bed overflow was then determined as a function of time. They found that their results for the concentration history of tracer in the overflow stream were identical in all cases considered, even though the holding time of material in the bed was different between the hot and cold runs, and the superficial gas velocity was mismatched in the second cold run. They found that the bed mixing behaviour could be modelled as a CSTR with stagnant zone. (The stagnant zone was attributed to unfluidized solids visually observed near the distributor.) However, they were unable to explain why the concentration/time profile was unaffected by holding time or gas velocity.

6.3 Electrical Capacitance Tomography Study of Axial Solids Mixing

Using the procedures outlined below the Electrical Capacitance Tomography system used for the dynamic voidage measurements presented in Chapter 5 was used to detect tracer solids in the 146 mm and 300 mm diameter scaled bubbling fluidized beds.

Despite the shortcomings of the ECT system in the comparisons made in Chapter 5, the nature of this application is somewhat less demanding as the ECT system is in essence only being operated as a tracer proximity detector. Importantly, even with possible differences in sensitivity between electrode systems at different scales as the evidence of Chapter 5 would tend to indicate, the peak response is still expected to be at the axial centre of the electrodes (Mathers *et al.*, 1998).

Tracer was deposited at the bed surface, and after a certain time delay it would be detected at the ECT electrode height within the bed. A number of particle size combinations of bed material and tracer were used in the experiments. The transient tracer response profiles generated from the ECT measurement were used to calculate the average downwards solids velocity for each case.

Specifically, the investigation sought to

1. Investigate the effects of relative tracer and bed material particle size on the solids mixing behaviour at a single scale; and
2. Compare solids mixing results from correctly scaled and mis-scaled solids mixing experiments at the two scales (146 mm and 300 mm beds).

6.3.1 Development of Technique

The ECT system uses the differences in dielectric constant (or permittivity) of the solids and the fluidizing gas to distinguish the emulsion from the bubbles in imaging of gas fluidization. Therefore, it follows (in theory) that the device should be equally capable of resolving two solids with sufficiently different dielectric constants. Readily available materials with suitably different dielectric constants were the silica sand (already prepared for use in the other similarity experiments), and glass ballotini. Values for the dielectric constants of the continuous solids are 3.75 to 4.1 for fused silica and 3.8 to 6.0 for various glasses (Weast, 1975). These values provide an approximate guide only, as the values can vary considerably from one specific material to another. Note also that the absolute values of the dielectric constants of the two materials are of little importance, provided that the relative difference between the materials is sufficient for them to be distinguished by the capacitance measurements of the ECT. Additionally, the ECT will not be measuring the capacitance of a continuous solid, but rather a bed of granular materials comprising particles of each solid. Thus, the effect of the air gaps

between the particles will tend to reduce the measured capacitance difference for the different materials.

Initial testing with the ECT unit indicated that for silica sand and glass ballotini, the relative difference in the measured capacitance of a packed bed of each material was approximately 0.44. That is, for the ECT system calibrated to read a packed bed of glass at full scale (ECT scale of 1.0), a packed bed of silica sand would register $1.0 - 0.44 = 0.66$. This was considered to be a sufficient difference to be able to distinguish tracer solids (glass) from bed material (sand). Note that although possible, it would not be as useful to reverse the situation and use sand as the tracer in a bed of glass. This is because of the presence of bubbles in the fluidized bed which constitute a third dielectric material with lower dielectric constant than either of the solids. If a bed of glass were to be used, and a tracer with lower dielectric constant (sand) added, it would not be possible to tell from the limited image resolution which of the regions of lower capacitance in the bed resulted from bubbles, and which resulted from tracer.

The calibration procedure for the ECT unit was modified to account for the different measurement range required for tracer detection as follows.

1. The initially empty bed vessel was used to set the lower limit of the ECT measurement range (so an empty vessel would appear on the ECT scale as 0).
2. The bed was then filled with glass ballotini to an aspect ratio of 2:1 (H/D) and gently fluidized for a few minutes (Recall that unlike the sands, longer fluidization was not required for this step when using glass beads – See Figure 5.6).
3. The fluidizing air was gently turned off allowing the bed of ballotini to settle into an evenly packed state.
4. The packed bed of glass was then used to set the upper limit of the ECT measurement range (corresponding to an ECT scale of 1.0, or 100%)
5. The bed was again gently fluidized and the drain valve in the distributor opened so that the ballotini could be removed.
6. The small layer of ballotini remaining on the distributor after draining was carefully removed with a vacuum cleaner.
7. The drain valve was closed and the bed now filled to the required height with the silica sand bed material.
8. Because of the drift problems associated with the use of the silica sand discussed earlier (see Section 5.6.2), the bed was gently fluidized for a period of 15 minutes, to allow the ECT measured baseline to stabilise.

At the completion of this process, a packed bed of silica sand would register 0.66 on the ECT scale and show very little drift even after extended time periods. It was not possible to calibrate the bed directly with sand and add the ballotini as a tracer, (which would have simplified the above calibration procedure), because in that case a packed bed of sand would register full scale on the ECT system, and there would have been no means of measuring the values higher than this associated with the addition of ballotini.

Once the system was calibrated, the solids mixing experiments could be carried out. A number of different solids addition procedures were attempted during the course of this work in order to determine the approach that would yield the most repeatable transient tracer response profiles. These were conducted in the 146 mm system and it was found that:

- Tracer added as an even layer to the bed surface prior to fluidization produced a very irregular response from one run to the next, even when the bed was suddenly fluidized to the correct velocity. (This was thought to be due to the unpredictable nature of the initial bubble paths through the bed occurring during the start-up transient, and their random initial effect on the tracer location. Consequently, all further attempts involved tracer addition to an already-fluidized bed.)
- Tracer was deposited evenly onto the bed surface through a mesh spreader whilst fluidized at the desired velocity (similar to one of the approaches used by Whitehead *et al.*, 1976, but covering the entire bed surface). This produced a slightly more reproducible result, but the measured response by the ECT was weak unless a lot of tracer was added.
- Tracer was deposited rapidly onto the bed surface in a cylindrical "plug" via delivery through a short pipe just above the bed surface. This gave reasonably reproducible results for smaller tracer quantities.
- The plug approach gave measurement anomalies when tracer was added adjacent to the bed wall, possibly as a result of a capacitive interaction between the delivery tube and the ECT electrodes.

From the above general observations it could be concluded that the initial surge of bubbles when a bed is suddenly fluidized are very unpredictable, leading to an uneven distribution of tracer prior to the bed reaching a steady fluidized state. Thus the "initial" position of the tracer once the bed reached stable fluidization varied greatly from one run to the next, making it not a good approach. When tracer was spread across the fluidized bed surface, there was a much greater distribution of apparent downwards

velocities (associated with the circulation patterns in the bed and tracer at some locations having to first move laterally to get into a downflow zone), thus the tracer was detected by the ECT in low concentration over a wide range of times. Tracer added as a plug to the bed surface tended to move downwards as a relatively coherent mass (as has been observed by others, *eg Fitzgerald et al. 1977*), so the downflow velocity could be easily determined since the mass of tracer arriving at the ECT measurement volume level was easily detectable. The plug approach was useful, but as a precaution it was limited to the bed centre only because of concerns about the influence of the delivery tube on the ECT measurements when the tube was close to the bed wall.

Thus the following procedure was adopted for the solids mixing experiments:

1. The system under investigation was calibrated as described previously.
2. The settled bed height was set to 295 (± 2) mm for the 146 mm bed or 590 (± 5) mm for the 300 mm bed.
3. The bed material was fluidized at the desired gas velocity (typically from 1.44 to 2 times the minimum fluidization velocity).
4. The ECT system started logging data at a sample rate of 10 frames per second.
5. After 100 seconds of initial data had been recorded, a quantity of ballotini tracer was added through a delivery tube placed just above the bed surface at the radial centreline. The delivery tube was 75 mm long and 45 or 85 mm in diameter for the 146 and 300 mm scales respectively. The quantity of tracer added was 250 mL for the 146 mm scale, and 2000 mL for the 300 mm scale. Tracer addition typically took about 1 second for the 146 mm scale, 2 seconds for the 300 mm scale.
6. The ECT system continued logging data at 10Hz for an additional 400 seconds for the 146 mm bed, or 900 seconds for the 300 mm bed. This was found to be well beyond the time taken for the long-term measured tracer concentration to reach a steady value.
7. For another experiment with the same bed material and tracer, a volume of bed material equivalent to the added tracer was drained from the bed using the drain valve in order to re-establish the original bed volume. Steps (3) to (6) were then repeated. It was found that tracer could be reliably detected for repeat runs of up to 10 times with no apparent influence of the increasing background tracer concentration on the results. However, as a precaution, the bed material was replaced after every 5 runs, when the overall tracer concentration in the solids phase was about 20%.

In initial experiments in the 146 mm bed, a 250mL volume of tracer solids was found to be sufficient for reliable detection by the ECT system. This quantity of material added to the bed only had a minor influence on the total bed volume, which was initially around 4940 mL when settled. The addition of tracer increased the bed height by only 5% (15 mm). It was not expected that this level of bed volume change would significantly affect the bed hydrodynamics.

The so-called "average volume fraction" output (see Figure 5.2) from the ECT was used to determine the change in tracer concentration with time, although in the current context the output is a tracer concentration profile and cannot be directly related to the volume of solids present without additional information about the relative capacitance contributions of the different solids present. Thus it will be referred to as simply "ECT measured output" from now on whenever a mixture of solids is involved.

The value for the initial and final packed bed percentage concentrations on the ECT scale were also recorded for each run. These could be used for a results check in order to determine whether the tracer concentration response measured by the ECT system corresponded to the expected increase for the known quantity of ballotini added. The calculation was carried out for mixing of the materials on an unfluidized basis, to avoid having to make assumptions about bed expansion and bubble throughflow.

Here is an example for a typical run. The packed bed concentration values recorded were $C_i = 72\%$ initially and $C_f = 73\%$ at the end of the run. The volume of tracer added was 250mL (packed bed) and the volume of the settled bed prior to tracer addition was calculated from the settled bed height $H_s = 29.6$ cm as:

$$V_{bed} = \pi r^2 H = \pi \left(\frac{14.6}{2} \right)^2 29.6 = 4955 \text{ mL} \quad (6.8)$$

So as a check of the measured C_f , the expected final concentration (assuming the bed is well mixed) can be calculated by:

$$C_f = C_i \frac{V_{bed}}{V_{bed} + V_{tracer}} + C_t \frac{V_{tracer}}{V_{bed} + V_{tracer}} \quad (6.9)$$

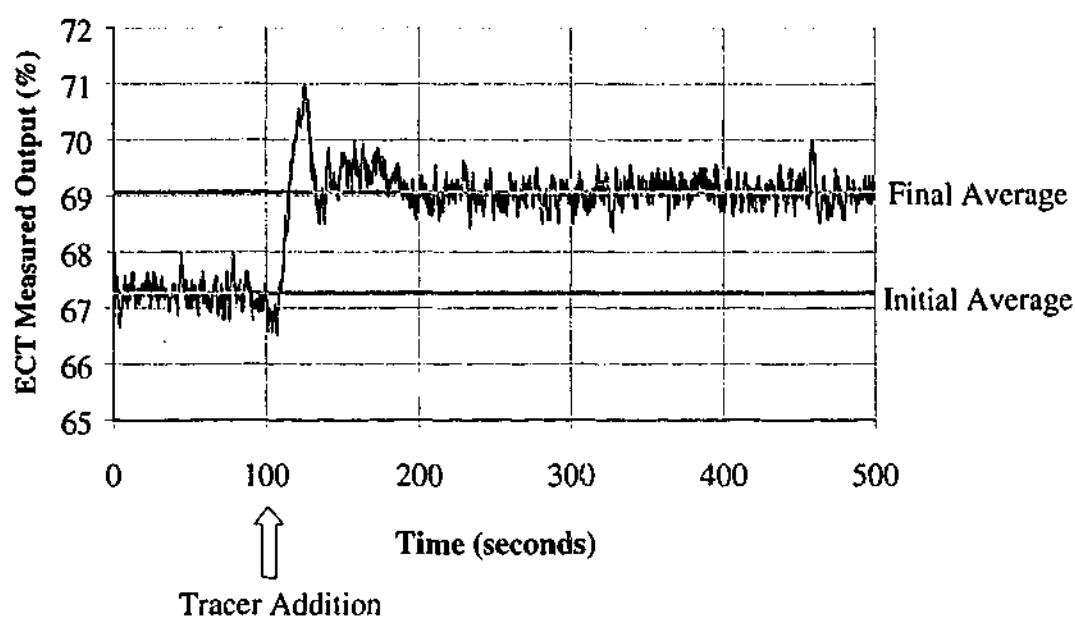
$$C_f = 72\% \frac{4955}{4955 + 250} + 100\% \frac{250}{4955 + 250}$$

$$\text{ie } C_f = 73.3\%$$

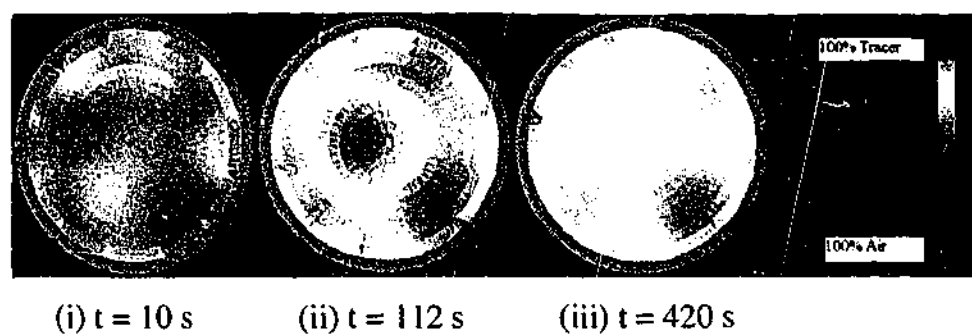
which, given the accuracy of the ECT system's on-screen presentation of the packed bed results (*ie* to the nearest whole percent only) is a reasonable agreement with the on-screen result of 73%. It should be noted, however, that although all the results were checked in this way and typically agreed within 0.5% (unless segregation occurred), the accuracy of such a comparison is somewhat limited, because the accuracy of the on-screen data is only $\pm 0.5\%$ anyway. The situation would be somewhat improved with the use of a tracer that resulted in a more significant change between initial and final concentrations (*eg* by using a tracer material with a higher dielectric constant relative to the bed material).

Another issue with the ECT sensitivity to tracer is the bubbles in the bed. Because the bubbles constitute a third dielectric medium, they also contribute to the fluctuations recorded, adding a layer of higher frequency "noise" to the dynamic tracer concentration signal. Therefore, the steady-state bubble fluctuation phenomena present in the signal were removed using a 2-second moving average applied to the ECT output. For downward moving solids, it was not expected that such a smoothing would affect the longer time-scale information relating to solids motion. (Note: Although image thresholding and windowed time-averaging approaches were tried, the simple moving average applied to the spatially-averaged ECT output was found to give the clearest transient tracer concentration response profiles.)

The resulting transient tracer response profile for a typical run is shown in Figure 6.1(a), with a number of reconstructed frames of the bed cross-section shown for various times in Figure 6.1(b).



6.1 (a)



6.1 (b)

Figure 6.1 Typical transient tracer response for the addition of ballotini tracer (at $t = 100$ s) to a 146 mm diameter bubbling bed of sand, measured with the ECT system:

- (a) 2-second moving average applied to the spatially-averaged ECT system output. 100% on the y-axis would correspond to a packed bed of tracer only, 0% corresponds to an empty vessel.
- (b) Reconstructed images from the ECT data showing (i) the initial bubbling bed of sand, (ii) the clump of descending tracer in the measurement volume, (iii) the bubbling bed mixture of sand and ballotini after the new steady-state tracer concentration is reached in the ECT measurement volume.

This kind of transient tracer response profile is qualitatively similar to that obtained by others (eg Avidan and Yerushalmi 1985; and Valenzuela and Glicksman 1984), using different tracer and detection systems in bubbling fluidization.

It is important to realise that the concentration response measured by the ECT electrodes cannot be attributed as originating from an "ideal" horizontal measurement plane (of zero thickness), although that is the usual practice for interpreting ECT images. This is critical in the current context, because the information being sought is *at what point in time do the downwards flowing solids reach a certain height in the bed*. The gradual increase in the ECT measurement output prior to the peak is the result of solids approaching the ECT measurement volume (not plane), and the value continues to increase as solids progress towards the axial centre of this measurement volume. It is reasonable to assume that the largest value in the peak will correspond to the largest quantity of solids spanning the axial centre of the measurement volume. In the current context the delay from tracer addition to measurement peak can be defined as the time taken for the "average" solids to reach the axial centre of the ECT measurement volume. However, the *slope* of the measurement increase prior to the peak is difficult to interpret because it depends to what extent the electric field is influenced by tracer in the axial direction. This may well extend beyond the height of the measurement electrodes – this is especially likely in the case of the 300 mm system as was found in the previous experiments of Chapter 5, as well as in other studies (Mathers *et al.*, 1998).

The other underlying assumption in this analysis of ECT measurement response to tracer is that if the tracer is subject to lateral dispersion between bed surface and electrode level, the tracer moves axi-symmetrically. This is important, because a small off-set clump of tracer near to the vessel wall will produce a bigger response than the same quantity at the radial centre due to increased measurement sensitivity near the electrodes (Huang *et al.*, 1993; Xie *et al.*, 1994; Mathers *et al.*, 1998). This assumption was found to be reasonable, since the on-line images (such as shown in Figure 6.1(b) above) always showed tracer appearing in the measurement volume in similar radial location to that at which it was added to the bed surface.

The problem with poor repeatability of experimentally observed solids mixing behaviour has been reported by many authors (*eg* Fitzgerald *et al.*, 1977; Valenzuela and Glicksman, 1984; Farrel, 1996). This variation in behaviour (within a given range) is a fundamental aspect of the solids mixing behaviour in fluidized beds, and confounds the experimenter who wants to obtain a single accurate value for (say) solids velocity. The approach taken here, like most experimental mixing studies, was to perform multiple runs, as mentioned earlier. Analysis of these runs has been carried out by taking the full set of transient tracer response profiles generated for a given set of conditions, removing the off-set associated with the initial measured concentration for each run, and averaging

the whole set of profiles, to generate one "average" tracer response profile for a given set of conditions. This average profile has then been used in subsequent calculations.

The procedure for generating the average tracer concentration response profile is shown as an example. Consider the transient tracer response profiles for a typical set of 5 consecutive runs, shown in Figure 6.2. (In order to improve the clarity, Figure 6.2 shows the data with a 5 second moving average applied, although a 2 second moving average was normally used on all data for calculation purposes.)

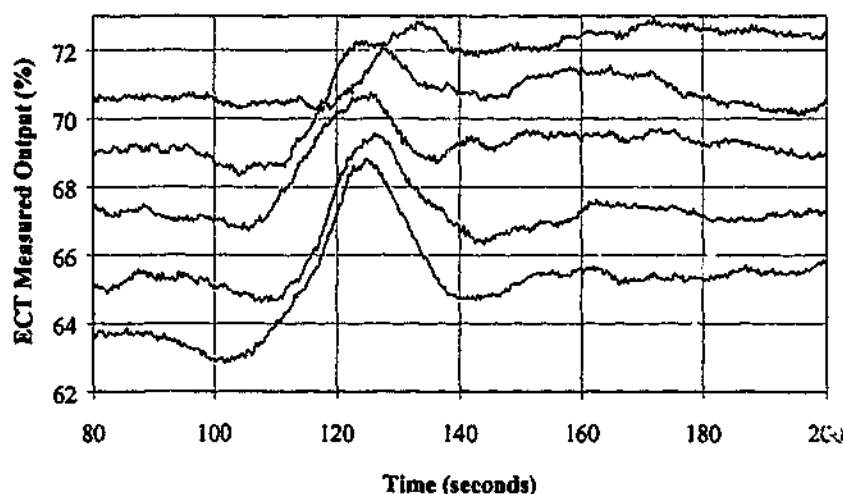


Figure 6.2 Tracer response profiles for five consecutive runs. Note that the initial concentration value for each subsequent run corresponds to the final value of the previous run. A 5 second moving average has been applied to this chart for clarity.

Data for the initial and final tracer concentration (on the original ECT output scale) can be calculated by taking the linear average for the first 50 seconds and last 50 seconds of data. The difference in the initial concentration for each run can then be subtracted, to remove the offset associated with each run (the first run of the set being used as the basis). This results in the data appearing as shown in Figure 6.3.

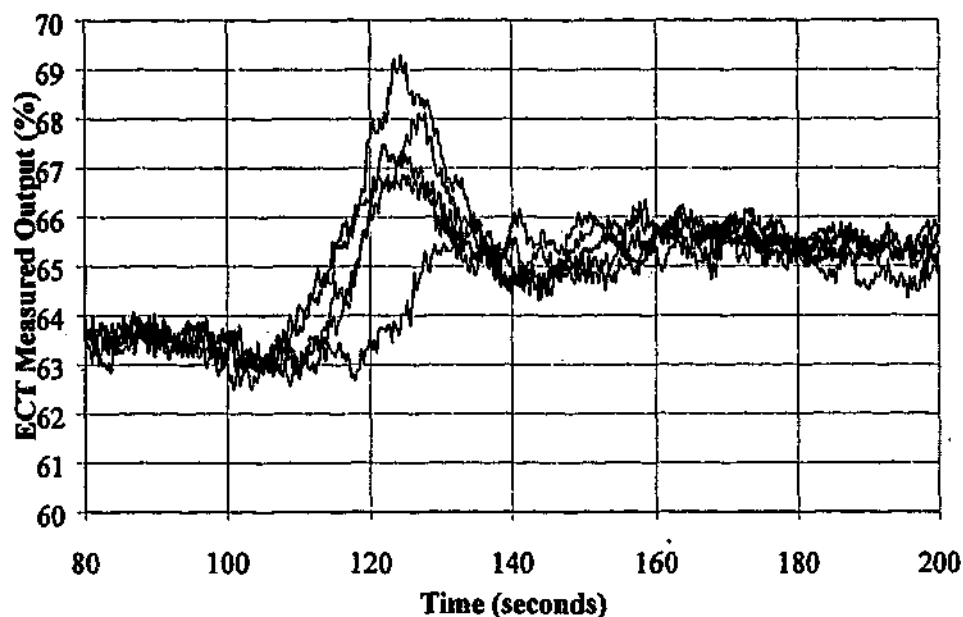


Figure 6.3 Tracer response profiles for five consecutive runs after the initial concentration off-set has been removed.

Note that strictly speaking this off-set removal approach is only approximately valid, due to the fact that the ratio of final tracer to initial tracer concentrations is not *exactly* the same for the runs. However, it is very close, and for the purposes of the analysis undertaken here, the error contributed by this simplified approach is not significant.

Having removed the off-set associated with the different runs, the data can be averaged to produce the average concentration response profile for the conditions under which these runs were conducted. The result is shown in Figure 6.4.

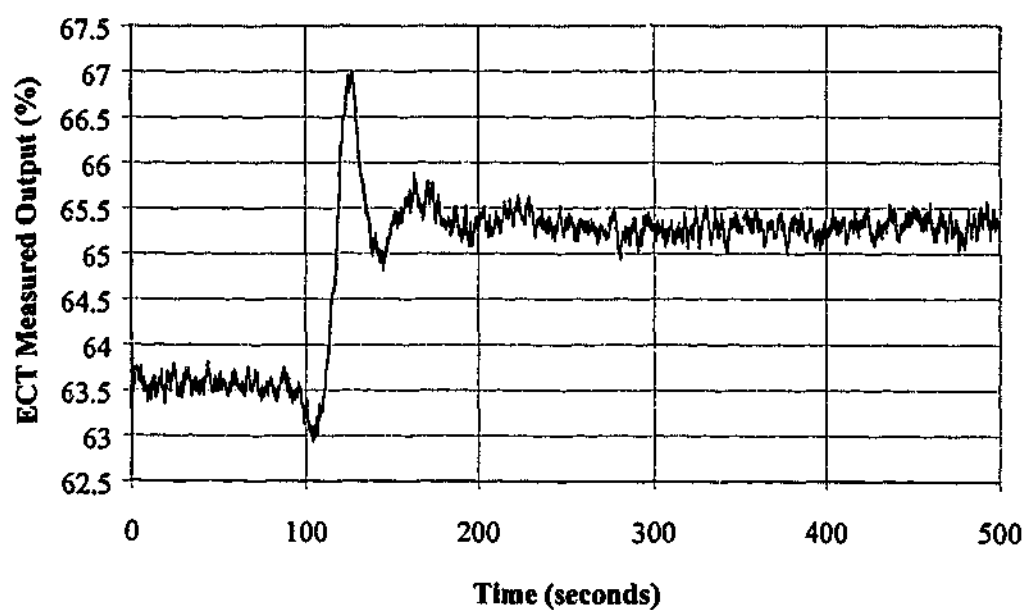


Figure 6.4 Average transient tracer concentration response profile for the original five runs.

Knowing that the tracer was added to the bed surface at $t = 100$ seconds, and the peak response (corresponding to the centre of the "clump" of tracer arriving at the centre of the measurement electrodes) occurs at $t = 127.5$ seconds on average, it is a simple matter to calculate the average solids downflow velocity, based on the distance between the bed surface and the centre of the measurement electrodes:

$$U_{sd} = \frac{\Delta h}{\Delta t} = \frac{H_s - H_e}{t_{peak} - t_{added}} \quad (6.10)$$

which, for the case presented here is:

$$U_{sd} = \frac{295 - 150}{127.5 - 100} = 5.3 \text{ mm/s}$$

Although the bed is gently bubbling and thus the operational bed height during mixing experiments is greater than H_s (typically by about 20 mm including bed expansion and tracer addition), the value of H_s was used to account for the fact that the tracer deposited on the bed surface doesn't sit "on" the surface, but sinks into it immediately, presenting an even bed surface at $t = 100$ s.

As far as the variation in the above solids downflow velocity is concerned for the example runs, the runs which deviated greatest either side of the average peak shown in Figure 6.4 result in U_{sd} values of 4.4 mm/s and 6.0 mm/s, with the standard deviation in solids downflow velocity for the set of 5 runs being 0.58mm/s, calculated from:

$$\sqrt{\frac{n\sum x^2 - (\sum x)^2}{n^2}} \quad (6.11)$$

(where x is the individual sample value and n is the number of samples.)

6.3.2 Preliminary Study – Effect of Tracer Particle Size

Although the primary goal of this work was to compare solids mixing characteristics at different scales, a choice for the tracer particle size had to be made for each bed scale and for each bed material. Ideally, the tracer particles would be of identical size, shape,

density and U_{mf} . Practically, however, a perfect match was not possible, and in one particular planned similarity experiment, it was known beforehand that the tracer and bed material particle sizes would be significantly different. Thus it was considered necessary to investigate the effect of differences between tracer and bed material properties, in order to assess what influence these differences might have on the mixing results.

First of all, there were some inherent differences between the two materials that could not be avoided. For example, the silica sand bed material had a sphericity of approximately 0.85, the ballotini had a sphericity of approximately 1. The particle density of the bed material was 2650 kg/m^3 , that of the ballotini was 2500 kg/m^3 (Burwell, 2000). As far as the similarity experiments go, these differences were maintained at both scales, so they are not likely to affect the results at one scale more than the other. From experiments (eg Figure 6.7) this small density difference was found to be insufficient to cause segregation of tracer particles and bed particles in situations where the particles were of similar size. Sphericity differences, however, can affect bubble wake fraction (eg Rowe and Partridge, 1965) for similar diameter particles. As can be seen from equations 6.3 and 6.4, the downwards solids velocity is generally taken to be a direct consequence of solids upflow due to bubbles (*ie* so that the net solids flux in the bed is zero), so a change in bubble wake fraction will ultimately affect solids downflow velocity. The same can be said for drift fraction and visible bubble fraction. However, providing that the tracer constitutes a negligible proportion of the total bed material and is of similar particle size, tracer addition is unlikely to alter bubble properties, and hence a sphericity difference alone between tracer and bed material will not affect the solids downflow velocity. Practically, tracer concentration was limited to less than 20% of the total bed inventory by replacing the bed with fresh material after every 5 runs. And as previously mentioned, even for the test case of 10 repeated runs there was no observed effect of the increasing tracer concentration on the transient tracer response profiles or the solids downflow velocity (see Appendix G).

However, if the particle size between tracer and bed material are sufficiently different that segregation occurs, the tracer will not follow the same behaviour as the bulk bed material. Because there was likely to be some discrepancy between the tracer and solids particle sizes, some initial experiments were performed to investigate the effect of the relative size of the tracer particles on results for solids downflow velocity. The bed material and tracer material combinations investigated in the 146 mm bed were as shown

in Table 6.1. (The silica sand bed material used in these preliminary experiments was Commercial Minerals Grade 50N – details are provided in Appendix C).

Combination	Bed Material	Tracer	U_{mfBM} (m/s)	U_{mfT} (m/s)	U (m/s)
1(a)	Silica Sand (125–355 μ m)	GB4 Ballotini	0.046	0.085	0.066
1(b)		(212–425 μ m)			0.090
2(a)	As above	GB3 Ballotini	As above	0.079	0.066
2(b)		(250–425 μ m)			0.090
3(a)	As above	GB5 Ballotini	As above	0.052	0.066
3(b)		(180–300 μ m)			0.090
4(a)	As above	GB6 Ballotini	As above	0.048	0.066
4(b)		(150–250 μ m)			0.090
5	As above	GB7 Ballotini (106–212 μ m)	As above	0.019	0.066

Table 6.1 Tracer and bed material combinations for investigating the effect of tracer to bed material particle size mis-match. U_{mfBM} and U_{mfT} correspond to the minimum fluidization velocities of the bed material and tracer respectively.

The same bed material was used for all of these experiments, and at least 5 runs were conducted at a given superficial gas velocity. The minimum fluidization velocities of all the tracer materials were measured experimentally (the method and results for these and other minimum fluidization tests are presented in Appendix C).

For the conditions shown in Table 6.1, it can be noted that Conditions 1 and 2 correspond to tracer particles with U_{mf} much greater than the bed material; Conditions 3 and 4 correspond to tracer particle and bed material fairly closely matched, and Condition 5 corresponds to a tracer material much finer than the bed material.

Observations about the effect of tracer particle size and superficial gas velocity were as follows:

When the $U_{mf}(\text{tracer}) \gg U_{mf}(\text{bed})$ and U was between the U_{mf} values of the two materials, tracer tended to descend rapidly as a single large coherent mass, causing a single strong peak in the tracer response profile. The solids downflow velocity of the tracer was high. Since the superficial gas velocity was less than that of the tracer, it is

highly likely that the clump of descending tracer was unfluidized, hence the solids downflow velocity for the tracer measured in this case is likely to be higher than that of the bed material. Figure 6.5 shows the average response profile for this situation (typical of all the individual runs) corresponding to Condition 2(a) in Table 6.1; results for Condition 1(a) were very similar.

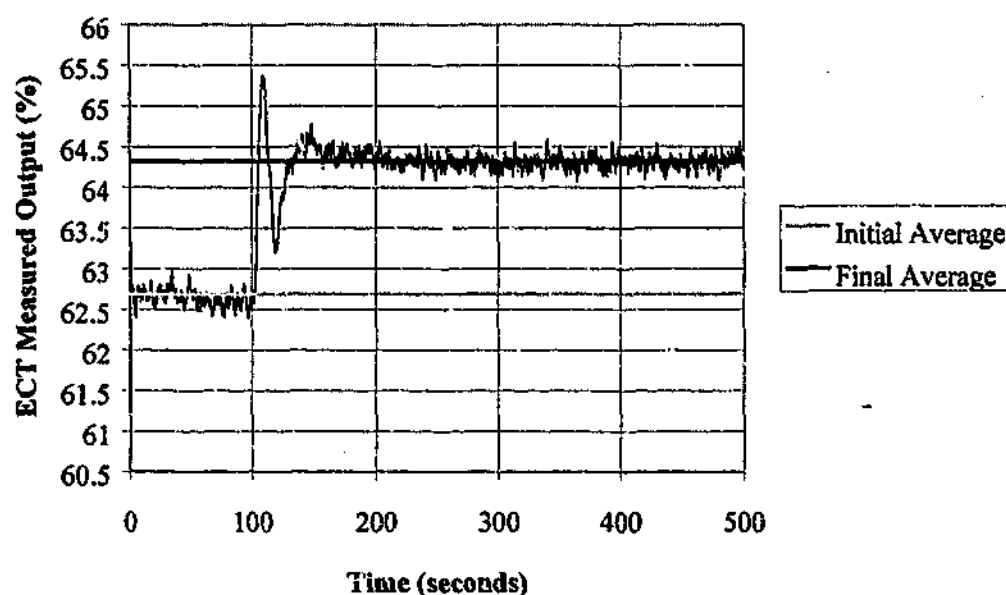


Figure 6.5 Transient trace response profile for tracer with $U_{mf}(\text{tracer}) > U > U_{mf}(\text{bed})$. The tracer descends rapidly through the ECT measurement volume as an unfluidized clump, mixing occurs only after the tracer reaches distributor level. The final concentration registered at ECT level may not be representative of the entire bed.

Note also in Figure 6.5 that the concentration response decreased after the initial peak at the same rate as the increase. This was because the tracer clump continued descending (below the ECT measurement height) towards the distributor. At the distributor the clump of tracer dispersed into the bed material, and ultimately the concentration registered at ECT electrode height became constant. Whether the *entire* bed was uniformly mixed at this point is open to conjecture.

When the $U_{mf}(\text{tracer}) \gg U_{mf}(\text{bed})$ and U was greater than the U_{mf} values of the two materials, tracer tended to mix with the bed material rapidly and no peaks were observed in the tracer response profile. It is not possible to identify a specific point on the concentration response profile corresponding to the appearance of downflowing material at ECT electrode height, hence no solids downflow velocity can be reliably calculated. An overall concentration increase with time can be observed, and the new steady-state

concentration was reached more rapidly than with the lower gas velocity in the previously described situation. Note also that the increased level of bubble activity registered by the ECT (compared with the previous situation) tends to "mask" the tracer behaviour somewhat. Figure 6.6 shows the average response profile for this situation, which was typical of all the individual runs. The data of Figure 6.6 correspond to Condition 2(b) in Table 6.1; again, results for Condition 1(b) were very similar.

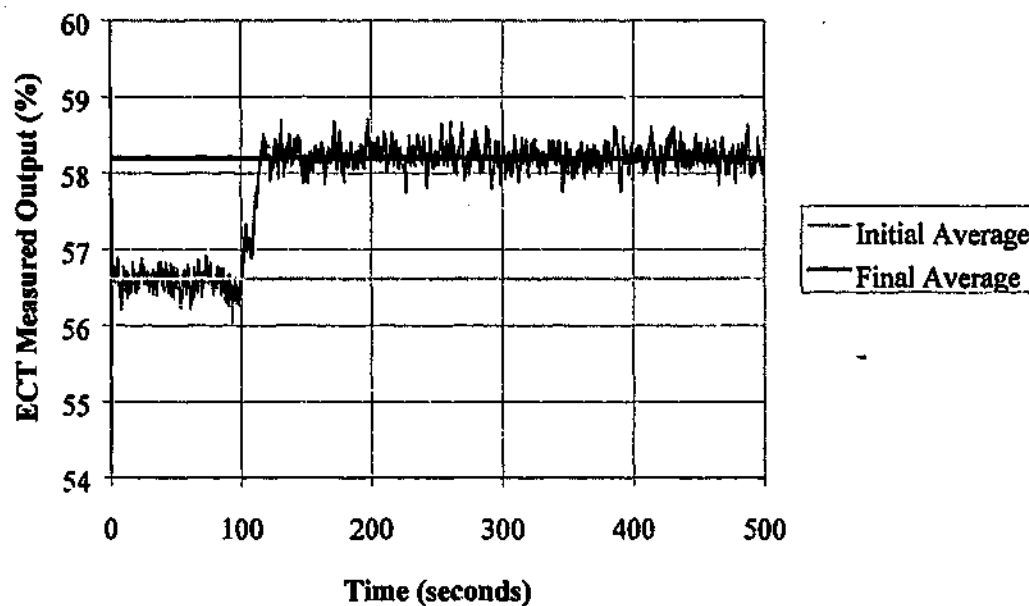


Figure 6.6 Transient trace response profile for tracer with $U > U_{mf}(\text{tracer}) > U_{mf}(\text{bed})$. The tracer mixes with bed material during descent, no individual clumps of tracer can be discerned. The final steady-state concentration (registered at ECT level) is reached rapidly.

When $U_{mf}(\text{tracer}) \approx U_{mf}(\text{bed})$, and U was slightly above the U_{mf} values of the two materials, tracer tended to mix with the bed material to some extent, producing a single small peak in the tracer response profile. Thus a solids downflow velocity could be determined by equation 6.11, which is likely to be representative of the bed material. The broad nature of the peak reflects the contributions of individual experiments. Figure 6.7 shows the typical averaged response curve for this situation (results of Condition 3(a), Table 6.1; results for Condition 4(a) were very similar).

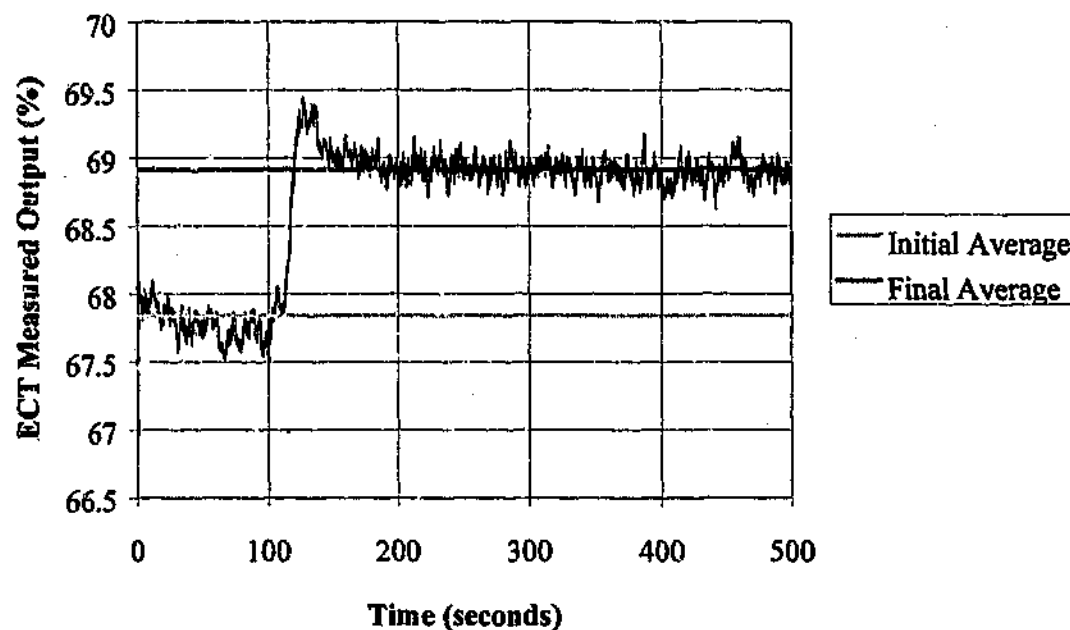


Figure 6.7 Transient trace response profile for tracer with $U > U_{mf}(\text{tracer}) \approx U_{mf}(\text{bed})$. The tracer descends with the bed material, a concentration peak corresponding to a high concentration region of tracer reaching the ECT measurement height can be identified, thus allowing the calculation of a solids downflow velocity. The final steady-state concentration (registered at ECT level) is reached gradually.

When $U_{mf}(\text{tracer}) \approx U_{mf}(\text{bed})$, and U was well above the U_{mf} values of the two materials, tracer tended to mix rapidly with the bed material, descending in a mixed state, producing no peaks in the tracer response profile, and reaching the final steady-state concentration more rapidly than the previous situation with lower superficial gas velocity. Thus a solids downflow velocity could not be determined for this situation. The increased level of bubble activity registered by the ECT also tended to "mask" the tracer behaviour somewhat. Figure 6.8 shows the average transient tracer response profile for this situation (data from Condition 3(b), Table 6.1; results for 4(b) were very similar).

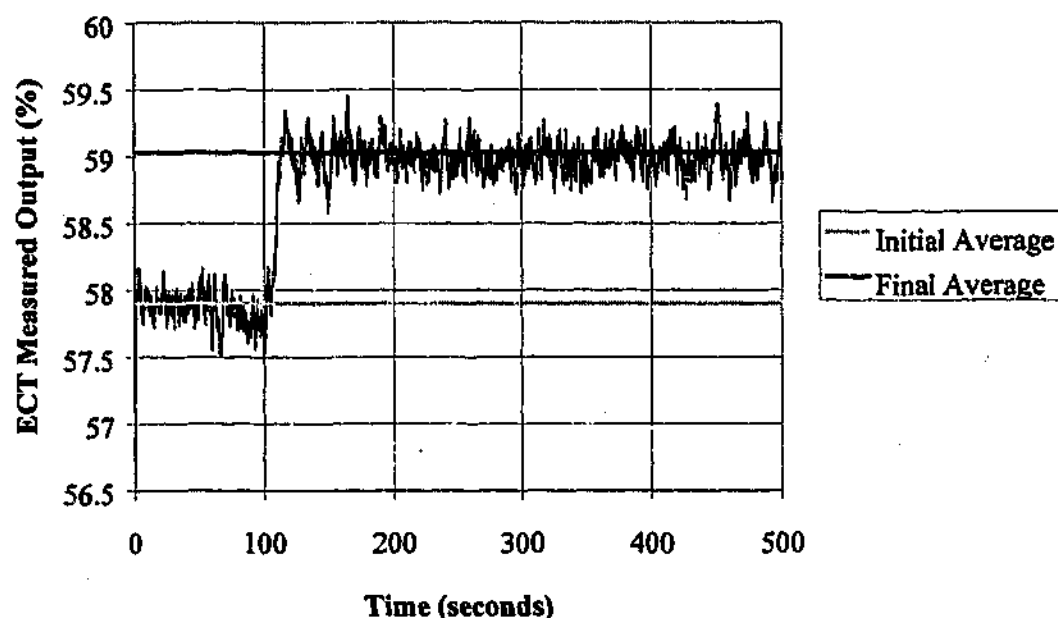


Figure 6.8 Transient trace response profile for tracer with $U \gg U_{mf}(\text{tracer}) \approx U_{mf}(\text{bed})$. The tracer mixes with bed material during descent, no individual clumps of tracer can be discerned. The final steady-state concentration is reached rapidly.

When $U_{mf}(\text{tracer}) < U_{mf}(\text{bed})$, and U was above the U_{mf} values of the two materials, tracer tended to segregate and remain on top of the bed. There was essentially no tracer concentration change at the ECT measurement level, even after several runs. Figure 6.9 shows the average transient tracer response profile for this situation (data from Condition 5, Table 6.1).

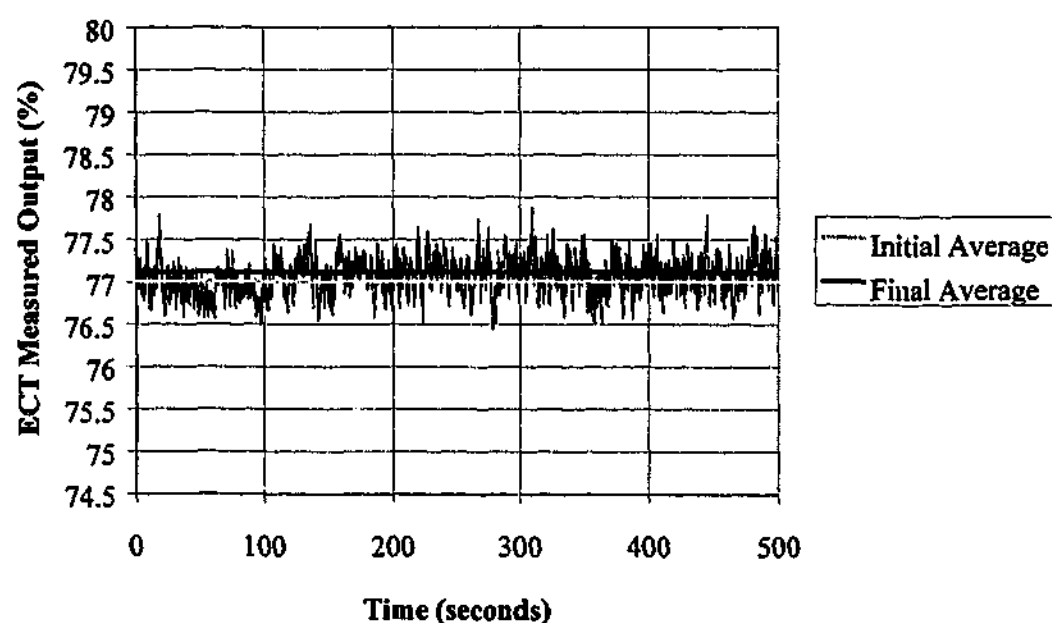


Figure 6.9 Transient trace response profile for tracer with $U \gg U_{mf}(\text{bed}) > U_{mf}(\text{tracer})$. Segregation occurs and the tracer remains on the bed surface. A very minor change in tracer concentration is noted at ECT level.

Where possible for the results of these initial tests, a solids downflow velocity was calculated using equation 6.10. Results for solids downflow velocities are given in Table 6.2, with the estimations of Baeyens and Geldart (1986) and Kunii and Levenspiel, (1969) calculated below.

U_{mfT}/U_{mfBM}	U/U_{mfBM}	U_{sd} average (mm/s)	Number of Runs	Standard Deviation (mm/s)
1.85	1.43	8.0	8	1.4
1.72	1.43	14	5	1.1
1.13	1.43	4.5	12	4.8
1.04	1.43	3.9	14	4.3

Table 6.2 results for solids downflow velocities of tracer particles of different sizes for the same bed material and superficial gas velocity. U_{mfBM} and U_{mfT} correspond to the minimum fluidization velocities of the bed material and tracer respectively.

Note that the standard deviation for the cases where the tracer and bed materials are closely matched is large (similar size to the average value of U_{sd}). This gives an indication of the extent to which the measured solids downflow velocity varies from one run to the next in this situation. Since the standard deviations for the results involving tracer much larger than the bed material are different (and much smaller) than the former case, this indicates that the rate of tracer downflow in these cases is not simply due to the bulk bed downflow. The tracer is settling faster than the solids downflow velocity of the bed material and in a far more repeatable way.

The correlations for solids downflow velocity of Baeyens and Geldart (1986) and Kunii and Levenspiel (1969) can be used to get an approximate estimate for the solids downflow velocity in the bed. (Note that for the purposes of comparison with the experimental data, the correlations do not in any way account for differences between tracer and bed material.)

In both cases, it is first necessary to calculate bubble properties. Equivalent bubble diameter d_{eq} can be estimated from the correlation of Darton *et al.* (1977), which was introduced in Chapter 2. For the purposes of this analysis, the bubble size will be calculated for the axial point midway between the centre of the measurement electrodes and the settled bed height, and assumed to be representative of the "average" bubble size present in the top half of the bed. The equation of Darton *et al.*, (1977) is:

$$d_{eq} = 0.54(U - U_{mf})^{0.4} (h + 4\sqrt{A_0})^{0.8} / g^{0.2} \quad (6.12)$$

where (in this case):

$$U = 0.066 \text{ m/s}$$

$$U_{mf} = 0.046 \text{ m/s}$$

$$h = 223 \text{ mm}$$

$$A_o \text{ (for the 146 mm bed with bubble cap distributor)} = 9.301 \times 10^{-4} \text{ m}^2 \text{ per orifice}$$

$$g = 9.81 \text{ ms}^{-2}.$$

Substituting these values yields an equivalent bubble diameter of $d_{eq} = 30.5 \text{ mm}$. Using the equation of Kunii and Levenspiel (1991) for bubble rise velocity,

$$U_{br} = \left[0.711(gd_{eq})^{1/2} \right] 1.2 \exp\left(-1.49 \frac{d_{eq}}{D}\right) \quad \text{for } 0.125 < \frac{d_{eq}}{D} < 0.6 \quad (6.13)$$

yields a bubble rise velocity of 0.343 m/s.

The bubble fraction ε_B can be estimated from

$$\varepsilon_B = \frac{Y(U - U_{mf})}{U - U_{mf} + U_{br}} \quad (6.14)$$

where Y for sand is taken as 0.67 (from Werther, 1978, 1983), which yields a value of $\varepsilon_B = 0.033$.

Kunii and Levenspiel (1969) provide two sources for estimating the wake fraction β_w ; from either source, for the bed material particles with a mean diameter of $d_p = 210 \mu\text{m}$, the value of $\beta_w = 0.21$ is arrived at. On the other hand, Baeyens and Geldart (1986) tabulate some values of both wake and drift fraction, from which the values $\beta_w = 0.26$ and $\beta_d = 0.42$. Given the differences in these values, it is expected that the Baeyens and Geldart correlation will result in a higher solids downflow, since they are assuming a greater proportion of each rising bubble is capable of solids transport.

Applying the data for bubble and wake fraction in the Kunii and Levenspiel (1969) approach;

$$U_{sd} = \frac{\beta_w \epsilon_B U_b}{1 - \epsilon_B - \beta_w \epsilon_B} \quad (6.15)$$

and noting that in their scheme they account for the difference between the rise of a single bubble and multiple bubbles by:

$$U_b = (U - U_{mf}) + U_{br} \quad (6.16)$$

the value of solids downflow velocity arrived at is $U_{sd} = 2.6$ mm/s.

The Baeyens and Geldart (1986) approach (with their various fraction estimates);

$$U_{sd} = \left(\frac{\beta_w + 0.38\beta_d}{1 - \epsilon_B - \epsilon_B(\beta_w + \beta_d)} Y \right) (U - U_{mf}) \quad (6.17)$$

yields $U_{sd} = 5.9$ mm/s. (Different assumptions for β_w , β_d , ϵ_B and Y will affect the result, of course, but ultimately the effect on U_{sd} is small for all parameters except Y , and this is likely to be constant for the conditions investigated – Baeyens and Geldart, 1986.)

Given the number of approximations involved in either one of these approaches, and the scatter in the experimental data with which the comparison is being made, closely matching results are not to be expected. However, the results of these correlations support the view that the larger-sized tracer particles descend at a velocity higher than that expected for the bulk bed material; and the experimental values for the more closely matched tracer particles agree better with the above literature estimates.

As a consequence of these initial experiments, it is possible to conclude that small variations in U_{mf} compared with U_{mfBM} are tolerable, having minimal effect on the measured solids downflow velocity, within the scatter of the experimental data. Large discrepancies, however, are to be avoided, because the measured solids downflow velocity in those cases will be influenced by segregation between tracer and bed material.

6.3.3 Solids Mixing Comparisons Between 146 mm and 300 mm Scales

For the similarity comparison, ballotini tracer materials and sand bed materials were chosen for the two scales (146 mm and 300 mm) such that the two minimum fluidization velocities were as closely matched as possible for the materials available. Where this was not possible, attempts were made to maintain the ratio U_{mfT}/U_{mfBM} similar at the two scales. Table 6.3 shows the situations explored:

Pair	Bed	U_{mfBM}	U_{mfT}	U	U_{mfT}/U_{mfBM}	U/U_{mfBM}
1	146 mm	0.039	0.048	0.056	1.23	1.44
	300 mm	0.058	0.079	0.084	1.36	1.45
2	146 mm	0.046	0.048	0.066	1.04	1.43
	300 mm	0.070	0.079	0.100	1.13	1.43
3	146 mm	0.085	0.085	0.122	1.00	1.44
	300 mm	0.125	0.085	0.180	0.68	1.44

Table 6.3 Operating conditions and tracer/bed material combinations for the solids mixing similarity experiments. 14 runs were carried out in each bed for each condition listed. Absolute velocities in m/s.

As can be seen from Table 6.3, neither the match between tracer and bed minimum fluidization velocities, or the match of their ratio for scaled pairs was perfect. The largest discrepancy occurred for the 300 mm bed in Pair 3 where the tracer U_{mf} was significantly lower than that of the bed. Given the conclusions of Section 6.3.3, it was not expected that this particular combination would give reliable results.

The bed materials chosen for each pair were silica sands matched according to the simplified scaling criteria of Horio *et al.*, (1986a). The value of m for the geometric scale change is:

$$m = \frac{D_2}{D_1} = \frac{300}{146} = 2.05 \quad (6.18)$$

and thus the value of \sqrt{m} required for scaling the U_{mf} values of the bed materials is 1.43. The U_{mf} ratios actually obtained for Pairs 1, 2 and 3 were 1.49, 1.52 and 1.47 respectively (all within 10% of the ideal ratio).

As mentioned previously, due to the nature of solids mixing and a range of individual experiments giving a range of results, the approach adopted here was to perform a number of independent experimental runs, and then take the average of the resulting transient tracer concentration. In the initial work at the 146 mm bed this worked well, resulting in average tracer response profiles which showed the characteristic trends of all the contributing experiments, but tending to improve the clarity of the trend when compared with the original results. In the case of the similarity experiments, 14 runs (in some cases more) were averaged to produce the final response profile, and once again, the procedure resulted in profiles which embodied the characteristics of the individual runs (for both the 146 mm and 300 mm beds).

In the following pages, results are presented for the three pairs of similarity runs. The ECT measured output in % is plotted as a function of time for the 14 or so runs in each set. Moving averages of 2 second and 3 second spans were applied to the runs from the 146 mm and 300 mm beds respectively to reduce the "bubble noise". It was noted that no further significant changes occurred in the concentration profile for the 300 mm bed beyond about 500 seconds, (even though data was recorded for a total of 1000 s for this scale). Because it is the peak in the profile which is of interest, all the profiles have been plotted for the time range 0 to 500 s. Elapsed time to peak (t_{peak}) values stated on the charts are for the maximum ordinate value recorded in the trend, although it should be noted that the peaks are generally wide, indicating that a range of solids downflow velocities have contributed to the results. The initial "spike" in the trends (close to $t = 0$) is due to the moving average calculations not having prior data to calculate, and can be safely ignored.

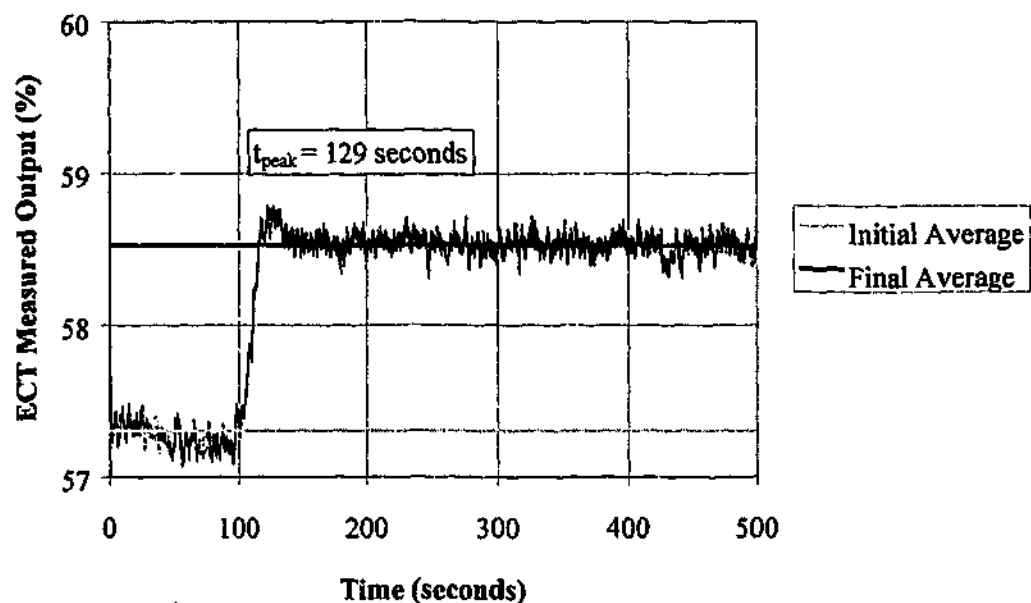


Figure 6.10 Average tracer response profile for the 146 mm bed, (Pair 1), with $U/U_{mfBM} = 1.44$ and $U_{mf}/U_{mfBM} = 1.23$. The system was scaled using the simplified criteria to match the 300 mm bed, results of which are shown in Figure 6.11.

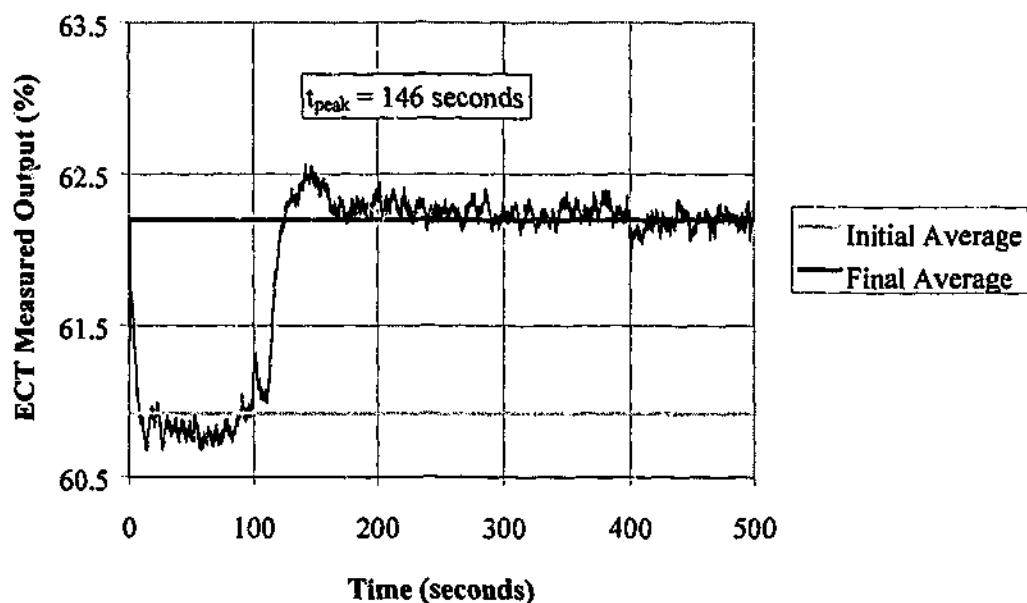


Figure 6.11 Average tracer response profile for the 300 mm bed, (Pair 1), with $U/U_{mfBM} = 1.45$ and $U_{mf}/U_{mfBM} = 1.36$. The system was scaled using the simplified criteria to match the 146 mm bed with results presented in the previous figure.

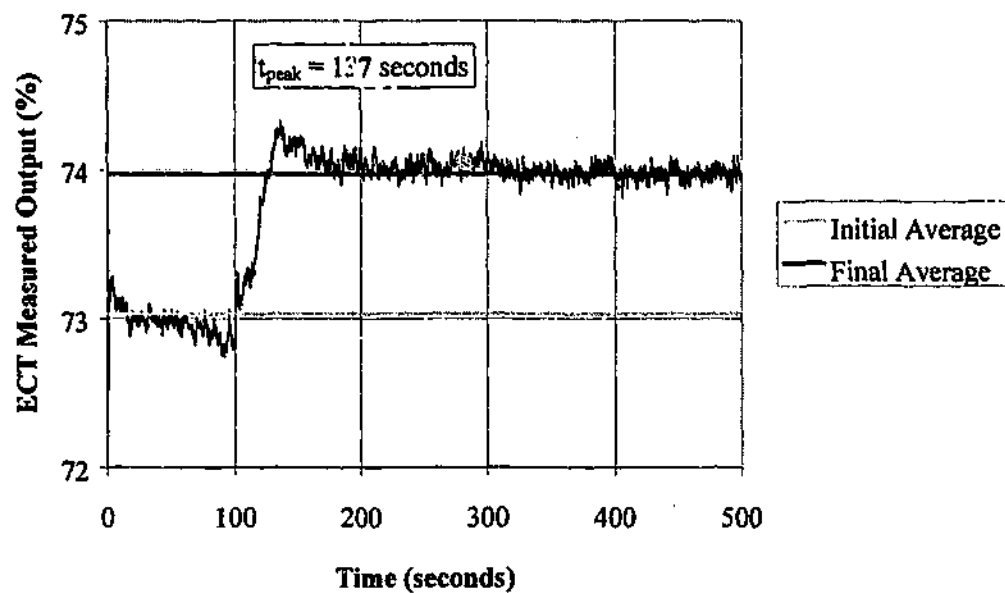


Figure 6.12 Average tracer response profile for the 146 mm bed, (Pair 2), with $U/U_{m/BM} = 1.43$ and $U_{mf}/U_{m/BM} = 1.04$. The system was scaled using the simplified criteria to match the 300 mm bed, results of which are shown in Figure 6.13.

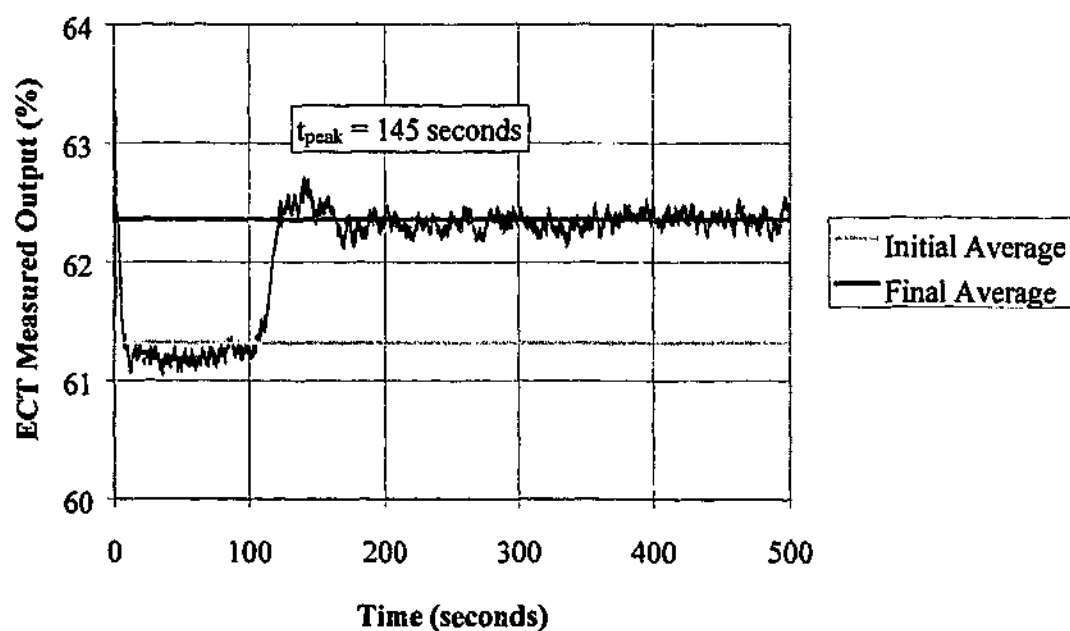


Figure 6.13 Average tracer response profile for the 300 mm bed, (Pair 2), with $U/U_{m/BM} = 1.43$ and $U_{mf}/U_{m/BM} = 1.13$. The system was scaled using the simplified criteria to match the 146 mm bed with results presented in the previous figure.

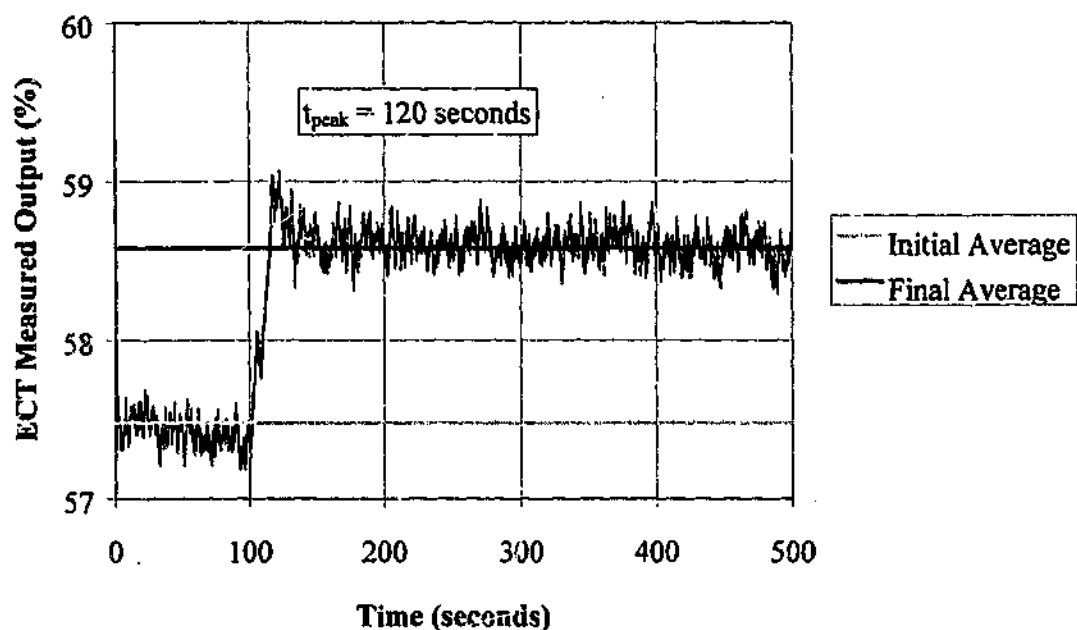


Figure 6.14 Average tracer response profile for the 146 mm bed, (Pair 3), with $U/U_{mfBM} = 1.44$ and $U_{mf}/U_{mfBM} = 1.00$. The system was scaled using the simplified criteria to match the 300 mm bed, results of which are shown in Figure 6.15.

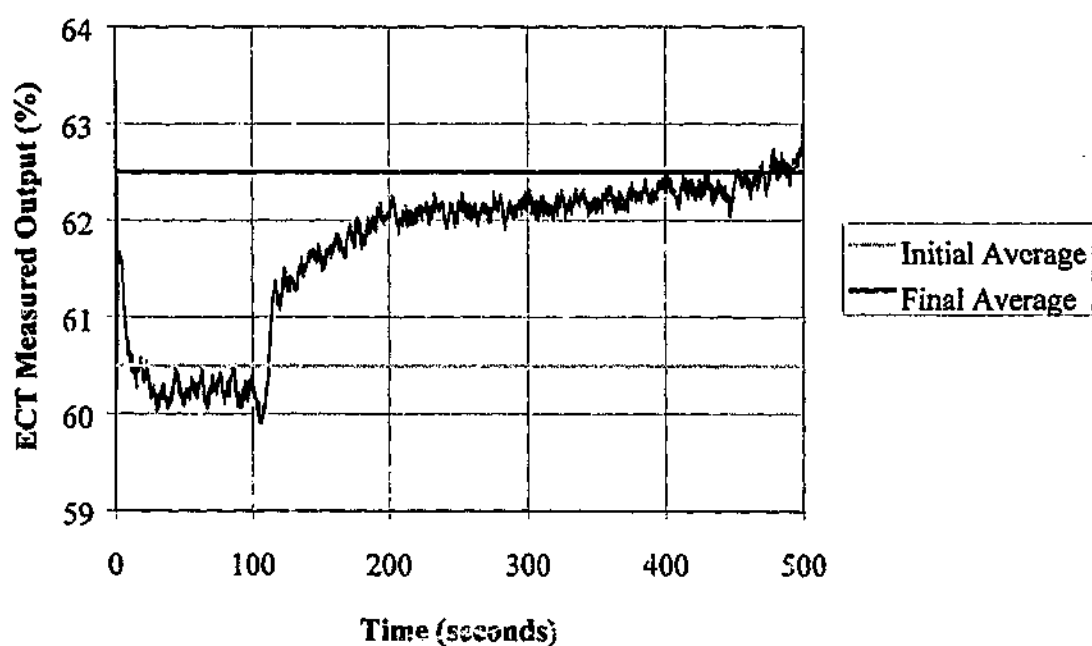


Figure 6.15 Average tracer response profile for the 300 mm bed, (Pair 3), with $U/U_{mfBM} = 1.44$ and $U_{mf}/U_{mfBM} = 0.68$. The system was scaled using the simplified criteria to match the 146 mm bed with results presented in the previous Figure, however, there was a significant discrepancy in tracer particle size.

A comparison of the results shown in Figures 6.10 to 6.15 yields the following points:

- In all except the final case (Figure 6.15), the trends are similar. This confirms that the tracer is mobile within the beds in the same general fashion, except in the last case where the tracer was undersized when compared with the bed material, and segregation effects dominate the results.
- The concentration peaks occur later at the larger scale. This is a qualitative indication of hydrodynamic similarity; as from dimensional analysis of the simplified similarity criteria it is to be expected that things occur in the larger system \sqrt{m} times more slowly.
- The concentration peaks are wider at the larger scale. This is also in accord with the expectations of the simplified similarity criteria; for similar dimensionless distribution of solids downflow travel times, the width of the distributions when plotted on the same scale should increase.
- The average t_{peak} times observed for the 300 mm scale are relatively unaffected by the change in particle size, (except in the case where segregation occurred). The peaks are broad, however, so a wide range of solids downflow velocities has contributed to each result.
- The average t_{peak} times observed for the 146 mm scale are slightly more diverse, with the fastest downflow occurring for the largest bed material particle size (Figure 6.14). The slowest downflow was for the bed material with intermediate U_{mf} , (Figure 6.12), however this material had a much wide particle size distribution than the others used at this scale, which may account for the behaviour.
- It is not possible to realistically calculate or compare the mixing times (ie time to new steady-state concentration) of any of the systems studied, given the fluctuations present in the data.
- Once again, the solids downflow velocities can be compared with the predictions of Kunii and Levenspiel, (1969) and Baeyens and Geldart (1986). Table 6.4 shows the comparison, with the estimated values of the various associated bubble-related fractions also provided.

Standard deviations were again of similar magnitude to the measured downflow velocities. As can be seen from Table 6.4, the measured values of solids downflow velocity and the correlations show qualitative agreement. Much, of course depends on the values of the fractions shown in the last column of the table. For the purposes of this

comparison, the values chosen follow the approach taken by the authors of the two solids downflow velocity correlations.

Pair	Bed	U_{sd} (expt)	U_{sd} (K&L)	U_{sd} (B&G)	$\varepsilon_p, \beta_w, \beta_d, Y$
1	146 mm	5.0	2.5	5.0	0.03, 0.26, 0.42, 0.67
	300 mm	6.3	3.8	7.4	0.03, 0.25, 0.4, 0.67
2	146 mm	3.9	2.9	6.0	0.04, 0.26, 0.42, 0.67
	300 mm	6.4	4.4	7.8	0.04, 0.23, 0.25, 0.67
3	146 mm	7.3	5.6	10.0	0.06, 0.23, 0.35, 0.67
	300 mm	N/A	8.7	14.6	0.05, 0.23, 0.35, 0.67

Table 6.4 Comparison of the experimentally measured solids downflow velocities and those calculated from the correlations of Kunii and Levenspiel (1969) and Baeyens and Geldart (1986). Velocities expressed in mm/s

Finally, the simplified similarity scaling criteria predict that for correct scale up, characteristic velocities should scale by \sqrt{m} ; and this ratio should be applicable to the solids downflow velocity. Because the bed materials have not been perfectly matched for the scale change, the value of \sqrt{m} determined either from the geometry change or the ratio of U_{mf} values in the two beds will yield slightly different results. In Table 6.5, a comparison is made between the \sqrt{m} values based on bed geometry, bed material U_{mf} , the measured U_{sd} , and the predicted values of U_{sd} .

Pair	\sqrt{m} (geo)	\sqrt{m} (U_{mf})	\sqrt{m} (U_{sd} expt)	\sqrt{m} (U_{sd} K&L)	\sqrt{m} (U_{sd} B&G)
1	1.43	1.49	1.26	1.52	1.48
2	1.43	1.52	1.64	1.52	1.30
3	1.43	1.47	N/A	1.55	1.46

Table 6.5 comparison of the similarity criteria scaling ratio \sqrt{m} calculated from bed geometry, measured bed material minimum fluidization velocity, measured solids downflow velocity and predicted solids downflow velocities.

The results here show that whilst the average solids velocities measured indicate some general trend in accord with the scaling criteria, a close numerical agreement is not achieved. The two correlations, however show a reasonable agreement with the predictions of the scaling criteria.

Although the novel ECT/tracer technique is successful, it is limited by the fact that the ECT system responds to both bubbles and tracer; the bubbles add an undesirable layer of "noise" to the tracer response profiles. The use of tracer with a higher dielectric constant, and the application of this technique to "bubbleless" fluidization may constitute worthwhile areas of future work.

With regards to the similarity comparisons made, it can only be concluded that the solids downflow velocity results from these experiments lend qualitative support to the simplified scaling law, but precise numerical agreement is lacking.

6.4 Float Tracer Study of Solids Motion

Solids motion was characterised in the three larger scaled beds using neutrally-buoyant spherical float tracers. The experimental arrangement has been described in Chapter 3. Three tracers with identical diameter and density (but different colour) were placed into a given bed for each experiment. The appearance and disappearance of the float tracers was recorded at the bed surface. "Blacklight" illumination and fluorescent paint on the float tracers made them easily distinguishable from the surrounding material at the bed surface. There were no pressure probes or other internals present in the beds during these experiments.

6.4.1 Basis for Comparison

The objective of the float tracer experiments is to verify whether the following theoretical scenario for hydrodynamic similarity is supported by experimental evidence from beds scaled by the simplified similarity criteria.

Consider two beds which are hydrodynamically similar in theory. In a horizontal plane at any dimensionless height, the proportions of upflowing and downflowing solids will be the same. Also, the dimensionless bubble rise and solids downflow velocities will be the same for the same dimensionless height. The dimensionless bubble sizes and their distribution will also be the same.

Now consider a neutrally buoyant spherical object of the same dimensionless size placed at random in each of the two similar beds. For a sufficiently large number of trials, the object has the same probability of being placed in an upflow or downflow region, and because it is geometrically similar, it will experience the same dimensionless upwards or downwards velocity. On average, it has the same probability of transferring from one phase direction to the other (*ie* upwards to downwards or vice versa).

Thus to an observer at the bed surface, for a sufficiently long number of trials, the object should appear at the bed surface for the same proportion of the (dimensionless) time, and should exhibit the same distribution of dimensionless cycle times in between appearances at the bed surface.

This proposal was put to the test experimentally.

6.4.2 Float Tracer Logging Procedure

The run-times for the solids mixing experiments were 90, 60 and 45 minutes in the 1560, 600 and 300 mm beds respectively. The reason that three tracers were used in each experiment was to increase (triple) the number of statistics generated for a given length of experiment. After the experiments were recorded, videotapes were viewed and the quantity of interest, namely the time between appearances of a given coloured tracer was logged.

The time between appearances of a given coloured tracer was logged on the pressure probe data acquisition computer using the following approach.

It was observed that the time spent by the tracers on the bed surface was very short compared with the time spent in the bed (by a factor of at least 10). Also, the time spent in the bed was very long compared with the reaction time of an observer watching the taped images (approx. 0.3 seconds – less with coffee). Therefore, a set of three push-buttons (one button for each tracer colour) were connected in place of the three pressure transducers used in the pressure probe experiments described in Chapter 4.

The buttons were set up to short circuit the analog input of a given line when in the “off” position (registering 0 volts), and send the computer’s own excitation signal (+5VDC) into the analog input when in the “on” position (registering 5 volts). The sampling rate

of the data acquisition software was set to a relatively low rate (5Hz). The tapes were played, with the observer pushing the appropriate button each time a given colour tracer was at the bed surface, and the button status for the three lines was logged. The concept for recording a single tracer appearance is illustrated in Figure 6.16.

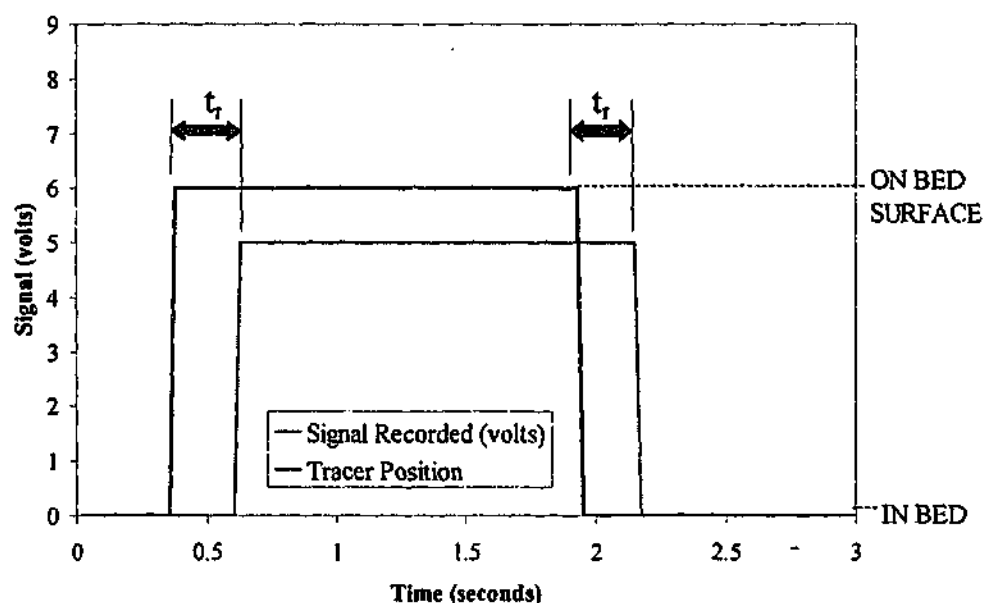


Figure 6.16 Illustration of the technique used to record float tracer location. t_r is the reaction time of the observer. The quantity of interest, namely the length of time spent by the tracer in the bed between surface appearances (not shown in full) was found to be at least an order of magnitude greater than the time spent at the bed surface in all the beds. The error introduced by t_r is minimal.

The resulting time-series of square wave pulses could then be used to interpret the time spent by the tracers as they circulated to different bed depths under the influence of solids downflow and bubble rise. This was done by measuring the time differential between rising edges of each successive square wave as shown in Figure 6.17 (via spreadsheet calculation).

Note again, that the assumption that the time spent on the bed surface is short in comparison with the time spent in the bed is necessary in order to interpret this time-delay between rising edges as the time taken for a single in-bed circuit by the tracer. Since the observed time on the bed surface was at least one-tenth of the time spent in the bed (and in most cases the ratio was a good deal higher than this), the assumption can be considered valid. An example of the typical circulation time distribution resulting from the analysis is given in Figure 6.19 a little further on.

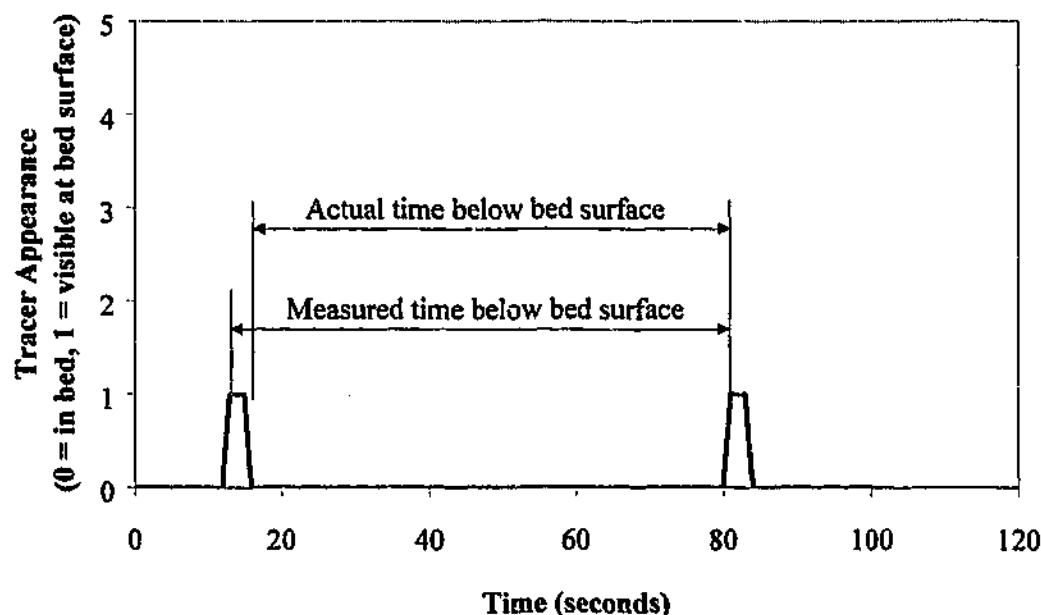


Figure 6.17 Conceptual example of the method for approximating the time spent below the bed surface from the tracer appearance log file. The approximation is good if the time spent at the bed surface is a small compared with the time spent in the bed.

6.4.3 Float Tracer Manufacture

The float tracers were chosen to be as small as possible, yet large enough to be reliably detectable at the bed surface. As a precaution, they were made slightly larger than the skirt-to-plate distance of the bubble caps to prevent the (unlikely) event that a tracer entered the bubble cap during shut-down. Initially, a number of different density tracers were trialled at the 1560 mm scale.

Tracers at the large scale were manufactured from ping-pong balls filled with a mixture of sand and polythene granules to give the required particle density. At the 600 mm and 300 mm scales, small wooden balls were machined to an appropriate diameter. For density adjustment, tight-fitting particles of lead shot were forced to the centre of a small hole through the diameter of each ball, which was then sealed at both ends with hot-melt glue.

(At the 146 mm scale, tracers made of hot-melt glue loaded with tungsten powder were tried, however these were too susceptible to electrostatic charging and adhered to the bed particles to such an extent that their movement was severely limited and their

presence at the bed surface was extremely difficult to detect. Hence experiments at this scale were abandoned.)

The tracers were geometrically scaled in proportion with the bed diameter in a similar fashion to the experimental approach of Horio *et al.*, (1986b). Float particle tracers are shown schematically in Figure 6.18.

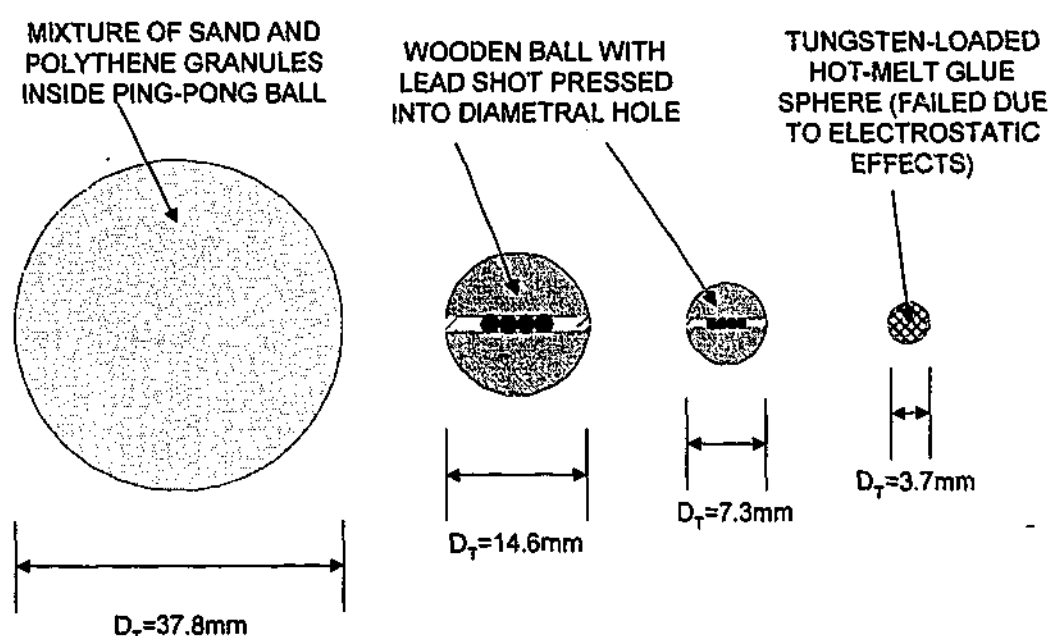


Figure 6.18 Schematic of float tracer particles used in similarity experiments (relative sizes approximately correct). Tracers were designed to be geometrically similar in the same ratio as the bed diameters.

6.4.4 Preliminary Experiment – Effect of Tracer Density

A number of preliminary experiments were conducted to see what effect relative tracer size and density had on the experimental results. These were carried out in the 1560 mm bed in two stages:

(1) Qualitative Observations

Five float tracers all of the same diameter (37.8 mm) were loaded with different ratios of sand/polythene and painted in five different fluorescent colours. These were tossed into the bed which was operated at $1.22 \cdot U_{mf}$ (Material D) and then at $3.05 \cdot U_{mf}$. Their behaviour (under UV illumination) was observed visually from the upper freeboard

hatch for a period of 1/2 hour for each gas velocity. The bed surface was also video-taped during this run to test the lighting and camera setup. Qualitative results were according to Table 6.6:

Colour	Density (kg/m ³)	Observations
Red	1260	Floats at low U , circulates at high U
Blue	1310	Floats at low U , circulates at high U
Orange	1360	Circulates at low and high U
Green	1410	Circulates at low and high U
Yellow	1460	Sinks at low U , circulates at high U

Table 6.6: Qualitative observations of density variation on float tracer behaviour in the 1560 mm bed (material D). Low U corresponds to $U/U_{mf} = 1.22$, high U corresponds to $U/U_{mf} = 3.05$.

No discernible radial pattern of upflow or downflow could be identified from the movement of the float tracers. Sites of appearance and disappearance seemed to be randomly distributed across the bed surface. At the higher velocity, the float tracers were often ejected from the bed quite violently. Occasionally this occurred with a considerable lateral velocity component and tracers bounced violently off the vessel wall in the freeboard region. (Subsequent examination of the tracers revealed no damage.) The qualitative observations of Table 6.6 agree well with results of the study by Rios *et al.* (1986) who report observations of the behaviour of cylindrical objects in a two-dimensional bed.

On analysis of the video-tape it was found that the camera was sensing light significantly into the near UV range; this "invisible" light reflecting from the bed surface was recorded as bright purple on the tape. This reduced the contrast between float tracers and background somewhat, so a near-UV filter (Kodak Wratten gelatin filter 2A) was subsequently installed on the lens to prevent this. In addition, it was quite difficult on the tape to distinguish between the float tracer colours of yellow and green, and also orange and red, although they could be easily differentiated with the naked eye. Consequently, the number of coloured balls was reduced to three (red, green, blue) for subsequent runs where video analysis was involved.

(2) Quantitative Observations

After considering the results of the first part of the density variation test and making appropriate changes to the setup, a second density variation experiment was performed involving the use of three float tracers with a narrower range of densities. Float tracers were of the same diameter as the previous experiment and were coloured red, green and blue. The tracers had respective densities of 1410, 1360 and 1310 kg/m³. An intermediate gas velocity of $U/U_{mf} = 2.7$ was used for this run, which lasted 90 minutes. The video-tape was analysed using the procedure outlined in Section 6.4.2. Results of the analysis are presented in Figure 6.19.

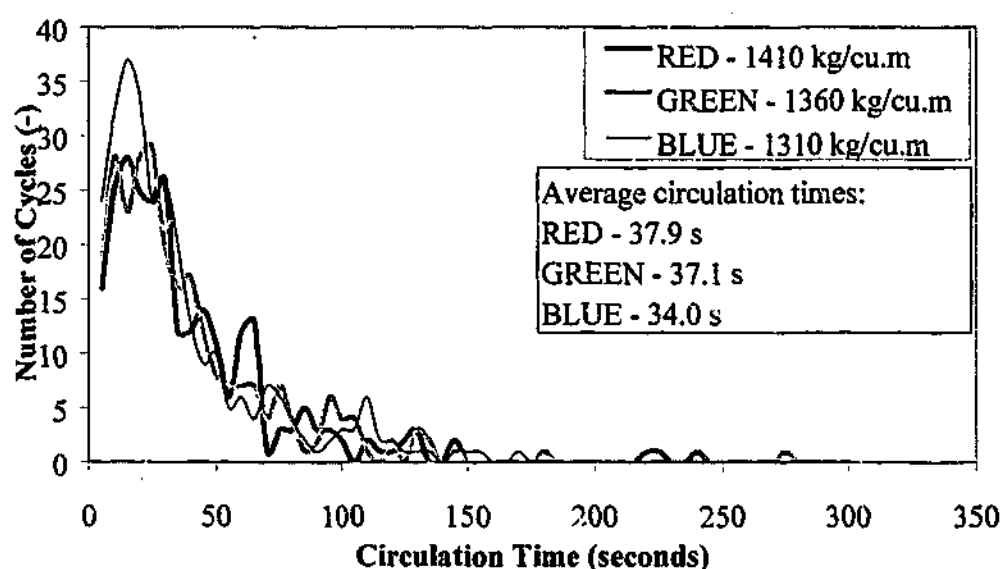


Figure 6.19 Distribution of circulation times for float tracers of the same size but different density in the 1560 mm bed fluidized at $U/U_{mf} = 2.7$. The circulation times are distributed into bins of 5 seconds width.

As can be seen from Figure 6.19, the peak and average circulation times compare well. There is very little difference in the distributions of circulation times for the three different density float tracers at this gas velocity. So as far as this measurement is concerned, tracer density has little effect. The circulation times have been distributed into bins with a 5 second width for this comparison.

Note that in the qualitative observations presented previously for the effect of float tracer density it was found that the 1410 kg/m³ density object sank at the lower U/U_{mf} . At this higher U/U_{mf} however, this is not the case. It is also possible that the 1410 kg/m³ density

object became trapped in a stagnant region between tuyeres during the experiment at the lower gas velocity. (This possibility will be further discussed in the next section.)

It can be concluded from the density variation experiments that within the range 1310 to 1410 kg/m³, the density of the float tracer is of little importance to the overall behaviour of the tracer. This point is also supported by the work of Merry and Davidson (1973), who (coincidentally) also used a 38 mm ping-pong ball as a float tracer. They made mention of the fact that varying the density of the ball did not alter their results, although the extent of the density variation was not specified.

As a result of the density variation tests, the tracer densities for the similarity experiments were selected to be 1360 kg/m³, although some minor deviations occurred at the smaller scales due to the very small masses involved. The specifics of the tracers used in the experiments are given in Table 6.7.

	1560 mm	600 mm	300 mm
D_{tracer} (mm)	37.8	14.6	7.3
D/D_{tracer}	41.3	41.1	41.1
ρ_{tracer} (kg/m ³)	1360	1350	1350
ρ_{bulk}^*	1566	1536	1535
$\rho_{\text{tracer}}/\rho_{\text{bulk}}$	0.868	0.879	0.879

* Taken from measured bed material bulk densities (reported in Section 4.9.1)

Table 6.7 Float tracer specifications for hydrodynamic similarity experiments. D refers to bed diameter, D_{tracer} is the tracer diameter; ρ_{tracer} is the tracer density and ρ_{bulk} is the bulk density of the bed materials.

Both the geometric scaling and the density scaling of the float tracers were reasonably accurate, with errors less than 0.5% and 2% respectively.

6.4.5 Comparison of Float Tracer Results at 300 mm, 600 mm and 1560 mm. Scales.

In the initial postulate of Section 6.4.1, it was proposed that for conditions of perfect hydrodynamic similarity, the distribution of float tracer circulation times should follow the scaling law prediction for a characteristic time, *ie* the circulation times should scale

by \sqrt{m} . In this section that supposition is put to the test. Experiments were carried out at the larger three scales with correctly scaled bed materials and float tracers, and operated at scaled superficial gas velocities. The operating conditions are shown in Table 6.8. Additionally, several runs were performed with a mis-scaled bed material (at the 600 mm scale) and a mis-scaled float tracer size (at the 300 mm scale). These details are also listed in Table 6.8.

Bed	Material	U_{mf} (m/s)	U/U_{mf} range	D/D_t	t (mins)
1560 mm	D	0.127	1.27-3.85	41.3	90
600 mm	C	0.07	1.32-3.81	41.1	60
	D	0.127	1.25-3.85	41.1	60
300 mm	B	0.058	1.27-3.85	41.1	45
	B	0.058	1.27-3.85	20.5	45

Table 6.8 Operating conditions for the float tracer circulation time similarity experiments. Within the range stated, 8 different velocities were considered. t refers to the duration of each experiment.

Within the U/U_{mf} ranges given, the specific velocities used in each experiment were matched as closely as possible at each scale. Some deviations were unavoidable however. The length of each experiment (given by the value t) was progressively decreased at the smaller scales. This was done on the basis that if the circulation times are decreasing with bed scale (as they should according to the similarity rule), a similar number of circulation statistics can be generated over a shorter time duration in a smaller scale bed. For a given run in any bed, there were typically several hundred circulation time statistics generated.

In order to compare the float tracer circulation results directly from one scale to another, the following approach has been used. The various circulation times recorded from the video tape during each experiment are presented in a histogram-style format, with the circulation times allocated into "bins" spanning a certain range of values. For example, the 600 mm bed results have been segregated in to circulation times falling in the ranges 0 to 2 seconds, 2 to 4 seconds, 6 to 8 seconds, etc. The bin width was chosen based on visual comparisons of the cycle time distributions for a number of runs. This was so that the distribution would be meaningful, ie if the bin widths are too small, every statistic is allocated to a separate bin and no useful distribution shape is generated, likewise if the

bin width is too wide, the detail of the distribution is lost because all the statistics fall into the same bin. For the 600 mm scale, 2 seconds was found to be a good compromise for characterising the distribution shape.

Note that the choice of bin widths for the other scales is no longer arbitrary and must now be *scaled* from this selection in order to make a meaningful comparison of the results. If the bin widths are not scaled, distributions at different scales will be altered to different extents by the bin width selection and the comparison will be meaningless. Thus, the bin widths (representing a time measurement) were scaled by \sqrt{m} , yielding bins of width 3.22 s and 1.41 s in the 1560 mm and 300 mm beds respectively. Once the circulation times had been sorted into the bins, the distribution was normalised by dividing the number of cycles falling into a given bin range by the total number of cycles over the whole range. Thus, the area under each distribution is unity, regardless of the bed scale being considered.

So that times could be compared directly, the circulation times were non-dimensionalised for each scale by relating time to two scaled bed properties, the bed diameter and the particle minimum fluidization velocity:

$$t^* = t \left(\frac{U_{mf}}{D} \right) \quad (6.19)$$

Having scaled the bin width, normalised the distribution results and non-dimensionalised the time axis, the characteristic shape of the circulation time distributions for the float tracers can now be directly compared. Figure 6.20 shows the comparison for the correctly scaled beds at the intermediate gas velocity of $U/U_{mf} \approx 2.75$.

The distributions compare well, with the peaks in the distributions occurring at very close to the same dimensionless circulation time in all three fluidized beds for this gas velocity. The size of the peaks are also similar, indicating that the distribution of circulation times for the float tracers within each bed are indeed very similar under these conditions. This sort of agreement in distribution size and shape was typical for the majority of the gas velocities considered. The full set of circulation distribution comparisons are included in Appendix G.

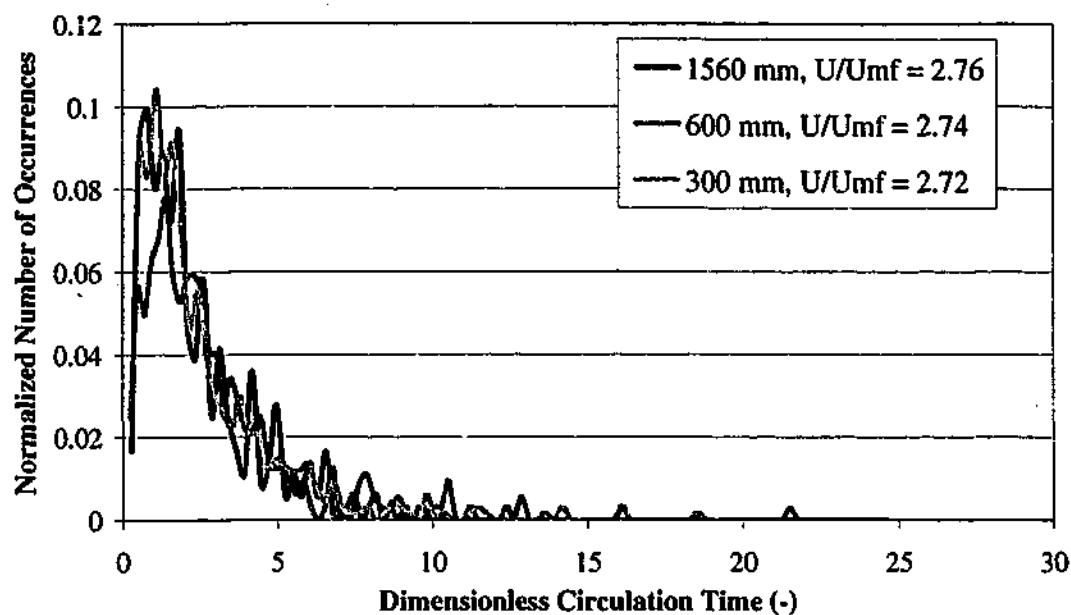


Figure 6.20 Comparison of the dimensionless circulation time distribution for geometrically scaled float tracers in scaled fluidized beds at $U/U_{mf} \approx 2.75$. Bed diameters and specific operating gas velocities are shown in the legend.

Qualitatively, it seems plausible that the measured circulation time may be directly related to the depth to which a tracer sinks in the bed. It is therefore tempting to try and interpret the circulation time results quantitatively in direct terms of the depth to which a tracer penetrates the bed, given that both the upwards and downwards velocities of the tracer can be related to the bubble rise velocity (Lim and Agarwal, 1994). However, it must be considered that the circulation time of the tracer within the bed does not necessarily represent the ideal case of a single downwards excursion via downflowing solids followed directly by a bubble-assisted return journey to the bed surface. As has been observed by Lim and Agarwal, (1994), Rios *et al.*, (1986) and others, the float tracers often exhibit "hesitating" motions and can transfer from upwards to downwards velocities a number of times before returning to the bed surface. Thus, without accurate quantification of the proportion of time spent moving upwards, downwards and hesitating within the bed, a penetration depth cannot be easily derived from these experimental data for circulation time.

The only significant departure from similarity in float tracer circulation behaviour occurred at the lowest gas velocity considered, $U/U_{mf} \approx 1.25$. Figure 6.21 shows this. Float tracers in the smaller two units disappeared at random for much longer times than their equivalents in the larger bed, which exhibited relatively regular and quite fast circulation times. This would tend to indicate that the tracers in the largest unit rarely

penetrated into the bed under this operating condition, whereas the tracers in the smaller beds penetrated to some extent and were only rarely returned to the bed surface due to the minimal bubble activity.

It is also worth pointing out that under these operating conditions, the gas velocity is slightly lower than that required to ensure continuous tuyere operation as discussed in Chapter 3 (Whitehead and Dent, 1967) so there is a possibility of float tracers becoming trapped in stagnant solids for extended periods of time. Occasionally, during a run at low velocity one of the float tracers would disappear permanently; this occurred at least once at all scales and was thought to be due to the tracer becoming lodged in permanently stagnant solids between tuyeres or in the defluidised "corners" between the distributor plate and the vessel wall. For some reason it was always the green one, (regardless of scale) however developing a theory to explain this colour-dependency is beyond the scope of the current work. The tracer could only be recovered in such cases by increasing the gas velocity significantly (to $>3U_{mf}$) for a short time until all tracers could be seen appearing at the bed surface once again.

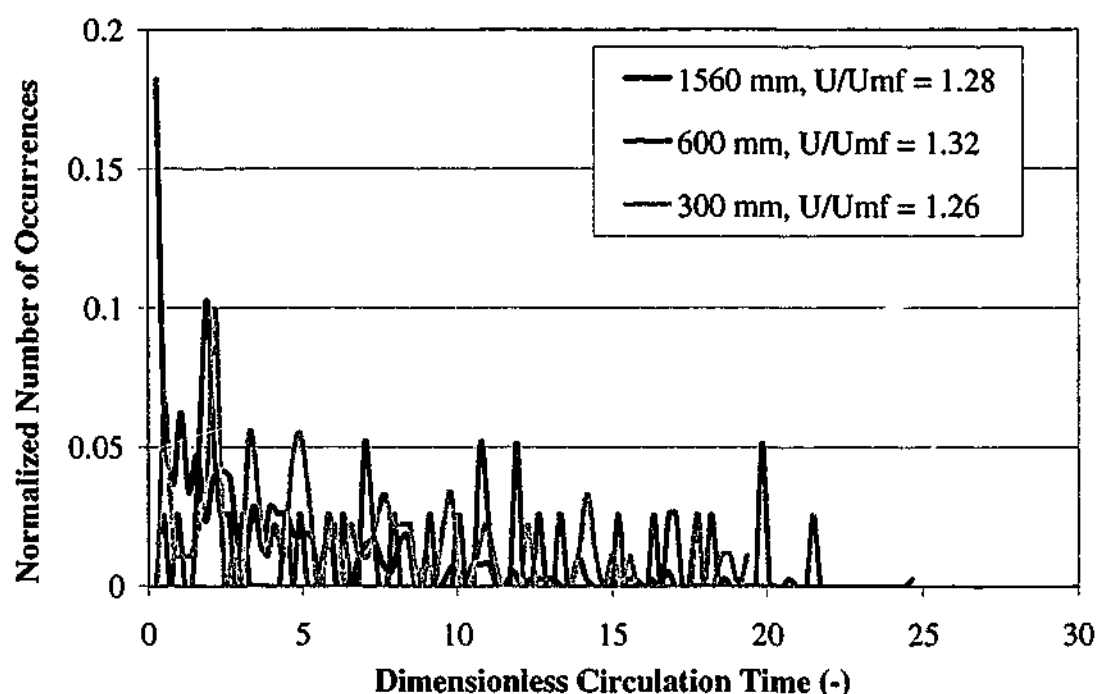


Figure 6.21 Tracer circulation time distributions for the lowest gas velocity studied ($U/U_{mf} \approx 1.27$). Bed diameters and specific operating gas velocities are shown in the legend.

At the highest velocity considered ($U/U_{mf} \approx 3.85$), the distributions were still well matched, as Figure 6.22 shows.

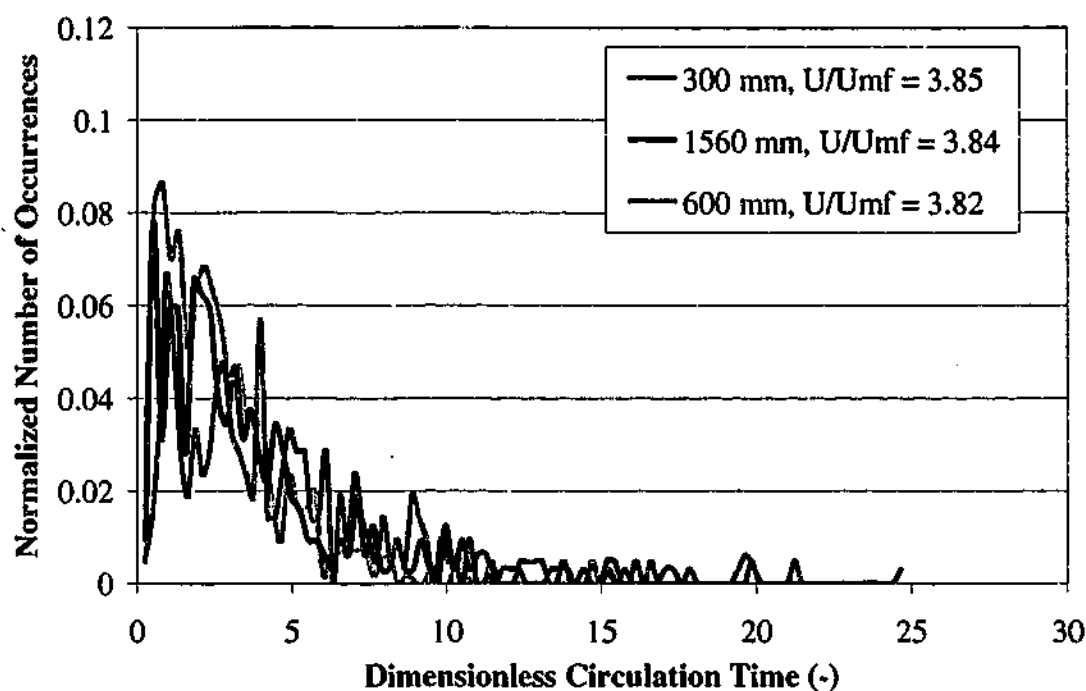


Figure 6.22 Comparison of the dimensionless circulation time distribution for geometrically scaled float tracers in scaled fluidized beds at $U/U_{mf} \approx 3.85$. Bed diameters and operating gas velocities are shown in the legend.

In order to compare the entire set of float tracer circulation results across the range of gas velocities studied, the peak dimensionless circulation time has been estimated from the distribution profiles shown, and plotted for each bed at each gas velocity. To account for the width and shape of the distribution, the circulation times that occur 50% as frequently (either side of the main peak) have also been graphically estimated and included on the chart. This comparison is shown in Figure 6.23. Unlike the pressure fluctuation frequency results of Chapter 4, the circulation time results for the 600 mm bed are not obviously affected by the non-dimensionalisation procedure (similar in approach to that used with pressure fluctuation frequencies in Chapter 4). Given that the minimum fluidization velocity for bed material C was not perfectly matched with the geometric scaling ratio, there is a possibility that there could be some discrepancy in the dimensionless circulation time values. However, given the relatively "noisy" appearance of the distributions, it cannot be easily discerned.

The results illustrate the similar behaviour of the float tracers for the majority of conditions considered in the correctly-scaled systems. Dimensionless peak circulation times generally agree well, and the shape of the distributions compare favourably.

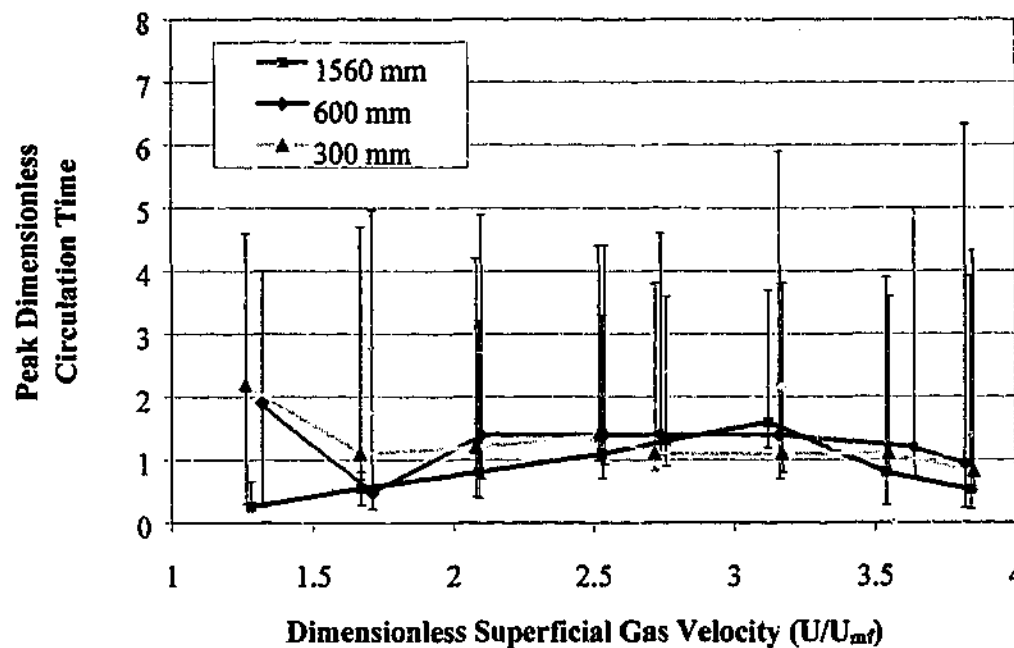


Figure 6.23. Peak circulation times for float tracers in the correctly scaled fluidized beds at all gas velocities considered. Error-bars have been used to indicate the circulation times that occur 50% as frequently (either side of the main peak) in order to give some indication of the "spread" in the circulation times about the peak value.

Having established that this is the level of agreement from correctly scaled systems, the incorrectly-scaled systems must now be addressed to determine the significance of the effect of mis-scaling on the circulation time distribution results. The two mis-scaled cases will now be considered.

In the first instance, larger-sized (mis-scaled) float tracers were used at the same operating conditions as the original tracers in the 300 mm bed. It was found that the effect of tracer size was significant. For the majority of conditions studied, the larger tracer particle size resulted in the shape of the circulation time distribution being altered, and the dominant circulation time increasing slightly. Figure 6.24 for the condition $U/U_{mf}=2.72$ shows the difference.

The larger float tracer shows a narrower distribution of circulation times appearing much more frequently at the bed surface. This has been observed previously by Rios *et al.*, (1986) who in their study found that at high gas velocities ($U/U_{mf}=3.6$), larger spheres tended to occupy the upper region of the bed more frequently than their same-density smaller counterparts. At the lowest gas velocity investigated, however, the larger float tracers spent considerable time in the bed, the resulting dimensionless circulation times are much greater than those of the smaller float tracer, as can be seen in Figure 6.25.

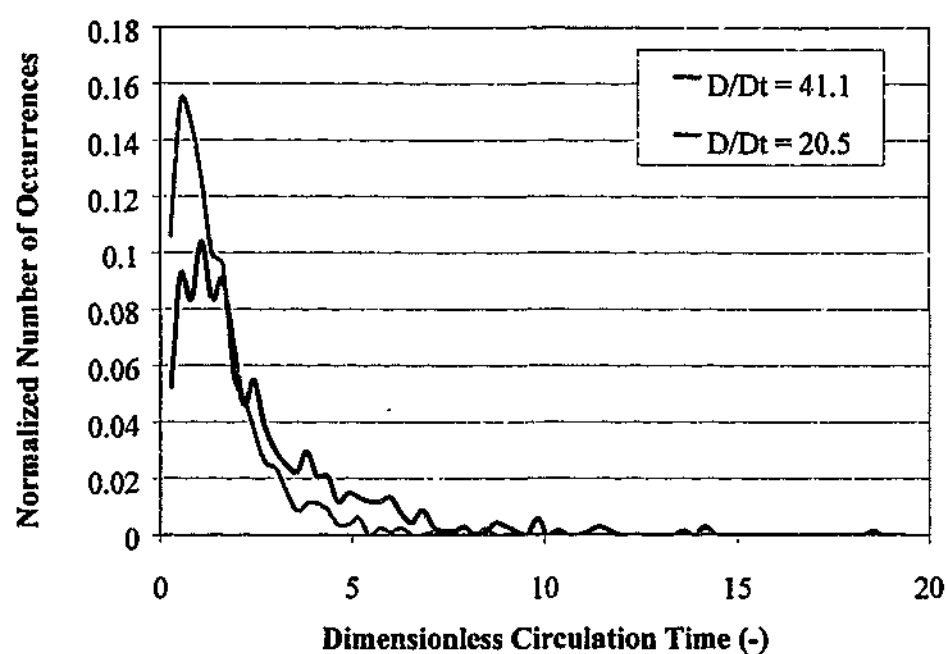


Figure 6.24 The effect of using a larger float tracer ($D/D_t = 20.5$) on the dimensionless circulation time distribution results, compared with the original size used in the similarity experiments ($D/D_t = 41.1$) for the 300 mm bed fluidized at $U/U_{mf} = 2.72$.

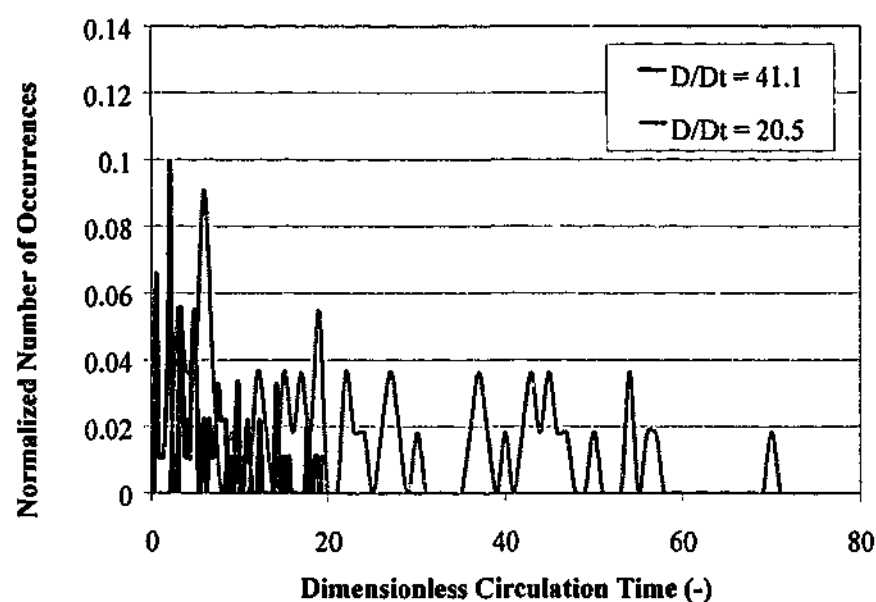


Figure 6.25 The effect of using a larger float tracer ($D/D_t = 20.5$) on the dimensionless circulation time distribution results, compared with the original size used in the similarity experiments ($D/D_t = 41.1$) for the 300 mm bed fluidized at $U/U_{mf} = 1.26$.

Although at low U/U_{mf} in shallow beds, density effects are expected to dominate the float tracer behaviour (Rios *et al.*, 1986); there is only a very small density difference

here between the two different sized objects. In the comparable experiments of Rios *et al.*, (1986) a 20 mm and 8 mm sphere each with density of 1350 kg/m^3 were fluidized in a shallow ($H/D \approx 1$) bed of $300 \mu\text{m}$ glass beads at $U/U_{mf} = 2.0$. Under these conditions, both objects circulated to a very similar extent throughout the whole bed, contrary to what is observed in the current work. In the case of the current work, it may be that bubbles are too small so close to U_{mf} to be able to lift the larger tracers back to the bed surface as effectively as the smaller ones. The effect of stagnant zones within the beds used in this work may again play a part.

A second investigation of a similarity mis-match was carried out in the 600 mm bed where the bed material was replaced with the coarser sand from the 1560 mm bed.

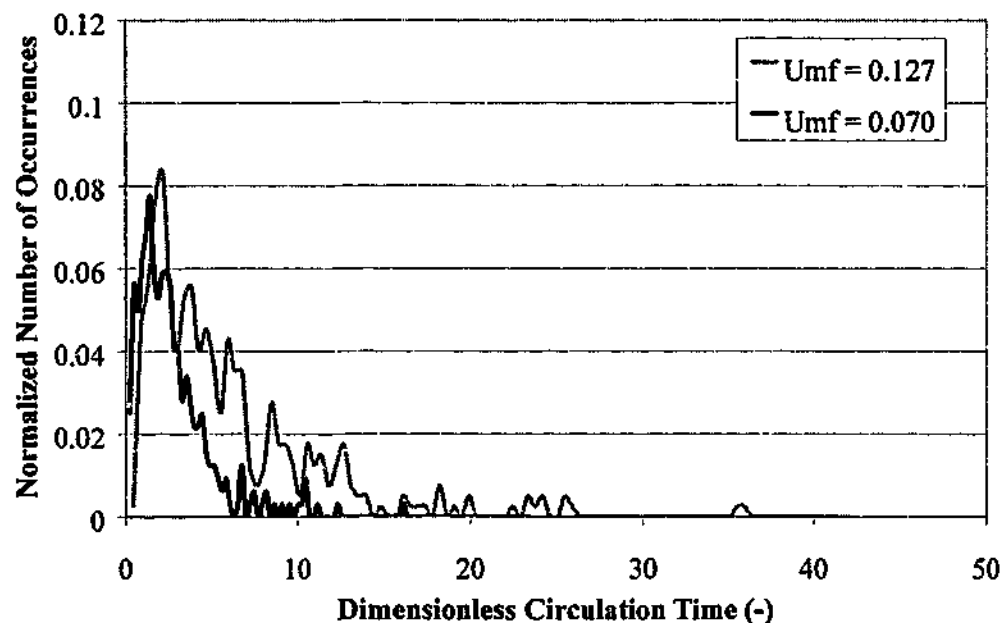


Figure 6.26 The effect of using a coarser bed material for a given bed diameter, float tracer size and dimensionless superficial gas velocity. The original material in the 600 mm bed ($U_{mf} = 0.070 \text{ m/s}$) was replaced with material from the 1560 mm bed ($U_{mf} = 0.127 \text{ m/s}$). The dimensionless circulation time distribution results are compared with those from the original bed material used in the similarity experiments for the 600 mm bed fluidized at $U/U_{mf} = 2.74$.

Higher gas velocities were used so that the same U/U_{mf} was maintained despite the larger particle size. In this case the distributions are distinctly shifted such that the float tracers circulating in the coarser bed material did so with a wider spread of dimensionless circulation rates (tending towards longer dimensionless times), and the peak dimensionless circulation time increased slightly. This is illustrated in Figure 6.26

for the intermediate velocity $U/U_{mf} = 2.74$. The comparison of results once again illustrates the influence of the U_{mf}/D ratio on the value of dimensionless time.

This was the typical result for all gas velocities except the lowest ($U/U_{mf} \approx 1.3$), where circulation times were widely distributed for tracers in either bed material. The difference between float tracer behaviours for the two bed materials did appear to gradually reduce as the gas velocity increased. As shown in Figure 6.27, at $U/U_{mf} \approx 3.83$, the highest velocity investigated, the difference between the circulation behaviours due to the effect of the bed material was marginal.

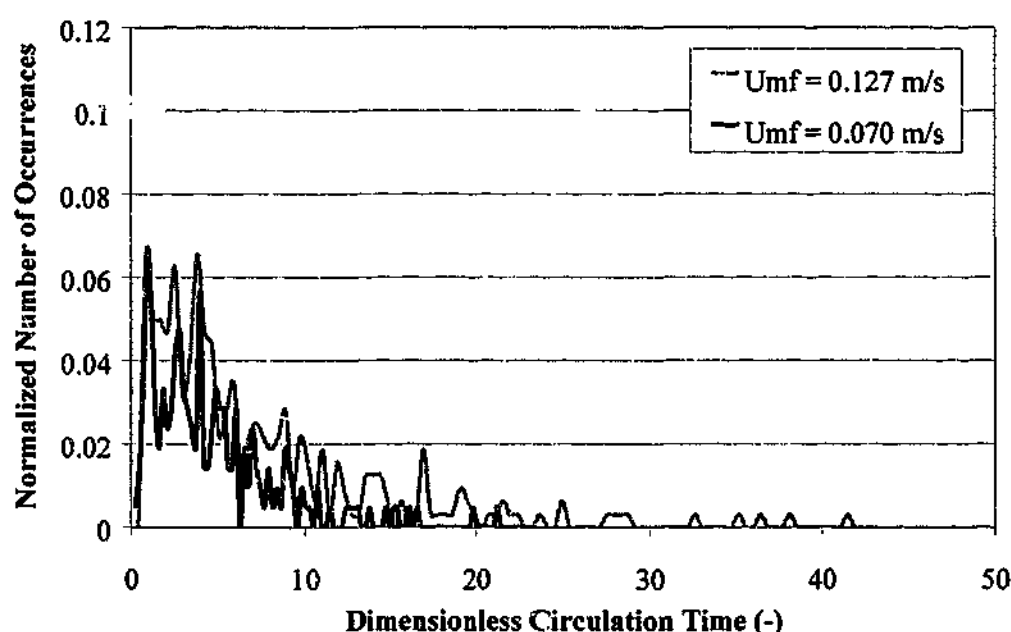


Figure 6.27 The reduced effect of mis-scaled bed material at higher gas velocity ($U/U_{mf} = 3.83$) on the dimensionless circulation time distribution results for the float tracers.

6.5 Conclusions from Solids Mixing Experiments

Conclusions from the experimental studies of solids mixing reported in this chapter are as follows:

1. The novel ECT/tracer technique was moderately successful, but it was limited by the fact that the ECT system responds to both bubbles and tracer; the bubbles add an undesirable layer of "noise" to the tracer response profiles. The use of tracer with a higher dielectric constant, and the application of this technique to "bubbleless" fluidization may be worthwhile areas of future work.

2. The measured solids downflow velocities were affected by mismatching of tracer and bed material sizes. Closely matched tracer and bed material minimum fluidization velocities resulted in solids downflow results that agreed better with the correlations of Kunii and Levenspiel (1969) and Baeyens and Geldart (1986) than the mis-matched cases, which were influenced by segregation.
3. Results for solids downflow velocity in the scaled beds showed qualitative agreement with the simplified scaling law and literature correlations, however precise numerical agreement was lacking, and the data were scattered (standard deviations of similar size to the mean velocity).
4. The experimental approach to active particle circulation monitoring was found to be a simple and effective method for solids motion comparisons.
5. The circulation behaviour of active particles within the correctly scaled bubbling beds followed the simplified scaling criteria across a wide scale range (300 mm to 1560 mm). This may have useful consequences for some fluidized bed applications involving larger and lighter particles (eg bubbling-bed combustors).
6. Altering the tracer density within a limited range had a negligible effect on the circulation time distributions, and the small errors in tracer density for tracers in the scaled experiments are therefore unlikely to have influenced the results.
7. The active particle dimensionless circulation rate was sensitive to both tracer particle size and bed material selection. This demonstrates that the active particle circulation time distributions are sensitive enough to correctly discriminate between scaled and mis-scaled conditions. Hence, the tracer behaviour is not inherently similar in bubbling beds, but is a scaleable phenomenon.

7. CONCLUSIONS AND RECOMMENDATIONS

7.1 Overview

This investigation has considered hydrodynamic similarity criteria for bubbling fluidization from an experimental standpoint. Specifically, the so-called "simplified" scaling criteria have been examined experimentally with emphasis on some areas which have been overlooked in previous analyses.

Large scale change – In this work, where possible, experimental work was carried out in bubbling beds from 146 mm in diameter to 1560 mm in diameter, representing the largest scale change over which experimental verification of the simplified scaling laws has been carried out thus far. Whilst there is evidence in previous work to suggest that the simplified scaling laws are successful over a small scale change, wall effects at the smaller scales may be significant. Data gathered from larger-scale units – and indeed spanning a larger range of relative bed sizes – is an important indicator of the feasibility of these scaling laws for industrial applications. In this work, a ten-fold increase in bed diameter (or 1000-fold increase in bed volume) has been evaluated using pressure fluctuation measurements. Solids motion experiments were also conducted at the large scale.

Multiple measurement techniques – Previous experimental evaluations have tended to focus on a single measurement, which has been assumed to characterise bed hydrodynamics sufficiently for a similarity comparison. In contrast, this work has employed a multiple-measurement approach. That way, not only can the separate measurement techniques be compared with one another in terms of their relative success as hydrodynamic indicators, but the larger range of independent experimental results provides a broader basis from which to draw conclusions about the success or failure of the similarity criteria under test.

Control experiments – A major shortcoming identified through the review of previous similarity criteria verification studies was the lack of appropriate "control" experiments. For a sound investigation of hydrodynamic similarity, it is of critical importance to not only verify the success of the scaling parameters, but also verify measurement deviations when parameters are deliberately mis-matched. This is necessary in order to

demonstrate that the measurement technique in use is able to distinguish between behaviour that is similar as a consequence of the successful application of the scaling laws and behaviour which is intrinsically similar in bubbling fluidization anyway. Given the practical difficulties associated with perfectly matching scaling law requirements in "real" applications, testing deliberate system mis-matches may also help to determine the extent to which parameter mis-matches are tolerable before a significant deviation from scaled behaviour occurs. (Particle size and solid-to-gas density ratio are good examples of such parameters.)

Distributor design – Many previous small-scale investigations have employed high pressure drop sintered or perforated plate distributors, which are not relevant to the majority of industrial applications. Whilst relatively high distributor pressure drops have been maintained in this work, a more industrially-relevant bubble-cap distributor configuration has been employed. Of particular interest was whether simplified scaling parameters would be successful for relatively shallow beds with only a small number of gas entry points in the distributor.

7.2 Work Summary

Experimental verification of the simplified scaling laws for bubbling fluidized beds was carried out for four fluidized beds of circular cross-section with sizes of 146 mm, 300 mm, 600 mm and 1560 mm in diameter. Scaled bubble-cap distributors were employed in all beds. Measurement techniques employed were pressure fluctuations from in-bed probes at various locations; voidage fluctuations using Electrical Capacitance Tomography (smaller scale beds); solids downflow velocities using the Electrical Capacitance Tomography system as a tracer detector (also in the smaller scale beds); and solids motion experiments involving neutrally bouoyant float-tracers (at the three larger scales).

Pressure fluctuation measurements were initially carried out in carefully controlled experiments at the smaller scales (146 mm and 300 mm beds with aspect ratios of approximately 2:1), in order to evaluate the measurements in systems similar to those studied previously in the literature. The effects of particle size and particle density mis-matches were investigated. Pressure fluctuation experiments were then extended to the full range of bed sizes for relatively shallow beds (aspect ratio of 0.67:1) of silica sands using single-ended probes at various radial and axial locations. In these experiments,

gas velocities from 1 to 4 times the minimum fluidization velocity of the bed materials were employed, with particle Reynolds numbers in the range 1 to 16. The effect of a mis-match in particle size was tested at the 600 mm scale.

Voidage fluctuation measurements were carried out in the two smallest beds using an Electrical Capacitance Tomography system. The beds were operated under the same conditions as for the initial small-scale pressure fluctuation experiments so that measurements could be compared. Some additional work was carried out investigating issues related to the use of the ECT system in fluidized bed work.

Solids downflow velocity experiments were also carried out at relatively low gas velocities using the ECT system as a detector for the tracer solids (glass ballotini). Once again, experiments were conducted in the 146 mm and 300 mm beds and various silica sands were used as bed materials.

Finally, the circulation times for neutrally-buoyant spheres were measured in the three larger fluidized beds using video analysis of the bed surface. The effects of mis-scaled particle size and mis-scaled sphere size were investigated. The question of whether small differences in sphere density would have a significant effect on results was also resolved. These solids motion experiments involved operating conditions for a slightly narrower range of gas velocities than the large-scale pressure fluctuation work.

7.3 Conclusions

Conclusions for this study can be broadly categorized into two groups: Conclusions that relate to measurement techniques as indicators of bed hydrodynamics, and conclusions that relate to the verification of the simplified scaling laws. The two areas will be addressed separately.

7.3.1 Measurement Techniques

Global pressure fluctuations (*ie* those originating from a single-ended in-bed probe) were found to be an adequate means of distinguishing between scaled and mis-scaled bubbling bed hydrodynamics in the small-scale experiments where a mis-matched gas velocity or particle size was involved. The amplitude of the fluctuations (in this case

characterised by the average absolute deviation) was sensitive to both particle size and gas velocity. The average pressure was found (particularly in the shallow bed experiments across the full range of bed sizes) to be very sensitive to bed inventory. Fluctuation frequency (as characterised by the average cycle frequency) was relatively insensitive to particle size or gas velocity. Generally speaking, the pressure fluctuation measurements were found to be a robust tool for comparing fluidized bed behaviour and entirely suitable for hydrodynamic similarity comparisons at different scales.

Electrical Capacitance Tomography, on the other hand, was found to be far less useful in fluidized bed diagnostics of the type required in this work. Images generated using the linear back-projection reconstruction algorithm did not accurately represent the behaviour of the fluidized beds. In the 300 mm bed, significant over-estimation of large void sizes and under-estimation of small void sizes occurred. Similar, but smaller errors were noted in the 146 mm system. Thus ultimately a quantitative comparison of voidage fluctuations results at different scales was of little use, except for the comparison of bed materials with different density which was undertaken at the same scale. Also, average cycle frequency results appeared to be only moderately affected and showed some encouraging agreement with the relevant pressure fluctuation results for the same systems.

The ECT system was also found to be very sensitive to extraneous effects. For example, it was found that the calibration procedure for the ECT system needed to include a suitable length of fluidization time in order to establish a stable baseline – a point not mentioned in previous literature. It was postulated that the time was required for any electrostatic charges generated whilst filling the vessel to dissipate. Note also that the fluidization time was found to be material dependent. For silica sand, this time was found to be of the order of 15 to 20 minutes, yet it was found to be negligible for glass ballotini. Whilst not separately identified, it is likely that the use of both driven shields and relatively small vessel diameters are both important in order to get the maximum measurement accuracy from the ECT system.

In its novel use as a detector for glass ballotini tracer in solids mixing experiments, the ECT system was moderately effective. However, it was limited by the fact that the system responds to both bubbles and tracer (as both have dielectric constants different from the bulk bed material). Consequently in the solids mixing application, the presence of bubbles was found to add an undesirable level of noise to the tracer response profiles.

The use of the large neutrally-buoyant spherical tracers was found to be an adequate indicator of bed hydrodynamics. Whilst the level to which quantitative comparisons could be made between beds was not as detailed as in the case of pressure fluctuations, the results indicated that the motion of the tracers was suitably sensitive to bed material particle size and tracer size, and suitably insensitive to small errors in relative density between the bed and the tracer. Thus this relatively simple method of monitoring bed behaviour at different scales was found to be a useful additional measurement.

7.3.2 Verification of the Simplified Similarity Criteria for Bubbling Fluidization

For the majority of the operating conditions and the full range of bed sizes, the measurements made at the different scales indicated hydrodynamic similarity had been achieved when the scaling laws were satisfied. Thus it is to be concluded that the simplified scaling laws were successful for the majority of the conditions tested experimentally in this work.

For the case of a small scale change involving bed materials with the same solid-to-gas density ratio, hydrodynamic similarity was achieved for the full range of gas velocities considered (U/U_{mf} from 1.5 to 8 and Re_p from 1 to 12).

For the case of a small scale change involving bed materials with the same solid-to-gas density ratio, solids motion trends (as characterised by the solids downflow velocity) exhibited a qualitative agreement with the simplified scaling criteria for the conditions studied ($U/U_{mf} = 1.4$ and Re_p from 1 to 2).

For the case of a small scale change involving beds of materials with different solid-to-gas density ratio, the experimental evidence (from both pressure fluctuations and voidage fluctuations) suggests that hydrodynamics similarity was achieved for the full range of gas velocities considered (U/U_{mf} from 1.5 to 5 and Re_p from 2 to 8). This indicates that for particle Reynolds numbers only moderately beyond the arbitrary value of $Re_p = 4$ (representing the limit of the viscous-dominated flow regime) the simplified scaling law may hold even with a mis-matched density ratio.

For the case of a large scale change, agreement was found to be generally good for gas velocities up to approximately $U/U_{mf} = 3.5$ and $Re_p = 13$, with agreement best towards the radial centre and in the lower portions of the bed. Beyond this velocity,

discrepancies in pressure fluctuation results were found in the behaviour of the largest bed when compared with the smaller three, but could not be discerned from the large spherical tracer particle results. The difference in pressure fluctuation results appears to represent a deviation from similarity not accounted for by the simplified scaling criteria and should be considered as an area for future work.

For a scale change from 300 mm to 1560 mm in bed diameter, the motion of neutrally buoyant spheres was found to follow the simplified scaling law when scaled correctly for the majority of operating conditions considered (U/U_{mf} from 1.8 to 3.8 and Re_p from 2 to 15). The tracer particle dimensionless circulation rate was sensitive to both tracer particle size and bed material selection. This demonstrates that the active particle circulation time distributions are sensitive enough to correctly discriminate between scaled and mis-scaled conditions. Hence, the tracer behaviour is not inherently similar in bubbling beds, but is a scaleable phenomenon.

7.4 Recommendations and Future Work

Although for the majority of the conditions tested experimentally in this work, the simplified scaling laws were found to be successful, there are a number of areas that have been identified as avenues for further investigation.

First and foremost is the discrepancy in pressure fluctuations noted for high gas velocities in the largest fluidized bed. As far as this author is aware, the observed behaviour does not correspond to anything reported for smaller scale beds and may indicate some fundamental difference in the behaviour of fluidized beds at large scales which has not been previously recognised (and thus is not accounted for in present scaling law developments).

The influence of wall effects and bed surface effects is often cited as a possible reason for otherwise unexpected differences in fluidization behavior from one bed to another. The present similarity criteria ignore these effects, and there may in fact be a minimum scale model size below which wall (or surface) effects dominate the behaviour and thus prevent accurate modelling. If the differences noted in pressure fluctuation behaviour for probes located close to the wall and bed surface in the present study are indeed a consequence of wall and surface effects, then the minimum scale model size may in fact be quite large. This is therefore an important area for future work.

A review of the available literature indicates that little or no experimental evaluation has been carried out for the simplified scaling criteria in systems corresponding to Geldart group A and D materials. The success or failure of the simplified criteria for these systems should be tested.

Although the present work went some way towards evaluating a distributor design more closely associated with industrial fluidized bed applications, it would be interesting and useful to study the effect of the distributor to bed pressure drop ratio on the success of fluidization scaling criteria. The issue is relevant because distributor pressure drop is often much lower in large scale industrial applications than laboratory facilities as a means of reducing upstream gas supply installed cost and power consumption.

Given that the experimental results of this investigation suggest that a solid-to-gas density ratio mis-match is tolerable at particle Reynolds numbers somewhat higher than 4, further work should be done to determine a more appropriate guideline for an acceptable density ratio and limiting particle Reynolds number applicable to viscous-limit scaling laws.

The novel application of Electrical Capacitance Tomography to solids mixing processes in fluidized beds is worthy of further investigation. For research groups with access to ECT equipment, the following points may be of use: In practical terms, selecting tracer and bed materials with greater differences in dielectric constant (up to a point) may improve the accuracy of the results. Additionally, investigations of mixing in non-bubbling fluidization may also be worthwhile.

Given the success of the simplified scaling criteria in regards to the motion of the large neutrally-buoyant spheres in freely bubbling beds, additional work involving beds with internals should be undertaken as this will relate more directly to fluidized bed combustor applications.

NOMENCLATURE

Generally, relevant algebraic symbols have been defined alongside the first occurrence of an equation throughout this text. Apart from two exceptions (noted in the text), SI units have been used throughout. This section summarises the notation used. Unless otherwise stated in the text, the following symbols apply:

A	Bed cross-sectional area
AAD	Average absolute deviation (<i>eg</i> of pressure fluctuations)
A_b	Amplitude of pressure fluctuations registered at bottom of bed
A_e	Electrode area
A_o	Distributor catchment area
A_{x-s}	Bed cross-sectional area
C	Capacitance
C_d	Orifice discharge coefficient
C_f	Final packed bed tracer concentration
C_i	Initial packed bed tracer concentration
C_s	Solids concentration
c_v	Volume fraction of one material in another
D	Bed diameter
d	distance between electrodes
D_B	Bubble diameter
d_{eq}	Diameter of a sphere of equivalent volume to that of the bubble
d_h	Distributor orifice diameter
d_p	Particle diameter
D_{sa}	Axial drift coefficient
D_{sr}	Radial drift coefficient
d_{sv}	Sauter mean diameter
D_T	Float tracer diameter
D_{tracer}	Float tracer diameter
D_v	Void diameter
f	Frequency
f^*	Dimensionless frequency
f_c	Nyquist critical frequency

f_d	Volumetric fraction of solids travelling upwards
f_u	Volumetric fraction of solids travelling upwards
f_w	Bubble wake fraction
g	Acceleration due to gravity ($= 9.81 \text{ ms}^{-2}$)
H	Bed height
h	Height above distributor
H_e	Height of ECT electrode axial centreline above distributor
H_{mf}	Bed height at minimum fluidization conditions
H_L	Critical bed height
H_s	Settled bed height
I	Information (<i>bits</i> is the SI unit)
\bar{i}	Unit vector in vertical direction
I_b	Bubble impact
J	Solids flux
K	Kolmogorov entropy
K_D	Grate flow factor
K_s	Solids exchange coefficient
K_T	Tuyere flow factor
L	Characteristic length dimension
L_e	Axial electrode length
M	Bed mass
m	Scaling factor (Horio rule)
m_{geo}	Scaling factor based on bed geometry
m_{part}	scaling factor based on particle characteristics
N	Number of orifices
n	Bubble hold-up coefficient
N_b	Flow of erupting bubbles (bubble flux)
N_o	Number of orifices
p	Pressure
P^*	Dimensionless pressure
ΔP_{bed}	Bed pressure drop
P_c	Windbox pressure
ΔP_{dist}	Distributor pressure drop
P_o	Freeboard pressure
P_w	Absolute pressure in windbox
Q	Volumetric gas flowrate

Q_B	"Visible" bubble flowrate
Q_{mf}	Volumetric gas flowrate at minimum fluidization conditions
Q_T	Volumetric flowrate of gas per tuyere
R	Bed radius
r	horizontal distance from radial centreline
t	Time
t^*	Dimensionless time
t_T	Bed turnover time
T_w	Absolute temperature in windbox
U	Superficial gas velocity
\bar{u}	Gas velocity vector
U_A	Average bubble rise velocity
U_B	Bubble rise velocity
U_D	Dense-phase gas velocity
U_{Drel}	Dense-phase gas velocity relative to particles
u_h	Gas velocity in orifice
U_{mb}	Minimum bubbling velocity
U_M	Minimum superficial gas velocity for complete tuyere operation
U_{mf}	Minimum fluidization velocity
U_{mBM}	Minimum fluidization velocity of the bed material
U_{mT}	Minimum fluidization velocity of the tracer material
U_{ms}	Minimum slugging velocity
U_s	Solids rise velocity
U_{sd}	Solids downflow velocity
U_{su}	Solids upflow velocity
\bar{v}	Particle velocity vector
V_b	Bubble volume
V_{bed}	Bulk volume of settled bed
V_c	Windbox volume
V_d	Drift volume
v_p	Average solids particle velocity
V_{tracer}	Bulk volume of tracer added
V_w	Volume of bubble wake
Y	Gas throughput factor

Greek Letters:

α	solids transport fraction
β	Drag coefficient
β_w	Bubble wake fraction
β_s	Fraction of solids dragged upwards
β_w	Fraction of solids in bubble wake
β_d	Fraction of solids in bubble drift
ε_{mf}	Voidage at minimum fluidization conditions
$\bar{\varepsilon}_B$	Bubble hold-up
ε_D	Dense-phase voidage
ε_m	Permittivity of mixture
ε_i	Permittivity of component i
ε_r	Relative permittivity
ε_0	Permittivity of a vacuum
ρ_s	solid density
ρ_f	Fluid density
ρ_{tracer}	Float tracer density
ρ_{bulk}	Bulk density of bed
ρ_p	Particle density
ρ_h	Gas density in orifice
ρ_{mf}	Bed density at minimum fluidization conditions
θ	Fraction of distributor open area
μ	Gas viscosity
τ_o	Characteristic time
Φ_s	Particle sphericity

Additional superscripts:

'	Denotes dimensionless quantity
*	Denotes dimensionless quantity
°	Denotes original scale (Horio rule)

$$Re_p \quad \text{Particle Reynolds number} = \frac{d_p U \rho_f}{\mu}$$

REFERENCES

- Acree Riley, C. and M. Y. Louge (1989) "Quantitative Capacitive Measurements of Voidage in Dense Gas-Solid Flows" Particulate Science and Technology 7: 51 – 59.
- Almstedt, A. E. and V. Zakkay (1990). "An Investigation of Fluidized Bed Scaling - Capacitance Probe Measurements in a Pressurized Fluidized-Bed Combustor and a Cold Model Bed." Chemical Engineering Science 45, No. 4: 1071 - 1078.
- Anderson, T. B., and R. Jackson (1967) "A Fluid Mechanical Description of Fluidized Beds" Industrial and Engineering Chemistry Fundamentals 6, No. 4: 527 – 539.
- Anderson, T. B., and R. Jackson (1969) "A Fluid Mechanical Description of Fluidized Beds – Comparison of Theory and Experiment" Industrial and Engineering Chemistry Fundamentals 8, No. 1: 137 – 144.
- Argyriou, D. T., H. L. List *et al.* (1971) "Bubble Growth by Coalescence in Gas Fluidized Beds" AIChE Journal 17, No. 1: 122 – 130.
- Arpaci, V. S., and A. Agarwal (1999) "Scaling Laws for Turbulent Ceiling Fires" Combustion and Flame 116: 84 – 93.
- Avidan, A. and J. Yerushalmi (1985) "Solids Mixing in an Expanded Top Fluid Bed." AIChE Journal 31, No. 5: 835 - 841.
- Baeyens J., and D. Geldart (1973) Proceedings of the International Symposium, Fluidization and Its Applications, (H. Angelino, J. P. Couderc, H. Gibert, C. Laquerie, Eds.) Toulouse 182.
- Baeyens, J., and D. Geldart (1974) "An Investigation into Slugging Fluidized Beds" Chemical Engineering Science 29: 255 – 265.
- Baeyens, J., and D. Geldart (1986) "Solids Mixing" In Gas Fluidization Technology, (D. Geldart ed.) John Wiley and Sons, 97 – 122.

Bair, M. S. and J. P. Oakley (1993) "Comparison of Excitation Methods for Electrical Capacitance Tomography" In: Tomographic Techniques for Process Design and Operation, (M.S. Beck *et al.*, Eds.), Computational Mechanics Publications, Southampton, 115 - 126.

Baird, M. H. I., and A. J. Klein (1973) "Spontaneous Oscillation of a Gas-Fluidized Bed" Chemical Engineering Science 28: 1039 - 1048.

Basesme, E. A. and E. K. Levy (1992) "Solids Exchange Between the Bubble Wake and the Emulsion Phase in a Two-Dimensional Gas-Fluidized Bed." Powder Technology 72: 45-50.

Baskakov, A. P., V. G. Tuponogov *et al.* (1986) "A Study of Pressure Fluctuations in a Bubbling Fluidized Bed" Powder Technology 45: 113 - 117.

Bellgardt, D. and J. Werther (1986) "A Novel Method for the Investigation of Particle Mixing in Gas-Solid Systems." Powder Technology 48: 173 - 180.

Bi, H. T., J. R. Grace *et al.* (1995) "Propagation of Pressure Waves and Forced Oscillations in Gas-Solid Fluidized Beds and their Influence on Diagnostics of Local Hydrodynamics" Powder Technology 82: 239 - 253.

Broadhurst, T. E. and H. A. Becker (1973) "The Application of the Theory of Dimensions to Fluidized Beds" Proceedings of the International Symposium, Fluidization et ses Applications, (H. Angelino *et al.*, Eds.), Tolouse, 10 - 27.

Brock, W. A. (1999) "Scaling in Economics: A Readers Guide" Technical Report 9912, University of Wisconsin, Department of Economics, Madison, WI.

Brown R. C. and E. Brue (1996) "Pressure Fluctuations as a Diagnostic Tool for Fluidized Beds" Quarterly Technical Report, 4th Quarter 1995, DE-FG22-94PC94210, Iowa State University.

Brown, R. C. and J. R. Schroeder (1997) "Pressure Fluctuations as a Diagnostic Tool for Fluidized Beds" Quarterly Technical Report, 3rd Quarter 1997, DE-FG22-94PC94210, Iowa State University.

Brue, E and R. C. Brown (2001) "Use of Pressure Fluctuations to Validate Hydrodynamic Similitude in Fluidized Media: Bubbling Beds" Powder Technology 119: 117 – 127.

Bunde, A., H-J. Schellnhuber *et al.* (2002) "Theories of Disaster: Scaling Laws Governing Weather, Body, and Stock Market Dynamics", Springer Verlag.

Burwell Abrasives Ballotini Impact Beads Product Specification Datasheet (2000).

Byars, M. (1998) "Application Note: Engineering Design Rules for ECT Sensors" – Draft Document. PTL - Process Tomography Limited.

Carman, P. C. (1956) "Flow of Gases Through Porous Media" Butterworth's Scientific Publications, London, 13.

Chen, Q., B. S. Hoyle *et al.* (1993) "Electric Field Interaction and an Enhanced Reconstruction Algorithm in Capacitance Process Tomography" in Tomographic Techniques for Process Design and Operation, (M.S. Beck *et al.*, Eds.), Computational Mechanics Publications, 205 – 212.

Clark, N. N. and C. M. Atkinson (1988) "Amplitude Reduction and PhaseLag in Fluidized Bed Pressure Measurements" Chemical Engineering Science, 43 No. 7: 1547 – 1557.

Clift, R. and J. Grace (1971) "Coalescence of Bubbles in Fluidized Beds." AIChE Symposium Series 67, No. 116: 23 - 33.

Commercial Minerals (1998) private communication – physical properties of mineral sands.

Darton, R. C., R. D. LaNauze *et al.* (1977) "Bubble Growth Due to Coalescence in Fluidized Beds." Transactions of the Institution of Chemical Engineers 55: 274 - 280.

Daw, C. S, W. F. Lawkins *et al.* (1990) "Chaotic Characteristics of a Complex Gas-Solids Flow" Physical Review A, 41, No. 2: 1179 – 1181.

Daw, C. S., and J. S. Halow (1991) "Characterization of Voidage and Pressure Signals

from Fluidized Beds Using Deterministic Chaos Theory" Proceedings: 11th International Conference on Fluidized Bed Combustion, ASME, 777 – 786.

Davidson, J. F., R. C. Paul *et al.* (1959) "The Rise of Bubbles in a Fluidised Bed" Transactions of the Institution of Chemical Engineers, 37: 323 – 326.

Davidson J. F. and D. Harrison (1963) "Fluidised Particles" Cambridge University Press, U.K.

Davidson, J. F. (1968) Rapporteur's Account, Tripartite Chemical Engineering Conference Symposium on Fluidization, Montreal, Instn. Of Chem. Engrs. Symp. Ser., 30: 3.

Deloughry, R., M. Young *et al.* (2001) "Cost Effective Loading of Road Tankers Using Process Tomography" Proceedings: 2nd World Congress on Industrial Process Tomography, Hannover, Germany, VCIPT, 565 – 572.

Di Felice, R., S. Rapagna *et al.* (1992a) "Dynamic Similarity Rules: Validity Check for Bubbling and Slugging Fluidized Beds." Powder Technology 71: 281-287.

Di Felice, R., S. Rapagna *et al.* (1992b) "Cold Modelling Studies of Fluidized Bed Reactors." Chemical Engineering Science 47, No. 9 - 11: 2233 - 2238.

Dhodapkar, S. V and G. E. Klinzing, (1993) "Pressure Fluctuation Analysis for a Fluidized Bed" AIChE Symposium Series 89, No. 296: 170 – 183.

Dickin, F. J., B. S. Hoyle *et al.* (1992) "Tomographic Imaging of Industrial Process Equipment: Techniques and Applications." IEE Proceedings-G 139(1): 72 - 82.

Dyakowski, T., L. F. C. Jeanmeure *et al.* (2000) "Applications of Electrical Tomography for Gas-Solids and Liquid-Solids Flows – A Review" Powder Technology, 112: 174 – 192.

Ergun, S. (1952) "Fluid Flow Through Packed Columns" Chemical Engineering Progress 48, 89 – 94.

Fan, L. T., T. C. Ho *et al.* (1981) "Pressure Fluctuations in a Fluidized Bed" AIChE

Journal 27, No. 3: 388 – 396.

Fan, L. T., S. Hiraoka *et al.* (1984) "Analysis of Pressure Fluctuations in a Gas-Solid Fluidized Bed" AIChE Journal, 30, No. 2: 346 – 349.

Farrel, P. A. (1996) "Hydrodynamic Scaling and Solids Mixing in Pressurised Bubbling Fluidized Bed Combustors" PhD dissertation, Massachusetts Institute of Technology, Mechanical Engineering Department, U.S.A..

Farrel, P. A., M. R. Hyre *et al.* (1998) "Importance of the Solid to Gas Density Ratio for Scaling Fluidized Bed Hydrodynamics" Proceedings: Fluidization IX, (T. M. Knowlton, Ed.), Engineering Foundation, New York, 85 – 92.

Fitzgerald T. J., N. Catipovic and G. Jovanovic (1977) "Solid Tracer Studies in a Tube-Filled Fluidized Bed" Proceedings: Fifth International Conference on Fluidized Bed Combustion, Vol. 3: 135 – 152.

Fitzgerald, T. J. and S. D. Crane (1980) "Cold Fluidized Bed Modelling" Proceedings of the Sixth International Conference on Fluidized Bed Combustion, Vol. III – Technical Sessions, 815 – 820b.

Fitzgerald, T., D. Bushnell *et al.* (1984) "Testing of Cold Scaled Bed Modelling for Fluidized Bed Combustors." Powder Technology 38: 107 - 120.

Foscolo, P. U. and L. G. Gibilaro (1984) "A Fully Predictive Criterion for the Transition Between Particulate and Aggregate Fluidization" Chemical Engineering Science 39 No. 12: 1667 – 1675.

Foscolo, P. U., R. Di Felice *et al.* (1990) "Scaling Relationships for Fluidization: The Generalized Particle Bed Model." Chemical Engineering Science 45 No. 6: 1647 -1651.

Fuller, T. S., C. S. Daw *et al.* (1993) "Interpretation of Pilot-Scale Fluidized Bed Behaviour Using Chaotic Time Series Analysis" Proceedings of the 1993 International Conference on Fluidized Bed Combustion, ASME, Vol. 1, 141 – 153.

Garncarek, Z., L. Przybylski *et al.* (1997) "A Quantitative Assessment of the Effect of Distributor Type on Particle Circulation" Powder Technology 91: 209 – 216.

Geldart, D. and J. R. Kelsey (1972) "The Use of Capacitance Probes in Gas-Fluidised Beds" Powder Technology, 6: 45 – 50.

Geldart, D. (1973) "Types of Gas Fluidization" Powder Technology, 7: 285 – 292.

Geldart, D. (1992) "Post-Experience Course on Gas Fluidization – Part C: Bubbles and Slugs" Course Notes, University of Bradford and the Institution of Chemical Engineers, July, 1992.

Glicksman, L. R. (1984) "Scaling Relationships for Fluidized Beds." Chemical Engineering Science 39 No. 9: 1373-1379.

Glicksman, L. R. and G. McAndrews (1985) "The Effect of Bed Width on the Hydrodynamics of Large Particle Fluidized Beds." Powder Technology 42: 159 - 167.

Glicksman, L. R. (1988) "Scaling Relationships for Fluidized Beds." Chemical Engineering Science 43 No. 6: 1419-1421.

Glicksman, L. R., D. Westphalen *et al.* (1990) "Verification of the Scaling Laws for Circulating Fluidized Beds" In Proceedings of Circulating Fluidized Bed Technology III, (P. Basu, M. Horio, M. Hasatani, Eds.), Nagoya, Japan, Pergamon Press, 119 – 124.

Glicksman, L. R., M. Hyre *et al.* (1993a) "Verification of Scaling Relations for Circulating Fluidized Beds" 1993 Conference on Fluidized Bed Combustion, ASME, Vol. 1, 69 – 80.

Glicksman, L. R., M. Hyre *et al.* (1993b) "Simplified Scaling Relationships for Fluidized Beds." Powder Technology 77: 177-199.

Glicksman, L. R. (1999a) "Fluidized Bed Scale-up" in Fluidization Solids Handling and Processing - Industrial Applications, (W-C. Yang, Ed.) Noyes Publications, New Jersey.

Glicksman, L. R. (1999b) "Scale-up of Fluidized Beds" Proceedings: Fluidization and Fluid-Particle Systems, AIChE Annual Meeting, Dallas, Texas, 166 – 174.

GMA Garnet Manufacturer's Product Sheet, (1999).

Grace, J. R. and R. Clift (1974) "On the Two-Phase Theory of Fluidization." Chemical Engineering Science **29**: 327 - 334.

Grace, J. R. (1986) "Contacting Modes and Behaviour Classification of Gas-Solid and Other Two-Phase Suspensions" Canadian Journal of Chemical Engineering, **64**: 353 - 365.

Grace, J. R. and J. Baeyens (1986) "Instrumentation and Experimental Techniques" in Gas Fluidization Technology, (D. Geldart, Ed.), John Wiley and Sons, 415 - 462.

Grassberger, P. (1986) "Estimating the Fractal Dimensions and Entropies of Strange Attractors" In: Chaos, (A. V. Holden, Ed.) Princeton University Press, 291-311.

Gwyn, J. E., J. H. Moser *et al.* (1970) "A Three-Phase Model for Gas-Solids Fluidized Beds" Chemical Engineering Progress Symposium Series No. 101 Vol. **66**: 19 - 27.

Habermann, A., F. Winter *et al.* (1998) "Residence Time Distribution of Particles in Fluidized Bed Reactors for Metallurgical Processes" Proceedings: Fluidization IX, (T. M. Knowlton, Ed.), Engineering Foundation, New York, 117 - 124.

Halow, J. S., G. E. Fasching, *et al.* (1990) "Preliminary Capacitance Imaging Experiments of a Fluidized Bed." AIChE Symposium Series No. 276 Vol. **86**: 41 - 50.

Halow, J. S. and P. Nicoletti (1992) "Observations of Fluidized Bed Coalescence Using Capacitance Imaging." Powder Technology **69**: 255 - 277.

Harrison D. and L. S. Leung (1961) Trans. Inst. Chem. Engrs. **39**: 409.

Hiby, J. W. (1967) "Periodic Phenomena Connected With Gas-Solid Fluidization" Proceedings: International Symposium on Fluidization, (A.A.H. Drinkenburg Ed.) Netherlands University Press, Amsterdam, 99 - 112.

Hirama, T., M. Ishida *et al.* (1975) "The Lateral Dispersion of Solid Particles in Fluidized Beds" Kagaku Kogaku Ronbunshu, **1**: 272.

Horio, M., A. Taki *et al.* (1980) "Elutriation and Particle Transport Through the

Freeboard of a Gas-Solid Fluidized Bed" In "Fluidization IV" Proceedings (J. R. Grace and J. M. Matsen Eds.) Engineering Foundation, 509 – 517.

Horio, M., T. Shibata, *et al.* (1983) "Design Criteria for the Fluidized Bed Freeboard" Proceedings: Fluidization IV, (D. Kunii and R. Toei, Eds.) Engineering Foundation, New York, 307 - 315.

Horio, M., A. Nonaka, *et al.* (1986a) "A New Similarity Rule for Fluidized Bed Scale-up." AICHE Journal 32 No. 9: 1466-1482.

Horio, M., M. Takada, *et al.* (1986b) "The Similarity Rule of Fluidization and its Application to Solid Mixing and Circulation Control", Proceedings: Fluidization V, (K. Ostergaard and A. Sorensen Eds.), Engineering Foundation, New York, 151 – 158.

Horio, M., H. Ishii, *et al.* (1989) "A Scaling Law for Circulating Fluidized Beds." Journal of Chemical Engineering of Japan 22, No. 6: 587 - 592.

Huang, S. M., C. G. Xie *et al.* (1992) "Process Tomography for Identification, Design and Measurement in Industrial Systems" Powder Technology 69: 85 – 92.

Huang, S. M., C. G. Xie, *et al.* (1993) "Experimental Evaluation of Capacitance Tomographic Flow Imaging Systems Using Physical Models", In Tomographic Techniques for Process Design and Operation, (M.S. Beck *et al.*, Eds.), Computational Mechanics Publications, Southampton, 347 – 360.

Isaksen, O., and J. E. Nordtvedt (1993a) "A New Reconstruction Algorithm for Process Tomography" Measurement Science and Technology 4: 1464 – 1475.

Isaksen, O. and J. E. Nordtvedt (1993b) "Capacitance Tomography: Reconstruction Based on Optimization Theory", In Tomographic Techniques for Process Design and Operation., (M.S. Beck *et al.*, Eds.), Computational Mechanics Publications, Southampton, 213 – 224.

Isaksen, O., A. S. Dico *et al.* (1994) "A Capacitance-Based Tomography System for Interface Measurement in Separation Vessels." Measurement Science and Technology 5: 1262 - 1271.

Johnsson, F., G. Larsson *et al.* (2002) "Pressure and Flow Fluctuations in a Fluidized Bed – Interaction with the Air-Feed System" Chemical Engineering Science 57: 1379 – 1392.

Kang, W. K., J. P. Sutherland *et al.* (1967) "Pressure Fluctuations in a Fluidized Bed With and Without Screen Cylindrical Packings." Industrial and Engineering Chemistry - Fundamentals 6, No. 4: 499 - 504.

Knowlton, T. M. (1997) "Distributor Design" In: Gas Fluidized Beds: Design and Operation, Course Notes, Monash University Department of Chemical Engineering Continuing Education Course, E1 – E17.

Kühn, F. T., J. C. Schouten, *et al.* (1996) "Analysis of Chaos in Fluidization Using Electrical Capacitance Tomography." Measurement Science and Technology 7: 361 - 368.

Kunii, D., and O. Levenspiel (1969) Fluidization Engineering", John Wiley and Sons, U.S.A., 155.

Kunii, D. and O. Levenspiel (1991) "Fluidization Engineering", Butterworth-Heinmann.

Leu, L. P., C. W. Lan (1992) "Scale-up of Gas-Solid Bubbling Fluidized Beds – Verification and Comment on Scale Up Rules" Journal of the Chinese Institute of Chemical Engineers, 23, No. 1: 35 – 44.

Lim, S. and P. Agarwal (1994) "Circulatory Motion of a Large and Lighter Sphere in a Bubbling Fluidized Bed of Smaller and Heavier Particles" Chemical Engineering Science 49, No. 3: 421 – 424.

Linjewile, T. M., A. S. Hull *et al.* (1993) "Heat Transfer to a Large Mobile Particle in Gas-Fluidized Beds of Smaller Particles" Chemical Engineering Science 48, No. 21: 3671 – 3675.

Lionheart, W. R. B. (2001) "Reconstruction Algorithms for Permittivity and Conductivity Imaging" Proceedings: 2nd World Congress on Industrial Process Tomography, Hannover, Germany, VCIPT, 4 – 11.

Lirag Jr, R. C. and H. Littman (1971) "Statistical Study of the Pressure Fluctuations in a Fluidized Bed." AIChE Symposium Series 67, No. 116: 11 - 22.

Liu, S., L. Fu *et al.* (2001) "Comparison of Three Image Reconstruction Algorithms for Electrical Capacitance Tomography" Proceedings: 2nd World Congress on Industrial Process Tomography, Hannover, Germany, VCIPT, 29 - 34.

Loser, T., R. Wajman, *et al.* (2001) "New Reconstruction Algorithm for Electrical Capacitance Tomography", Proceedings: 2nd World Congress on Industrial Process Tomography, Hannover, Germany, VCIPT, 20 - 28.

Louge, S. and M. Opie (1990) "Measurements of the Dielectric Permittivity of Suspensions." Powder Technology 62: 85 - 94.

Louge, M. (1997) "Experimental Techniques" In: Circulating Fluidized Beds (J. Grace, A. Avidan, T. Knowlton, Eds), Chapman & Hall, London, 312 - 368.

Mathers, B. J. and M. J. Rhodes (1996) "Use of Process Tomography to Study the Structure of a Gas-Solid Fluidized Bed" Proceedings: Chemeca '96, IEAust, 57 - 62

Mathers, B. J., P. J. Sanderson, *et al.* (1998) "Determination of the Resolution of Electrical Capacitance Tomography for Use in Fluidized Bed Applications" Proceedings, Chemeca, '98, Port Douglas, Australia.

Mathers, B. J. (1998) "Hydrodynamics of a Fluidized Bed with Circulating Fines" PhD dissertation, Monash University Department of Chemical Engineering, Australia.

Maxwell, J. C. (1873) "A Treatise on Electricity and Magnetism" Vol. 1, Clarendon Press, Oxford.

May, W. G. (1959) "Fluidized Bed Reactor Studies" Chemical Engineering Progress, Vol 55 No. 12: 49 - 56.

Merry, J. M. D. and J. F. Davidson (1973) "'Gulf-Stream' Circulation in Shallow Fluidized Beds." Transactions of the Institution of Chemical Engineers 51: 361 - 368.

Mori, S. and C. Wen (1975) "Estimation of Bubble Diameter in Gaseous Fluidized

Beds." AIChE Journal 21, No. 1: 109 - 115.

Morse, R. D. and C. O. Ballou (1951) "The Uniformity of Fluidization - Its Measurement and Use" Chemical Engineering Progress 47, No. 4: 199 - 204.

Mostoufi, N. and J. Chaouki (2001) "Local Solids Mixing in Gas-Solid Fluidized Beds" Powder Technology 114: 23 - 31.

Musmarra, D., M. Poletto *et al.* (1995) "Dynamic Waves in Fluidized Beds." Powder Technology 82: 255 - 268.

Newby, R. A. and D. L. Keairns (1986) "Test of the Scaling Relationships for Fluid-Bed Dynamics" Proceedings: Fluidization V, (K. Ostergaard and A. Sorensen Eds.), Engineering Foundation, New York, 31 - 38.

Nguyen, T. H. and J. R. Grace (1978) "Forces on Objects Immersed in Fluidized Beds" Powder Technology 19: 255 - 264.

Nicastro, M. T. and L. R. Glicksman (1984) "Experimental Verification of Scaling Relationships for Fluidized Beds" Chemical Engineering Science 39 No. 9: 1381-1391.

Nienow, A. W., P. N. Rowe *et al.* (1978) "Mixing and Segregation of a Small Proportion of Large Particles in Gas Fluidized Beds of Considerably Smaller Ones" AIChE Symposium Series, No. 176, Vol 74: 45 - 53.

Nienow, A. W. and Cheesman, D. J. (1980) In "Fluidization" (J. R. Grace and J. M. Matsen Eds.) Plenum, 373.

Ormiston, R. M., F. R. G. Mitchell, *et al.* (1965) "The Velocities of Slugs in Fluidised Beds" Transactions of the Institution of Chemical Engineers, 43: T209 - T216.

Ostrowski, K., S. P. Luke *et al.* (1999) "Real Time Visualisation and Analysis of Dense Phase Powder Conveying" Powder Technology 102: 1 - 13.

Pacho, D., and G. Davies (2001) "Application of Electrical Capacitance Measurements to Study the Collapse of Oil Foams" Proceedings: 2nd World Congress on Industrial Process Tomography, Hannover, Germany, VCIPT, 618 - 627.

Plaskowski, A., M. S. Beck *et al.* (1995) "Imaging Industrial Flows" Bristol, Institute of Physics Publishing.

Plaskowski, A., T. Piotrowski *et al.* (2001) "Progress of the ECT Application in Dust-Air Explosibility Research" Proceedings: 2nd World Congress on Industrial Process Tomography, Hannover, Germany, VCIPT, 339 – 345.

Potter, O. E. (1971) "Mixing" Chapter 7 in Fluidization, (J. F. Davidson and D. Harrison, Eds.), Academic Press, London, 293 – 381.

Press, W. H., S. A. Teukolsky, *et al.* (1992) "Numerical Recipes in C" Second Edition, Cambridge University Press, UK, 501.

Rapagna, S., R. Di Felice *et al.* (1992) "Experimental Verification of the Scaling Rules for Fine Powder Fluidization", Fluidization VII, (O. E. Potter, D. J. Nicklin, Eds.), Engineering Foundation, 579 – 587.

Rhodes, M. J., S. Zhou *et al.*, (1991) "Effects of Operating Conditions on Longitudinal Solids Mixing in a Circulating Fluidized Bed Riser" AIChE Journal, 37 No. 10: 1450 – 1458.

Rios, G. M., K. D. Tran *et al.*, (1986) "Free Object Motion in a Gas Fluidized Bed" Chemical Engineering Communications, 47: 247 – 272.

Romero, J. B. and L. N. Johanson (1962). "Factors Affecting Fluidized Bed Quality." Chemical Engineering Progress Symposium Series No. 38, Vol. 58: 28 - 37.

Rowe, P. N. and B. A. Partridge (1962) "Particle Movement Caused by Bubbles in a Fluidised Bed" In: Interaction Between Fluids and Particles, Institution of Chemical Engineers, London, 135 - 142.

Rowe, P. N., and B. A. Partridge (1965) "An X-Ray Study of Bubbles in Fluidised Beds" Transactions of the Institution of Chemical Engineers 43: T157 – T175.

Rowe, P. N., B. A. Partridge, *et al.* (1965) "The Mechanisms of Solids Mixing in Fluidized Beds." Transactions of the Institution of Chemical Engineers 43: T271 - T286.

Rowe, P. N. (1971) "Experimental Properties of Bubbles" in Fluidization (J.F Davidson and D. Harrison, Eds.), Academic Press, London, 121 – 191.

Rowe, P. N. (1976) "Prediction of Bubble Size in a Gas Fluidized Bed." Chemical Engineering Science **31**: 285 - 288.

Rowe, P. and H. Masson (1981) "Interaction of Bubbles with Probes in Gas Fluidized Beds." Transactions of The Institution of Chemical Engineers **59**: 177 - 185.

Roy, R. and J. F. Davidson (1989) "Similarity Between Gas-fluidized Beds at Elevated Temperature and Pressure", Proceedings: Fluidization VI, (J.R. Grace, L.W. Shemilt and M.A. Bergougnou, Eds.), Engineering Foundation, New York, 293 – 300.

Roy, R. (1989) "Pressure Fluctuations and Scale-up in Fluidized Beds" PhD Dissertation, Department of Chemical Engineering, University of Cambridge, U.K.

Roy, R. J. F. Davidson *et al.* (1990) "The Velocity of Sound in Fluidised Beds" Chemical Engineering Science **45**, No. 11: 3233 – 3245.

Sadasivan, N., D. Barreteau *et al.* (1980) "Studies on Frequency and Magnitude of Fluctuations of Pressure Drop in Gas-Solid Fluidised Beds" Powder Technology **26**: 67 – 74.

Sanders, W. C., S. L. Ceccio *et al.* (2001) "Applicability of Electrical Capacitance Tomography to the Study of Gasoline Direct Injection Sprays and Combustion" Proceedings: 2nd World Congress on Industrial Process Tomography, Hannover, Germany, VCIPT, 603 – 607.

Sanderson, P. J., M. J. Rhodes *et al.*, (2001) "Testing the Simplified Scaling Laws for Bubbling Fluidized Beds" Proceedings, Fluidization X, (M. Kwauk and J. Li, Eds.), Engineering Foundation, New York, 381 – 388.

Sanderson P. J. and M. J. Rhodes (2001) "An Experimental Investigation of the Simplified Scaling Laws for Bubbling Fluidized Beds" In Proceedings: 6th World Congress in Chemical Engineering, Melbourne, Australia.

Sanderson and Rhodes (2001a) "A Scale-up Comparison of Solids Motion and Mixing in Bubbling Fluidized Beds" In Proceedings: AIChE Annual Meeting, Reno, Nevada.

Sanderson P. J. and M. J. Rhodes (2002) "Verification of the Simplified Scaling Laws for Bubbling Fluidized Beds at Large Scales" In Proceedings: Fourth World Congress on Particle Technology, Sydney, Australia.

Schouten, J. C. and C. M. van den Bleek (1992) "Chaotic Hydrodynamics of Fluidization: Consequences for Scaling and Modelling of Fluid Bed Reactors." AIChE Symposium Series 88, No. 289: 70 - 84.

Schouten, J. C., M. L. M. van der Stappen *et al.* (1992) "Deterministic Chaos Analysis of Gas-Solids Fluidization" Fluidization VII, (O. E. Potter, D. J. Nicklin, Eds.), Engineering Foundation, 103 - 111.

Schouten, J. C., M. L. M. van der Stappen *et al.* (1996) "Scale-up of Chaotic Fluidized Bed Hydrodynamics." Chemical Engineering Science 51 No. 10: 1991 - 2000.

Shen, L., M. Zhang *et al.* (1995) "Solids Mixing in Fluidized Beds" Powder Technology 84: 207 - 212.

Shi, Y. F and L. T. Fan (1985) Powder Technology 41: 23.

Shuster, W. W. and P. Kisliak (1952) "The Measurement of Fluidization Quality." Chemical Engineering Progress 48, No. 9: 455 - 458.

Sitnai, O. (1981) "Solids Mixing in a Fluidized Bed with Horizontal Tubes" Ind. Eng. Chem. Process. Des. Dev. 20: 533 - 538

Stein, M., J. Seville *et al.* (1998) "Scale-up of Particle Motion in Fluidized Beds Using Positron Emission Particle Tracking" Proceedings: Fluidization IX, (T. M. Knowlton, Ed.), Engineering Foundation, 77 - 84.

Stewart, P. S. B., and J. F. Davidson (1967) "Slug Flow in Fluidised Beds" Powder Technology 1: 61 - 80.

Svensson, A., F. Johnsson *et al.* (1996) "Fluidization Regimes in Non-Slugging Fluidized Beds: The Influence of Pressure Drop Across the Air Distributor." Powder Technology 86: 299 - 312.

Tailby, S. R. and M. A. T. Cocquerel (1961) "Some Studies of Solids Mixing in Fluidised Beds" Transactions of the Institution of Chemical Engineers 39: 195 - 201.

Tamarin, A. I. (1964) "The Origin of Self-Excited Oscillations in Fluidized Beds" Int. Chem. Engng. 4 No.1: 50.

Taylor, P. A., M. H. Lorenz *et al.* (1973) "Spectral Analysis of Pressure Noise in a Fluidized Bed" Fluidization and its Applications, Toulouse, France, 90 - 98.

Tinga, W. R., W. A. G. Voss *et al.* (1973) "Generalized Approach to Multiphase Dielectric Mixture Theory" Journal of Applied Physics 44: 3897 - 3902.

Toei, R., R. Matsuno *et al.* (1974) "Deformation and Splitting of a Bubble in a Two-Dimensional Fluidized Bed" Journal of Chemical Engineering of Japan 7, No. 6: 447-455.

Toomey, R. D. and H. F. Johnstone (1952) "Gaseous Fluidization of Solid Particles." Chemical Engineering Progress 48, No. 5: 220 - 226.

Tsuji, Y., T. Kawaguchi *et al.* (1993) "Discrete Particle Simulation of Two-Dimensional Fluidized Bed" Powder Technology 77: 79 - 87.

Valenzuela, J. A., and L. R. Glicksman (1984) "An Experimental Study of Solids Mixing in a Freely Bubbling Two-Dimensional Fluidized Bed" Powder Technology 38: 63 - 72.

van Deemter, J. J. (1967) In the Proceedings of the International Symposium on Fluidization (A. A. H. Drinkenburg, Ed.) Netherlands University Press, 334 - 347.

van Deemter, J. J. (1985) "Mixing" In Fluidization 2nd Ed. (J. F. Davidson, R. Clift, and D. Harrison, Eds.), Academic Press, London, 331 - 355.

van den Bleek, C. M. and J. C. Schouten (1993a) "Deterministic Chaos: a New Tool in

Fluidized Bed Design and Operation." The Chemical Engineering Journal **53**: 75 - 87.

van den Bleek, C. M. and J. C. Schouten (1993b) "Can Deterministic Chaos Create Order in Fluidized Bed Scale-up." Chemical Engineering Science **48**, No. 13: 2367 - 2373.

van der Schaaf, J., J. C. Schouten *et al.* (1998) "Origin, Propagation and Attenuation of Pressure Waves in Gas-solid Fluidized Beds." Powder Technology **95**: 220 - 233.

van der Stappen, M. L. M., J. C. Schouten *et al.* (1995) "Chaotic Hydrodynamics and Scale-up of gas-solid Fluidized Beds" Proceedings: Fluidization VIII, (J-F. Large, and C. Laguerie, Eds.), AIChE, 625 - 632.

van der Stappen, M. L. M. (1996) "Chaotic Hydrodynamics of Fluidized Beds" PhD Dissertation, Delft University of Technology, The Netherlands.

van Ommen, J. R., J. C. Schouten *et al.* (1999) "Response Characteristics of Probe-Transducer Systems for Pressure Measurements in Gas-Solid Fluidized Beds: How to Prevent Pitfalls in Dynamic Pressure Measurements" Powder Technology **106**: 199-218.

Verloop, J., and P. M. Heertjes (1974) "Periodic Pressure Fluctuations in Fluidized Beds" Chemical Engineering Science **29**: 1035 - 1042.

Verloop, J., de Nie, L. H. *et al.* (1968/1969) "The Residence Time of Solids in Gas-Fluidized Beds" Powder Technology, **2**: 32 - 42.

Wace, P. F., and S. J. Burnett, (1961) "Flow Patterns in Gas-Fluidised Beds" Transactions of the Institution of Chemical Engineers, **39**: 168 - 174.

Wang, S. J., T. Dyakowski, *et al.* (1995) "Real Time Capacitance Imaging of Bubble Formation at the Distributor of a Fluidized Bed." The Chemical Engineering Journal **56**: 95 - 100.

Weast, R. C. (1975) "Handbook of Chemistry and Physics - 56th Edition" CRC Press, Ohio, U.S.A.

Wei, F., Y. Cheng *et al.* (1998) "Axial and Lateral Dispersion of Fine Particles in a

Binary Solids Riser" Canadian Journal of Chemical Engineering, 76: 19 – 26.

Weinall, C. E., K. Dam-Johansen *et al.* (1997) "Single Particle Behaviour in Circulating Fluidized Beds" Powder Technology 92: 241 – 252.

Werther, J., and O. Molerus (1973a) "The Local Structure of Gas-Fluidized Beds – I. A Statistically Based Measuring System" Int. Journal of Multiphase Flow, 1:103- 122.

Werther, J., and O. Molerus (1973b) "The Local Structure of Gas-Fluidized Beds – II. The Spatial Distribution of Bubbles" Int. Journal of Multiphase Flow, 1: 123 - 138.

Werther, J. (1974) "Influence of the Bed Diameter on the Hydrodynamics of Gas Fluidized Beds." AIChE Symposium Series 70, No. 141: 53 - 62.

Werther, J. (1978) "Scale-up of Fluidized Bed Reactors" Ger. Chem. Eng. 1: 243 – 251.

Werther, J. (1983) "Hydrodynamics and Mass Transfer Between the Bubble and Emulsion Phases in Fluidized Beds of Sand and Cracking Catalyst" in Fluidization IV (D. Kunii and R. Toei, Eds.) Engineering Foundation, New York, 93 – 101.

Werther, J. (1999) "Measurement Techniques in Fluidized Beds" Powder Technology 102: 15 – 36.

West, G.B., Brown, J.H. *et al.* (1997) "A General Model for the Origin of Allometric Scaling Laws in Biology" Science 276: 122-126.

White, R. B. and A. Zakhari (1998). "Lateral Mixing in a 1.56m Diameter Cold Fluid Bed Model" Proceedings: Fluidization IX, (T. M. Knowlton, Ed.), Engineering Foundation, New York, 349 – 355.

Whitehead, A. B., D. C. Dent (1967) "Behaviour of Multiple Tuyere Assemblies in Large Fluidized Beds" Proceedings of the International Symposium on Fluidization, (A. A.H Drinkenberg Ed.) Eindhoven, Netherlands University Press, Amsterdam, 802 -820.

Whitehead, A. B. (1970) "Some Problems in Large-Scale Fluidized Beds" in Fluidization, (J. F. Davidson and D. Harrison, Eds.) 781 – 814.

Whitehead, A. B., G. Gartside *et al.* (1976) "Fluidization Studies in Large Gas-Solid Systems. Part III. The Effect of Bed Depth and Fluidizing Velocity on Solids Circulation Patterns." Powder Technology 14: 61 - 70.

Wirth, K. E., M. Seiter *et al.* (1991) "Concentration and Velocities of Solids in Areas Close to the Walls in Circulating Fluidized Bed Systems." VGB Kraftwerkstechnik 71, No. 10: 824 - 828.

Witt, P. J., J. H. Perry *et al.* (1997) "Application of CFD to Fluidized Bed Systems" 4th Annual Conference, CRC for New Technologies for Power Generation from Low-Rank Coal.

Wong, H. W., and M. H. I. Baird (1971) "Fluidization in Pulsed Gas Flow" The Chemical Engineering Journal, 2: 104.

Woollard, I. N. M., and O. E. Potter (1968) "Solids Mixing in Fluidized Beds" AIChE Journal, Vol 14 No. 3: 388 - 391.

Xie, C. G., S. M. Huang *et al.* (1994) "Experimental Evaluation of Capacitance Tomographic Flow Imaging Systems Using Physical Models." IEE Proceedings - Circuits Systems and Devices Vol. 141, No. 5, October, 357 - 368.

Yagi, S. and I. Muchi (1952) Chem. Eng. (Japan) 16: 307.

Yang, W. Q. and A. L. Stott (1993) "Low Value Capacitance Measurements for Process Tomography" In: Tomographic Techniques for Process Design and Operation, (M.S. Beck *et al.*, Eds.), Computational Mechanics Publications, Southampton, 107 - 114.

Yang, W. Q., J. C. Gamio *et al.* (1997) "A Fast Iterative Image Reconstruction Algorithm for Capacitance Tomography" in Sensors and Their Applications, Vol. VIII A. (T. Augousti and M. N. White, Eds.), IOP Publisher, 47 - 52.

Yates, J. G. and S. J. R. Simons (1994) "Experimental Methods in Fluidization Research." International Journal of Multiphase Flow 20: 297 - 330.

Zhang, M. C. and R. Y. K. Yang (1987) "On the Scaling Laws for Bubbling Gas-Fluidized Bed Dynamics." Powder Technology 51: 159 - 165.

APPENDIX A – LITERATURE DATA

This appendix contains supporting information for the literature review of scaling law experimental verification work that was presented in Chapter 2 (Section 2.9). Summary data have been tabulated for the scales and operating conditions used by previous investigators of both the simplified and the full scaling laws for bubbling fluidized beds. Summary data for this study are also presented for comparative purposes.

The following points apply to the data presented:

- The consequences of rounding, occasional errors in the original data and the necessity to back-calculate (or assume) some of the values will result in small discrepancies between the tabulated values in this appendix and some of the original literature results. (However, the data presented here should all be within 10% of the originally reported values.)
- Sphericity details were often not reported in the original references, hence the abbreviation "N/R" is used in these cases.
- Geldart group classification has been made in accordance with Equations 6 and 8 of the original paper (Geldart, 1973). A $\pm 10\%$ margin was applied within which a "transition" classification (eg A/B or B/D) would be selected. However, for all literature data, no transition classification was necessary as systems fell clearly into a particular group.
- Grace regime map parameters have been calculated as per Grace (1986) and correspond to coordinates of the regime map presented in Chapter 1, Figure 1.2.
- The nomenclature for the tabulated data is defined below the table on each page.

Experimental Verification for Bubbling Beds - Review of Experimental Details

Reference	Authors	System ID	d _p (μm)	Φ	L (m)	ρ _s (g/cm ³)	U _{mf} (m/s)	ρ _f (g/cm ³)	μ (kg/ms)	Geldart Classification		d _p (μm)	ρ _s (g/cm ³)	Group*	Grace Regime Map			Dimensionless Groups									
										LOW U (m/s)	HIGH U (m/s)				d _p *	U* (low)	U* (high)	ρ _s /ρ _f	Fr _{mf} (low)	Fr _{mf} (high)	U/U _{mf} (low)	U/U _{mf} (high)	Re _p (low)	Re _p (high)	D/d _p	Ar	
1	This Work	A	230	Matched	0.146	2.65	0.039	1.23E-03	1.79E-05	0.058	0.327	230	2.65	B	10.67	8.59E-02	4.85E-01	2154	2.35E-03	0.075	1.49	8.38	0.9	5.2	635	0.56	
		B	286		0.3	2.65	0.058	1.21E-03	1.81E-05	0.092	0.614	286	2.65	B	13.08	1.34E-01	8.94E-01	2199	2.88E-03	0.128	1.59	10.59	1.8	11.7	1049	1.02	
		C	326		0.6	2.65	0.07	1.23E-03	1.79E-05	0.100	0.650	326	2.65	B	15.12	1.48E-01	9.63E-01	2154	1.70E-03	0.072	1.43	9.29	2.2	14.6	1840	1.60	
		D	479		1.56	2.65	0.127	1.18E-03	1.85E-05	0.150	0.500	479	2.65	B	21.43	2.14E-01	7.13E-01	2246	1.47E-03	0.016	1.18	3.94	4.6	15.3	3257	4.39	
		A*	344		0.146	2.65	0.085	1.23E-03	1.79E-05	0.101	0.327	344	2.65	B	15.95	1.50E-01	4.85E-01	2154	7.12E-03	0.075	1.19	3.85	2.4	7.7	424	1.89	
		B*	388		0.3	2.65	0.125	1.21E-03	1.81E-05	0.159	0.614	388	2.65	B	17.74	2.32E-01	8.94E-01	2199	8.59E-03	0.128	1.27	4.91	4.1	15.9	773	2.54	
		G	300		0.146	4.1	0.082	1.23E-03	1.79E-05	0.101	0.327	300	4.10	B	16.09	1.29E-01	4.19E-01	3333	7.12E-03	0.075	1.23	3.99	2.1	6.7	487	1.25	
		D*	479		0.6	2.65	0.127	1.23E-03	1.79E-05	0.100	0.650	479	2.65	B	22.21	1.48E-01	9.63E-01	2154	1.70E-03	0.072	0.79	5.12	3.3	21.4	1253	5.09	
2	Fitzgerald & Crane (1980)	small	240	N/R	0.0564	2.65	N/R	2.41E-02	1.47E-05	0.160	0.122	240	2.63	B	34.12	1.15E+00	1.41E+00	110	0.018	0.027			39.3	48.0	235	364.50	
		large	2068		0.483	0.15	N/R	1.19E-03	1.85E-05	0.292	0.358	2068	0.15	B	35.54	1.09E+00	1.34E+00	126	0.018	0.027			38.8	47.6	234	358.98	
3	Fitzgerald et al (1984)	AFBC	2000	N/R	1.83	2.5	N/R	3.04E-04	4.70E-05	2.440		2000	2.50	D	30.00	1.05E+00		8224	0.332				31.6		915	3.28	
		3D cold	500		0.46	9	N/R	1.12E-03	1.90E-05	1.180		500	9.00	D	32.47	1.07E+00		8036	0.309				34.8		920	4.76	
		2D helium	1000		0.483	2.5	N/R	3.04E-04	1.80E-05	1.770		1000	2.50	D	28.44	1.05E+00		8224	0.661				29.9		483	2.80	
		2D thin air	500		0.242	9	N/R	1.12E-03	1.90E-05	1.170		500	9.00	D	32.47	1.06E+00		8036	0.577				34.5		484	4.26	
4	Nicasro & Glicksman (1984)	Hot Bed	677	0.80	0.61	2.63	0.16	3.61E-04	4.40E-05	0.930		677	2.63	D	11.43	4.52E-01		7285	0.145		5.81		5.2		901	0.20	
		Cold Bed	170	0.80	0.15	7.38	0.1	1.25E-03	1.85E-05	0.470		170	7.38	B	10.91	4.95E-01		5904	0.150		4.70		5.4		882	0.22	
		Cold Bed MS	677	0.80	0.15	2.63	0.18	1.21E-03	1.85E-05	0.940		677	2.63	D	30.47	1.37E+00		2174	0.600		5.22		41.6		222	13.02	
5	Horio et al (1986)	I	376	N/R	0.24	2.66	0.112	1.21E-03	1.85E-05	0.224		376	2.66	B	16.99	3.24E-01		2198	0.021		2.00		5.5		638	2.23	
		II	305		0.1	2.66	0.074	1.21E-03	1.85E-05	0.146		305	2.66	B	13.78	2.11E-01		2198	0.022		1.97		2.9		328	1.19	
		III	236		0.041	2.66	0.046	1.21E-03	1.85E-05	0.092		236	2.66	B	10.66	1.33E-01		2198	0.021		2.00		1.4		174	0.55	
		IV	376		0.1	2.66	0.112	1.21E-03	1.85E-05	0.184		376	2.66	B	16.99	2.66E-01		2198	0.035		1.64		4.5		266	2.23	
		I	236		0.1	2.66	0.046	1.21E-03	1.85E-05	0.118		236	2.66	B	10.66	1.71E-01		2198	0.014		2.57		1.8		424	0.55	
		VI	376		0.041	2.66	0.112	1.21E-03	1.85E-05	0.158		376	2.66	B	16.99	2.29E-01		2198	0.062		1.41		3.9		109	2.23	
6	Horio et al (1986a)	A	182	N/R	0.6	2.6	0.027	1.21E-03	1.85E-05	0.120		182	2.60	B	8.16	1.75E-01		2149	2.45E-03		4.44		1.4		3297	0.25	
		B	150		0.3	2.6	0.018	1.21E-03	1.85E-05	0.082		150	2.60	B	6.73	1.20E-01		2149	2.28E-03		4.56		0.8		2000	0.14	
		C	129		0.15	2.6	0.011	1.21E-03	1.85E-05	0.058		129	2.60	B	5.78	8.46E-02		2149	2.29E-03		5.27		0.5		1163	0.09	
		D	106		0.05	2.6	0.0072	1.21E-03	1.85E-05	0.034		106	2.60	B	4.75	4.96E-02		2149	2.36E-03		4.72		0.2		472	0.05	
		A2	182		0.6	2.6	0.027	1.21E-03	1.85E-05	0.120		182	2.60	B	8.16	1.75E-01		2149	2.45E-03		4.44		1.4		3297	0.25	
		B2	150		0.3	2.6	0.018	1.21E-03	1.85E-05	0.082		150	2.60	B	6.73	1.20E-01		2149	2.28E-03		4.56		0.8		2000	0.14	
		C2	129		0.15	2.6	0.011	1.21E-03	1.85E-05	0.058		129	2.60	B	5.78	8.46E-02		2149	2.29E-03		5.27		0.5		1163	0.09	
		B'	150		0.194	2.6	0.018	1.21E-03	1.85E-05	0.082		150	2.60	B	6.73	1.20E-01		2149	3.53E-03		4.56		0.8		1293	0.14	
		C'	129		0.097	2.6	0.011	1.21E-03	1.85E-05	0.058		129	2.60	B	5.78	8.46E-02		2149	3.54E-03		5.27		0.5		752	0.09	
		B2'	150		0.194	2.6	0.018	1.21E-03	1.85E-05	0.082		150	2.60	B	6.73	1.20E-01		2149	3.53E-03		4.56		0.8		1293	0.14	
		C2'	129		0.097	2.6	0.011	1.21E-03	1.85E-05	0.058		129	2.60	B	5.78	8.46E-02		2149	3.54E-03		5.27		0.5		752	0.09	
7	Newby & Kearns (1986)	Half-scale	100	1.00	0.18	7.625	N/R	3.06E-03	1.82E-05	0.033	0.075	100	7.62	B	8.84	6.28E-02	1.43E-01	2492	6.17E-04	3.19E-03			0.6	1.3	1800	0.28	
		Full-scale1	200	1.00	0.36	2.467	N/R	1.18E-03	1.85E-05	0.049	0.110	200	2.47	B	8.74	7.15E-02	1.61E-01	2091	6.80E-04	3.43E-03			0.6	1.4	1800	0.32	
		Full-scale2	200	1.00	0.36	2.931	N/R	1.25E-03	1.85E-05	0.049	0.110	200	2.93	B	9.43	7.02E-02	1.58E-01	2345	6.80E-04	3.43E-03			0.7	1.5	1800	0.36	
8	Zhang & Yang (1987)	2D Full-scale	805	Matched	0.915	2.65	0.615	1.21E-03	1.85E-05	1.107	1.480	805	2.65	D	36.32	1.60E+00	2.15E+00	2190	0.137	0.244	1.80	2.41	58.3	77.9	1137	21.89	
		2D Half-scale	557		0.305	2.65	0.355	1.21E-03	1.85E-05	0.639	0.852	557	2.65	B	25.13	9.26E-01	1.24E+00	2190	0.136	0.243	1.80	2.40	23.3	31.0	548	7.25	
9	Roy & Davidson (1989)	A (Hot)	600	N/R	0.135	2.65	0.15	3.98E-04	4.50E-05	0.780		600	2.65	B	10.33	4.01E-01		6658	0.459		5.20		4.1		225	0.17	
		B	180		0.045	11.1	0.09	1.22E-03	1.85E-05	0.450		180	11.10	B	13.13	4.07E-01		9098	0.459		5.00		5.3		250	0.25	
		C	500		0.045	11.1	0																				

Experimental Verification for Bubbling Beds - Review of Experimental Details (continued)

												Geldart Classification:			Grace Regime Map:			Dimensionless Groups										
Reference	Authors	System ID	d_p (μm)	Φ	L (m)	ρ_s (g/cm^3)	U_{mf} (m/s)	ρ_f (g/cm^3)	μ (kg/ms)	LOW U (m/s)	HIGH U (m/s)	d_p (μm)	ρ_s/ρ_f (g/cm^3)	Group*	d_p^*	U^* (low)	U^* (high)	ρ_f/ρ_f	Fr_{bed} (low)	Fr_{bed} (high)	U/U_{mf} (low)	U/U_{mf} (high)	Re_p (low)	Re_p (high)	D/d_p	Ar		
10	Almstedt & Zukay (1990)	Hot Bed	962	0.82	0.78	2.2	0.19	2.41E-03	4.41E-05	1.270		962	2.20	D	28.76	2.32E+00		913	0.211		6.68		66.8		811	26.08		
		Cold Bed	486	0.75	0.394	3	0.14	2.81E-03	1.85E-05	0.900		486	3.00	B	30.26	2.20E+00		1068	0.210		6.43		66.4		811	25.98		
		Cold Bed	486	0.82	0.394	2.2	0.12	2.81E-03	1.85E-05	0.900		486	2.20	B	27.29	2.43E+00		783	0.210		7.50		66.4		811	25.98		
		Cold Bed	962	0.82	0.394	2.2	0.28	2.81E-03	1.85E-05	0.900		962	2.20	D	54.01	2.43E+00		783	0.210		3.21		131.5		410	201.49		
11	Liu & Lan (1992)	Case 1: 1 (Hot)	290	N/R	0.208	3.865	0.065	6.51E-04	2.84E-05	0.100	0.700	290	3.86	B	9.07	7.33E-02	5.13E-01	5937	0.005	0.240	1.54	10.77	0.7	4.7	717	0.13		
		2	290		0.208	2.64	0.045	4.44E-04	1.95E-05	0.100	0.500	290	2.64	B	9.03	7.31E-02	3.65E-01	5946	0.005	0.123	2.22	11.11	0.7	3.3	717	0.12		
		3	290		0.208	3.865	0.1	1.22E-03	1.80E-05	0.100	0.500	290	3.86	B	15.16	1.30E-01	6.48E-01	3168	0.005	0.123	1.00	5.00	2.0	9.8	717	1.10		
		Case 2: 1	2770		0.728	0.24	0.41	1.15E-03	1.80E-05	0.710	0.880	2770	0.24	D	56.12	2.24E+00	2.77E+00	209	0.071	0.108	1.73	2.15	125.7	155.7	263	851.06		
		2	390		0.104	2.67	0.14	1.23E-02	1.20E-05	0.245	0.303	390	2.66	B	50.93	1.92E+00	2.38E+00	217	0.059	0.090	1.75	2.16	97.9	121.1	267	611.38		
		3	390		0.104	2.67	0.17	1.18E-03	1.80E-05	0.290	0.360	390	2.67	B	17.82	4.16E-01	5.17E-01	2263	0.082	0.127	1.71	2.12	7.4	9.2	267	2.50		
		Horio Case 1 A	290		0.208	3.865	0.1	1.18E-03	1.80E-05	0.200	0.500	290	3.86	B	14.99	2.54E-01	6.34E-01	3275	0.020	0.123	2.00	5.00	3.8	9.5	717	1.03		
		B	423		0.208	2.64	0.1	1.18E-03	1.80E-05	0.200	0.500	423	2.64	B	19.25	2.88E-01	7.20E-01	2237	0.020	0.123	2.00	5.00	5.5	13.9	492	3.19		
		Horio C2 A (Hot)	423		0.208	2.64	0.05	6.51E-04	2.84E-05	0.15	0.6	423	2.64	B	11.65	1.25E-01	4.99E-01	4055	0.011	0.176	3.00	12.00	1.5	5.8	492	0.39		
		B	290		0.208	2.34	0.05	1.18E-03	1.80E-05	0.1	0.4	290	2.34	B	12.68	1.50E-01	6.00E-01	1983	0.005	0.078	2.00	8.00	1.9	7.6	717	1.03		
		12	Di Felice, Rapagna et al (1992a)	A	597	1.00	0.192	1.216	0.13	1.10E-03	1.80E-05	0.183	0.707	597	1.21	B	20.50	3.26E-01	1.26E+00	1105	0.018	0.266	1.41	5.44	6.7	25.8	322	7.80
				B	348	1.00	0.106	2.64	0.11	2.40E-03	1.80E-05	0.119	0.495	348	2.64	B	20.06	2.75E-01	1.14E+00	1100	0.014	0.236	1.08	4.50	5.5	23.0	305	7.35
C	158			1.00	0.0495	8.77	0.08	7.80E-03	1.76E-05	0.094	0.362	158	8.76	B	20.44	3.21E-01	1.24E+00	1124	0.018	0.270	1.17	4.52	6.6	25.3	313	7.60		
D	163			0.60	0.0495	7.3	0.12	7.69E-03	1.82E-05	0.125	0.413	163	7.29	B	19.23	4.43E-01	1.46E+00	961	0.032	0.350	1.04	3.44	8.5	28.1	304	7.41		
E	348			1.00	0.192	2.64	0.11	1.10E-03	1.80E-05	0.130	0.622	348	2.64	B	15.47	1.78E-01	8.54E-01	2400	0.009	0.205	1.18	5.65	2.8	13.2	552	1.54		
13	Di Felice, Rapagna et al (1992b)	1	14	N/R	0.0495	8.92	0.001	1.16E-02	1.90E-05	0.001	0.015	14	8.91	A	1.98	4.33E-03	6.49E-02	769	2.06E-06	4.63E-04	1.00	15.00	0.0	0.1	3536	0.01		
		2	68		0.192	0.873	0.0016	1.10E-03	1.90E-05	0.005	0.035	68	0.87	A	2.02	9.76E-03	6.83E-02	794	1.33E-05	6.50E-04	3.13	21.88	0.0	0.1	2824	0.01		
		3	348		0.106	2.64	0.11	2.40E-03	1.80E-05	0.180	0.500	348	2.64	B	20.06	4.16E-01	1.16E+00	1100	0.031	0.240	1.64	4.55	8.4	23.2	305	7.35		
		4	597		0.192	1.216	0.13	1.10E-03	1.80E-05	0.200	0.650	597	1.21	B	20.50	3.26E-01	1.16E+00	1105	0.021	0.224	1.54	5.00	7.3	23.7	322	7.80		
		5	950		0.106	8.8	0.85	4.40E-03	1.80E-05	0.700	1.400	950	8.80	D	100.15	1.62E+00	3.25E+00	2000	0.471	1.885	0.82	1.65	162.6	325.1	112	502.57		
		6	2400		0.275	2.24	1.1	1.10E-03	1.80E-05	1.500	2.600	2400	2.24	D	101.02	2.18E+00	3.77E+00	2036	0.834	2.506	1.36	2.36	220.0	381.3	115	506.46		
14	Rapagna et al (1992)	A1	86	N/R	0.106	1.054	0.0039	0.001054	1.85E-05	0.005	0.070	86	1.05	A	2.72	8.99E-03	1.26E-01	1000	2.403E-05	0.005	1.28	17.95	0.0	0.3	1233	0.02		
		A2	47		0.053	2.54	0.0025	0.00254	1.85E-05	0.005	0.050	47	2.54	A	2.68	1.21E-02	1.21E-01	1000	4.398E-05	0.004	2.00	20.00	0.0	0.3	1233	0.02		
		B1	96		0.118	0.873	0.0038	0.0011349	1.85E-05	0.005	0.070	96	0.87	A	2.93	1.01E-02	1.41E-01	769	2.153E-05	0.004	1.32	18.42	0.0	0.4	1233	0.03		
		B2	47		0.058	2.54	0.0024	0.003302	1.85E-05	0.005	0.050	47	2.54	A	2.92	1.44E-02	1.44E-01	769	4.398E-05	0.004	2.08	20.83	0.0	0.4	1233	0.03		
		C1	61		0.075	1.5	0.0021	0.00105	1.85E-05	0.003	0.040	61	1.50	A	2.17	4.78E-03	6.38E-02	1429	1.220E-05	0.002	1.43	19.05	0.0	0.1	1233	0.01		
		C2	42		0.052	2.54	0.0018	0.001778	1.85E-05	0.003	0.040	42	2.54	A	2.12	5.70E-03	7.63E-02	1429	1.772E-05	0.003	1.67	22.22	0.0	0.2	1233	0.01		
		D1	61		0.075	1.5	0.0021	0.0015	1.85E-05	0.005	0.050	61	1.50	A	2.45	1.01E-02	1.01E-01	1000	3.388E-05	0.003	2.38	23.81	0.0	0.2	1233	0.01		
		D2	92		0.113	0.873	0.0032	0.000873	1.85E-05	0.005	0.060	92	0.87	A	2.57	8.44E-03	1.01E-01	1000	2.247E-05	0.003	1.56	18.75	0.0	0.3	1233	0.02		
		E1	14		0.017	8.92	0.001	0.00892	1.80E-05	0.002	0.015	14	8.91	A	1.88	7.40E-03	5.55E-02	1000	2.362E-05	0.001	2.00	15.00	0.0	0.1	1233	0.01		
		E2	68		0.084	0.873	0.0016	0.000873	1.85E-05	0.002	0.033	68	0.87	A	1.90	3.38E-03	5.57E-02	1000	4.863E-06	0.001	1.25	20.63	0.0	0.1	1233	0.01		
		15	van der Stappen (1996)	1 (large)	400	Matched	0.384	2.64	0.142	1.29E-03	1.85E-05	0.260	0.884	400	2.64	B	0.65	7.39E-02	2.51E-01	2047	0.018	0.207	1.83	6.23	7.3	24.7	960	3.05
				2 (small)	280		0.1	2.64	0.075	1.29E-03	1.85E-05	0.133	0.451	280	2.64	B	0.58	4.26E-02	1.44E-01	2047	0.018	0.207	1.77	6.01	2.6	8.9	357	1.05
				3 (large PS)	560	Mis-matched	0.384	1.102	0.14	1.29E-03	1.85E-05	0.350	0.884	560	1.10	B	0.30	8.89E-02	2.24E-01	854	0.033	0.207	2.50	6.31	13.7	34.5	686	8.38
				4 (small mis-scaled)	280		0.1	2.64	0.069	1.29E-03	1.85E-05	0.097	0.4	280	2.64	B	0.58	3.10E-02	1.28E-01	2047	0.010	0.163	1.41	5.80	1.2	7.8	357	1.05
16	Farrel et al (1998)	polythene	379	0.85	0.1016	0.94	0.23	1.21E-03	1.85E-05	0.230	0.550	379	0.94	B	0.22	6.37E-02	1.52E-01	777	0.053	0.304	1.00	2.39	5.7	13.6	268	2.28		
		limestone	653	0.82	0.1016	2.74	0.24	1.21E-03	1.85E-05	0.240	0.580	653	2.74	D	0.78	5.55E-02	1.34E-01	2264	0.058	0.338	1.00	2.42	10.3	24.8	156	11.69		
17	Stein et al (1998)	Resin Beads	650	1.00	0.07	1.1	0.11	1.21E-03	1.85E-05	0.110																		

APPENDIX B – FLOW MEASUREMENTS

B.1 Introduction – Sources of Error

In the preceding technical chapters of this work, an indication of the random errors in results data has been provided by presenting data for a limited number of repeated experiments on the same charts. Thus the "scatter" on the charts immediately give the reader a feel for the reproducibility of results. Now, one of the primary sources of experimental error in hydrodynamic similarity experiments is the measurement of gas flow, and the size of the likely flow measurement error can be estimated from the measurement data. However, in order to present the experimental results of this study with reasonable clarity, estimated errors for the gas flow have not been included on the results charts. In this appendix, the procedure for flow measurements is described, and the associated error estimates are presented.

Unlike many other experimental studies of fluidization where small errors in gas velocity would tend to go unnoticed, the comparative nature of hydrodynamic similarity experiments requires that gas velocities be set very accurately. This was emphasized in the current work when significant and unexpected deviations from similarity were found on two separate occasions in some early experimental comparisons. In both cases, ultimately the source of these deviations was found to be flow measurement error. In one case, the diaphragm gasmeter used to calibrate the variable area flowmeters was found to be faulty; repairs and recalibration of the gasmeter by the manufacturer and subsequent recalibration of the flowmeters solved the problem. In the other case, there was mis-communication about the orifice diameter used for flow measurement in the large-scale work. (The actual orifice size was 4 inches; however this had been reported as 100 mm).

The basis for reporting air flow in the fluidized beds used in this study was the superficial gas velocity just above the bed surface. In this appendix, the calibration data for the flowmeters, the basis for the orifice plate measurements and the estimated errors for flow measurement are presented. Also reported are the changes in gas transport properties due to air heating by the blowers (where used) and the effect this has on the calculation of the scaling criteria dimensionless groups.

B.2 Flowmeter Calibration Charts and Error Estimates

B.2.1 146 mm System

The 146 mm system used 2 flowmeters for low and higher gas flow measurements. The flowmeters were manufactured by Fischer and Porter and had the following specifications:

Size	Tube No.	Float No.
Small	FP-1/2-17-G-10	1/2-GSVT-45-A
Large	FP-3/4-27-G-10	3/4-GNSVGT-59

Table B.1 Flowmeter tube and float specifications for the 146 mm system

The flowmeters were calibrated with an "Aluminumcase" Diaphragm Meter Model AL-1400 manufactured by the American Meter Company, which had a maximum throughput capacity of $39.6 \text{ m}^3/\text{h}$. The diaphragm meter was serviced and calibrated by the manufacturer prior to use.

The flowmeter calibration procedure was as follows:

- 1) The supply line was removed from the windbox and connected to the meter inlet.
- 2) The supply system was turned on and adjusted as normal for an experimental run (nominal supply pressure; 100 kPag).
- 3) The flow was set to a given value on the flowmeter under consideration (other flowmeter turned off).
- 4) With a stable flow, the volume of air passing through gas meter in a given time period was measured. Note that this volumetric flowrate was recorded at temperature and pressure conditions identical to those at the bed surface during the experiments.
- 5) A simple conversion from volumetric flow to superficial gas velocity (based on the cross-sectional area of the bed) provided the necessary data for calibrating the flowmeters.

Errors in the calibration data for the flowmeters were estimated based on the following assumptions:

- The error in the volume measured by the gasmeter was assumed to be one-half of a division on the meter's volume scale (*ie* 0.5 L).
- The error in timing was approximately the reaction time of the timekeeper (0.3 s).
- The flowmeter scale reading error was one division (*ie* 1 % of full scale).

Errors calculations were based on the maximum error approach, *viz*:

If $y = a + b$ and $x = a.b$, then

$$\delta y = \delta a + \delta b \quad (B.1)$$

and

$$\%y = \%a + \%b \quad (B.2)$$

where δ refers to the absolute error and $\%$ refers to the relative error. Note that absolute and relative errors are related by:

$$\%x = \frac{\delta x}{x} \quad (B.3)$$

Addition and subtraction operations cause addition of absolute errors; multiplication and division cause addition of relative errors.

Figures B.1 and B.2 show the resulting calibration chart for the smaller flowmeter and larger flowmeters respectively. The calibration points are presented with estimated errors in the form of errorbars around each point. A (straight) line of best fit has been calculated for the calibration points and an upper and lower limiting line denotes the maximum and minimum errors possible.

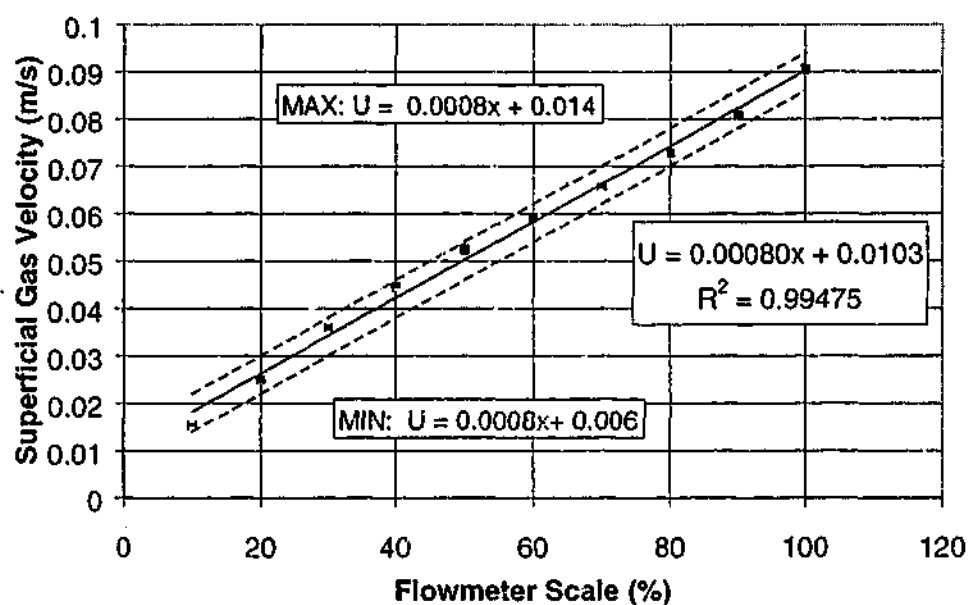


Figure B.1 Calibration chart for the small flowmeter used at the 146 mm scale. Solid line is the line of best-fit (equation shown at top right). Dashed lines refer to the maximum and minimum values expected given the estimated error on the measurements. Maximum and minimum values can be calculated from the equations shown on the chart. In the equations, "x" refers to the flowmeter reading.

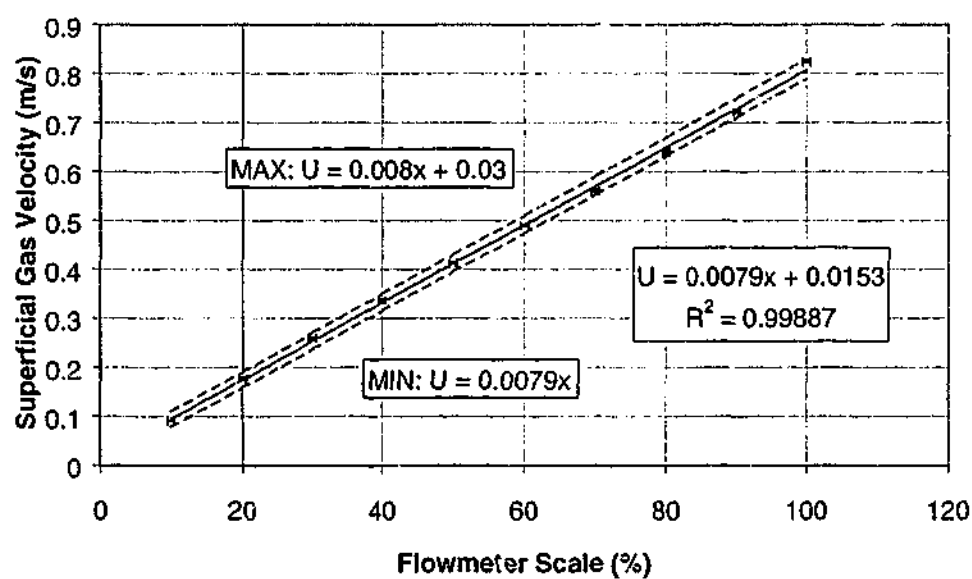


Figure B.2 Calibration chart for the large flowmeter used at the 146 mm scale. Solid line is the line of best-fit (equation shown at top right). Dashed lines refer to the maximum and minimum values expected given the estimated error on the measurements. Maximum and minimum values can be calculated from the equations shown on the chart. In the equations, "x" refers to the flowmeter reading.

B.2.2 300 mm System

The 300 mm system also used 2 flowmeters for low and higher gas flow measurements. Again, the flowmeters were manufactured by Fischer and Porter. They had the following specifications:

Size	Tube No.	Float No.
Small	FP-3/4-27-G-10	¾-GNSVGT-59
Large	FP-2-27-G-10	2-GSVGT-97

Table B.2 Flowmeter tube and float specifications for the 300 mm system

The flowmeters were calibrated with the same diaphragm gasmeter as was used for the 146 mm bed.

The flowmeter calibration procedure was as follows:

- 1) The supply line was removed from the windbox and connect to the meter inlet.
- 2) The supply system (blower, etc) was turned on and adjusted as normal for an experimental run (nominal supply pressure 80 kPag; supply air temperature 15°C at low gas velocity to 35°C at high gas velocity).
- 3) The flow was set to a given value on the flowmeter under consideration (other flowmeter turned off).
- 4) With a stable flow, the volume of air passing through gas meter in a given time period was measured. This volumetric flowrate was also recorded at temperature and pressure conditions identical to those at the bed surface during the experiments. (This was achieved by adjusting the set-point of the supply air cooling system to give the same exit temperature from the gasmeter as had been measured in the freeboard during preliminary experiments).
- 5) A simple conversion from volumetric flow to superficial gas velocity (based on the cross-sectional area of the 300 mm bed) provided the necessary data for calibrating the flowmeters.

Errors in the calibration data for the flowmeters were estimated based on the same assumptions as in the 146 mm bed case. The same approach was also used to quantify the errors in the calibration data. Figure B.3 shows the resulting calibration chart for the smaller flowmeter. The calibration points are presented with estimated errors in the

form of errorbars around each point. A (straight) line of best fit has been calculated for the calibration points and an upper and lower limiting line denote the maximum and minimum errors possible.

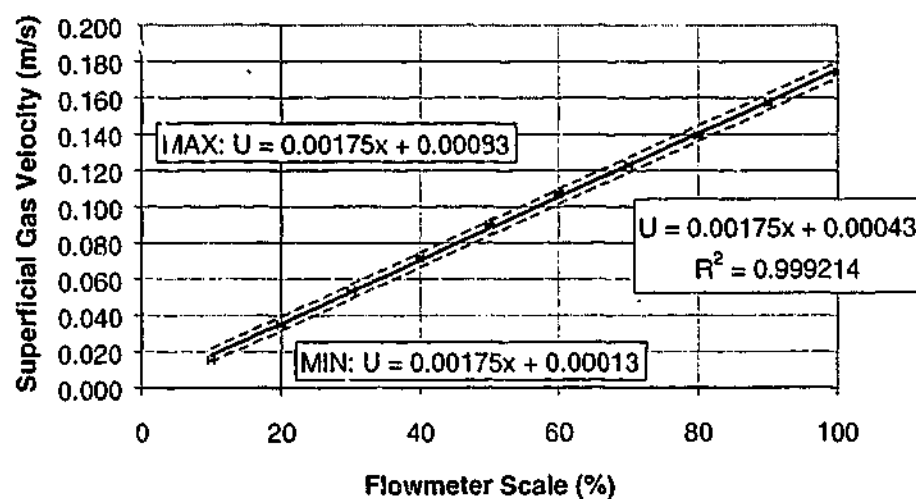


Figure B.3 Calibration chart for the small flowmeter used at the 300 mm scale. Solid line refers to the fitted equation (shown top right). Dashed lines refer to the maximum and minimum values expected given the estimated error on the measurements. Maximum and minimum values can be calculated from the equations shown on the chart. In the equations, "x" refers to the flowmeter reading.

The case of the larger flowmeter was a little more complicated, due to the fact that the flowmeter range exceeded the maximum gas capacity of the gasmeter. Calibration data with estimated errors are presented in Figure B.4. Figure B.5 shows the same data with an extrapolated line of best fit to the full-scale range of the flowmeter. Two alternative extrapolated lines passing through the limiting-case errors in the calibration data show the increase in possible error in the extrapolated line as the gas velocity increases.

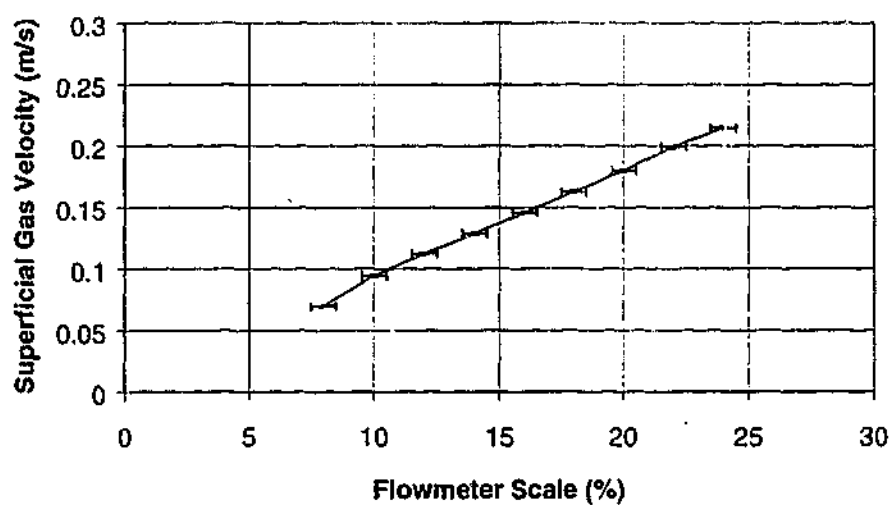


Figure B.4 Calibration values measured for the large flowmeter used with the 300 mm bed, showing estimated measurement errors. Unfortunately, higher flowrates than those shown could not be measured using the calibrated diaphragm gas meter and extrapolation was required (see Figure B.5).

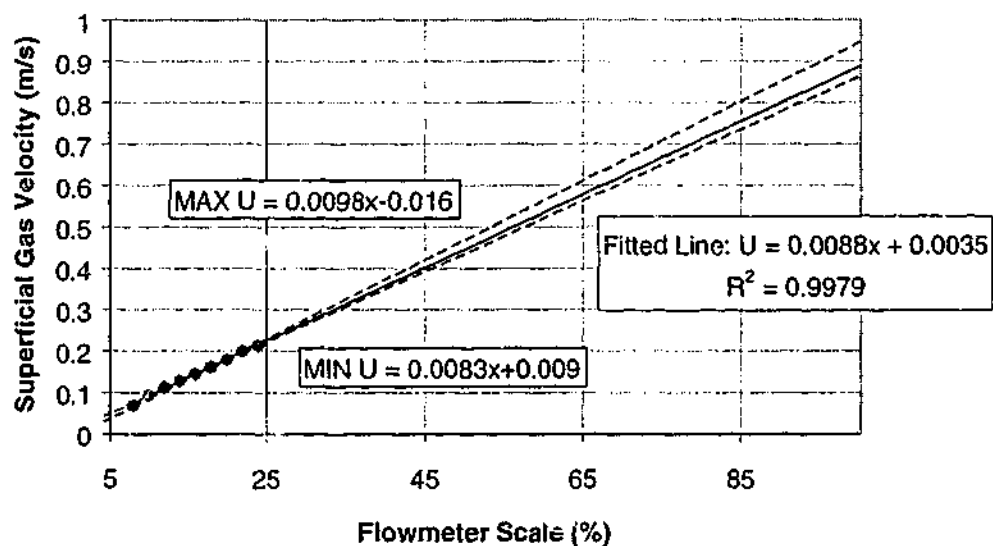


Figure B.5 Extrapolation of calibration data for the large flowmeter used at the 300 mm scale. The solid line is the extrapolated line of best fit through the data, (equation shown at top right). Dotted lines refer to the possible maximum and minimum values of the extrapolation. Equations for these lines are printed on the chart. In the equations, "x" refers to the flowmeter reading.

B.3 Orifice Plate Flow Measurements

Both the 600 mm and 1560 mm fluidized beds employed the same basic orifice plate arrangement for air flowrate measurements, although the diameters of the orifices differed. The pressure drop across the orifice was measured with standard D and D/2 tapping points and the plates themselves were manufactured in accordance with British Standard BS 1042 : 1943.

B.3.1 Orifice Plate Sample Calculation

A sample calculation for the superficial gas velocity in the 1560 mm bed is presented below, with reference to Figure B.6.

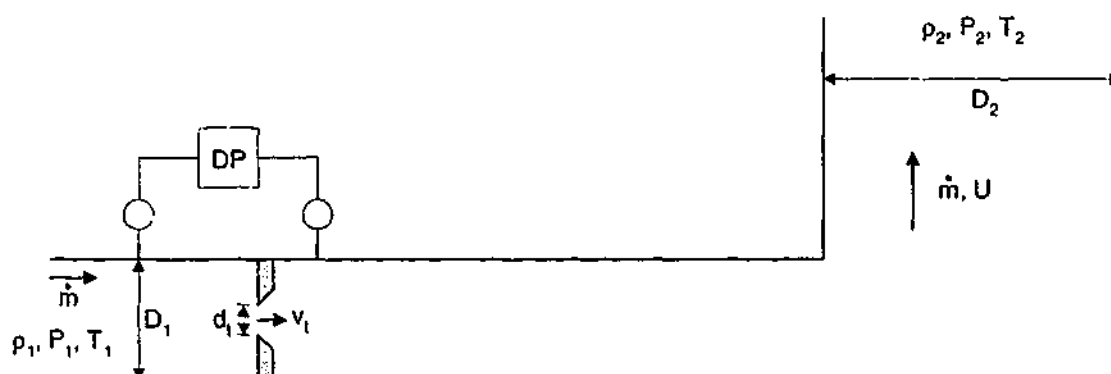


Figure B.6 Basis for orifice plate sample calculation

Measured parameters:

Upstream line pressure $P_1 = 68.5$ kPag

Orifice pressure drop $DP = 14.71$ kPa

Air temperature at orifice plate $T_1 = 83$ °C

Downstream pressure $P_2 = 0$ kPag (bed surface)

Downstream temperature $T_2 = 35$ °C (bed surface)

Other information:

Supply line diameter $D_1 = 16$ inches (406.4 mm)

Orifice throat diameter $d_1 = 4$ inches (101.6 mm)

Bed diameter $D_2 = 1560$ mm

Average molecular weight of air $MW = 29$

Universal gas constant $R = 8.314 \text{ J/g-moleK}$

Air viscosity at T_1 $\mu = 1.885 \times 10^{-5} \text{ Pa.s}$ (Holman, 1986)

The procedure is as follows:

(1) Calculate the density of the air upstream of the orifice.

$$\rho_1 = \frac{P_1 MW}{RT_1} = \frac{(68.5 + 101.325) * 29}{8.314 * (83 + 273)} = 1.664 \text{ kg/m}^3 \quad (\text{B.4})$$

(2) Calculate the value of the orifice coefficient.

$$K = \frac{0.61}{\sqrt{1 - \left(\frac{d_t}{D_1}\right)^4}} = \frac{0.61}{\sqrt{1 - \left(\frac{101.6}{406.4}\right)^4}} = 0.6112 \quad (\text{B.5})$$

(3) Calculate the cross-sectional area of the orifice throat.

$$A_t = \frac{\pi}{4} d_t^2 = \frac{\pi}{4} (101.6 * 10^{-3})^2 = 0.008107 \text{ m}^2 \quad (\text{B.6})$$

(4) Calculate the gas velocity in the orifice throat.

$$v_t = K \sqrt{\frac{2 * DP}{\rho_1}} = 0.6112 * \sqrt{\frac{2 * 14710}{1.664}} = 81.27 \text{ m/s} \quad (\text{B.7})$$

(5) Calculate the mass flow of air in the system.

$$\dot{m} = \rho_1 * v_t * A_t = 1.664 * 81.27 * 0.008107 = 1.096 \text{ kg/s} \quad (\text{B.8})$$

(6) Calculate the density of the air at the exit conditions (bed surface).

$$\rho_2 = \frac{P_2 * MW}{R * T_2} = \frac{(0 + 101.325) * 29}{8.314 * 35} = 1.148 \text{ kg/m}^3 \quad (\text{B.9})$$

(7) Calculate the cross-sectional area of the exit pipe (bed vessel).

$$A_2 = \frac{\pi}{4} D_2^2 = \frac{\pi}{4} * 1.56^2 = 1.911 \text{ m}^2 \quad (\text{B.10})$$

(8) Calculate the superficial gas velocity at the bed surface.

$$U = \frac{\dot{m}}{\rho_2 * A_2} = \frac{1.096}{1.148 * 1.911} = 0.4996 \text{ m/s} \quad (\text{B.11})$$

(9) Check the assumption that the flow through the orifice is fully turbulent (*ie* the Reynolds number of the flow through the orifice throat is $> 10,000$).

$$\text{Re}_t = \frac{d_t v_t \rho_t}{\mu} = \frac{101.6 * 10^{-3} * 81.27 * 1.664}{1.885 * 10^{-5}} = 728,900 \text{ (ie } > 10,000) \quad (\text{B.12})$$

B.3.2 Estimated Errors in Flow From Orifice Plate Measurements

The major sources of error in the above calculation are likely to be the measured parameters listed at the start of Section B.3.1. Estimated errors for these parameters are as follows (for both the 600 mm and 1560 mm beds):

Upstream line pressure $P_1 \pm 2.5 \text{ kPa}$

Orifice pressure drop $DP \pm 0.05 \text{ kPa}$

Air temperature at orifice plate $T_1 \pm 1 \text{ }^\circ\text{C}$

Downstream pressure $P_2 \pm 0.01 \text{ kPa}$ (bed surface)

Downstream temperature $T_2 \pm 3 \text{ }^\circ\text{C}$ (bed surface)

Once again, the resulting error in velocity has been estimated using the maximum error approach (see Section B.2.1). Typical values of the error in superficial gas velocity are presented in Figure B.7 and B.8 for the 1560 and 600 mm beds respectively.

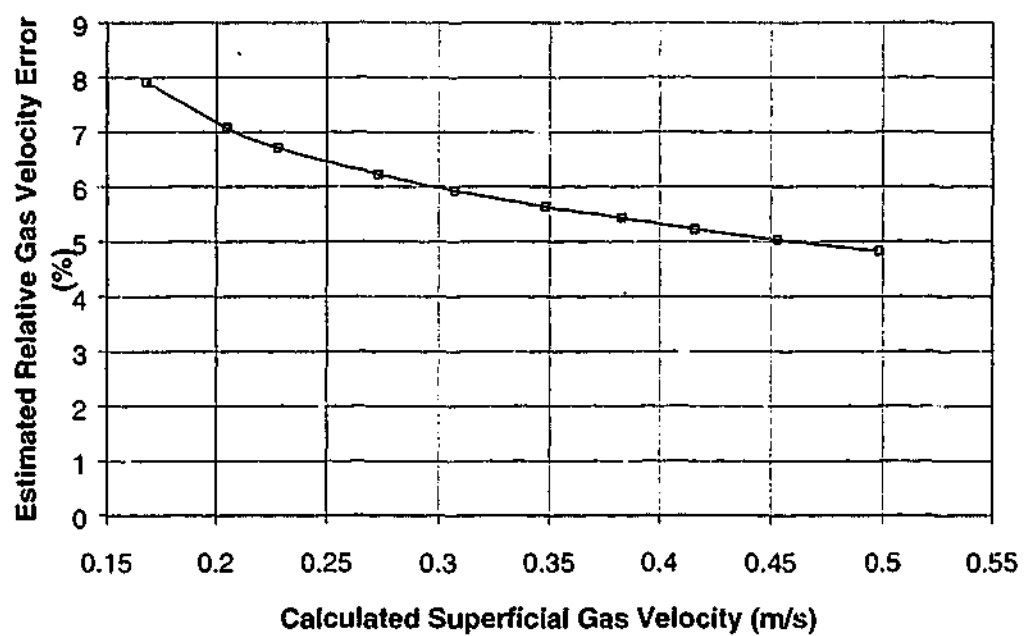


Figure B.7 Estimated relative error in superficial gas velocity for the 1560 mm bed as a function of gas velocity (based on typical operating conditions).

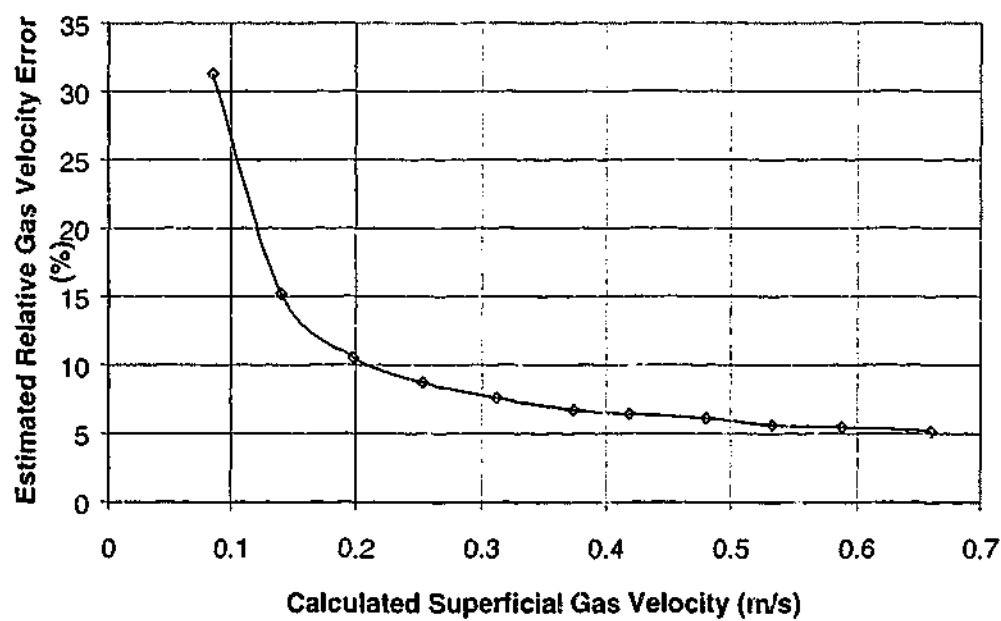


Figure B.8 Estimated relative error in superficial gas velocity for the 600 mm bed as a function of gas velocity (based on typical operating conditions).

B.4 Assumed Transport Properties for Other Calculations

The air flow in the fluidized beds used in this study was reported as the superficial gas velocity just above the bed surface. This means that in all cases (see Chapter 3, Section 3.4) the pressure can be assumed to be atmospheric. However, the air temperature at the bed surface was in some cases slightly above ambient due to the heating effects of the blowers, (most noticeable at the 300 mm and 1560 mm scales). This affects the transport properties of the air to a small extent and has some minor consequences for the calculation of the scaling law dimensionless groups. (-In fact, there would actually be a slight temperature gradient present within the bed, as the heated air cooled during its passage through the bed. The in-bed effects of such a thermal gradient are likely to be small, and will not be accounted for here.)

Note that gas density has been *directly* calculated from the ideal gas law where required for flow calculations (*ie* orifice plate calculations such as those above) and estimated bed surface temperatures used for downstream conditions. However, for general comparisons (dimensionless groups), average transport properties have been used for each bed. These average transport properties are given below.

In the case of the 146 mm bed, there was no temperature change, so transport properties at atmospheric pressure and 15°C have been used. The transport properties of the air at the bed surface for the 300 mm bed have been taken at atmospheric pressure and 20°C, which was the average operating condition. In the case of the 600 mm bed, the air temperature at the bed surface was approximately the same as the air temperature in the windbox for all experiments, so the transport properties for this scale were therefore taken at atmospheric pressure and 15°C. In the 1560 mm scale bed, gas velocity was normally calculated from the orifice plate data and the estimated bed surface temperature, which was found to maintain a value almost exactly 10°C lower than the measured windbox temperature in every case where it was measured. Therefore, for the 1560 mm bed, the transport properties of air were taken at atmospheric pressure and 25°C, representing the typical average conditions at the bed surface. Transport properties were determined from the data of Holman (1986) and are presented in Table B.3.

Bed	Pressure (kPag)	Temperature (°C)	Density (kg/m ³)	Viscosity (Pas)
146 mm	0	15±2	1.230±0.01	1.79E-5±1E-7
300 mm	0	20±5	1.205±0.02	1.81E-5±2.2E-7
600 mm	0	15±3	1.230±0.02	1.79E-5±1.5E-7
1560 mm	0	25±10	1.1805±0.02	1.85E-5±5E-7

Table B.3 Air conditions at the bed surface and transport properties, with estimated errors. Based on linear interpolation of data presented in Holman (1986).

APPENDIX C – PARTICLE CHARACTERISTICS

This appendix contains the particle size distributions and minimum fluidization velocity results for all bed materials used in the experimental work. Particle size distributions were characterised using the Malvern Mastersizer particle size analyser at CSIRO Division of Minerals. Minimum fluidization velocity experiments were carried out for all bed materials using the 146 mm diameter bed with sintered brass distributor (pressure drop characteristics are presented in Appendix D)

C.1 Particle Size Analysis Results

The Malvern Mastersizer is a laser light-scattering particle sizer. Collimated laser light is passed through an essentially laser transparent medium containing the sample to be analysed. Light is scattered by the sample material in a direct relation to the size of the particles making up the sample. Angle of scatter light gives size information and intensity of various scattered fractions gives quantity information. The scattered light is detected by a series of forward and backscatter detectors and the resultant pattern of light and intensity is fitted to a number of models depending on the size range measured. A composite size distribution results. Unlike sieving, the method measures a particle size approximating the largest axis of the particle (sieving measures the smallest). In the case of materials analysed for this work, water was used as the dispersant medium.

Table C.1 shows the calculated surface to volume diameter (also known as the Sauter mean diameter) based on the particle size results. Surface to volume mean diameter is evaluated by:

$$d_{sv} = \frac{1}{\sum \frac{V_i}{d_i}} \quad (C1)$$

where V_i is the relative volume of the i^{th} sample with mean class diameter of d_i . (These d_{sv} values have been used in calculating particle Reynolds numbers in previous sections of this work.)

Material Designation	d_{sv} Sauter mean diameter (μm)
A	230
B	286
C	326
D	479
A*	344
B*	388
G	300
CM50N	304
GB3	347
GB4	369
GB5	279
GB6	269
GB7	155

Table C.1 Surface to volume mean particle size calculated from size analysis results for all bed and tracer materials.

Figures C.1 to C.14 show the particle size analysis results for all bed materials, as well as results for glass bead tracers used in the solids downflow velocity experiments of Chapter 6.

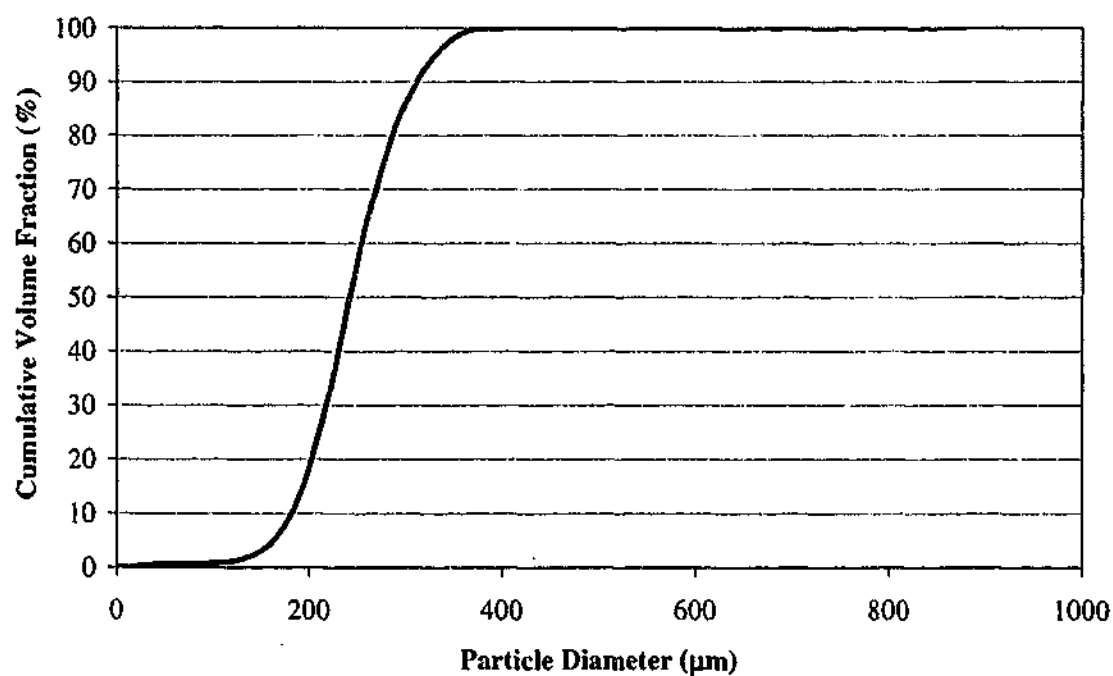


Figure C.1 Cumulative particle size distribution result (from Malvern Mastersizer) for Bed Material "A".

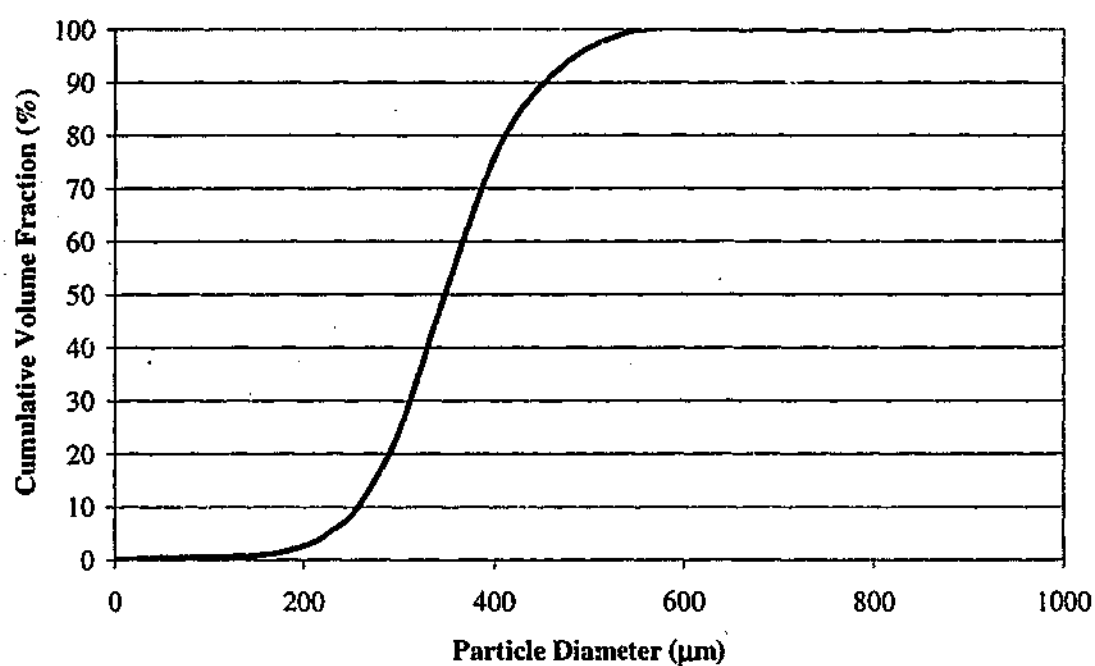


Figure C.2 Cumulative particle size distribution result (from Malvern Mastersizer) for Bed Material "B".

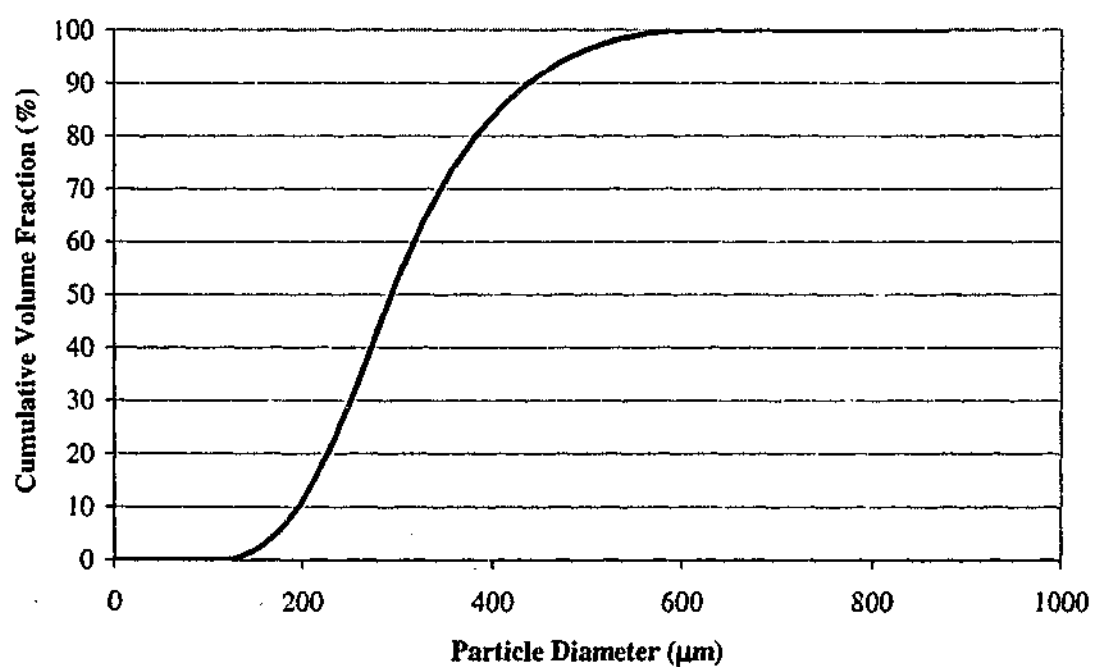


Figure C.3 Cumulative particle size distribution result (from Malvern Mastersizer) for Bed Material "C".

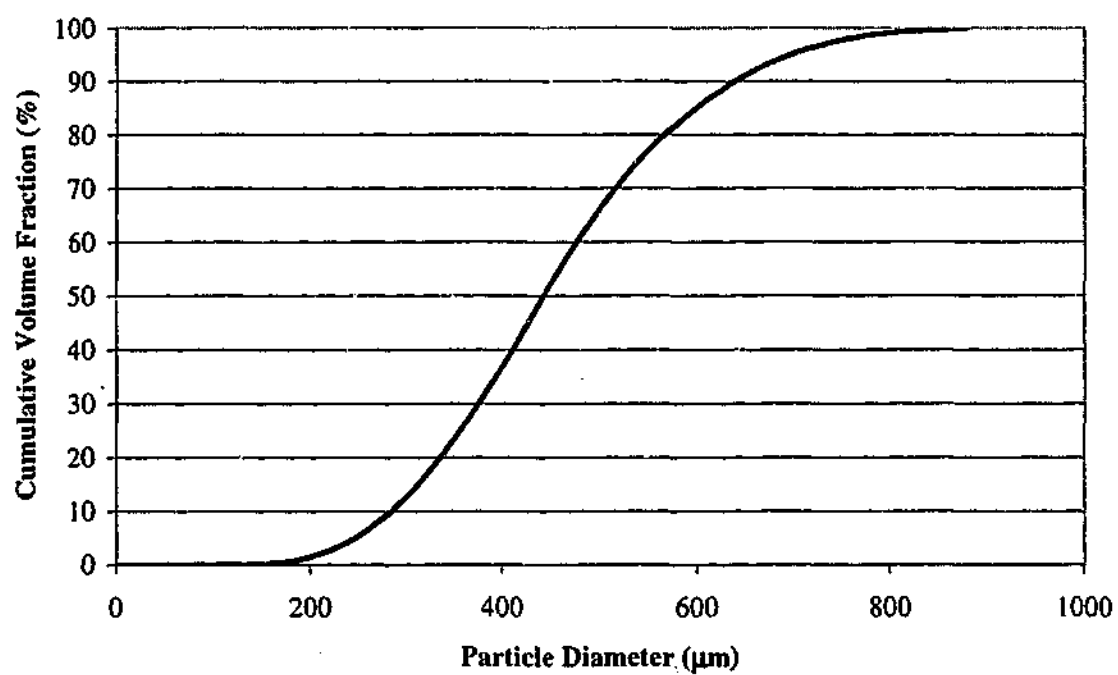


Figure C.4 Cumulative particle size distribution result (from Malvern Mastersizer) for Bed Material "D".

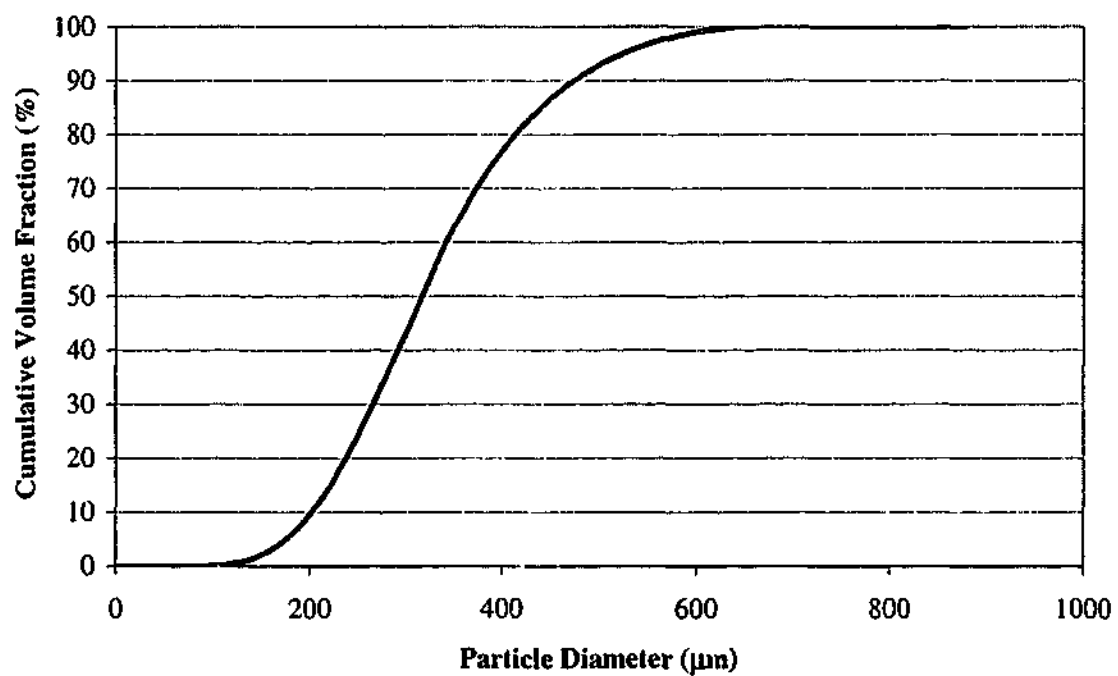


Figure C.5 Cumulative particle size distribution result (from Malvern Mastersizer) for Bed Material "A*".

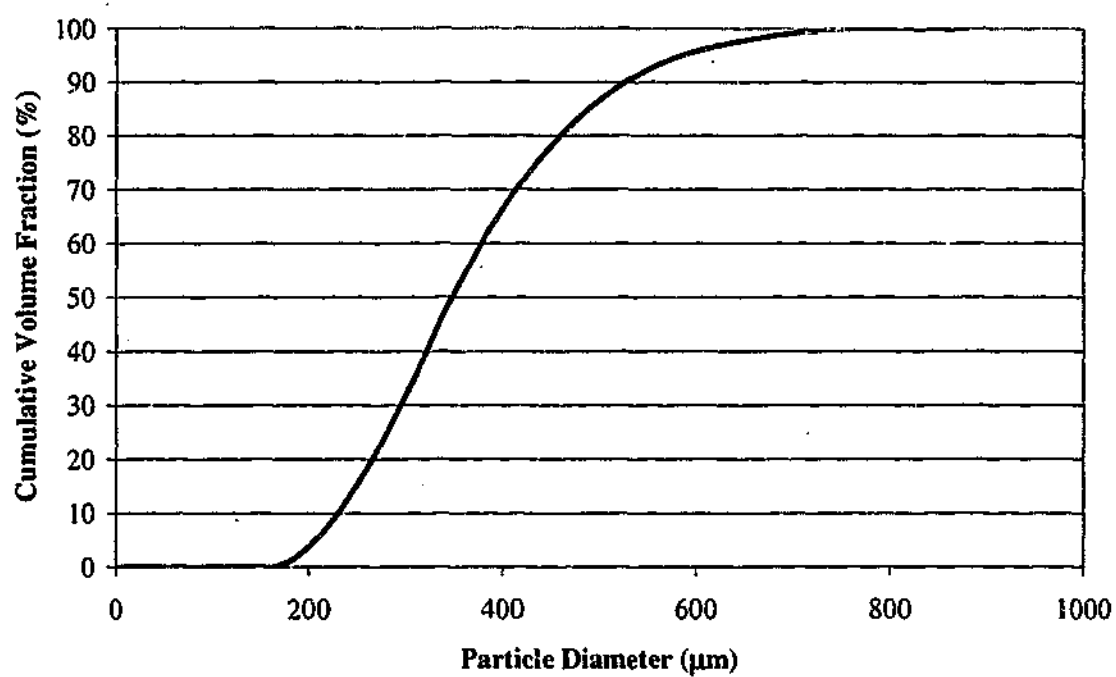


Figure C.6 Cumulative particle size distribution result (from Malvern Mastersizer) for Bed Material "B*".

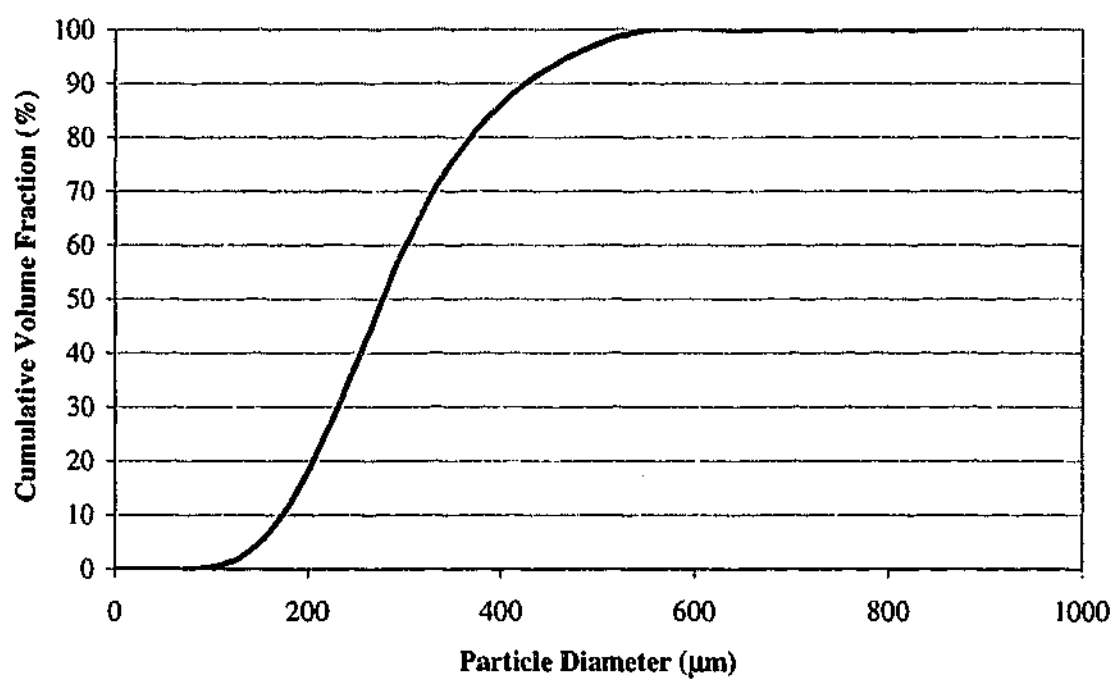


Figure C.7 Cumulative particle size distribution result (from Malvern Mastersizer) for Bed Material "G".

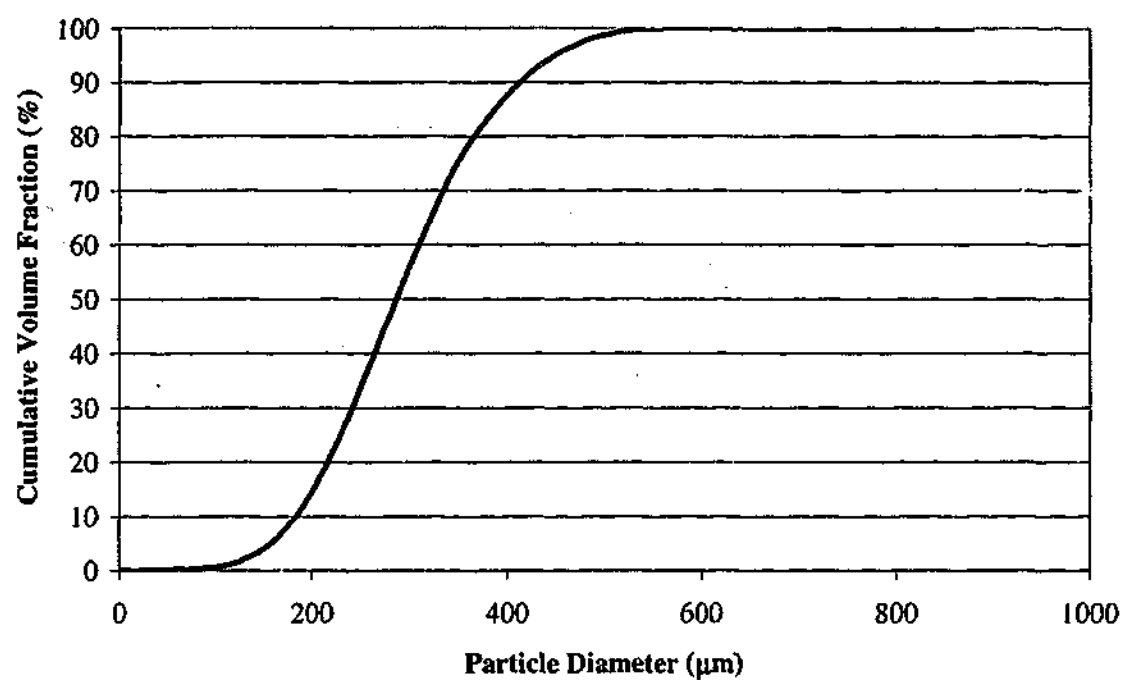


Figure C.8 Cumulative particle size distribution result (from Malvern Mastersizer) for Bed Material "CM50N" used in solids downflow experiments of Chapter 6.

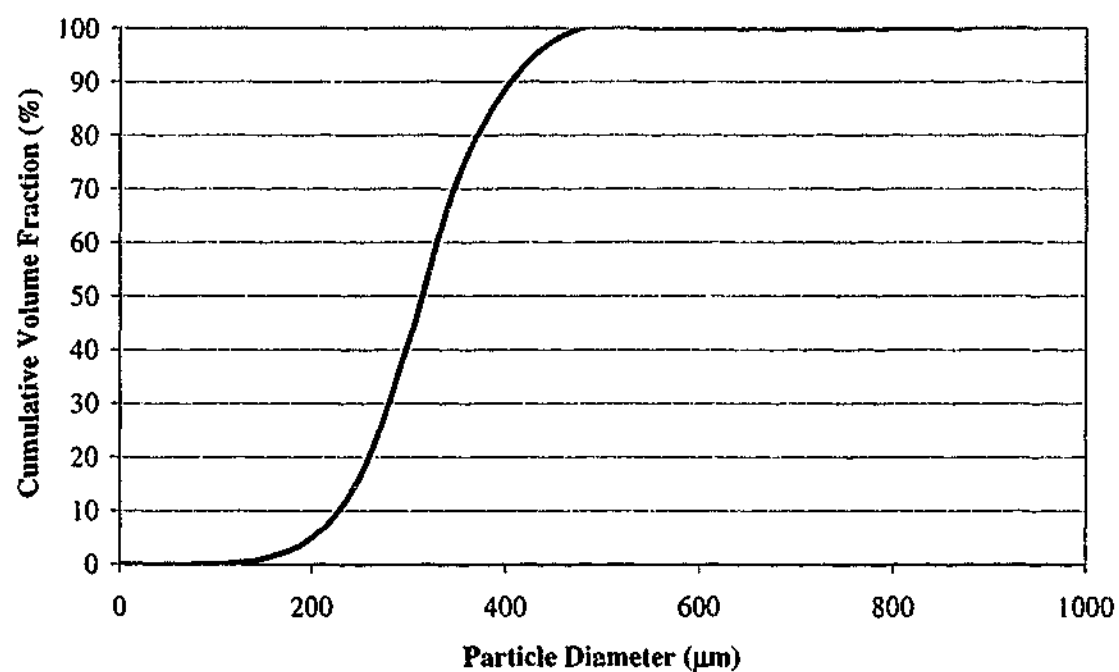


Figure C.9 Cumulative particle size distribution result (from Malvern Mastersizer) for Tracer Material "GB3" used in solids downflow experiments of Chapter 6.

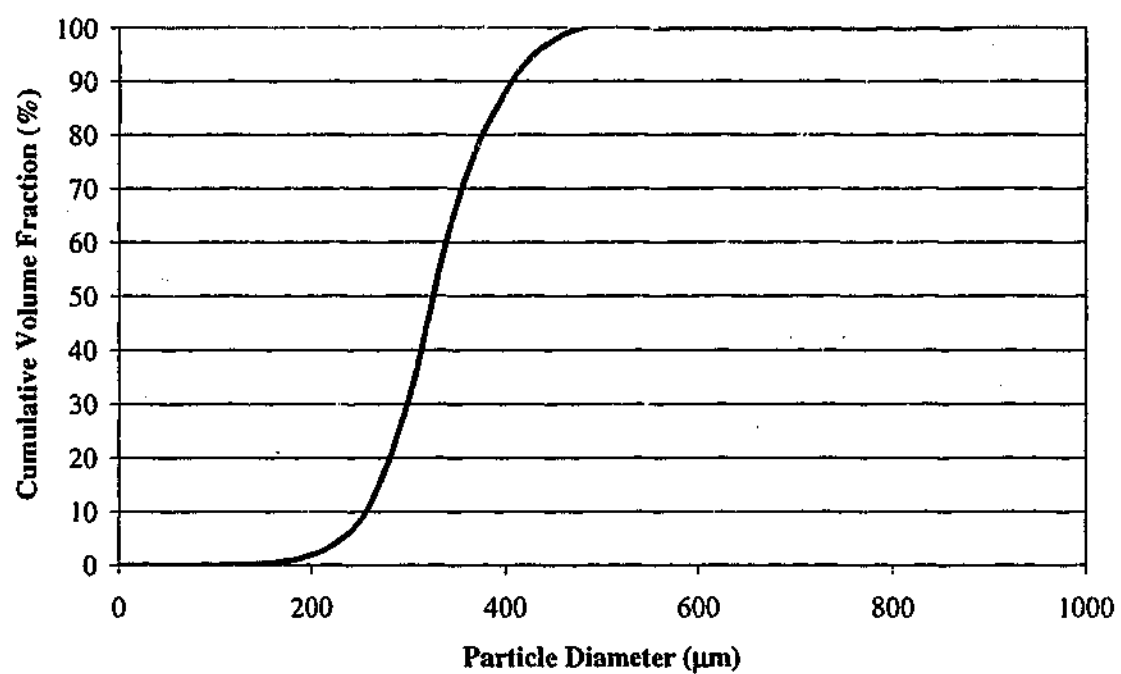


Figure C.10 Cumulative particle size distribution result (from Malvern Mastersizer) for Tracer Material "GB4" used in solids downflow experiments of Chapter 6.

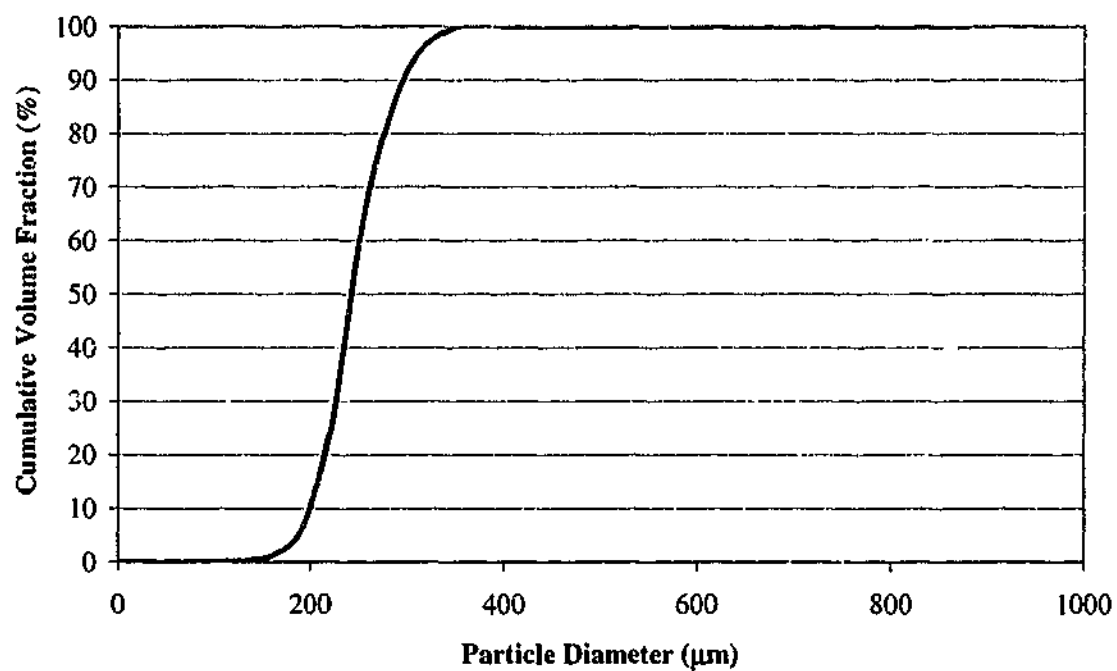


Figure C.11 Cumulative particle size distribution result (from Malvern Mastersizer) for Tracer Material "GB5" used in solids downflow experiments of Chapter 6.

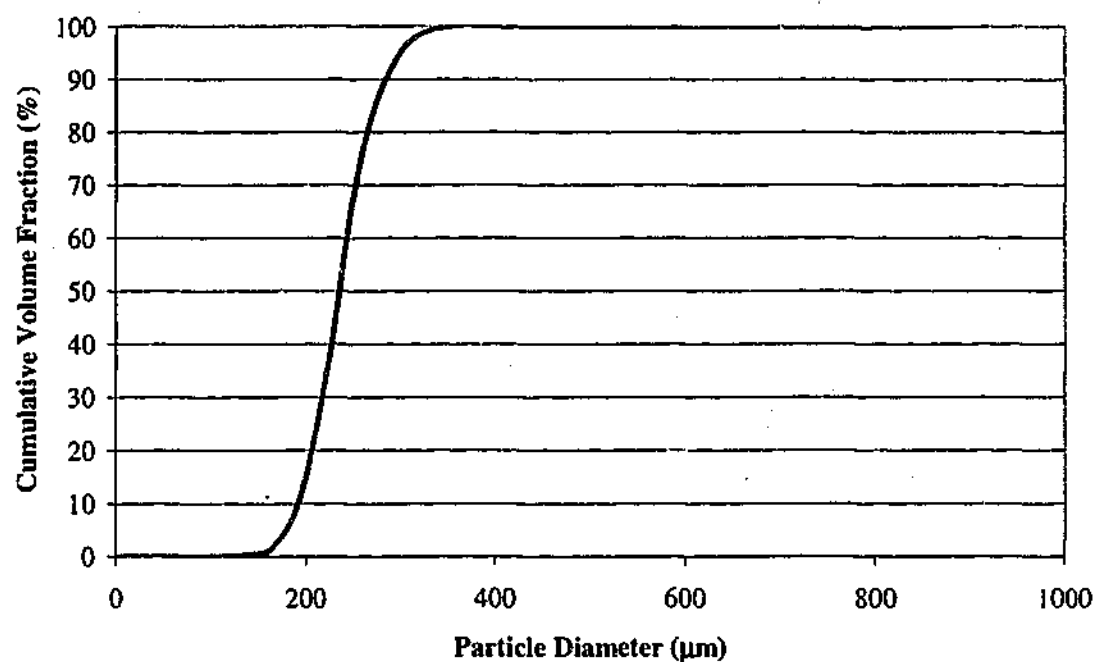


Figure C.12 Cumulative particle size distribution result (from Malvern Mastersizer) for Tracer Material "GB6" used in solids downflow experiments of Chapter 6.

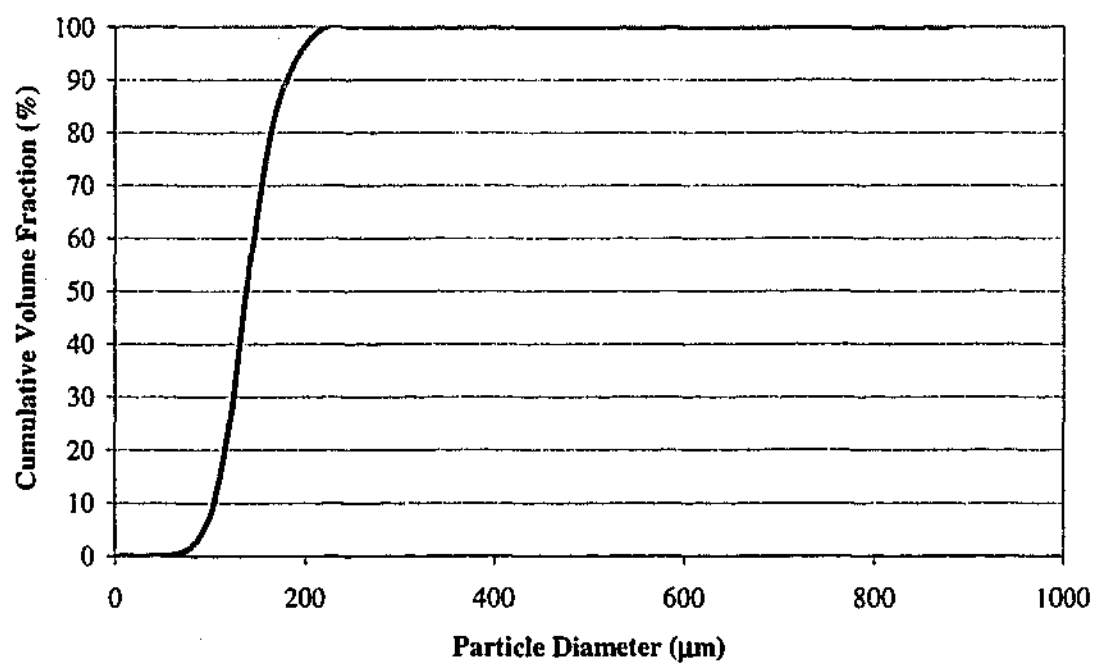


Figure C.13 Cumulative particle size distribution result (from Malvern Mastersizer) for Tracer Material "GB7" used in solids downflow experiments of Chapter 6.

C.2 Minimum Fluidization Velocity Results

Before presenting the results the procedure for conducting minimum fluidization velocity experiments will be outlined. A standard approach was used for all materials which can be summarised as follows:

- (1) A bed material sample was placed in the 146 mm diameter bed (with sintered brass distributor) to give a settled bed height of 150 to 200 mm.
- (2) The bed was fluidized and the gas velocity adjusted to provide some rough indication of approximately what the minimum fluidization velocity was on the flowmeter scales so that an appropriate range of test gas velocities could be determined.
- (3) Gas velocity was then set to an initial value (well above the expected U_{mf} based on the rough observation).
- (4) Bed pressure drop was measured between a pressure probe located at port A, 48 mm above the distributor (See Figure 3.11 and Table 3.8) and the bed surface. - The probe tip was at the radial centreline. Pressure data was recorded using a pressure transducer and the PC-based data acquisition system described in Chapter 3, Section 3.6.5. Typically, a 0 to 6.9 kPa range transducer (XCX01DNQ series – see Table 3.9 and Appendix E for further details) was used. Sampling frequency was 100 Hz, with 20 seconds of data recorded.
- (5) Once pressure data for that gas velocity had been recorded, gas velocity was decreased and the measurement process repeated. Gas velocity was typically decreased in increments of the order of 20% of the anticipated U_{mf} , until reaching the lower limit of the flowmeter scale.
- (6) In order to present the results, the measured pressure signal was averaged for the 20 second record, thus providing a single pressure value (representing pressure drop between the in-bed probe and the freeboard) and the flowmeter readings were converted to superficial gas velocity using the calibration data of Appendix B.
- (7) Minimum fluidization velocities were calculated by drawing “lines of best fit” through the data points corresponding to the packed bed condition (large positive slope) and also the data corresponding to fluidized bed conditions (small positive slope). The x-coordinate of the intersection point was recorded as the minimum fluidization velocity of the material.

Figures C.14 to C.26 present the minimum fluidization velocity data for the various bed materials employed in the experimental work. Based on the error analysis for

flowmeters presented in Appendix B, the estimated *maximum* error for U_{mf} values is likely to be ± 0.004 m/s for $0.02 < U_{mf} < 0.09$ and ± 0.02 m/s for $0.09 < U_{mf} < 0.8$.

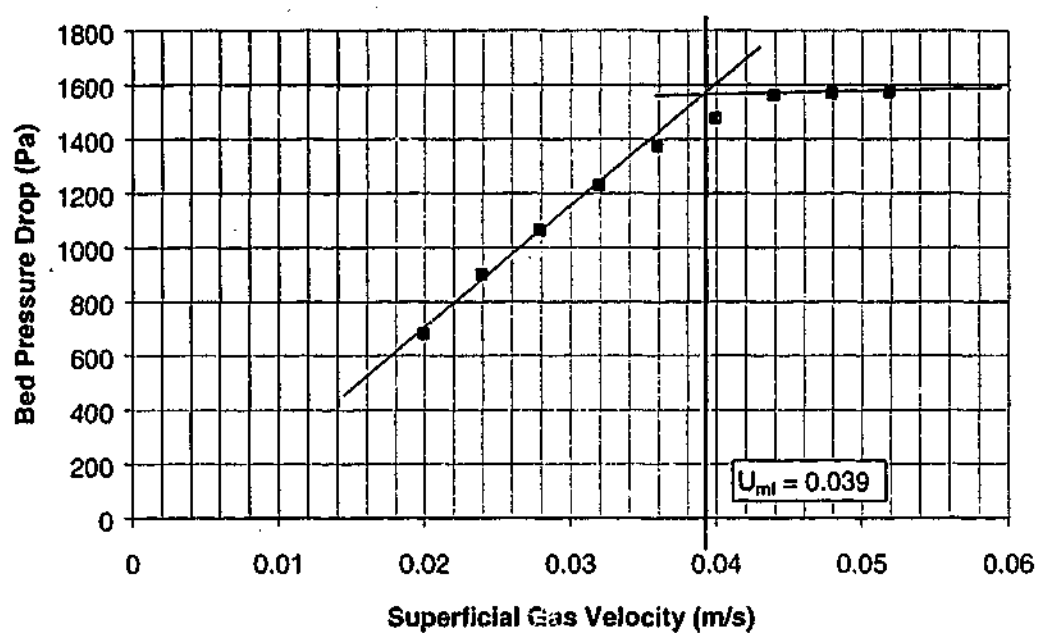


Figure C.14 Results of minimum fluidization experiment for Material A silica sand.

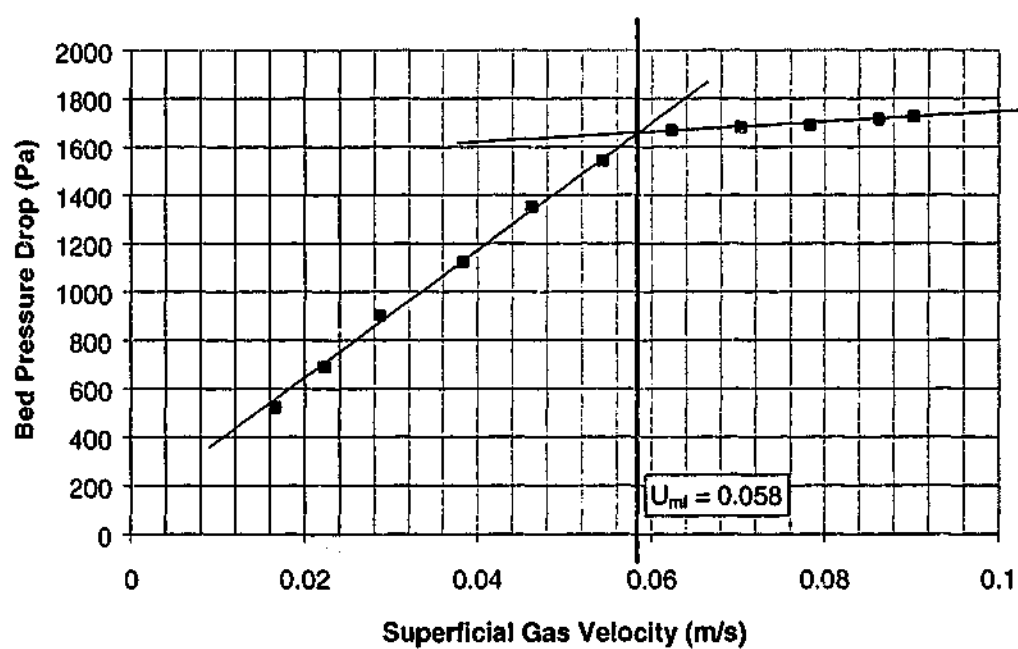


Figure C.15 Results of minimum fluidization experiment for Material B silica sand.

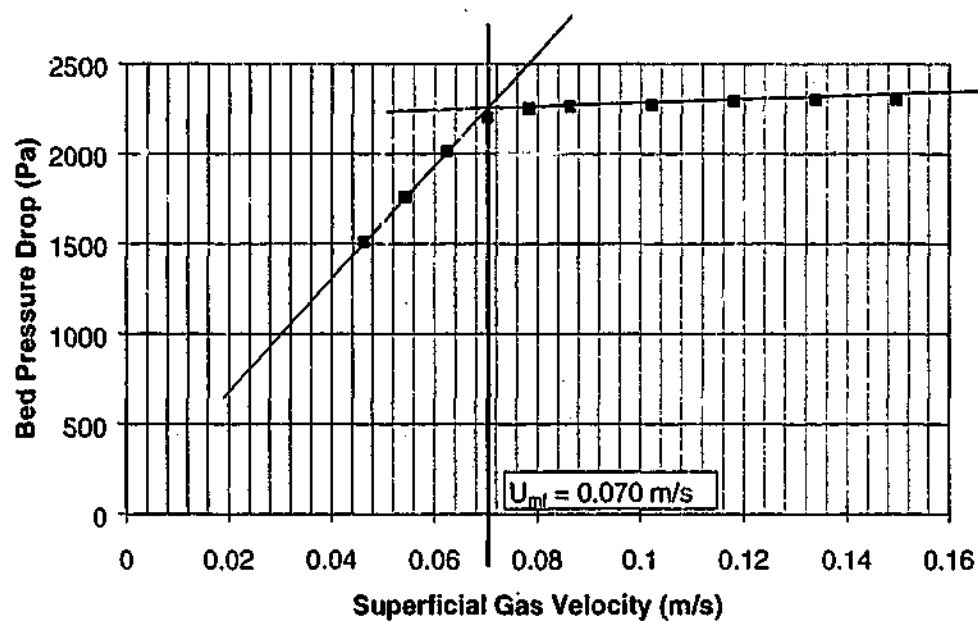


Figure C.16 Results of minimum fluidization experiment for Material C silica sand.

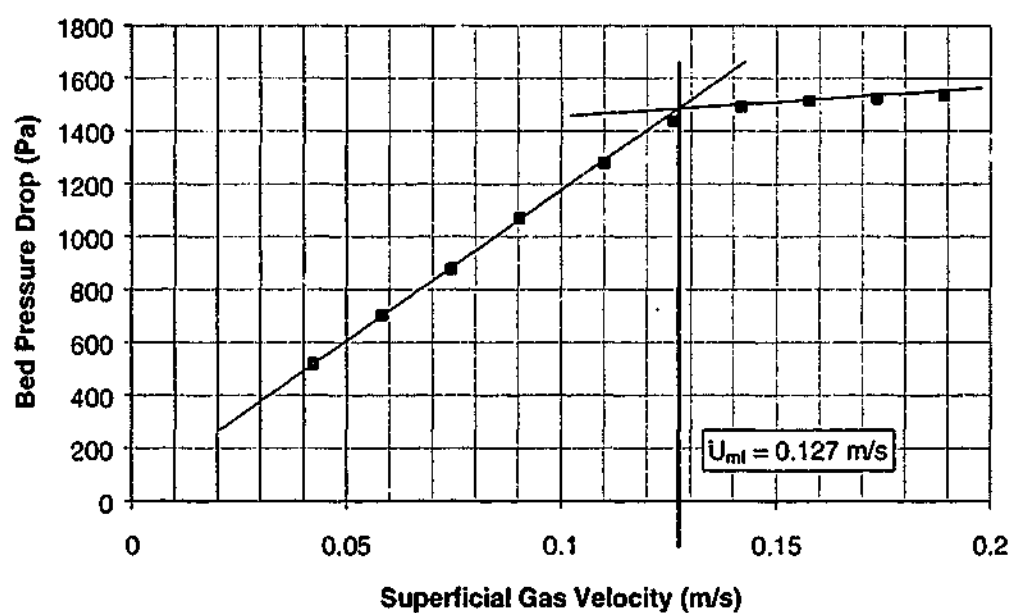


Figure C.17 Results of minimum fluidization experiment for Material D silica sand.

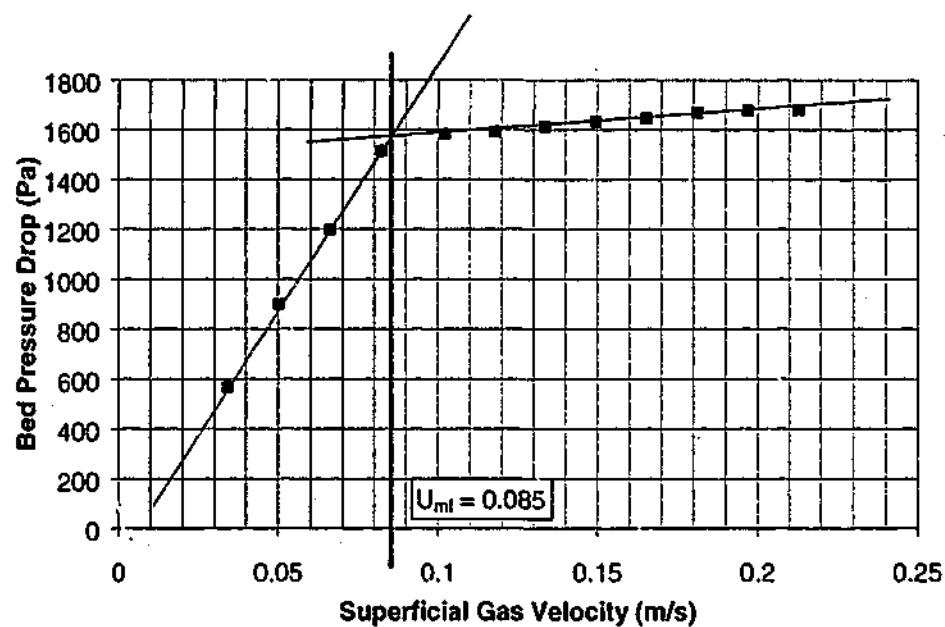


Figure C.18 Results of minimum fluidization experiment for Material A* silica sand.

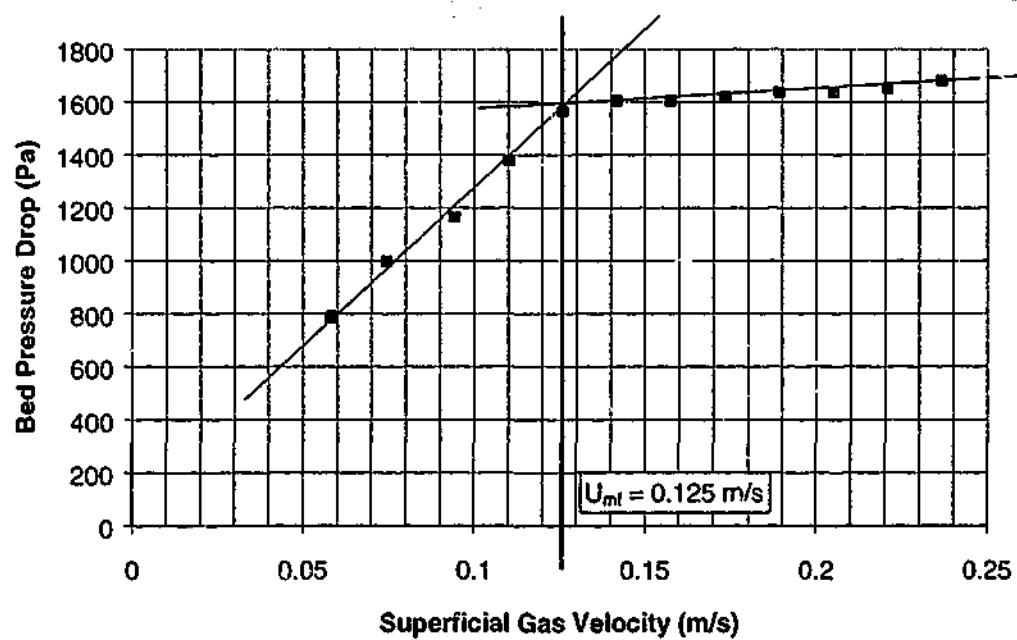


Figure C.19 Results of minimum fluidization experiment for Material B* silica sand.

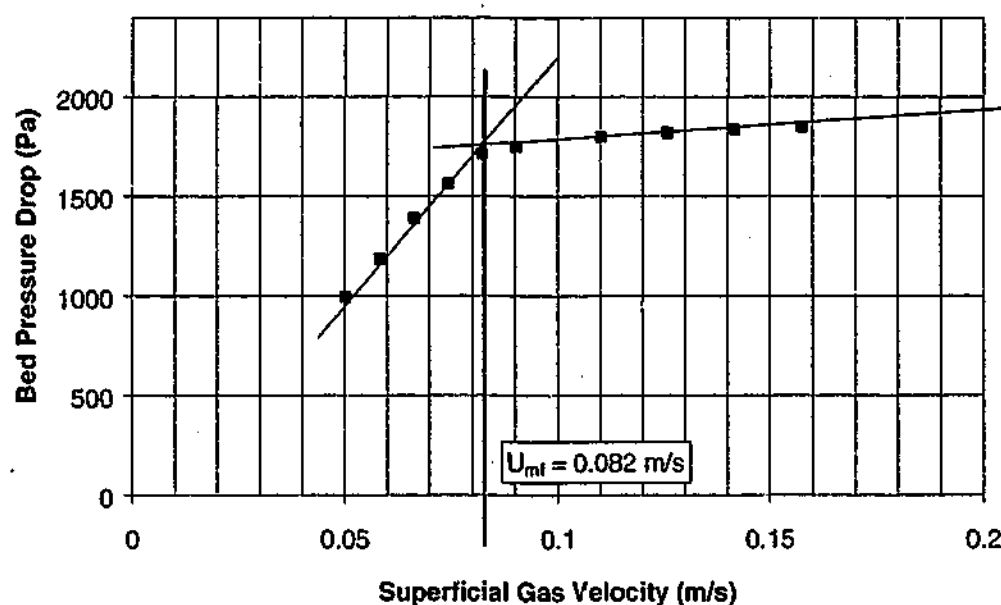


Figure C.20 Results of minimum fluidization experiment for Material G garnet sand.

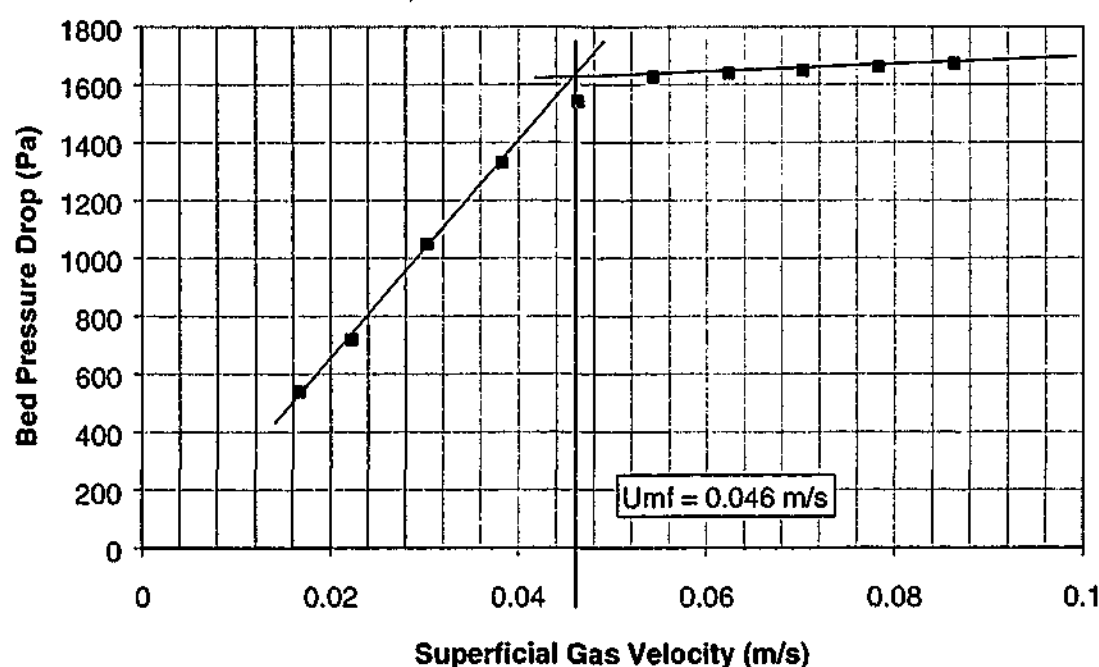


Figure C.21 Results of minimum fluidization experiment for Commercial Minerals 50N silica sand (125 – 355 micron bed material used in solids mixing experiments – See Table 6.1).

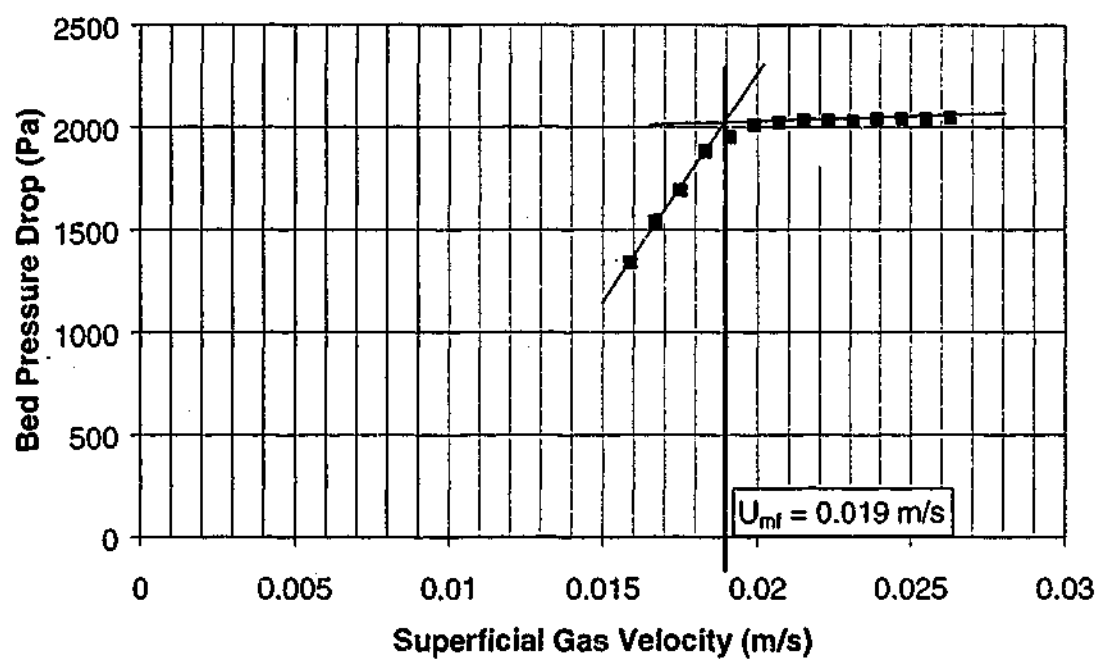


Figure C.22 Results of minimum fluidization experiment for Burwell glass beads GB#7 (solids mixing experiments).

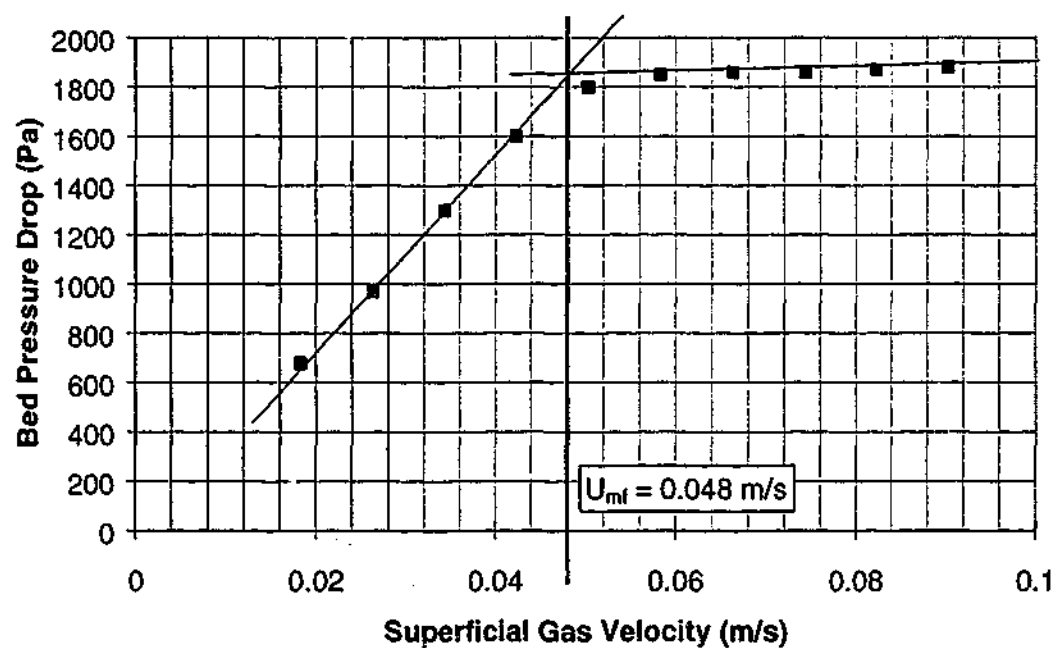


Figure C.23 Results of minimum fluidization experiment for Burwell glass beads GB#6 (solids mixing experiments).

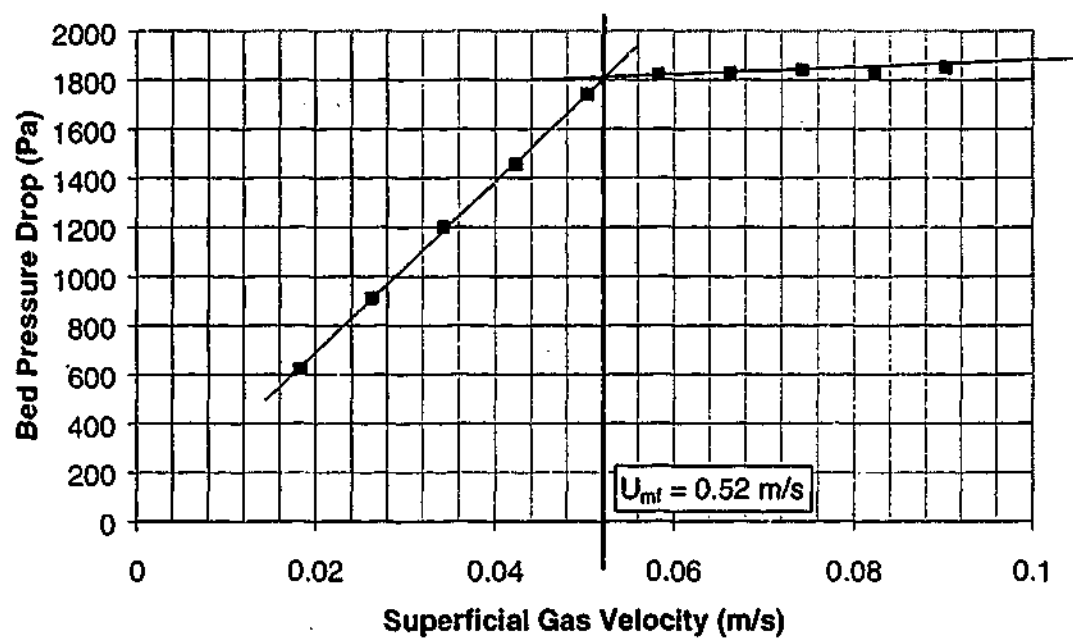


Figure C.24 Results of minimum fluidization experiment for Burwell glass beads #GB5 (solids mixing experiments).

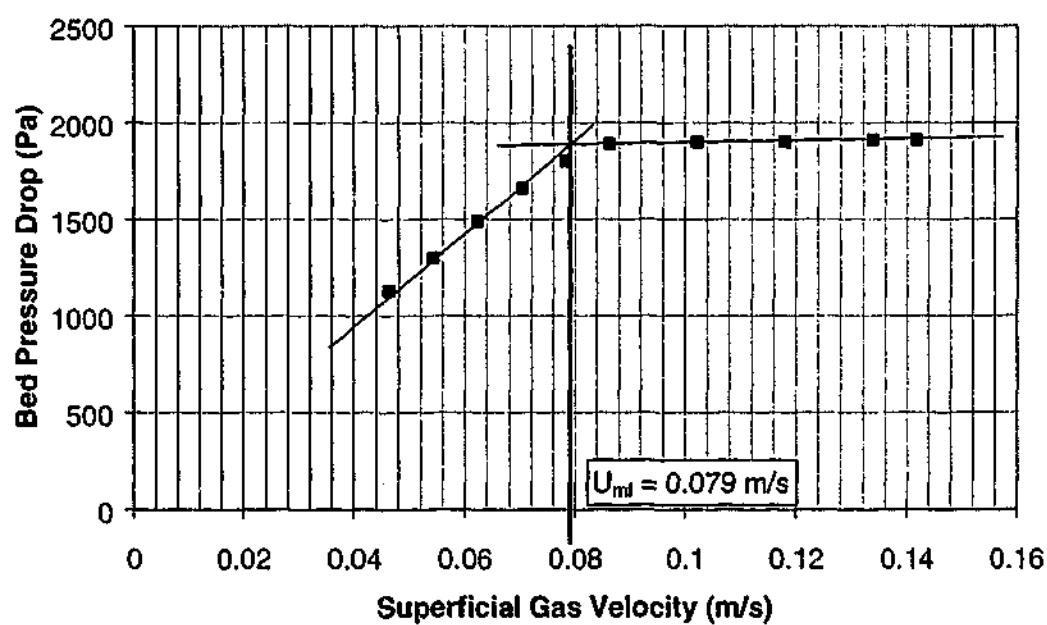


Figure C.25 Results of minimum fluidization experiment for Burwell glass beads GB#3 (solids mixing experiments).

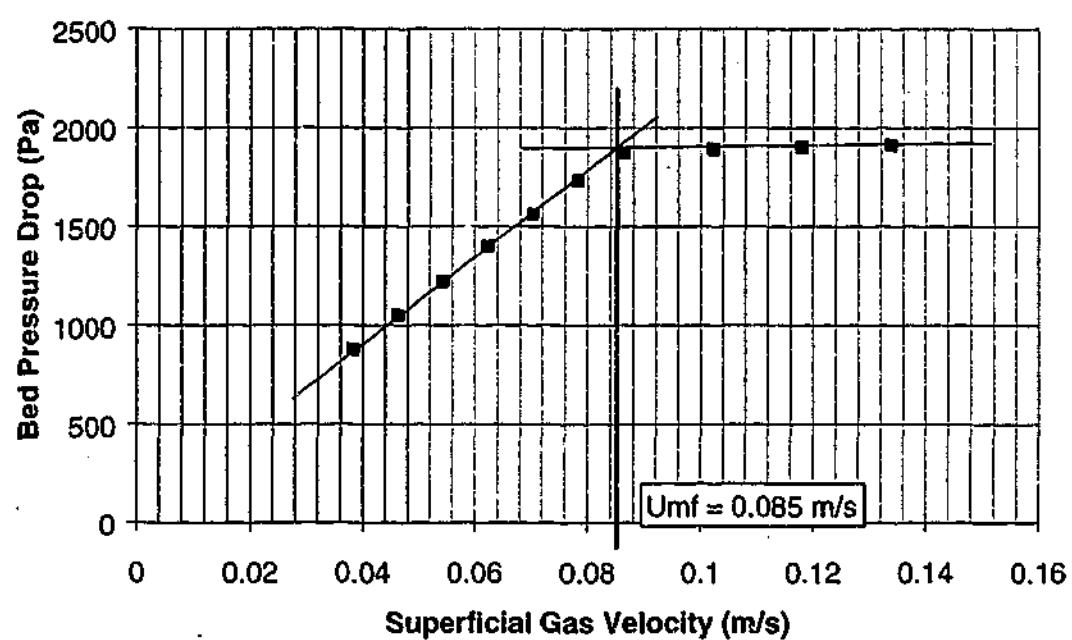


Figure C.26 Results of minimum fluidization experiment for Burwell glass beads GB#4 (solids mixing experiments).

APPENDIX D – DISTRIBUTOR CHARACTERISTICS

This appendix provides the pressure drop characteristics of all the gas distributors used in this work. Specifically, there were four bubble-cap distributors used at the four different scales, plus an additional sintered brass distributor used in the 146 mm bed for the minimum fluidization velocity experiments presented in Appendix C. Measurements were carried out using a calibrated Eirelec MP320 digital manometer attached to the windbox tapping point in each of the four beds. Vessels were emptied of all bed materials, prior to the measurements. A range of gas velocities was chosen such that it gave some indication of the likely pressure drops across the distributors during the similarity experiments.

Bubble-cap distributor characteristics have been presented on the same chart (Figure D.1), for comparison purposes. It should be noted that when presented in this way, for perfect scaling by the simplified criteria the pressure drop profiles should be identical.

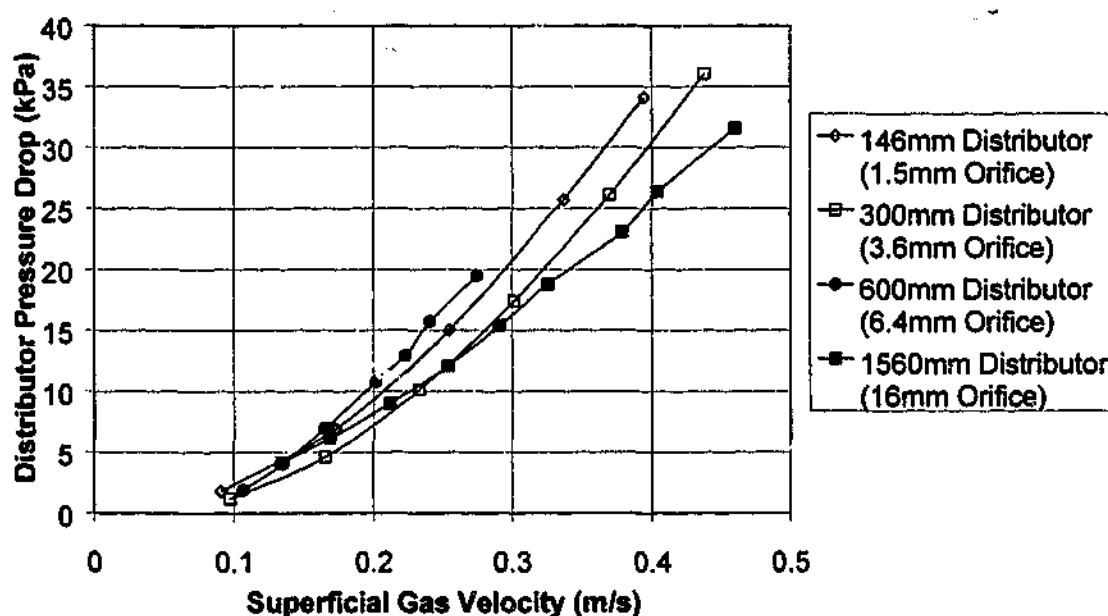


Figure D.1 Pressure drop profiles for bubble cap distributors used in the similarity experiments.

As can be seen in the figure, after adjustment of orifice sizes, they are certainly relatively close. The most marginal case for good gas distribution is the lowest gas velocities involved in experiments in the 146 mm bed, (approximately 0.04 m/s for material A) with the largest bed inventory ($H_s = 0.295$ m). The distributor pressure drop

(estimated) for this case would probably be around 1 to 1.5 kPa. The estimated bed pressure drop would be approximately 4.5 kPa for the silica sand. Thus the normal criterion of $DP_{dist} > 0.3 \cdot DP_{bed}$ is possibly *just* satisfied under these conditions. At higher gas velocities the criterion is easily exceeded.

Figure D.2 shows the pressure drop characteristic for the sintered brass distributor plate used in the 146 mm bed for minimum fluidization velocity experiments. Note that the majority of U_{mf} experiments were conducted at gas velocities lower than 0.2 m/s, so it is the lower part of the graph that is of importance. *Total* bed pressure drops were generally around 2 to 2.5 kPa in these experiments, hence the distributor pressure drop of approximately 1 kPa at 0.025 m/s should be sufficient to ensure good distribution for U_{mf} measurements (ie $DP_{dist} > 0.3 DP_{bed}$ for most conditions).

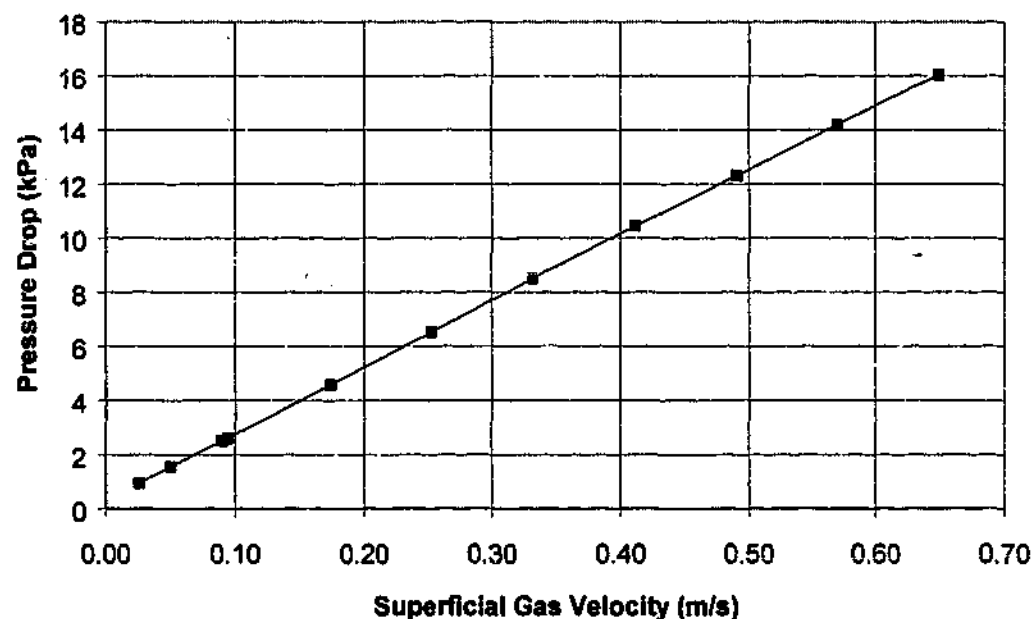


Figure D.2 Pressure drop characteristic for sintered brass distributor plate used in minimum fluidization velocity experiments at the 146 mm scale.

APPENDIX E – PRESSURE TRANSDUCER CALIBRATION DATA

This appendix provides the calibration results for the various Data Instruments pressure transducers employed in pressure probe measurements (Chapter 4). Transducers were calibrated using a Druck DPI-601 digital pressure indicator (with internal pressure reference volume). Once the transducer under test had been connected to the DPI, mechanical adjustment of the pressure reference volume could be used to apply a known pressure to the high pressure port on the transducer. Pressure was indicated on the DPI display, and the output voltage from the transducer was recorded using the data acquisition computer.

Results for the transducer calibrations are presented in the following figures. Straight-line fits for the calibration data are presented next to the graphs. Figures E.1 to E.4 show data for the four low-range transducers (0 to 2 kPa), Figures E.5 to E.7 show data for the three intermediate range transducers (0 to 7 kPa) and Figures E.8 to E.10 show the calibration data for the three higher range transducers (0 to 35 kPa). Note that in the actual similarity experiments of Chapter 4, transducers were often swapped around on the various cold models to ensure maximum use of the dynamic range for a given experimental condition.

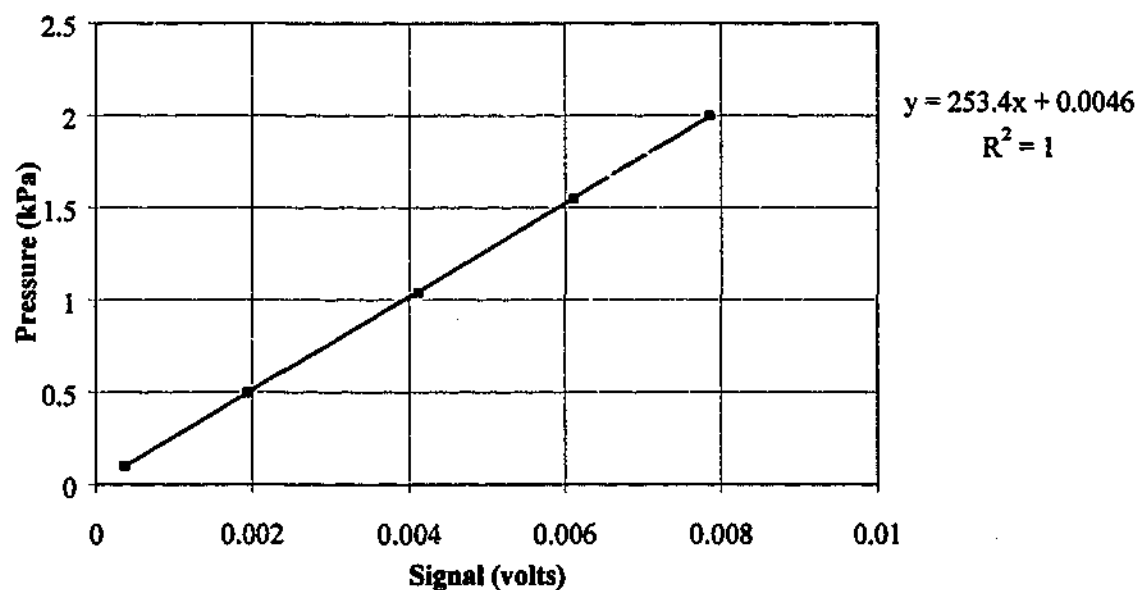


Figure E.1 Calibration data for low-range pressure transducer (designation XCX0.3#2). Straight-line fit for data conversions shown at top right corner.

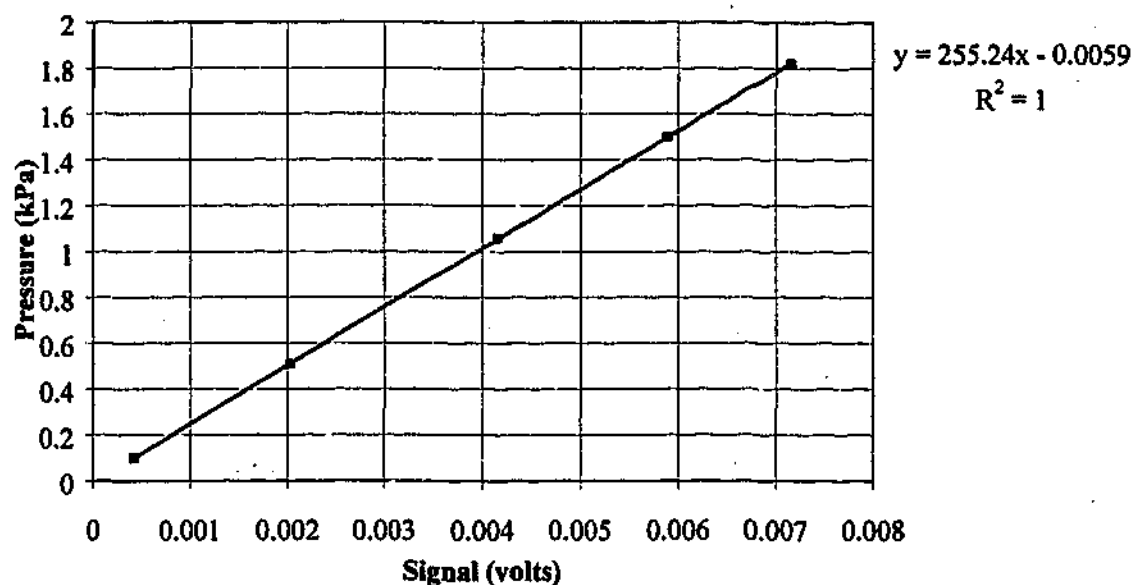


Figure E.2 Calibration data for low-range pressure transducer (designation XCX0.3#3). Straight-line fit for data conversions shown at top right corner.

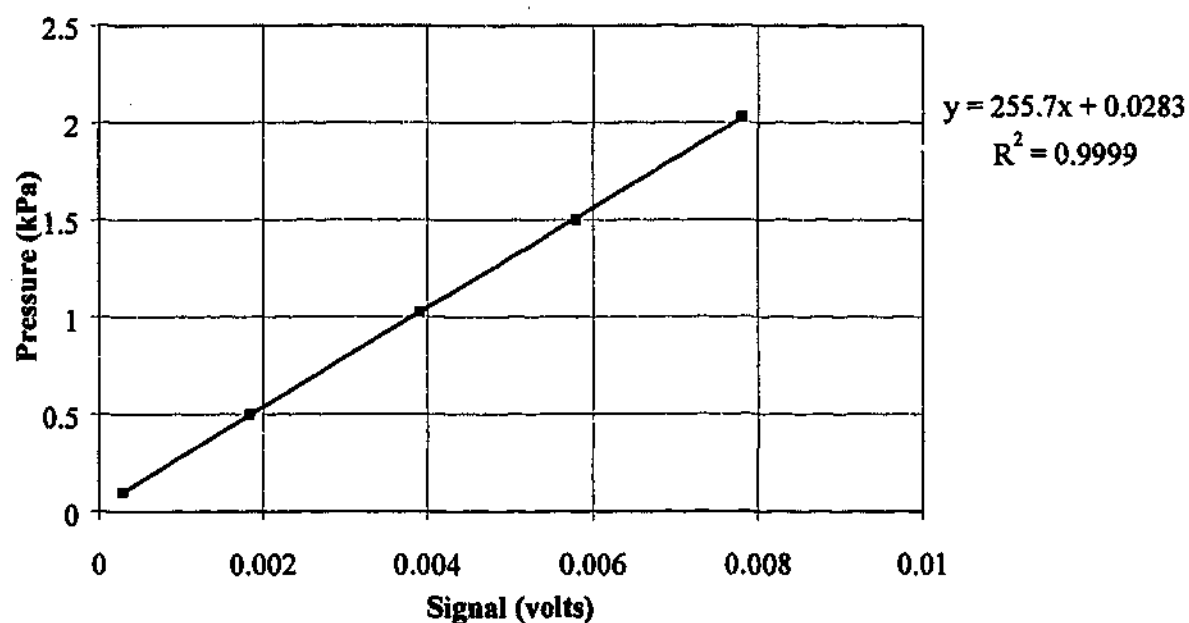


Figure E.3 Calibration data for low-range pressure transducer (designation XCX0.3#4). Straight-line fit for data conversions shown at top right corner.

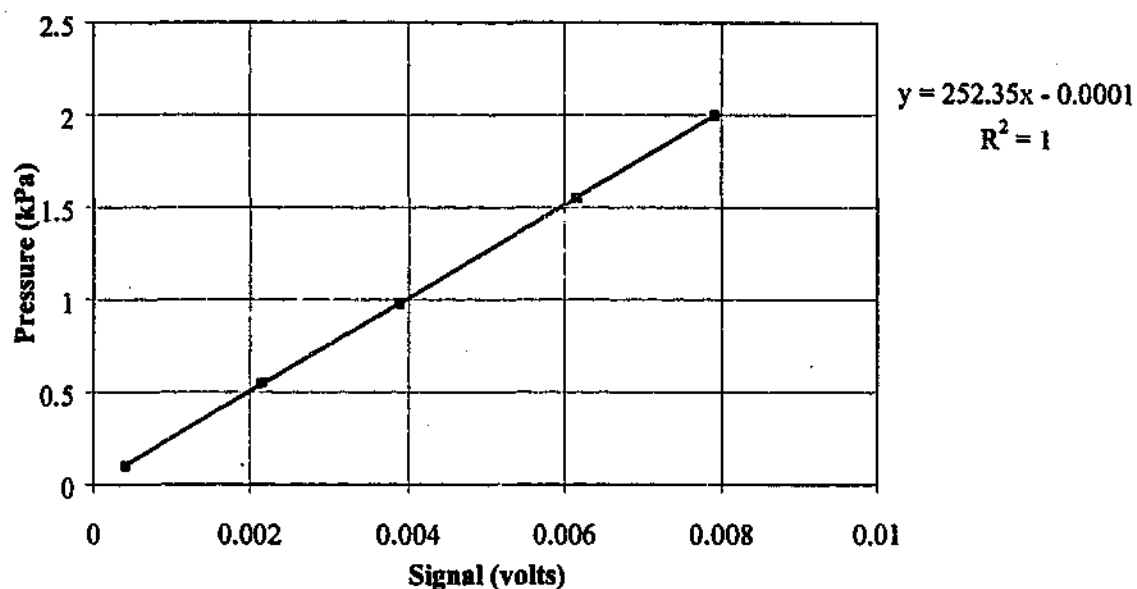


Figure E.4 Calibration data for low-range pressure transducer (designation XCX0.3#5). Straight-line fit for data conversions shown at top right corner.

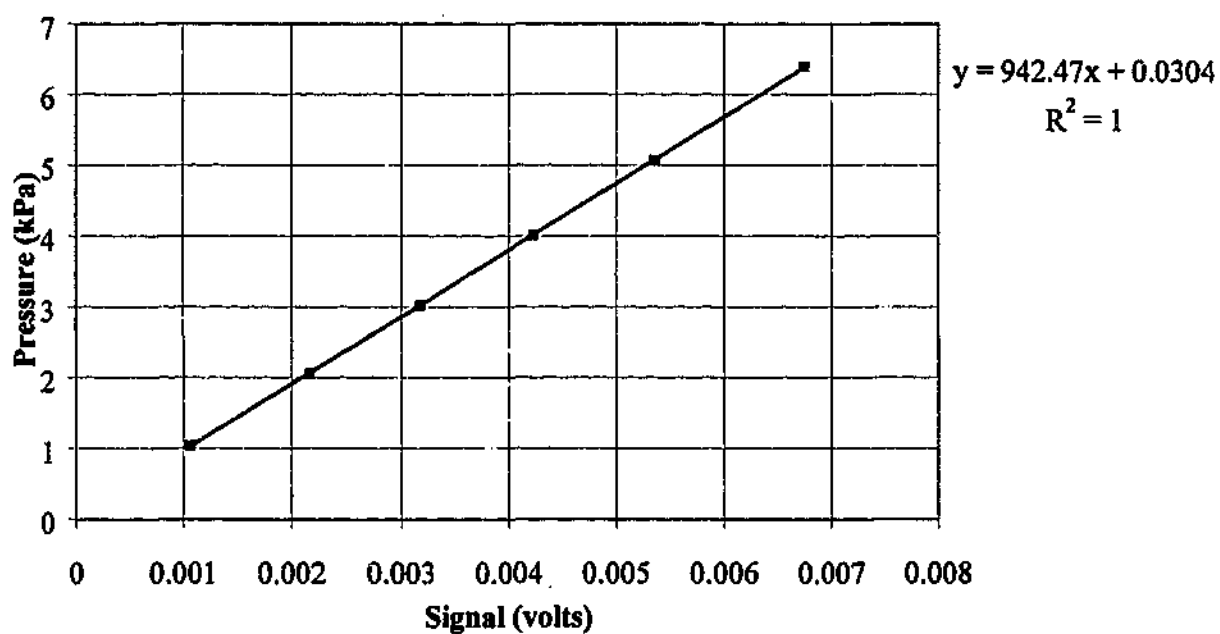


Figure E.5 Calibration data for low-range pressure transducer (designation XCX01#1). Straight-line fit for data conversions shown at top right corner.

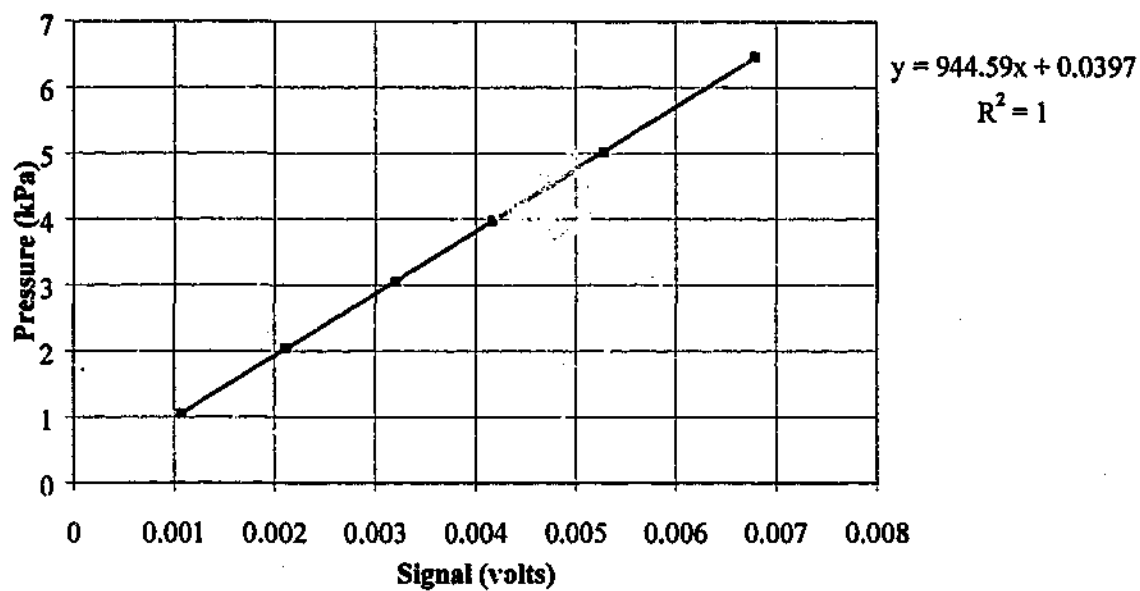


Figure E.6 Calibration data for low-range pressure transducer (designation XCX01#2).
Straight-line fit for data conversions shown at top right corner.

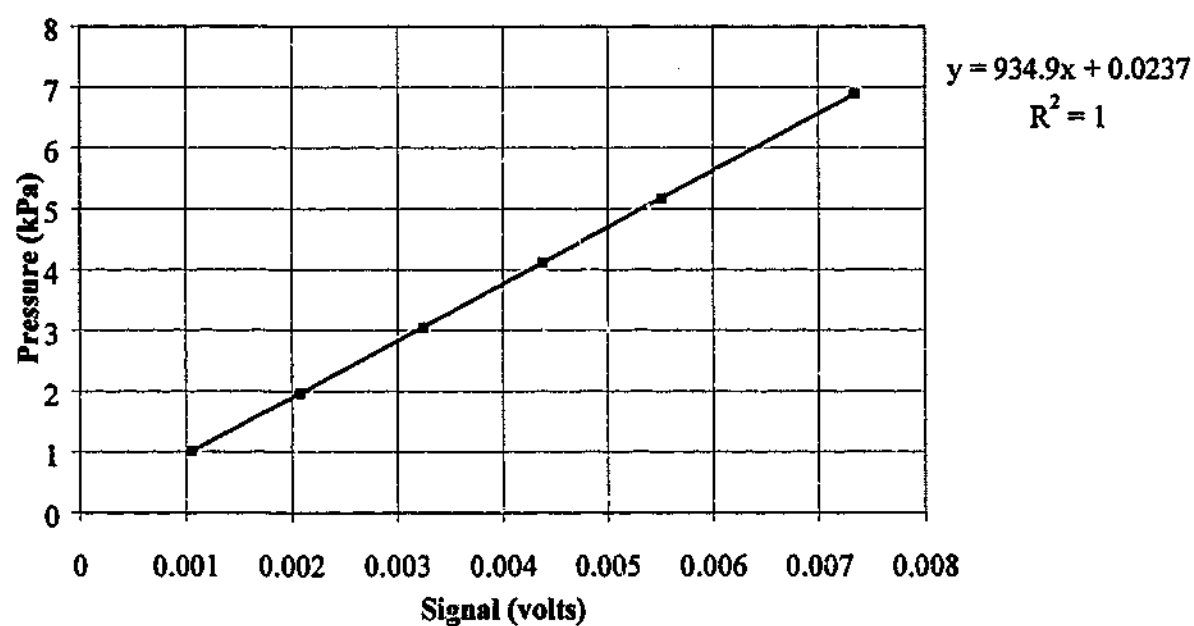


Figure E.7 Calibration data for low-range pressure transducer (designation XCX01#4).
Straight-line fit for data conversions shown at top right corner.

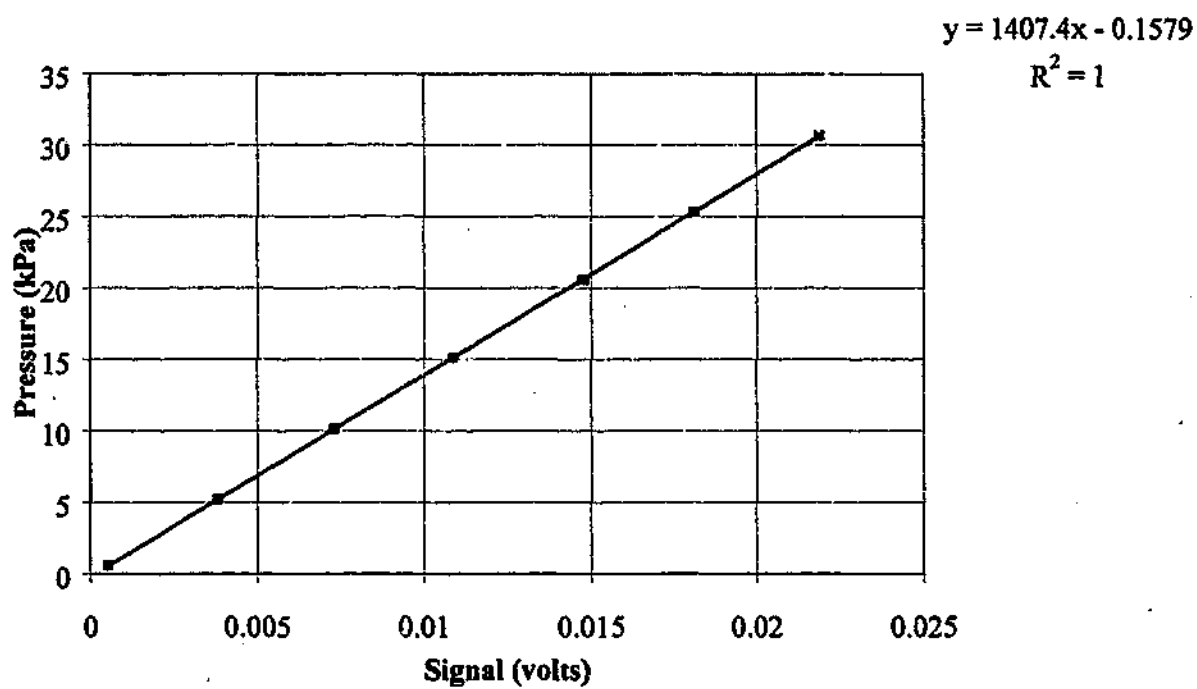


Figure E.8 Calibration data for low-range pressure transducer (designation XCX05#1). Straight-line fit for data conversions shown at top right corner.

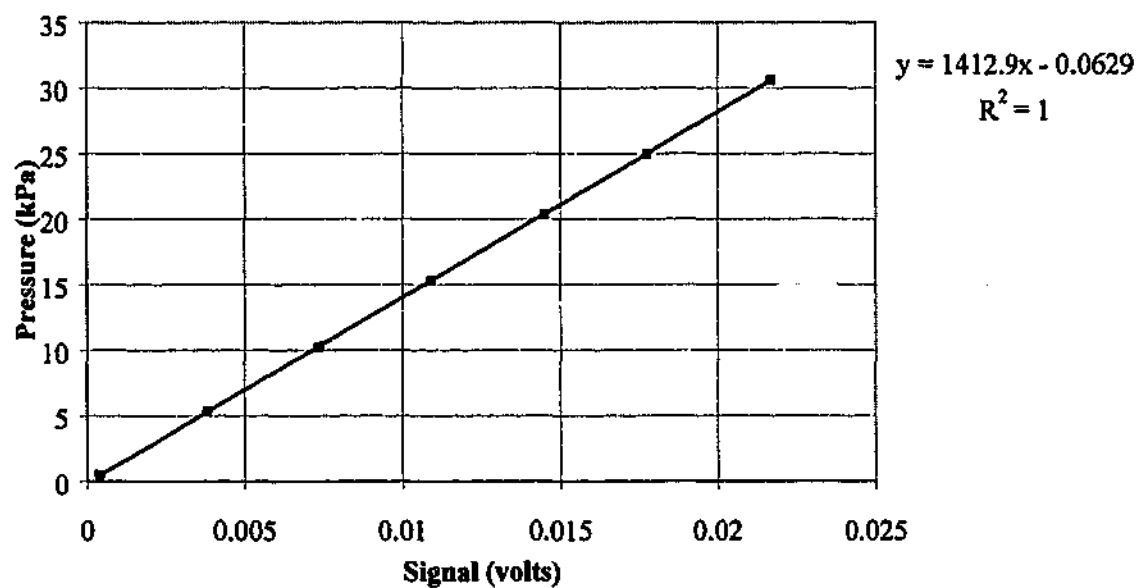


Figure E.9 Calibration data for low-range pressure transducer (designation XCX05#3). Straight-line fit for data conversions shown at top right corner.

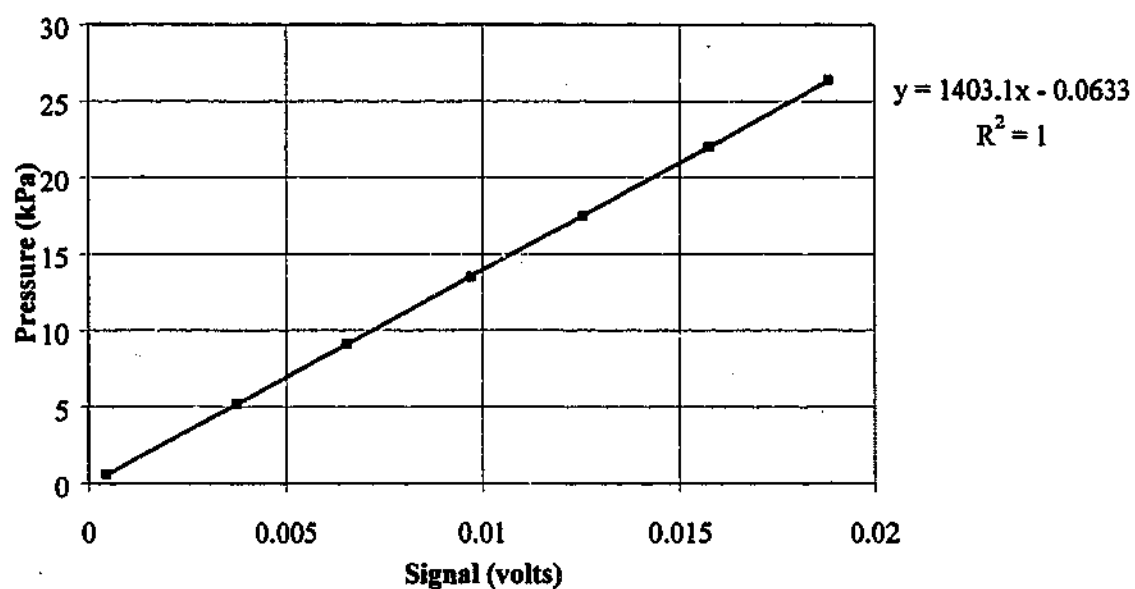


Figure E.10 Calibration data for low-range pressure transducer (designation XCX05#4). Straight-line fit for data conversions shown at top right corner.

APPENDIX F – PRESSURE FLUCTUATION RESULTS

In this appendix the entire set of single value pressure fluctuation results for the four cold models are presented at all gas velocities and for all probe positions. The data are presented for use in conjunction with Chapter 4. The first set of results, Figures F.1 to F.27, correspond to the results for all four correctly-scaled beds at gas velocities from $U/U_{mf} = 1.25$ to 4.0. Figure F.28 to F.54 are results for the subsequent experiments in the smaller three beds at higher gas velocities ($U/U_{mf} = 1.25$ to $U/U_{mf} = 9.3$)

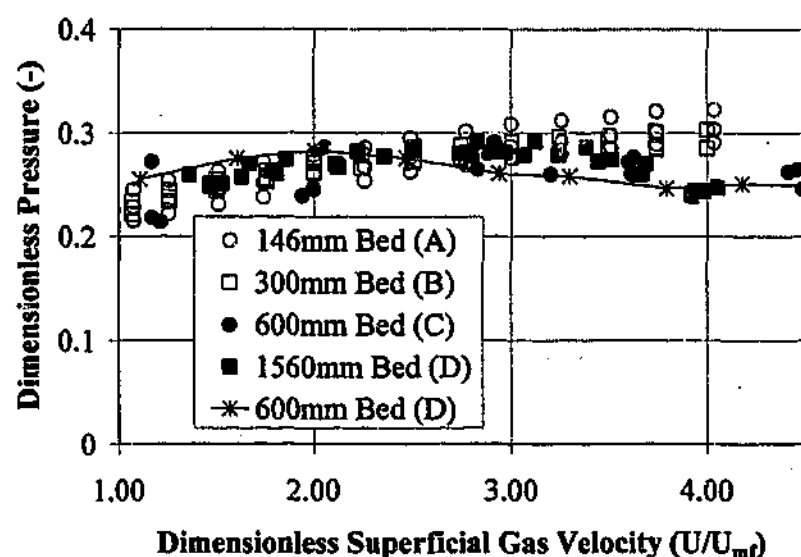


Figure F.1 Comparison of the dimensionless average pressure from the four correctly scaled beds (146 mm A, 300 mm B, 600 mm C, and 1560 mm D) and the one mis-scaled bed (600 mm D). Probe positioned at $r/R = 0$ and $h/H = 0.77$.

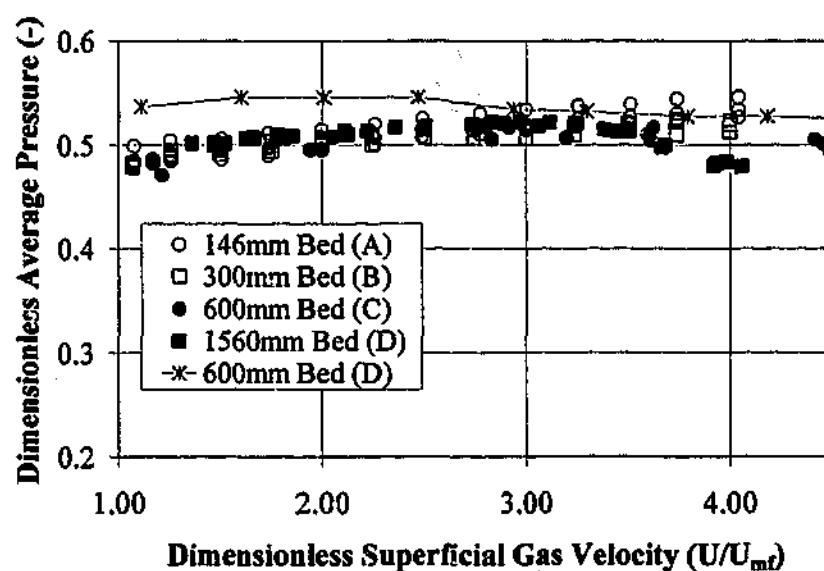


Figure F.2 Comparison of the dimensionless average pressure from the four correctly scaled beds (146 mm A, 300 mm B, 600 mm C, and 1560 mm D) and the one mis-scaled bed (600 mm D). Probe positioned at $r/R = 0$ and $h/H = 0.46$.

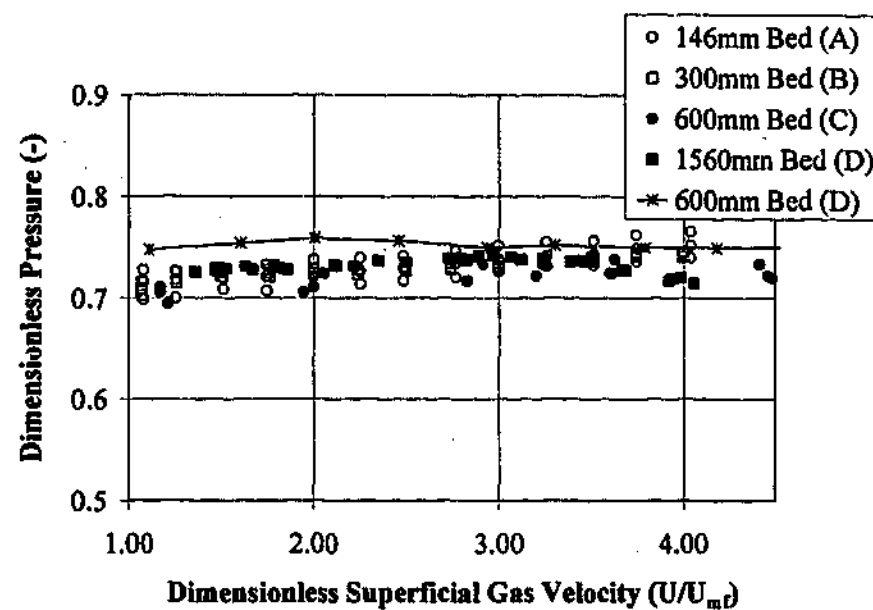


Figure F.3 Comparison of the dimensionless average pressure from the four correctly scaled beds (146 mm A, 300 mm B, 600 mm C, and 1560 mm D) and the one mis-scaled bed (600 mm D). Probe positioned at $r/R = 0$ and $h/H = 0.2$.

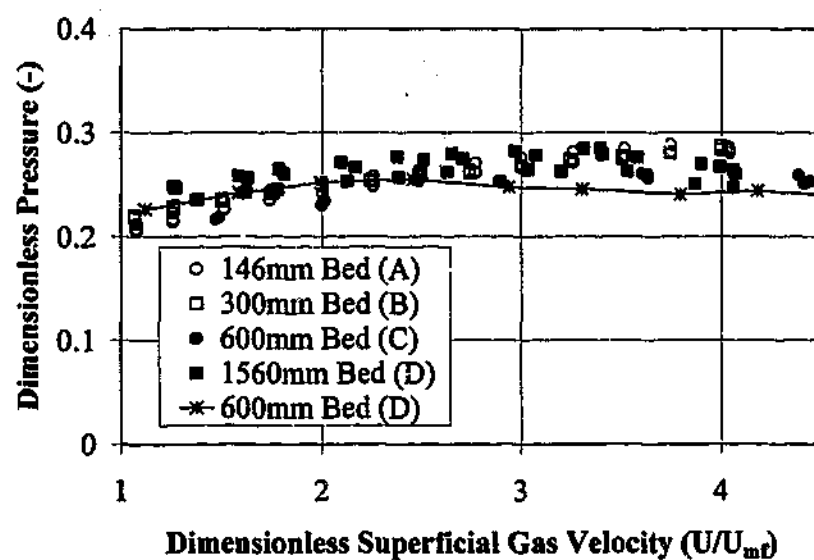


Figure F.4 Comparison of the dimensionless average pressure from the four correctly scaled beds (146 mm A, 300 mm B, 600 mm C, and 1560 mm D) and the one mis-scaled bed (600 mm D). Probe positioned at $r/R = 0.5$ and $h/H = 0.77$.

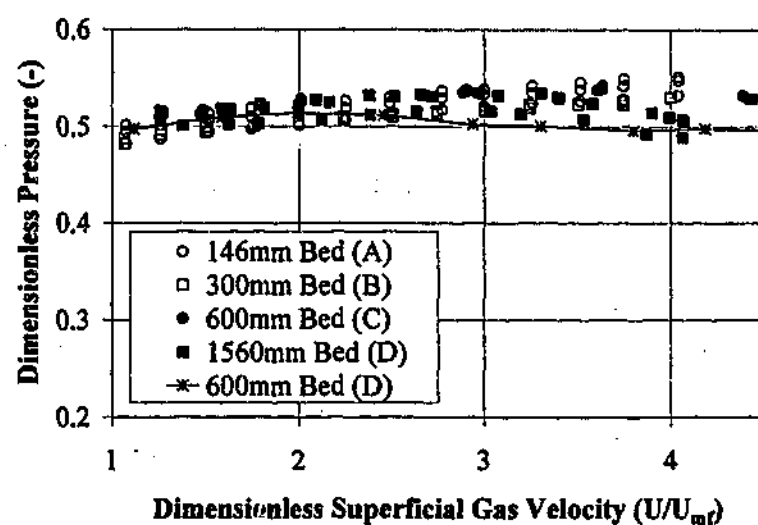


Figure F.5 Comparison of the dimensionless average pressure from the four correctly scaled beds (146 mm A, 300 mm B, 600 mm C, and 1560 mm D) and the one mis-scaled bed (600 mm D). Probe positioned at $r/R = 0.5$ and $h/H = 0.46$.

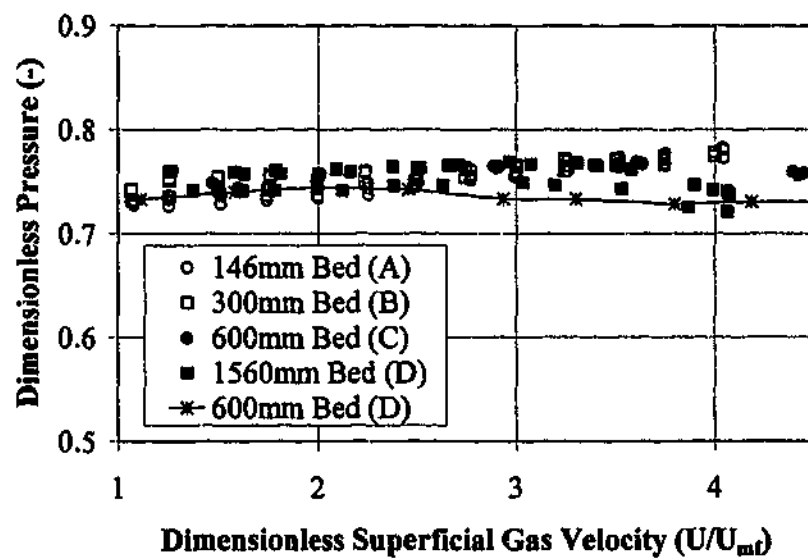


Figure F.6 Comparison of the dimensionless average pressure from the four correctly scaled beds (146 mm A, 300 mm B, 600 mm C, and 1560 mm D) and the one mis-scaled bed (600 mm D). Probe positioned at $r/R = 0.5$ and $h/H = 0.2$.

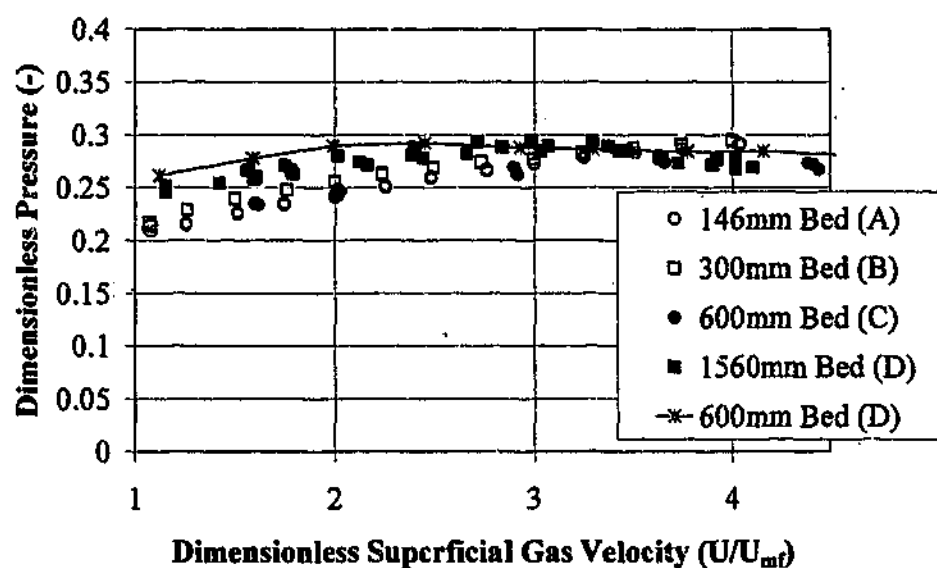


Figure F.7 Comparison of the dimensionless average pressure from the four correctly scaled beds (146 mm A, 300 mm B, 600 mm C, and 1560 mm D) and the one mis-scaled bed (600 mm D). Probe positioned at $r/R = 1$ and $H = 0.77$.

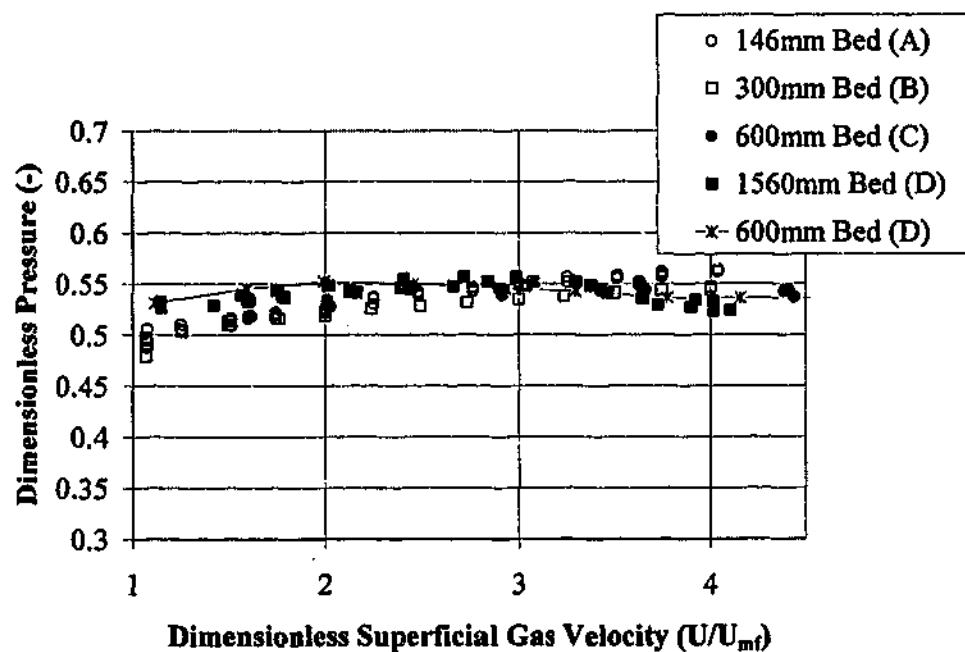


Figure F.8 Comparison of the dimensionless average pressure from the four correctly scaled beds (146 mm A, 300 mm B, 600 mm C, and 1560 mm D) and the one mis-scaled bed (600 mm D). Probe positioned at $r/R = 1$ and $H = 0.46$.

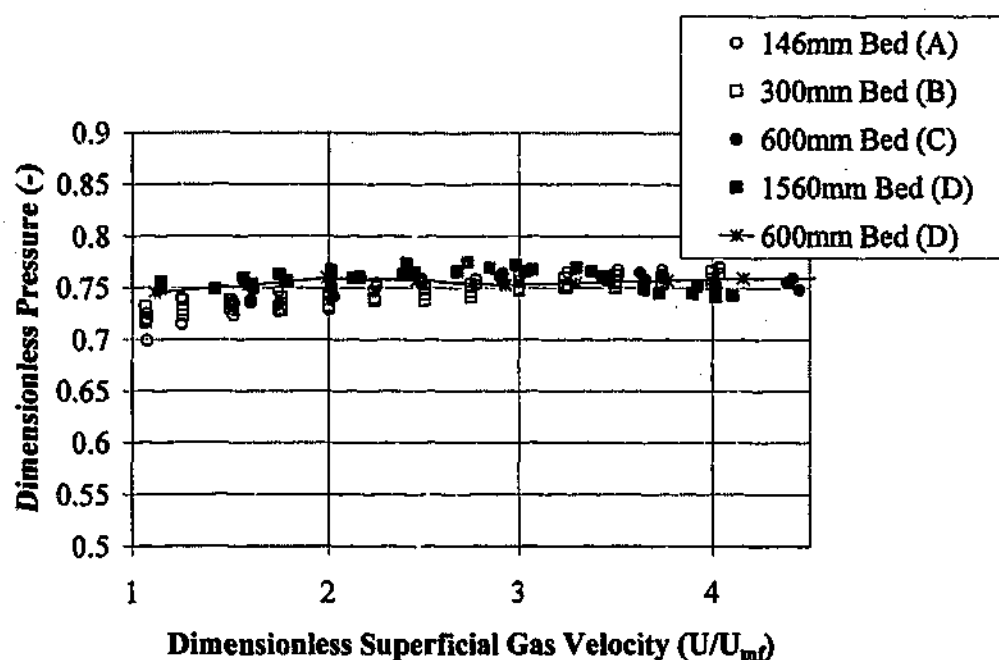


Figure F.9 Comparison of the dimensionless average pressure from the four correctly scaled beds (146 mm A, 300 mm B, 600 mm C, and 1560 mm D) and the one mis-scaled bed (600 mm D). Probe positioned at $r/R = 1$ and $H = 0.2$.

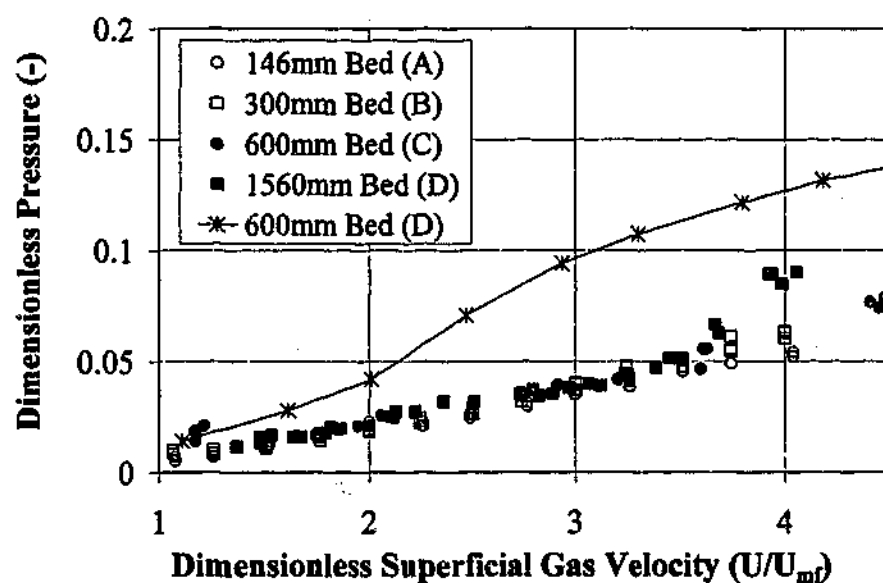


Figure F.10 Comparison of the dimensionless average absolute deviation of pressure from the four correctly scaled beds (146 mm A, 300 mm B, 600 mm C, and 1560 mm D) and the one mis-scaled bed (600 mm D). Probe positioned at $r/R = 0$ and $H = 0.77$.

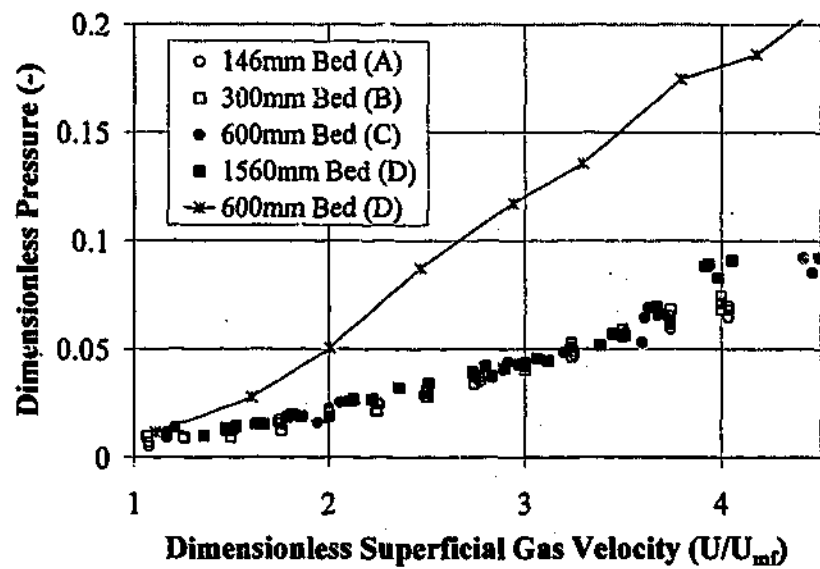


Figure F.11 Comparison of the dimensionless average absolute deviation of pressure from the four correctly scaled beds (146 mm A, 300 mm B, 600 mm C, and 1560 mm D) and the one mis-scaled bed (600 mm D). Probe positioned at $r/R = 0$ and $H = 0.46$.

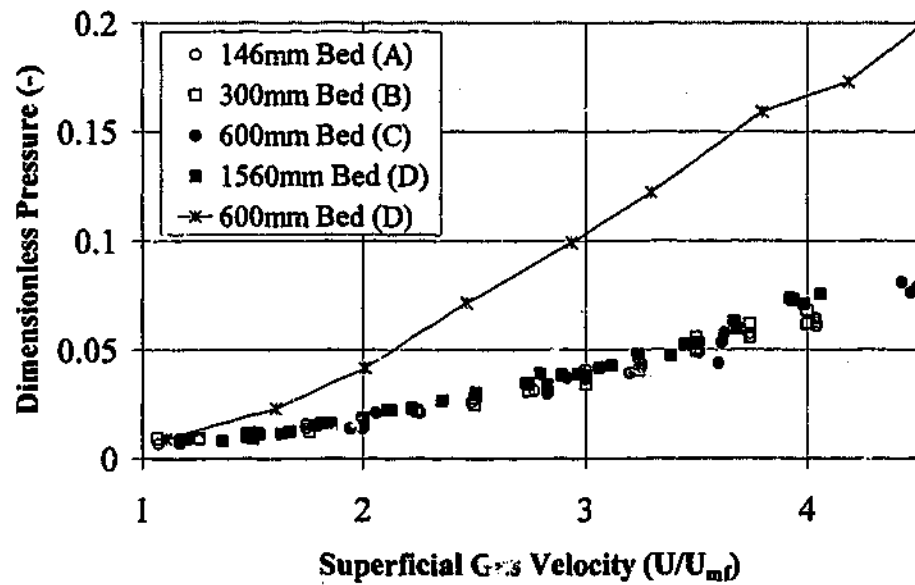


Figure F.12 Comparison of the dimensionless average absolute deviation of pressure from the four correctly scaled beds (146 mm A, 300 mm B, 600 mm C, and 1560 mm D) and the one mis-scaled bed (600 mm D). Probe positioned at $r/R = 0$ and $H = 0.46$.

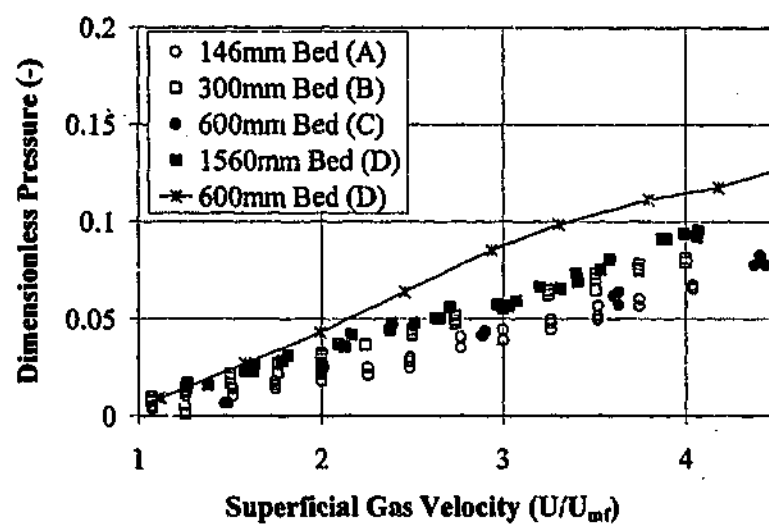


Figure F.13 Comparison of the dimensionless average absolute deviation of pressure from the four correctly scaled beds (146 mm A, 300 mm B, 600 mm C, and 1560 mm D) and the one mis-scaled bed (600 mm D). Probe positioned at $r/R = 0.5$ and $H = 0.77$.

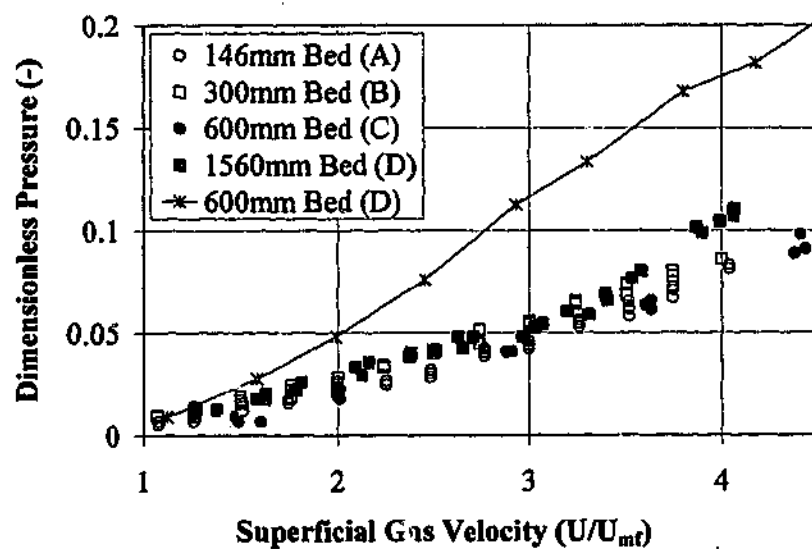


Figure F.14 Comparison of the dimensionless average absolute deviation of pressure from the four correctly scaled beds (146 mm A, 300 mm B, 600 mm C, and 1560 mm D) and the one mis-scaled bed (600 mm D). Probe positioned at $r/R = 0.5$ and $H = 0.46$.

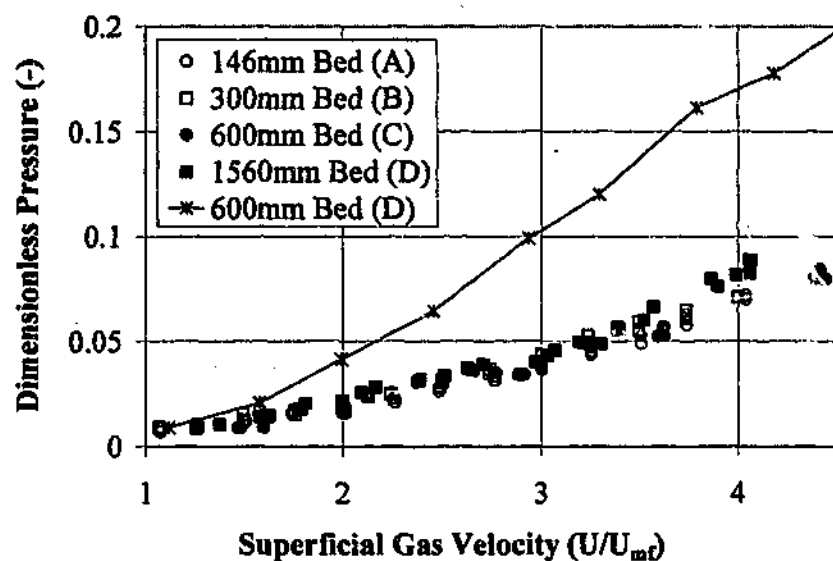


Figure F.15 Comparison of the dimensionless average absolute deviation of pressure from the four correctly scaled beds (146 mm A, 300 mm B, 600 mm C, and 1560 mm D) and the one mis-scaled bed (600 mm D). Probe positioned at $r/R = 0.5$ and $H = 0.2$.

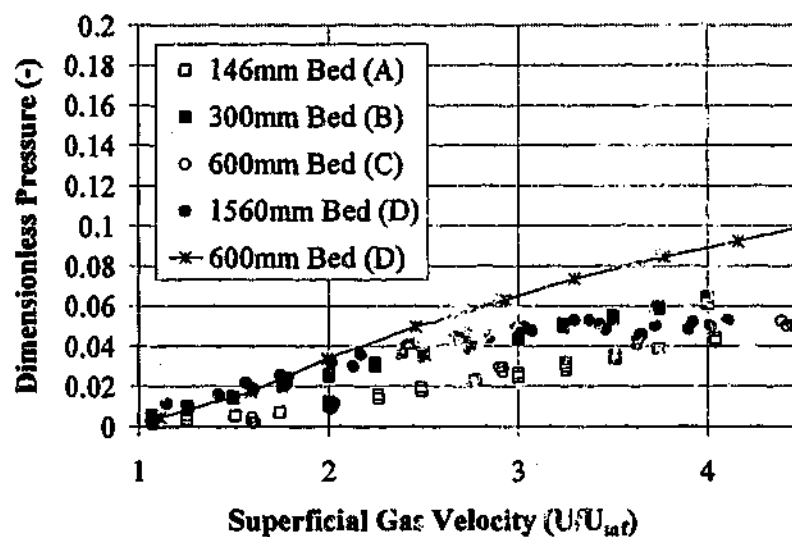


Figure F.16 Comparison of the dimensionless average absolute deviation of pressure from the four correctly scaled beds (146 mm A, 300 mm B, 600 mm C, and 1560 mm D) and the one mis-scaled bed (600 mm D). Probe positioned at $r/R = 1$ and $H = 0.77$.

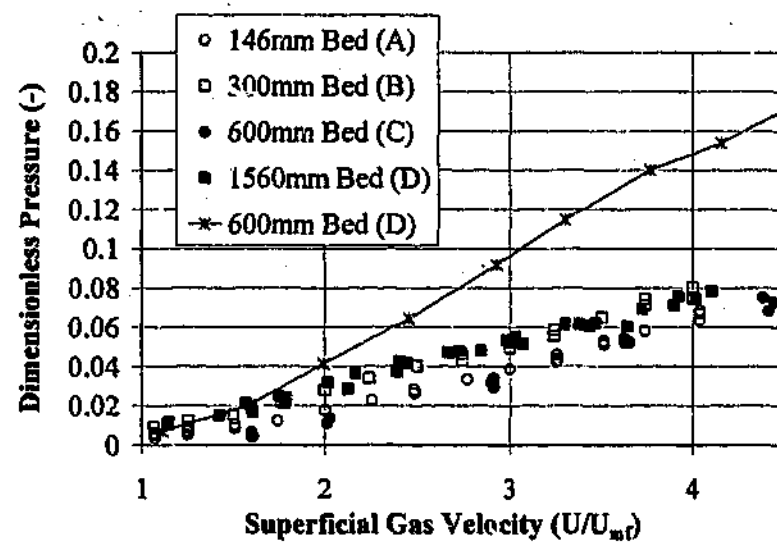


Figure F.17 Comparison of the dimensionless average absolute deviation of pressure from the four correctly scaled beds (146 mm A, 300 mm B, 600 mm C, and 1560 mm D) and the one mis-scaled bed (600 mm D). Probe positioned at $r/R = 1$ and $H = 0.46$.

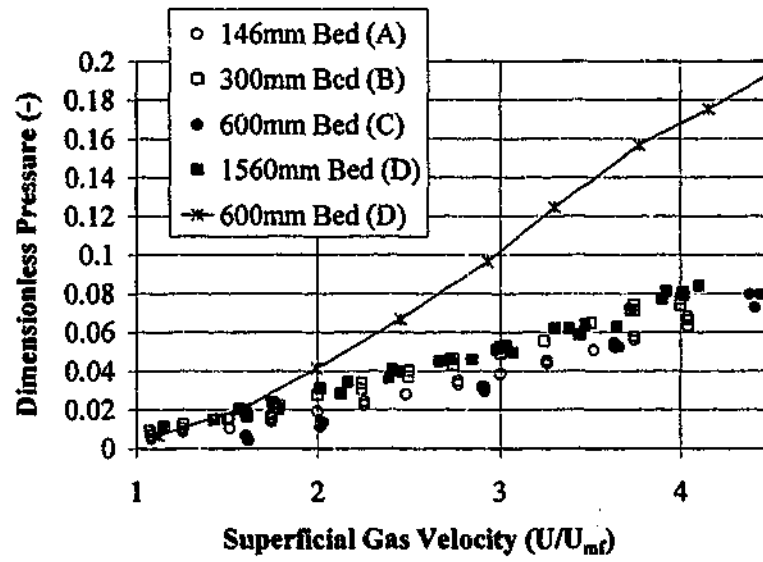


Figure F.18 Comparison of the dimensionless average absolute deviation of pressure from the four correctly scaled beds (146 mm A, 300 mm B, 600 mm C, and 1560 mm D) and the one mis-scaled bed (600 mm D). Probe positioned at $r/R = 1$ and $H = 0.2$.

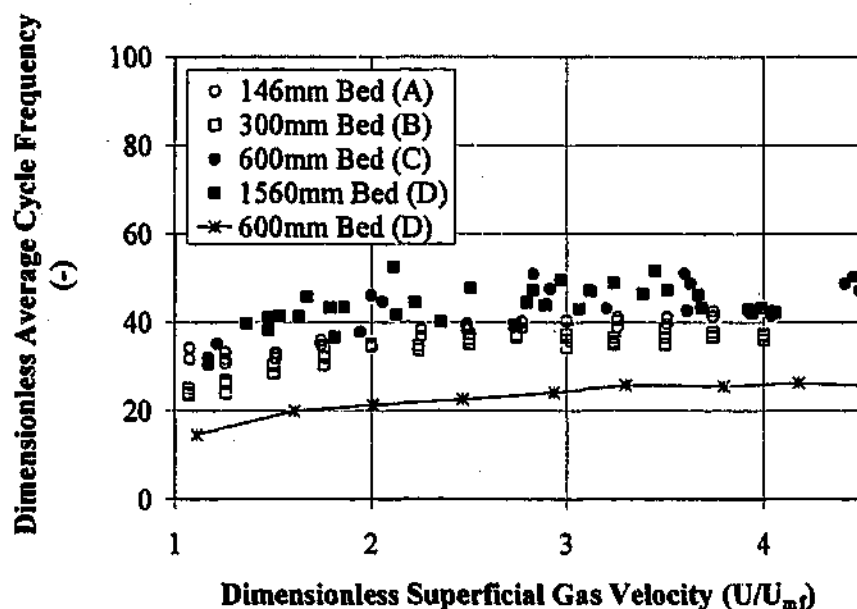


Figure F.19 Comparison of the dimensionless average cycle frequency of pressure fluctuations from the four correctly scaled beds (146 mm A, 300 mm B, 600 mm C, and 1560 mm D) and the one mis-scaled bed (600 mm D). Probe positioned at $r/R = 0$ and $H = 0.77$.

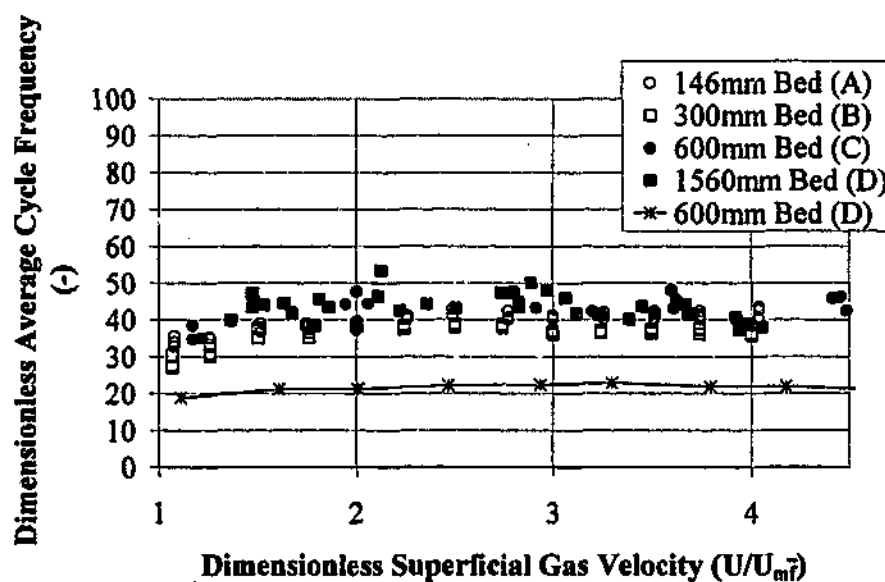


Figure F.20 Comparison of the dimensionless average cycle frequency of pressure fluctuations from the four correctly scaled beds (146 mm A, 300 mm B, 600 mm C, and 1560 mm D) and the one mis-scaled bed (600 mm D). Probe positioned at $r/R = 0$ and $H = 0.46$.

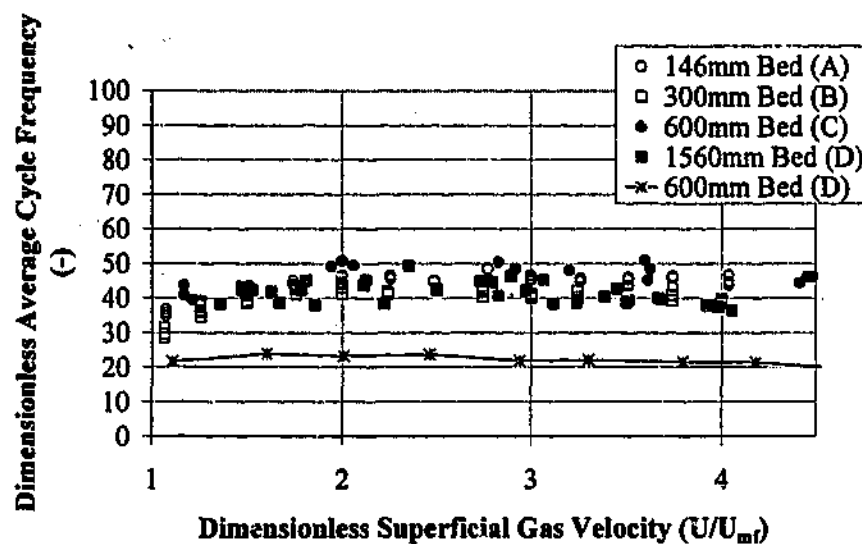


Figure F.21 Comparison of the dimensionless average cycle frequency of pressure fluctuations from the four correctly scaled beds (146 mm A, 300 mm B, 600 mm C, and 1560 mm D) and the one mis-scaled bed (600 mm D). Probe positioned at $r/R = 0$ and $H = 0.2$.

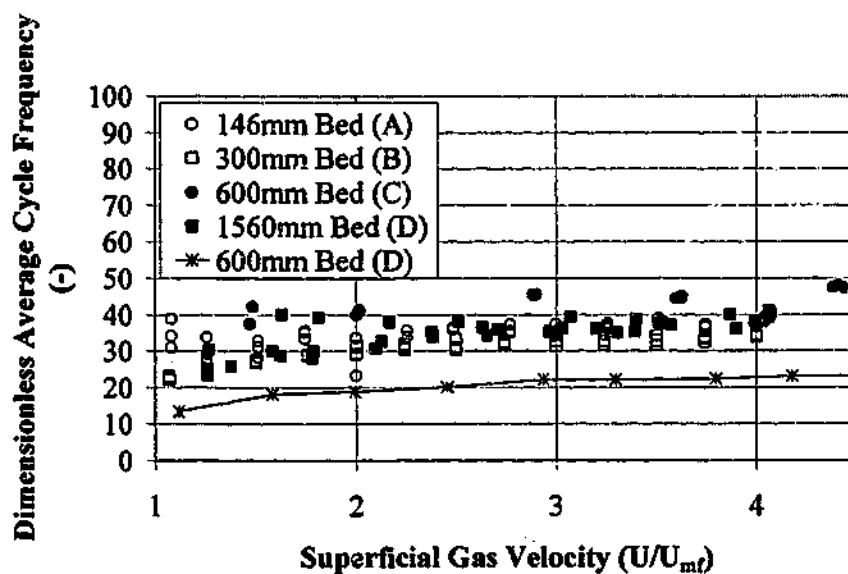


Figure F.22 Comparison of the dimensionless average cycle frequency of pressure fluctuations from the four correctly scaled beds (146 mm A, 300 mm B, 600 mm C, and 1560 mm D) and the one mis-scaled bed (600 mm D). Probe positioned at $r/R = 0.5$ and $H = 0.77$.

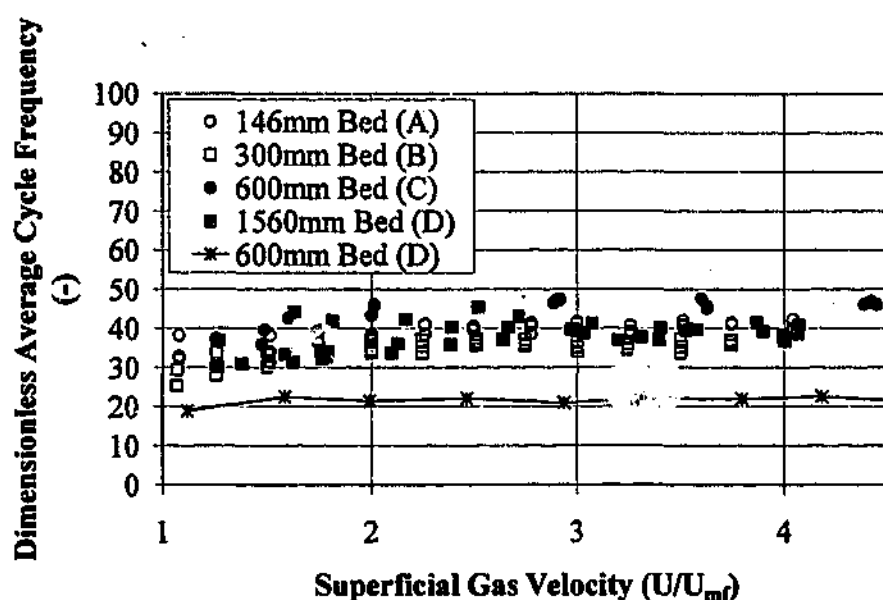


Figure F.23 Comparison of the dimensionless average cycle frequency of pressure fluctuations from the four correctly scaled beds (146 mm A, 300 mm B, 600 mm C, and 1560 mm D) and the one mis-scaled bed (600 mm D). Probe positioned at $r/R = 0.5$ and $H = 0.46$.

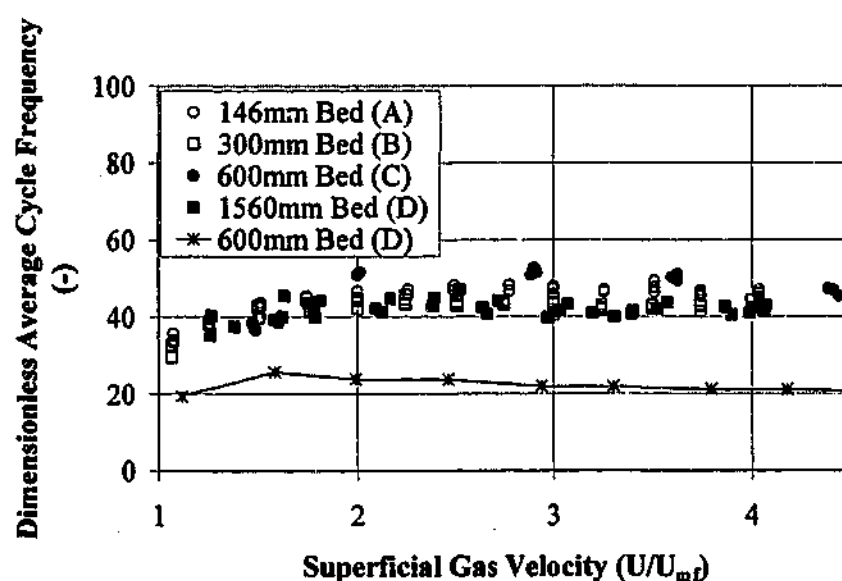


Figure F.24 Comparison of the dimensionless average cycle frequency of pressure fluctuations from the four correctly scaled beds (146 mm A, 300 mm B, 600 mm C, and 1560 mm D) and the one mis-scaled bed (600 mm D). Probe positioned at $r/R = 0.5$ and $H = 0.2$.

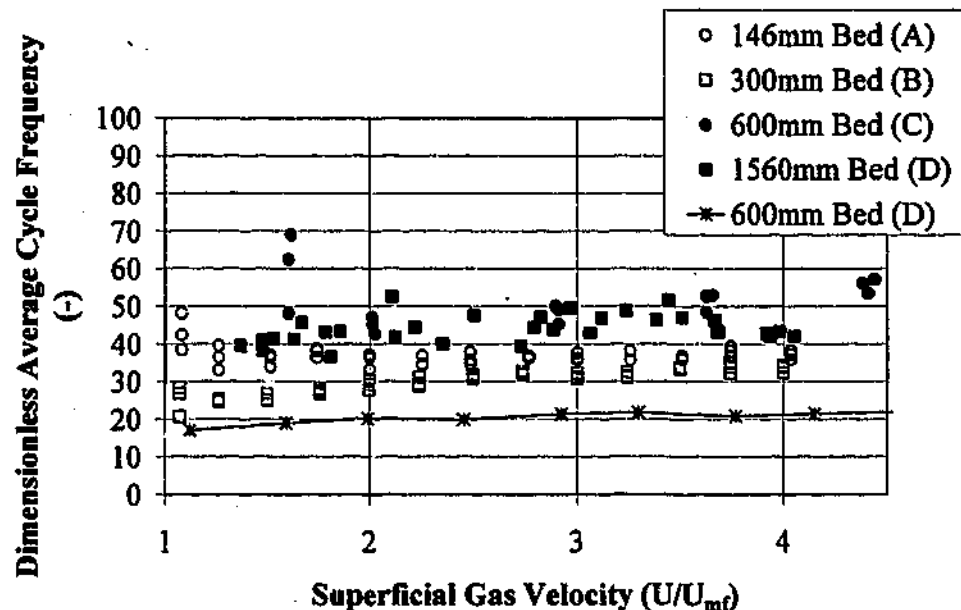


Figure F.25 Comparison of the dimensionless average cycle frequency of pressure fluctuations from the four correctly scaled beds (146 mm A, 300 mm B, 600 mm C, and 1560 mm D) and the one mis-scaled bed (600 mm D). Probe positioned at $r/R = 1$ and $H = 0.77$.

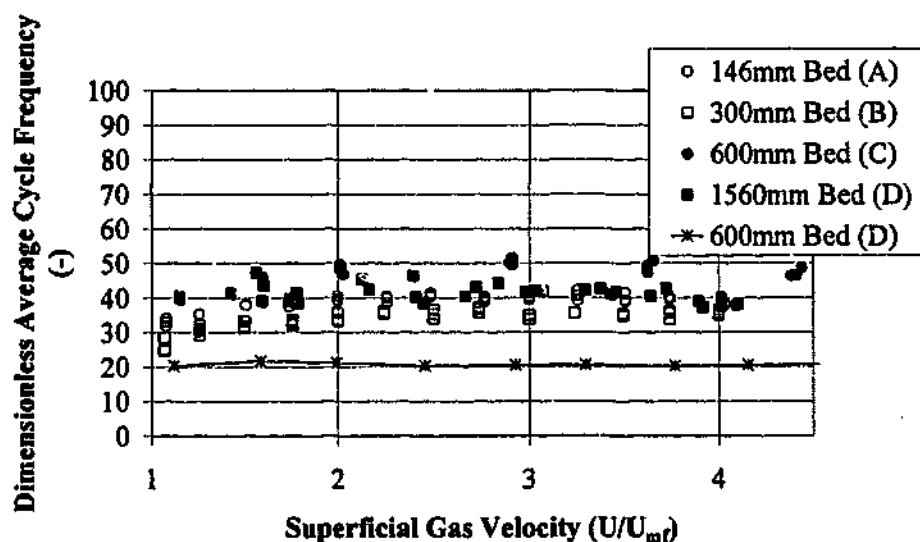


Figure F.26 Comparison of the dimensionless average cycle frequency of pressure fluctuations from the four correctly scaled beds (146 mm A, 300 mm B, 600 mm C, and 1560 mm D) and the one mis-scaled bed (600 mm D). Probe positioned at $r/R = 1$ and $H = 0.46$.

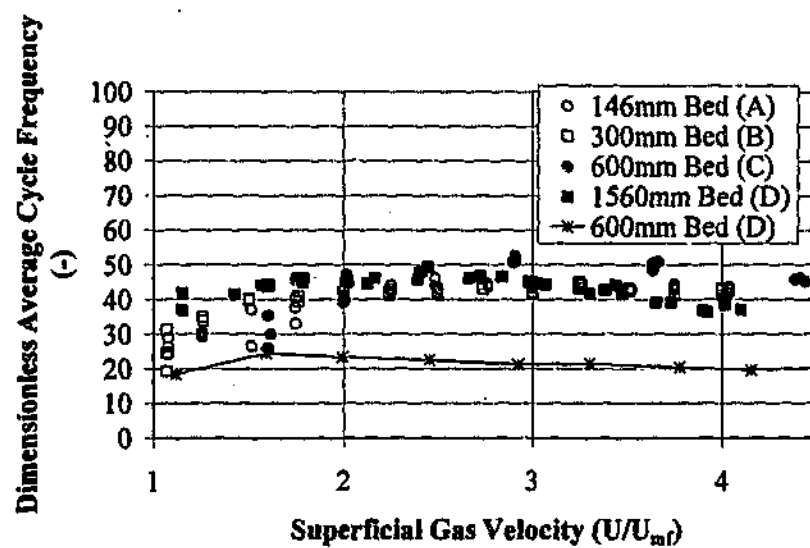


Figure F.27 Comparison of the dimensionless average cycle frequency of pressure fluctuations from the four correctly scaled beds (146 mm A, 300 mm B, 600 mm C, and 1560 mm D) and the one mis-scaled bed (600 mm D). Probe positioned at $r/R = 1$ and $H = 0.2$.

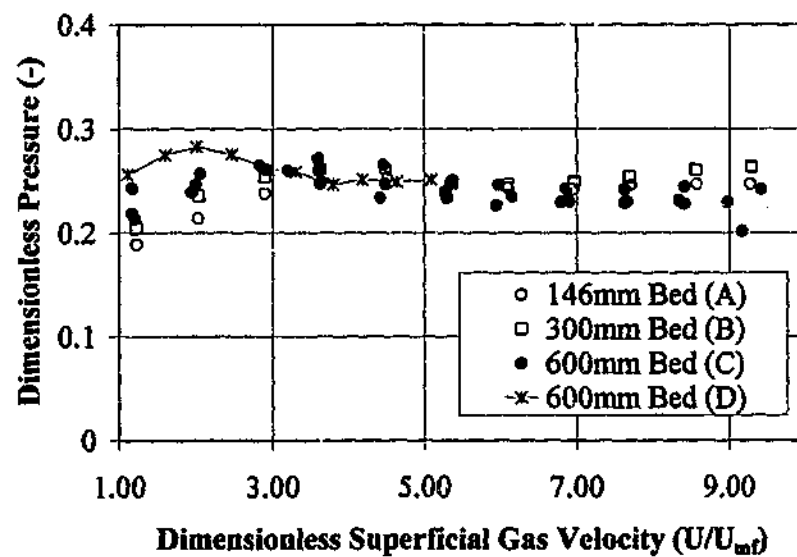


Figure F.28 Comparison of the dimensionless average pressure from the three correctly scaled beds (146 mm A, 300 mm B, and 600 mm C) and the one mis-scaled bed (600 mm D). Probe positioned at $r/R = 0$ and $H = 0.77$.

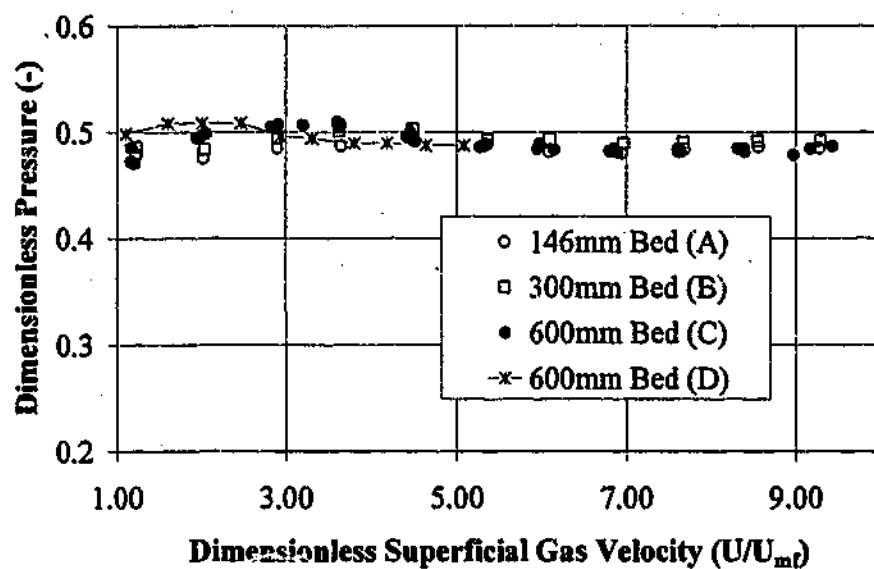


Figure F.29 Comparison of the dimensionless average pressure from the three correctly scaled beds (146 mm A, 500 mm B, and 600 mm C) and the one mis-scaled bed (600 mm D). Probe positioned at $r/R = 0$ and $H = 0.46$.

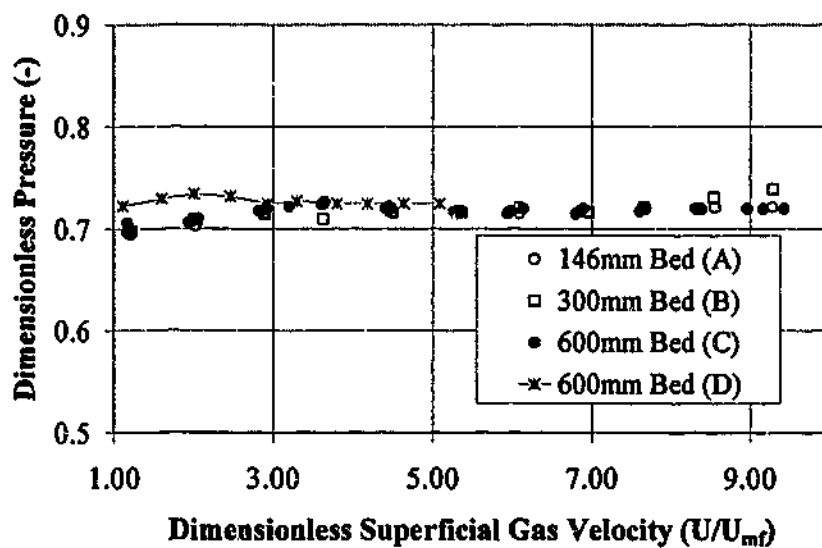


Figure F.30 Comparison of the dimensionless average pressure from the three correctly scaled beds (146 mm A, 300 mm B, and 600 mm C) and the one mis-scaled bed (600 mm D). Probe positioned at $r/R = 0$ and $H = 0.2$.

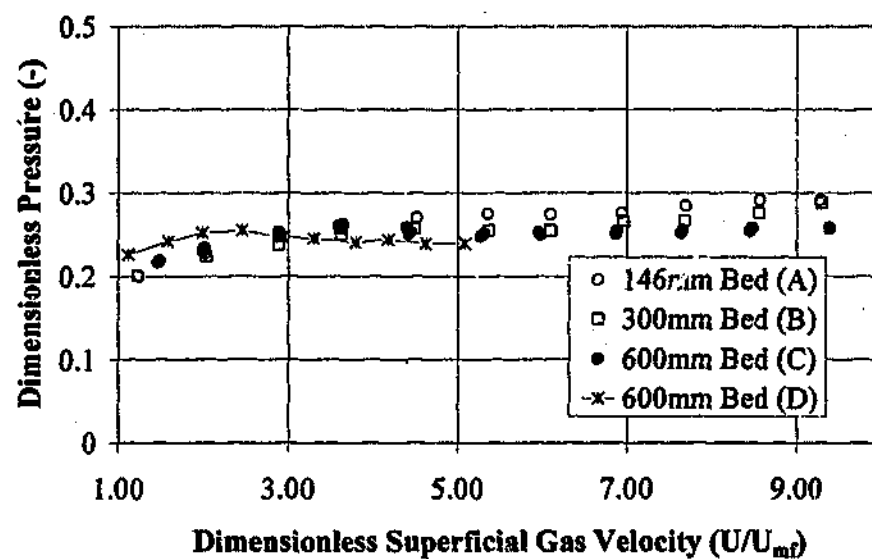


Figure F.31 Comparison of the dimensionless average pressure from the three correctly scaled beds (146 mm A, 300 mm B, and 600 mm C) and the one mis-scaled bed (600 mm D). Probe positioned at $r/R = 0.5$ and $H = 0.77$.

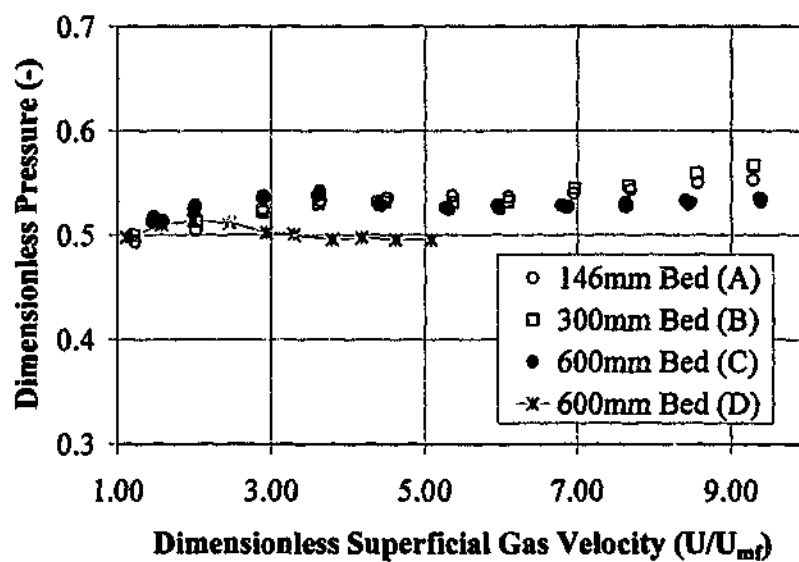


Figure F.32 Comparison of the dimensionless average pressure from the three correctly scaled beds (146 mm A, 300 mm B, and 600 mm C) and the one mis-scaled bed (600 mm D). Probe positioned at $r/R = 0.5$ and $H = 0.46$.

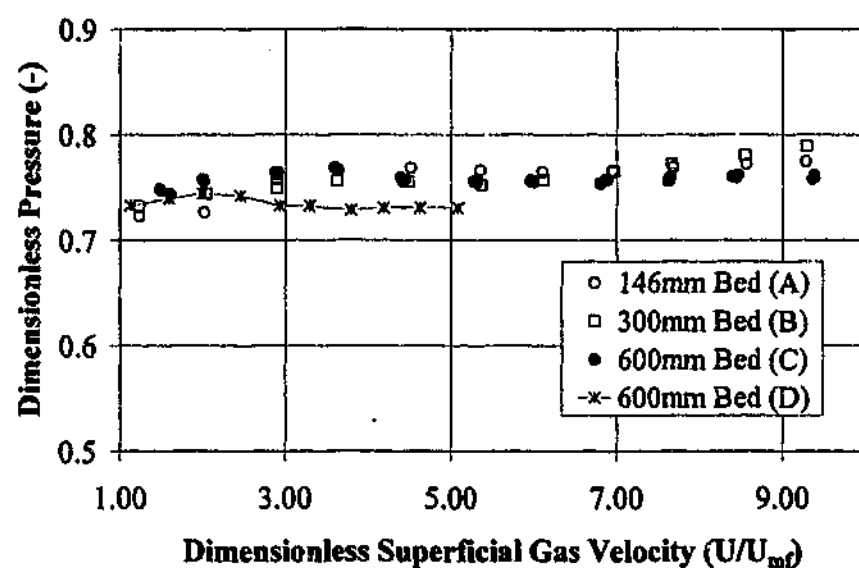


Figure F.33 Comparison of the dimensionless average pressure from the three correctly scaled beds (146 mm A, 300 mm B, and 600 mm C) and the one mis-scaled bed (600 mm D). Probe positioned at $r/R = 0.5$ and $H = 0.2$.

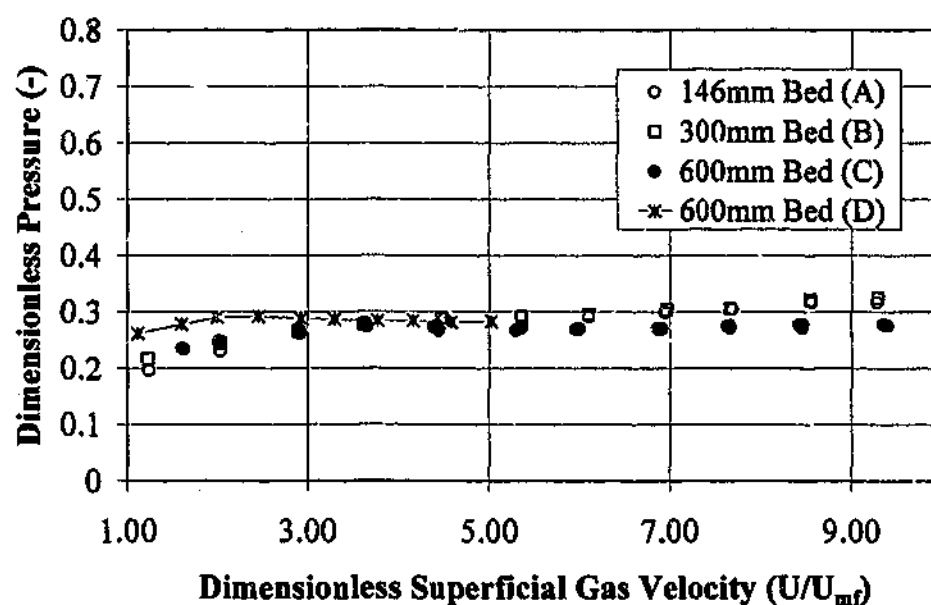


Figure F.34 Comparison of the dimensionless average pressure from the three correctly scaled beds (146 mm A, 300 mm B, and 600 mm C) and the one mis-scaled bed (600 mm D). Probe positioned at $r/R = 1$ and $H = 0.77$.

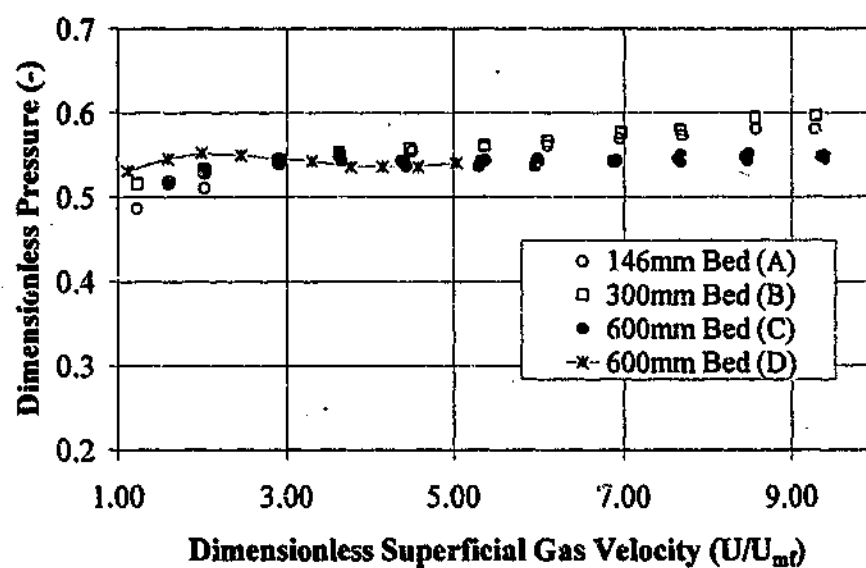


Figure F.35 Comparison of the dimensionless average pressure from the three correctly scaled beds (146 mm A, 300 mm B, and 600 mm C) and the one mis-scaled bed (600 mm D). Probe positioned at $r/R = 1$ and $H = 0.46$.

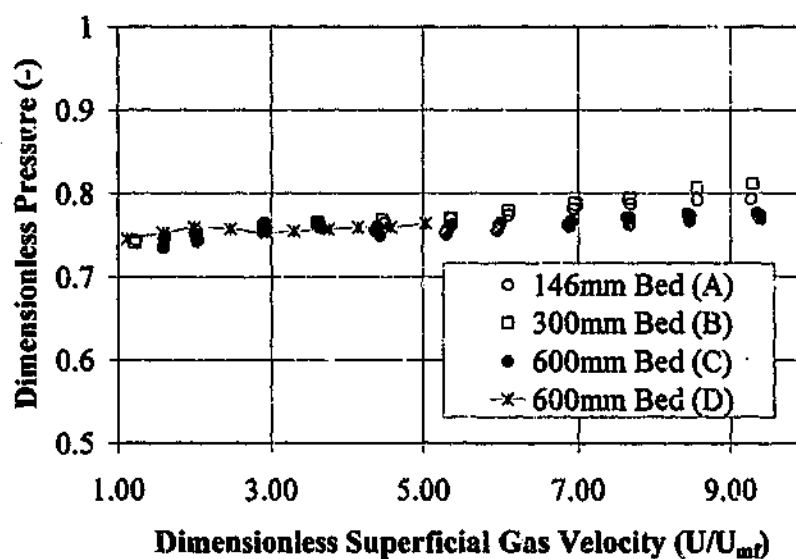


Figure F.36 Comparison of the dimensionless average pressure from the three correctly scaled beds (146 mm A, 300 mm B, and 600 mm C) and the one mis-scaled bed (600 mm D). Probe positioned at $r/R = 1$ and $H = 0.2$.

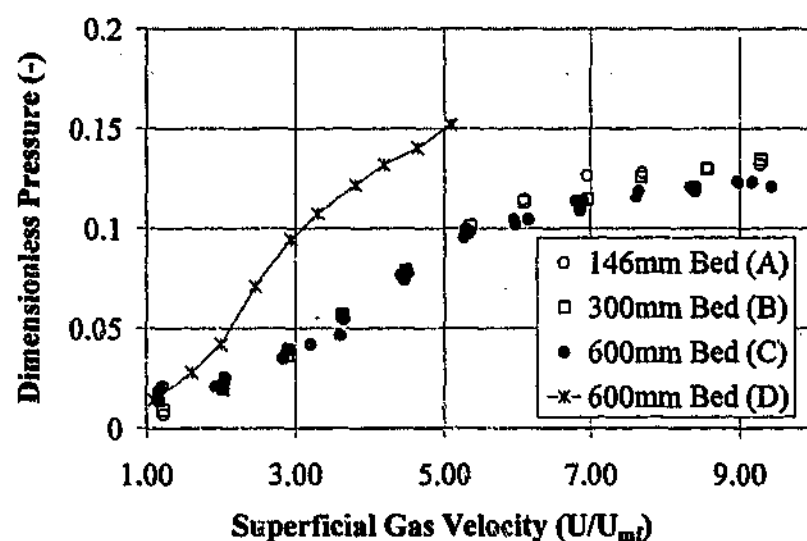


Figure F.37 Comparison of the dimensionless average absolute deviation of pressure from the three correctly scaled beds (146 mm A, 300 mm B, and 600 mm C) and the one mis-scaled bed (600 mm D). Probe positioned at $r/R = 0$ and $H = 0.77$.

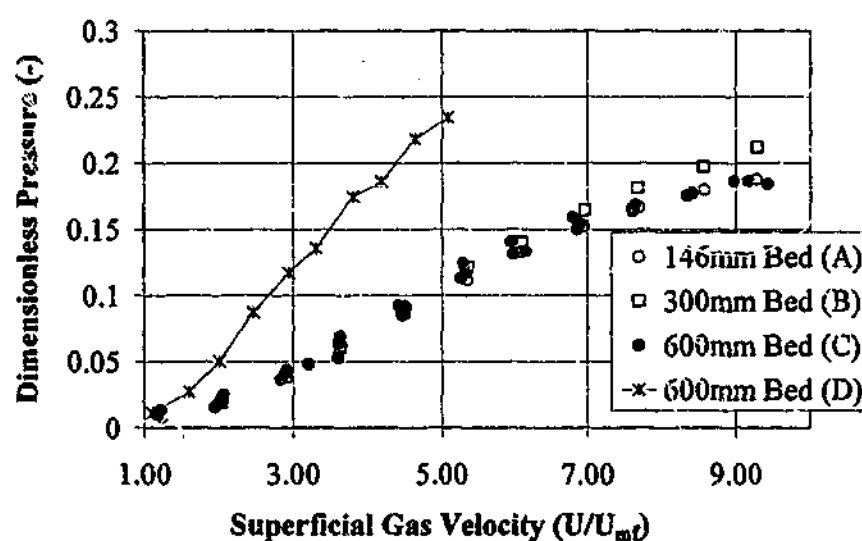


Figure F.38 Comparison of the dimensionless average absolute deviation of pressure from the three correctly scaled beds (146 mm A, 300 mm B, and 600 mm C) and the one mis-scaled bed (600 mm D). Probe positioned at $r/R = 0$ and $H = 0.46$.

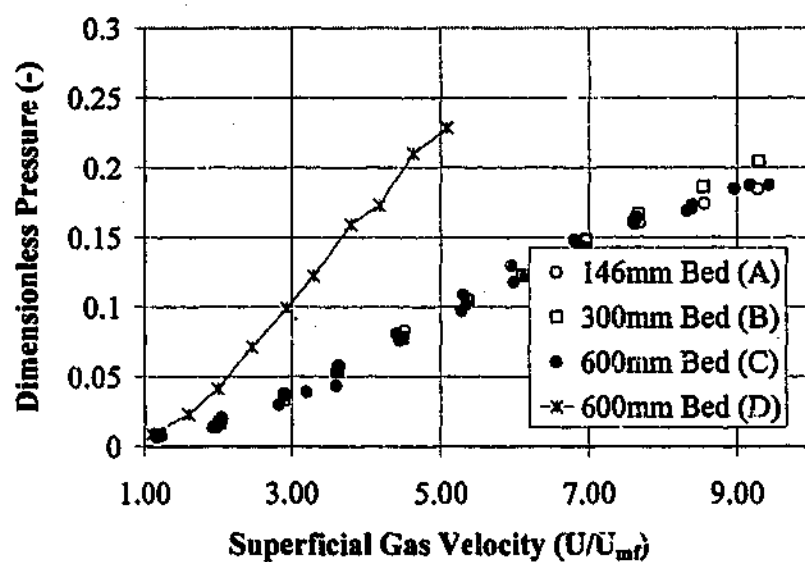


Figure F.39 Comparison of the dimensionless average absolute deviation of pressure from the three correctly scaled beds (146 mm A, 300 mm B, and 600 mm C) and the one mis-scaled bed (600 mm D). Probe positioned at $r/R = 0$ and $H = 0.2$.

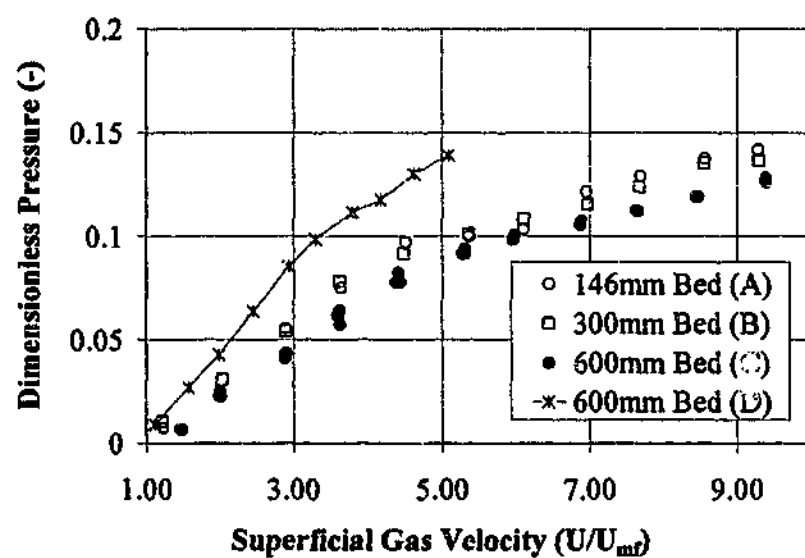


Figure F.40 Comparison of the dimensionless average absolute deviation of pressure from the three correctly scaled beds (146 mm A, 300 mm B, and 600 mm C) and the one mis-scaled bed (600 mm D). Probe positioned at $r/R = 0.5$ and $H = 0.77$.

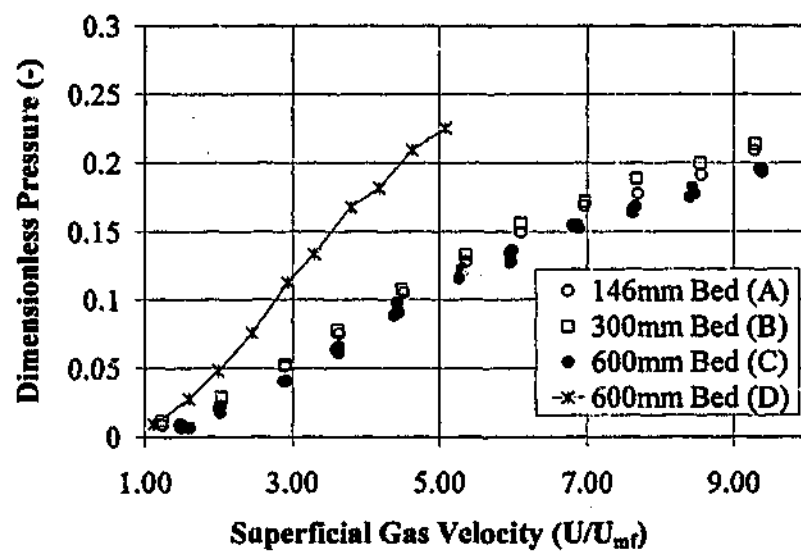


Figure F.41 Comparison of the dimensionless average absolute deviation of pressure from the three correctly scaled beds (146 mm A, 300 mm B, and 600 mm C) and the one mis-scaled bed (600 mm D). Probe positioned at $r/R = 0.5$ and $H = 0.46$.

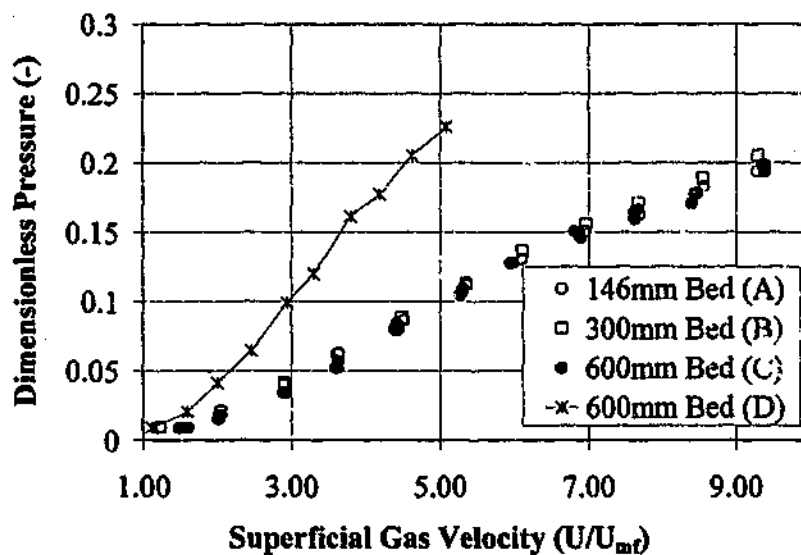


Figure F.42 Comparison of the dimensionless average absolute deviation of pressure from the three correctly scaled beds (146 mm A, 300 mm B, and 600 mm C) and the one mis-scaled bed (600 mm D). Probe positioned at $r/R = 0.5$ and $H = 0.2$.

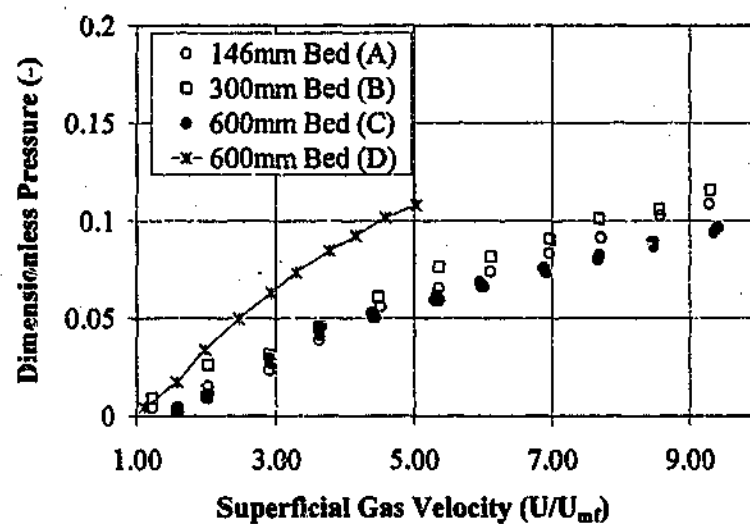


Figure F.43 Comparison of the dimensionless average absolute deviation of pressure from the three correctly scaled beds (146 mm A, 300 mm B, and 600 mm C) and the one mis-scaled bed (600 mm D). Probe positioned at $r/R = 1$ and $H = 0.77$.

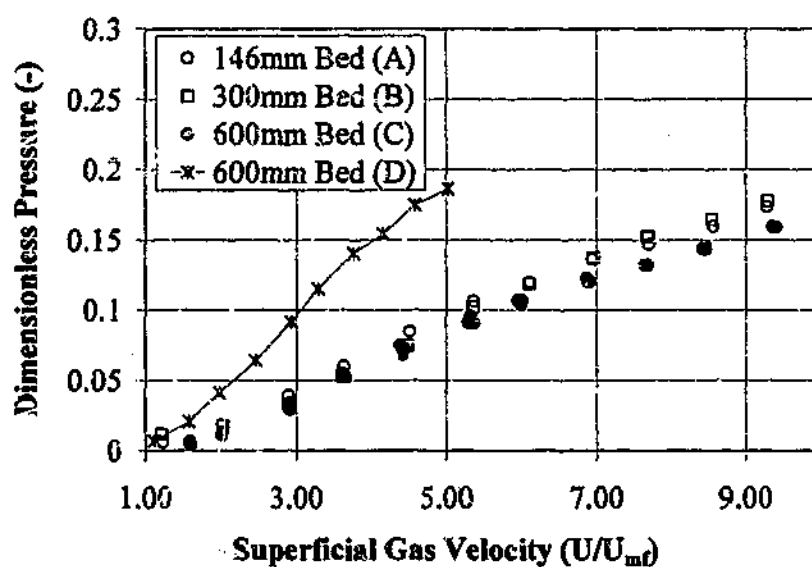


Figure F.44 Comparison of the dimensionless average absolute deviation of pressure from the three correctly scaled beds (146 mm A, 300 mm B, and 600 mm C) and the one mis-scaled bed (600 mm D). Probe positioned at $r/R = 1$ and $H = 0.46$.

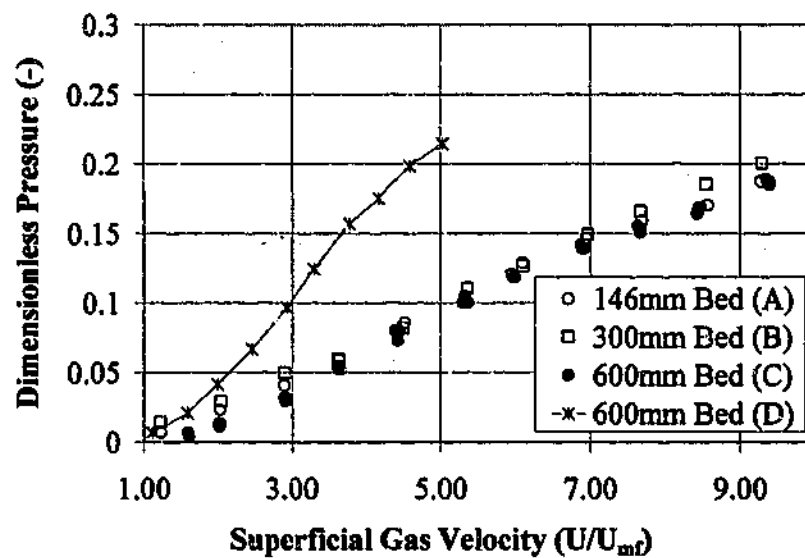


Figure F.45 Comparison of the dimensionless average absolute deviation of pressure from the three correctly scaled beds (146 mm A, 300 mm B, and 600 mm C) and the one mis-scaled bed (600 mm D). Probe positioned at $r/R = 1$ and $H = 0.2$.

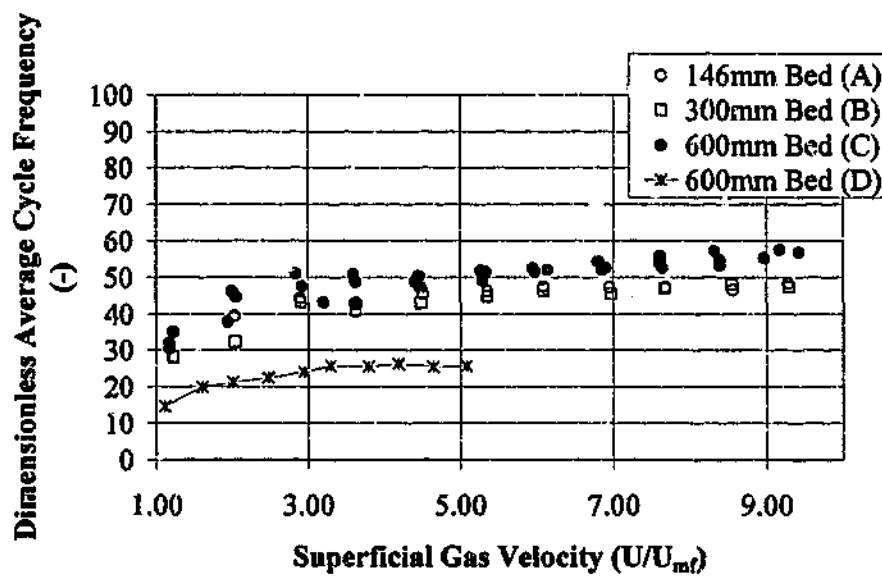


Figure F.46 Comparison of the dimensionless average cycle frequency of pressure fluctuations from the three correctly scaled beds (146 mm A, 300 mm B, and 600 mm C) and the one mis-scaled bed (600 mm D). Probe positioned at $r/R = 0$ and $H = 0.77$.

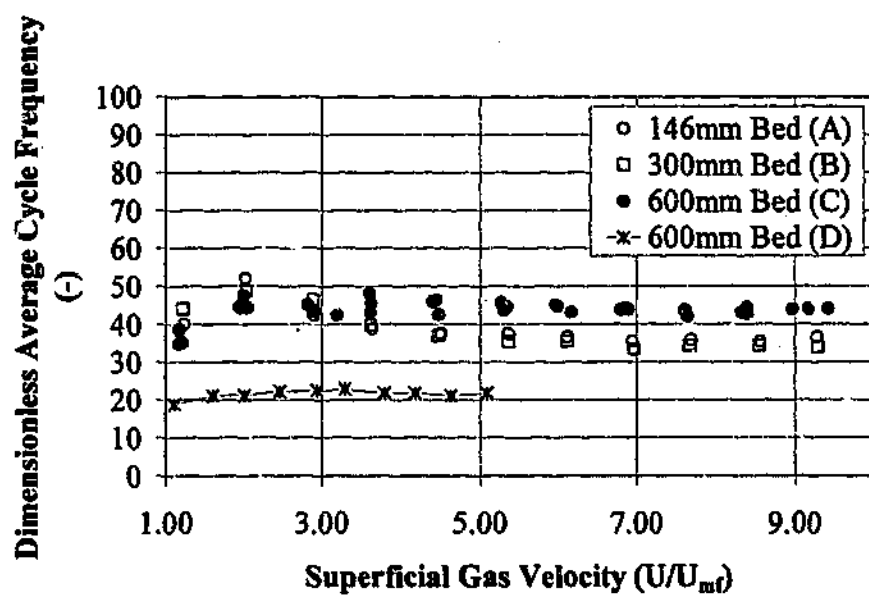


Figure F.47 Comparison of the dimensionless average cycle frequency of pressure fluctuations from the three correctly scaled beds (146 mm A, 300 mm B, and 600 mm C) and the one mis-scaled bed (600 mm D). Probe positioned at $r/R = 0$ and $H = 0.46$.

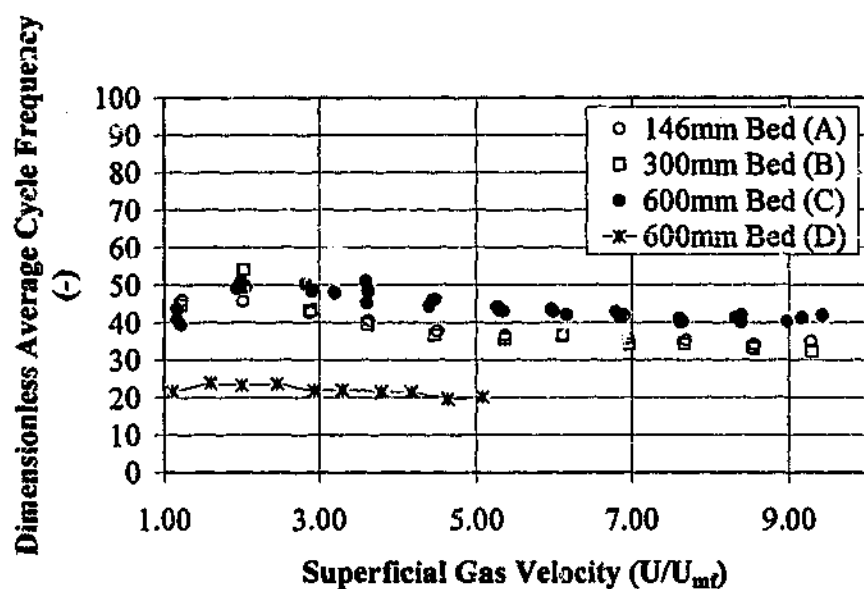


Figure F.48 Comparison of the dimensionless average cycle frequency of pressure fluctuations from the three correctly scaled beds (146 mm A, 300 mm B, and 600 mm C) and the one mis-scaled bed (600 mm D). Probe positioned at $r/R = 0$ and $H = 0.2$.

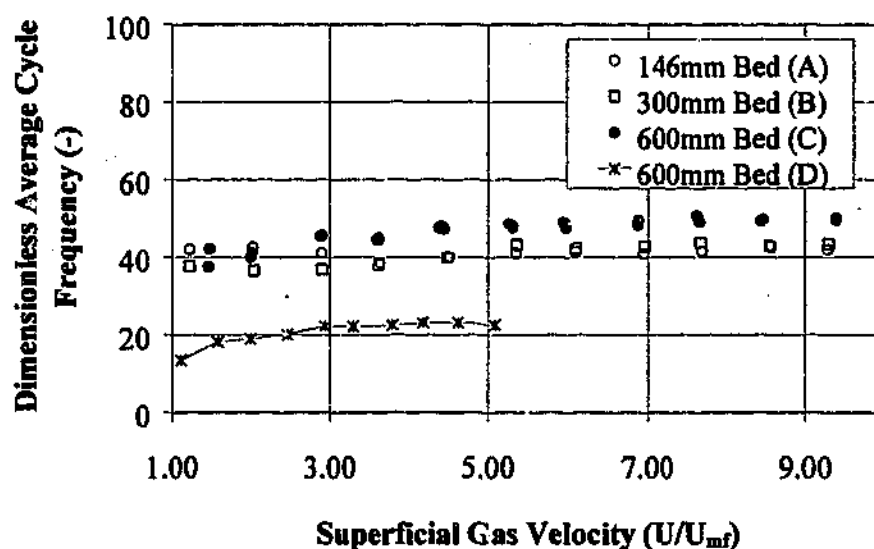


Figure F.49 Comparison of the dimensionless average cycle frequency of pressure fluctuations from the three correctly scaled beds (146 mm A, 300 mm B, and 600 mm C) and the one mis-scaled bed (600 mm D). Probe positioned at $r/R = 0.5$ and $H = 0.77$.

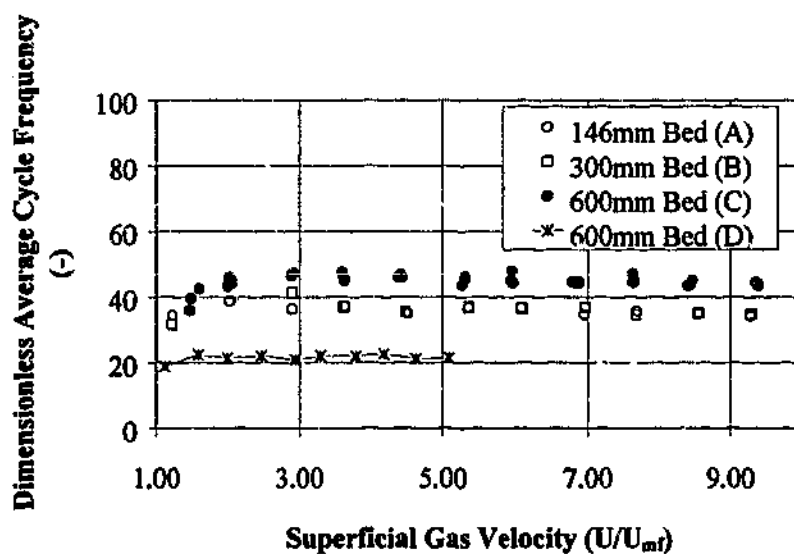


Figure F.50 Comparison of the dimensionless average cycle frequency of pressure fluctuations from the three correctly scaled beds (146 mm A, 300 mm B, and 600 mm C) and the one mis-scaled bed (600 mm D). Probe positioned at $r/R = 0.5$ and $H = 0.46$.

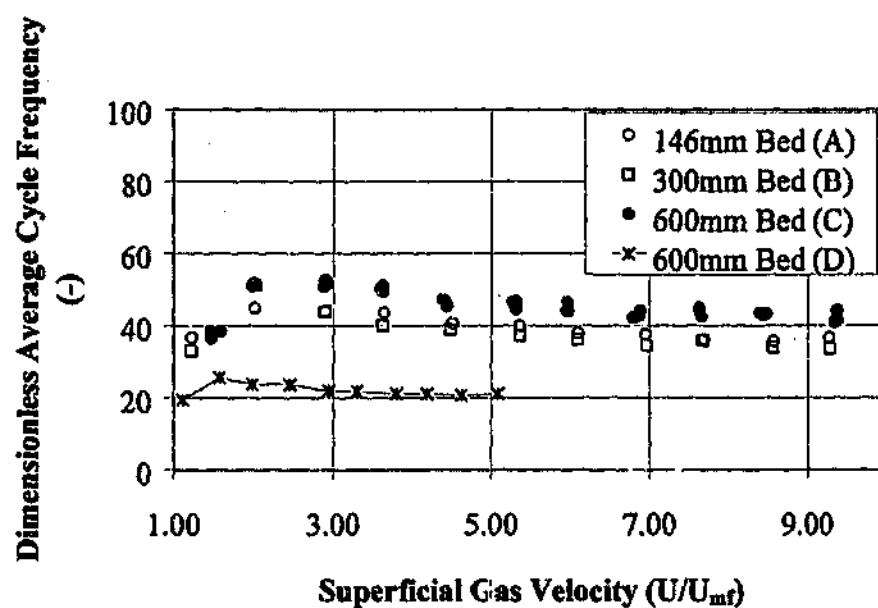


Figure F.51 Comparison of the dimensionless average cycle frequency of pressure fluctuations from the three correctly scaled beds (146 mm A, 300 mm B, and 600 mm C) and the one mis-scaled bed (600 mm D). Probe positioned at $r/R = 0.5$ and $H = 0.2$.

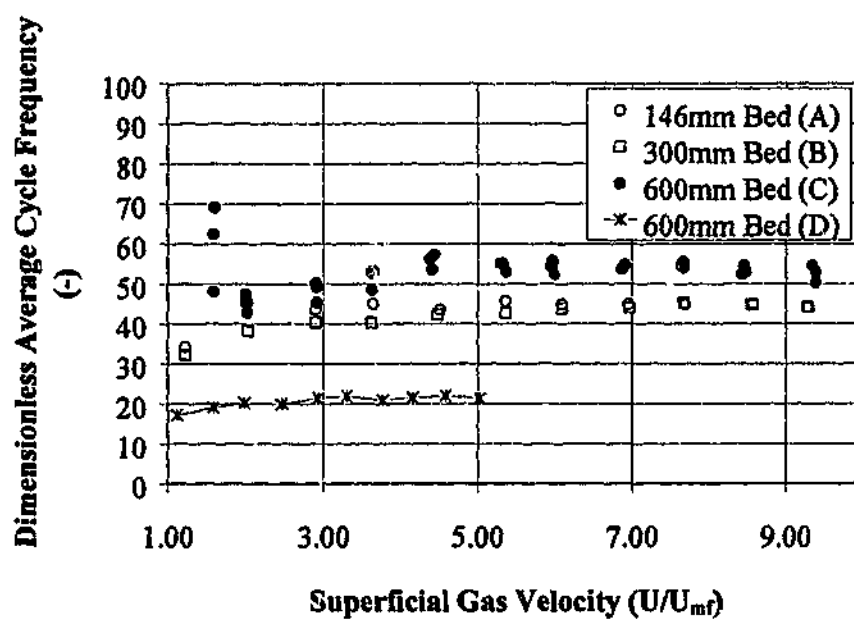


Figure F.52 Comparison of the dimensionless average cycle frequency of pressure fluctuations from the three correctly scaled beds (146 mm A, 300 mm B, and 600 mm C) and the one mis-scaled bed (600 mm D). Probe positioned at $r/R = 1$ and $H = 0.77$.

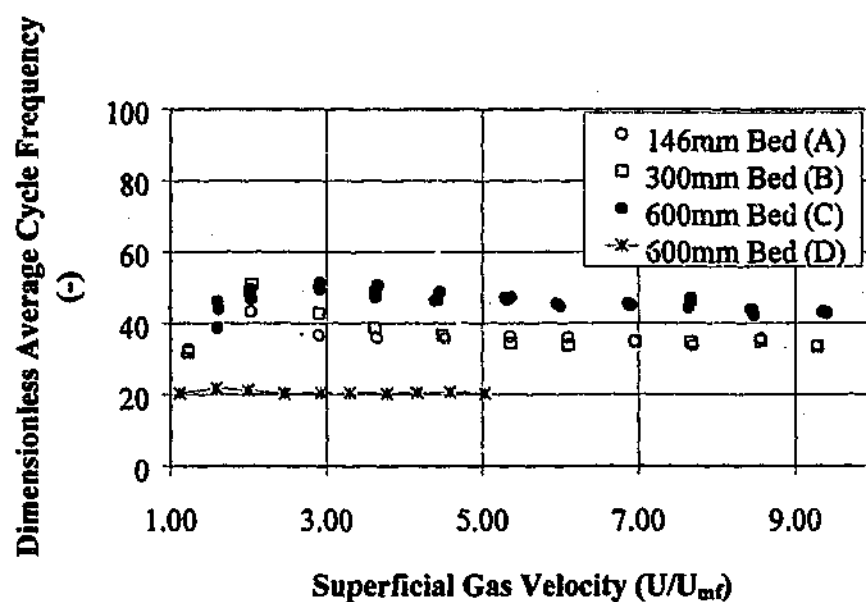


Figure F.53 Comparison of the dimensionless average cycle frequency of pressure fluctuations from the three correctly scaled beds (146 mm A, 300 mm B, and 600 mm C) and the one mis-scaled bed (600 mm D). Probe positioned at $r/R = 1$ and $H = 0.46$.

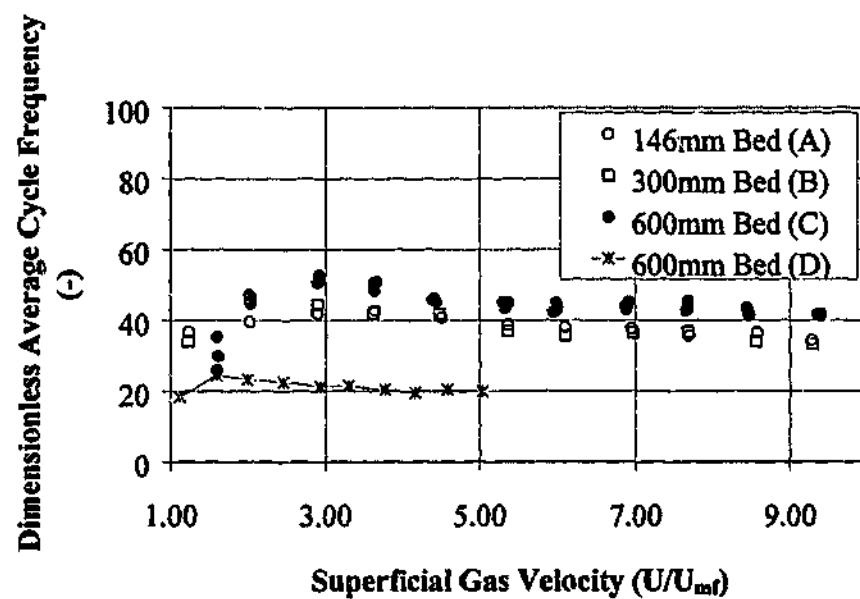


Figure F.54 Comparison of the dimensionless average cycle frequency of pressure fluctuations from the three correctly scaled beds (146 mm A, 300 mm B, and 600 mm C) and the one mis-scaled bed (600 mm D). Probe positioned at $r/R = 1$ and $H = 0.2$.

APPENDIX G – SOLIDS MIXING RESULTS

In this appendix, additional results for the solids mixing experiments and solids motion experiments of Chapter 6 are presented. The first set of results, Figures G.1 to G.5, correspond to the additional small-scale solids mixing results referred to in Section 6.3.2. Figures G.6 to G.22 are additional dimensionless circulation time results for the neutrally-buoyant large tracer experiments in the larger three beds.

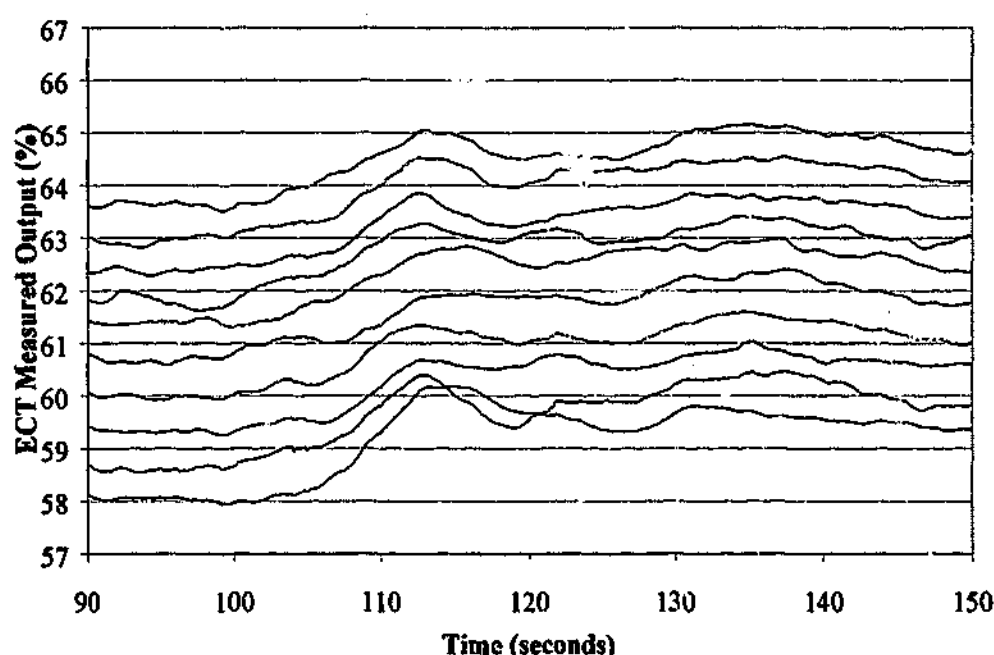


Figure G.1 Tracer response profiles for ten consecutive runs carried out without bed material changeover in order to test how increasing levels of tracer concentration in the bed would affect subsequent response profiles. Results correspond to Condition 3(b) of Table 6.1. Silica sand ($U_{mf} = 0.046$ m/s) fluidized at 0.09 m/s with GB5 ballotini as tracer.

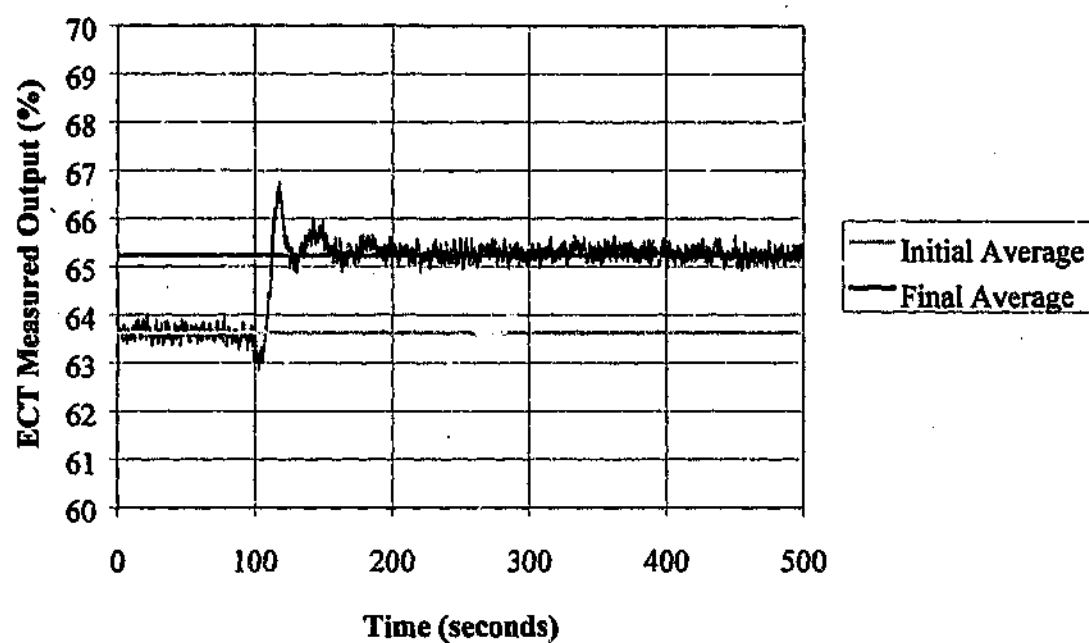


Figure G.2 Transient tracer response profile for Condition 1(a) of Table 6.1: Silica sand ($U_{mf} = 0.046$ m/s) fluidized at 0.066 m/s with GB4 ballotini as tracer.

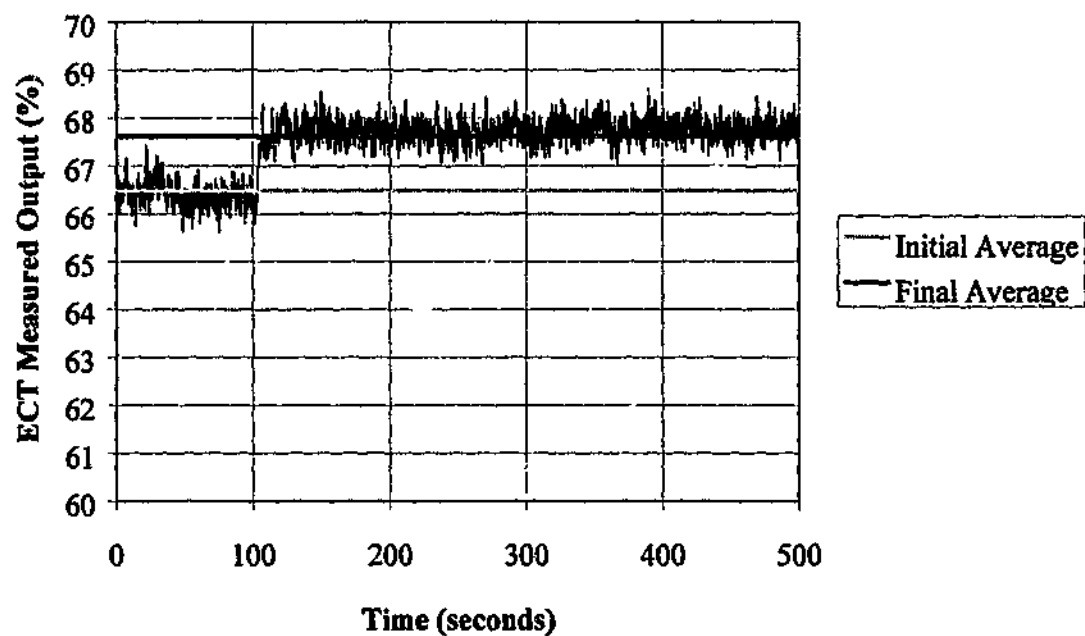


Figure G.3 Transient tracer response profile for Condition 1(b) of Table 6.1: Silica sand ($U_{mf} = 0.046$ m/s) fluidized at 0.09 m/s with GB4 ballotini as tracer.

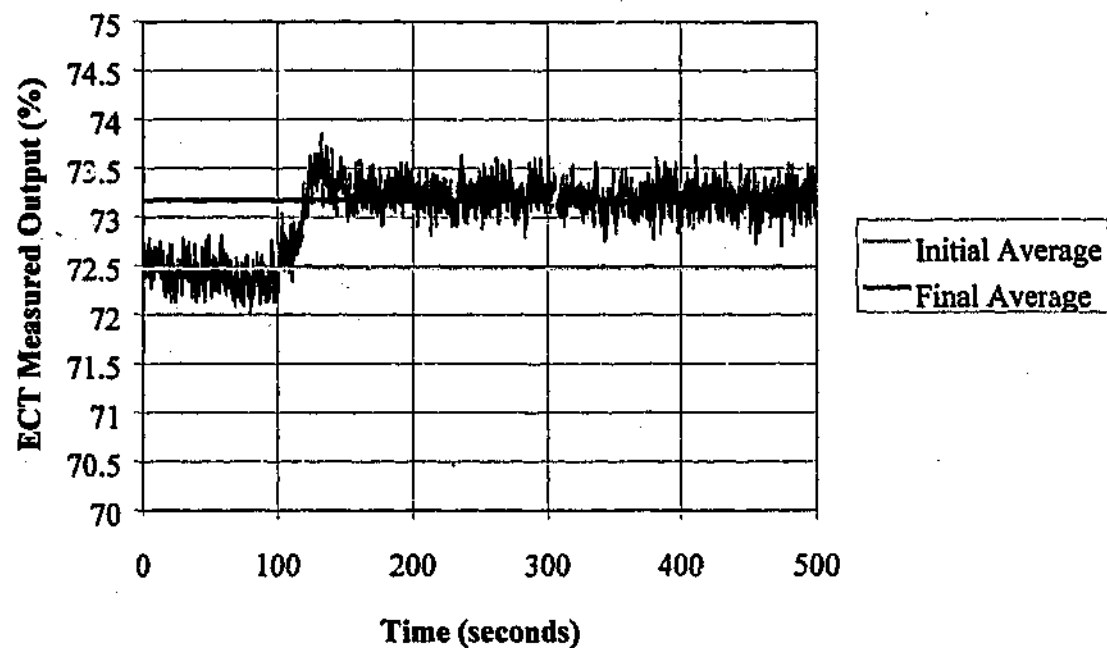


Figure G.4 Transient tracer response profile for Condition 4(a) of Table 6.1: Silica sand ($U_{mf} = 0.046$ m/s) fluidized at 0.066 m/s with GB6 ballotini as tracer.

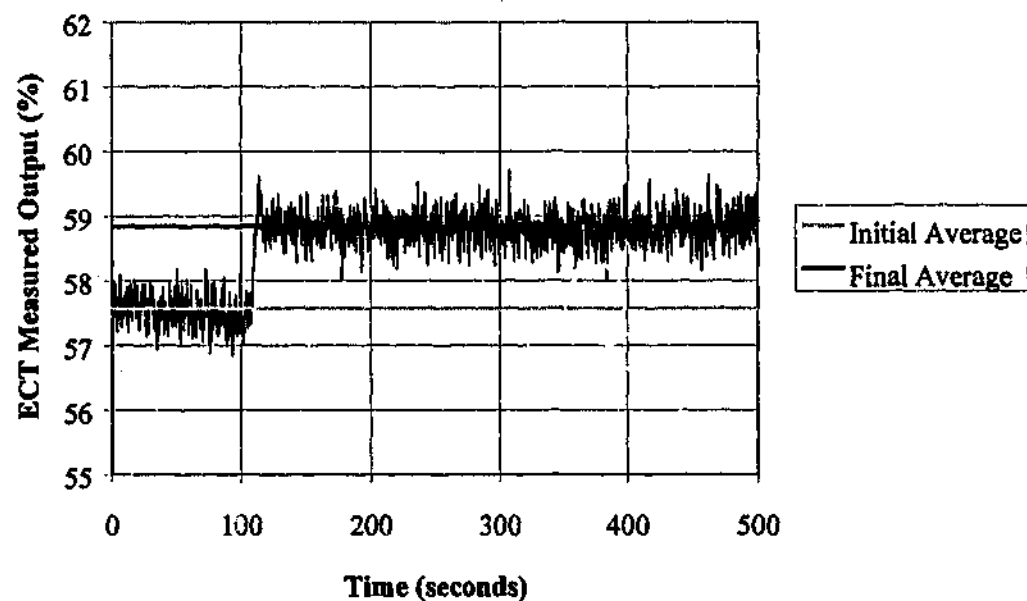


Figure G.5 Transient tracer response profile for Condition 4(b) of Table 6.1: Silica sand ($U_{mf} = 0.045$ m/s) fluidized at 0.09 m/s with GB6 ballotini as tracer.

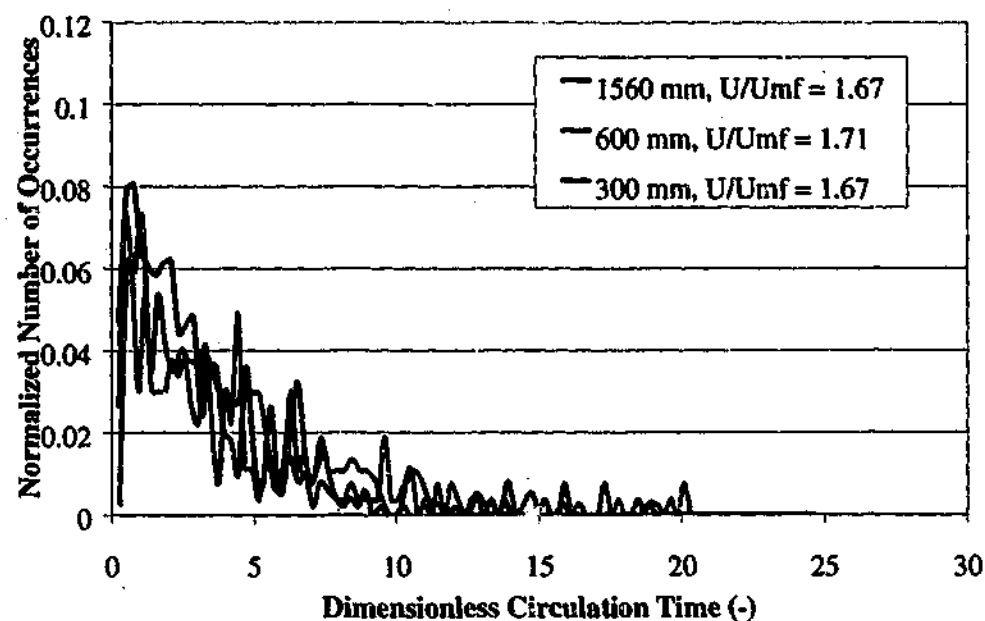


Figure G.6 Comparison of the dimensionless circulation time distribution for geometrically scaled float tracers in scaled fluidized beds at $U/U_{mf} \approx 1.7$. Bed diameters and specific operating gas velocities are shown in the legend.

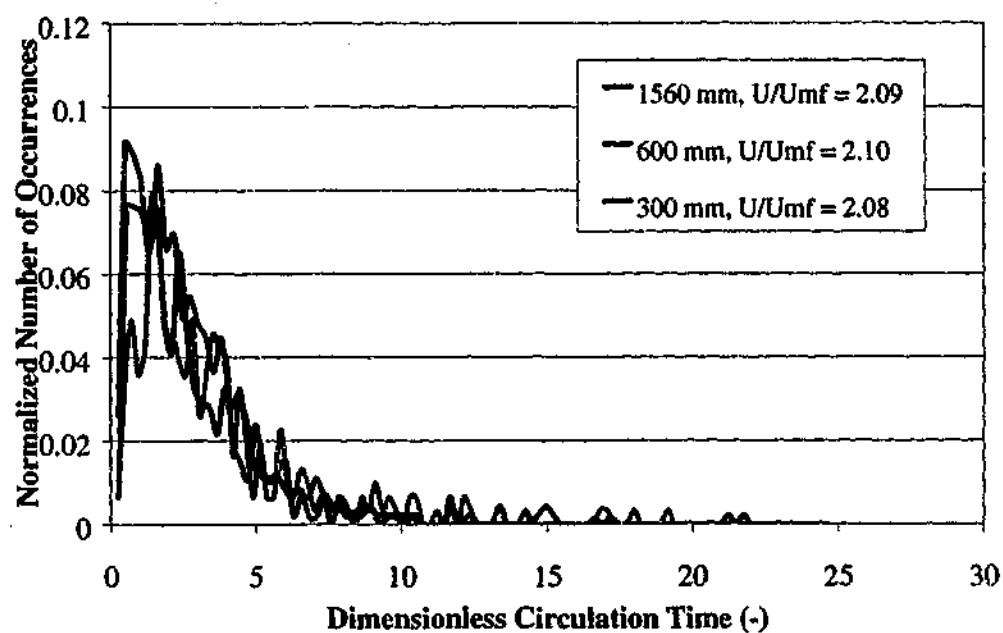


Figure G.7 Comparison of the dimensionless circulation time distribution for geometrically scaled float tracers in scaled fluidized beds at $U/U_{mf} \approx 2.1$. Bed diameters and specific operating gas velocities are shown in the legend.

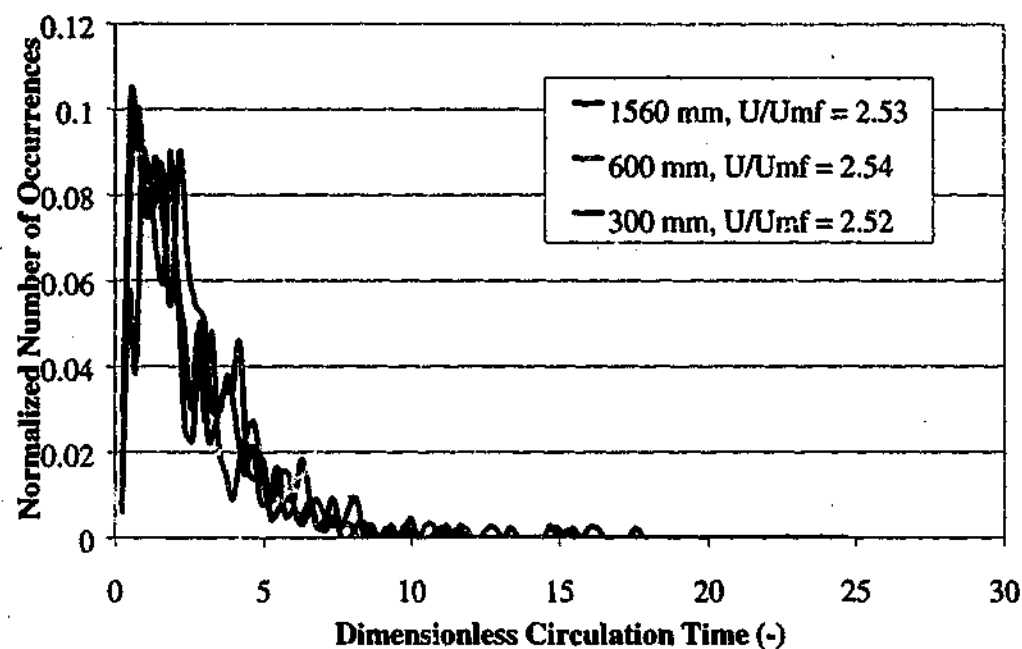


Figure G.8 Comparison of the dimensionless circulation time distribution for geometrically scaled float tracers in scaled fluidized beds at $U/U_{mf} \approx 2.5$. Bed diameters and specific operating gas velocities are shown in the legend.

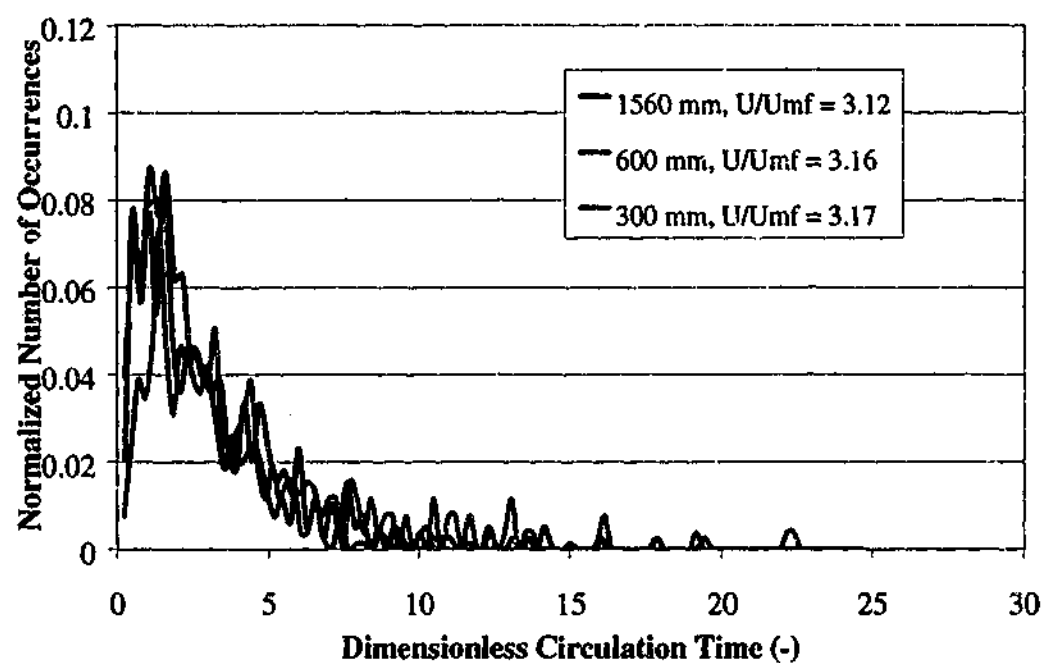


Figure G.9 Comparison of the dimensionless circulation time distribution for geometrically scaled float tracers in scaled fluidized beds at $U/U_{mf} \approx 3.15$. Bed diameters and specific operating gas velocities are shown in the legend.

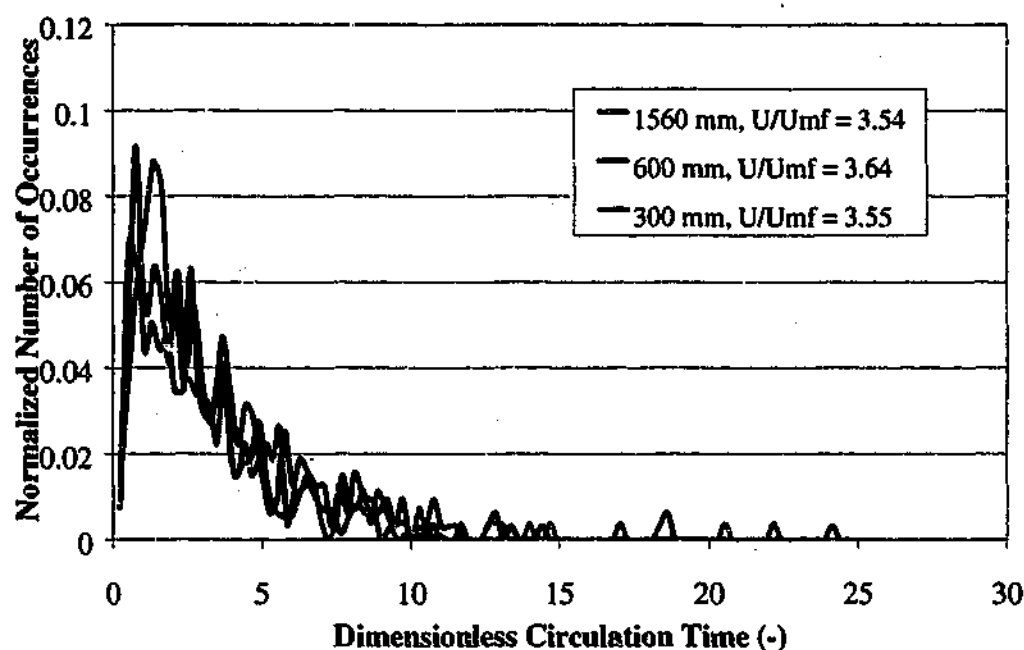


Figure G.10 Comparison of the dimensionless circulation time distribution for geometrically scaled float tracers in scaled fluidized beds at $U/U_{mf} \approx 3.6$. Bed diameters and specific operating gas velocities are shown in the legend.

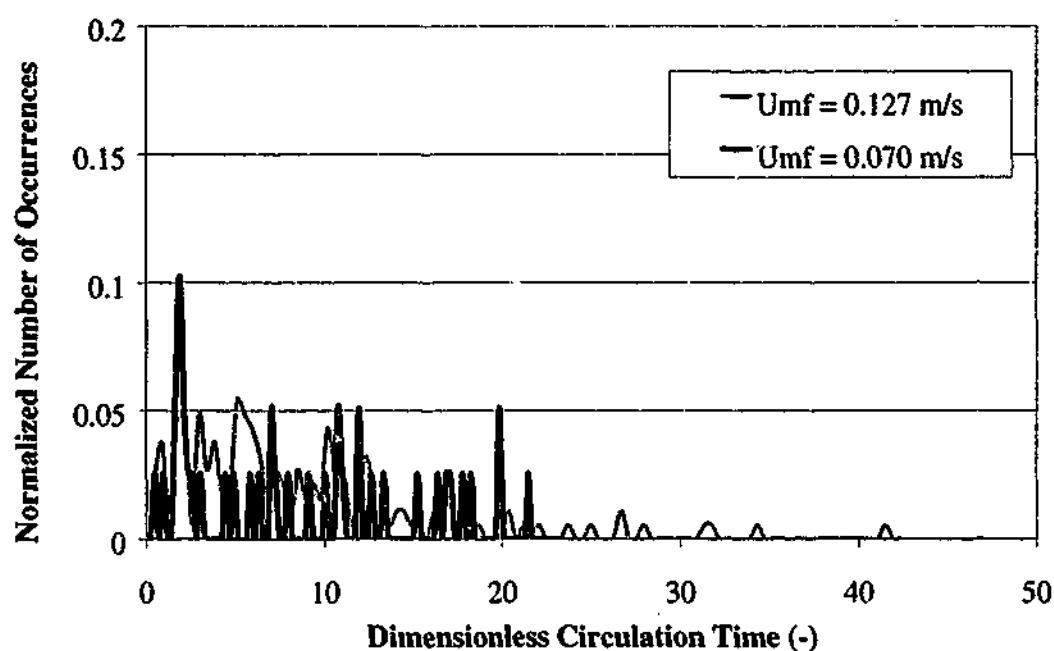


Figure G.11 Comparison of the dimensionless circulation time distribution for correct and mis-scaled bed materials (materials C and D respectively) in the 600 mm fluidized bed operated at $U/U_{mf} \approx 1.24$.

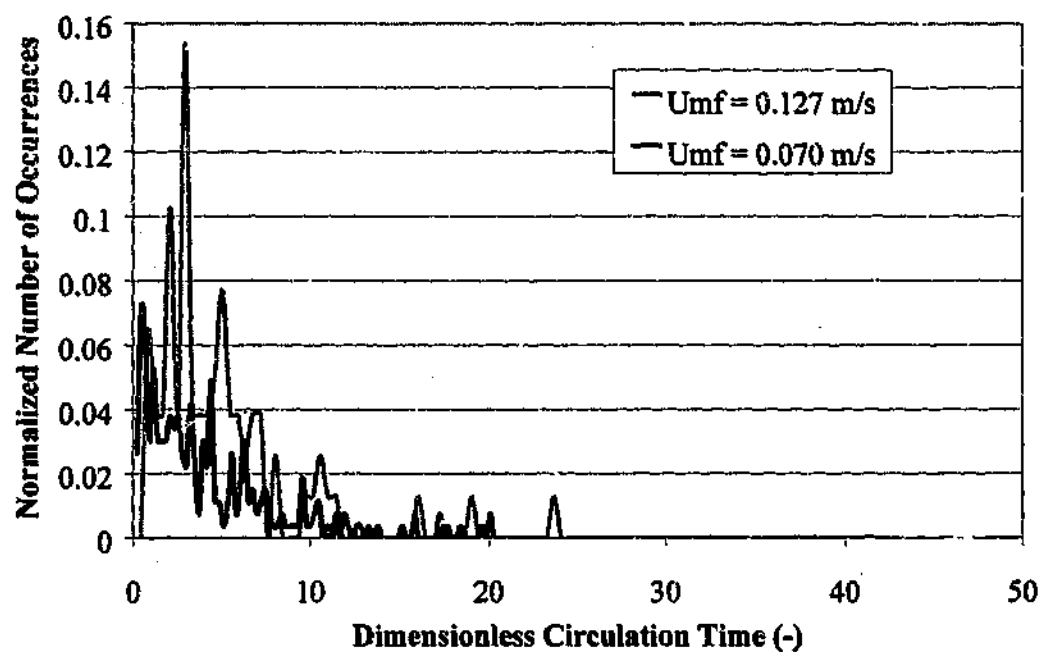


Figure G.12 Comparison of the dimensionless circulation time distribution for correct and mis-scaled bed materials (materials C and D respectively) in the 600 mm fluidized bed operated at $U/U_{mf} \approx 1.70$.

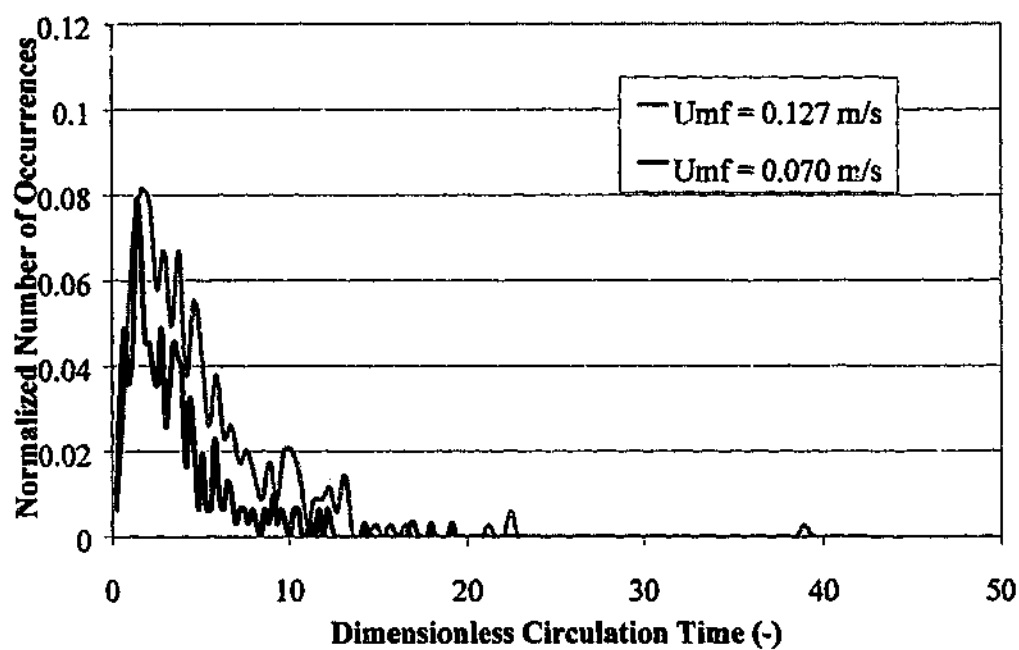


Figure G.13 Comparison of the dimensionless circulation time distribution for correct and mis-scaled bed materials (materials C and D respectively) in the 600 mm fluidized bed operated at $U/U_{mf} \approx 2.10$.

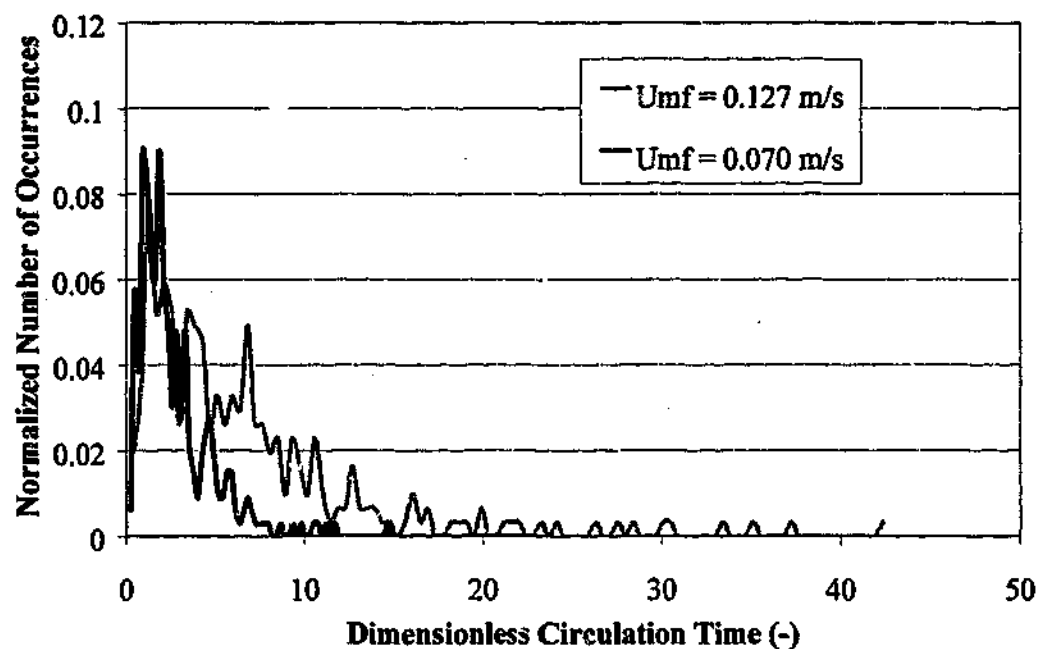


Figure G.14 Comparison of the dimensionless circulation time distribution for correct and mis-scaled bed materials (materials C and D respectively) in the 600 mm fluidized bed operated at $U/U_{mf} \approx 2.52$.

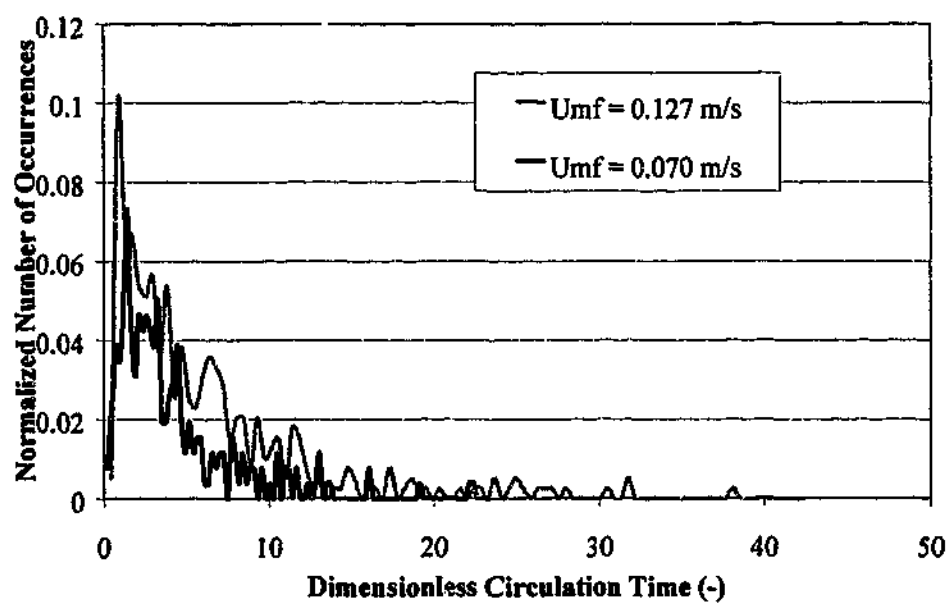


Figure G.15 Comparison of the dimensionless circulation time distribution for correct and mis-scaled bed materials (materials C and D respectively) in the 600 mm fluidized bed operated at $U/U_{mf} \approx 3.12$.

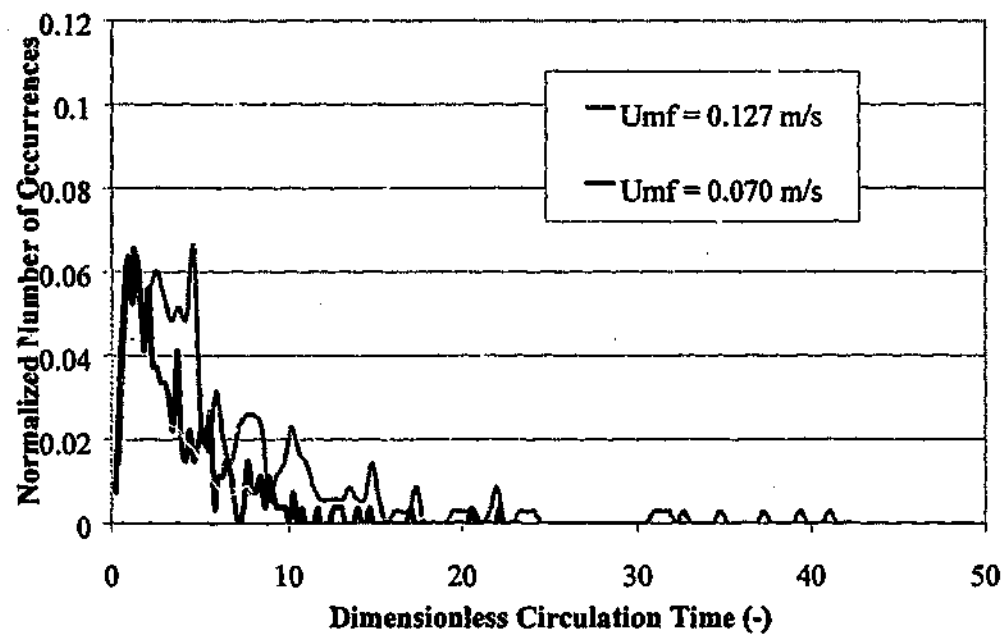


Figure G.16 Comparison of the dimensionless circulation time distribution for correct and mis-scaled bed materials (materials C and D respectively) in the 600 mm fluidized bed operated at $U/U_{mf} \approx 3.61$.

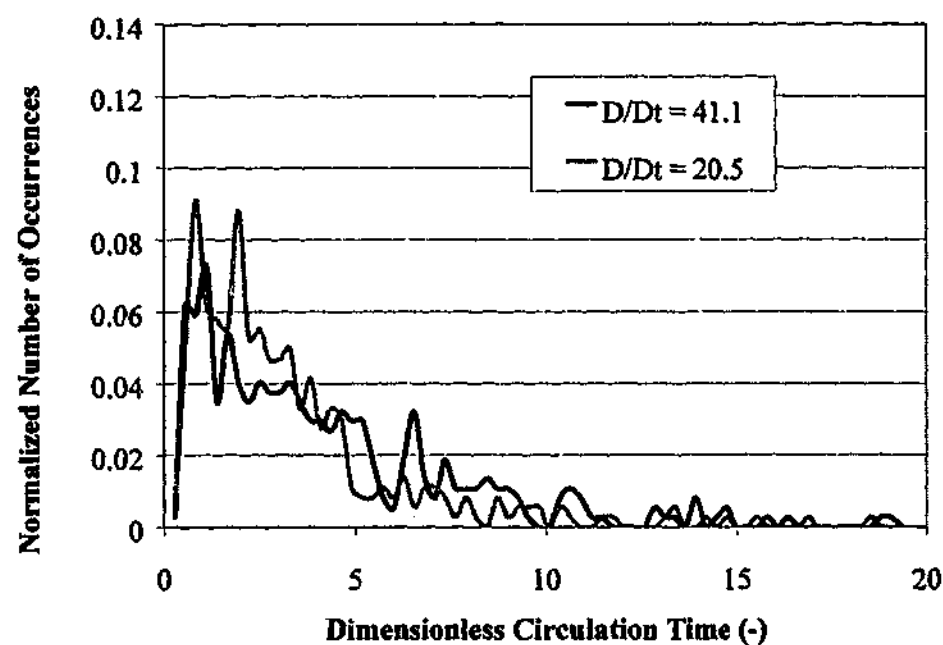


Figure G.17 Comparison of the dimensionless circulation time distribution for correct and mis-scaled float tracer sizes ($D/D_t = 41.1$ "correct", $D/D_t = 20.5$ "oversize") in the 300 mm bed with material B. Fluidized bed operated at $U/U_{mf} \approx 1.67$.

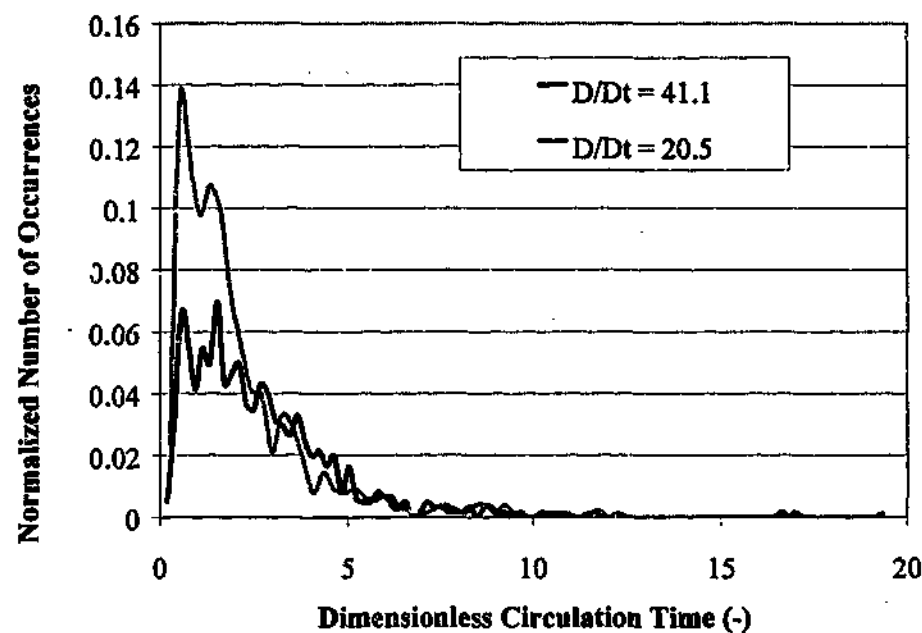


Figure G.18 Comparison of the dimensionless circulation time distribution for correct and mis-scaled float tracer sizes ($D/D_t = 41.1$ "correct", $D/D_t = 20.5$ "oversize") in the 300 mm bed with material B. Fluidized bed operated at $U/U_{mf} \approx 2.08$.

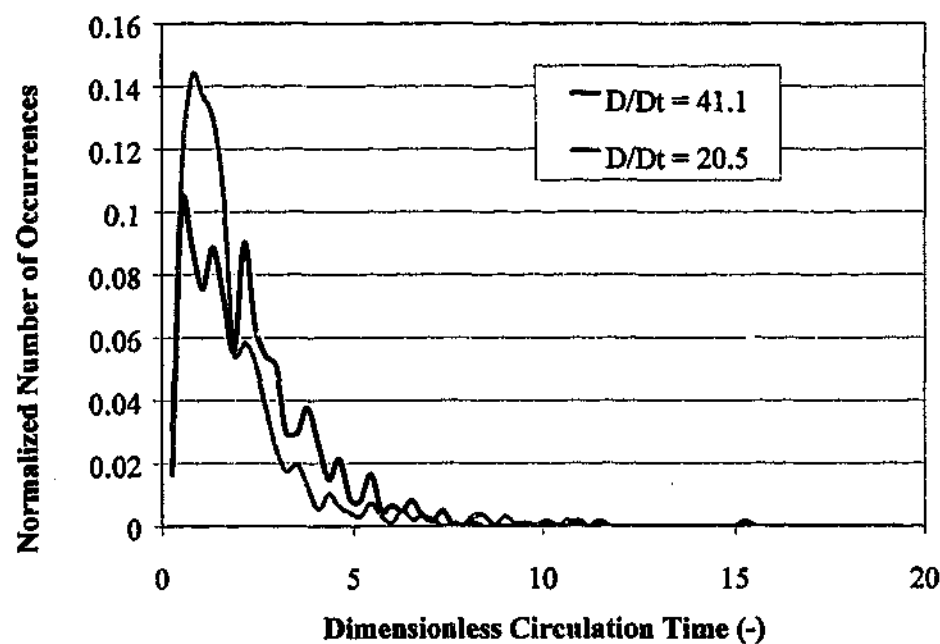


Figure G.19 Comparison of the dimensionless circulation time distribution for correct and mis-scaled float tracer sizes ($D/D_t = 41.1$ "correct", $D/D_t = 20.5$ "oversize") in the 300 mm bed with material B. Fluidized bed operated at $U/U_{mf} \approx 2.52$.

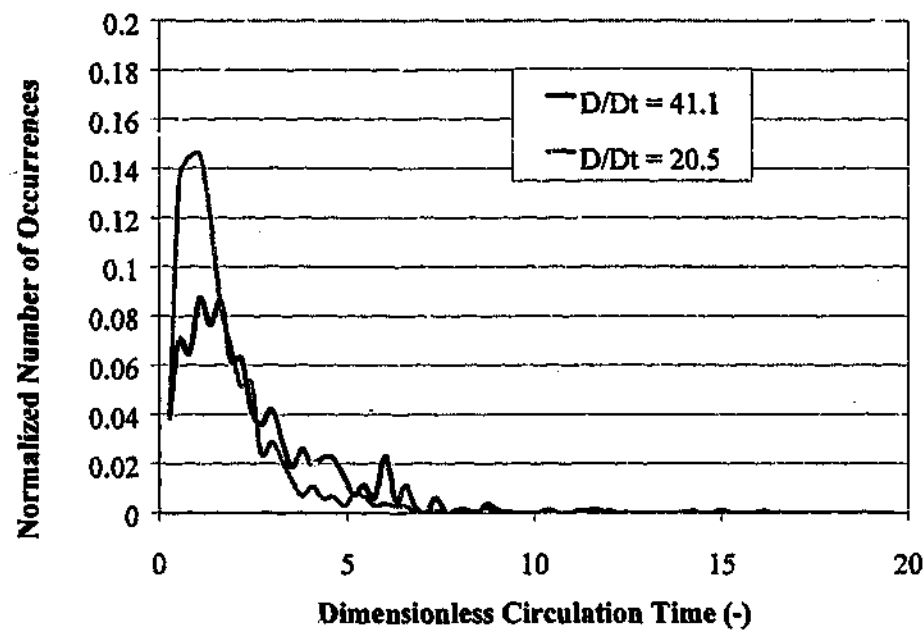


Figure G.20 Comparison of the dimensionless circulation time distribution for correct and mis-scaled float tracer sizes ($D/D_t = 41.1$ "correct", $D/D_t = 20.5$ "oversize") in the 300 mm bed with material B. Fluidized bed operated at $U/U_{mf} \approx 3.17$.

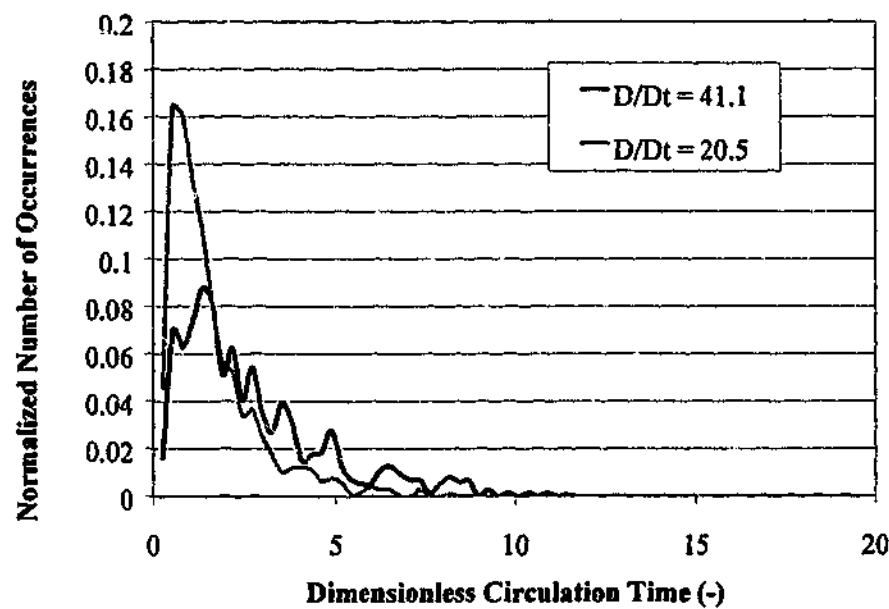


Figure G.21 Comparison of the dimensionless circulation time distribution for correct and mis-scaled float tracer sizes ($D/D_t = 41.1$ "correct", $D/D_t = 20.5$ "oversize") in the 300 mm bed with material B. Fluidized bed operated at $U/U_{mf} \approx 3.55$.